UNIVERSIDAD COMPLUTENSE DE MADRID

FACULTAD DE CIENCIAS QUÍMICAS
Departamento de Química Física I

DYNAMICS OF INTERFACIAL SYSTEMS.

MEMORIA PARA OPTAR AL GRADO DE DOCTOR
PRESENTADA POR

Armando Maestro Martín

Bajo la dirección de los doctores

Ramón González Rubio
Francisco Ortega Gómez

Madrid, 2010

ISBN: 978-84-693-8777-1

Universidad Complutense de Madrid
Facultad de Ciencias Químicas
Departamento de Química Física I

Dynamics of Interfacial Systems
(Dinámica de Sistemas Interfaciales)

Memoria para optar al Grado de Doctor presentada por:
Armando Maestro Martín

Dirigida por:
Ramón González Rubio
Francisco Ortega Gómez

Madrid, 2010

Contents

Resumen

Dinámica de Sistemas Interfaciales

(Dynamics of Interfacial Systems)

1. Introducción

En general, se considera el término *superficie* como la región del espacio comprendida entre una fase condensada (líquido y/o sólido) y una fase gaseosa o en condiciones de vacío, mientras que el término *interfase* se aplica normalmente a la región que separa dos fases condensadas; sin embargo no existe ninguna diferencia física fundamental entre ambas.

Una monocapa es una película, con un tamaño cercano al espesor monomolecular, formada por un compuesto superficialmente activo (*tensioactivo*). Ésta puede ser obtenida por la deposición del material si es insoluble en una de las fases o bien, mediante su adsorción directa si es soluble en una de ellas.

La caracterización de compuestos tensioactivos, polímeros o en general moléculas anfifílicas depositadas en una interfase fluida en forma de monocapas consiste en la medida de la presión superficial $\Pi(=\gamma_0-\gamma)$. Desde un punto de vista de equilibrio, la tensión superficial de la interfase en presencia de la monocapa (γ) disminuye respecto al valor de la interfase sin material adsorbido (γ_0). En este sentido, la monocapa adsorbida ejerce una presión superficial que puede ser interpretada con la disminución de la energía libre superficial (G_s) por unidad de área (A) resultante de la adsorción espontánea de la monocapa a temperatura y presión constante: $\Pi = (dG_S/dA)_{T,p}$. Por tanto, la tensión superficial no es más que un parámetro termodinámico que caracteriza la estabilidad del estado de equilibrio de la película adsorbida.[1, 2] Sin embargo, como se ha venido demostrando durante las últimas décadas, este parámetro no es sensible a la existencia de transiciones de fase o conformacionales dentro de la región interfacial.[3]

La tensión superficial por sí sola no puede describir completamente la respuesta de una monocapa de material adsorbido en una interfase aire–líquido o líquido–líquido ante una deformación externa, siendo necesario tener en cuenta su comportamiento reológico. Este comportamiento viscoelástico relativo a una monocapa de tensioactivo juega un papel decisivo en muchas aplicaciones prácticas de interés actual: estabilidad de emulsiones y espumas, formación de depósitos Langmuir–Blodgett, extracciones líquido–líquido, etc.[4, 5] Además, en general, el estudio del comportamiento de monocapas de tensioactivos, tales como los sistemas estudiados en la presente tesis, tiene gran importancia en diversos

campos científicos: biomedicina, ciencia y tecnología de alimentos, industria farmacéutica, cosmética, y en el campo emergente de la nanociencia y nanotecnología.[6, 7] En este sentido, es importante el conocimiento de las propiedades de equilibrio de monocapas solubles o insolubles, además de la comprensión de los procesos dinámicos característicos a estas monocapas: cinéticas de adsorción a la interfase, procesos dinámicos intrínsecos a la monocapa tales como reorganización, etc.

En este contexto, la reología interfacial es una herramienta importante en la comprensión del comportamiento dinámico de monocapas interfaciales constituidas por moléculas tensioactivas de cualquier índole. Como en los estudios relativos a sistemas tridimensionales, la reología en interfases estudia la respuesta de los sistemas adsorbidos en interfases respecto a deformaciones externas. Boussinesq[8] fue el primero que caracterizó la dinámica de interfases introduciendo los conceptos de módulo viscoelástico de cizalla y dilacional. Boussinesq expresó la relación entre el esfuerzo y la velocidad de deformación en una interfase a través de la definición de la existencia de unos modos superficiales. Años más tarde, Scriven[9] y Slattery[10] adecuaron las ecuaciones matemáticas propuestas por Boussinesq para describir las condiciones dinámicas en la interfase teniendo en cuenta la existencia de una viscosidad interfacial. Estos tratamientos suponen que moléculas adsorbidas en interfases dan lugar a un comportamiento viscoelástico completamente diferente a una interfase sin ninguna sustancia adsorbida; esta situación se debe al acoplamiento existente entre las moléculas tensioactivas y la interfase a la que se adsorben.

2. Objetivos

La presente Tesis Doctoral recoge el estudio experimental de la dinámica de sistemas poliméricos de diferente naturaleza en geometría restringida, es decir en condiciones de baja dimensionalidad como son las *interfases*. En concreto, se ha estudiado el comportamiento *reológico* de compuestos poliméricos en forma de monocapas de *Langmuir* y de sistemas mixtos constituidos por *nano*particulas-tensioactivo y proteína-tensioactivo, constituyendo ambos monocapas de *Gibbs* en interfases aire-agua. Con el propósito de realizar un estudio de la reología de interfases fluidas en una escala espacio-temporal lo más amplia posible se han desarrollado diversas metodologías específicas, las cuales extienden la reología interfacial desde la escala *mesoscópica* hasta la *macroscópica*. Tanto la descripción detallada de las metodologías experimentales específicas como los argumentos que avalan las hipótesis de partida, referentes al estudio de la dinámica interfacial de sistemas complejos en formas de monocapas solubles (*Gibbs*) e insolubles (*Langmuir*), se encuentran perfectamente formulados en la literatura especializada. Incluso algunas de las obras de referencia en este ámbito

pertenecen a la trayectoria del grupo de investigación del doctorando. Además, gracias al concurso del conjunto de técnicas de reología interfacial, enriquecido con técnicas auxiliares, se ha obtenido un soporte desde el punto de vista estructural en relación a las conclusiones alcanzadas.

Un nexo en común entre los diferentes sistemas estudiados es el uso de la interfase aire – agua en la que polímeros hidrofóbicos dan lugar a monocapas insolubles, mientras que proteínas solubles y nanopartículas dan lugar a películas solubles en el que su respuesta mecánica (reológica) está acoplada a diversos procesos de adsorción.

Bajo esta perspectiva general de estudio de la dinámica de sistemas interfaciales, la estructura formal de la presente Tesis Doctoral se ha organizado en diferentes partes temáticas atendiendo exactamente a cada uno de los objetivos planteados:

La **Parte I** presenta una visión general del estado actual del comportamiento interfacial de fluidos, atendiendo principalmente a los antecedentes teóricos relacionados con las propiedades mecánicas de las diferentes monocapas estudiadas, e incluyendo además una breve descripción de algunos de los problemas que aún no están resueltos o son relativamente controvertidos.

La **Parte II** muestra un estudio detallado del comportamiento dinámico de monocapas de polímeros insolubles (monocapas de Langmuir). En concreto, se hace hincapié en la existencia de movimientos colectivos de cadenas poliméricas accesibles mediante experimentos mecánicos realizados a frecuencias relativamente bajas (< 1Hz). Es habitual describir a los sistemas poliméricos esparcidos en un espacio bidimensional, como la interfase aire–agua, en términos de los conceptos de disoluciones poliméricas perfectamente conocidos. En este sentido, la calidad de la interfase como disolvente juega un papel determinante en el comportamiento reológico de las monocapas de polímeros. Esta parte está dividida en dos capítulos que reflejan el comportamiento de la interfase aire–agua como *buen* y *mal* disolvente. Condiciones de buen disolvente tienen lugar cuando la energía de adsorción excede a la energía de interacción entre monómeros ($E_{ads} > E_{mon\text{-}mon}$), posibilitando que las cadenas de polímero adopten conformaciones extendidas en la superficie. Por otro lado, la condición de mal disolvente supone que la energía de interacción entre monómeros es favorable frente a la de adsorción en la interfase ($E_{ads} < E_{mon\text{-}mon}$), dando lugar a una posible conformación de ovillo denso en la interfase.

En el **Capítulo 1** se estudia tanto el comportamiento de equilibrio como dinámico de monocapas de poli (acrilato de *tert*-butilo) (PTBA), el cual se puede considerar como un paradigma de polímero adsorbido en la interfase aire–agua en

condiciones de buen disolvente. En concreto, se ha evaluado la dinámica de relajación terminal (tiempos largos, bajas frecuencias) en términos de la existencia de movimiento de reptación característico de las cadenas de polímero flexibles en un estado de alto grado de entrecruzamiento de las mismas. Es precisamente el carácter *quasi*−2D de la monocapa de PTBA, entendido como presencia de segmentos de cadena no adsorbidos completamente o *bucles* que penetran en las fases adyacentes, el que posibilita la existencia de cruces entre cadenas (*entanglements*) los cuales se encuentran prohibidos en un espacio estrictamente bidimensional.

En el **Capítulo 2** se muestra el estudio realizado al poli (metacrilato de metilo) (PMMA), para el que la interfase se comporta como un mal disolvente. En este sentido, cabe destacar que las cadenas de PMMA adoptan una conformación de ovillo colapsado. Este comportamiento da lugar a un diferente comportamiento mecánico en comparación con las monocapas de PTBA. Concretamente, las dependencias dinámicas encontradas para el peso molecular y la concentración superficial de polímero son características de un proceso de percolación donde las cadenas comienzan a conectarse a partir de una densidad de empaquetamiento crítica. Este hecho sugiere que la fase percolada pueda ser identificada como un sólido amorfo bidimensional o en términos dinámicos, un vidrio bidimensional.

Durante el transcurso de esta tesis, merece una mención especial el desarrollo de una técnica experimental para el estudio reológico interfacial en un intervalo de frecuencias no alcanzable por otras técnicas experimentales. Dicha técnica permite estudiar las interfases en el intervalo de frecuencias que va desde las decenas de *Hertzio* hasta el *kilohertzio*. La técnica de generación de ondas capilares por excitación eléctrica (ECW) se describe en detalle en la **Parte III**. En concreto, con este instrumento y la teoría Hidrodinámica Interfacial ha sido posible obtener información acerca de las propiedades viscoelásticas de los sistemas bidimensionales formados fundamentalmente por polímeros y compuestos tensioactivos, en forma de monocapas o películas adsorbidas en interfases fluidas, comentados con anterioridad.

En el **Capítulo 3** se comentan los aspectos técnicos de la técnica CEW construida en nuestro laboratorio. Como se ha mencionado, la técnica genera, y es capaz de detectar, ondas superficiales en interfases fluidas utilizando el fenómeno de deformación Ponderomotriz. De esta forma se generan ondas superficiales transversales restauradas por capilaridad, esto es, el incremento de área y curvatura de la superficie, que implica la formación de la onda, genera una fuerza que tiende a restaurar la superficie plana: la tensión superficial. Estas ondas Capilares son detectadas por reflectometría láser, es decir, las desviaciones de la

superficie respecto a la planitud son detectadas mediante la reflexión especular de un haz láser en la superficie de un fluido.

En el **Capítulo 4** se complementan los estudios reológicos de las monocapas de Langmuir de PTBA y PMMA realizados a bajas frecuencias, por métodos mecánicos mostrados en la Parte II, con experimentos a frecuencias mayores (concretamente desde 10Hz hasta 1kHz) realizados por la técnica de ondas capilares desarrollada. Partiendo de la premisa de que la escala espacial involucrada en los experimentos de ondas capilares se encuentra cercana al micrómetro, las relajaciones de estos sistemas se corresponden con movimiento colectivos de segmentos correspondientes a las cadenas de ambos polímeros.

Además, se ha utilizado la técnica de ondas capilares para estudiar el comportamiento dinámico de sistemas interfaciales mixtos constituidos por tensioactivos y nanoparticulas, y por tensioactivos y proteínas. Se han comparado estos resultados a altas frecuencias con experimentos reológicos en un régimen de bajas frecuencias. En este sentido, el **Capítulo 5** muestra un estudio sistemático del comportamiento dinámico de capas adsorbidas formadas desde disoluciones de nanopartículas de sílice y tensioactivos catiónicos (En concreto, Bromuro de trimetil alquil amonio, C_nTAB, donde n=12 para DTAB y n=16 para CTAB). El modulo de elasticidad dilacional complejo ha sido medido en el intervalo de frecuencias accesible combinando diferentes técnicas (desde 0.02Hz hasta 1.5kHz). Por último estos resultados se han evaluado en términos de un modelo teórico, previamente propuesto, basado en la formación de complejos tensioactivo-nanoparticula en el seno de la disolución y transferidos a la interfase.

Finalmente, el **Capítulo 6** muestra un estudio similar para mezclas de una proteína como la β–caseina (BCS) con tensioactivos de diferente naturaleza química y carga superficial: por un lado el no-iónico óxido de dodecil dimetil fosfina ($C_{12}DMPO$), y por otro el catiónico bromuro de dodecil trimetil amonio (DTAB). El comportamiento dilacional de estas mezclas depende en gran medida de la naturaleza del tensioactivo utilizado. Además, se ha evaluado un modelo teórico previamente sugerido para este tipo de sistemas interfaciales, el cual está basado en la depleción de las proteínas en las capas interfaciales a medida que la concentración de tensioactivos aumenta.

Por último en la **Parte IV** se ha demostrado la validez en la utilización de *micropartículas* como sondas para medir la reología de cizalla monocapas de *Langmuir* compuestas por tensioactivos o polímeros, en diferentes interfases. El **Capítulo 7** consiste en un estudio sistemático de la influencia de diferentes factores en las monocapas formadas por micropartículas en diferentes interfases. En concreto, se ha estudiado la dependencia del disolvente de esparcimiento, además de la naturaleza química y el tamaño de las partículas, en el ángulo de

contacto (θ) de las micropartículas esparcidas en interfases aire/aceite–agua. En el **Capítulo 8** se ha utilizado una técnica de seguimiento de partículas la cual se fundamenta en la definición de un modelo hidrodinámico apropiado. Los resultados obtenidos se han comparado con los valores obtenidos mediante otras técnicas de cizalla de carácter macroscópico, utilizando diferentes aproximaciones teóricas, y partículas con diferente naturaleza química y carga superficial.

Tras la parte III de la memoria se exponen las conclusiones generales obtenidas de los capítulos de la presente Tesis Doctoral.

Para finalizar, en el **Apéndice** se describen las técnicas experimentales utilizadas para el desarrollo de los experimentos tanto de equilibrio como reológicos de este estudio de sistemas interfaciales, con la excepción de la técnica de ondas capilares y de seguimiento de partículas, las cuales se describen en sus correspondientes capítulos.

3. Conclusiones

A continuación, se expone un resumen de las conclusiones más importantes obtenidas de la presente Tesis Doctoral:

Desde un punto de vista metodológico, la técnica de ondas capilares desarrollada nos ha permitido evaluar el comportamiento viscoelastico de diferentes sistemas interfaciales tales como polímeros insolubles en forma de monocapas de Langmuir y complejos mixtos nanoparticula–tensioactivo y proteína – tensioactivo en forma de monocapas de Gibbs en una región de frecuencia (10Hz–2kHz) no accesible por medio de las técnicas mecánicas. Además se ha demostrado la validez de la medida del movimiento aleatorio de micropartículas adsorbidas en interfases fluidas debidas a fluctuaciones de carácter Browniano para el cálculo de la reología interfacial de cizalla de monocapas de polímeros esparcidas en la interfase. Se han evaluado partículas con diferente naturaleza química y carga superficial, además de diferentes aproximaciones teóricas, tales como la teoría hidrodinámica de Fischer y otras basadas en el cálculo de la ecuación generalizada de Stokes (GSE). Dentro de esta última se han seguido dos procedimientos de análisis: el tratamiento de una partícula, y la correlación de dos partículas. Todos los tratamientos teóricos realizados han dado lugar a resultados similares de viscosidad de cizalla interfacial. Sin embargo, en comparación con los resultados de viscosidad de cizalla obtenidos con reómetros macroscópicos, estos son superiores en más de tres órdenes de magnitud, poniendo de manifiesto la diferencia relativa entre estas dos metodologías.

En relación al objetivo fundamental de la Tesis doctoral, el conocimiento del comportamiento dinámico de diversos sistemas interfaciales y su relación con

las propiedades de equilibrio, los aspectos más relevantes a destacar de cada capítulo son los siguientes:

Capítulo 1: El estudio del comportamiento dinámico de monocapas de PTBA por medio de experimentos de reología de cizalla y dilacional a frecuencias bajas, ha puesto de manifiesto la dependencia del comportamiento viscoelastico en función de la concentración superficial de polímero y de su peso molecular de acuerdo a las teorías convencionales de redes entrecruzadas. Las leyes de escala encontradas han resultado compatibles con el transporte molecular gobernado por movimientos de reptación. Se ha demostrado que tanto el comportamiento de equilibrio como la dinámica de los sistemas suponen una evidencia experimental de una relajación compatible con movimientos de reptación en un monocapa de polímero altamente entrecruzada, para valores de longitud de cadena lo suficientemente largos (más de 100 monómeros).

Capítulo 2: La correlación entre las propiedades de equilibrio y el comportamiento dinámico, estudiado a través de experimentos reológicos, de monocapas de PMMA en función de la densidad de empaquetamiento del polímero y de su peso molecular ha demostrado la existencia de un estado percolado por encima de un umbral de empaquetamiento. La fase percolada se manifiesta a partir del estado en que los ovillos poliméricos comienzan a interconectarse dando lugar a un sólido amorfo *quasi*–bidimensional. Para comprender mejor las dependencias con el peso molecular y la densidad de empaquetamiento tanto del módulo elástico de cizalla como del dilacional, además de los resultados de equilibrio, se han utilizado modelos teóricos existentes basados en un escenario de percolación. Por otro lado, los experimentos de relajación mecánica llevados a cabo han puesto de manifiesto una serie de características relacionadas con un estado vítreo bidimendional: la existencia de carácter no exponencial (no *Debye*), y la dependencia no *Arrhenius* con la concentración de polímero. Por último, la existencia de un vidrio *quasi*–bidimensional ha sido apoyada por la dependencia con la temperatura del comportamiento reológico y de equilibrio de la monocapa de PMMA.

Capítulo 4: En virtud del espectro de relajación obtenido a partir de la combinación de experimentos mecánicos y de ondas capilares para monocapas de PMMA se han encontrado dos procesos de relajación tipo Maxwell. Un modo de carácter macroscópico el cual tiene en cuenta la relajación a tiempos largos de movimientos colectivos correspondientes a dominios de PMMA. El otro modo, de carácter microscópico, se ha encontrado en un dominio de tiempos inferior, pudiendo deberse al movimiento colectivo de segmentos poliméricos. Las leyes de potencias encontradas con la concentración superficial de PMMA son compatibles con la descripción realizada en el capítulo 2 en base a un estado

percolado de cadenas de PMMA. Por otro lado, en el caso de monocapas de PTBA, los resultados de los parámetros viscoelásticos dilacionales a alta frecuencia han puesto de manifiesto la compatibilidad de las leyes de escala predichas por de Gennes para un movimiento de reptación característico de un estado entrecruzado. Los tiempos característicos encontrados son compatibles con la difusión colectiva de segmentos de cadenas flexibles de PTBA.

Capítulo 5: Los complejos mixtos de nanopartículas de sílice y tensioactivo catiónicos, tales como CTAB y DTAB, adsorbidos en la interfase aire-agua han sido estudiados desde diferentes puntos de vista. El escenario conformacional elucidado por medidas elipsométricas, e interpretado por medio de un modelo de dos-capas, nos ha permitido conocer el grado de hidrofobicidad de los complejos en función de la concentración de tensioactivo. Este parámetro es importante pues determina el grado de afinidad de la partícula por el medio interfacial. Por otro lado, se ha determinado la dependencia con la concentración, y de la naturaleza del tensioactivo, del módulo elástico dilacional de los complejos en un amplio intervalo de frecuencias, utilizando la combinación de las técnicas basada en la gota pendiente y la basada en la excitación de ondas capilares. Estos resultados han puesto de manifiesto que la interacción entre la superficie de las partículas y los tensioactivos juegan un papel decisivo en los procesos dinámicos de adsorción. En este sentido, los datos reológicos se han correlacionado con un modelo teórico basado en la existencia de un acoplamiento entre la reología interfacial y la cinética de adsorción. En virtud del mismo se ha demostrado que junto a la adsorción de los complejos desde el seno de la subfase acuosa, es importante un proceso de reorganización de los tensioactivos en los complejos mixtos y en la interfase.

Capítulo 6: El comportamiento del módulo viscoelástico dilacional de las mezclas de β–caseina (BCS) con tensioactivos ha mostrado una dependencia fuerte con la naturaleza del tensioactivo utilizado. Con el objetivo de entender el comportamiento del complejo formado, se ha evaluado un modelo teórico previamente sugerido para este tipo de sistemas mixtos. Éste se basa en la reducción de las moléculas proteicas adsorbidas en la interfase a medida que se incrementa la concentración de tensioactivo. En este sentido, la descripción de los resultados en base al modelo propuesto sugiere que el comportamiento mostrado por los complejos BCS-tensioactivo se debe a un mecanismo de competencia entre ambos componentes. Las diferencias encontradas entre ambos tensioactivos apuntan a que probablemente el C_{12}DMPO desplaza a las moléculas de BCS de la interfase de una manera más eficaz comparadas con el efecto del DTAB. Este situación se encuentra en perfecto acuerdo con la existencia de una mayor actividad superficial del C_{12}DMPO a la vista de los valores del módulo

viscoelástico. Por tanto, existe una interacción más efectiva entre la proteína y las moléculas de DTAB, dando lugar a menor actividad superficial.

Capítulo 7: El estudio sistemático de las monocapas de partículas esparcidas en interfases aire/aceite–agua en función de diversos factores experimentales, nos ha revelado que el ángulo de contacto (θ) determinado por varias técnicas experimentales depende del tamaño y de la composición química de la partícula. Además, cabe destacar, la influencia del disolvente de esparcimiento en el ángulo de contacto de las partículas. El comportamiento obtenido apunta a que la porosidad y/o rugosidad de las partículas juega un papel fundamental en su hidrofobicidad, tenida en cuenta a partir de las medidas de θ. La existencia de un efecto disolvente ha sido apoyada por los valores obtenidos de tensión de línea estimados para los diferentes sistemas estudiados.

Capítulo 8: Se ha demostrado que a pesar de que la metodología basada en el seguimiento del movimiento Browniano de micropartículas conduce a resultados de la viscosidad de cizalla para monocapas de PTBA órdenes de magnitud inferior en comparación con reómetros interfaciales de carácter macroscópico. Los resultados son compatibles con las leyes de escala propuestas para sistemas entrecruzados donde pueden existir movimientos de reptación, por encima de una longitud de cadena crítica.

En definitiva, fruto de este trabajo experimental se han alcanzado importantes conclusiones acerca del comportamiento dinámico de los diferentes sistemas estudiados, además de la adecuada correlación de éste con la conformación estructural a nivel molecular planteada para estos sistemas. Esto nos ha llevado a un importante avance conceptual en la disposición de estas películas bidimensionales gracias a la interpretación de los resultados con las diferentes teorías aplicadas.

4. Referencias

1. Gaines, L., Insoluble monolayers at liquid-gas interfaces Interscience: New York, 1966.
2. Mingotaud, A.-F.; Mingotaud, C.; Patterson, L. K., Handbook of Monolayers. Academic Press: San Diego, 1993.
3. Liggieri, L.; Ferrari, M.; Mondelli, D.; Ravera, F., Surface rheology as a tool for the investigation of processes internal to surfactant adsorption layers. Faraday Discussions **2005,** 129, 125-140.
4. Langevin, D., Viscoelasticity of Monolayers. In Encyclopedia of Surface and Colloid Science Hubbard, A. T., Ed. Marcel Dekker: New York, 2002; Vol. 3.
5. Miller, R.; Liggieri, L. Eds., Interfacial Rheology. VSP: UK, 2009.
6. Schaefer, H.-E., Nanoscience: The Science of the Small in Physics, Engineering, Chemistry, Biology and Medicine (Nanoscience and Technology) Springer: 2010.
7. Starov, V., Nanoscience: Colloidal and Interfacial Aspects. Surfactant Science Vol.147 CRC Press: 2010.
8. Boussinesq, M. J., On the existence of a superficial viscosity grade , in the thin layer of transition which separates a liquid from another adjacent fluid Ann. Chim. Phys. **1913,** 29, 349.
9. Scriven, L. E., On the dynamics of phase growth Chem Eng Sci **1960,** 12, 98.
10. Slattery, J. C., Interfacial Transport Phenomena. Chem Eng Sci **1964,** 19, 379.

Aims and Scope

THis Ph. D. Thesis deals with the study of the physicochemical properties of fluid interfaces. One usually finds that the term *surface* is applied to the region between a condensed phase (liquid or solid) and a gas phase or vacuum, while *interface* is normally applied to systems involving two condensed phases. However, there is no fundamental physical difference between the two terms.

The presence of an interface in a two-phase system tends to increase the free energy of the system, thus the system will tend to reduce spontaneously the interface whenever possible. If the composition of the interface is modified, e.g., by the adsorption or deposition of surface active molecules, the interfacial contribution to the free energy is also changed in order to reduce the interfacial energy. In general, it may be said that there exists an entropic penalty on adsorption because molecules become confined. However, the driving–force for spontaneous adsorption is the decrease in interfacial tension, i.e., the decrease of the interfacial free energy per unit area, keeping the temperature and pressure constant.

The behaviour of surface active molecules (in short, surfactants) at interfaces is an important phenomenon involved in multiple research fields: physics, chemistry, biology, etc., as well as in many technological applications. In order to optimize the use of these surfactants, it is essential to know their behaviour at interfaces. Thus, it is necessary to understand first the equilibrium properties of monolayers either adsorbed or spread of these materials. Second, it is important to study the mechanisms involved in the dynamic processes involved: the kinetics of adsorption, and eventually of any internal processes after adsorption (e.g. conformational changes).

Interfacial rheology is a key tool to understand the dynamical behaviour of interfaces. As in bulk systems, rheology deals with the response of interfacial layers against deformations in size or shape. Interfaces with molecules adsorbed lead to complex viscoelastic modulus that are quite different to that of an interface with no adsorbed molecules, as a consequence of the coupling between the surfactants and the fluid interface.

The overall objective of this thesis is to obtain information about the dynamic behaviour of several interfacial systems and its relation with the equilibrium features. Systems such as polymers, proteins, surfactants, particles and their mixtures at fluid interfaces will be studied. Our work involves

completely different systems which allow us to explore very different equilibrium and dynamics behaviours. The common aspect between the different systems is the use of the air–water interface as support. Hydrophobic polymers give rise to insoluble spread monolayers at the interface, while soluble proteins and nanoparticles lead to soluble layers in which the mechanical behaviours are coupled to the adsorption processes.

From this framework, the thesis has been organized in four different parts as follows:

Part I presents a general overview of the current knowledge of interfacial phenomena, emphasizing the theoretical background involved in the mechanical properties of different monolayer as well as a brief description of the some of the problems that still remain unresolved and/or not well understood.

Part II focus on the dynamical behaviour of spread polymer films (*Langmuir* monolayers). More specifically, in the existence of collective motions that can be accessed from mechanical experiments probed in the low frequency range. It has been usual to describe the polymer chains adsorbed at a two-dimensional space, such as an interface, using the concept of polymer solutions. Thus the solvent quality plays a major role in the rheology of polymer monolayers. This part is divided in two different chapters that reflect the two different cases: the interface as a *good* solvent, and the interface as a *poor* solvent. In **Chapter 1**, we point out the existence of reptation motion for flexible polymer chains based on an entangled quasi-bidimensional scenario. The study focuses in the equilibrium and rheological features of poly (*tert*–butyl acrylate) (PTBA) monolayer, which is considered as a paradigmatic example of a polymer in good-solvent conditions. In **Chapter 2**, we present the results for poly (methyl methacrylate) (PMMA) for which the interface is a poor solvent. Thus, it is expected that PMMA adopts a near collapsed conformation at the interface. This lead to a different mechanical behaviour than in PTBA monolayers. Concretely, the dynamical dependencies found for the polymer chain length, and of concentration are characteristic of a percolation process where the chains get connected above a percolation threshold. This fact suggests the existence of a *quasi*-bidimensional soft–glass. Moreover, the existence of a 2D-glassy state is also supported by the temperature dependencies of the PMMA rheological parameters as well as the equilibrium features.

In **Part III**, we describe a high-frequency dynamical study of different interfacial systems. The technique that has been built is based on the excitation of electro–capillary waves at fluid surfaces (ECW). This part is divided in four chapters as follows: In Chapter 3 we describe the set-up designed and built, which is based on the detection of electrically excited capillary waves created by means

of an oscillating electrical field. This methodology allow us to obtain the complex dilational elasticity modulus of the interface in a frequency range from10Hz to 2kHz, depending on the interfacial system considered. **Chapter 4** extends to higher frequencies the study of Langmuir polymer monolayers considered, PTBA and PMMA monolayers previously described by mechanical relaxation methods. We demonstrate that the spatial scale involved in ECW experiments lies within the micrometers scale, then the relaxation found will correspond to collective segmental motions. We have also used this technique to study the dynamical behaviour of adsorbed mixed layers of surfactants and nanoparticles, and of surfactants and proteins, in order to compare with previous dynamical results of each system performed in a low frequency range. Thus, **Chapter 5** will show the dynamical viscoelastic behaviour of adsorbed layers formed from solutions of silica nanoparticles and cationic surfactants (Alkyl trimethy lammonium bromide, C_nTAB, with DTAB for n=12 and CTAB for n=16). The complex dilational elastic modulus has been measured in the whole range of frequencies experimentally accessible (from 0.02 Hz to 1.5 kHz). These results have been evaluated by a previously developed theoretical model. Finally, **Chapter 6** shows a similar study for mixtures of β−casein (BCS) and surfactants with different chemical nature and charge: the non-ionic dodecyl dimethyl phosphine oxide (C12DMPO) and the cationic dodecyl trimethyl ammonium bromide (DTAB). The surface dilational behaviour of the mixtures depends on the nature of the surfactant used. We also tested a theoretical model previously suggested for this type of systems, based on the depletion of the proteins at the interfacial layers as the surfactant concentration increases.

In **Part IV** , we describe another technique included in the so-called *microrheology*. It is based on measuring the passive motions of microparticles attached to fluid interfaces due to thermal Brownian fluctuations. Microparticles are used as probes to measure the surface shear rheology of interfacial films adsorbed at the air-water interface. This part is organized as follows: **Chapter 7** consists on a systematic study of the different factors that affect the particles attached at fluid interfaces as revealed by their contact angle (θ). We use different experimental methods to obtain reliable values of θ, and we evaluate these values taking into account the effect of the spreading solvent used, as well as the size and chemical nature of the particles. Finally, **Chapter 8** shows a study of the interfacial shear modulus of PTBA monolayers by using the particle tracking technique. We use particles of different chemical nature and size. Different theoretical approaches have been used to obtain the shear viscosity, (or the complex shear modulus), and we found that the shear viscosity obtained by all the methods are in reasonable agreement. The results obtained by microrheology have been compared with the ones obtained from macroscopic rheometers.

In addition, to perform all the experimental study above commented, we have used a set of experimental techniques and methodologies that allow us to study the equilibrium properties of the interfacial systems, as well as their mechanical properties, which accounts for the dynamical mechanism involved. They are described in Appendix 1 (Methods summary), with exception of the ECW technique and the particle tracking techniques that are described in their respective chapters.

Part I

Dynamics of Interfacial systems: A general overview

Preface

Soft Matter refers to a group of systems that includes polymers, colloids, surfactants, amphiphiles, membranes, micelles, emulsions, dendrimers, liquid crystals, polyelectrolytes, and their mixtures. These soft matter systems usually have structural length scales in the region from one nanometer to several hundred nanometers. The soft matter length scales are often characterized by interactions that are in the order of thermal energy (k_BT) so that relatively small perturbations can cause dramatic structural changes in them. Relaxation on such long distance scales is often relatively slow so that such systems may, in some situations, not be in thermal equilibrium.

Soft Matter is important in many industrial processes and in Biology among which one can mention paints, plastics, porous media, pharmaceuticals, ceramic precursors, textiles, proteins, polysaccharides, etc. Many of these systems have formerly been grouped together under the more foreboding term *complex fluids*. Soft matter is an interdisciplinary field involving Physics, Chemistry, Biology and Engineering among others. Progress in basic Soft Matter research is driven largely by the new experimental techniques available. Much of the work is concerned with understanding them at the microscope level, especially at the nanometer length scales, which give soft matter studies a wide overlap with nanotechnology.

In soft matter systems, new properties appear that are not observed for each individual component. While it is trivial that electrons and nuclei form atoms (sub-ångstrom scale), that atoms form molecules (ångstrom scale) or that monomers can be transformed into polymers (nanometer scale), we are just beginning to explore the potential of supramolecular assemblies or of large multifunctional objects (e.g. copolymers of complex architecture). Therefore, a particularly interesting length scale is, of course, the nanoscopic organization of matter.

State of the Art

In 1915 Wolfgang Ostwald described the subject matter of colloid and surface science as a "*world of neglected dimensions*". The reason for such a description stemmed from the unique nature of interfaces and related colloidal phenomena. They could not be readily interpreted based on classical atomic theories, and the regions of space involved were beyond the reach of existent experimental techniques. Science has since taken a firm theoretical and experimental hold on the nature of matter at its two extremes: at the molecular and atomic levels, and in the area of materials science. But…

…Why are Interfacial Phenomena of Interest?

Interfacial phenomena may be defined as those related to the interaction of at least one bulk phase (solid or liquid) with another phase (solid, liquid or gas) or a vacuum in the narrow region in which the transition from one phase to the other occurs. Hence, observe interfacial phenomena everywhere in daily life.[1-3] They concern aspect like adhesion, friction, wetting, or dewetting. These phenomena can be essential for the faultless performance of various applications. Interestingly, such performance often depends on very tiny changes only. For instance, the wetting behaviour can be easily switched from perfect wetting to non-wetting by modifying the very surface, i.e., the last monolayer or, in some cases, the end-group of the molecules at this surface.[1, 3] Accordingly, small variations on a molecular scale can lead to dramatic effects on macroscopically observable scales.

1. Introduction: Monolayers at fluid interfaces

It is well known that a molecular layer or, briefly, monolayer, is a film considered to be close to one molecule thick. It can be obtained either by adsorption of surface-active substances (in short, surfactants) at the surface of solutions (*adsorbed* or *Gibbs* layers), or being insoluble in the fluid phase by its deposition using a volatile solvent (*spread* or *Langmuir* layers).

If a monolayer formed by amphiphilic molecules, is attached at a gas–liquid or a liquid–liquid interface, surface tension (γ) alone cannot fully describe their response to external perturbations; the surface complex elasticity moduli have to be taken into account. Hence, monolayer viscoelasticity plays important roles in many practical applications: spray, coating, wetting and dewetting phenomenon, foaming and emulsification, foam and emulsion stability, Langmuir–Blodgett deposition, liquid–liquid extraction, two-phase flow, etc.[4, 5] In general, the behaviour of monolayers is important in many technological and scientific fields: biomedicine, food science, pharmacy, cosmetics, oil recovery, and nanoscience and nanotechnology.[6, 7]

Most frequently, the characterization of surfactants, polymers and amphiphilic molecules adsorbed at the fluid-fluid interface is carried out by measuring the surface pressure Π ($= \gamma_0 - \gamma$) as a function of the interfacial area (A). From an equilibrium point of view, the surface tension of the interface in the presence of the monolayer γ, is decreased with respect to the value of the bare interface γ_0. Hence, the adsorbed monolayer exerts a certain surface pressure that can be interpreted as the decrease of the surface free energy (G_S) per area unit resulting from the spontaneous adsorption of the film, at constant temperature and pressure ($\Pi = (dG_S/dA)_{T,p}$). The surface pressure is therefore a thermodynamic parameter that characterizes the stability of the equilibrium state of the adsorbed film.[8, 9] However, as it has been shown during the last decades, the surface pressure may be insensitive to the existence of some structural or conformational transitions within the interfacial region.[10, 11] The apparition of new suitable experimental techniques, such as ellipsometry,[12] infrared or UV reflectivity,[13, 14] surface plasmon resonance,[15] and non-liner optical techniques[16], as well as the development of computer simulation methods,[17-20] have allowed to understand some important aspects of the structural description of the monolayer.

Time-resolved versions of the scattering techniques, i.e., X–ray photon correlation spectroscopy (XPCS) and neutron spin-echo (NSE), have emerged as powerful probes of the microscopic dynamics in these soft and fragile systems.[21] However, in the case of polymer monolayers, long time relaxation phenomena, like collective diffusion, or other dynamic mechanisms of relaxation like polymer

reptation motions, arm retractions, etc. are too slow to accomplish the coherence requirements of these techniques. For instance, XPCS has been successfully used to follow slow collective dynamics in solid-supported thin polymer films close to the glass transition.[22] However, high-brilliance synchrotron sources are needed to carry out these experiments.

In the context of fluid interfaces, the surface rheology emerged as a most adequate probe of the slow interfacial dynamics. The experimental advances in the last decades allow the researcher to explore a rather broad frequency range, from 1mHz to 1MHz, by combining different experimental techniques. [23-25] Thus the surface rheology has been routinely used in this Ph.D. thesis.

2. Surface Rheology at fluid Interfaces

In general, Rheology is the study of the deformation and flow of a material in response to an applied stress. Simple solids store energy and provide spring-like, elastic response, whereas simple liquids dissipate energy trough viscous flow. For more complex viscoelastic materials, rheological measurements reveal both solid– and fluid–like response, depending on the time scale at which the sample is probed.[26] Surface rheology, like its 3D analogue, defines the relationship between stress, deformation and rate of deformation. Boussinesq[27] was the first who propose a two-dimensional analogue of the Newtonian fluid to explain the retardation in the terminal velocity of drops and bubbles. He characterized the dynamics of interfaces introducing the concept of surface shear and dilational complex elasticity moduli. Boussinesq expressed the relation between stress and the rate of deformation in a special coordinate system coinciding with the principle axes of strain.[27] Several years later Scriven [28] and Slattery [29] derived the mathematical equations required to describe the dynamic conditions at the interface taking into account the interfacial viscosity.

An important difference between the rheological behaviour of interfaces and bulk fluids is that the latter can be considered incompressible in many practical applications. However, monolayers attached at fluid surfaces can be compressed and expanded over a large range of areas per molecule.[30] Let us note that isotropic bulk systems are characterized by only two types of viscoelastic parameters: compression and shear. Because of the uniaxial symmetry, there is an additional surface viscoelastic parameter in monolayers, associated with transverse shear.[4, 25]

The modes of deformation possible for a surfactant monolayer adsorbed at a fluid interface can be classified into two main classes:[23] *a)* out–of–plane (*Transversal*) modes and *b)* in–plane modes, including shear and compression contributions (see Figure 1). The transverse out-of-plane deformations result in

curvature motions that are ultimately restored by surface-tension-driven Laplace forces. On the other hand, if a surfactant monolayer is present, longitudinal in-plane modes are restored by surface tension gradients due to surface concentration gradients. Since dissipative effects do exist within the film, each of these dynamics modes contain of elastic and viscous components. The material parameters consist in general of two components characterizing, respectively, the elastic and dissipative properties of the surface layer.

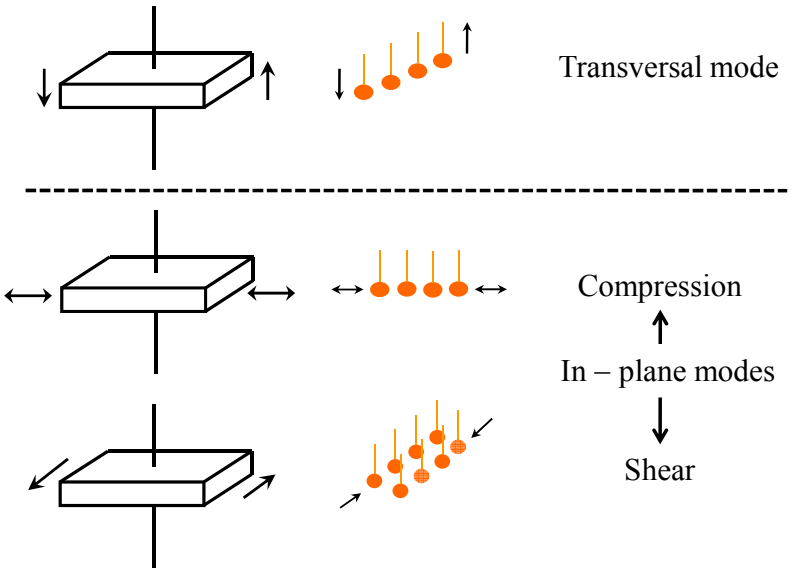

Figure 1. Sketch of different surface relaxation modes: Transversal (out-of-plane) and Dilational (in-plane) that is composed by shear and compression Adapted from Ref. [23].

When the surface is subject to a small amplitude sinusoidal deformation, the response is linear and single surface modes may be excited. Let us consider a surface deformation mode of wave vector q parallel to x-axis: $u(x,y,z,t)=u_i(t)\ e^{iqx}$; where u_x describes compression deformation modes, u_y shear modes, and u_z transverse modes (see Figure 1). The total surface energy is:[4, 31]

$$F = \frac{1}{2}\varepsilon q^2 u_x^2 + \frac{1}{2}Gq^2 u_y^2 + \frac{1}{2}\left(\gamma q^2 + \rho g + Kq^4\right)u_z^2 \qquad (1)$$

The transversal mode has several contributions: surface tension contribution (γ), gravity contribution (ρg), where ρ is the density of the bulk fluid and curvature contribution (K). When q is longer than $q_1=(\rho g)^{1/2}$, the u_z modes are capillary modes, which are very important for the rheological study of monolayers, as it will be demonstrated in Part III.

2.1 Monolayers dilational viscoelasticity

Let us consider an infinitesimal change of the surface area, δA(t) produced by an uniaxial stress). The area perturbation induces a change in the surface

pressure δΠ(t) which evolves in time until a new equilibrium state is reached. The change in surface pressure depends on the time scale probed in the experiment, and, to first order, it can be expressed as:[32]

$$\delta\Pi(t) = \Pi(t) - \Pi_0 = \frac{\partial \Pi}{\partial A}\delta A = -\varepsilon(t)u(t) \qquad (2)$$

where: $\varepsilon(t) = -A_0(\partial\Pi / \partial A)_T$ is the time-dependent dilational modulus, that accounts for the elastic energy storage on compressing the film. This equation can be in fact conceived as a general time-dependent response function, where a surface stress δΠ appears as the consequence of an stimulus applied as a compression strain $u(t)=\delta A/A_0$. In this context, the proportionally constant ε(t) accounts for the material function, which usually contains both dilational and shear components: $\varepsilon(t) = \varepsilon_k + G$. This is because uniaxial compression always involve shear. For fluid systems, the shear component is usually very small compared to the compression one, whereas it is nonzero only in solid or gel-like monolayers.[33] Therefore, for fluid films at equilibrium the dynamic modulus equals the Gibbs elasticity ε_0:

$$\varepsilon(t) \to \varepsilon_0 = \Gamma\left(\frac{\partial \Pi}{\partial \Gamma}\right)_{eq} \qquad (3)$$

where $\Gamma=1/A$ is the surface concentration.

In the limit of constant elasticity modulus, Equation 1 is formally equivalent to Hooke's law for a pure elastic 2D-body. If friction is present, some delay may exist in the response function that can be written in terms of a viscoelastic modulus including a dissipation operator:

$$-\delta\Pi(t) = \tilde{\varepsilon}(t)\cdot u(t) = \left[\varepsilon(t) + \kappa(t)\frac{\partial}{\partial t}\right]\cdot u(t) \qquad (4)$$

The second dissipative term in Equation 4 accounts for the viscous losses, that are proportional to the dilation rate (Newton's law). The proportionality factors are respectively the elastic modulus ε(t) and the dilational viscosity κ(t), that also depend on time, t. A linear viscoelastic modulus can be defined as:

$$\tilde{\varepsilon}(t) = -\left(\frac{\partial \Pi}{(\partial A/A)}\right)_T \qquad (5)$$

For an small-amplitude oscillatory motion [$\delta A(t) \sim e^{i\omega t}$] of frequency ω, this modulus is a complex quantity:

$$\tilde{\varepsilon}(\omega) = \varepsilon(\omega) + i\omega\kappa(\omega) \qquad (6)$$

The viscoelastic dilational modulus contains information about how the surface pressure changes on dilating the film, and thus, about the changes on the adsorption state and the molecular conformation stressed by the external deformation. These changes are, in general, dependent of the time scale probed in the particular rheological experiment (or of the frequency ω of the applied deformation in surface wave experiments). The constitutive viscoelastic parameters ε(ω) and ωκ(ω) obtained as a function of ω contain the time-dependent response of the system subject to a small disturbance.

At equilibrium, or when the film is disturbed along a long-times quasi-static path (ω→0 for oscillatory strains), no viscous losses are effectively present in the stress response which becomes purely elastic, The surface dilation causes an instantaneous change in surface concentration, $\delta A/A = -\delta\Gamma/\Gamma$. Then, the elasticity modulus equals the compression modulus, which can be obtained from the relative slope of a equilibrium isotherm Π–Γ,

$$\varepsilon(\omega \to 0) = \varepsilon_0 = \Gamma\left(\frac{\partial \Pi}{\partial \Gamma}\right)_T . \qquad (7)$$

And the dilational viscosity reaches its frequency-independent Newtonian limit,

$$\kappa(\omega \to 0) = \kappa_0 \qquad (8)$$

The linear viscoelastic response of the adsorbed films obeys the Krammers-Kronig relationships, from which one can conclude that the elastic response increases monotonically with the frequency of the deformation, while the viscosity decreases with frequency.[34] In addition, the following inequalities must be fulfilled:

$$\begin{aligned} &\varepsilon(\omega) \geq \varepsilon_0 \\ &\omega\kappa(\omega) \leq \varepsilon(\omega) \end{aligned} \qquad (9)$$

Figure 2 summarizes the expected material response for a viscoelastic insoluble monolayer exhibiting a relaxation due to diffusion process at the fluid interface.

When surfactant molecules can be exchanged between the surface and the bulk liquid, the monolayer can be considered as soluble. Thus, the surface concentration in the monolayer also changes because of adsorption–desorption equilibrium. Many authors apply the Lucassen-van den Tempel model to describe the viscoelasticity of soluble surfactants adsorbed layers.[30] This model assumes that upon monolayer compression, some surfactant molecules dissolve into the underlying water, to restore the equilibrium surface concentration. When the monolayer is expanded again, surfactant molecules re–adsorbe at the interface. As a result, Equation 6 can only be used when the rate of compression is faster than

the rate of dissolution. When this is not the situation, models have been proposed to relate ε and $\varepsilon_0 = \Gamma(\partial\Pi / \partial\Gamma)$, which is the limit value at infinite frequency (very fast compression rates).[5]

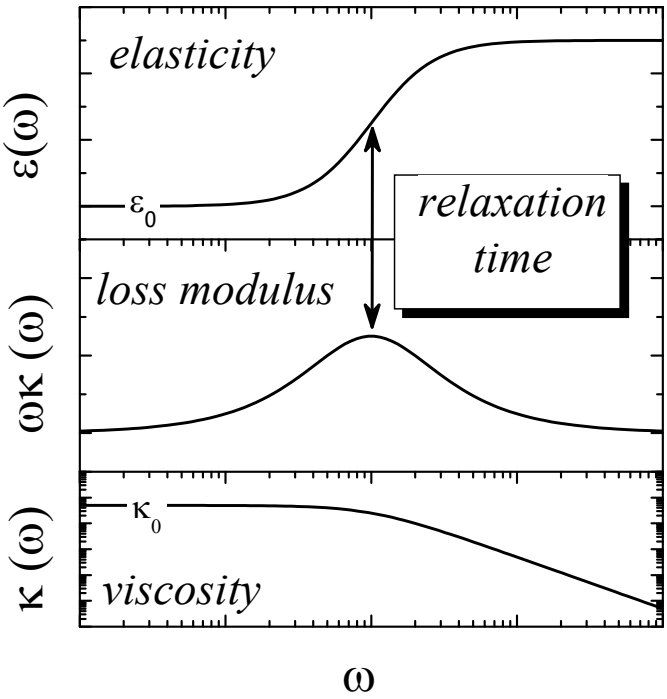

Figure 2. Typical frequency dependence of the elasticity, loss modulus and viscosity of a viscoelastic insoluble monolayer undergoing a near-exponential dynamic process.

The Lucassen-van den Tempel model assumes that desorption and adsorption proceed freely, without energy barriers, and exchanges between bulk and surface are controlled by simple diffusion[24, 30] leading to the following expression of the complex modulus ε:

$$\varepsilon = \varepsilon_0 \frac{1 + \xi + i\xi}{1 + 2\xi + 2\xi^2} \tag{10}$$

Where:

$$\xi = \sqrt{\frac{\omega_D}{2\omega}}$$
$$\omega_D = \frac{D}{2\pi}\left(\frac{dc}{d\Gamma}\right)_{eq}^2 \tag{11}$$

ν_D being the characteristic frequency of the diffusion mechanism; *D* the diffusion coefficient and *c* is the bulk concentration. Two limit can be assumed: When $\omega\to\infty$, $\omega_D \to 0$, $\varepsilon_r \to \varepsilon_0$ and $\varepsilon_i = \omega\kappa\to 0$, the monolayer behaves as if it were insoluble, as expected. When $\omega\to 0$, $\omega_D \to \infty$, and both ε_r and ωκ go to zero and thus, there is no resistance to compression, and the equilibrium between bulk and

surface has time to establish during the compression. When ω takes intermediate values, $0 < \varepsilon_r < \varepsilon_0$ and $\omega\kappa \neq 0$.

2.2 Shear viscoelasticity

The concepts of three-dimensional rheology may be applied to two-dimensional rheology, although there are some notable limitations. (a) For a correct analysis the stress tensor at the interface must be symmetric. (b) Due to the drag forces the interfacial shear properties depend on the geometry of the apparatus and the effect of the coupled subphase must be considered in the data analysis. (c) Each element of the interface must be deformed at constant area, and any radial flow at the interface must be avoided.[35, 36]

Hydrodynamic equations show that the motion along *y* evolves independently from the motion along *x* and *z*. Shear modes are then completely decoupled from capillary and compression modes: both their amplitude and time evolution are independent.[25, 34] For 2D deformations in the *x*–*y* plane one can define the interfacial shear elasticity *G* as the proportionality factor between the applied strain (u_{xy}) and the stress response exerted by the monolayer (σ_{xy}). "Solid" films exhibit elastic (Hookean) behaviour characterized by: $\sigma_{xy} = G\, u_{xy}$. Low strain amplitudes ($u \leq 1\%$, typically) guarantees measurements of the zero-shear limit ($G = \sigma/u$ at $u \rightarrow 0$).[37] For totally "fluid" films, a viscous (Newtonian) behaviour is observed: $\sigma_{xy} = \eta\, du_{xy} / dt = \eta\, \dot{u}_{xy}$; where $\dot{u}_{xy}$ is the strain rate and η is the interfacial shear viscosity.

Attractive interactions between the surface elements (e.g. segments of adsorbed and/or spread polymer, surfactant molecules, etc.) lead to an increase of *G* and η because energy is dissipated to overcome these interactions and let the surface elements flow. However, most interfacial layers exhibit both elastic and viscous behaviour, and the response of such viscoelastic layer to periodic deformations, accordingly to bulk rheology , is a complex shear modulus G^* with a real and imaginary component:

$$G^*(\omega) = G'(\omega) + iG''(\omega) \equiv G' + i\omega\eta \qquad (12)$$

where *G'* is the shear storage component and *G''* is the loss component. For a small amplitude oscillatory motion of frequency ω ($u \sim u_0\, e^{i\omega t}$) the loss modulus is related to the viscous friction $G'' = \omega\eta$, where η is the shear viscosity.

2.3 Curvature Elasticity

In some particular systems, such as microstructures formed by surfactant mono or bilayers in bulk, they can also deform in the normal direction (out of the

plane), there is an additional set of modes describing the conformations of the film. These out-of -plane deformations are known as bending or curvature modes and the free energy associated with such modes is known as the curvature free energy F_c:

$$F_c = \frac{1}{2} K \left(C_1 + C_2 - 2C_0 \right)^2 + \bar{K} C_1 C_2 \qquad (13)$$

where C_1 and C_2 are the principal curvatures, and C_0 is the spontaneous curvature of the layer, by convention, it is positive if the curvature is against water. Flat aggregated correspond to $C_0 = 0$. The elastic constants K and $\bar{K}$ are related to deviations from the mean curvature, and from Gaussian curvature. The latter is known as the saddle-splay or Gaussian curvature modulus. This expression for F_c, which is essentially an expansion of the free energy for small curvatures, is correct in the limit of radii of curvatures that are large compared with the thickness of the film. It is well known that $\bar{K}$ plays an important role: If it is negative, the second term in Equation 12 is smaller if C1 and C2 have the same sign, i.e., favouring vesicles. If $\bar{K}$ is positive, structures with saddles (regions where C1 and C2 have opposite signs) are favored: These are the "sponge" phases.

In the case of monolayers adsorbed at macroscopic flat interfaces, the Gaussian curvature modulus does not play any role (saddle formation is not possible, the surface topology is invariant), but K leads to an additional surface energy term which can be generally neglected, except in systems with very low surface tensions and for surface deformations of small enough wavelengths (less than $q_u = \sqrt{\gamma}/K$).[38]

2.4 Experimental techniques*

There are several types of experimental methods for the measurement of interfacial viscoelastic parameters, all of them are based on a perturbation of the mechanical equilibrium at interface and the subsequent measurement of the system response.

2.4.1 Compression Viscoelasticity

If the perturbation can be reduced to a small change of the surface area, this response is determined by a fundamental surface property: the viscoelastic dilational modulus $\varepsilon^*(\omega)$. Figure 3 shows the frequency ranges corresponding to different methods of the dilational surface rheology.[39]

* Further description of the experiments used in this work is shown in Appendix I: Methods Summary.

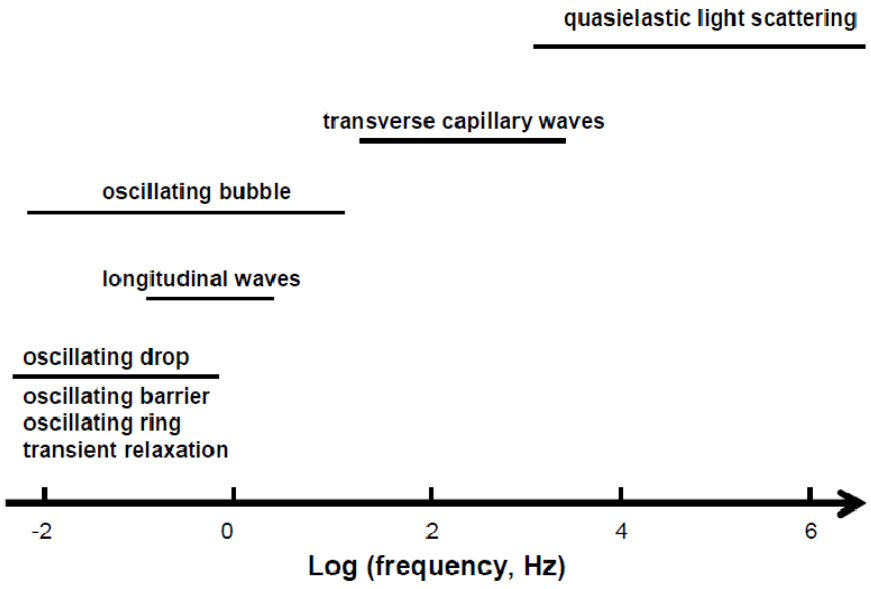

Figure 3. Frequency ranges of different experimental methods of the dilational surface rheology. Adapted from Ref. [39].

ε*(ω) have been investigated using mechanical experiments in moving barrier devices such as Langmuir trough, in which longitudinal deformations are applied directly onto the fluid surface; also techniques based on the excitation of surfaces waves, either capillary or compression waves have been used.[25, 40-42] Methods that use mechanically induced waves in the low frequency range (≤ 1Hz), whereas the capillary wave techniques work at higher frequencies.[25] Other methods such as oscillations of bubbles or drops have also been described. The use of the latter menisci in these devices has the advantage of the use of small liquid volumes up to a few microliters.[43, 44] The frequency of this kind of techniques is generally small (≤ 1Hz), although recent improvements, such as capillary pressure tensiometry, leads to higher frequency regime (≤ 100Hz).[45, 46] In these methods, the geometry is radial and pure compression viscoelastic moduli are determined, whereas in techniques based on mobile barriers the compression mode is coupled to the shear one, as stated above.

2.4.2 Shear viscoelasticity

Surface shear properties have been the most frequently studied viscoelastic properties. The most common techniques have been channel viscosimeters for insoluble monolayers, and oscillating disk and bi-cones surface rheometers for both soluble and insoluble monolayers.[37, 41, 47] In these shear experiments the contribution of the fluid subphase must not be dominant in the friction process. The degree of hydrodynamic interaction between the monolayer and the fluid subphase depends on the Boussinesq number,[27] B_0 ($= \eta / \eta_w l$), where l is the

characteristic length scale of the velocity gradient, η is the surface shear viscosity and η_w is the viscosity of the subphase, normally water.[†]

Recently, a new class of rheological experiments have been described, the so-called Microrheology, which probes the material response on micrometer length scales with microliter sample volumes. Surface microrheology methods use embedded micro-size probes to locally deform the fluid surfaces where they are adsorbed. There are two broad classes of microrheological techniques: those involving the active manipulation of probes by the local application of stress, such as optical or magnetical tweezers, and those measuring the passive motions of particles due to thermal or Brownian fluctuations.[48-51]

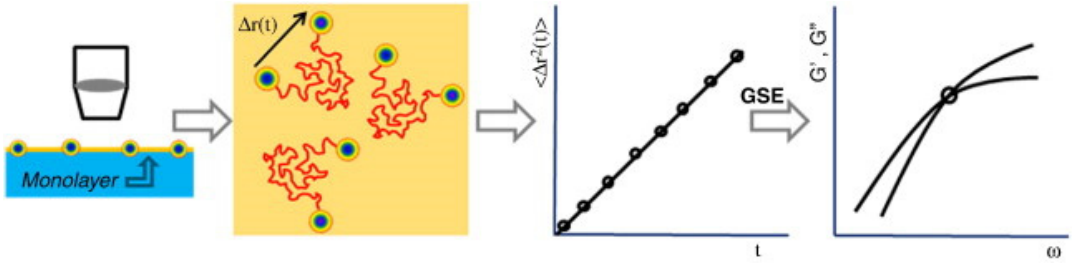

Figure 4. Typical experiment of 2D-microrheology based on the analysis of the Brownian trajectories of beads adsorbed at fluid interfaces by particle tracking methodology. With the respective mean square displacement of the particles $< \Delta r^2 >$, and by using different theoretical approaches is possible to obtain the t Shear complex moduli $G^*(\omega)$ of the material adsorbed along the particles at the fluid surface. Adapted from Ref. [51].

2.4.3 Curvature Elasticity

Curvature elasticity can be determined by a variety of techniques involving bulk microstructure perturbations. We begin with the monolayers found in microemulsions. Measurements and analysis of the dynamical fluctuations of microemulsion drops provide information on the restoring forces which resist these fluctuations and hence on the bending energy. In bilayer systems, there have been many experimental attempts to estimate bending moduli of isolated globules such as vesicles, mostly by analysis of the amplitude of the thermal fluctuations of the vesicle.[52]

3. Spread polymer monolayers

3.1 Polymers: General overview

Polymers are long-chain molecules of very high molecular weight based on a large number of covalently linked atomic groups. The entire structure of a

[†] Further Information about the Boussinesq number (B_0) in the experiments performed is shown in Appendix 1.

polymer is generated during polymerization, the process by which elemental units (chemical monomers) are covalently bonded together. The number of monomers in a polymer molecule is called its degree of polymerization (N). The molecular weight M of a polymer is equal to its degree of polymerization N times the molar mass M_0 of its chemical monomer: $M = N / M_0$.[53] Macromolecules are of great importance. From a technological point of view, natural and synthetic polymer materials offer a wide assortment of useful properties (mechanical, thermal, electric, optical, etc.) which can explain their ubiquity as fibbers, films processing aids, rheology modifiers, and as structural or packaging materials (e.g. plastics in general). From a biological point of view, the most important are proteins, viewed as poly amino acids, polyssacharides and DNA (poly nucleic acids). In general, polymeric systems are characterized by: (1) an extremely high entropic content arising from a high number of degrees of freedom. Since entropy governs the physics of neutral polymer systems, no strong influence from the intermolecular forces is expected, thus polymer behaviour is truly universal depending only on the molecular weight, M and on temperature, T but not of the chemical detail. (2) long-range correlations that show themselves in strong fluctuation effects and long relaxation times, anomalously small enthalpies, and accordingly, anomalously high susceptibilities to external forces. (3) a long-term memory for the preparation conditions where the system' connectivity and topology become quenched.[53]

Many physical properties of polymers are due to their conformation; i.e., the spatial arrangement and motion of atoms and atomic groups in a macromolecule which determine the basic behaviour of both biological and synthetic polymers. This conformational phenomenon characteristic of polymers occur on length and times scales larger than atomic ones, and it is due to their enormous length in comparison with regular molecules. Thus, the conformation adopted by the polymeric systems can be determined according to: (1) Properties of the constituent monomers (existence of several types of monomers, monomer interaction with solvent and each other, monomers flexibility, etc.). (2) Chains connectivity, i.e., the molecular configuration of the chains: linear, branched, crosslinked networks (molecules linked by covalent bonds), etc. (3) Polymer concentration regimes. It is possible to differentiate different situations: Dilute solutions well dominated by single chain properties. Semi-dilute solutions, where a strong overlap between coils exists even at very low monomer concentrations; and finally, Concentrated solutions, with low or vanishing solvent content that may lead to a semicrystalline, glassy or melt state.

Finally, macromolecules (polymers) show characteristic adsorption properties at interfaces due to their flexibility, when attracted to surfaces and interfaces. In the following, we will comment the relevant features to the

adsorption of polymers that are flexible, insoluble and neutral at the air–water interface. The effect of solvent quality, surface concentration, and chain length will be discussed. Also soluble, flexible, and charged proteins adsorbed at the air–water interface will be studied.

3.2 Equilibrium behaviour

3.2.1 Generalities

Neutral polymers of intermediate hydrophobicity are well known to form Langmuir monolayers. They are formed by spreading a relatively dilute polymer solution in an organic volatile solvent on the water surface. After solvent evaporation, and a lag time that depends on the polymer concentration, the surface tension reaches a constant value corresponding to a reproducible state of the monolayer.[42] A considerable amount of theoretical and experimental work has been devoted to polymer systems spread at interfaces;[54, 55] however, most of the studies deal with structural and equilibrium properties of the monolayers, and their dynamics is not yet well understood.

Langmuir polymer films are usually considered as two-dimensional systems since their thickness (h) does not exceed the polymeric chain radius of gyration (known as Flory radius: R_F). Unless charges or strong dipoles are present the adsorption energy is of the order of k_BT in adsorbed polymer films, and then no strong constraints are imposed by the adsorbing interface, thus polymer monolayers behave like free-standing films.

The first classification of polymer monolayers into expanded or condensed monolayers is traced by Crisp,[56] and is similar to that of fatty acids. Several years ago, De Gennes used scaling theories to predict that the chain radius of gyration should scale with the number of monomers in the chain N as: $R_F \sim a\, N^{\nu}$ (Flory's law); ν being the Flory exponent and a is the size of the monomer ($a \approx 0.1$nm for flexible chains). [57, 58] This power-law is influenced by the strength of interactions with the surrounding medium through the Flory scaling exponent. Thus, for good solvent conditions $\nu \sim 3/(d+2)$, d being the dimensionality (in two dimensions, $\nu \approx 3/4$). Polymers with polar groups are in extended conformations: the monolayer is of the expanded type. In this situation, the chains are able to interpenetrate above the overlap concentration, Γ^*, at which the chains become in contact. Above Γ^* the chains form a gel-like network characterized by a correlation length ξ. This behaviour has been found for a variety of linear polymers with polar monomers, such as poly (vinyl acetate) (PVAc), poly acrylates in general (PMA), poly (*t*-butyl acrylates) (PTBA), etc.[23, 59, 60] For Θ solvent conditions, $\nu \approx 1/2$, independently of the dimension, while values of ν between ½ and ¾ are expected

for poor solvent conditions. This case occurs with more hydrophobic polymers, with are in near collapsed conformation at the surface: the monolayer is of the condensed type. In this case, the chains do not interpenetrate and behave as individual particles. Studies of a few hydrophobic polymers, such as polystyrene derivatives, poly (methyl methacrylates) (PMMA) and poly (dimethyl siloxanes) (PDMS) have confirmed this view.[33, 61-63] In addition, a limit condition for rigid rods is $\nu = 1$; i.e., the maximum contour length (L) of a rigid chain in the highest extension limit is $R_F = L = bN$.

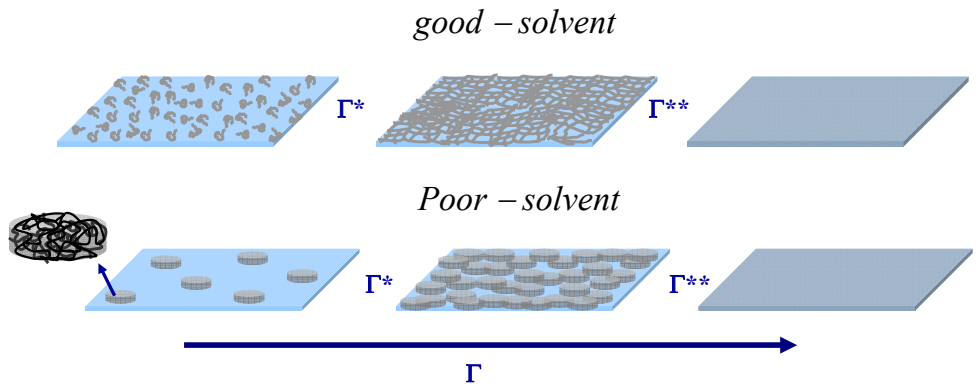

Figure 5. Scheme showing the different polymer coils configuration adopted in a monolayer under good solvent conditions, and bad ones.

3.2.2 Importance of the nature of the interfacial solvent

The nature of the solvent is not obvious in the case of polymer monolayers adsorbed at fluid interfaces. In adsorbed two-dimensional films, the polymer chains lye at the interface between two bulk media consequently losing one degree of freedom with respect to the 3D conformation. Thus, there exists an entropic penalty on adsorption, the driving-force for spontaneous adsorption being the decrease in surface tension. One can therefore conceive an adsorbed polymer chain as the result of the interplay between different forces: monomer–monomer, (or chain–chain) and the adsorption forces, including all the interactions between the polymer and the fluid surface. In this situation, the interface itself plays the role of the solvent in bulk solutions, and it is in this sense that one must define the thermodynamic quality of the solvent. This concept, usual in bulk, refers to the strength of the adsorption interaction in the case of interfacial films. Then, good solvent conditions refer to net cohesive adsorption interactions between the polymer and the interface. On the other hand, weak adsorption, as compared with the monomer–monomer interactions leads to adsorbed polymers at poor solvent conditions. Chain conformation at adsorbed films is then governed by the strength and directionality of the adsorption forces compared with the intra- and inter-chain interactions. From a structural point of view, good solvent conditions are

equivalent to high excluded volume conformations like the extended coil or the flexible worm-like ones while the poor condition leads to smaller excluded volume interactions, and as a result the polymer adopt a collapsed coil conformation to minimize the number of contacts with the interface, and to increase those between monomers inside the chain. The viscoelastic properties strongly depend upon the solvent quality of the interface, as will be seen later. Note that when adsorption energy outweighs the entropy lost upon adsorption, polymer chains might flatten and adopt a pancake conformation at the surface.

3.2.3 Π–Γ *isotherms and scaling theory*

The measurement of the surface pressure Π as a function of the surface concentration Γ at constant temperature (hereinafter called Isotherm) provides the basic equilibrium thermodynamic information about the system. Equilibrium isotherms have been measured for many insoluble neutral homopolymers.[23, 54, 55, 63-65] For instance, Figure 6 shows the typical isotherms for polymer monolayers in good and poor solvent conditions; in both cases the isotherm can divided in three different regime. In the dilute regime (usually $\Pi < 1$ mN·m^{-1}), Π slightly increases with the surface concentration of the polymer in the film, Γ, closely following the ideal gas law at high dilution, $\Pi \sim k_B T \Gamma$. As Γ is increased in this regime, chain interactions emerge imposing deviations from the ideal behaviour well quantified as virial contributions to the surface pressure.[66] At higher concentrations it is possible to describe the surface pressure by a power law $\Pi \sim \Gamma^{y}$, y being a constant that depends on the solvent quality of the interface in terms of de Gennes theory of polymer solutions.[57] The value of Γ where the two types of behaviours merge is the *overlapping concentration* Γ*; it marks the onset of the semidilute regime. At still higher concentrations (above Γ**, see Figure 6), the power law does not describe the experimental behaviour any longer, and Π increases more slowly with Γ. Γ** marks the onset of the concentrated regime, where the surface solvent is almost excluded and the film becomes pure polymeric. The surface pressure reaches a plateau value which corresponds to the film collapse. The collapse point and multilayer formation is sometimes called Γ***.[67, 68] Figure 6 shows the two limiting values of the exponent y found for different polymer-interface pairs.

Contrary to what happens in the monolayers of many insoluble surfactants[8, 69], most monolayers of insoluble neutral homopolymers do not show regions in which $\Gamma \approx$ constant ($\Pi \sim \Gamma^{0}$), that are associated to interfacial phase transitions. However, they exist for monolayers of copolymers with a block soluble in the subphase,[70-72] or in the case of polyelectrolytes.[73, 74] They are also observed when there is a transition from monolayer to multilayer.[19]

Although, it was demonstrated by de Gennes that chain overlap and entanglements are not possible in a strict two-dimensional scenario,[57] the domains occupied by an individual chain are not strictly 2D, and in addition, loops and tails might penetrate the subphase, as suggested by Noskov[75]; as a consequence interpenetration of the domains of neighbouring chains cannot be discarded.[75] Moreover computer simulations have supported the idea that polymers tend to be more extended than predicted by de Gennes[57], thus forming an interpenetrated network.[20, 22] Also recent AFM experiments on monolayers deposited on mica have shown that in some situations the individual chains do not form condensed patches. Two-photon correlation fluorescence experiments of Granik's group seem to suggest that the polymer coils do not always form condensed patches in monolayers onto mica. In addition, the existence of entanglements in very thin PMMA films (up to 1nm thick) has been demonstrated by Itagaki et al.[76] from measurement of the Försters distance. Finally, Wang and Folz, using AFM experiments on nanorope monolayers, have shown that they do not form isolated coil pancakes except for extremely diluted conditions.[77]

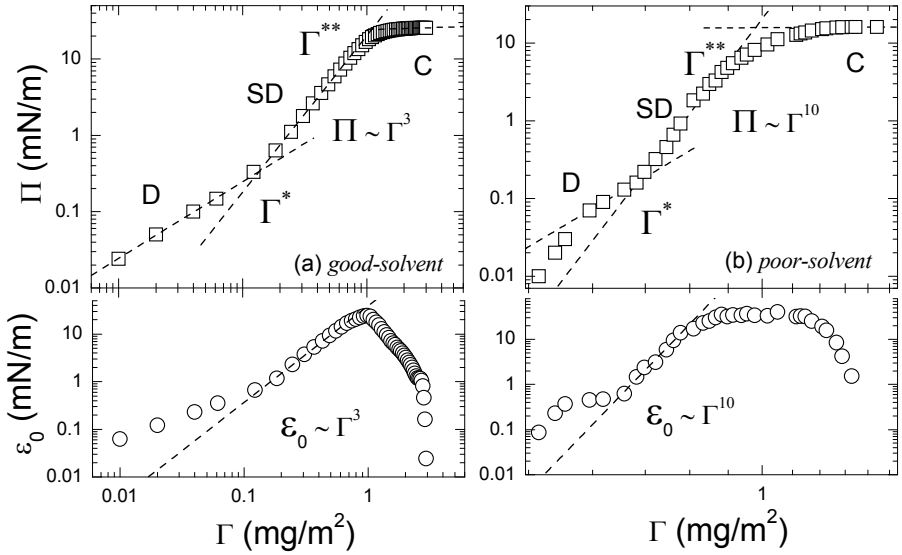

Figure 6. Experimental Π–Γ isotherm for (a) PVAc monolayer (good-solvent scenario) obtained from ref. [78] and (b) PMMA monolayer (poor-solvent scenario) adapted from ref. [33]. Three well defined concentrations regimes are shown in each isotherm: diluted (D), semidilute (SD), and concentrated (C). Γ* marks the onset of the semidilute regime and Γ** marks the onset of the concentrated regime. Also (a) and (b) plot the respective compression modulus (ε_0) as a function of Γ.

Within the segregated disk argument proposed by de Gennes, a simple interpretation for the overlapping concentration (see Figures 5 and 6) comes from the state at which individual polymer coils start to contact to each other. Then, at Γ*, the polymer concentration in the monolayer becomes similar to the monomer concentration within a single chain, making possible to relate with R_F ($\Gamma^*=1/A^*$, with $A^*=\pi\ R_F^2$). To describe the scaling behaviour in the Π–Γ

isotherms it is possible to use the same arguments of des Cloizeaux and Jannik used with polymer solutions.[79] Thus, ξ is viewed as a re-scalable characteristic distance that can be related to Γ, $\xi \sim \Gamma^{-\nu/(\nu-1)}$. Accordingly, Π in the semidilute regime can be written by the power law:[79] $\Pi \sim k_B T / \xi^2 \sim N^0 \sim \Gamma^{2\nu/(\nu-1)}$, from it is possible identify $y = 2\nu/(\nu-1)$. In addition, the compression modulus, calculated by Equation 7, can be written following similar power-law dependencies: $\varepsilon_0 \sim y\Pi \sim \Gamma^y$. It is possible to interpret the values of the exponent y for different monolayers in terms of the solvent-quality concept commented above.

The good solvent conditions is observed for several polymer monolayers at the air-water interface: PVAc[78], PMA[56, 60], PTBA[80], etc. where $\nu \approx 3/4$ ($y \approx 3$) leading to a relatively low compression modulus (e.g. PVAc monolayer in Figure 6.a). At high Γ, when the surface is saturated by monomers, some segments of the flexible chains may extend out of the interface: the layer form quasi-bidimensional gels where the polymer chains well swollen by the solvent are mutually interpenetrated.

For Θ–solvent conditions ν is predicted to be ½ ($y = 10$), while large values of *y* are found for poor solvent conditions ($y \geq 10$, $\nu > 0.5$; e.g. PMMA monolayer in Figure 6.b) is found for hydrophobic polymers such as P4HS[63], PMMA[33], PDMS[62], etc. The consequence of poor-solvent conditions is a condensation in a dense globular state, which result in a significant increase of the compression rigidity. Moreover, within a poor-solvent scenario, the surface pressure and viscoelastic properties are observed to increase suddenly when the polymer chains come into contact. This abrupt increase with chain concentration is characteristic of percolation lattices where the sites (polymer chains or patches) become connected above a critical fraction of surface coverage (ϕ_c) forming a continuous network of non-entangled chains only partially overlapping, with properties typical of a soft glass. ϕ_c is usually identified with Γ^*, and a description in terms of soft glasses made of tightly packed globules is suitable in these cases, whereas a description in terms of polymer gels with entangled chains is more appropriate in the good solvent case. This collapsed state has been comparatively much less studied.[81, 82]

3.3 Compression rheology of polymer monolayers

3.3.1 Temperature dependence

To the best of our knowledge, only few studies on polymer monolayers have been dedicated to the temperature dependence of the dilational viscoelasticity moduli. Yoo and Yu first studied PVAc and poly (*tert*-butyl methacrylate) (PTBMA) as example of good and poor solvent cases, but not clear temperature dependence of

the compression parameter was detected.[83] Later, PVAc was re-examined by different techniques over a large temperature range.[84, 85] In the semidilute regime, a glass type of transition was identified from these rheological studies: a discontinuous change in the thermal expansivity was detected around T≈15ºC, just coinciding with a non-trivial increase of the compression modulus below this temperature.[84] The temperature dependence of the long-time relaxation for polymers in poor-solvent conditions, such as P4HS suggest important features common to glassy systems, in terms of their singular dynamics, which can be easily probed in mechanical experiments. In effect the stress relaxation of P4HS monolayers evolves from a single exponential behaviour to a progressively stretched exponential decay as temperature increased (non-Debye linear response) and a non-Arrhenius temperature dependence of the relaxation times.[86, 87] A divergence of the relaxation times was observed at the percolation threshold of the polymer patches, which is a clear signature of a dynamical arrest at the fluid-solid transition. This fluid-to-solid transition in two dimensional systems has been speculated to be suppressed by large scale fluctuations, mainly when the substrate is fluid, as in the case of Langmuir films. However, the freezing transition to a 2D crystalline state has been experimentally observed in Langmuir films of colloidal particles[82, 88] and small surfactants[89], with an excellent theoretical support.[90] However, amorphous freezing in two dimensions is still a matter of controversy, till now there is a few experimental evidences of the existence of the glass transition on polymer Langmuir monolayers.[86, 87] Additional evidences of the glass transition in a two dimensional scenario, such as emerging shear rigidity[68, 82] and the formation of monolayer structures compatible with frozen amorphous states support this conjecture.[63]

3.3.2 *Low frequency rheology: Reptation motion*

Collective motions of polymer chains can be accessed from mechanical experiments that probe a low frequency range (≤ 1Hz). P.G. de Gennes first conjectured the possible existence of 3D gels made of entangled chains.[57] Later, M. Kawaguchi suggested that the semidilute and concentrated Langmuir monolayers of flexible polymers in good solvent conditions were indeed 2D gels.[23] Polymer chains are confined into a network with many obstacles formed by other adjacent chains; thus, an entangled system is potentially able to undergo terminal reptation motion under external deformation. Relaxation times (τ) increase with surface concentration and with chain size (N).[91-93]

The most frequently used scaling description of the rheology of 3D semidilute polymer solutions is based on the concept of reptation of a polymer chain within a tube defined by the entanglements with the neighbour chains.[57, 94] If excluded volume interactions are screened, the diffusion of a self-avoiding walk

chain through a distance comparable to its own size R_F takes place during the so-called Rouse time, $\tau_R = R_F^2 / D_R$ (D_R, being the diffusion coefficient), independently of the polymer concentration Γ. In the semidilute regime and if chain entanglements are present, the characteristic time depends on both N and Γ through:

$$\tau \sim R_G^d \left(\frac{\Gamma}{\Gamma^*} \right)^m \sim N^{vd+m(vd-1)} \Gamma^m \qquad (14)$$

For good solvent conditions, it has been quite usual to assume that the dependency of τ on N is $\tau \sim N^3$, and therefore, one can write m = 3, and $\tau \sim N^3\Gamma^3$. This N^3 law represents a much stronger dependence than the simpler Rouse dynamics expected for individual chains, $\tau \sim N$. It must be stressed that the N^3 law implicitly assumes that the polymer chain is formed by blobs within which the excluded volume interactions are screened. As a consequence, the scaling law for the Newtonian limit of the dilational viscosity can be written as $\kappa \sim \varepsilon\tau \sim N^3\Gamma^6$. The strong Γ dependence of τ and of κ have been tested for PVAC monolayer obtained from low-frequency mechanical relaxation experiments as shown Figure 7.[78]

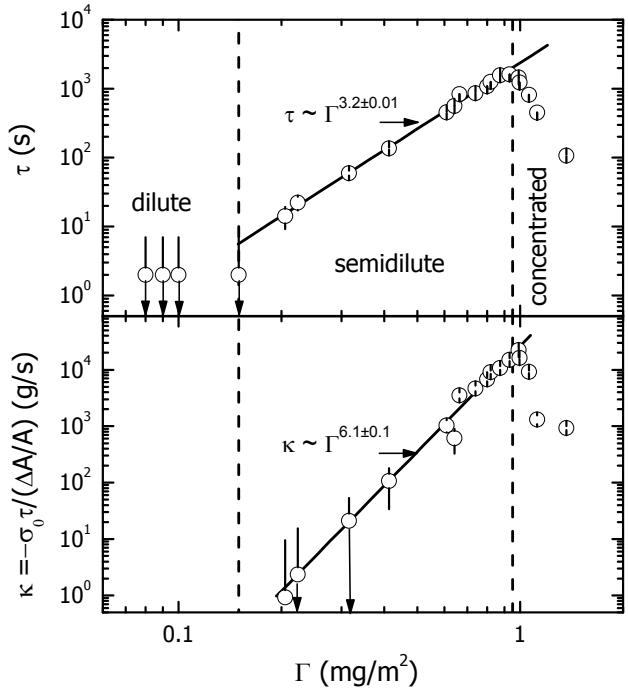

Figure 7. Surface concentration dependence of the relaxation time and of the dilational viscosity of poly(vinyl acetate) monolayers at 25 ºC. The straight lines are the fits to the scaling laws. Taken from Ref. [78].

The results shown in Figure 7 represent a strong support for reptation as the mechanism for long-time motion of the polymer chains in the monolayer, such a mechanism assumes the existence of entanglements that can give rise to the tube

concept; however, the N^3 law is not free from controversy . The existence of entanglements at polymer interfaces has been discussed by Brown and Russell,[95] who found that the density of entanglements at the interface was lower than in the bulk. Recent studies by Jiang et al.[96] confirm the qualitative conclusions of Brown and Russell. This opens the possibility for allowing the existence of chain entanglements and the reptation motion in Langmuir polymer monolayers where long chains are interpenetrated forming two-dimensional scenario compatible with good-solvent conditions contrary to the segregated pancake model for chains in poor solvent conditions.[58, 97]

3.3.3 *High frequency dynamics: segmental motions*

Poly (vinyl acetate) is the most studied polymer by the surface light scattering technique. The high frequency dependence of the dilational elastic module is larger than the equilibrium value. The frequency dependence has been found Maxwell-like in the 1kHz–10kHz regime,[84] with a viscoelastic relaxation characterized by a rather strength (≈ 0.5) and a relaxation time $\tau_0 \approx 20$ μs. As the involved spatial scale lies within the nanometric scale, these relaxations were assigned to highly correlated segmental motions. An analysis of the temperature dependence of this relaxation time lead to a high value of the Arrhenius activation energy $E_A \approx 30 k_B T$, corresponding to collective relaxation of segmental motions.[84] Other types of fast motions have been found in excited capillary wave experiments. Concretely, for PVAc, two Maxwell-like relaxation was found in the 100 Hz –1kHz range where slow motions are tested. ($\tau \approx 10$ ms).[84] On the other hand, for a polymer in poor conditions, such as P4HS, a broader distribution of relaxation times was found, extending from 100 Hz–10kHz regime.[63] This hydrophobic polymer is practically collapsed at the air-water interface. Hence, the relaxation display solid material features, such as: $\varepsilon \approx$ constant, $\omega\kappa > \varepsilon$, instead of $\omega\kappa < \varepsilon$ for viscoelastic gels.

The Γ–dependence of these high frequency relaxations is also interesting. The group of Yu performed a further study of the viscoelastic parameters by *quasi*-elastic light scattering (SQELS).[65, 98] They found a clear correspondence between the static features, such as Π–Γ isotherms, and the dilational viscoelastic moduli of different polymer monolayers (e.g. PEO, PVAc, PMA, PMMA, PTBMA, etc) taking into account the different solvent condition. The polymer monolayers in a good solvent scenario exhibit a viscoelastic profile characterized as nearly perfect elastic behaviour over a wide range of surface concentration. In contrast, polymer monolayers under poor solvent conditions, show a viscoelastic profile of incompressible films with the dynamics approaching the limit of the dilational viscoelasticity moduli ($\varepsilon^* \rightarrow \infty$).

Furthermore, systems involving different classes of polymers, where ν changes from good and poor solvent values have been measured by high-frequency rheology techniques. For instance, miscible blends of PVAc and P4HS;[99, 100] where ν varies in a sigmoid fashion between $\nu^{(P4HS)} \approx 0.52$ and $\nu^{(PVAC)} \approx 0.75$. The intrinsic viscosity measured at high frequency (≈ 1 kHz) was found to increase monotonically, from a low value corresponding to P4HS ($\kappa \approx 4\times10^{-5}$ mN·s/m at Π=8mN/m) to a comparatively high viscosity for PVAc (4×10^{-4} mN·s/m at the same Π), typical of a entangled polymer. This decrease in dilational surface viscosity correlates well with the increase of the entanglement density, as measured by the increase of ξ in the surface blend.

Block copolymers of PEO–PMMA[71], PEO–PS[70] and PTBA–PS[101] were also studied. These systems forms brush-like structures when one block is soluble in the water subphase (e.g. PEO). In these cases, monolayer rheology is dominated by the diffusion dynamics of the soluble tail resulting in a behaviour similar to adsorbed monolayers of soluble surfactants but characterized by much longer relaxation times as expected for larger macromolecule.[102] A different behaviour was reported for copolymers with hydrophobic blocks. A typical case is a copolymer made of flexible PTBA followed by a glass–like PS block. Depending on the relatively size of the block, the monolayer displays a behaviour characteristic of an entangled polymer (PTBA-rich) or a glassy-like (PS-rich). The existence of complex lyotropic organization as two-dimenional micelles has been conjectured for these systems.[103]

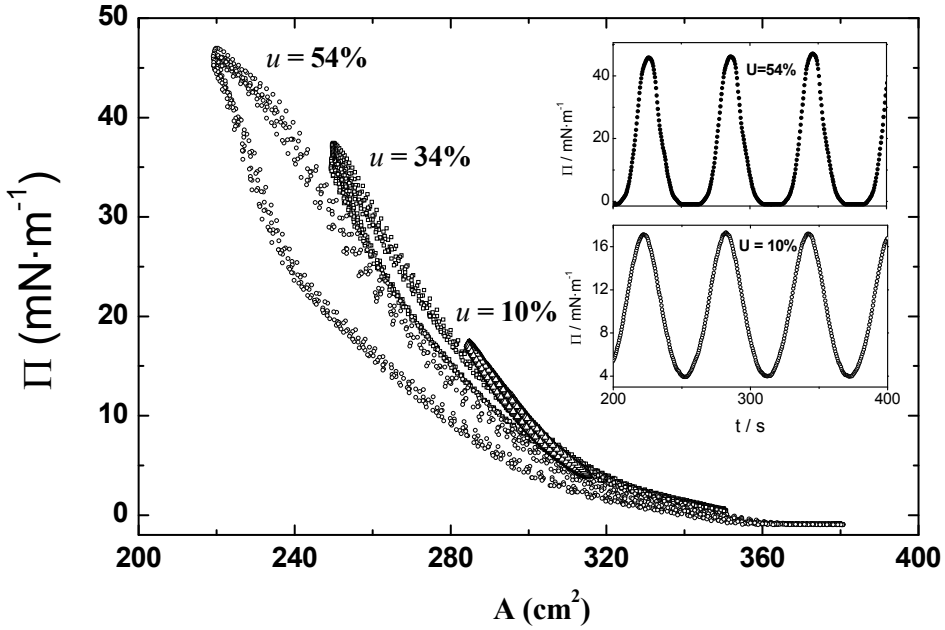

Figure 8. Oscillatory barrier experiment for a poly (octadecyl acrylate) monolayer at constant frequency, and for different values of the strain amplitude (*u*). The inset shows part of the oscillatory response function for two strains. Taken from Ref. [104].

3.3.4 Non-linear elasticity

Oscillatory barrier experiments have been demonstrated to provide further insight into the mechanical response of Langmuir polymer films in linear and non-liner regimes.[68, 105-107] As in 3D systems, for polymer Langmuir films, non-linear elasticity appears for above a certain value of the strain. As Γ increases, a pseudo-plastic plateau develops at strain increases. Above the yield strain, the film becomes softer and the effective elasticity modulus smaller. The stress-strain curves obtained from PVAc monolayers have been quantitatively described by a theoretical constitutive model of rubber elasticity in two-dimensions.[107] Moreover, non-equilibrium features have been observed when larger compression stresses are exerted by the barriers of the Langmuir trough. For rigid polymers, metastability and hysteresis effects emerge as a consequence of stress, for faster strain rates.[104] For instance, Figure 8 shows the response of poly (octadecyl acrylate) monolayer for oscillatory barrier experiments at the same frequency but different amplitudes. It is noteworthy the apparition of hysteresis effects as the strain amplitude increases at constant Γ.[104]

3.4 Shear rheology

Using homemade shear rheometers, Sachetti et al.[108] and more recently Barentin et al.[109], measured the shear viscosity of polymer monolayers in good solvent conditions (such as PVAc and PEO). They found that the shear viscosities are several orders of magnitude lower than the compression viscosities. This difference is due to the fact that a large entropy is lost by the chains during compression, whereas little conformational change is caused by shear (at least for relatively small shear rates). As a consequence, the viscous relaxation is much faster in the case of a shear deformation. Moreover, shear rheology may be an adequate probe of reptation-like motions. Evidences were reported by Luap and Goedel for spread end-tethered polyisoprenes.[110] Recently, Spignone et al. have performed an interesting study about Γ– and *N*–dependence of the shear viscoelasticity moduli of PVAc monolayers.[68] On the other hand, hydrophobic polymers such as poly (vinyl octanal) (PVO) exhibit a size-dependent shear elasticity modulus characterized by linear dependencies, much weaker than for polymers in good solvent conditions.[111] Also, the shear viscoelastic moduli of cross-linked polymer networks were also studied by the group of Fuller.[112, 113] They found relaxation times much larger than the previously reported.[114] Finally, when an insoluble monolayer is uniaxially compressed, both shear and compression stresses are present. Following the analysis proposed by Petkov et al.[115], Cicuta and Terentjev[116] have measured the shear modulus of polymer monolayers from the analysis of the surface stresses along two perpendicular directions, parallel and perpendicular to the compression direction. Unfortunately,

no comparison with surface shear rheometer measurements confirmed yet the validity of this approach.

4. Adsorbed layers

4.1 Surfactant adsorbed at fluid interfaces

4.1.1 Surfactants

Surface tension of pure liquids can be modified by Surfactants, which are usually organic compounds containing in their structure both hydrophobic (and hydrophilic groups. Their structure consists in polar group (hydroxyl, carboxyl, ionic groups, polyether chains) that interacts strongly with polar liquids, while the hydrophobic groups have affinity with non-polar solvents and with air. This dual physicochemical nature determines the surfactant surface activity, as they are soluble both in polar and non-polar liquids, so they are "attracted" to an interface separating aqueous and non-aqueous phases. These molecules can change of the interfacial properties of liquid/liquid and air/liquid systems. Indeed, the hydrophobic group is oriented towards the non-polar phase (air or oil), while the hydrophilic group towards the more polar phase (e.g. water) (Figure 9). Thus, the surfactant tends to adsorb at the liquid/fluid interface, this determines the surface free energy decrease of the system.

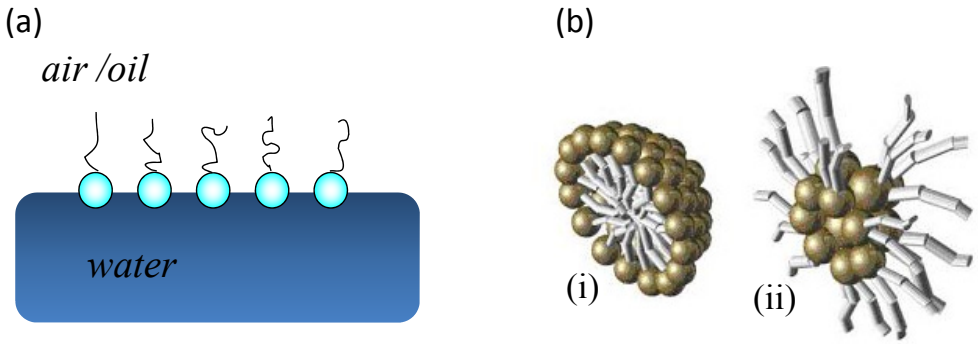

Figure 9. (a) Surfactant adsorption at a fluid interface. (b) Scheme of a normal micelle (i) and an inverse micelle (ii).

For high surfactant concentration, when there is the saturation of the aqueous solution, the formation of micelles in the bulk solution occurs. The concentration at which surfactants begin to form micelles is known as the critical micelle concentration (cmc). Typical micelles in aqueous solution form an aggregate with the hydrophilic "head" regions in contact with the surrounding solvent, with the hydrophobic tail regions in the micelle centre. This type of micelle is known as a normal micelle (oil-in-water micelle). Inverse micelles have the headgroups at the centre with the tails extending out (water-in-oil micelle).

4.1.2 *Adsorption Isotherms and Superficial State equations: Models*

For studying the surfactant adsorption properties, it is necessary to obtain reliable equilibrium surface tension data. They can be obtained by monitoring the surface tension as a function of time (dynamic surface tension) behaviour of a solution until the tension reaches a constant value for different surfactant bulk concentrations *c*. An abrupt change of the slope in the γ–*c* curve occurs at the cmc (Figure 10). Above the cmc, the equilibrium tensions of the solutions remain essentially constant, because only the monomeric form of the surfactant contributes to the surfactant activity or chemical potential, and hence to the tension reduction. In fact, due to their structure, micelles are not surface active, so they do not influence the surface tension value of the system. In fact γ (*c* >*cmc*) is not strictly constant because the chemical potential of the surfactant may change as *c* is increased.

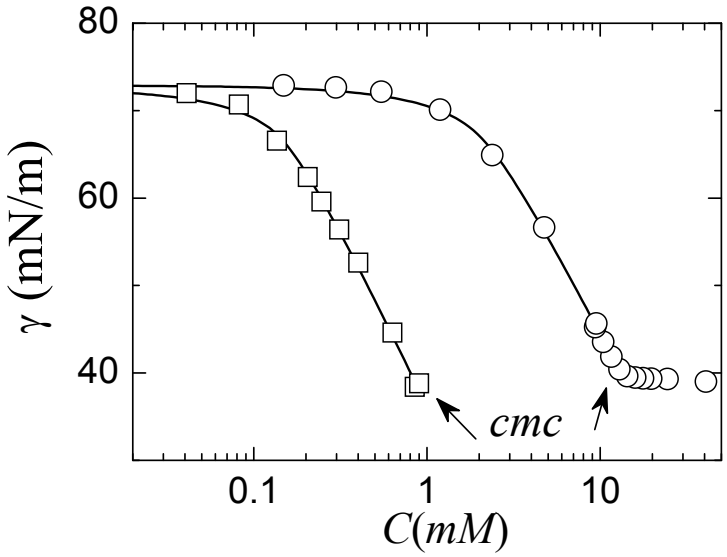

Figure 10. Equilibrium interfacial tension as a function of the surfactant concentration; symbols as follows: CTAB (□) and DTAB (○). Solid lines represent the fits with the Frumkin equation of state. The break points of both curves indicate respectively the *cmc* of the surfactants.

For surfactant concentrations below the cmc, therefore, the surface concentrations Γ at the interface may be estimated from Gibbs adsorption equation:

$$\Gamma = \frac{1}{RT}\left(\frac{\partial \gamma}{\partial \ln a}\right)_{T,P} \qquad (15.a)$$

where *a* is the surface activity. Assuming ideal dilute solution behaviour, Γ may be estimated from the slope of a γ – *c* plot:[117]

$$\Gamma = -\frac{1}{nRT}\left(\frac{\partial \gamma}{\partial \ln c}\right)_{T} \qquad (15.b)$$

where R is the gas constant and T is the temperature. The factor n is a constant that depends on the number of species constituting the surfactant and adsorbing at the interface. Equation 15.b has been tested by C. Bain et al. using neutron reflectance experiments[118], but this has been shown not to be valid for systems in which the surfactant suffers a reorganization (such as aggregation) after adsorption.[119] Usually, for single-component surfactants, the equilibrium tension decreases monotonically with increasing surfactant concentration, or stays approximately constant above the critical micelle concentration (cmc).

The equilibrium relationship between the surface tension γ, or surface pressure $\Pi(=\gamma_0-\gamma)$ and the bulk surfactant concentration c is usually called the adsorption isotherm of the system. When this is used coupled with the Gibbs equation (Eq. 15) it provides also the relationship between γ and the adsorption Γ, usually called surface equation of state, and the $\Gamma - c$ equilibrium relationship.

The most commonly adsorption model used for soluble surfactants is the Langmuir isotherm, which provides:

$$\Gamma = \Gamma^{\infty} \frac{K_L c}{1 + K_L c} \tag{16}$$

where Γ^{∞} is the maximum surface concentration, and K_L, is the Langmuir equilibrium adsorption–desorption equilibrium constant. Here, the parameter Γ^{∞} is a theoretical limit, which is important but cannot normally be reached because of the constraint of a maximum concentration, such as the cmc or the solubility. From the maximum slope of $d\gamma/d\ln c$ at concentrations near the cmc, one can only obtain a maximum surface concentration (for the available bulk concentration), which is usually lower than the theoretical Γ^{∞} value. At low concentrations, or when $K_L c << 1$, the Langmuir isotherm can be approximated by the Henry isotherm. Then:

$$K_H = \Gamma^{\infty} K_L \tag{17}$$

For assessing "high" or "low" concentrations, the reference concentration is $1/K_L$. Hence, the value of K_L provides a useful measure of the surfactant activity, as does the value of K_H. Langmuir's equation accounts for a lattice-type model of the surface molecules, which are assumed not to interact with each other or the solvent (or uncovered) sites.[120] Non-ideal non-localized adsorption isotherms accounting for the finite size of molecules and their lateral interactions have also been developed based on statistical mechanics. A two-dimensional van der Walls equation of state lead to adsorption isotherms which differ significantly from the Henry/Langmuir isotherms.

The Frumkin isotherm, which considers solute-solute interactions at a non-ideal surface, has also been used for several systems.[121, 122] This equation is appropriate mostly for non-ionic surfactants:

$$c = \frac{1}{K_F}\frac{\Gamma}{\Gamma^{\infty} - \Gamma}\exp\left(-A\left(\frac{\Gamma}{\Gamma^{\infty}}\right)\right) \qquad (18)$$

where K_F is the Frumkin equilibrium adsorption constant, and the parameter A is a measure of the non-ideality of mixing at the interface layer. When $A = 0$, the surface is ideal, and the Frumkin isotherm reduces to the Langmuir isotherm. The parameter Γ^{∞} may differ from the parameter Γ^{∞} derived from Langmuir's isotherm.

Using the Gibbs adsorption equation for an ideal (usually dilute) solution, without aggregation of micellization, one can derive the following surface equation of state for the Henry isotherm:

$$\Pi = nRTK_H c = nRT\Gamma \qquad (19)$$

Considering that $\Gamma=1/\bar{A}$, where $\bar{A}$ is the molar area, one obtains $\Pi\bar{A}= n$RT. Note that n is not the number of moles. The analogous surface equations of state for the Langmuir isotherm are the Szyszkowski equation (Eq. 17) and the Frumkin equation (Eq. 18):

$$\Pi = nRT\Gamma^{\infty}\ln(1 + K_L c) \qquad (20)$$

$$\Pi = nRT\Gamma^{\infty}\ln\left(1 - \frac{\Gamma}{\Gamma^{\infty}}\right) \qquad (21)$$

The surface equation of state for the Frumkin isotherm is:[122]

$$\Pi = \gamma_0 - \gamma = -nRT\Gamma^{\infty}\ln\left(1 - \frac{\Gamma}{\Gamma^{\infty}}\right) - \frac{1}{2}nRTA\Gamma^{\infty}\left(\frac{\Gamma}{\Gamma^{\infty}}\right)^2 \qquad (22)$$

From $c(\Gamma)$, and $\gamma(\Gamma)$ in Eq. 19, one can see that a relation between γ and c exists, involving the three parameters Γ^{∞}, K_F, and A (as well as T and n). However, because these equations are nonlinear, no analytical expression for $\gamma(c)$ is available, and $\gamma(c)$ has to be found numerically.

4.1.3 *Dynamic surface tension*

A fresh surface is said to be of *zero age* when the composition of the surface layer is identical with that of the bulk. In this case, the surface excess concentration or adsorption Γ is zero. Thus, dynamic surface tension decreases from the solvent value to the equilibrium one, which is called *equilibrium surface*

tension. The behaviour of surface tension between the pure and equilibrium values represents the *dynamic interfacial tension*.[117]

When a solute is adsorbed from the solution, its concentration first decreases in the immediate neighbourhood of the surface layer. Then diffusion tends to restore the initial concentration by bringing solute from the bulk. The region in which diffusion takes place may be much larger than the thickness of the adsorption layer. For non-charged small molecule surfactants usually, the adsorption process is faster than diffusion, so diffusion is the controlling mechanism of the adsorption dynamics.[117]

The first quantitative model for diffusion controlled adsorption was established by Ward and Tordai.[123] In this model the exchange of mass at the interface is considered at equilibrium compared with the bulk diffusion local equilibrium. Under this assumption, the increase of the adsorption equals the diffusion flux at the surface.

$$\frac{d\Gamma}{dt} = \Phi_{diff} \tag{23}$$

Thus, by considering the adsorption of a single component from a semi-infinite volume on the plane interface defined by $x = 0$, the x-axis being directed towards the solution, this balance reads

$$\frac{d\Gamma}{dt} = D\frac{\partial c}{\partial x}\bigg|_{x=0^+} \tag{24}$$

where $c \equiv c(x,t)$ is the concentration profile at the time t, and D is the surfactant diffusion coefficient. The diffusion in the bulk is described by the Fick equation:

$$\frac{\partial c}{\partial t} = D\frac{\partial^2 c}{\partial^2 x} \tag{25}$$

The solution of Eq. 24 with the boundary condition $c(0^+,t) = c_s(t)$ and the initial conditions $c(x,0) = c_0$ supplies $c(x,t)$, provides the classical Ward-Tordai equation:

$$\Gamma(t) = \sqrt{\frac{D}{\pi}}\left[2c_0\sqrt{t} - \int_0^t \frac{c_s(\tau)}{\sqrt{t-\tau}}\,d\tau\right] \tag{26}$$

The most critical point in this modelling is the correct choice of the adsorption isotherm. In fact, apparent deviations from the diffusion controlled behaviour[124] have re-entered this scheme after introducing new isotherms[125] instead of the more classical ones. Basically, two models involving the internal reorganisation of the adsorbed layer have been developed so far:[126] considering a redistribution between states characterised by different molecular area,[127] and an aggregation process,[128] respectively.

The first model assumes that the surfactant molecules can adsorb in different states whose relative area per molecule occupation changes with the total adsorption, Γ. Therefore it is representative of a situation where rotations and conformational changes are possible for the adsorbed molecules. A model considering only two states, characterised by the areas per molecule, ω_1 and ω_2, has been successfully applied to describe both the equilibrium and dynamic adsorption of poly-oxyethyled surfactants at the air-water interface.[129] In this case for the adsorption in each state Γ_1 and Γ_2, it is possible to write a kinetics equation similar to Eq. 25, with Φ_{int}, representing the flux of molecules transforming from a state to the other:

$$\Phi_{\text{int}}^{2} = -\Phi_{\text{int}}^{1} = k_{12}\left(\left(\frac{\omega_1}{\omega_2}\right)^{\alpha}\left(1-\omega_{\Sigma}\Gamma\right)^{(\omega_1-\omega_2)/\omega_{\Sigma}}\Gamma_2 - \Gamma_1\right) \qquad (27)$$

where k_{12} is the rate constant of the process, α is a parameter linked to the relative surface activity of the molecules in the two state and

$$\omega_{\Sigma} = \frac{\omega_1\Gamma_1 + \omega_2\Gamma_2}{\Gamma_1 + \Gamma_2} \qquad (28)$$

is the average area. Each process involved in the adsorption dynamics has its own characteristic time. Assuming the ratio between the equilibrium adsorption, Γ^0, and concentration, c^0, as the diffusion length, the characteristic time for the diffusion process can be defined as:

$$\tau_D = \frac{1}{D}\left(\frac{\Gamma^0}{c^0}\right)^2 \qquad (29)$$

It has to be underlined that Γ^0/c^0 is also representative of the surface activity properties. Thus, assuming that the diffusion coefficients of all surfactants are about of the same order of magnitude, the characteristic time of the diffusion process contributing to the adsorption, is essentially controlled by the surface activity and by the initial bulk concentration c_0. It is possible to give an expression of the characteristic times of all the processes involved in the adsorption dynamics, by assuming all the other processes at the equilibrium, and by using the kinetic equation. For example, the characteristic time of the re-orientation of the adsorbed molecules can be written as:

$$\tau_{or} = \frac{1}{k_{12}\left(1+\frac{\Gamma_1^0}{\Gamma_2^0}\right)} \qquad (30)$$

which depends both on the orientation rate, k_{12} , and on the partitioning between the two adsorption states, while the characteristic time of the transfer kinetics can be estimated as:

$$\tau_k = \frac{1}{k_a \omega_\Sigma c_0} \tag{31}$$

The comparison of these characteristic times allows the controlling processes to be identified and the appropriate model picture to be assumed. Accordingly, the adsorption is diffusion controlled if the characteristic time for the bulk diffusion is the dominant one ($\tau_D \gg \tau_k, \tau_{or}$). Other significant cases are the kinetic controlled adsorption ($\tau_k \gg \tau_D, \tau_{or}$) the diffusion-orientation controlled adsorption ($\tau_D \approx \tau_{or} \gg \tau_k$). Finally, it is also interesting to model the most general case, referred to as mixed adsorption dynamics.

4.1.4 *Dilational rheology*

According to the expression obtained for a soluble monolayer in section 2, for a surfactant adsorption layer with a pure diffusional relaxation mechanism both real and imaginary parts of the surface dilational complex modulus $\varepsilon^*(\omega)$ can be described by the classical Lucassen-van den Tempel (LVT) model (see Eqs. 10-11).[30] The use of the Lucassen–van den Tempel equation is correct only if the surface relaxation processes can be assumed at equilibrium with respect both to the diffusion exchange with the bulk and to the perturbation of the surface. This model assumes that the relaxation of surface dilational stresses occurs only at the expense of pure diffusion mass exchange between the surface layer and bulk phase, and neglects all other possible relaxation mechanism in the surface layers. However, in some situations, other kinetic processes can occur inside the adsorbed layer depending on the nature of the surface-active species and of the liquid bulk phases. For some non-ionic surfactants, for example, molecular surface re-orientation and surface aggregation have been observed[130, 131], while in other cases other transformations in the surface layer like surface reactions or molecular conformational changes[132] can be important. Each process involved in the adsorption dynamics has its own characteristic time that can be evaluated using appropriate models and experiments, and compared with those of the other processes in order to define the principal controlling process. When these characteristic times are much shorter than the characteristic time of the bulk diffusion, the adsorption is diffusion controlled and the other processes can be considered at equilibrium in the time scale of diffusion. An accurate study of a particular relaxation process is possible only if the appropriate theoretical approach is available, providing the relation between the visco-elastic modulus and the kinetic parameters proper of the process. For studying these cases in

which other relaxation processes are involved, extensions to the classical Lucassen- van der Tempel can be used.[10]

For a more general case of a mixed adsorption mechanism, including the transport by diffusion and an adsorption step governed by a kinetic barrier, the dynamic surface elasticity is given by[35]:

$$\varepsilon = \varepsilon_0 \frac{i\omega\tau + (1+i)/2\xi}{1 + i\omega\tau + (1+i)/2\xi} \qquad (32)$$

The relaxation time τ depends on the adsorption model. For a Langmuir adsorption model, we have $\tau = (\alpha_k + \beta_k c / \Gamma_\infty)^{-1}$ with the kinetic coefficients of adsorption and desorption, α_k and β_k respectively, and the maximum adsorbed amount Γ_∞. For small relaxation times, Equation 32 simplifies to Equation 10.

The dilational viscoelastic behaviour of many surfactants are systematically investigated. Classical studies were done with surfactants like fatty acids, fatty alcohols or alkyl sulphates using capillary wave[30] and oscillating bubble techniques[133]. Because oscillating drop and bubble instruments have became rather accessible, many surfactant systems have been investigated. For instance, in a recent study, the dilational rheology of C12 dodecyl dimethyl phosphine oxide (DMPO) was measured at various concentrations at low frequencies using the oscillating drop profile analysis methods,[134] and compared with data obtained from oscillating bubble experiments.[135] The consideration of the internal compressibility discussed by Ref.[136] lead to good agreement between the experimental and theoretical dependencies for ε_0.

4.2 Mixed surfactant/polymer adsorbed layers

4.2.1 Polyelectrolyte/surfactant mixed layers

The association between oppositely charged polymers (polyelectrolytes) and surfactants in water is driven by both electrostatic and hydrophobic interactions. Many factors can influence the phase behaviour of these mixtures such as molecular weight, degree of branching, charge density, backbone rigidity, and concentration of the polymer, as well as polar head, chain length and concentration of the surfactants.[118, 137, 138]

The formation of surface complexes is revealed by a decrease of surface tension. Although synthetic charged polymers have low surface activity, their mixtures with conventional surfactants can decrease strongly the surface tension, even in a concentration range where the surfactants alone does not change the surface tension of the water. This strong synergistic effect was known for many decades, and explained by the formation of relatively hydrophobic

polyelectrolyte–surfactant complexes.[39] Several years ago, Goddard proposed a simple model of the surface structure of dilute polyelectrolyte–surfactant solutions: the surfactant ions form a monolayer at the liquid surface and attract electrostatically the elongated charged macromolecules, where the charged groups of the polymer plays the role of counterions.[139] Recently, by the application of ellipsometry[140] and neutron reflectivity[141], it has been shown that the surface structure can be essentially more complex. For instance, the adsorption film formed by poly (styrene sulfonate) and dodecyl trimethyl ammonium bromide (PSS/DTAB) solutions contains microaggregates in a broad concentration range, and can consist of a few layers at high surfactant concentrations. This structural arrangement was also suggested by the rheological behaviour of this interfacial system.[142, 143] The real part of the dynamic surface elasticity was extremely high at low DTAB concentrations and dropped abruptly to low values when the surfactant concentration was a little less than the molar concentration of the sulfonate groups.

In general, both parts of the dilational elastic complex modulus show large frequency variations in the case of soluble mixed monolayers, because of the important coupling with the bulk. Here, once adsorbed, the monolayers behave as insoluble. It should be noted that the intrinsic elasticity can be frequency dependent as a result of the relaxation processes in the surface, such as surfactant or polymer chain reorientation.[138] For soluble mixed monolayers, the frequency dependence of the intrinsic dilational complex moduli is smaller than the one associated to exchanges between surface and bulk, and is usually not taken into account in data interpretation. In the case of non-ionic surfactants, the diffusion controlled mechanism for exchanges between surface and bulk is generally in good agreement with experiments.[144] In the case of ionic surfactants, the diffusion process is affected by the surface charges, and the theory is more complicated, but again in good agreement with the experiments.[145] The diffusion controlled models lead to a maximum of elasticity at a particular surfactant concentration. Because the polymer-surfactant layers are insoluble, the diffusion controlled models cannot in fact be used.

One open question in these systems is the following: are the polyelectrolyte/surfactant aggregates adsorbed from the bulk phase or are they formed directly in the surface layer? It should be noted that the dynamic surface elasticity can reach high values at the surfactant concentrations much lower than the critical aggregation concentration (CAC) corresponding to the cooperative polyelectrolyte/surfactant aggregation in the bulk phase.[146] The complexes in the bulk phase in the concentration range below the CAC are probably formed due to ion pair formation between the polyelectrolyte charged groups and surfactant ions.

It is hardly possible that a mere adsorption of these complexes is sufficient to create a rigid surface structure. The kinetics of the adsorption film formation is really much slower that the diffusion of the components from the bulk phase to the surface.[146] A strong argument in favour of the distinction between the complexes in the bulk solution and in the surface layer stems from the comparison between the surface properties of the solutions of polyelectrolyte/surfactant complexes and polysoaps with the same content and length of alkyl groups. The surface activity of the complexes proved to be much higher and thereby the structure of the corresponding adsorption layers is different.[147] This means that the complexes at the surface must contain a larger number of surfactant ions per polyelectrolyte chain than the complexes in the bulk, and the distribution of alkyl chains in the former case must favour their contact with the gas phase.

The formation of polyelectrolyte/surfactant aggregates leading to the abrupt drop of the dynamic surface elasticity can also proceed directly in the surface layer. The corresponding narrow surfactant concentration range usually does not coincide with the range of large aggregate formation in the bulk phase.[148] The analysis of the surface elasticity kinetic dependencies gives more direct evidence of the aggregate formation in the surface layer. The dynamic surface elasticity of polyelectrolyte/surfactant solutions can be a nonmonotonous function of the surface age and go through one or two local maxima.[148] The strong decrease of the surface elasticity of PAA/DTAB and PMA/DTAB solutions beyond the first maximum corresponds exactly to the beginning of the surface tension plateau.[148] This can indicate something like a phase transition in the surface layer.

4.2.2 *Protein/surfactant adsorbed layers*

As stated above, the analysis of the kinetic dependencies of the surface rheological properties gives important details of the mechanism of adsorption film formation. Hence, although the surface rheological properties of protein solutions have been studied for many years,[149] only a few kinetic dependencies of the dynamic surface elasticity have been published so far. These dependencies for solutions of non-globular proteins; e.g., of β-casein (*BCS*) display a few local maximum.[150] It is generally accepted that the first maximum is caused by the loop and tail formation at the expense of N-terminals-hydrophilic parts of *BCS* molecules, which form the distal region of the surface layer while more hydrophobic parts remain at the boundary with the gas phase. One can assume, using the analogy with block copolymers, that more hydrophobic parts also go into the subphase in the region beyond the second maximum of the surface elasticity and mix with N-terminals.[150] Different charges of the hydrophobic and hydrophilic parts of *BCS* molecules give a possibility to use small additions of ionic surfactant as probes of the adsorption mechanism. The cationic and anionic

surfactants have really different influence on the position and height of the local maxima of the surface elasticity.[151] The cationic surfactants interact mainly with the negatively charged N-terminals which become more hydrophobic. The formation of loops and tails becomes more difficult in this case and the surface elasticity increases in the region of the first maximum and the maximum shifts in the direction of higher surface pressures. The second maximum disappears gradually as the concentration increases. Anionic surfactants have the opposite effect. The first maximum disappears gradually, and the second one increases and shifts towards higher surface pressures.[151] This approach cannot be applied directly to the adsorption of globular proteins. For example, the surface elasticity of β-lactoglobulin (*BLG*) solutions increases monotonically with the surface age, and reaches high values close to the equilibrium.[152] However, one can disrupt entirely the globular structure by the addition of a denaturant, for instance guanidine hydrochloride (GH). The kinetic dependencies of the surface elasticity change only slightly when the GH concentration increases from zero to a certain critical value. This slight influence is caused by the increase of the solution ionic strength.[152] However, the shape of the kinetic curves becomes entirely different beyond a narrow critical concentration range of the denaturant. The dependencies are nonmonotonous at high GH concentrations as a result of the protein unfolding. Unlike the case of β-casein, one can observe only a single local maximum for the mixed solutions of *BLG* and GH because of the more homogeneous distribution of hydrophobic and hydrophilic groups along the protein chain.

5. Interfacial layers containing particles

5.1 Generalities

Surface layers of micro- and nanoparticles at fluid interfaces in absence or in the presence of surfactants are of high importance in processes, such as emulsion and foam stabilization by particles.[153-155]

Micro- and nanoparticles can adsorb at the air-water and oil-water interfaces when they are partly hydrophobic, forming surface layers.[156] When their free energy of attachment, which strongly depends on their contact angle (θ), exceeds the thermal energy by many orders of magnitude ($\Delta G >> k_B T$), the adsorption is *quasi*-irreversible.[157] Even for small particles of radius a =10nm, γ =36mN/m and θ =90º the free energy, $\Delta G = 2750 k_B T$.[158, 159] It is comparable to $k_B T$ only in case of extremely small particles (a < 0.5nm), or for contact angles very close to 0º or 180º.

Similar to surfactant adsorption, the attachment of particles at a fluid interface results in a change of the interfacial tension. The creation of interfacial area assumes the transfer of particles from the bulk phase to the interface. When the thermodynamic equilibrium is established between particles at the interface and in the bulk, then an *adsorption isotherm* can be used to describe the particle distribution.[156] However, particles at an interface behave usually like insoluble molecules, an in such situation an adsorption isotherm cannot be applied. Moreover, because of the high adsorption energy of particles, and the very slow adsorption/desorption kinetics, spread particle monolayer at fluid interfaces behave also as insoluble, and can be handled in a similar way as insoluble surfactant or polymer monolayer, e.g., they can be studied trough Π–Γ isotherms.[156] Studies of particle' isotherms were performed with special emphasis on spherical monodisperse polystyrene particles. These studies allow one to get information on particles sizes and particle-particle repulsive interactions.[160-162] It is noteworthy that particles can organise differently at interfaces: a well-ordered two-dimensional structure was first observed for polystyrene particles,[163] whereas a disordered structure were observed for silica microparticles at the oil-water interface. [126] These different structures reflect the different interactions between particles at the interface.[164] In general, the interactions between particles adsorbed at fluid interfaces depend on their size and shape, on the nature of their surface (wettability, surface charge), and the nature and composition of the bulk phases. Moreover, these interactions influence the partitioning of particles between the bulk phase and the interface, the effective interfacial tension and the shape of surface pressure isotherms, as well as stability of emulsions and foams containing particles. Besides attractive capillary interactions, spherical charged colloidal particles can experience either Coulombic repulsion because of their vertically asymmetric charge distribution, and long range attraction due to non-uniform horizontal charge distribution.[163] Attraction forces between the particles lead to the formation of aggregates and/or clusters of different shape (from fractal-like to dense) at the interface.[89] However, the existence of repulsion forces leads to formation of ordered arrays of particles.[160] The inter-particle interaction energy can be calculated on the basis of the classical DLVO theory,[165] with additional consideration of hydrophobic interaction energy, or other non-DLVO forces acting between particles.[166]

5.2 Surface tension and Rheological behaviour

The effective interfacial tension of an interface containing particles is determined essentially by two factors: i) lateral particle–particle interaction (repulsion) and ii) thermal motion of particles. In particular the interactions between particles adsorbed at liquid interfaces depend on their size and shape, on

the nature of their surface (wettability, surface charge) and the nature and composition of the contacting bulk phases, e.g. on the presence of surfactants and/or electrolytes. These interactions influence the partitioning of particles between the bulk phase and the interface.

The thermodynamic similarity between the ensembles of particles and molecules gives the possibility to derive expressions for the effective surface pressure, produced by particles or composite particles-surfactant systems. For the description of particle monolayers at liquid interface an equation of state is proposed by Fainerman et al.[167]:

$$\Pi = -\frac{kT}{\omega_0}\left[ln\left(1-\theta_p\right)+\theta_p\right]-\Pi_{coh} \qquad (33)$$

where Π is the surface pressure, θ_p=ω/A is the surface coverage of particles, ω and ω_0 are the average molecular area of particles and solvent molecules respectively ($\omega >> \omega_0$), Π_{coh} is the cohesion pressure (the interaction between the monolayer components), k is the Boltzmann constant, T is the temperature. It is important to note that this equation does not involve other particle geometrical characteristics except their coverage in the monolayer.

Particles adsorbed at fluid interfaces modify the interfacial rheological properties.[168, 169] It is well known, that at sufficiently high interfacial concentrations the interface exhibits viscoelastic features.[170] An expression for the "effective" dilational modulus, ε, was derived by Lucassen in 1992:[168]

$$\frac{1}{\varepsilon}=\sum_{1}^{n}\frac{\chi_i}{\varepsilon_i} \qquad (34)$$

where χ_i is the surface fraction having the dilational modulus ε_i. This equation corresponds to the case of particles that do not interact and do not move but are characterised by a certain internal compressibility. In this case, the macroscopic and local surface tensions coincide.

6. References

1. De Gennes, P. G.; Brochard-Wyart, F.; Quere, D., *Gouttes, bulles, Perles et Ondes.* Belin: Paris 2002.
2. De Gennes, P. G., Wetting: statics and dynamics. *Rev. Mod. Phys.* **1985,** 57, 827.
3. Israelachvili, J. N., *Intermolecular and Surface Forces*. 2nd ed.; Academic Press: San Diego, 1991.
4. Langevin, D., Viscoelasticity of Monolayers. In *Encyclopedia of Surface and Colloid Science* Hubbard, A. T., Ed. Marcel Dekker: New York, 2002; Vol. 3.
5. Miller, R.; Liggieri, L. Eds., *Interfacial Rheology*. VSP: UK, 2009.
6. Schaefer, H.-E., *Nanoscience: The Science of the Small in Physics, Engineering, Chemistry, Biology and Medicine (Nanoscience and Technology)* Springer: 2010.
7. Starov, V., *Nanoscience: Colloidal and Interfacial Aspects. Surfactant Science Vol.147* CRC Press: 2010.
8. Gaines, L., *Insoluble monolayers at liquid-gas interfaces* Interscience: New York, 1966.
9. Mingotaud, A.-F.; Mingotaud, C.; Patterson, L. K., *Handbook of Monolayers*. Academic Press: San Diego, 1993.
10. Liggieri, L.; Ferrari, M.; Mondelli, D.; Ravera, F., Surface rheology as a tool for the investigation of processes internal to surfactant adsorption layers. *Faraday Discussions* **2005,** 129, 125-140.
11. Noskov, B. A.; Akentiev, A. V.; Bilibin, A. Y.; Zorin, I. M.; Miller, R., Dilational surface viscoelasticity of polymer solutions. *Advances in Colloid and Interface Science* **2003,** 104, 245-271.
12. Kapilashrami, A.; Malmsten, M.; Eskilsson, K.; Benjamins, J.-W.; Nylander, T., Ellipsometric studies of nonionic block copolymers adsorbed at the solid/water and oil/water interfaces. *Colloids and Surfaces A* **2003,** 225, 181-192.
13. Mendelsohn, R.; Brauner, J. W.; Gericke, A., External Infrared Reflection Absorption Spectrometry of Monolayer Films at the Air-Water Interface. *Annu. Rev. Phys. Chem.* **1995,** 46, 305.

14. Dynarowicz-Latka, P.; Dhanabalan, A.; Oliveira JR, O. N., Modern physicochemical research on Langmuir monolayers. *Adv. Colloid Interface Sci.* **2001,** 91, 221-293.

15. Kambhampati, D. K.; Knoll, W., Surface-plasmon optical techniques. *Current Opinion in Colloid & Interface Science* **1999,** 4, 273-280.

16. Vogel, V.; Shen, Y. R., Air/Liquid Interfaces and Adsorbed Molecular Monolayers Studied with Nonlinear Optical Techniques. *Annual Rev. Matter Sci.* **1991,** 21, 515.

17. Müller, M.; MacDowell, L. G., Wetting of polymer liquids: Monte Carlo simulations and self-consistent field calculations *J. Phys.: Condens. Matter* **2003,** 15, R609-R653

18. Chang, R.; Yethiraj, A., Osmotic Pressure of Salt-Free Polyelectrolyte Solutions: A Monte Carlo Simulation Study. *Macromolecules* **2005,** 38, 607–616.

19. Gavranovic, G. T.; Deutsch, J. M.; Fuller, G. G., Two-dimensional melts: Polymer chains at the air-water interface. *Macromolecules* **2005,** 38, 6672-6679.

20. Carmesin, I.; Kremer, K., Static and dynamic properties of two-dimensional polymer melts *J phys (Paris)* **1990,** 51, 915-932.

21. Sikharulidze, I.; Farago, B.; Dolbnya, I. P.; Madsen, A.; de Jeu, W. H., Surface and Bulk Elasticity Determined Fluctuation Regimes in Smectic Membranes. *Physical Review Letters* **2003,** 91, 166504.

22. Ki, H.; Rühm, A.; Lurio, L. B.; Basu, J. K.; Lal, J.; Lumma, D.; Mochrie, S. G. J.; Sinha, S. K., Surface Dynamics of Polymer Films. *Physical Review Letters* **2003,** 90, 068302.

23. Kawaguchi, M., Thermodynamic, structural and rheological properties of polymer films at the air-water interface. *Prog. Polym. Sci.* **1993,** 18, 341.

24. Levich, V. G., *Physico-Chemical Hydrodynamics*. Prentice Hall: 1962.

25. Langevin, D., *Light Scattering by Liquid Surfaces and Complementary Techniques*. Marcel Dekker: New York, 1992; Vol. 41.

26. Larson, R. G., *The structure and rheology of complex fluids*. Oxford University Press: New York, 1999.

27. Boussinesq, On the existence of a superficial viscosity grade , in the thin layer of transition which separates a liquid from another adjacent fluid. M. J., *Ann. Chim. Phys.* **1913,** 29, 349.

28. Scriven, L. E., On the dynamics of phase growth *Chem Eng Sci* **1960,** 12, 98.

29. Slattery, J. C., Interfacial Transport Phenomena. *Chem Eng Sci* **1964,** 19, 379.

30. Lucassen, J.; Van der Tempel, M., Dynamic measurements of dilational properties of a liquid interface. *Chemical Engineering Science* **1972,** 27, (6), 1283.

31. Krammer, L., Theory of light scattering from fluctuations of membranes and monolayers. *Journal of chemical physics* **1971,** 55, 2097.

32. Noskov, B. A., Fast adsorption at the liquid-gas interface. *Advances in Colloid and Interface Science* **1996,** 69, 63-129.

33. Maestro, A.; Ortega, F.; Monroy, F.; Kragel, J.; Miller, R., Molecular Weight Dependence of the Shear Rheology of Poly (methyl methacrylate) Langmuir Films: A Comparison between Two Different Rheometry Techniques. *Langmuir* **2009,** 25, (13), 7393-7400.

34. Ferry, J. D., *Viscoelastic Properties of Polymers*. 3 ed.; Wiley: New york, 1980.

35. Van den Tempel, M.; Lucassen-Reynders, E., Relaxation processes at fluid interfaces. *Adv Colloid Interface Sci* **1983,** 18, 281.

36. Kragel, J.; Derkatch, S. R.; Miller, R., Interfacial shear rheology of protein-surfactant layers. *Adv Colloid Interface Sci* **2008,** 144, (1-2), 38-53.

37. Kragel, J.; Kretzschmar, G.; Li, J. B.; Loglio, G.; Miller, R.; Mohwald, H., Surface rheology of monolayers. *Thin Solid Films* **1996,** 284, 361-364.

38. Langevin, D.; Meunier, J., Micelles, membranes, Microemulsions and Monolayers. In *Interfacial Tension, Theory and Experiments*, Gelbart, W. M.; Ben-Shaul, A.; Roux, D., Eds. Springer: New York, 1994.

39. Noskov, B. A., Dilational surface rheology of polymer and polymer/surfactant solutions. *Current Opinion in Colloid & Interface Science* **2010,** DOI:10.1016/j.cocis.2010.01.006.

40. Lucassen, E. H.; Lucassen, J., Properties of Capillary waves. *Advances in Colloid and Interface Science* **1969,** 2, 347-395.

41. Miller, R.; Wustneck, R.; Kragel, J.; Kretzschmar, G., Dilational and shear rheology of adsorption layers at liquid interfaces. *Colloids and Surfaces a-Physicochemical and Engineering Aspects* **1996,** 111, (1-2), 75-118.

42. Monroy, F.; Ortega, F.; Rubio, R. G.; Velarde, M. G., Surface rheology, equilibrium and dynamic features at interfaces, with emphasis on efficient tools for probing polymer dynamics at interfaces. *Advances in Colloid and Interface Science* **2007,** 134-35, 175-189.

43. Loglio, G.; Pandolfini, P.; Miller, R.; Makievski, A.; Ravera, F.; Ferrari, M.; Liggieri, L., Drop and Bubble Shape Analysis as Tool for Dilational Rheology Studies of Interfacial Layers. In *"Novel Methods to Study Interfacial Layers", Studies in Interface Science*, Mobius, D.; Miller, R., Eds. Elsevier: Amsterdam, 2001.

44. Ravera, F.; Ferrari, M.; Santini, E.; Liggieri, L., Influence of surface processes on the dilational visco-elasticity of surfactant solutions. *Advances in Colloid and Interface Science* **2005,** 117, (1-3), 75-100.

45. Liggieri, L.; Ravera, F.; Passerone, A.; Sanfeld, A.; Steinchen, A., The capillary pressure method: A new tool for interfacial tension measurements. *Dynamics of Multiphase Flows across Interfaces* **1996,** 467, 175-185.

46. Liggieri, L.; Ravera, F.; Passerone, A., Dynamic interfacial-tension measurements by a capillary-pressure method. *Journal of Colloid and Interface Science* **1995,** 169, (1), 226-237.

47. Sacchetti, M.; Yu, H.; Zografi, G., A canal surface viscometer for the inplane steady shear viscosity of monolayers at the air-water-interface. *Review of Scientific Instruments* **1993,** 64, (7), 1941-1946.

48. Gardel, M.; Valentine, M.; Weitz, D. A., Microrheology. In *Microscale diagnostic techniques*, Brauer, K., Ed. Springer: Berlin, 2005.

49. Waigh, T. A., Microrheology of complex fluids. *Rep. Prog. Phys.* **2005,** 68, 685-742.

50. Cicuta, P.; Donald, A. M., Microrheology: a review of the method and applications. *Soft Matter* **2007,** 3, (12), 1449-1455.

51. Ortega, F.; Ritacco, H.; Rubio, R. G., Interfacial Microrheology: Particle tracking and related techniques. *Current Opinion in Colloid & Interface Science* **2010,** DOI:10.1016/J.cocis.2010.03.001.

52. Safran, S. A., Curvature elasticity of thin films. *Advances in Physics* **1999,** 48, 395-448.

53. Rubinstein, M.; Colby, R. H., *Polymer Physics*. Oxford Univ. Press: New York, 2003.

54. Scheutjens, J. M. H. M.; Fleer, G.; Cohen-Stuart, M.; Cosgrove; Vincent, B., *Polymer at Interfaces*. Chapman and Hall: London, 1993.

55. Jones, R. A. L.; Richards, R. W., *Polymers at Surfaces and Interfaces*. Cambridge Univ. Press: Cambridge, 1999.

56. Crisp, D. J., Surface films of polymers .1. Films of the fluid type. *Journal of Colloid Science* **1946,** 1, (1), 49-70.

57. Gennes, P.-G. d., *Scaling Concepts in Polymer Physics*. Cornell University Press: Ithaca, 1979.

58. Kumaki, J.; Kawauchi, T.; Yashima, E., "Reptational" Movements of Single Synthetic Polymer Chains on Substrate Observed by in-Situ Atomic Force Microscopy. *Macromolecules* **2006,** 39, 1209-1215.

59. Vilanove, R.; Rondelez, F., Scaling description of two-Dimensional Chain Conformations in Polymer monolayers. *Phys. Rev. Lett.* **1980,** 45, (18), 1502.

60. Kawaguchi, M.; Sano, M.; Chen, Y. L.; Zografi, G.; Yu, H., Interfacial properties of polyvinyl acetate) films - surface-wave scattering at an air-water-interface. *Macromolecules* **1986,** 19, (10), 2606-2612.

61. Bae, S. Y.; Granick, S., Molecular Motion at Soft and Hard Interfaces: From Phospolipid Bilayers to Polymers and Lubricants. *Annual Review of Physical Chemistry* **2007,** 58, 353-374.

62. Mann, E. K.; Langevin, D., Poly(dimethylsiloxane) molecular layers at the surface of water and of aqueous surfactant solutions. *Langmuir* **1991,** 7, (6), 1112-1117.

63. Monroy, F.; Rivillon, S.; Ortega, F.; Rubio, R. G., Dilational rheology of Langmuir polymer monolayers: Poor-solvent conditions. *Journal of Chemical Physics* **2001,** 115, (1), 530-539.

64. Cicuta, P.; Hopkinson, I., Studies of a weak polyampholyte at the air-buffer interface: The effect of varying pH and ionic strength. *Journal of Chemical Physics* **2001,** 114, (19), 8659-8670.

65. Esker, A. R.; Kim, C.; Yu, H., Polymer monolayer dynamics. *Functional Materials and Biomaterials* **2007,** 209, 59-110.

66. Skarlupka, R.; Seo, Y.; Yu, H. U., A study of the surface viscoelasticity of poly(vinyl acetate) at the air-water interface using the electrocapillary wave diffraction technique. *Polymer* **1998,** 39, (2), 387-392.

67. Cicuta, P.; Hopkinson, I., Scaling of dynamics in 2d semi-dilute polymer solutions. *Europhysics Letters* **2004,** 68, (1), 65-71.

68. Spigone, E.; Cho, G. Y.; Fuller, G. G.; Cicuta, P., Surface Rheology of a Polymer Monolayer: Effects of Polymer Chain Length and Compression Rate. *Langmuir* **2009,** 25, (13), 7457-7464.

69. Knoebler, C. M.; Desai, R. C., Phase Transitions in Monolayers. *Annu. Rev. Phys. Chem.* **1992,** 43, 207.

70. Rivillon, S.; Munoz, M. G.; Monroy, F.; Ortega, F.; Rubio, R. G., Experimental study of the dynamic properties of monolayers of PS-PEO block copolymers: The attractive monomer surface case. *Macromolecules* **2003,** 36, (11), 4068-4077.

71. Richards, R. W.; R, R. B.; TAylor, M. R., Surface Quasi-Elastic Light Scattering From Spread Monolayers of a Poly(methyl methacrylate)−Poly(ethylene oxide) Block Copolymer. *Macromolecules* **1996,** 29, 1980.

72. Fauré, M. C.; Bassereau, P.; Lee, L. T.; Menelle, A.; Lhevender, C., Phase Transitions in Monolayers of PS−PEO Copolymer at the Air−Water Interface. *Macromolecules* **1999,** 32, 8538.

73. Kawaguchi, M., Thermodynamic, structural and rheological properties of polymer films at the air-water interface. *Prog. Polym. Sci.* **2007,** 18.

74. Miranda, B.; Hilles, H. M.; Rubio, R. G.; Ritacco, H.; Radic, D.; Gargallo, L.; Sferrazza, M.; Ortega, F., Equilibrium and Surface Rheology of Monolayers of Insoluble Polycations with Side Chains. *Langmuir* **2009,** 25, (21), 12561-12568.

75. Noskov, B. A., Dynamic surface elasticity of polymer-solutions. *Colloid and Polymer Science* **1995,** 273, (3), 263-270.

76. Itagaki, H., Segmental motion of polystyrene in fluid solution revealed by means of the fluorescent probe method. *Macromolecules* **1991,** 24, 6531–6535.

77. Wang, B.; Guan, J.; Anthony, S. M.; Bae, S. C.; Schweizer, K. S.; Granick, S., Confining Potential when a Biopolymer Filament Reptates. *Physical Review Letters* 104, (11).

78. Monroy, F.; Hilles, H. M.; Ortega, F.; Rubio, R. G., Relaxation dynamics of Langmuir polymer films: A power-law analysis. *Physical Review Letters* **2003,** 91, (26).

79. Cloizeaux, J. d.; Jannick, G., *Polymers in Solution*. Clarendon Press: Oxford, 1990.

80. Maestro, A.; Hilles, H.; Ortega, F.; Rubio, R. G.; Langevin, D.; Monroy, F., Reptation in Langmuir polymer monolayers. *Soft Matter* **2010,** accepted 2010.

81. Adams, J.; Buske, A.; Duran, R. S., Viscoelastic properties and collapse behavior of a smectic liquid-crystalline polymer at the air/water interface. *Macromolecules* **1993,** 26, 2871-2877.

82. Cicuta, P.; Stancik, E. J.; Fuller, G. G., Shearing or compressing a soft glass in 2D: Time-concentration superposition. *Physical Review Letters* **2003,** 90, (23).

83. Yoo, K. H.; Yu, H., Temperature-dependence of polymer film properties on the air water interface - polyvinyl acetate) and poly(n-butyl methacrylate). *Macromolecules* **1989,** 22, (10), 4019-4026.

84. Monroy, F.; Ortega, F.; Rubio, R. G., Dilatational rheology of insoluble polymer monolayers: Poly(vinylacetate). *Physical Review E* **1998,** 58, (6), 7629-7641.

85. Monroy, F.; Ortega, F.; Rubio, R. G., Thermoelastic behaviour of polyvinylacetate monolayers at the air-water interface: Evidences for liquid-solid phase transition. *European Physical Journal B* **2000,** 13, (4), 745-754.

86. Hilles, H. M.; Ortega, F.; Rubio, R. G.; Monroy, F., Long-time relaxation dynamics of langmuir films of a glass-forming polymer: Evidence of glasslike dynamics in two dimensions. *Physical Review Letters* **2004,** 92, (25).

87. Hilles, H. M.; Ritacco, H.; Monroy, F.; Ortega, F.; Rubio, R. G., Temperature and Concentration Effects on the Equilibrium and Dynamic Behavior of a Langmuir Monolayer: From Fluid to Gel-like Behavior. *Langmuir* **2009,** 25, (19), 11528-11532.

88. Denkov, N. D.; Velev, O. D.; Kralchevsky, P. A., Two-dimensional crystallization *Nature* **193,** 361, 26.

89. Sharpe, D.; Earnshaw, J.; Haig, K.; Li, Y., Apparently universal changes in the elastic properties of monomolecular films. *Phys Rev B* **1997,** 55, 6260-6264.

90. Strandburg, K., Two-dimensional melting. *Rev. Mod. Phys.* **1988,** 55, 161–207

91. Maier, B.; Radler, J. O., Conformation and self-diffusion of single DNA molecules confined to two dimensions. *Physical Review Letters* **1999,** 82, (9), 1911-1914.

92. Maier, B.; Radler, J. O., DNA on fluid membranes: A model polymer in two dimensions. *Macromolecules* **2000,** 33, (19), 7185-7194.

93. Zhao, J.; Granick, S., Polymer lateral diffusion at the solid-liquid interface. *Journal of the American Chemical Society* **2004,** 126, (20), 6242-6243.

94. Doi, M.; Edwards, S. F., *The theory of polymer dynamics*. Oxford: Clarendon, 1986.

95. Brown, H. R.; Russell, T. P., Entanglements at Polymer Surfaces and Interfaces. *Macromolecules* **1996,** 29, **798–800**.

96. Jiang, Z.; Kim, Z.; Jiao, X.; Lee, H.; Lee, Y.-J.; Byun, Y.; Song, S.; Eom, D.; Li, C.; Rafailovich, M. H.; Lurio, L. B.; Sinha, S. K., Evidence for Viscoelastic Effects in Surface Capillary Waves of Molten Polymer Films. *Phys Rev Lett* **2007,** 98, 227801.

97. Semenov, A.; Johner, A., Theoretical notes on dense polymers in two dimensions. *Eur. Phys. J E* **2003,** 12, 469.

98. Esker, A. R.; Zhang, L. H.; Sauer, B. B.; Lee, W.; Yu, H., Dilational viscoelastic behaviors of homopolymer monolayers: surface light scattering analysis. *Colloids and Surfaces a-Physicochemical and Engineering Aspects* **2000,** 171, (1-3), 131-148.

99. Monroy, F.; Ortega, F.; Rubio, R. G., Rheology of a miscible polymer blend at the air-water interface. Quasielastic surface light scattering study and analysis in terms of static and dynamic scaling laws. *Journal of Physical Chemistry B* **1999,** 103, (12), 2061-2071.

100. Rivillon, S.; Monroy, F.; Ortega, F.; Rubio, R. G., Dilational rheology of monolayers of a miscible polymer blend: From good- to poor-solvent conditions. *European Physical Journal E* **2002,** 9, (4), 375-385.

101. Hilles, H. M.; Sferrazza, M.; Monroy, F.; Ortega, F.; Rubio, R. G., Equilibrium and dynamics of Langmuir monolayers when the interface is a selective solvent: Polystyrene-b-poly(t-butyl acrylate) block copolymers. *Journal of Chemical Physics* **2006,** 125, (7).

102. Diez-Pascual, A. M.; Monroy, F.; Ortega, F.; Rubio, R. G.; Miller, R.; Noskov, B. A., Adsorption of water-soluble polymers with surfactant character. Dilational viscoelasticity. *Langmuir* **2007,** 23, (7), 3802-3808.

103. Zhu, J.; Eisenberg, A.; Lennox, R., Interfacial behavior of block polyelectrolytes. 1. Evidence for novel surface micelle formation. *J Am Chem Soc* **1991,** 113, 5583.

104. Hilles, H.; Maestro, A.; Monroy, F.; Ortega, F.; Rubio, R. G.; Velarde, M. G., Polymer monolayers with a small viscoelastic linear regime: Equilibrium and rheology of poly(octadecyl acrylate) and poly(vinyl stearate). *Journal of Chemical Physics* **2007,** 126, (12).

105. Ferenczi, T. A. M.; Cicuta, P., Shear and compression viscoelasticity in polymer monolayers. *Journal of Physics-Condensed Matter* **2005,** 17, (45), S3445-S3453.

106. Cicuta, P., Compression and shear surface rheology in spread layers of beta-casein and beta-lactoglobulin. *Journal of Colloid and Interface Science* **2007,** 308, (1), 93-99.

107. Hilles, H.; Monroy, F.; Bonales, L. J.; Ortega, F.; Rubio, R. G., Fourier-transform rheology of polymer Langmuir monolayers: Analysis of the non-linear and plastic behaviors. *Advances in Colloid and Interface Science* **2006,** 122, (1-3), 67-77.

108. Sacchetti, M.; Yu, H.; Zografi, G., In-Plane Steady Shear Viscosity of Monolayers a the Air/water Interface and Its dependence on Free Area. *Langmuir* **1993,** 9, 2168-2171.

109. Barentin, C.; Muller, P.; Ybert, C.; Joanny, J.-F.; di Meglio, J.-M., Shear viscosity of polymer and surfactant monolayers. *Eur. Phys. J E* **2000,** 2, 153-159.

110. Luap, C.; Goedel, W. A., Linear viscoelastic behavior of end-tethered polymer monolayers at the air/water interface. *Macromolecules* **2001,** 34, 1343-1351.

111. Sato, N.; Ito, S.; Yamamoto, M., Molecular Weight Dependence of Shear Viscosity of a Polymer Monolayer: Evidence for the Lack of Chain Entanglement in the Two-Dimensional Plane. *Macromolecules* **1998,** 31, 2673.

112. Brooks, C. F.; Thiele, J.; Frank, C. W.; O'Brien, D. F.; Knoll, W.; Fuller, G. G.; Robertson, C. R., Surface shear rheology of a polymerizable lipopolymer monolayer. *Langmuir* **2002,** 18, (6), 2166-2173.

113. Naumann, C. A.; Brooks, C. F.; Fuller, G. G.; Lehmann, T.; Ruhe, J.; Knoll, W.; Kuhn, P.; Nuyken, O.; Frank, C. W., Two-dimensional physical networks of lipopolymers at the air/water interface: Correlation of molecular structure and surface rheological behavior. *Langmuir* **2001,** 17, (9), 2801-2806.

114. Brooks, C. F.; Fuller, G. G.; Frank, C. W.; Robertson, C. R., An interfacial stress rheometer to study rheological transitions in monolayers at the air-water interface. *Langmuir* **1999,** 15, (7), 2450-2459.

115. Petkov, J. T.; Gurkov, T. D.; Campbell, B. E.; Borwankar, R. P., Dilatational and Shear Elasticity of Gel-like Protein Layers on Air/Water Interface. *Langmuir* **2000,** 16, 3703.

116. Cicuta, P.; Terentjev, E. M., Viscoelasticity of a protein monolayer from anisotropic surface pressure measurements. *European Physical Journal E* **2005,** 16, (2), 147-158.

117. Adamson, A. W., *Physical chemistry of surfaces*. 5th ed.; Wiley: New York, 1990.

118. Bain, C. D.; Claesson, P. M.; Langevin, D.; Meszaros, R.; Nylander, T.; Stubenrauch, C.; Titmuss, S., Complexes of surfactants with oppositely charged polymers at surfaces and in bulk. *Advances in Colloid and Interface Science* **2010,** 155, 32-49.

119. Fainerman, V. B.; Miller, R., Surface tension isotherms for surfactant adsorption layers including surface aggregation. *Langmuir* **1996,** 12, (25), 6011-6014.

120. Aveyard, R.; Haydon, D. A., *An Introduction to the Principles of Surface Chemistry*. Cambridge University press: 1973.

121. Fainerman, V. B., Kinetics of adsorption of ionic surfactants at the solution-air interface and the nature of the adsorption barrier. *Colloid Surfaces* **1991,** 57, 249.

122. Borwankar, R. P.; Wasan, D. T., The kinetics of adsorption of surface active agents at gas-liquid surfaces. *Chem. Eng. Sci.* **1983,** 38, 1637.

123. Ward, A. F.; Tordai, L., Time-Dependence of Boundary Tensions of Solutions I. The Role of Diffusion in Time-Effects. *J Chem Phys* **1946,** 14, 453.

124. Eastoe, J.; Dalton, J.; Rogueda, P. G. A.; Crooks, E. R.; Pitt, A. R.; Simister, E. A., Dynamic Surface Tensions of Nonionic Surfactant Solutions. *J. Colloid Interface Sci.* **1997,** 188, 423.

125. Chang, H. C.; Hsu, C.-T.; Lin, S.-Y., Adsorption Kinetics of C10E8 at the Air−Water Interface. *Langmuir* **1998,** 14, 2476.

126. Ravera, F.; Ferrari, M.; Liggieri, L., Adsorption and partitioning of surfactants in liquid-liquid systems. *Advances in Colloid and Interface Science* **2000,** 88, (1-2), 129-177.

127. Fainerman, V. B.; Miller, R.; Wustneck, R.; Makievski, A. V., Adsorption isotherm and surface tension equation for a surfactant with changing partial molar area .1. Ideal surface layer. *Journal of Physical Chemistry* **1996,** 100, (18), 7669-7675.

128. Fainerman, V. B.; Miller, R., Equation of state for concentrated protein surface layers at the water/air interface. *Langmuir* **1999,** 15, (5), 1812-1816.

129. Miller, R.; Aksenenko, E. V.; Liggieri, L.; Ravera, F.; Ferrari, M.; Fainerman, V. B., Effect of the reorientation of oxyethylated alcohol molecules within the surface layer on equilibrium and dynamic surface pressure. *Langmuir* **1999,** 15, (4), 1328-1336.

130. Liggieri, L.; Ferrari, M.; Massa, A.; Ravera, F., Molecular reorientation in the adsorption of some CiEj at the water-air interface. *Colloids and Surfaces a-Physicochemical and Engineering Aspects* **1999,** 156, (1-3), 455-463.

131. Ravera, F.; Liggieri, L.; Miller, R., Molecular orientation as a controlling process in adsorption dynamics. *Colloids and Surfaces a-Physicochemical and Engineering Aspects* **2000,** 175, (1-2), 51-60.

132. Maldonado-Valderrama, J.; Fainerman, V. B.; Aksenenko, E.; Galvez-Ruiz, M. J.; Cabrerizo-Vilchez, M. A.; Miller, R., Dynamics of protein adsorption at the oil-water interface: comparison with a theoretical model. *Colloids and Surfaces a-Physicochemical and Engineering Aspects* **2005,** 261, (1-3), 85-92.

133. Miller, R.; Kretzschmar, G.; Dukhin, S. S., On the theory of adsorption-kinetics of ionic surfactants at fluid interfaces .4. deceleration of the adsorption rate due to nonequilibrium distribution of absorbed ions in the diffuse layer. *Colloid and Polymer Science* **1994,** 272, (5), 548-553.

134. Kotsmar, C.; Kragel, J.; Kovalchuk, V. I.; Aksenenko, E. V.; Fainerman, V. B.; Miller, R., Dilation and Shear Rheology of Mixed beta-Casein/Surfactant Adsorption Layers. *Journal of Physical Chemistry B* **2009,** 113, (1), 103-113.

135. Kovalchuk, V. I.; Loglio, G.; Fainerman, V. B.; Miller, R., Interpretation of surface dilational elasticity data based on an intrinsic two-dimensional interfacial compressibility model. *Journal of Colloid and Interface Science* **2004,** 270, (2), 475-482.

136. Fainerman, V. B.; Kovalchuk, V. I.; Aksenenko, E. V.; Michel, M.; Leser, M. E.; Miller, R., Models of two-dimensional solution assuming the internal compressibility of adsorbed molecules: A comparative analysis. *Journal of Physical Chemistry B* **2004,** 108, (36), 13700-13705.

137. Langevin, D., Complexation of oppositely charged polyelectrolytes and surfactants in aqueous solutions. A review. *Advances in Colloid and Interface Science* **2009,** 147-48, 170-177.

138. Langevin, D.; Monroy, F., Interfacial rheology of polyelectrolytes and polymer monolayers at the air-water interface. *Current Opinion in Colloid & Interface Science* **2010,** doi:10.1016/j.cocis.2010.02.002.

139. Goddard, E. D., Polymer-surfactant interaction part II. Polymer and surfactant of opposite charge. *Colloids and Surfaces A* **1986,** 19, 301-329.

140. Monteux, C.; Williams, C. E.; Meunier, J.; Anthony, O.; Bergeron, V., Adsorption of oppositely charged polyelectrolyte/surfactant complexes at the air/water interface: formation of interfacial gels. *Langmuir* **2004,** 20, 57-63.

141. Taylor, D. J. F.; Thomas, R. K.; Penfold, J., Polymer/surfactant interactions at the air/water interface. *Adv Colloid Interface Sci* **2007,** 132, 69-110.

142. Noskov, B. A.; Loglio, G.; Miller, R., Dilational viscoelasticity of polyelectolyte/surfactant adsorption films at the air/water interface: Dodecyltrimethylammonium bromide and sodium poly(styrenesulfonate). *Journal of Physical Chemistry B* **2004,** 108, (48), 18615-18622.

143. Monteux, C.; Fuller, G. G.; Bergeron, V., Shear and dilational surface rheology of oppositely charged polyelectrolyte/surfactant microgels adsorbed at the air-water interface. Influence on foam stability. *Journal of Physical Chemistry B* **2004,** 108, (42), 16473-16482.

144. Lucassen, J.; Giles, D., Dynamic surface properties of nonionic surfactant solutions. *Journal of the Chemical Society-Faraday Transactions I* **1975,** 71, (2), 217-232.

145. Bonfillon, A.; Langevin, D., Electrostatic model for the viscoelasticity of ionic surfactant monolayers. *Langmuir* **1994,** 10, (9), 2965-2971.

146. Noskov, B. A.; Grigoriev, D. O.; Lin, S. Y.; Loglio, G.; Miller, R., Dynamic surface properties of polyelectrolyte/surfactant adsorption films at the Air/Water interface: Poly(dially1dimethylammonium chloride) and sodium dodecylsulfate. *Langmuir* **2007,** 23, (19), 9641-9651.

147. Babak, V. G.; Baros, F.; Boury, F.; Desbrieres, J., Effect of electrolyte concentration on the dynamic surface tension and dilational viscoelasticity of adsorption layers of chitosan and dodecyl chitosan. *J phys Chem B* **2007,** 32, 9519-9529.

148. Bykov, A. G.; Lin, S. Y.; Loglio, G.; Miller, R.; Noskov, B. A., Kinetics of Adsorption Layer Formation in Solutions of Polyacid/Surfactant Complexes. *Journal of Physical Chemistry C* **2009,** 113, (14), 5664-5671.

149. Bos, M. A.; van Vliet, T., Interfacial rheological properties of adsorbed protein layers and surfactants: a review. *Adv Colloid Interface Sci* **2001,** 91, 43-471.

150. Noskov, B. A.; Latnikova, A. V.; Lin, S. Y.; Loglio, G.; Miller, R., Dynamic surface elasticity of beta-casein solutions during adsorption. *Journal of Physical Chemistry C* **2007,** 111, 16895-16901.

151. Latnikova, A. V.; Lin, S. Y.; Loglio, G.; Miller, R.; Noskov, B. A., Impact of surfactant additions on dynamic properties of beta-casein adsorption layers. *Journal of Physical Chemistry C* **2008,** 112, (15), 6126-6131.

152. Latnikova, A. V.; Lin, S. Y.; Noskov, B. A., Dynamic surface properties of the solutions of beta-casein-surfactant complexes. *Colloid Journal* **2009,** 71, (2), 208-218.

153. Pickering, S. U., *J Chem Soc* **1907,** 97.

154. Binks, B. P.; Lumsdon, S. O., Pickering emulsions stabilized by monodisperse latex particles: Effects of particle size. *Langmuir* **2001,** 17, (15), 4540-4547.

155. Binks, B. P.; Horozov, T. S., *Colloidal Particles at Liquid Interfaces*. Cambridge University Press: Cambridge, U.K., 2006.

156. Miller, R.; Fainerman, V. B.; Kovalchuk, V. I.; Grigoriev, D. O.; Leser, M. E.; Michel, M., Composite interfacial layers containing micro-size and nano-size particles. *Advances in Colloid and Interface Science* **2006,** 128, 17-26.

157. Pieranski, P., Two-Dimensional Interfacial Colloidal Crystals. *Physical Review Letters* **1980,** 45, 569-572.

158. Binks, B. P., Particles as surfactants - similarities and differences. *Current Opinion in Colloid & Interface Science* **2002,** 7, (1-2), 21-41.

159. Aveyard, R.; Binks, B. P.; Clint, J. H., Emulsions stabilised solely by colloidal particles. *Advances in Colloid and Interface Science* **2003,** 100, 503-546.

160. Aveyard, R.; Clint, J. H.; Nees, D.; Paunov, V. N., Compression and structure of monolayers of charged latex particles at air/water and octane/water interfaces. *Langmuir* **2000,** 16, (4), 1969-1979.

161. Aveyard, R.; Clint, J. H.; Nees, D.; Quirke, N., Structure and collapse of particle monolayers under lateral pressure at the octane/aqueous surfactant solution interface. *Langmuir* **2000,** 16, (23), 8820-8828.

162. Aveyard, R.; Binks, B. P.; Clint, J. H.; Fletcher, P. D. I.; Horozov, T. S.; Neumann, B.; Paunov, V. N.; Annesley, J.; Botchway, S. W.; Nees, D.; Parker, A. W.; Ward, A. D.; Burgess, A. N., Measurement of long-range repulsive forces between charged particles at an oil-water interface. *Physical Review Letters* **2002,** 88, (24).

163. Chen, W.; Tan, S.; Ng, T.-K.; Ford, W. T.; Tong, P., Long-Ranged Attraction between Charged Polystyrene Spheres at Aqueous Interfaces. *Physical Review Letters* **2005,** 95, (21).

164. Frydel, D.; Dietrich, S.; Oettel, M., Charge renormalization for effective interactions of colloids at water interfaces. *Physical Review Letters* **2007,** 99, 118302

165. Hórvölgyi, Z.; Németh, S.; Fendler, J. H., Spreading of hydrophobic silica beads at water—air interfaces. *Colloids and Surfaces A: Physicochem. Eng. Aspects* **1993,** 71, 327-335.

166. Levine, S.; Bowen, D. B.; Partridge, S. J., Stabilization of emulsions by fine particles I. Partitioning of particles between continuous phase and oil/water interface. *Colloids and Surfaces* **1989,** 38, 325-343.

167. Fainerman, V. B.; Kovalchuk, V. I.; Lucassen-Reynders, E. H.; Grigoriev, D. O.; Ferri, J. K.; Leser, M. E.; Michel, M.; Miller, R.; Mohwald, H., Surface-pressure isotherms of monolayers formed by microsize and nanosize particles. *Langmuir* **2006,** 22, (4), 1701-1705.

168. Lucassen, J., Capillary forces between solid particles in fluid interfaces. *Colloids and Surfaces* **1992,** 65, (2-3), 131-137.

169. Stancik, E. J.; Widenbrant, M. J. O.; Laschitsch, A. T.; Vermant, J.; Fuller, G. G., Structure and dynamics of particle monolayers at a liquid-liquid interface subjected to extensional flow. *Langmuir* **2002,** 18, (11), 4372-4375.

170. Sharma, R.; Yang, Z. H.; Yu, H.; Green, M.; Pak, H. K., Dynamic surface tension and relaxation of thermally stimulated PEO-PPO-PEO and PPO-PEO-PPO copolymers at the air-water interface. *Abstracts of Papers of the American Chemical Society* **1999,** 217, 015-PMSE.

Part II

Equilibrium and Dynamics of Langmuir Polymer films: From '*good*' to '*poor*' solvent conditions

Aim

Inspired by the principle that changing the dimensionality of the space a system could modify its physical properties we highlights a study of the equilibrium properties and rheology of polymers forced to be conformed at a two-dimensional space. Indeed, the knowledge of the conformation and dynamics of confined materials to *nanometric* dimensions plays an important role as paradigmatic model to get physical insight on the materials at reduced dimensionality. Actually, Polymer systems confined at interfaces as Langmuir monolayers have been extensively described leading to a set of several theories and models within the framework of polymer solutions in a *quasi*-bidimensional state. However, there are still quite a number of unsolved questions in the physical mechanism underlying the dynamics of polymer monolayers. Therefore, this part of the thesis has been formally divided in two chapters to get physical insight of the dynamics related to the different conformational scenarios proposed for the polymers at reduced dimensionality.

In **Chapter 1** we demonstrated the existence of the *Reptation motion* for flexible linear polymer chains confined in a quasi two-dimensional space. To test our hypothesis we thus studied the rheology of poly (*tert*–butyl acrylate) Langmuir films. In **Chapter 2** we studied the monolayers of poly (methyl methacrylate), a glass former polymer and weakly adsorbed at the air-water interface, to suggest the existence of a *quasi-bidimensional glass* above the *percolation* threshold of the collapsed coil conformation showed by the polymer.

Chapter 1

Polymer reptation in fluid monolayers

Abstract

We report the existence of reptation motion typical of entangled polymer chains in dense polymer monolayers spread at the air-water interface. Ellipsometry determinations of the layer thickness reveal a thickening of the layers in the semi-dilute region, enabling the existence of entanglements. Relaxation measurements were performed using compression and shear surface deformations. The resulting dependences on chain concentration and size are compatible with the existence of diffusional reptation motions controlling molecular transport inside the monolayer. As in bulk, these features are observed above a critical number of monomers N_e for which chain entanglements become possible.

1. Introduction

The great success of scaling concepts is grounded in their simplicity and had an enormous influence on the development of polymer physics[1-3]. They describe chain conformation and dynamics of polymers in solution in terms of two parameters, number of monomers in the chain N and concentration c. Scaling concepts can be extended to describe polymer near surfaces, and both conformation and dynamics of polymer chains are predicted to differ significantly from the behaviour in the bulk. Based on the argument that adsorption energy outweighs the entropy loss from a bulk conformation, de Gennes theoretically postulated that a fully adsorbed chain might adopt a *pancake* conformation with most monomers adsorbed at the interface[1]. In this case, the chains take conformations of SAWs *self-avoiding walks* for which chain intersections are forbidden[1,4]. Such strong adsorption conditions do not prevail when the adsorbed chains are in contact with a good solvent. In this case, de Gennes showed that adsorbed chains adopt a self similar conformation with a density decaying algebraically away from the interface[5]. These self-similar profiles were evidenced experimentally later on[6,7]. De Gennes also predicted that reptation-like motions could occur in these adsorbed layers, and derived a scaling law for the relaxation time, $\tau \sim N^3 \log N$, that differs from the law established in bulk ($\tau_{bulk} \sim N^3$) by a logarithmic correction[8]. Experimental evidence for this prediction is still lacking. One major difficulty comes from the fact that non-equilibrium effects are dominant whenever monomer-surface sticking energies are somewhat larger than k_BT, a common case for polymers layers supported on solid surfaces. Polymer relaxation kinetics within the layer are then severely retarded, leading to non-equilibrium layers whose structure and dynamics depend on adsorption kinetics and layer ageing [9]. The method of fluorescence correlation spectroscopy was used extensively by Granick and collaborators to study diffusion of synthetic polymer chains weakly adsorbed at solid surfaces avoiding aggregation or crystallization in the adsorbed state.[10] Despite these precautions, no well-defined power laws were yet observed. Fluid interfaces offer an interesting option for probing polymer dynamics in the weak adsorption regime where slowing-down effects typical of solid surfaces are avoided, since the substrate does not impose topological constraints to chain motion. They appear ideal to probe ensemble averaged equilibrium and dynamical scaling through changes in surface free energy, easily accessible from the surface pressure observable.[11]

In this work, we present an extensive body of experimental evidence on the structure and mechanics monolayers of flexible polymer spread at the air-water interface (Langmuir layers). A crossover from Rouse- to reptation-like behaviour

was observed for highly monodisperse polymers when increasing chain size above a critical entanglement value N_e. Our results show that long enough flexible chains can entangle in the monolayer evidencing reptation-like motion.

2. Materials and Methods

2.1 Chemicals

We used in this study eleven different high monodisperse samples of poly(*tert*-butyl-acrylate) (PTBA) obtained from Polymer Source, Canada, with molecular weights ranging from 1.44×10^3 to 1.095×10^6 g·mol^{-1}. Scheme 1.1 shows the constitutive unit of this polymer and the properties of the samples used have been summarized in the Table 1.1. Chloroform (Sigma Aldrich, 99% of purity) was used as spreading solvent. The concentration of the spreading solution was 0.1mg/ml for all the samples.

Scheme 1.1. Chemical structure of the repetitive units of poly(*tert*-butyl-acrylate)

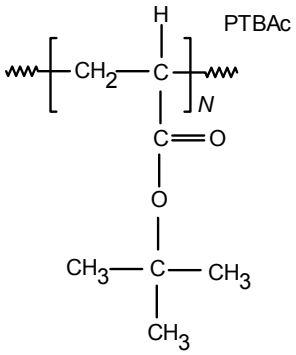

Double distilled and deionized water from a MilliQ-RG system was used to prepare the subphase, having a resistivity higher than 18mΩ·cm^{-1}, organic matter lower than 1 ppb and a surface tension of $\gamma = 72.6 mN\cdot m^{-1}$ at 20ºC. For the Langmuir monolayers preparation, Small aliquots of the spreading solution (10-20 µl) were slowly dispensed at different places onto the A/W interface with a Hamilton microsyringe. The surface polymer concentration was changed by subsequent additions of the spreading solution. Times ranging 15 to 50 min were allowed for solvent evaporation and equilibration.

The temperature of the monolayers was controlled by a thermostat and a water jacket of the trough. Near the interface, the temperature was measured with a precision of 0.01ºC, and the temperature control was better than ±0.05 ºC. Care

was taken to avoid any changes on the height of the monolayer during the experiments due to evaporation.

2.2 Methods

We studied the equilibrium features of PTBA monolayers by the surface pressure – surface polymer concentration (Π–Γ) isotherms at 23ºC. Structural information about the PTBA films was obtained by ellipsometry. Furthermore, the dilational rheological behaviour of our samples were studied; we thus performed relaxation experiments to PTBA monolayers upon a mechanical uniaxial compression imposed by the barriers of the Langmuir trough. To study the shear rheology, we used two different oscillatory rheometers working in the plate (ISR-1, Sinterface) and bi-cone (MCR301-IRS, Anton Paar) geometries. In both cases, the rheometer tool is carefully placed at the interface and the linear mechanical response measured at a constant shear rate (0.1Hz) corresponding to deformation times shorter than the terminal relaxation time (> 10s) but much longer than typical segmental relaxations. This oscillatory mode assigns the observed rheology to a plateau regime (almost independent on the deformation frequency). Control experiments performed on polymer monolayers yield identical results with both instruments. All the methods details have been further described in the Appendix 1 (Methods summary).

Table 1.1. Properties of different samples of poly(*ter*-butyl-acrylate)

Commercial Name	M_w (10^3g mol^{-1})	M_n (10^3g mol^{-1})	M_w/M_n
P1828-TBA	1.56	1.45	0.93
P2213- TBA	3.47	3.03	0.87
P2532- TBA	4.6	4.0	0.87
P1670- TBA	7.5	7.0	0.93
P1036- TBA	16.3	14.4	0.88
P2009- TBA	21.2	19.6	0.92
P1148- TBA	39.2	37.0	0.94
P1598- TBA	52.1	46.5	0.89
P2450- TBA	103.0	79.0	0.77
P1592 TBA	327.0	287.0	0.88
P346 TBA	1094.8	870.0	0.79

3. Results and Discussion

3.1 Equilibrium Behaviour

We have studied poly(*tert*-butyl-acrylate) (PTBA) of different molecular weights spread onto the air/water interface at increasing surface concentration, Γ. In the dilute $\Gamma < \Gamma^*$ and semi-dilute $\Gamma^* < \Gamma < \Gamma^{**}$ regimes the surface layer thickness is well below the typical sizes of the polymer coil, hence these layers can be considered as "monolayers" (for vinyl polymers with a bulk density $\rho \approx 1\text{g/cm}^3$, if $\Gamma \leq 10\text{mg/m}^2$, the layer thickness h ($\approx \Gamma/\rho$) ≤ 10nm). Twelve different PTBA samples were chosen, spanning a quite broad range of molecular weights ($10^3 - 10^6$ Da) with a low polydispersity ($M_w/M_n \approx 1.1$) (see caption in Figure 1.1 for details). Figure 1.1.a shows the three usual equilibrium concentration regimes, as identified from the surface pressure curves[11] (see caption for details). The shift observed towards lower concentrations at increasing polymerisation degree clearly manifests the influence of chain size and concentration on monolayer energetics (see Figure 1.1.a–c). This makes the system particularly suitable for mechanical studies since these variables can be easily modulated. At the overlapping state (∗) the system crosses over from the isolated-chain dilute regime to a dense regime structurally dominated by the collective behaviour of a strongly packed arrangement of polymer chains. The overlapping concentration is of a fundamental importance as it informs us about the size of a single chain on the interface, R_F ($\Gamma^* = N/\pi R_F^2$; see Figure 1.1b). Above a critical size N_e (≈ 100 monomers), R_F displays 2D-scaling behaviour $R_F = a\,N^{\nu}$. The experimental value of the scaling exponent $\nu = 0.74 \pm 0.01$ is found close to the 2D-Flory exponent in good solvent conditions ($\nu = 3/4$). The Kuhn length $a = 0.45 \pm 0.05$nm is found in agreement with reported bulk values at good-solvent conditions[12]. Below N_e, the chain size scales as $R_F \approx aN$ (as expected for small oligomers). Note that below Γ*, the polymer layer thickness is comparable to the monomer size (at $\Gamma < \Gamma^*$, $h \approx a$; see Figure 1.1.e), hence finding an exponent corresponding to 2D theories in the dilute regime is as expected.

In the semidilute regime (see Figure 1.1.a), theory predicts that there is only one characteristic length ξ(Γ), *N*-independent[1]. In bulk, the characteristic length is the distance between entanglement points, which varies as $\xi(\Gamma) \sim N^0\,\Gamma^{-\nu/(3\nu-1)}$. The osmotic pressure, for instance, which is proportional to the average density of contact points in the gel, is expected to scale as $\Pi(\xi) \sim k_B T/\xi^3$. By analogy to bulk, the scaling law usually used to interpret surface pressure isotherms[13] reads as $\Pi(\Gamma) = \Pi^* (\Gamma/\Gamma^*)^m N^0$, with an exponent $m = 2\nu/(2\nu-1)$ (see Figure 1.1.b). For flexible chains at good-solvent conditions, the Flory exponent is $\nu = ¾$, leading to $\Pi(\Gamma, N)$

$\sim \Gamma^3 N^0$ (see Refs. [14,15] for recent reviews on polymer monolayers). In the present case, experimental values of $\nu \approx 0.75$, compatible with good-solvent conditions, are systematically obtained from fittings for $N > N_e$, similarly to spread monolayers of other flexible polymers[16,17]. Figure 1.1.d shows a strong proof of scaling: almost all isotherms in Figure1.1.a can be merged into a master curve where the semidilute regime is described by the universal law $\Pi(\Gamma)/\pi^* = (\Gamma/\Gamma^*)^3 N^0$ defined for interpenetrated adsorbed flexible chains. An additional piece of evidence for the structural scenario arises from ellipsometry measurements of the film thickness, h (see Fig. 1.1.e). A very thin monolayer (all monomers adsorbed) is already built up at Γ^* ($h^* \approx a \approx 0.3$nm). As lateral overlapping increases the monolayer thickens, which is compatible with the existence of chain loops in the semidilute regime. Finally, at Γ^{**} the polymer monolayer reaches a plateau thickness compatible with a flattened conformation thinner than the bulk coil ($a << h^{**} < R_F$). A sketch of the possible evolution is shown in Figure 1.2.

It may seem strange that the surface pressure varies in the semi-dilute regime (between Γ^* and Γ^{**}) according to scaling laws derived for two dimensions. In fact, de Gennes predicted that the region of the layer closest to the surface, with thickness of the order of the monomer size (proximal layer) is the densest and its contribution to the surface pressure dominates over that of the self similar region.

In the semidilute regime, the thickness is related to the first moment of the concentration profile and scales as $h \sim R_{F(bulk)}^{2/3}$, $R_{F(bulk)}$ being the Flory radius in bulk. Since $R_{F(bulk)} \sim N^{3/5}$, one finds $h \sim a N^{2/5}$. Estimations of h for $M = 50$ kDa ($N = 350$), leads to $h \approx 5$nm, close to the measured thickness. The difference with the value measured for the largest molecular weight is however too small; for the sample with $M = 870.7$ kDa, h should be three times larger and is only about 8nm. It is possible that the polymer concentration profile is not truly self-similar but as discussed recently.[18] Further investigations are planned to clarify this point.

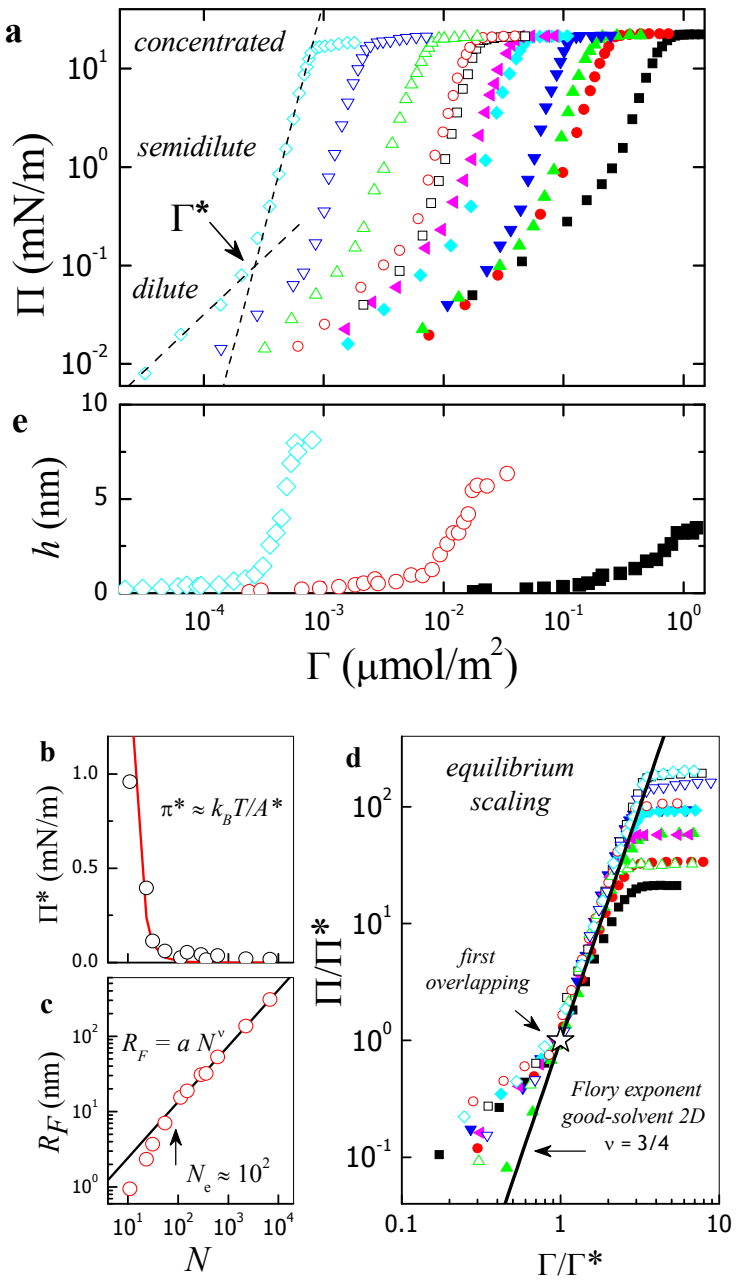

Figure 1.1. Equilibrium behavior of PTBA layers spread on water (25ºC). (a) Surface pressure isotherms (Π–Γ) at different molecular weights *(from right to left)* : M_n : M_w (in kDa) and polydispersity index σ between parentheses: (■) 1.45 : 1.56 (1.07); (●) 3.03 : 3.47 (1.14); (▲) 4.00 : 4.60 (1.15); (▼) 7.00 : 7.50 (1.07); (◆) 14.4 : 16.30 (1.13); (◀) 19.6 : 21.2 (1.08); (□) 37.0 : 39.2 (1.06); (○) 46.5 : 52.1 (1.12); (△) 79.0 : 103.0 (1.3); (▽) 287.0 : 327.0 (1.14) and (◇) 870.7 : 1094.8 (1.25). For clarity, the concentration regimes are only signalled for the highest polymer (◇ 870.7 kDa; $N = 6800$). Dashed lines represent power law behavior at the dilute (D; $\Pi \sim \Gamma^1$) and semidilute regime (SD; $\Pi \sim \Gamma^3$). The overlapping concentration is obtained as the crossover point between both regimes. (**b**) Surface pressure at the overlapping point (π*) as a function of the polymerization degree N. Symbols are experimental values inferred from the *log-log* plots in **1a**. Solid line is the prediction from the ideal-gas law, $\Pi \approx k_BT/A_0$ ($A^* = 1/\Gamma^*$ is the molecular area occupied for a single chain at the *-state). (**c**) Chain dimensions at the overlapping concentration ($A^* = \Pi R^2_F$) as a function of N. The line represent scaling predictions for adsorbed chains, $R_F = a\ N^\nu$. (**d**) Universal scaling of the Π isotherms versus Γ/Γ*. (**e**) Ellipsometric thickness for different molecular weights (symbols as in 1a).

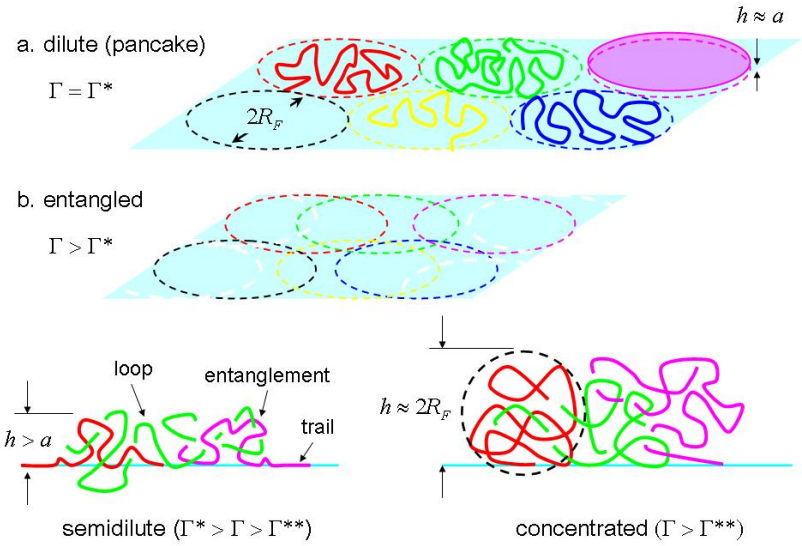

Figure 1.2. Conformational scenario for spread monolayers of flexible polymers at good solvent conditions: (**a**) Dilute regime, below the overlapping concentration (Γ*) : all monomers in a chain are adsorbed at the interface resulting in the ideal pancake conformation, with a thickness similar to the monomer size but much smaller than the in-plane dimensions ($h \approx a < R_F$). (**b**) Above Γ* chains laterally overlap. All adsorption sites (trails) being saturated, some chain segments can be found dangling below the interface in an entropically favourable conformation (loops). This favours chain entangling upon lateral overlapping.

2.2 Compression relaxation

This technique accesses the dynamics of conformational changes produced after a compression of the spread monolayers.[19,20] To compare equivalent states, experiments were performed at a constant surface pressure ($\pi^{**} = 16$mN/m) which corresponds to a quite dense surface state at the onset of the concentrated regime (at $\Gamma \approx \Gamma^{**}$ one gets $\xi^{**}/R_F \approx (\Gamma^*/\Gamma^{**})^{3/2} \approx 0.1$ and $h^{**} >> a$).

Figure 1.3.a shows the experimental relaxation curves which evidence a significant slowing-down for increasing N. The time to reach equilibrium strongly increases with N. The monolayers made with the smaller molecular weight polymers equilibrate after a few seconds, but those of the two highest ($M_w = 287.0$ and 870.7 kDa) take more than one day to relax, being in these cases impossible an accurate determination of the relaxation times. As expected for a linear mechanical response, the relaxation profiles are described by an exponential decay with a single relaxation time (see Fig. 1.3.b). Above $N_e \approx 100$ the compression modulus reaches a constant value ($\varepsilon \approx 48$mN/m) independent of the molecular weight (see Fig. 1.3.c). The compression elastic modulus is expected to scale as k_BT/ξ^2, hence to be independent of N, as observed above N_e. The smaller values below N_e may be due to the absence of entanglement and a decoupling of the behaviour of the chains. For polymers above N_e, in the semidilute regime, $\Pi \sim \Gamma^3$,

so one gets $\varepsilon(\Gamma) = -\Gamma(\partial\pi/\partial\Gamma) \approx 3\pi$, as experimentally observed above N_e (see Fig. 1.3.c; at Γ^{**} the surface pressure is $\Gamma^{**} \approx 16$ mN/m so one gets $\Gamma^{**} \approx 48$ mN/m). Figure 1.3.d, e and f show the concentration and molecular weight dependences of the terminal relaxation times.

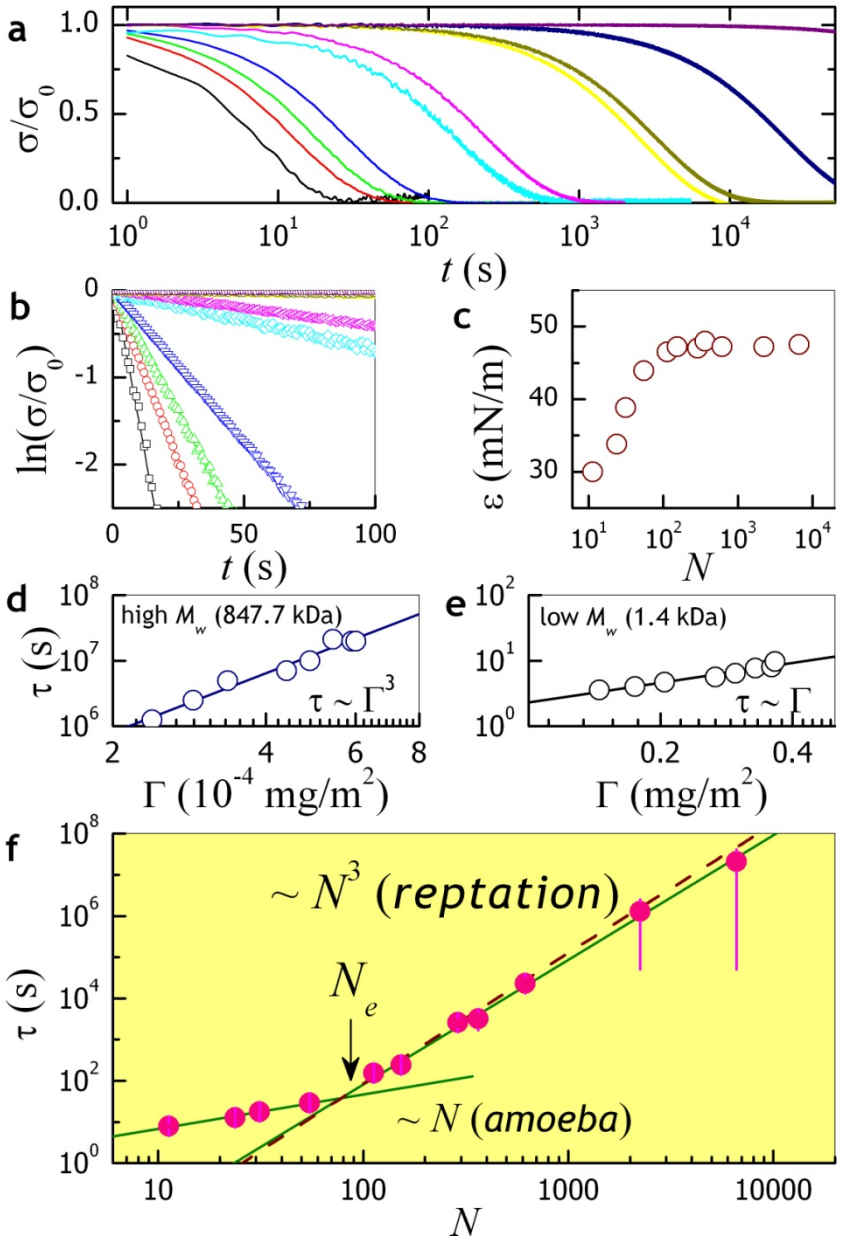

Figure 1.3. Compression stress relaxation of PTBA spread monolayers at the dense state (Π^{**} = 16mN/m). (a) Normalised stress-relaxation curves at different molecular weights (the same that in Fig. 1a) after a sudden compression (see Methods). **(b)** Linearised plot for obtaining the terminal relaxation time of the exponential decays of Fig. 1.1a. **(c)** Compression elasticity modulus as obtained from the relaxation amplitudes. Above $N_e \approx 100$, data are found compatible with predictions for an entangled gel of flexible chains at two dimensions ($\varepsilon^{**} \approx 3\pi^{**} \approx 48$mN/m; dashed line). **(d, e)** Typical concentration dependence of the relaxation times for (**d**) high and (**e**) low molecular weights. (**f**) Chain length dependence of the terminal relaxation times at the Γ^{**} state. The solid line represent scaling behaviour ($\sim N^3$ above N_e). The dashed line includes the logarithmic correction expected for adsorbed layers ($\sim N^3 \log N$).

Above N_e, the times τ follow a scaling law $\tau \sim \Gamma^3 N^3$ characteristic of reptation events, suggesting that reptation is the dominant mechanism for molecular transport in the studied polymer layers[1]. Reptation requires well defined tubes to occur, which is compatible with the structural scenario obtained from the equilibrium properties (see Fig. 1.2).

The scaling $\tau \sim \Gamma^3$ is in agreement with data previously reported for similar flexible polymers[25,26]. Below N_e, the relaxation times are weakly dependent on N and increase linearly with concentration, a feature typical of non-entangled chains ($\tau \sim \Gamma$ at $N < N_e$; see Fig. 1.3.f).

Let us now discuss the logarithmic correction predicted by de Gennes for entangled chains adsorbed at interfaces. In view of the error bars of the experimental relaxation times there is a certain uncertainty in the scaling exponent, $\tau \sim N^{3.0\pm0.2}$. Relaxation times corresponding to the two highest molecular weights are so long ($\tau > 24$h) that experimental data must be considered just as a shorter estimation, which introduces a certain degree of uncertainty in the effective scaling exponent at high N. If we discard the data for the two highest molecular weights, we have a span of N between 100 and 1000, for which according to the prediction: $\tau \sim N^3 \log N$, τ should vary by a factor 2000, instead of 1000 without the correction. This is close to $\tau \sim N^{3.3}$, and consistent with the error bar quoted. Distinguishing between $N^3 \log N$ and $N^{3.3}$ is therefore unfortunately completely out of reach.

As expected, a much weaker dependence is experimentally observed below the critical entanglement size ($\tau \sim N$ at $N < N_e$). In this case, amoeboid-like motions are possible in the crowded environment accessible to a given chain, resulting in a sub-diffusive transport mechanism characterised by an N-dependence weaker than those expected from the Rouse model[1-3]. Depending on the main dissipation mechanism, such a kind of amoeboid motion has been predicted to give relaxation times varying either as $\sim N^{15/8}$ if elastic forces dominate (internal friction) or as $\sim N$ if friction at the boundaries of the pancakes does[21]. Here, the data are compatible with the second friction mechanism (see Fig. 1.3.f; $\tau \sim N$ at $N < N_e$)

Srivastava and Basu have reported recently similar compression relaxation measurements on PVAc spread monolayers at the air-water interface[22]. They used three different molecular weight (N = 720, 2856 and 4191) with a rather high polydispersity (M_w/M_n = 1.5, 2.2 and 2.2, respectively). The concentration dependence of the compression relaxation times was also found compatible with reptation motion ($\tau \sim \Gamma^3$) except for the largest polymer ($\tau \sim \Gamma^{1.4\pm0.1}$ for $N = 4191$). The N-dependence of the relaxation times is weaker than expected for reptation

motions ($\tau \sim N^2$), but at a relatively low concentration ($\Gamma \approx 2\Gamma^* < \Gamma^{**}$). Srivastava and Basu argue that these data rule out the existence of reptation. However, their polymers are much more polydisperse as compared to the PTBA chains studied in our work. The smallest chains contained in the polydisperse samples may accelerate the diffusion and relax the constraints without requiring long reptation events.[1-3]

2.3 Shear viscoelasticity

Oscillatory shear experiments performed at small deformation and relatively low frequency allow exploring reptation-like motions in polymer spread monolayers (see Methods for details). Figure 1.4.a plots the concentration dependence of the shear viscosity measured in the semidilute regime at different molecular weights. Similarly to compression[13-20], the frictional resistance to shear increases strongly with chain size and concentration, as expected from a highly entangled system: the viscous friction being determined by the product of the shear rigidity, $G \sim \Gamma^3$, and the relaxation time, $\tau \sim \Gamma^3$, the shear viscosity should scale as $\eta_S \sim G\,\tau \sim \Gamma^6$ [1-3]. Similar behavior has been recently reported for spread monolayers of PVAc[23]. An additional proof of scaling is provided by the master plot of Figure 1.4.b, which demonstrates universal behavior, $\eta/\eta^* = (\Gamma/\Gamma^*)^6\ N^0$. Weaker concentration dependencies are found only for the smallest chains, well below N_e (see a representative example in Fig. 1.4.b). Similarly to compression, the shear modulus does not depend on chain size (see Fig. 1.4.c), again a strong evidence for the existence of entanglements[1-3]. Otherwise, chains segregating into self-avoiding conformations should be characterized by a size-dependent shear elasticity modulus[1,24]. Indeed, as extensively verified in bulk systems[2,3], the shear modulus is determined by the effective surface monomer density between entanglement points, ρ: $G_0/k_BT \approx \rho/N_e$; for polymer monolayers at the considered state ($\Gamma^{**} \approx 1\text{mg/m}^2$, $\rho^{**} \approx a\,\Gamma^{**}/h^{**} \approx 0.1\text{mg/m}^2$) and $N_e \approx 100$, the predicted value $G_0 \approx 15\mu\text{N/m}$, is in good quantitative agreement with the experimental value (see Fig. 1.4.c). For N smaller than N_e, the plateau shear modulus is not observed to decrease, at the difference of the compression modulus (see Fig. 1.3.c). This is probably because G_0 is still linked to the effective monomer density, which is independent of the molecular weight.

Figure 1.4.d shows the experimental values of the shear viscosity measured at the same state than compression data in Fig. 1.3 ($\Pi^{**} = 16\text{mN/m}$). Again, above the critical entanglement size ($N_e \approx 100$), we found a reptation-like dependence of the shear viscosity on the molecular weight ($\eta_S \sim N^{3.0\pm0.3}$). However, shear viscosities measured for the layers of the two highest molecular

weights are found systematically higher than expected for ideal reptation ($\eta_S \sim N^{3.3}$ at $N > 10\ N_e$). Such a positive deviation is compatible with the slowing down effects expected from large loops and tails dangling out the outer portion of the layer. Again, the experimental uncertainty although smaller than in compression experiments, prevents us from demonstrating the existence of a logarithmic correction to the ideal reptation law.

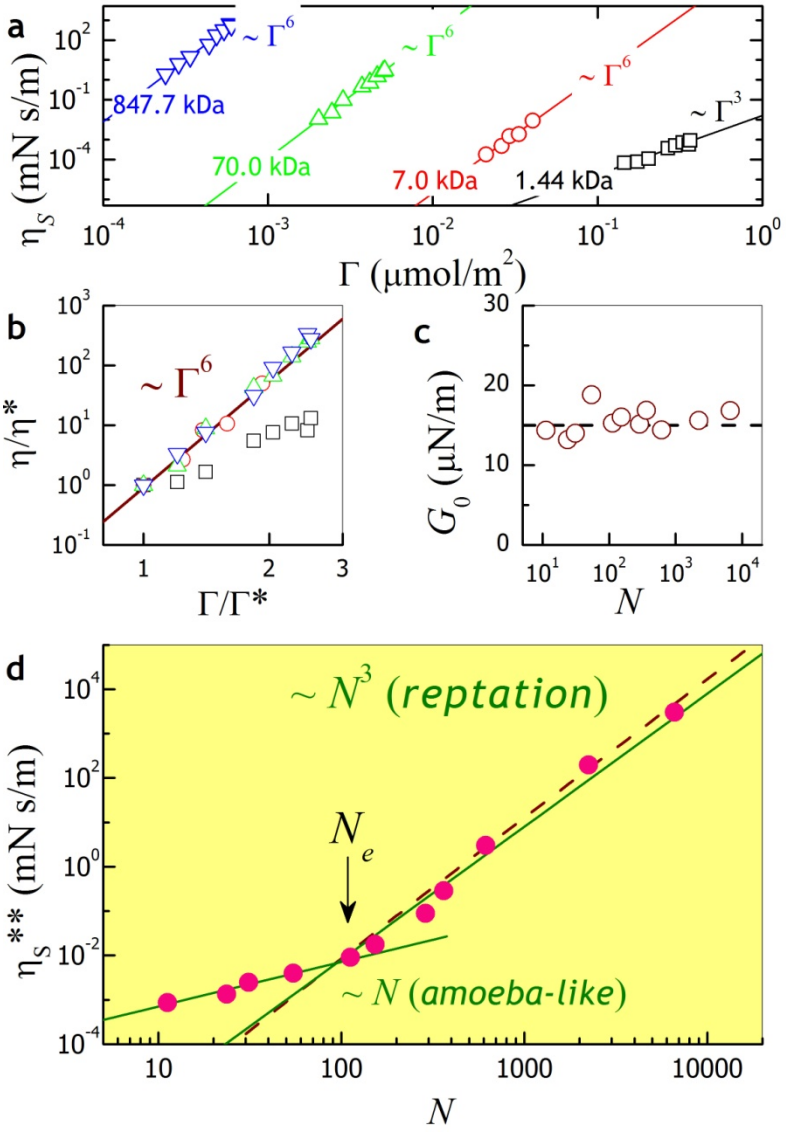

Figure 1.4. Shear rheology of PTBA spread monolayers at the dense states (π = 16mN/m).** **a**, Shear viscosity as a function of the surface concentration. **b**, Scaled viscosity η/η∗ **c**, Plateau value of the shear modulus as a function of the molecular weight.. **d**, Scaling behaviour of the shear viscosity at increasing molecular weight. The experimental error bars are smaller than the symbol size. The dashed line includes a logarithmic correction (*~N^3 logN)* to the reptation-like scaling law ~ N^3.

Strong evidences for reptation-like shear viscoelasticity have been also reported by Luap and Goedel for brushes of end-tethered polyisoprenes at the air-water interface[25]. In this work, the high values of the shear viscosity and the

amazing exponential dependence observed on the chain length ($\eta_S \sim \exp(N)$) are suggestive of a certain sequestration of the terminal disengagement process that, similarly to star-polymers, may be provoked by chain tethering at the interface. A much weaker, linear dependence ($\eta_S \sim N$) was reported by Sato *et al.*[26] from measurements of the shear viscosity of spread monolayers of a highly hydrophobic polymer, as expected for polymer pancakes. As little entanglements are expected for polymer monolayers in poor-solvent conditions amoeboid-like motions could account for these results.

Obviously, highly monodisperse samples such as the ones used here (with a polydispersity ratio, $M_w/M_n \leq 1.1$) are absolutely mandatory to allow for a clean measurement of the terminal disengagement time, otherwise small chain components drive faster stress relaxation. In a recent paper, Spigone *et al.*[23] have performed a similar shear rheology study of spread layers of PVAc using three different molecular weights spanning less than one decade above N_e. The concentration dependence of the shear viscosity is similar to the one found for PTBA($\eta_S \sim \Gamma^6$). The shear viscosity was also observed to increase with molecular weight in the semidilute regime (reached after continuous compression at a finite compression rate, whereas we used successive depositions to avoid non equilibrium conformations, see methods). Spigone et al found that the viscosities depended on the compression rates, suggesting that their monolayers were not fully in equilibrium. Furthermore the polydispersity of their samples was larger than ours, possibly masking the reptation events. No molecular weight dependence of η_S was observed in the concentrated regime, which was used to exclude reptation-like mechanisms. However, the structure of the layer in this region changes, possibly accounting for this puzzling result.

If small chains with degree of polymerization less than $N_e \approx 100$ do not make entanglements, the fact that the shear modulus remains non-vanishing at $G_0 \approx 15\mu N/m$ implies that, at the considered dense state Γ^{**}, as the large chains as the small ones connect into a structural solid-like network able to support shear rigidity,[27] the effective monomer density being similar independently of the molecular weight.

Finally, a strong evidence in support of a dynamics driven by reptation motions is displayed by Figure 1.4.d, which plots the experimental values of the shear viscosity measured at the same state than compression data in Figure 1.3 ($\Pi^{**} = 16mN/m$). Again, above the critical entanglement size ($N_e \approx 100$), we found a reptation-like dependence of the shear viscosity on the molecular weight ($\eta_S \sim N^{3.0\pm0.1}$). Strong evidences for reptation-like shear viscoelasticity have been also reported by Luap and Goedel for Langmuir brushes of end-tethered polyisoprenes[28]. In that work, the high values of the shear viscosity and the

amazing exponential dependence observed on the chain length ($\eta_S \sim \exp(N)$) are suggestive of a certain sequestration of the terminal disengagement process that, similarly to star-polymers, may be provoked by chain tethering at the interface. A much weaker, linear dependence ($\eta_S \sim N$) was reported by Sato *et al.*[29] from measurements of the shear viscosity of Langmuir monolayers of a highly hydrophobic polymer as expected for polymer pancakes. As little entanglement is expected for a polymer in poor-solvent conditions ($\nu = ½$) those results must be interpreted as an example of amoeboid-like motion rather than a proof of the absence of reptation in two dimensions, which would require better solvent conditions.

4. Conclusions

We have studied Langmuir monolayers of flexible polymers adsorbed at the air water interface and in good solvent conditions. The concentration and size dependence of the surface pressure is compatible with theoretical scaling laws. Ellipsometric determination of the layer thickness shows that they are much thinner than the 3D Flory radius, but thicker than the monomer size above Γ^*, consistent with the existence of a self-similar structure as postulated by de Gennes close to Γ^{**}. The dynamic behaviour of the dense polymer layers strongly depend on the chain length N. The relaxation after sudden compressions is characterized by relaxation times increasing as N^3 as in 3D reptation. The shear viscosity also varies as N^3, whereas the modulus is independent of N. The results are compatible with molecular transport governed by reptation motions. As in bulk, a crossover from a non-entangled to entangled systems is observed for $N_e \approx 100$. The logarithmic corrections predicted by de Gennes, on the basis of the existence of a self similar profile were not seen here, but the experimental accuracy was not sufficient to evidence the corresponding very small deviations to the scaling laws. We can conclude therefore that the behaviour observed represents the first experimental evidence of a relaxation phenomenology compatible with reptation motions in a polymer monolayer.

5. References

1. P.G. de Gennes, *Scaling Concepts in Polymer Physics*, (Cornell Univ. Press, Ithaca NY, 1979);
2. P.G.de Gennes, Dynamics of entangled polymer solutions. I. The Rouse model, *Macromolecules* **9**, 587 (1976); Dynamics of entangled polymer solutions. II. Inclusion of hydrodynamic interactions *ibid.* 594 (1976).
3. M. Rubinstein and R.H. Colby, *Polymer Physics* (Oxford Univ. Press, NY, 2003).
4. B. Duplantier and H. Saleur, Exact surface and wedge exponents for polymers in 2 dimensions, *Phys. Rev. Lett.* **57**, 3179 (1986).
5. P.G.de Gennes, Polymer solutions near an interface. 1.Adsorption and depletion layers *Macromolecules* **14**, 1637, (1981)
6. O. Guiselin, L.T.Lee, B.Farnoux and A.Lapp, Adsorbed polymers: Neutron reflectivity and concentration profiles, *J.Phys.Chem.*, **95**, 4632 (1991)
7. L. Auvray and J. P. Cotton, Self-similar structure of an adsorbed polymer layer: comparison between theory and scattering experiments, *Macromolecules***, 20,** 202 (1987)
8. P.G. de Gennes, Motion of polymer near a solid surface, in *Liquids at interfaces*, J. Charvolin, J.F. Joanny and J. Zinn-Justin edts. (Les Houches, Session XLVIII, Elsevier publishers) p311, 1988.
9. B. O'Shaughnessy and D. Vavylonis, Non-equilibrium in adsorbed polymer layers, *J. Phys.: Condens. Matter* **17**, R63 (2005).
10. S.C. Bae and S. Granick, Molecular motion at soft and hard interfaces, *Annu. Rev. Phys. Chem.* **58**, 553 (2007).
11. F. Monroy, F. Ortega, R. G. Rubio and M. G. Velarde, Surface rheology, equilibrium and dynamic features at interfaces, with emphasis on efficient tools for probing polymer dynamics at interfaces, *Adv. Colloid Interface Sci*. **134-135**, 175, (2007).
12. J. Brandrup, E.H. Immergut and E.A. Grulke, eds., *Polymer Handbook 4th ed.* (Wiley, New York, 1999).
13. M. Kawaguchi, Thermodynamic, structural and rheological properties of polymer-films at the air-water interface, *Prog. Polym. Sci.* **18**, 341 (1993).

14. A. R. Esker, C. Kim and H. Yu., Polymer monolayer dynamics, *Adv. Polym. Sci*. **209**, 59 (2007).

15. F. Monroy and D. Langevin, Interfacial Rheology of Polyelectrolytes and Polymers Monolayers at the Air-Water Interface, *Curr. Opin. Colloid Interface Sci*. (in press-2010).

16. F. Monroy, F. Ortega and R.G. Rubio, Dilatational rheology of insoluble polymer monolayers: poly(vinylacetate), *Phys. Rev. E* **58**, 7629 (1998).

17. P. Cicuta and I. Hopkinson, Scaling of dynamics in 2D semidilute polymer solutions, *Europhys. Lett., **68**, 65 (2004)*.

18. J.C. Marshall, J.C., T. Cosgrove, F. Leermakers, T.M. Obey, C.A. Dreiss, Detailed modeling of the volume fraction profile of adsorbed polymer layers using small-angle neutron scattering, *Langmuir*, 20, 4480 (2004)

19. F. Monroy, H. Hilles, F. Ortega and R.G. Rubio, Relaxation dynamics of Langmuir polymer films: a power-law analysis, *Phys. Rev. Lett.* **91**, 268302 (2003).

20. F. Monroy, S. Rivillon, F. Ortega and R.G. Rubio. Dilational rheology of Langmuir polymer monolayers: poor-solvent conditions, *J. Chem. Phys*. **115**, 530 (2001).

21. A.N. Semenov and A. Johner, Theoretical notes on dense polymers in two dimensions, *Eur. Phys. J E* **12**, 469 (2003).

22. S. Srivastava and J. K. Basu, Absence of reptation in highly confined polymers, J. Chem. Phys. **130**, 224907 (2009).

23. E. Spigone, G.Y. Cho, G.G. Fuller and P. Cicuta, Surface rheology of a polymer monolayer: effects of polymer chain length and compression rate, *Langmuir* **25**, 7457 (2009).

24. A. Maestro, F. Ortega, F. Monroy, J. Krägel and R. Miller, Molecular weight dependence of the shear rheology of poly (methyl methacrylate) Langmuir films: a comparison between two different rheometry techniques, *Langmuir* **25**, 7393 (2009).

25. C. Luap and W.A. Goedel, Linear viscoelastic behavior of end-tethered polymer monolayers at the air/water interface, *Macromolecules* **34**, 1343-51 (2001).

26. N. Sato, S. Ito and M. Yamamoto, Molecular weight dependence of shear viscosity of a polymer monolayer: evidence for the lack of chain

entanglement in the two-dimensional plane*, Macromolecules* **31**, 2673 (1998).

27. A. Maestro, D. Langevin and F. Monroy, Amorphous freezing in two dimensions: from soft coils to rigid particles, *Eur. Phys. J E* **31**, 89-94 (2010)

28. C. Luap and W.A. Goedel, Linear viscoelastic behavior of end-tethered polymer monolayers at the air/water interface, *Macromolecules* **34**, 1343-51 (2001).

29. N. Sato, S. Ito and M. Yamamoto, Molecular weight dependence of shear viscosity of a polymer monolayer: evidence for the lack of chain entanglement in the two-dimensional plane*, Macromolecules* **31**, 2673 (1998).

Chapter 2

Rheological behaviour of Poly (methyl methacrylate) Langmuir films: a *Percolation* description and *Glass* – like dynamics

Abstract

We have carried out an experimental study on the surface rheology of Langmuir monolayers of poly(methyl methacrylate) (PMMA) as a function of polymer concentration (Γ), Molecular Weight (M_w) and temperature (*T*). Indeed, both Dilational and Shear rheological techniques were used, covering a frequency range from 10^{-3} to 0.2 *Hz*. It was found that under *poor* solvent conditions, the polymer coils rearrange to form collapsed soft-disks (*pancakes*) at the interface. Therefore, the physical mechanism underlying the dynamics of the polymer chains have been interpreted in terms of the existence of a percolation transition of deformable PMMA pancakes. We have demonstrated the existence of a sol-gel transition which can be reached by increasing the polymer concentration above a critical packing fraction at constant Temperature. Here we show that the rheological behaviour of PMMA monolayers could be interpreted in terms of a percolation network with both *Central* and *Bond Bending* forces. Furthermore, we found in PMMA films remarkable hallmarks of the glass formation in molecular materials. Indeed, the existence of a glassy state has been pointed out by the Γ-dependence of the relaxation dynamics of the PMMA monolayers in terms of a *Vogel-Fulcher-Tamman* function. We found a fragile-behaviour for the percolated system which is strongly influenced by the underlying *energy landscape* associated to the structural configurations that it may adopt. As a final proof of our hypothesis come from the *T*-dependence of both equilibrium and rheological features.

1. Introduction

Polymer films at fluid interfaces have been the subject of extensive research for many years.[1] The reason for these studies is that the possibility to effectively confine the polymers in two dimensional systems appears important from both the theoretical and technological point of view.[2, 3] Polymer monolayers adsorbed at fluid interfaces are considered as a paradigmatic example for exploring soft matter physics at two dimensional topologies.[4]

For a Langmuir film compared to a bulk solution, the interface plays the same role as the solvent and the adsorption energy as the solvation interactions. Consequently, as for bulk solutions, it is possible to characterize the Langmuir polymer film by a "solvent quality" parameter which accounts for the balance between the polymer-interface adsorption interaction and polymer cohesion. For Langmuir polymer films, it is the quality of the air-water interface as a surface solvent for the polymer that defines the distinct conformational scenarios, from a swollen random-coil at good- to a near-collapsed chain at poor-solvent conditions. The results of high-frequency capillary-wave experiments reported by Esker et al. suggest that there is a strong correlation between the rheological behaviour of the film and the solvent quality of the air-water interface.[5, 6]

The equilibrium behaviour of poly (methyl methacrylate) (PMMA) films have been studied extensively by surface pressure-area isotherms,[5, 7, 8] surface light scattering,[6, 8] ellipsometry,[9, 10] atomic force microscopy[11, 12] and dielectric spectroscopy.[7] From these studies PMMA is known to adsorb at the air/water interface at poor-solvent conditions,[5, 8] thus PMMA Langmuir films might provide an adequate system for probing the shear properties of a two-dimensional arrangement of self-avoiding chains conformed as polymer pancakes. The dilational properties of PMMA monolayers have been previously studied from surface light scattering experiments.[13] Cardenas-Valera and Bailey[13] used the stress-relaxation method to study the dilational behaviour of Langmuir films of PEO/PMMA graft polymers. By using the torsion pendulum technique, Cardenas-Valera and Bailey[14] and Peng et al.[14] have also studied the interfacial shear rheology of PEO-*g*-PMMA spread at an oil/water interface. A strong correlation between the shear properties of the adsorbed film and emulsion stability was deduced in these works, particularly, emulsions with a higher interfacial shear viscosity were found to have a higher stability. This is due to the enhancement of the mechanical resistance of the interfacial film and their ability to respond to local variations in film thickness.[15]

To our knowledge only very few data have been published about the interfacial shear rheology of PMMA monolayers adsorbed at the air/water

interface. Using a torsion surface rheometer Peng et al.[16, 17] have studied Langmuir films of atactic PMMA with different molecular mass under different states of compression. While at low densities the torsion pendulum technique works well in oscillatory mode, at a certain stage of compression the interfacial shear viscosity became so large that the measuring body got stuck in the interfacial layer and the rotation mode had been employed. However, published data on the interfacial shear viscosity versus surface pressure dependencies show different slopes for different measuring mode, and therefore the experimental results have been discussed for the different states of compression separately. It was also shown that the viscosity depends on the molecular weight, where very small differences were observed when comparing data at the same surface pressure.

The aim of the present study is to get further insight in the dynamical behaviour of a two-dimensional arrangement of self-avoiding chains conformed as PMMA pancakes according to a *poor* solvent scenario. We thus studied the effects of surface concentration (Γ), chain length (N) and temperature (T) on the interfacial rheology of PMMA Langmuir monolayers and discuss it in structural terms. It will be pointed out that the rheological parameters follow scaling-law dependencies with Γ and N. A larger range of polymer weights were studied to demonstrate the universal behaviour found in the relation between the conformation of the PMMA monolayers and their dynamical characteristics. From a theoretical point of view, in the present work we corroborate the existence of a percolation transition of deformable soft polymer coils.[18] we thus explain in terms of scaling dependencies the relation between the shear and dilational rheological features and corroborate the conformational scenario proposed by means of the percolation approach. Here we find a description of dynamical behaviour of PMMA monolayers directly related to a percolation network with both *Central* and *Bond Bending* forces.[19-21] Furthermore, we report direct evidences of a glassy-like long time dynamics, which remained as an open question of the physics of polymer in confined systems. Indeed, the existence of a glassy-state appears as a reliable scenario for amorphous 2D solid. The relaxation experiments performed allow us to discover marked glassy-like features characteristics of *fragile* systems as *non-Debye* relaxation and *non-Arrhenius* Γ–dependence of relaxation times and viscosity. We found that PMMA monolayers had a crossover from single molecule to a collective dynamics as Γ increased at fixed temperature, which highlights the existence of a glass transition. It should be noted that similar results which corroborate ours were previously published in colloidal and polymeric systems.[22, 23] As a remark, the correlation between the equilibrium properties and dynamical behaviour is due to the fact that polymer at poor solvent conditions have monomer-monomer interactions largely exceed the adsorption energy, so the

pancake conformation promote the plausible existence of a percolation-glass transition. We must suggest that sol-gel transition explored by a percolation approach is compatible with the glassy-like features found in polymer monolayers. Thus, there is not any argument against the existence of 2D-glassy solids of amorphous matter like polymers or colloids at temperatures below the glass transition temperature.[24] Under these assumptions, recent experiments have further demonstrated that both temperature and density play relevant roles in the understanding of the glass transition.[25, 26] It is noteworthy that the mode-coupling (*MC*) model established by Ngai is useful describing the behaviour of systems wherein the motion of the structural units is constrained by mutual interactions.[27, 28] Moreover, a further description of cooperative motions depends on the existence of a length scale over which the dynamics are cooperative. Indeed, the cooperative rearrangement region (*CRR*) concept which measured the spatial scale where the system shows dynamic homogeneity had been defined.[4] Actually, recent studies showed that the influence of the thickness of polymer films on the glass transition is important.[29] The fact that monolayer thickness is smaller than the radius of gyration of the polymer coils leads to a dynamic heterogeneity which characterizes the glass transition.[30]

From the *T*-dependence of equilibrium properties we highlight the existence of a glass-transition temperature, $T_g \approx 25^{\circ}C$ value was significantly lower than the bulk $T_g \approx 105^{\circ}C$ for PMMA.[31] This behaviour could be explained because polymers in confined environments show deviations from their bulk properties. To further explore the glass-transition we also study the dependence of the film thickness, *h* with the temperature. We thus pointed out the existence of a T_g from the sharp crossover between the two linear dependencies of *h vs.T*. As a final proof of our hypothesis come from for the study of the dilational rheological behaviour of our system. We found that PMMA monolayers could be described by a *T*-dependence of the dilational viscosity by a *Vogel-Fulcher-Tamman* function in terms of a *fragility* glass former.[32] These results have been corroborated by the dilational elasticity dependence on T which show a further increase when the system is cooled below T_g.

2. Materials and Methods

2.1 Chemicals

The six different samples of poly (methyl methacrylate)-atactic (PMMA) used in this study were obtained from Polymer Source, Canada, with molecular weights ranging from 14×10^3 to 270.8×10^3 g·mol^{-1}. The microstructure of these atactic samples has the following percentages: syndio about 56%, hetero 38% and

iso 6%. Scheme 2.1 shows the constitutive unit of this polymer and the properties of these samples have been summarized in the Table 2.1. Chloroform (Sigma Aldrich, 99% of purity) was used as spreading solvent. The concentration of the spreading solution was 0.01mg/ml.

Scheme 2.1. Chemical structure of the repetitive units of poly(methyl methacrylate)

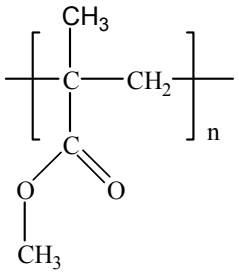

Double distilled and deionized water from a MilliQ-RG system was used to prepare the subphase, having a resistivity higher than 18mΩ·cm-1 and a surface tension of $\gamma = 72.6 mN \cdot m^{-1}$ at 20ºC. For the equilibrium measurements, the spreading solution was slowly applied by a micro syringe at different places onto the surface. The surface concentration was changed by subsequent additions of the polymer solution waiting adequate time to reach the equilibration of surface pressure. The temperature of the monolayers was controlled by a thermostat and a water jacket of the trough. Near the interface, the temperature was measured with a precision of 0.01ºC, and the temperature control was better than ±0.05 ºC. Care was taken to avoid any changes on the height of the monolayer during the experiments due to evaporation.

Table 2.1. Properties of different samples of *atactic*-poly(methyl metacrylate)

Commercial Name	M_w (10^3g mol^{-1})	M_n (10^3g mol^{-1})	M_w/M_n
PMMA10	270.8	146.4	1.85
P4938MMA	159	105	1.5
P3243MMA	104.3	64.6	1.61
P5177MMA	80	40	2.0
P7399MMA	30	21.5	1.4
P4943MMA	14	10	1.4

2.2 Methods

We studied the equilibrium features of PMMA monolayers by the surface pressure – surface polymer concentration (π–Γ) isotherms in a Langmuir trough. Structural information about the PMMA films was obtained by ellipsometry. The dynamical behaviour of our PMMA monolayers was studied by both dilational and shear rheological experiments covering a frequency range from 10^{-3} to 0.2 *Hz*.

We have taken advantage of dilational rheology by oscillatory experiments and relaxation ones performed in a Langmuir trough. Furthermore, to study the shear rheology, we used two different oscillatory rheometers using different principles of measurement, i.e working in the plate (ISR-1, Sinterface) and bi-cone (MCR301-IRS, Anton Paar) geometries. However, we demonstrated that they provide complementary and mutually compatible data. All the methods performed have been further described in the Appendix 1 (Methods summary).

3. Results and Discussion

3.1 Equilibrium Properties

Our experiment system consisted of PMMA of different molecular weights adsorbed onto the air-water interface at increasing surface concentration, Γ. Figure 2.1.a shows the surface pressure equilibrium isotherms Π – Γ for the PMMA monolayers at 23ºC. The isotherms display similar qualitative behaviour, however the shift observed towards lower surface concentrations at increasing the polymerization degree $N\ (=M_w/M_0)$ points out a strong influence of chain size on the conformational scenario formed by this flexible polymer.

Three well-defined concentration regimes are clearly visible in the log-log plots (see Figure 2.1b): (a) A diluted regime at low pressures ($\Pi<1 mN\cdot m^{-1}$), which displays an N-dependent shape as a consequence of the influence of the interchain pair potential. In this regime Π follows ideal-gas behavior at high dilution, $\Pi \sim \Gamma^1$. (b) At $\Gamma = \Gamma^*$, defined as the overlapping concentration, the adsorbed chains become into lateral contact and a semidilute regime is entered. From a structural point of view, the chains become strongly packed in this concentration regime ($\Gamma^* > \Gamma > \Gamma^{**}$), consequently Π strongly increases. (c) At $\Gamma > \Gamma^{**}$ the concentrated regime is entered. Here, the surface solvent is almost excluded and the film becomes purely polymeric. At this state ($\Gamma > \Gamma^{**}$) the isotherm reaches a plateau value corresponding to the saturation of the film. For the present system, no clear dependence of the plateau pressures on the molecular weight is observed ($\Pi_{plateau} \approx 16\pm1$ mN/m), suggesting the structural similarity of the concentrated regime with the bulky molten state, where chains mutually overlap and every one forgets its own entity in a continuous entangled state.

In the semidilute regime it is plausible to describe the Π – Γ isotherms as a power law, $\pi \sim \Gamma^y$, where $y = 2\nu/(\nu-1)$ and ν is the *2D-Flory* exponent.[7] From the linear slopes of the log-log plots the power-law exponent is obtained *ca.* $y \sim 10 \pm 2$ for all molecular weights. This is compatible with a value of the Flory exponent $\nu \sim 0.55 \pm 0.02$, corresponding to poor-solvent conditions, in agreement with previous experiments by Vilanove and Rondelez.[33] A strong proof of scaling is

highlighted by Figure 2.1d where all the Π–Γ isotherms in Figure 2.1a can be merged into a master curve where the semidilute regime is described by the universal law $\Pi = \Pi^* (\Gamma/\Gamma^*)^y N^0$, where *y=10* as suggest Kawaguchi.[31]

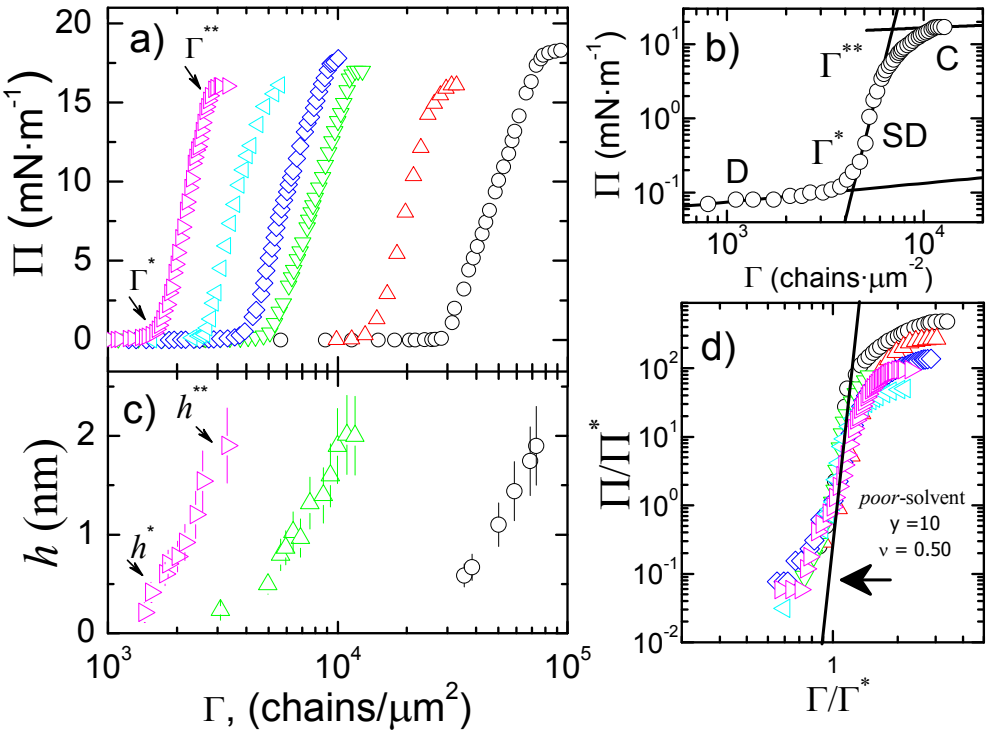

Figure 2.1. Equilibrium behavior of PMMA monolayers spread at the air-water interface at 23ºC. **(a)** Surface Pressure isotherms (π) as a function of the Surface concentration (Γ) of the Langmuir monolayers of PMMA. Symbols: M_W's in g·mol^{-1}; (○) 1.4·10^4; (Δ) 3·10^4; (▽) 8·10^4; (◊) 1.043·10^5; (◁) 1.59·10^5 and (▷) 2.708·10^5 obtained by the subsequent aliquot-addition method. **(b)**, The *log-log* plot points out three well-defined concentration regimes: diluted *(D)*, semidilute *(SD)* and concentrated (*C*). The overlapping concentration Γ^* separates the dilute from the semidilute regimes. Γ^{**} defines the onset of the concentrated regime. **(c)** Optical thickness obtained by ellipsometric measurements at different molecular weights; symbols as in (a). According to the thickness measured, PMMA monolayers are always at the sub-monolayer quasi-2D regime ($h<R_F$). **(d)** Universal scaling of the π–Γ isotherms when reduced with the coordinates of the overlapping point., the semidilute regime is described by the universal, *N*-independent, scaling law $\pi = \pi^* (\Gamma/\Gamma^*)^{d\nu/(d\nu-1)} N^0 \sim \Gamma^{10} N^0$ ($d = 10$, $\nu = 0.55$).

Another hallmark of the plausible scaling description is shown by Figure 2.2a which highlights the scaling behaviour of the limits of the semidilute regime, Γ^* and Γ^{**} with *N* as $\Gamma^* \sim N^{1-2\nu} \sim N^{-1}$ in agreement with the exponent previously found. It is noteworthy that Γ^* has fundamental importance because it provides direct experimental values for the Flory radius of the coils:

$$\Gamma^* = \frac{1}{\pi R_F^2} \qquad (2.1)$$

This is defined as the hydrodynamic radius of an isolated polymer coil, which gives an idea of the molecular dimensions in the monolayer. Figure 2.2b shows as the experimental values of R_F scales with the chain length as Eq. 2.1. Experimentally a scaling regime is found as $R_F \sim N^{0.55\pm0.02}$. The Flory exponent $\nu \sim 0.55 \pm 0.02$ is found compatible with *poor*-solvent conditions, which is structurally compatible with a flat coiled conformation as near-collapsed pancakes for which intrachain interactions dominates over polymer-surface forces. The *Kuhn* length found, $a \approx 0.22 \pm 0.02 nm$ is close to the monomer size, in agreement with this value in the literature.[30]

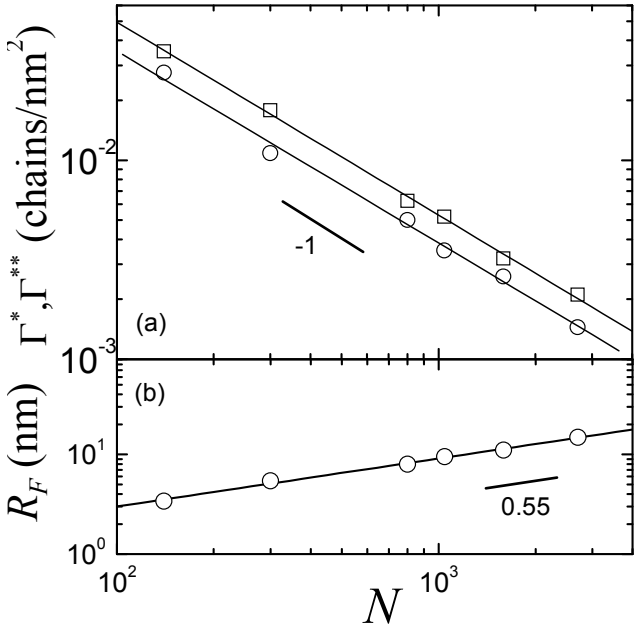

Figure 2.2. (a) Overlapping concentration, Γ^* (○) and double overlapping packing fraction, Γ^{**} (□) as a function of the chain length (*N*). *N*-dependence follows from scaling arguments: $\Gamma^* \sim N^{1-2\nu}$ where the scaling exponent $\nu \sim 0.55$ takes a value equal to the 2D Flory's exponent. **(b)** Flory radius, R_F as a function of N. Data are well described by a scaling law $R_F \sim N^{0.55}$ with a critical, characteristic for Langmuir films at *poor*-solvent conditions.

Other piece of evidence for this structural scenario comes from the ellipsometry experiments of the averaged film thickness, *h*. Figure 2.1c shows *h* as a function of the increasing Γ for three different monolayers of PMMA. These data clearly show the *quasi*-2D character of PMMA conformations. PMMA *ultra*-thin films are always at the sub-monolayer quasi-2D regime ($h<R_F$). At Γ^* all monomers are adsorbed building a thin monolayer as shown the values of $h^* \approx a \approx$ 0.22nm. At Dense states ($\Gamma>\Gamma^*$) the monolayer was built up much more than one monomer thicker films ($h>a$) but more or less compatible with flatten conformations ($h \leq R_F$) characteristics of soft flexible coils. Ellipsometric results show clearly that h^{**} is the same for all polymer weights instead of R_F which

increase with *N* as shown Figure 2.2b. Therefore, higher molecular weights favour a thicker conformation with more segments of polymer attached to the water surface as a result entropically rich, and short chains, for which entropy penalty is relative small, have tendency to be less dense. These results constitute a proof of the existence of 2D pancake-like configuration in all the polymer weights.

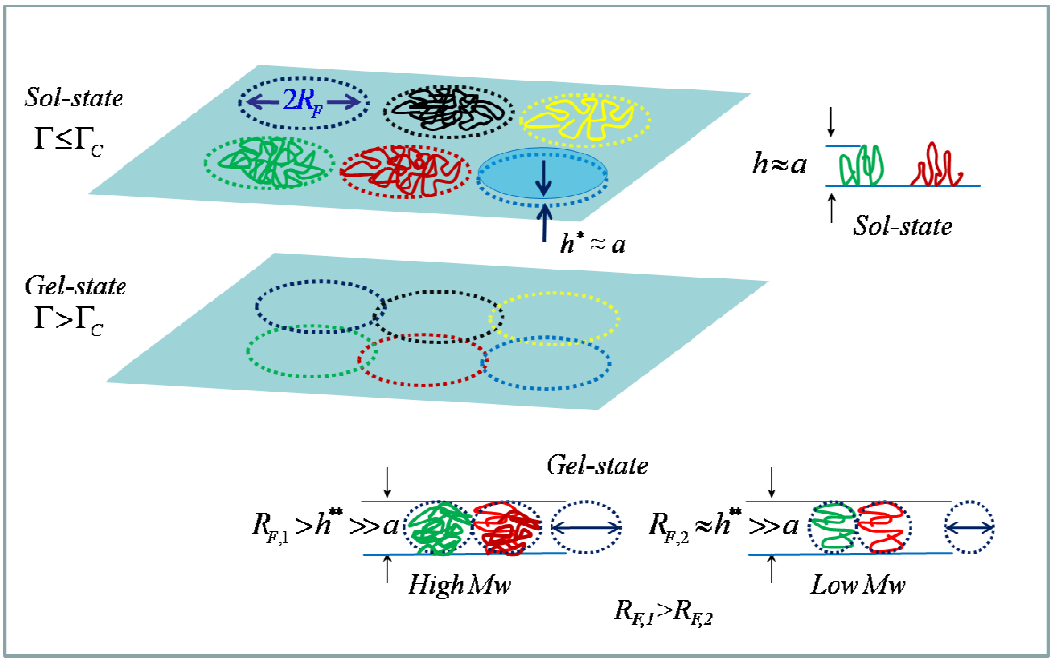

Figure 2.3. Picture of the conformational scenario for Langmuir monolayers of PMMA at *poor* solvent conditions in the air-water interface. **(a)** In the sol-state, below the overlapping concentration viewed as a percolation treshold ($\Gamma_c \approx \Gamma^*$), the polymer chains adopt a flat coiled conformation as a *pancake* as a result of the dominance of the intrachain interactions over polymer-surface ones. Every pancake show a flattened conformation where it thickness is similar to the monomer size but much smaller than the in-plane dimensions ($h^* \approx a << R_F$). **(b)** Above the percolation threshold (Γ_c) although chain overlap and entanglements are not possible, the domain occupied by an individual pancake came into contact with the domains of neighbour chains forming a percolated gel regime. At concentrated regime the thickness is larger than the monomer size and relative close to the in-plane dimensions ($a < h^{**} \leq R_F$). Expecting behavior for a *poor*-solvent scenario. Two different polymer weights have been proposed ($M_{W,1} > M_{W,2}$) suggesting that higher molecular weights favour a thicker conformation as a result entropically rich, and short chains, have tendency to be less dense; however in both situations the pancake conformation is plausible hypothesized due to the existence of similar *thickness at* Γ^{**}.

It is noteworthy that the *poor*-solvent character of the air-water interface for PMMA has been evidenced, as deduced from values of the Flory exponent, calculated from the Γ-dependence of the surface pressure ($\Pi \sim \Gamma^{10}$, thus $\nu = 0.55 \pm 0.02$) and from the chain dimensions deduced from Γ* ($R_F \sim N^{0.55}$). From these data the flatten pancake conformation is expected.[5, 8] This structural picture agrees with the conclusions drawn by Yu[18] about the influence of solvent quality on the structure and dynamics of insoluble polymer monolayers. Because each chain excludes out its own volume, PMMA monolayers above Γ^* can be

structurally conceived as a percolation network, viewed as a disordered gel phase of connected chains thus characterized by a finite shear modulus, *G*. Indeed, when the monolayer is compressed from the diluted state a sol-gel transition is expected at a percolation threshold in the polymer fractional area defined as $\phi=NA_0/A=A_0\Gamma$, as the ratio of the occupied are by *N* pancakes at the available surface Area, *A*.[34] It is noteworthy that in Langmuir monolayers of polymers, a chain can be considered as an individual pancake with surface area, $A_0=1/\Gamma=\pi R_F^2$. Therefore, if ϕ is increased above a critical packing fraction ϕ_c, the polymer coils come into random physical contact and form an interconnected 2D–network.[35]

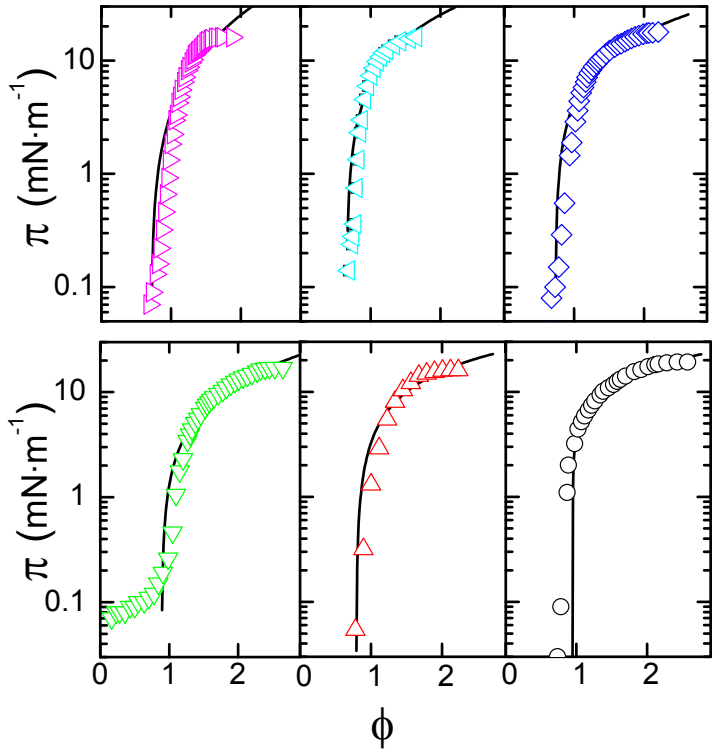

Figure 2.4. Experimental isotherms of Figure 1.a re-plotted in terms of the fractional area occupied by the polymer ϕ ($\phi = A_0/A = A_0\Gamma$). Below a percolation threshold, $\phi < \phi_C$, the isotherms obey gas-like behavior. Above ϕ_C the π–data follow the prediction from the Princen's equation (Eq. 4.2) for $\phi_C = 0.78$. (Experimental data as in Figure 2.1)

To get further insight in the percolation scenario proposed for the PMMA pancakes at *poor* solvent conditions in the air-water interface, it is schematically highlighted in Figure 2.3. For the percolated network proposed, we have re-plotted the experimental Π–isotherms as a function of the fractional area, ϕ as shown Figure 2.4. This plot thus point outs the existence of a crossover from a diluted regime to a percolated one at Γ^* can be plausibly hypothesized. At the percolation threshold, $\phi_c \sim 0.78$, close to the random-lattice close packing, the surface pressure is characterized by a sudden increase typical of a percolation network of compressed circles.[36-38] Beyond the percolated threshold, $\phi > \phi_c$, Π

can be plausibly described by the *Princen's* equation of state of a disordered 2D array of soft disks:[20]

$$\pi(\phi)/(\sigma/R) \sim \left(\frac{\phi}{\phi_c}\right)^{1/2} (\phi - \phi_c)^f \qquad (2.2)$$

where the elemental interaction energy σ/R is governed by the lateral contact between neighbouring discs (σ is a line tension and R the circle radius). We have included in Figure 2.4 a prediction from the Princen's equation for each polymer weight studied, which reproduces rather well the experimental π–ϕ isotherms, making plausible the sketched percolation scenario.

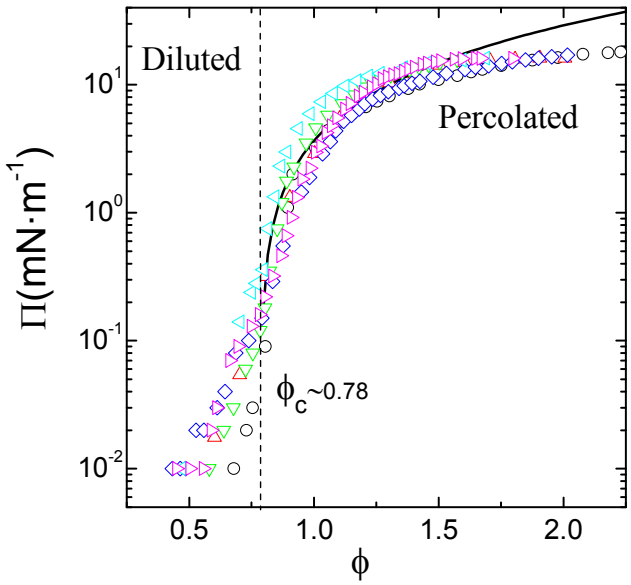

Figure 2.5. Master plot of π–ϕ isotherms of Figure 2.4. Above ϕ_C, π–data follow a prediction from the Princen's equation (Eq. 4.2) for $\phi_C = 0.78$. (Experimental data as in Figure 2.4)

We have demonstrated that above ϕ_c Eq. 4.2 is closely obeyed for all the polymer weights studied. Indeed, our experimental fits display the same percolation power-law behaviour is found, $\pi(\phi) \sim (\phi - \phi_c)^p$ with $p \approx 1.3 \pm 0.3$. This universal exponent found can be corroborated by the fact that all of the π–ϕ isotherms merge in a near-universal isotherm dependent on the on the *re*-scaled density ϕ as points out Figure 2.5. To test the universality behaviour, we thus have proposed in Figure 2.5a prediction from the Princen's equation with the universal exponent $p \approx 1.3$ taking plausible values of $\sigma \approx 10^{-9}$N, $R \approx 10$nm, the ratio $\sigma/R \approx$ 100mN/m. In the context of the percolation theory, we thus explain this power-law at $\phi > \phi_c$ as a consequence of ϕ increases the pancakes deform, increasing their contact perimeter and hence the energy of the system; it leads to the system to store interfacial energy. The Laplace pressure σ/R, where σ is the line tension and R the pancake radius) would be an approach of the characteristic energy

required to deform the pancakes. Therefore, the power-law $\Pi \sim (\phi - \phi_c)^{1.3}$ is rather compatible with a *central-force* problem as driven by rotationally-invariant osmotic forces independent of the coil size and primarily determined by entropy.[20, 39] We thus viewed the polymer-pancakes similarly to a pure entropic network.[40]

3.2 Oscillatory dilational viscoelasticity

We have performed oscillatory-barrier experiments on PMMA monolayers to study the dilational viscoelasticity of these systems. They are used to get insight on the material response functions of polymer films in linear and non-linear regimes. Therefore to test for non-linear elastic effects, the strain amplitude (*u)* was changed from 0.01 to 0.50 keeping constant the amplitude frequency, ν of $0.1 s^{-1}$. Figure 2.6a–b shows the stress (σ) as a function of the strain applied (*u*) for two different PMMA monolayers (M_w*'s* = $2.708 \cdot 10^5$ and $1.4 \cdot 10^4$ *g·mol*$^{-1}$) within the semidilute regime, $\Gamma > \Gamma^*$, concretely at $\pi \approx 8mN/m$.

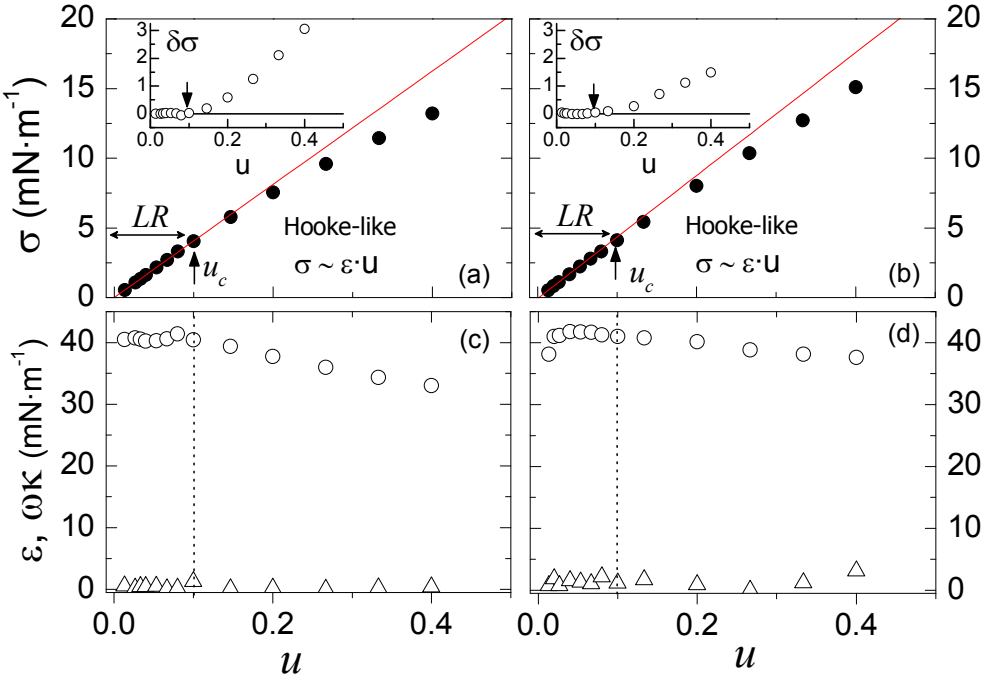

Figure 2.6. Experimental stress–strain (σ–*u*) curves of the Langmuir monolayers of PMMA at π=8mN/m obtained by the oscillatory experiments. Concretely: (a) $2.708 \cdot 10^5$; (b) $1.4 \cdot 10^4$ g·mol^{-1}. The region defined by *u<10%* characterizes the Hooke-like regime. The straight lines show the linear fits performed in this regime which represent Hookean behavior ($\sigma = \varepsilon_{hooke} \cdot u$). The Insets in a) and b) show well the linear regime (*LR*) of the σ–*u* curves. (c) and (d) show respectively the elasticity modulus, ε (○) and the loss modulus, ωκ (Δ) for each monolayer studied in (a) and (b). It is found the same dilational storage modulus and loss modulus in both cases (ε>ωκ). Beyond the linear regime the storage modulus decays as the strain increase.

Note that negative deviations from the linear elastic response viewed as plastic effects appear clearly in the two systems above a strain of 0.1 (u_c). Thus; this linear elastic response of the system can be explained in terms of a Hooke-like elastic modulus ε_{Hooke} defined as $\sigma = \varepsilon_{Hooke} \cdot u$ with constant ε independent of the applied strain. The insets in Figure 2.6a-b show the difference between the experimental strain and the one obtained by fitting ($\delta_\sigma=\sigma_{fit}-\sigma_{exp}$). They allow us to identified well the linear regime in both monolayers. Thus, it is important to note that we found the same linear regime in the two monolayers studied which represent the two limit cases of PMMA weight. A *yield stress* is observed in both of these $\sigma-u$ curves, *i.e.* their intercept at the origin is not zero in all cases ($\sigma \rightarrow 0$ when $u \rightarrow 0$) as expected for an elastic body free of plastic effects. Then, the strength of this plastic-plateau is characterized by the yield-stress extrapolated at zero strain. This plastic-like feature found is characterized by a decrease of the u^n-dependence of the response, from the Hooke-like $n = 1$ behaviour, characteristic of the linear regime ($u_C > u \rightarrow 0$), to a weaker $n \leq 1$ dependence at $u > u_C$. Here, the film becomes softer than at lower strains, *i.e.* the effective elasticity modulus (ε), obtained from the $\sigma-u$ curves decreases as the film is strained as shown in Figure 2.6c-d. From a phenomenological point of view this means that when the pseudo-plastic plateau is entered, a large deformation does not need a proportionally higher applied force, $f \sim \sigma$, or conversely, small changes in f produce large plastic-like deformations. Furthermore, the Figure 2.6c-d show the loss modulus calculated ($\varepsilon'' = \omega\kappa$). It should be mention that the values of ε'' are found lower than ε' ones for all the cases studied, even for $u > u_c$ as expected for a *solid*-like monolayer.

From this point, we have studied the structural resistance of the PMMA monolayers against a dilational deformation to evaluate the rigid character of these films. Moreover, we have been able to characterize the fluid-to-solid transition as a mechanical rigidity emerging above Γ^*. For these aims we have carried out oscillatory experiments at a frequency and strain rate compatible with the linear response. Thus the strain amplitude was fixed at 4% and the frequency ranged from 0.001 to 0.2 s^{-1}. Figure 2.7 shows the values of the dilational viscoelasticity parameters calculated, ε', ε'' and κ as a function of the frequency (ν) at different surface pressures (π*'s*) above Γ^* of a PMMA monolayer with $2.708 \cdot 10^5 g \cdot mol^{-1}$.

The storage modulus, ε' are higher than the loss one, ε'' in the interval of frequencies studied as well as in all the increasing π's regimes studied which demonstrates the solid character of the PMMA monolayers. Furthermore, the increase of the mechanical rigidity above Γ^* is due to the existence of a dense

monolayer arrangement according to the previous conformational scenario proposed. For the sake of comparison, we also have included in the Figure 2.7 the experimental values of the equilibrium elasticity, ε_0. The values of storage modulus, ε' obtained has found higher than the equilibrium ones which clearly indicates that the monolayer have viscoelastic character. As expected, the low frequency limit of the dilational elasticity $\varepsilon'(w \rightarrow 0)$, extrapolates rather well the value of ε_0 and the loss modulus extrapolates to a near-zero value which indicate the absence of relaxation processes when the deformation is slow enough ($w < 0.001 s^{-1}$).

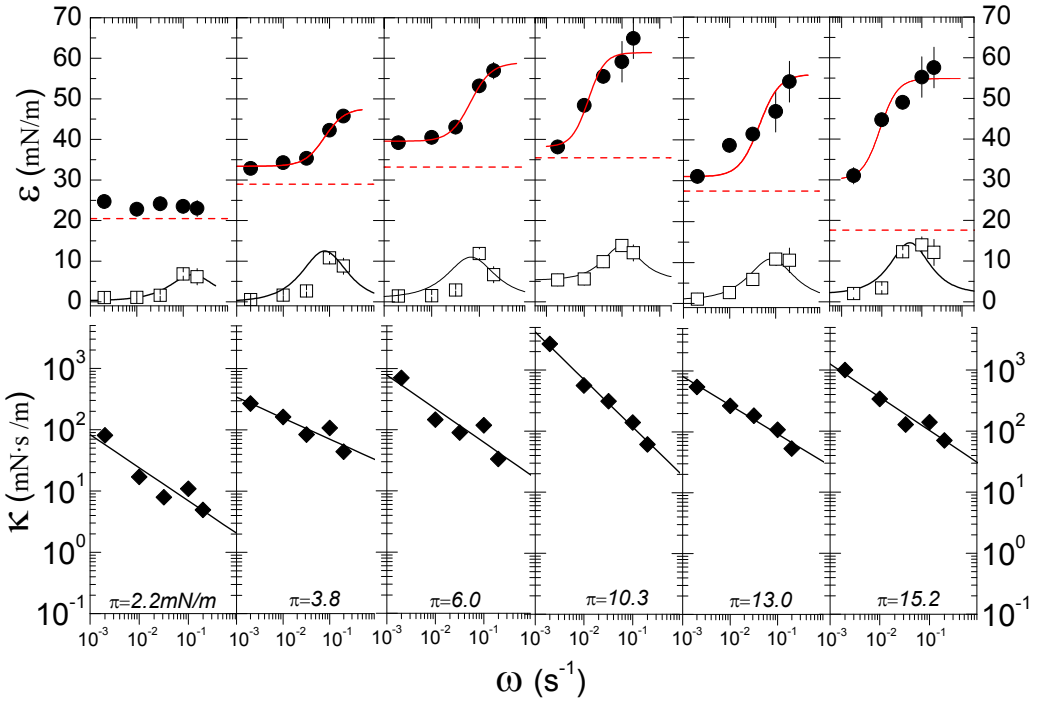

Figure 2.7. Dilational viscoelasticity behaviour of the PMMA monolayer ($2.708 \cdot 10^5 g \cdot mol^{-1}$) as a function of the frequency (ν) for different surface concentration regimes obtained by oscillatory experiments. Symbols: (●) Elasticity modulus, ε'; (□) loss modulus, ε'' = ωκ and (♦) Viscosity, κ. For comparison, the equilibrium elasticity (ε_0) for each regime has been showed calculated from the π–Γ isotherm (---). In all the surface concentration regimes ε is larger than ε_0. The experimental results (ε and ωκ) have been fitted by Maxwell relaxation modes. The straight lines exhibit the linear relation between κ and ν. Therefore PMMA monolayer exhibit a *dilational-thinning* ($\kappa < \omega^{-f}$; $f \approx 0.5 \pm 0.1$) typical of non-Newtonian behaviour in all the regimes studied.

The relaxation behaviour observed for ε', ε'' of different π-regions above Γ^* may be due to the rearrangement of the density distribution of a collection of individual coils on the surface. Therefore, it may be plausible to fit the observed viscoelastic relaxation to a Maxwell-type dependency, which the expected ω-functionality of the dilational modulus is given by [41, 42]:

$$\tilde{\varepsilon}(\omega) = \varepsilon(\omega) + i\omega\kappa = \varepsilon_0 + \varepsilon_1 \frac{\omega^2\tau^2 + i\omega\tau}{1 + \omega^2\tau^2} \qquad (2.3)$$

The viscoelastic relaxation in Eq. 2.3 is described by two parameters: ε_1 accounts for the amplitude of the relaxation process and τ is the relaxation time. All the results obtained from the fits have been summarized in the Table 2.2. It should be note that the increase of the relaxation time with the surface pressure can be quantitatively explained considering the Γ-dependence of the dilational properties trough a power-law description which is shown in Figure 2.8.

Table 2.2. Parameters of the Maxwell-Relaxation processes

π (mN/m)	$\varepsilon_0 \pm 0.5$ (mN/m)	$\varepsilon_1 \pm 0.75$ (mN/m)	$\tau \pm 3$ (s)
2.2	25	12.8	6.3
3.8	33.4	14.3	12.8
6.0	39.5	19.4	15.2
10.3	38.2	23.3	77.8
13.0	34.3	18.6	88.8
15.2	30.1	24.9	110.2

An additionally piece of evidence of the *non-Newtonian* behaviour of the PMMA monolayers is pointed out by the below panel in Figure 2.7 where the experimental values of the surface dilational viscosity κ, obtained from the phase-difference between the experimental stress response decreases with increasing ν. This "*thinning-behaviour"* characteristics of a *non-Newtonian* response of the system might be explained by the power law: $\kappa \sim \omega^{-f}$, where $f \approx 0.5 \pm 0.1$ suggesting a solid-like description of the system. These exponents found characteristics of a weak κ-dependence with ω are consistent with a soft glassy rheology model proposed for materials close to the glass transition.[43] A similar power-like behaviour have been obtained for shear rheology performed in proteins monolayers with a similar conformational picture.[16]

To explore the Γ-dependence of ε, we performed experiments restricted to the semidilute regime ($\Gamma > \Gamma^*$) under identical conditions, i.e. frequency of 0.1 *Hz* and strain amplitude at 4%, rather compatible with the linear response previously defined. Figure 2.8 shows the dilational elasticity modulus ε' as function of the surface concentration, Γ for three different molecular weights studied at a frequency of the sinusoidal dilatation of 0.1*Hz*. For each M_w, the dilational modulus is found strongly dependent on Γ, exhibiting a power-law behaviour as $\varepsilon' \sim \Gamma^{y'}$. The power law exponent is found to be $y' \approx 11 \pm 2$, irrespectively of the molecular weight of the polymer sample. This value is very reproducible for the different PMMA monolayers, thus suggesting a strong correlation between dilational elasticity and molecular packing. Note that the scaling description of ε' is not suitable in the concentrated regime ($\Gamma > \Gamma^{**}$) where is not be allowed according to the de Gennes theory.[30] For the sake of comparison the values of compression modulus, ε_0 (calculated from the slope of the $\pi - \Gamma$ isotherms) are

plot also in Figure 2.8 as a function of Γ. It should be take into account that the same power-law behaviour is found for the dilational elasticity and the equilibrium elasticity, ε_0 which is in agreement with the *de Gennes* scaling-law described as $\varepsilon_0 = \Gamma(\partial\Pi/\partial\Gamma) = y\,\Pi \sim \Gamma^y$.[30] Further insight into the scaling behaviour found leads us to demonstrate the strong dependence of dilational and equilibrium viscoelasticity is based in a percolated scenario formed by polymer gels at poor-solvent conditions; where above the overlapping threshold, all the viscoelasticity moduli increase strongly with polymer concentration.

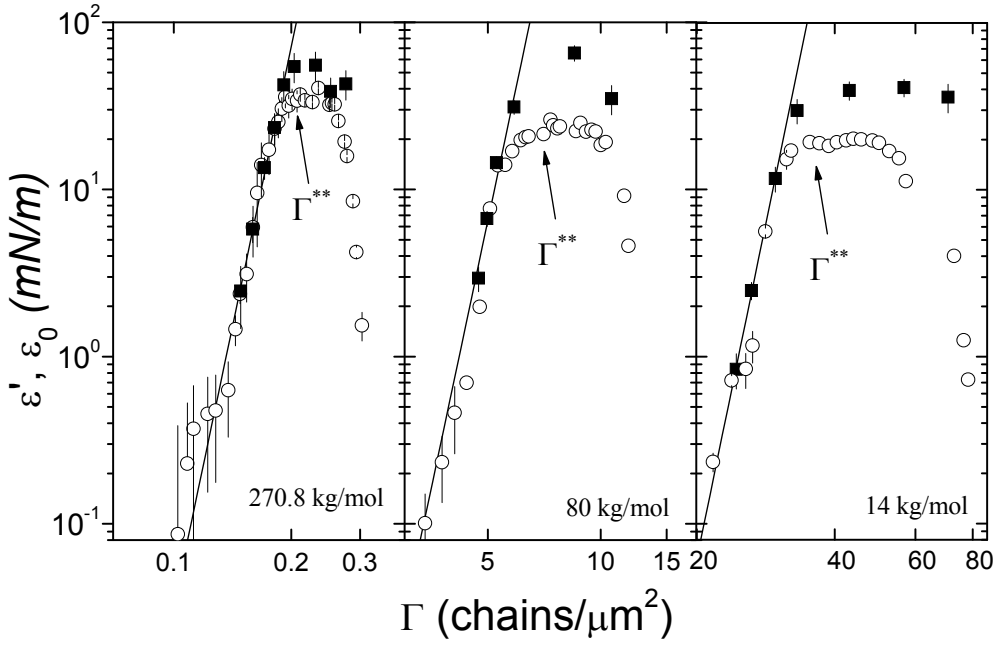

Figure 2.8. Dilational Elastic modulus, ε' (■) and Equilibrium elasticity, ε_0 (○) as a function of the polymer concentration from the semidilute to concentrate regime. Each panel corresponds to a sample with different molecular weight; from left to right: $2.708\cdot10^5$, $8\cdot10^4$ and $1.4\cdot10^4$, in g·mol^{-1}. Straight lines represent power-law fits against the polymer concentration, ε_0, $\varepsilon' \sim \Gamma^y$ with exponent *ca.* 11±2 in all cases.

3.3 Shear viscoelasticity

The interfacial shear storage modulus *G'* and the interfacial shear loss modulus, *G''* have been studied as a function of the surface concentration Γ for the PMMA monolayers with different molecular weights. Two different rheometers using different principle of measurement have been used: the ISR-1 working in the free oscillatory regime of the ring and the MCR301-IRS exerting a forced oscillatory stress on a biconical disk. At $\Gamma < \Gamma^*$ the shear parameters vanishes at values smaller than the instrumental sensibility, as expected for a diluted solution. The experiments have been restricted to the semidilute regime, between Γ^* and Γ^{**}. Experiments have been carried out under identical experimental conditions, at a frequency and strain rate compatible with the linear

response. In both experiments frequency was fixed at 0.7rad·s^{-1} and the strain amplitude at 4%.

Figure 2.9 shows the interfacial shear storage modulus *G'* as function of the surface concentration for six different molecular weights studied. Experimental values of *G'* are found between 10^{-4} and 15 mN·m^{-1}, at high concentration and molecular weight. Values of the shear modulus lower than 10^{-4} mN·m^{-1}, below the sensitivity limit of the ISR-1 rheometer, are not adequately resolved. Values higher than 1 mN·m^{-1} are measured with the MCR301-ISR rheometer. Because data measured with the two rheometers are quantitatively identical, both techniques can be considered to produce complementary and reproducible measurements. For each M_w, the shear modulus is found strongly dependent on Γ, exhibiting power-law behaviour as $G' \sim \Gamma^{y'}$. The power law exponent is found to be $y' \approx 10$, irrespectively of the molecular weight of the polymer sample. This value is very reproducible for the different PMMA monolayers thus suggesting a strong correlation between shear elasticity and molecular packing. As discussed below, if data at equal packing (constant Γ) are compared, the shear modulus shows a strong increase with the molecular weight. Indeed, our results confirm that the system supports shear elasticity which eventually becomes similar to hydrostatic compression at molecular weights high enough.

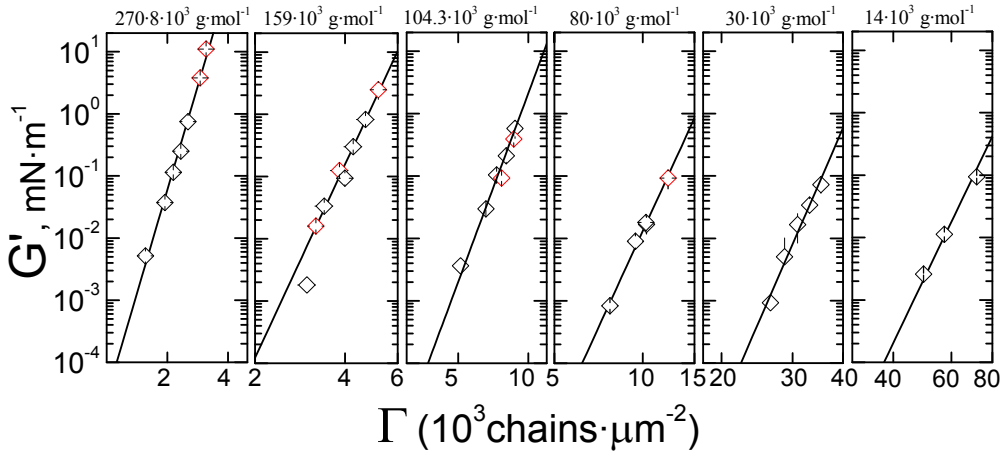

Figure 2.9. Shear elasticity, *G'* as a function of the polymer concentration in the semidilute regime. Each panel corresponds to a sample with different molecular weight; from left to right: 2.708·10^5, 1.59·10^5, 8·10^4, 3·10^4 and 1.4·10^4 in g·mol^{-1}. Measurements were made with two different rheometers: (◇) *ISR* from *Sinterface* and (◇) *MCR301* from *Anton Paar*. Straight lines represent power-law fits of the shear modulus against the polymer concentration, $G \sim \Gamma^{y'}$, with exponent *ca.* 10±1 in all cases.

Figure 2.10 shows the shear loss modulus, *G''* as a function of the surface concentration. For comparison, data corresponding to two different rheometers are plotted. The lower *G''* values were measured with the more sensible ISR-1 rheometer while all values higher than 1mN·m^{-1} were measured with the

MCR301-IRS. Data obtained by the two different devices are found in quantitative agreement. Similarly to the storage modulus, the shear viscous losses display power-law behaviour $G'' \sim \Gamma^{y''}$, with an experimental exponent *ca.* 10 for all molecular weights. It is noteworthy that for a given packing state, values of the loss modulus are found similar to the shear elasticity, *i.e.* $G' \approx G''$. As for G', the absolute values of G'' are found strongly dependent on the molecular weight.

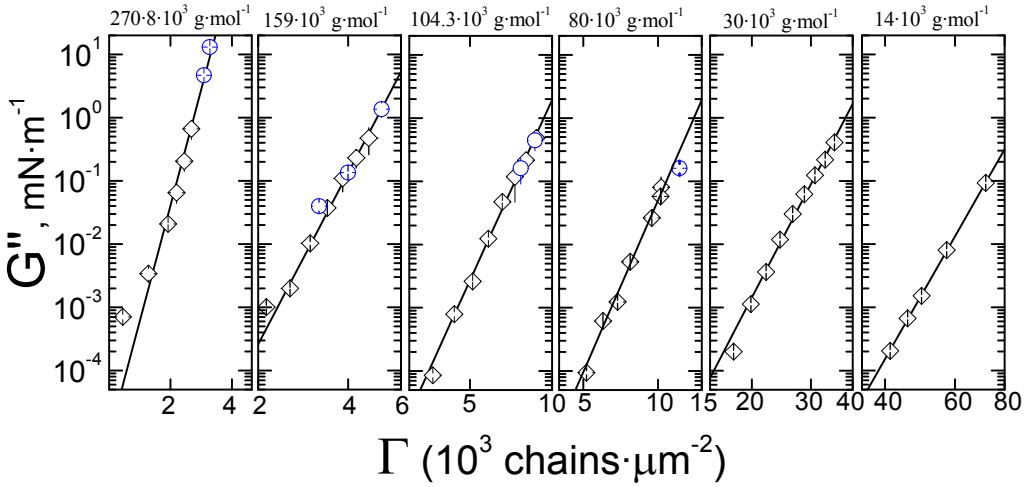

Figure 2.10. Shear loss modulus, G'' as a function of the polymer concentration in the semidilute regime. Each panel corresponds to a sample with different molecular weight (as in Fig. 3). Measurements were made with two different rheometers: (◇) *ISR* from *Sinterface* and (○) *MCR301* from *Anton Paar*. Straight lines represent power-law fits of the shear modulus against the polymer concentration, $G \sim \Gamma^{y''}$, with exponent *ca.* 10±1 in all cases.

Figure 2.10 shows the shear loss modulus, G'' as a function of the surface concentration. For comparison, data corresponding to two different rheometers are plotted. The lower G'' values were measured with the more sensible ISR-1 rheometer while all values higher than 1mN·m^{-1} were measured with the MCR301-IRS. Data obtained by the two different devices are found in quantitative agreement. Similarly to the storage modulus, the shear viscous losses display power-law behaviour $G'' \sim \Gamma^{y''}$, with an experimental exponent *ca.* 10 for all molecular weights. It is noteworthy that for a given packing state, values of the loss modulus are found similar to the shear elasticity, *i.e.* $G' \approx G''$. As for G', the absolute values of G'' are found strongly dependent on the molecular weight.

The absolute values of the shear parameters found here are similar to those previously reported by Saccheti et al.[44] for Langmuir films of poly(*tert*-butyl methacrylate). These results measured by canal viscosimetry actually correspond to a polymer at good-solvent conditions. Several groups have reported shear parameters for Langmuir protein films.[45-47] Those data are quantitatively similar to the shear viscoelasticity reported here.

3.4 Dilational and Shear Viscoelasticity: A scaling description

The analysis of the experimental surface viscoelasticity of polymer monolayers leads to gain better insight into the dynamics of structural changes occurred in the monolayer film. Therefore, changes in area are controlled by the dilational modulus, $\varepsilon'$and if the area is kept constant, the shape of the interfacial area is controlled by the shear modulus, G'. As expected from the dynamical behaviour previously shown, we could highlight the existence of a clear correlation between the shear and dilational mechanical behaviour of PMMA monolayers with different weights and the quality of the interface pointed out by the *Flory* exponent. To demonstrate this fact, we thus plot the Γ-dependence of the dilational elasticity modulus, ε, the hydrostatic compression modulus, ε_0 and the shear elasticity, G for three different molecular weights studied at a frequency of 0.1*Hz*. It should be note that similar strong power-law behaviour is found for the dilational elasticity and the shear one suggesting a similar energetic mechanism ($\varepsilon', G' \sim \Gamma^{10\pm2}$). Furthermore, the shear and dilational viscoelastic response is found similar to the equilibrium elasticity, ε_0 which is well known that scales rather well with Γ.[33, 48]

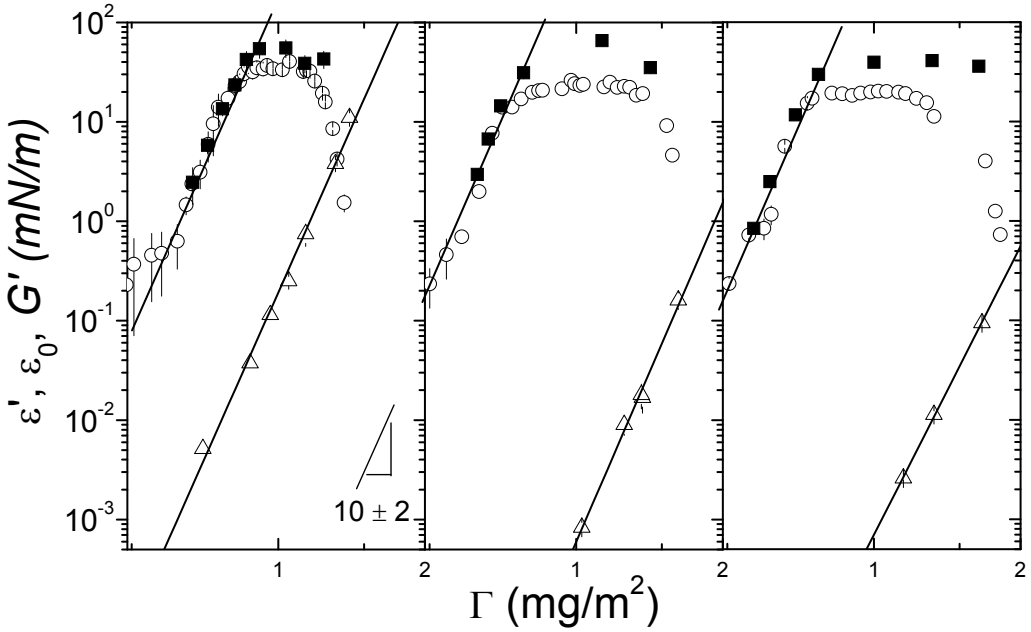

Figure 2.11. Dilational Elastic modulus, ε' (■) and Equilibrium elasticity, ε_0 (○) as a function of the polymer concentration from the semidilute to concentrate regime. Each panel corresponds to a sample with different molecular weight; from left to right: $2.708 \cdot 10^5$, $8 \cdot 10^4$ and $1.4 \cdot 10^4$, in g·mol^{-1}. Also these experimental results have been compared with the Shear one, G' (Δ). Straight lines represent power-law fits against the polymer concentration, ε_0, ε' and $G \sim \Gamma^{y'}$, with exponent *ca.* 10±2 in all cases.

Further insight into the scaling behaviour found leads us to demonstrate the strong dependence of dilational and shear viscoelasticity is based in a percolated scenario formed by polymer gels at *poor*-solvent conditions; where above the overlapping threshold, all the viscoelasticity moduli increase strongly with polymer concentration. Moreover, the power-law exponents are found close for every mechanical property (ε', G' and ε_0), a similar compositional mechanism for energy storage can be hypothesised under shear and compression.[49] However, while the values of ε and ε_0 are found to be essentially independent of the molecular weight, those of G' display a strong increase for larger M_w's. Consequently, for molecular weights high enough shear and compression elasticity are found progressively similar (see Fig. 2.11). Furthermore, while ε and ε_0 is found to be essentially chain-size independent, ε , $\varepsilon_0 \sim N^0$, G' displays scaling behaviour. As discussed below, if data at equal packing (constant Γ) are compared, the shear modulus shows a strong increase with the molecular weight. Our results confirm that the dilational modulus dominates the viscoelastic response but the system also supports shear elasticity which eventually becomes similar to hydrostatic compression at molecular weights high enough. The dominance of dilational over shear is a well-known fact already described for different surface systems in the classical textbook by Edwards, Brenner and Wasan.[50] Recently, this dominance also has been discussed for protein monolayers by Cicuta and Terentjev.[45]

Because the power-law exponents are found close for every mechanical property (G', ε and ε_0), a similar compositional mechanism can be hypothesised under shear and compression, not only for energy storage but also for dissipation. On the other hand as discussed above, in the semidilute regime shear parameters correlate with chain size but compression is found independent on the molecular weight, $\varepsilon \sim N^0$. In other words, the shear elastic energy is strongly influenced by changes in chain-shape or distortions of the two-dimensional percolated gel. However, lateral compression is neither sensible to chain size nor to the relative distance between chains. Contrarily to entangled gels, for which hydrostatic and shear elasticity are governed by a N-independent distance between entanglement points, a percolation network supports shear elasticity which is ultimately governed by the size of the structural unit. The observed elasticity suggests the plausibility of the percolation scenario instead of the entangled gel-like typical of polymers at good-solvent conditions. A plausible explanation for the strong power-law dependencies found above the percolation threshold is the high cooperativity between the interacting pancakes in the percolation network.

3.5 Percolated properties of viscoelasticity of PMMA films

The solid character of a Langmuir monolayer might be characterised by a structural resistance against a shear deformation; we thus have taken advantage of shear rheology to characterise the fluid-to-solid transition as a mechanical rigidity emerging above a critical packing ϕ_C. In the context of the classical percolation theory,[18] this sol-gel transition is defined as a geometrical packing process primarily driven by lattice connectivity which is proportional to the fraction of gel phase ($\phi - \phi_C$). In random percolation networks, near the percolation threshold ϕ_C, the effective connectivity scales as $(\phi - \phi_C)^f$.[30] Above ϕ_C the system freezes into a rigid gel state and both dilational and shear modulus follow power law behaviour as:

$$\begin{aligned} \varepsilon(\phi) &\approx \varepsilon_0 (\phi - \phi_C)^p \\ G(\phi) &\approx G_0 (\phi - \phi_C)^f \end{aligned} \qquad (2.4)$$

where *p* and *f* respectively represent the power exponents. To further explore the dynamical behaviour of our system, we thus defined it as a percolation network with both *Central* and *Bond Bending* forces. Actually, it is well known that theories have classified bond-related forces into two different classes, *central forces (CF)* and *angular bond-bending* ones *(BBF)*.[20, 21] For central-force conditions, the structural rigidity exclusively arises from the tensile stiffness of elemental clusters defining the network, consequently high rigidity requires not only stiff cross-links but also high connectivity, similarly to the pure entropic case.[40] On the other hand, bond-bending forces emerge only if the orientation of crosslinks is distorted by shear, resulting in conformational changes susceptible to store elastic energy.[21]

Figure 2.12 re-plots the experimental dilational and shear moduli for the different *Mw's* presented in Figure 2.11, in reduced units, i.e. G/G_0, $\varepsilon/\varepsilon_0$ as a function of the fraction of gel phase, $\phi - \phi_c$. This master-plot highlights the plausible explanation of the dynamics in terms of *CF* and *BBF's*. Dilational elasticity shows power-law behaviour as $\varepsilon(\phi) \sim (\phi - \phi_c)^p$, with $p \approx 1.4$. It should be noted that this exponent is rather compatible with a central-force model driven by rotationally-invariant osmotic forces. On the other hand, the shear elasticity data could be fitted to a power-law behaviour as $G(\phi) \sim (\phi - \phi_c)^f$, with $f \approx 4.6$. Thus, it has been demonstrated the strong dependence of the shear strength as a function of the molecular weight as expected for bond-bending interactions between the structural elements. This behaviour could be explained in terms of the rough penetrable surface which has the swollen coils of PMMA. They can mutually stick upon lateral compaction resulting in non-sliding contacts resembling highly-

directional bonds. It should be remarked that bond bending forces emerge if the orientation of the PMMA-pancakes is modified by shear. In fact, the conformational change of the percolation network promoted by shear could store elastic energy.[21]

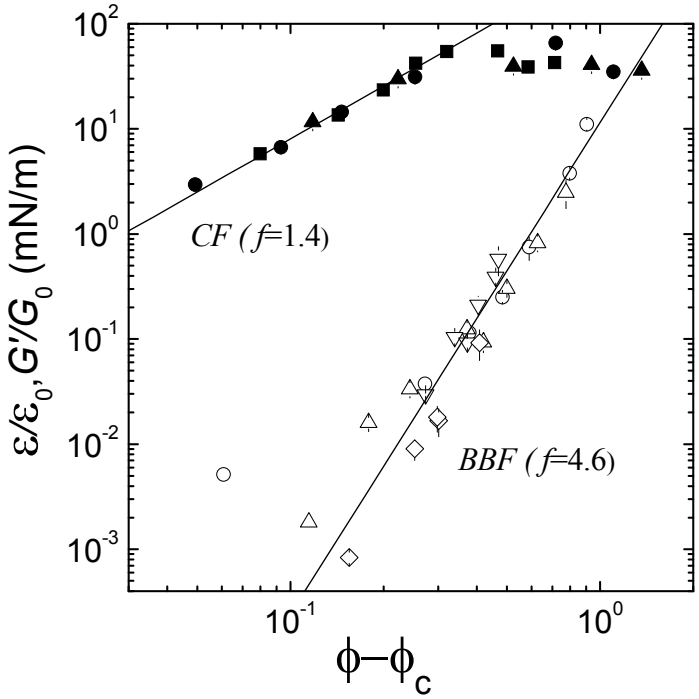

Figure 2.12. *Master Curve* of the Dilational Elastic moduli, ε and Shear ones, G as a function of the difference between the packing fraction (ϕ) and the percolation threshold (ϕ_c). Straight lines represent power-law fits in terms of a percolation behaviour: $\sim (\phi - \phi_C)^{p, f}$; where p=1.4 for the dilational elasticity and f=4.6 for the shear one. These two different power laws have been explained respectively by the *Central Force* (*CF*) and *Bond Bending one* (*BBF*) models for a percolation network. Symbols, M_w's in kDa: **(a)** $\varepsilon / \varepsilon_0$ = (■) 270.8; (●) 80 and (▲) 14. **(b)** G/G_0= (○) 270.8; (△) 80; (△)30 and (◇)14.

To summarize, the power-law behaviour of the dilational elasticity as a function of $\phi-\phi_c$ can be explained in terms of a central-force problem where the network rigidity increases near-linearly with the fraction of the gel phase ($f \approx 1$). This fact may be explained due to dilational stress do not cause the emergence of directional bond-bending forces and only the stiff cross-links and the high connectivity between the polymeric-pancakes influences the network rigidity similarly to a pure entropic network.[40] However, the shear test promotes directional lateral interactions which introduces strong structural stiffening in percolation networks. This percolated scenario can be explained by the bond-bending interactions of the soft coils of PMMA. Thus, a symmetry is broken by the directional lateral interactions and, as a result a strong increase of the shear modulus on the fraction of the gel phase can be found ($f \approx 4$).[21]

Moreover, bond-bending forces are dependent to the size of the structural elements as shown Figure 2.13 which displays the experimental values of the shear modulus as a function of the chain length, *N* above the percolation threshold for all the PMMA monolayers studied. A strong increase of *G* with the molecular weight is shown as expected from increasing bond-bending interactions between the structural pancakes at increasing size. However, the power-law exponent remains essentially constant at a value of $f \approx 4$ compatible with the universality class of bond-bending forces. On the other hand, ε and ε_0 are found to be nearly chain-size independent as expected for the interpretation of the system in terms of a central force percolation network. In addition, as expected for the power law exponents found which remain essentially constant with the size of structural units, we have demonstrated the universality class of Central forces and Bond-bending forces for the PMMA percolated network at different polymer weights.

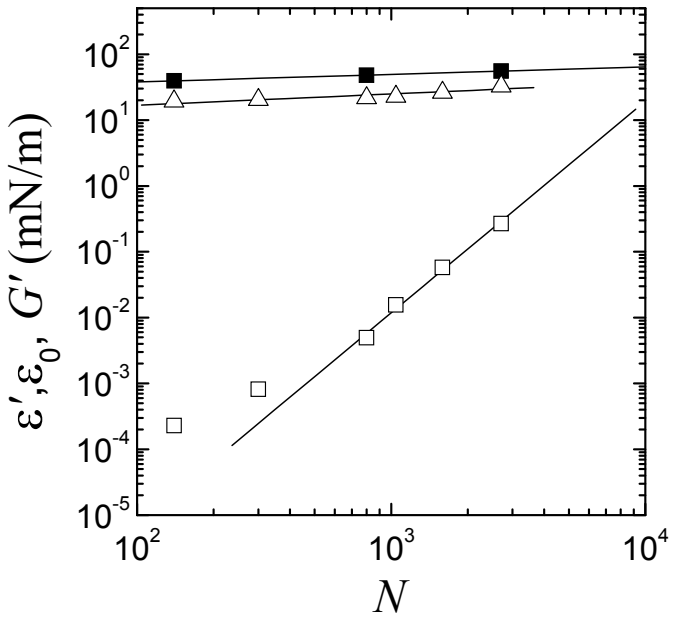

Figure 2.13. Dilational Elastic modulus, ε (■), equilibrium elastic modulus, ε (Δ), and Shear ones, G (□) as a function of the Chain length for all the PMMA monolayers studied. *G'* shows power law dependence with *N* as expected from increasing bond-bending interactions between the structural elements at increasing size, explained in terms of *Bond Bending forces theory* (*BBF*). Contrary to this behavior, ε' and ε_0 do not show any power-law dependence with *N*, as expected for the *central-force* model (*CF*) driven by rotationally-invariant osmotic forces.

In the framework of the percolation scenario proposed, we have found an apparent correlation between the exponent shown by dilational elasticity as a function of the fraction of gel and the previously found for the surface pressure, Π (Figure 2.5). On the basis of our Π–Γ isotherms, we have explored the possibility that both follow a percolation power-law dependence in terms of a central-force problem. [35, 49, 51] Our experimental fits show that for all the PMMA

monolayers studied, the same behaviour is found, $\Pi(\phi) \sim (\phi - \phi_c)^f$ with $f \approx 1.3 \pm 0.3$. As expected, this behaviour is compatible with a central-force description of the system governed by the lateral contact between neighbouring soft discs. Indeed, the power-law dependency correlates well with the dilational elasticity previously mentioned, $\Pi(\phi) \sim \varepsilon(\phi) \sim \varepsilon_0(\phi) \sim (\phi - \phi_c)^{1.3}$. However, only if the symmetry of the system is broken by directional lateral interactions when it is distorted by shear; it will produce strong structural stiffening. It is characterized by a sharp increase of *G* with the dependency on the fraction of gel as explain the bond-bending behaviour. In addition, these results constitute an additional proof of the percolated description of the equilibrium and rheological features of PMMA films.

3.6 Relaxation experiments: a 2D glass-like dynamics

There is no unequivocal evidence of the existence of two dimensional glasses. [52, 53] Indeed, the possibility that molecules rearrange cooperatively has been postulated to explain the phenomenology observed in a glassy state.[54] From a structural point of view, a two dimensional-glassy polymer film can be conceived as made of frozen units interconnected in a solid amorphous network after a percolation density transition undergoes. These structural units can be viewed as soft-flexible pancakes which describe a percolation scenario.[55] To investigate the role of the existence of a glasslike dynamics in PMMA monolayers, we used relaxation experiments to determine the surface concentration and chain length dependence of the timescale which characterize the relaxation motion of these percolated systems.

We have performed relaxation experiments for three PMMA films with different M_w at different surface concentrations, Γ ranging from the percolation threshold, Γ_c to the concentrated regime and at constant temperature of 23ºC. No stress-relaxation ($\sigma \approx cte$) has been observed below Γ_c pointing out that no-collective motions exist when the polymer pancakes remains isolated at the air-water interface. Figure 2.14 shows a representative result of the reduced stress-relaxation experiments performed in PMMA film with $270.8 \cdot 10^3$ g·mol^{-1} at 5 different Γ's. It should be note that as Γ increases, there are marked changes in the dynamics; indeed, a non-exponential character of the relaxation curves is clearly pointed out as an increasing curvature of the *ln* (σ/σ_0) as a function of time plotted as Γ increases.[32] This non-Debye response constitutes an evidence of a typical glasslike dynamical behaviour in a 2D-system upon approach the glass transition. Similar results has been obtained for other glass forming polymer at poor solvent conditions, poly-(4-hydroxistyrene).[17] The relaxation curves obtained have been

well fitted to a stretched exponential in terms of the *Kohlrausch-Williams-Watts* (*KWW*) function,[56, 57]

$$\sigma(t) = \sigma_0 \exp\left[-(t/\tau)^{\beta}\right] \qquad (2.5)$$

where τ is the relaxation time, σ_0 the amplitude of the relaxation and the stretching exponent, β is related to the coupling parameter n of the coupling model (*CM*) developed by Ngai by $n=1-\beta$.[25, 26] It takes values from 0 to 1 depending on the cooperativity of the intermolecular interactions. [26] To summarize, our experiments shows that for the PMMA monolayers the relaxation function deviates from the Debye-like shape ($\sim exp[-t/\tau]$) to a stretched-exponential behaviour ($\sim exp[-t/\tau]^{\beta}$, $\beta<1$) as the system enter into the percolated solid-like phase ($\Gamma>\Gamma_c$). This behaviour highlights the heterogeneous collective relaxation of a disordered solid-like arrangement of rigid elements. Furthermore, it can be understood in terms of a dynamical arrest of these disordered structure, which relaxes trough a kinetic "bottleneck" mechanism.[58] To quantify the Γ dependence of the final decay time, we determined the average structural relaxation time, $\tau_\alpha = (\tau/\beta)\,\Gamma(1/\beta)$, where Γ denotes the gamma function.

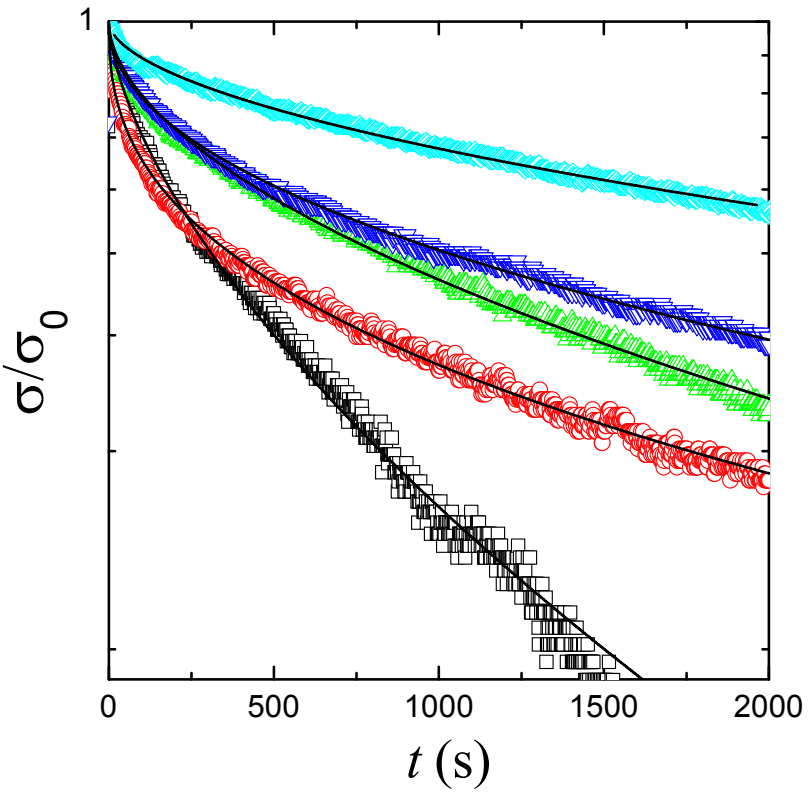

Figure 2.14. a) Reduced stress-relaxation plots of PMMA Langmuir film with $270.8\cdot10^3$ g·mol^{-1} at different surface concentration, Γ = (□) 0.83; (○) 0.86; (Δ) 0.89; (∇) 0.92 and (◊) 0.96 mg·m^{-2}. The straight lines are fits to a stretched exponential, KWW function.

The Γ-dependence of the structural relaxation times, τ_α for the different M_w's studied is highlighted in Figure 2.15. For each PMMA monolayer studied, the relaxation times show a sharp increase with the surface concentration following a power law, $\tau_\alpha \sim \Gamma^y$, where y =15±2. Indeed, this Γ-dependence characterizing structural relaxation is robust due to be observed in all the molecular weights studied. Furthermore, this scaling-behaviour found is similar to Γ-dependence of π and the dynamical features, ε and *G* obtained by other experimental techniques. Indeed, the hypothesis of a 'poor' solvent scenario explained in terms of a percolation theory becomes plausible. We thus confirm our hypothesis that the Γ-dependence of dynamical features (both dilational and shear) can be explained in terms of a universal power-law behaviour.

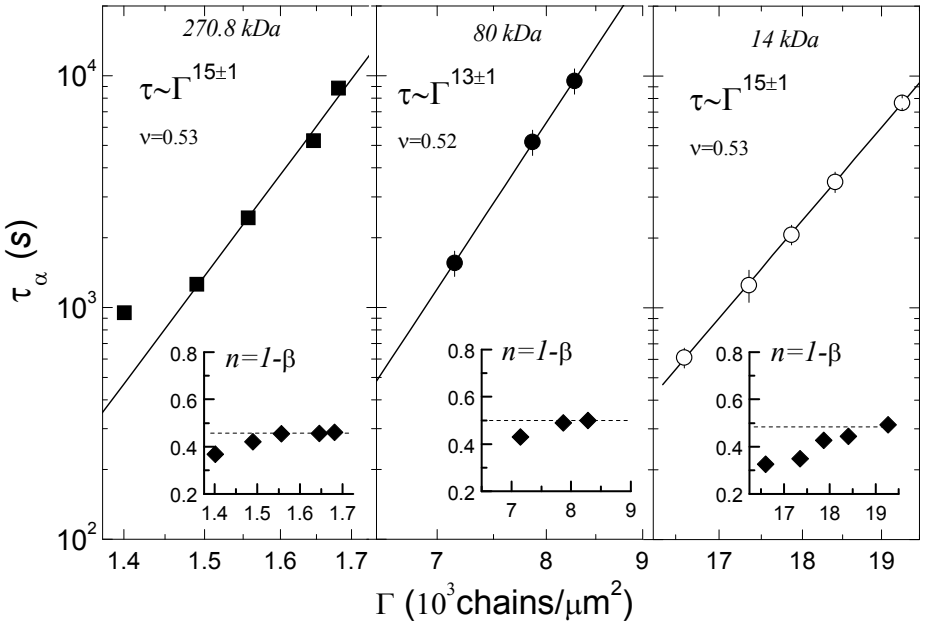

Figure 2.15. Scaling law behavior of the experimental relaxation times obtained from the experimental stress-relaxation curves for PMMA monolayers with different molecular weight; symbols as: $270.8 \cdot 10^3$g·mol^{-1} (■); $80 \cdot 10^3$g·mol^{-1} (●); $14 \cdot 10^3$g·mol^{-1} (○). Straight line represent a power-law fit of the relaxation time, τ_α against the polymer concentration, $\tau \sim \Gamma^y$, with exponent ca. 15±2. Each inset shows the coupling parameter, *n* as a function of Γ.

For the amorphous system studied, we find that the coupling parameter, *n* increases with Γ reaching a constant value close to 0.5 for all the PMMA monolayers, as shown the respective insets in Figure 2.15. This value of *n* points out the existence of high cooperative motions in the range $\Gamma > \Gamma_c$, where the molecular connectivity is high enough.[59] In the context of the coupling model, two different relaxation times must exist in an amorphous system like a glass. A microscope one, τ_0 related to the fast independent relaxation of an individual unit, and τ, the macroscopic one which is related to the cooperative and dynamically heterogeneous relaxation of the system. The macroscopic relaxation motion

relaxes following a KWW function instead of a Debye-like fashion which characterizes the microscopic one.[59] In sharp contrast to the diffusive relaxation of an isolated coil of radius, $R_F \approx 14.9$nm calculated by $\tau_0 = R_F^2/D \approx 0.01 ms$,[60] we thus confirm our long range relaxation times, τ_α as the timescale which underlie a cooperative motion of the PMMA pancakes. Moreover, if we compare the results for the different molecular weights studied we found that the τ_α values do not dependent on the chain length. Indeed, we can suggest an '*universa*l' description of dynamical arrest in these glassy-polymer films.

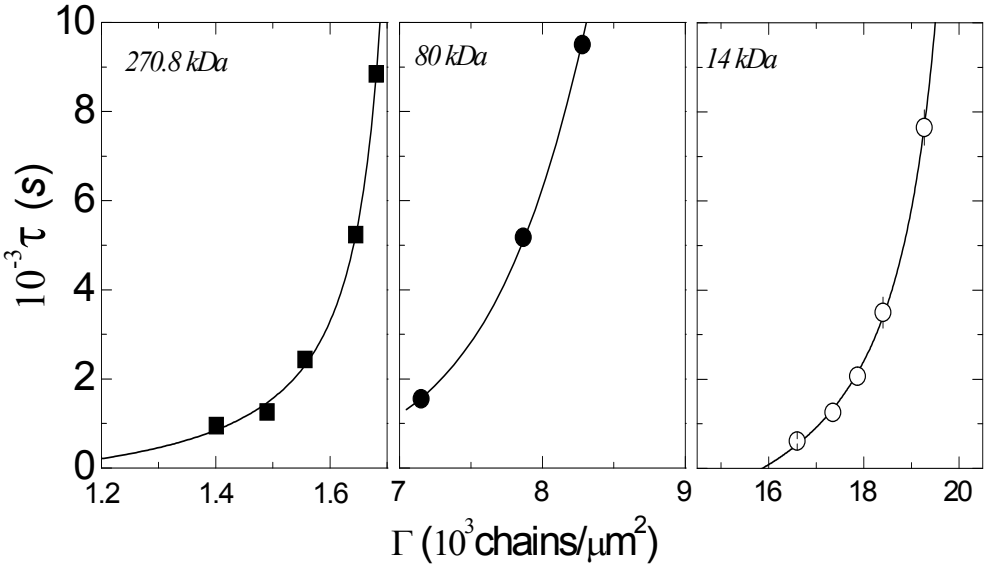

Figure 2.16. Experimental relaxation times, τ_α fitted in terms of the Vogel-Fulcher-Tammann equation with $1/\Gamma$exchanged for T. (symbols as in Figure 2.15). As expected Γ plays a role analogous of 1/T in molecular systems.

In addition, to describe the relaxation-time data, we can use a Vogel-Fulcher-Tammann (VFT) function[32]:

$$\tau_\alpha = \tau_0 \exp\left(A\Gamma/\left(\Gamma_0 - \Gamma\right)\right), \qquad (2.6)$$

Where Γ_0 sets the apparent divergence, *A* controls the growth of τ_α on approach to Γ_0 and τ_0 is the characteristic relaxation times for low values of Γ. This empirical function, with $1/\Gamma$ exchanged for *T,* provides a good description of the T dependence of τ_α for supercooled molecular liquids near the glass transition[32]. Weitz and col. use this new approach to confirm that for suspensions of soft particles, Γ plays a role analogous to that of *1/T* in molecular systems.[24] Our experimental values of τ_α for PMMA monolayers show that in the same way for soft colloidal particles, the approach to a Γ-description of these by the *VFT* function is plausible as pointed out Figure 2.16. Our experiments show that the Γ-dependence of τ_α can be explained by an exponential behaviour in terms of the

modified *VFT* function. Moreover the same behaviour is found for all the molecular weights studied. It should be note that *VFT* dependence with $\Gamma_0 >> \Gamma$ found leads us to restrict PMMA monolayers to a *fragile* behaviour instead of *strong* molecular glass-formers as silica which follows an Arrhenius dependence, but in our situation with T exchanged for $1/\Gamma$.[24, 32] Our results thus further confirm that for polymer films, Γ plays a role analogous to 1/T in molecular systems and by analogy, similarly results have been previously published in soft colloidal systems.[24]

To summarize, we have explored the non-Debye long-time dynamics of a glass-forming polymer film. Thus, a glassy state appears as a reliable scenario for amorphous matter in 2D-arrangements. Our results thus suggest that the Γ-dependence observed upon compressing the film can be correlated with the percolation of the polymer pancakes and this structural relaxation in Langmuir monolayers of glass-polymer formers can be described by thermal activation strongly influenced by the underlying energy landscape associated, which reflects the possible configurations of the system.[52, 61] The concept of *fragility* is reflected in the topology of the energy landscape (*EL*). Indeed, for fragile glasses the *EL* is very heterogeneous which promotes larges activation energies ~$65K_BT$ (calculated from the *VFT* parameters[32]) due to the existence of cooperative many-bodies rearrangements.

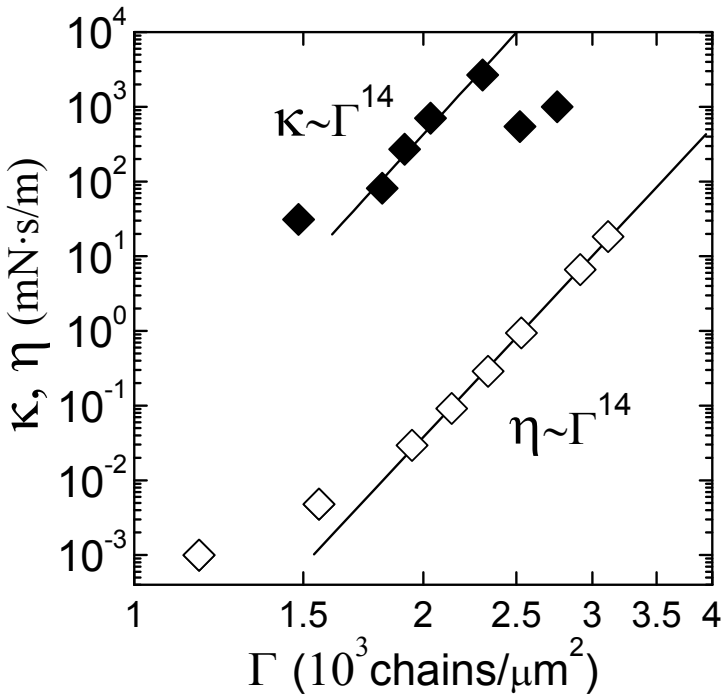

Figure 2.17. Comparison between dilational viscosity, κ and shear viscosity one, η as a function of the surface concentration, Γ of a PMMA monolayer *(Mw: 270.8KDa)*. A similar power law dependency is showed by dilational and shears viscosities: $\kappa,\eta \sim \Gamma^{\alpha}$,where α=14 underlying the cooperative motion of the percolated pancakes of PMMA.

A final proof of the existence of a 2D glass polymer film comes from the noteworthy emergence of viscosity in a fluid to glass transition. To further investigate the role of the viscosity in the dynamic arrest of polymer monolayers, we used dilational oscillatory rheology and shear one to determine the density dependence of the dilational and shear viscosities, κ and η respectively. This behaviour is highlighted in Figure 2.17 which plots κ and η as a function of Γ for the PMMA monolayer with *Mw: 270.8KDa* at a fixed Temperature of 23ºC. A similar power law dependency is showed by dilational and shears viscosities: $\kappa,\eta \sim\Gamma^{\alpha}$,where α=14 in both cases. It should be note that the strong Γ-dependence of κ and η highlights the emergence of a cooperative motion of the percolated pancakes of PMMA. Thus, we confirm our hypothesis that the collective rearrangements necessary to make flow the percolate system, follow a bottleneck mechanism typical of glasses. A transition from fluid to glassy regime are clearly identified trough the variation of Γ by analogy with the definition of the glassy state by the sharp change in the temperature dependence of rheological features for many systems. [62] Furthermore, we can hypothesize that to enter in the glassy state of polymer monolayers not only the temperature must be decreased below T_g, but also the film density, Γ, must be increased above the percolation transition point.

3.7 Temperature effects on the equilibrium and rheology of poly (methyl methacrylate) Langmuir films: Towards a *glassy* state

In the framework of the physics of glass transition, the hypothesis of the existence of a 2D-glassy state in thin polymer films is one of the major current challenges to deal.[53] Indeed, the concept that molecules could rearrange cooperatively quantify a characteristic length scale for glass transition dynamics.[27] Furthermore, it is well known that changes in the glass transition temperature, T_g and dynamics from bulk behaviour emerge when the system is confined near the cooperativity size.[63] The study of systems of restricted dimensionality highlights the existence of the cooperative rearrangement regions which suggest the possibility of finite size effects.[29] Thus, thin polymer films are interesting to test the dominance role of finite-size effects when the molecular weight is high enough and the thickness, h, smaller than the coil size, R_F (defined as the 2D-Flory-radius of polymer films).[4] Both experimental and theoretical evidences have shown that a strong decrease of T_g below the bulk glass transition values appears in freely standing films as well as the decreasing found of T_g should lead to an increased molecular mobility of these polymer systems.[4, 64]

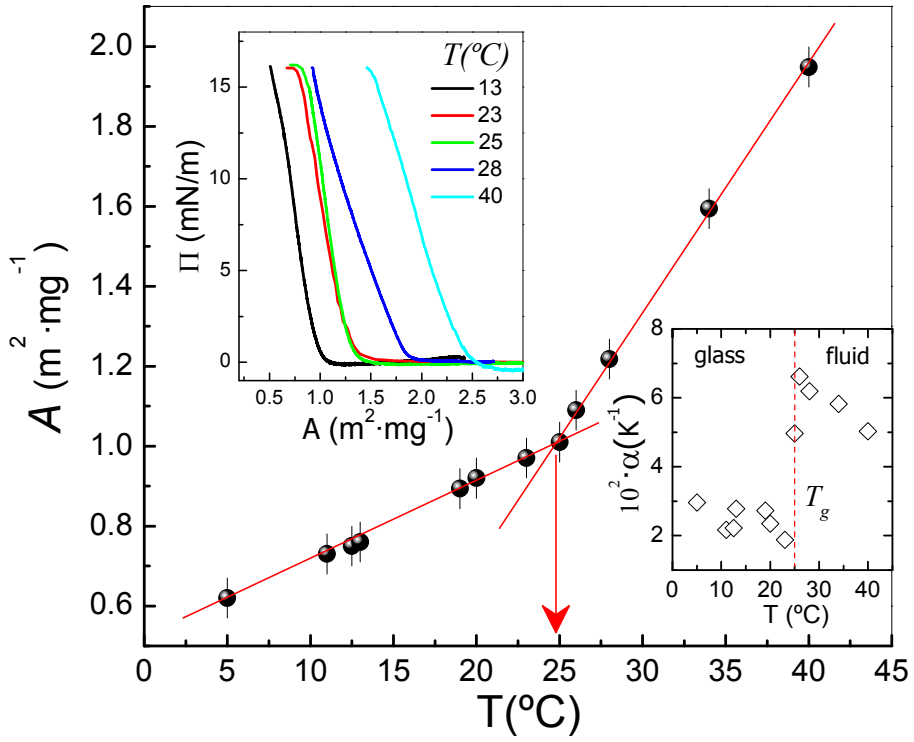

Figure 2.18. Isobaric compression of PMMA Langmuir monolayers *(Mw: 270.8KDa)* at a constant surface pressure, Π ≈ 8mN/m. A transition is identified at T~25ºC as a meaningful increase of the surface area as the temperature increase. A glass transition temperature (T_g) could be pointed out from 2D melt to a *solid*-like state. The right-bottom inset shows the thermal dilation coefficient (α) as a function of the temperature. An evident decrease of α from the T_g to lower temperatures point out the existence of a *glassy*-state. The value of a of the glassy films, is found to be more than twice lower than one of the fluid-like films. This glass transition has been identified by Π–A experiments at different temperatures (see upper inset).

In this section we highlight the evidences of a glass transition and cooperative motions in a Langmuir polymer film of atactic poly (methyl methacrylate) (PMMA) a glass-forming polymer described by an arrangement of self-avoiding chains conformed as collapsed soft disk-shaped coils (pancakes) at the air-water interface. It should be mention that in a previous work we demonstrated that Langmuir PMMA monolayers are in the monomolecular size ($h < R_F$) and show weak interaction with the substrate ($\sim K_BT$)[49]; indeed, it lead us to determine an hypothetic glassy-like transition from a 2D-melt to an amorphous solid-like state. The existence of a glass transition in quasi-2D films has not been clearly demonstrated;[65] however, some polymer monolayers showed soft glasslike features e.g. *percolation-like rigidity* as a result of lateral compression,[49] *non-Debye* mechanical relaxation characterized by deviations of the relaxation times from the *Arrhenius* behaviour at decreasing temperature and increasing density.[17, 66] In the context that Langmuir monolayers are the thinnest possible films these

experimental evidences points out a dynamic heterogeneity typical of glass-former systems.[29]

We thus take advantage of both equilibrium and rheological behaviour of Langmuir films of an amorphous glass-forming polymer, i.e. PMMA (M_W =270.8·10^3 *g/mol*; M_W/M_N=1.85) at different temperatures to gain a conclusive insight into the glass transition in quasi-2D systems.

We studied the equilibrium surface pressure as a function of surface area isotherms $\pi(A)$ of PMMA monolayers in the air-water interface varying the temperature, from 5 to 40^oC using a Langmuir trough (Methods Summary). The upper inset in Figure 2.18 highlights that $\pi(A)$ isotherms had a qualitative similar shape according to the 'poor' solvent scenario previously proposed for this polymer.[6, 49] However, the shift observed towards lower surfaces areas, A at decreasing the temperature points out a strong influence of T on the conformational scenario based on collapsed pancakes formed by this polymer. The concept of glass transition is best highlighted in a plot of the surface area per monomer as a function of temperature. The T_g is well defined as the sharp break in the slope of the A vs. T plot at a constant surface pressure, $\pi\approx$8mN/m as shown Figure 2.18; we thus concretely identifies the break point as the fluid-to-glass transition, $T_g \approx 25^oC$; this value was significantly lower than the bulk $T_g \approx 105^oC$ for PMMA.[31] This difference on T_g could be due to the enhanced chain mobility promoted by the existence of the cooperatives regions in this free-standing film. Furthermore the emergence of dynamical arrest is plausible hypothesized when cooling below 25^oC. It is noteworthy that at $\pi\approx$8mN/m, well above the percolation threshold, the system is well defined in terms of an arrangement of PMMA-pancakes.[49] In this context, is plausible the existence an expanded-like behaviour found at high temperatures in sharp contrast to an intrinsically condensed-like as T decreases which highlights the glassy-state. We thus found a similar conclusion from the variation of the thermal dilation coefficient, $\alpha=(1/A)(\Delta A/\Delta T)$ with T (right-bottom inset of Figure 2.18). Similarly to bulk glasses, the values of α in the solid-state are $\alpha_G \approx 0.021\pm0.005K^{-1}$, it is found a sharp increase when the temperature increasing over 25^oC, entering in a fluid-like regime where α increases taking larger values, $\alpha_F \approx 0.075\pm0.005K^{-1}$.

Similar results which points outs the existence of a glass transition from the isobaric compression of Langmuir films have been found for other polymer monolayers; e.g. poly (vinyl stearate)[67] and poly (4-hydroxystyrene)[68], for both a *poo*r solvent scenario were plausible hypothesized.

To confirm our hypothesis about the existence of a glassy state in polymer monolayers, we investigated the role of the film thickness, h of the PMMA monolayers in the existence of a glass transition temperature by standard plots of h as a function of T performed by ellipsometric measurements (Methods

Summary). In Figure 2.19 we report the T dependence of *h* for the PMMA monolayers in the surface state characterized by π≈8mN/m. The crossover between the two linear dependencies, *h vs.T* pointed out by the experimental data is generally used to determine the glass transition temperature.[69, 70] *h* is found as the relevant length scale to investigate the role of the finite sizes effects on the glass transition. Indeed, the thickness obtained are comparable with the dimensions of cooperatively rearranging regions previously estimated for several glass forming materials by Donth et al.[29] Moreover for our PMMA monolayers (where $h<R_F$)[49] the explanation of the decrease of T_g could be due to the existence of chain confinements; however this hypothesis as nowadays a matter of theoretical controversy.[71]

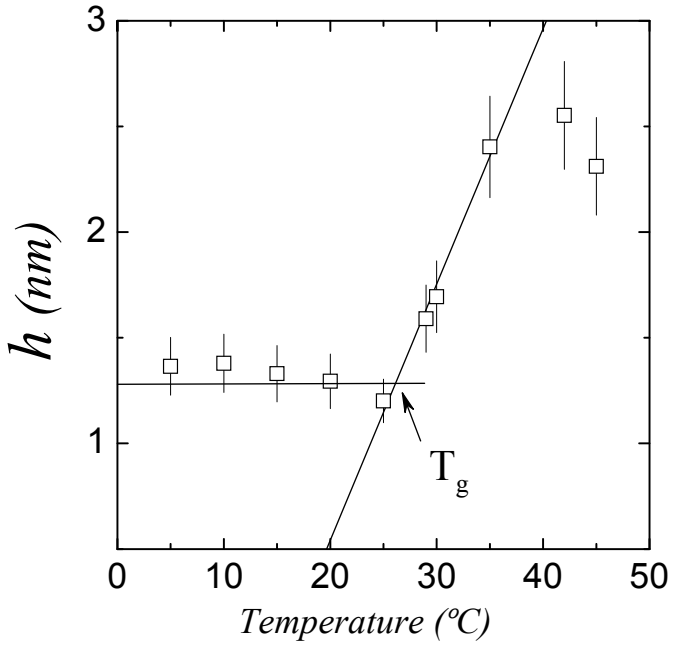

Figure 2.19. Temperature dependence of the optical thickness measured by ellipsometry of PMMA monolayers at π≈8mN/m. A transition is identified at T~25ºC as an increase of *h* as the temperature increase. The solid lines illustrate the linear regions of *h* in the glassy and melt regimes.

For our PMMA monolayer, we also determined the temperature-dependence of both dilational elasticity modulus, ε and dilational viscosity, κ by oscillatory rheology. The T-dependence of the dilational viscosity, κ is shown in Figure 2.20a. This plot is rather characteristic of a system undergoing a fluid to glass transition from the point of view as an important increase of the dilational viscosity. Indeed, the data shown further confirm that for polymer monolayers, κ plays a role analogous to the well known shear viscosity, η in the dependence with $1/T$.[62] It should be note that the density of the monolayer is further above the percolation threshold as demonstrated our previous works; thus, we point out clearly that the density plays an important role in the glass transition of polymer

monolayers. This is in agreement with the works of Weitz and col. in colloidal systems.[24] To describe the dilational viscosity data we used a *Vogel-Fulcher-Tammann* (*VFT*) function[32], $\kappa = \kappa_0 \, exp(A/(T-T_0))$, where A and T_0 are system dependent parameters. This empirical function provides a good description of the T-dependence of κ for polymer monolayers near their glass transition as pointed out Figure 2.20.a. It should be note that *VFT* dependence found for our results leads us to describe the PMMA monolayers as a *fragile*-glass forming solid instead of strong molecular glass-formers which follows an Arrhenius dependence.[32] To test our hypothesis about the existence of a fragile-glass former, we investigated the behaviour of the *fragility* concept, m defined by the logarithmic slope at T_g by Angell[32, 72] in the whole T-range studied. Assuming that 25ºC is the T_g of our films, the dependence of m with T in a normalized plot by T_g is shown in Figure 2.20b. It is noteworthy that approached from the melt, when the kinetic arrest starts, the fragility parameter increases up to a value close to 100, typical of fragile glasses in the Angell's clasification.[72, 73] From the VFT parameters[32] we calculated the apparent activation energy involved in this process, $E_a \approx 40 K_B T$ which this large value showed highlights the existence of cooperative rearrangements.

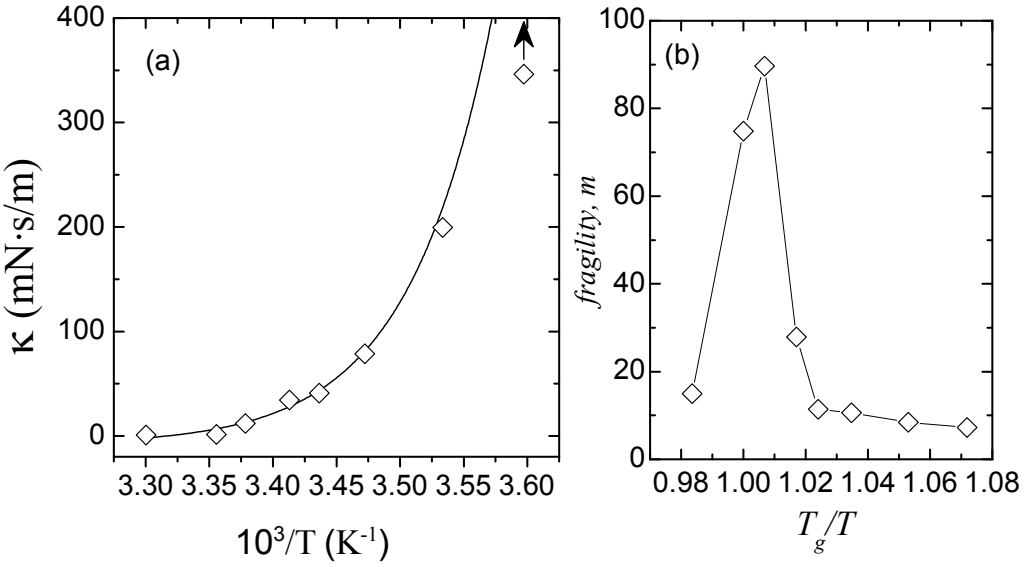

Figure 2.20. (a) Temperature dependence of the dilational viscosity, κ of PMMA monolayers at π≈8mN/m (diamonds). The solid line represent the fit of the experimental values by a Vogel-Fulcher-Tammann (*VFT*) function characteristic of a fragile-glass forming materials.[32] (b) Dependence of *fragility* parameter, m as a function of T renormalized by T_g.

Moreover, for molecular glass-formers, it is expected that the dilational elasticity modulus further increases when the system is cooling below T_g as the previously showed by k. Figure 2.21 highlights a definitive proof of the glass transition in Langmuir PMMA films. To investigate the role of ε we plot it as a function of T. For the sake of comparison we also plot the equilibrium elastic

modulus calculated from the Π–*A* isotherms of Figure 2.21 as: $\varepsilon_0 = -A(\partial\Pi/\partial A)$. Both parameters, ε and ε_0 present a further growth when the monolayer is cooled below the T_g. By analogy with the T-dependences of the other glassy features shown previously, there is a sharp crossover from the fluid-like state, where elasticity takes values close to 2-4*mN/m* to the glassy-like, where the elasticity of the system increase to higher values according to a solid-like phase. Indeed, the behaviour of the dilational elasticity is perfectly compatible with the existence of soft glass state.

To conclude, the results presented here demonstrate the plausible existence of a glass-transition in a Langmuir polymer films. Many conclusive evidences for an understanding of glass formation may come from exploring both the equilibrium and the rheological behaviour of polymer monolayers in a *poor* conditions where the polymer coils collapsed forming soft disk-shaped in a percolation network.[49]

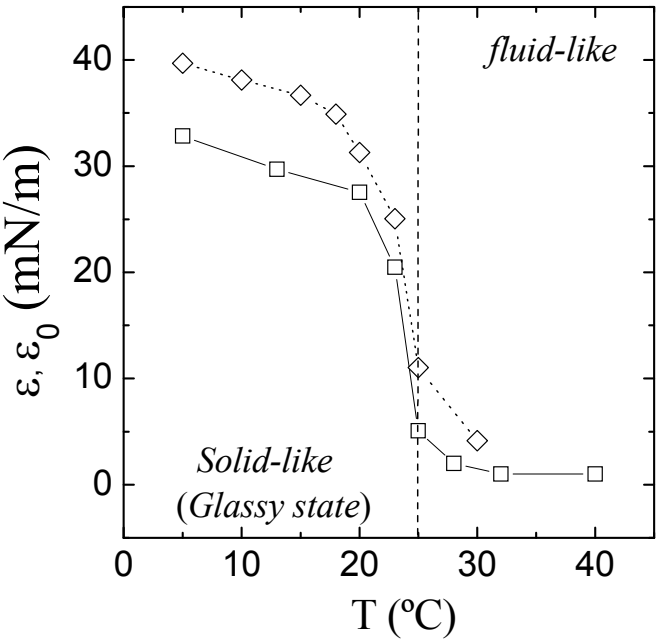

Figure 2.4. Temperature dependence of the equilibrium elasticity modulus, ε_0 (□) and the dilational one, ε (◊) of PMMA monolayers *(Mw: 270.8KDa)* at a constant surface pressure, π≈8mN/m. A transition is identified at T~25ºC as a meaningful decrease of both ε and ε_0 as the temperature increase.

4. Conclusions and Remarks

Our results points out the plausible existence of an amorphous 2D solid viewed as a percolation network of poly (methyl methacrylate) (PMMA) pancakes at high density and low enough temperature. The study of the dynamical behaviour has contributed to a better understanding of our system; indeed, the Γ-dependence which characterizes both dilational and shear rheological features is

robust, as it is independently determined by several different methods. Concretely, the studies of the density packing and molecular weight in terms of the correlation between equilibrium and dynamical properties have demonstrated the existence of a percolation scenario. It has been found that under *poor* solvent conditions, PMMA coils rearrange form collapsed pancakes at the air-water interface. A further understanding of the Dynamical behaviour of PMMA monolayers come from the description of our system in terms of a percolation network with *Central-forces* and *Bond-Bending* ones. Equilibrium features and dilational rheology could be explained by *CF*s, however shear response obey to *BBFs* problematic. Furthermore, the relaxation experiments have suggested striking glassy-like features: non-Debye relaxation and non-Arrhenius Γ-dependence of the relaxation times and viscosity. Therefore, our results here point out the *fragility* of PMMA monolayer independent on the chain size trough the variation on Γ within the percolation regime. Finally, in the context of 2D-glassy systems many conclusive evidences for an understanding of glass formation may come from exploring the *T*-dependence of both equilibrium and rheological behaviour of PMMA monolayers. We thus highlights that polymer monolayers in a *poor* conditions where the polymer coils collapsed forming soft disk-shaped in a percolation network could be show glassy features.[49]

On the experimental point of view, we used several techniques suitable to study both dilational and shear rheology of monolayers in a broad frequency range.[74] In fact, The results obtained for polymer monolayers clearly show the existence of a rather complex dynamical behaviour, strongly dependent on the solvent quality of the interface, surface density and temperature.[6] Furthermore, it is well known that the dynamics of fluid monolayers is governed by the dilational viscoelasticity moduli instead of the in-plane shear ones.[16, 75] However, amorphous solid systems support shear elasticity, for our dense polymer monolayers, shear effects could indeed become comparable to the compression component, being *G* a relevant contribution in the dynamics.[49, 51]

5. References

1. Scheutjens, J. M. H. M.; Fleer, G.; Cohen-Stuart, M.; Grosgove, T.; Vincent, B., *Polymer at Interfaces*. Chapman and Hall: London, 1993.
2. Decher, G.; Schlenoff, J. B., *Multilayer Thin Films*. Wiley-VCH: Weinheim, 2003.
3. Jones, R. A. L.; Richards, R. W., *Polymers at Surfaces and Interfaces*. Cambridge Univ. Press: Cambridge, 1999.
4. Forrest, J. A.; Jones, R. A. L., The glass transition and relaxation dynamics in thin polymer films. In *Thin polymer surfaces and thin films*, Karim, A.; Kumar, S., Eds. World Scientific Publishing: Singapure, 2000.
5. Esker, A. R.; Zhang, L. H.; Sauer, B. B.; Lee, W.; Yu, H., *Colloids and Surfaces A* **2000,** 171, 131-148.
6. Esker, A. R.; Kim, C.; Yu, H., Polymer monolayer dynamics. *Functional Materials and Biomaterials* **2007,** 209, 59-110.
7. Vilanove, R.; Rondelez, F., Scaling description of two-Dimensional Chain Conformations in Polymer monolayers. *Phys. Rev. Lett.* **1980,** 45, (18), 1502.
8. Kawaguchi, M.; Sauer, B. B.; Yu, H., *Macromolecules* **1989,** 22, 1735.
9. Kumaki, J.; Kawauchi, T.; Okoshi, K.; Kusanagi, H.; Yashima, E., Supramolecular Helical Structure of the Stereocomplex Composed ofComplementary Isotactic and Syndiotactic Poly(methyl methacrylate)sas Revealed by Atomic Force Microscopy. *Angew. Chem. Int. Ed* **2007,** 46, 5348-5351.
10. Kumaki, J.; Kawauchi, T.; Yashima, E., "Reptational" Movements of Single Synthetic Polymer Chains on Substrate Observed by in-Situ Atomic Force Microscopy. *Macromolecules* **2006,** 39, 1209-1215.
11. Forrest, J. A.; Sharp, J. S., Dielectric and ellipsometric studies of the dynamics in thin films of isotactic poly(methylmethacrylate) with one free surface. *Phys. Rev. E* **2003,** 67, 031805.
12. Hartmann, L.; Gorbatschow, W.; Hauwede, J.; Kremer, F., Molecular dynamics in thin films of isotactic poly(methylmethacrylate). *Eur. Phys. J. E* **2002,** 8, 145-154.

13. Cardenas-Valera, A. E.; Bailey, A. I.; The interfacial rheological behaviour of monolayers of PEO/PMMA graft copolymers spread at the air/water and oil/water interfaces, *Colloids and Surfaces A* **1993,** 79, 115-127.

14. Peng, J. B.; Barnes, G. T.; Abraham, B. M., The shear viscoelastic properties of poly(methyl methacrylate) and poly(vinyl stearate) monolayers on water. *Langmuir* **1993,** 9, 3574-3579.

15. Bain, C. D.; Claesson, P. M.; Langevin, D.; Meszaros, R.; Nylander, T.; Stubenrauch, C.; Titmuss, S., Complexes of surfactants with oppositely charged polymers at surfaces and in bulk. *Advances in Colloid and Interface Science* **2010,** 155, 32-49.

16. Cicuta, P.; Stancik, E. J.; Fuller, G. G., Shearing or compressing a soft glass in 2D: time-concentration superposition. *Physical Review Letters* **2003,** 90, (23), 236101/1-4.

17. Hilles, H. M.; Ortega, F.; Rubio, R. G.; Monroy, F., Long-time relaxation dynamics of langmuir films of a glass-forming polymer: Evidence of glasslike dynamics in two dimensions. *Physical Review Letters* **2004,** 92, (25).

18. Stauffer, D.; Aharony, A., *Introduction to Percolation Theory*. Taylor & Francis: London, 1992.

19. Kantor, Y.; Webman, I., Elastic properties of random percolating systems. *Physical Review Letters* **1984,** 52, (21), 1891-1894.

20. Arbabi, S.; Sahimi, M., Mechanics of disordered solids .1. percolation on elastic networks with central forces. *Physical Review B* **1993,** 47, (2), 695-702.

21. Sahimi, M.; Arbabi, S., Mechanics of disordered solids .2. percolation on elastic networks with bond-bending forces. *Physical Review B* **1993,** 47, (2), 703-712.

22. Cicuta, P.; Stancik, E. J.; Fuller, G. G., Shearing or compressing a soft glass in 2D: Time-concentration superposition. *Physical Review Letters* **2003,** 90, (23).

23. Monroy, F.; Ortega, F.; Rubio, R. G.; Ritacco, H.; Langevin, D., Surface rheology of two-dimensional percolating networks: Langmuir films of polymer pancakes. *Physical Review Letters* **2005,** 95, (5), 056103/1-4.

24. Mattsson, J.; Wyss, H. M.; Fernandez-Nieves, A.; Miyazaki, K.; Hu, z.; Reichman, D. R.; Weitz, D. A., Soft colloids make strong glasses. *Nature* **2009,** 462, (5), 83-86.

25. Ngai, K. L.; Tsang, K. Y., Similarity of relaxation in supercooled liquids and interacting arrays of oscillators. *Physical Review E* **1999,** 60, (4), 4511-4517.

26. Ngai, K. L., Mobility in thin polymer films ranging from local segmental motion, Rouse modes to whole chain motion: A coupling model consideration. *European Physical Journal E* **2002,** 8, 225-235.

27. Adam, G.; Gibbs, J. H., On temperature dependence of cooperative relaxation properties in glass-forming liquids. *Journal of Chemical Physics* **1965,** 43, (1), 139-&.

28. Ngai, K. L., Dynamic and thermodynamic properties of glass-forming substances. *Journal of Non-Crystalline Solids* **2000,** 275, (1-2), 7-51.

29. Donth, E.; Hempel, E.; Schick, C., Does temperature fluctuate? Indirect proof by dynamic glass transition in confined geometries. *Journal of Physics-Condensed Matter* **2000,** 12, (16), L281-L286.

30. Gennes, P.-G. d., *Scaling Concepts in Polymer Physics*. Cornell University Press: Ithaca, 1979.

31. Brandrup, J.; Immergut, E. H.; Grulke, E. A., *Polymer Handbook*. 4 ed.; Wiley: New York, 1999.

32. Angell, C. A.; Ngai, K. L.; McKenna, G. B.; McMillan, P. F.; Martin, S. W., Relaxation in glassforming liquids and amorphous solids. *Journal of Applied Physics* **2000,** 88, (6), 3113-3157.

33. Kawaguchi, M., Thermodynamic, structural and rheological properties of polymer films at the air-water interface. *Prog. Polym. Sci.* **1993,** 18, 341.

34. Adam, M.; Lairez, D., *Physical Properties of Polymeric Gels*. Willey: Chichester, UK, 1996.

35. Monroy, F.; Ortega, F.; Rubio, R. G.; Rittaco, H.; Langevin, D., *Phys. Rev. Lett.* **2005,** 95, 056103.

36. Princen, H. M., Osmotic pressure of foams and highly concentrated emulsions. 2. Determination from the variation in volume fraction with height in an equilibrated column. *Langmuir* **1987,** 3, 36.

37. Mason, T. G.; Weitz, D. A., Linear Viscoelasticity of Colloidal Hard Sphere Suspensions near the Glass Transition. *Phys. Rev. Lett.* **1995,** 75, 2770.

38. Hutzler, S.; Weaire, D., The osmotic pressure of a two-dimensional disordered foam. *J. Phys. Condens. Matter* **1995,** 7, L657.

39. Farago, O.; Kantor, Y., Entropic elasticity of two-dimensional self-avoiding percolation systems. *Physical Review Letters* **2000,** 85, (12), 2533-2536.

40. Feng, S.; Sen, P. N., Percolation on elastic networks - new exponent and threshold. *Physical Review Letters* **1984,** 52, (3), 216-219.

41. Monroy, F.; Rivillon, S.; Ortega, F.; Rubio, R. G., Dilational rheology of Langmuir polymer monolayers: Poor-solvent conditions. *Journal of Chemical Physics* **2001,** 115, (1), 530-539.

42. Monroy, F.; Ortega, F.; Rubio, R. G., Dilatational rheology of insoluble polymer monolayers: Poly(vinylacetate). *Physical Review E* **1998,** 58, (6), 7629-7641.

43. Sollich, P.; Lequeux, F.; Hebraud, P.; Cates, M. E., Rhelogy of Soft Glassy Materials. *physical Review Letters* **1997,** 78, (10), 2020-2023.

44. Sacchetti, M.; Yu, H.; Zografi, G., In-Plane Steady Shear Viscosity of Monolayers a the Air/water Interface and Its dependence on Free Area. *Langmuir* **1993,** 9, 2168-2171.

45. Cicuta, P.; Terentjev, E. M., Viscoelasticity of a protein monolayer from anisotropic surface pressure measurements. *European Physical Journal E* **2005,** 16, (2), 147-158.

46. Krägel, J.; Derkatch, S. R.; Miller, R., Interfacial shear rheology of protein–surfactant layers. *Adv. Colloid Interface Sci.* **2008,** 144, 38.

47. Bantchev, G. B.; Schwartz, D. k., Surface Shear Rheology of β-Casein Layers at the Air/Solution Interface: Formation of a Two-Dimensional Physical Gel. *Langmuir* **2003,** 19, 2673.

48. Gennes, P. G. d., Reptation of a Polymer Chain in the Presence of Fixed Obstacles. *J. Chem. Phys.* **1971,** 55, 572.

49. Maestro, A.; Ortega, F.; Monroy, F.; Kragel, J.; Miller, R., Molecular Weight Dependence of the Shear Rheology of Poly (methyl methacrylate) Langmuir Films: A Comparison between Two Different Rheometry Techniques. *Langmuir* **2009,** 25, (13), 7393-7400.

50. Edwards, D. A.; Brenner, H.; Wasan, D. T., In *Interfacial Transport Processes and Rheology*, Butterworth-Heinemann: Boston, 1991.

51. Maestro, A.; Langevin, D.; Monroy, F., Amorphous freezing in two dimensions: from soft coils to rigid particles. *European Physical Journal E* **2010,** in press.

52. Angell, C. A., Formation of glasses from liquids and biopolymers. *Science* **1995,** 267, 1924-1939.

53. Binder, K.; Baschnagel, J.; Kob, W.; Paul, W., Glass physics: still not transparent. *Phys. World* **1999,** 12, 54.

54. Weeks, E. R.; Crocker, J. C.; Levitt, A. C.; Schofield, A.; Weitz, D. A., Three-dimensional direct imaging of structural relaxation near the colloidal glass transition. *Science* **2000,** 287, (5453), 627-631.

55. Monroy, F.; Ortega, F.; Rubio, R. G.; Ritacco, H.; Langevin, D., Surface rheology of two-dimensional percolating networks: Langmuir films of polymer pancakes. *Physical Review Letters* **2005,** 95, (5).

56. Kohlrausch, R., *Prog. Ann Phys* **1847,** 12, 393.

57. Williams, G.; Watts, D. C., Non-symmetrical dielectric relaxation behaviour arising from a simple empirical decay function. *Trans Faraday Soc* **1970,** 66, 80.

58. Das, S. P., Mode-coupling theory and the glass transition in supercooled liquids. *Rev. Mod. Phys.* **2004,** 76, 785-851.

59. Ngai, K. L., Short-time and long-time relaxation dynamics of glass-forming substances: a coupling model perspective. *Journal of Physics-Condensed Matter* **2000,** 12, (29), 6437-6451.

60. Leblanc, N.; Le Cerf, D.; Chappey, C.; Langevin, D.; Metayer, M.; Muller, G., Polyimide asymmetric membranes: Elaboration, morphology, and gas permeation performance. *Journal of Applied Polymer Science* **2003,** 89, (7), 1838-1848.

61. Sastry, S.; Debenedetti, P. G.; Stillinger, F. H., Signatures of distinct dynamical regimes in the energy landscape of a glass-forming liquid. *Nature* **1998,** 393, (6685), 554-557.

62. Riande, E.; Diaz-Calleja, R.; Prolongo, M.; Masegosa, R.; Salom, C., *Polymer Viscoelasticity. Stress and Strain in practice*. New York, 2000.

63. Bennemann, C.; Donati, C.; Baschnagel, J.; Glotzer, S. C., Growing range of correlated motion in a polymer melt on cooling towards the glass transition. *Nature* **1999,** 399, (6733), 246-249.

64. Gennes, P.-G. d., Glass transitions in thin polymer films. *Eur. Phys. J. E* **2000,** 2, 201.

65. Cicuta, P.; Stancik, E. J.; Fuller, G. G., Shearing or Compresing a Soft Glass in 2D: Time-concentration Superposition. *Phys. Rev. Lett.* **2003,** 90, 236101-.

66. Maestro, A.; Ortega, F.; Rubio, R. G., Surface Rheology of poly (methyl methacrylate) Langmuir monolayers: Evidences of a Glassy-like dynamic. *in preparation* **2010**.

67. Hilles, H.; Maestro, A.; Monroy, F.; Ortega, F.; Rubio, R. G.; Velarde, M. G., Polymer monolayers with a small viscoelastic linear regime: Equilibrium and rheology of poly(octadecyl acrylate) and poly(vinyl stearate). *Journal of Chemical Physics* **2007,** 126, (12).

68. Hilles, H. M.; Ritacco, H.; Monroy, F.; Ortega, F.; Rubio, R. G., Temperature and Concentration Effects on the Equilibrium and Dynamic Behavior of a Langmuir Monolayer: From Fluid to Gel-like Behavior. *Langmuir* **2009,** 25, (19), 11528-11532.

69. Keddie, J. L.; Jones, R. A. L.; Cory, R. A., SIZE-DEPENDENT DEPRESSION OF THE GLASS-TRANSITION TEMPERATURE IN POLYMER-FILMS. *Europhysics Letters* **1994,** 27, (1), 59-64.

70. Forrest, J. A.; DalnokiVeress, K.; Stevens, J. R.; Dutcher, J. R., Effect of free surfaces on the glass transition temperature of thin polymer films. *Physical Review Letters* **1996,** 77, (10), 2002-2005.

71. Gennes, P.-G. d., *Eur. Phys. J. E* **2000,** 2, 201.

72. Ngai, K. L.; Yamamuro, O., Thermodynamic fragility and kinetic fragility in supercooling liquids: A missing link in molecular liquids. *Journal of Chemical Physics* **1999,** 111, (23), 10403-10406.

73. Debenedetti, P. G.; Stillinger, F. H., Supercooled liquids and the glass transition. *Nature* **2001,** 410, (6825), 259-267.

74. Monroy, F.; Ortega, F.; Rubio, R. G.; Velarde, M. G., Surface rheology, equilibrium and dynamic features at interfaces, with emphasis on efficient tools for probing polymer dynamics at interfaces. *Advances in Colloid and Interface Science* **2007,** 134-35, 175-189.

75. Giermanska-Kahn, J.; Monroy, F.; Langevin, D., Negative effective surface viscosities in insoluble fatty acid monolayers: Effect of phase transitions on dilational viscoelasticity. *Physical Review E* **1999,** 60, (6), 7163-7173.

Part III

High-Frequency rheology of
Interfacial Complex systems

Aim

It is well known that transversal or capillary and dilational motions are found coupled at fluid interfaces; thus, the dilational viscoelastic behaviour of many complex systems adsorbed at these fluid interfaces can be obtained from the analysis of the propagation characteristics of capillary waves excited by transverse waves devices. From this perspective we have developed a device in which it is possible generate capillary waves onto the surface of a fluid by non-invasive electrical excitation. This method allows one to obtain further insight in the dynamical behaviour at moderate-high frequencies (concretely, from 10*Hz to 1.2kHz*) of surfactants, polymers or other systems, including their mixtures, adsorbed as *Gibbs* or *Langmuir* monolayers at fluid interfaces. Under the capillary waves phenomenon framework, the next chapters are organized as follows:

In **Chapter 3** we highlighted the set up of the non-invasive technique developed, which is based in the excitation of capillary waves by means of an electrical field onto arbitrary fluid surfaces. In **Chapter 4** we studied the dilational viscoelastic behaviour at high frequencies (short time domain) by the capillary waves method of monolayers of poly (methyl methacrylate) and poly (*tert*-butyl-acrylate). This study is focused in the relation between the 2D-conformational scenario adopted by each polymer and their dynamical behaviour. In **Chapter 5** we addressed the dynamical viscoelastic of the complex system formed by silica-nanoparticles and negative-charged surfactants over a broad frequency range by means of the combination of several rheological methods including *ECW*. Finally, in **Chapter 6**, we report the dilational rheology of the mixtures based on a protein, such as βeta-Casein, and surfactants with different charge.

Chapter 3

Capillary waves to study Interfacial viscoelasticity: New improvements in an old technique

Abstract

The study of the propagation of excited surface waves leads to a method to highlight the dilational viscoelasticity behaviour of many interfacial complex systems. We thus have developed a non-invasive technique based on the excitation of capillary waves by means of an electrical field on liquid surfaces. Furthermore, the spatial profile of the capillary waves is scanned by the reflection of a laser beam from the fluid surface to a position–sensitive photodiode. The dilational viscoelasticity behaviour of fluid surface may be obtained from the analysis of the propagation of the capillary waves by means of the dispersion relation of the surface modes explained by surface hydrodynamics. We describe our set up and review work in this area to get further insight in the theoretical and experimental understanding of this problem.

1. Introduction

Fluid–fluid interfaces when monolayers of amphiphilic molecules are present can be important both in nature and in many industrial applications.[1, 2] Thus, the knowledge of monolayer viscoelasticity is important to improve the understanding of technological processes where these soft surfaces play an essential role, e.g.: coating, wetting, foaming and emulsification, foam and emulsion stability, Langmuir-Blodgett deposition, two phase flow in porous media, etc.[3]

It is well known that many surfactants, polymers with polar groups among them, tend to adsorb at air–water interfaces, forming either Gibbs monolayers, when adsorbed from a bulk solution of the polymer or surfactant, or Langmuir films when, being insoluble in the adjacent bulk fluid phases, the surface active material can be spread and later adsorbed at the interface. All of these monolayers adsorbed have been found to support several rheological modes at equilibrium and present viscoelastic character.[4] *Capillary* and *longitudinal* motions have been found the most important ones for thin adsorbed monolayers of small monomeric amphiphiles.[5] However for thicker monolayers other modes as *bending* and *splay* could be important as well.[6] It is should be note that at a free liquid surface, that is, the air–water interface, the viscoelastic behaviour depends of the coupling between transverse (capillary) and longitudinal (dilational) modes.[7] Consequently, the observation of surface viscoelastic properties should be interpretable in terms of the surface organization of amphiphilic molecules like polymers, surfactants, etc. Furthermore, the surface viscoelastic behaviour is of intrinsic interest due to the insight into the stability of interfaces, a relevant aspect in emulsions and fluid flow.

It was shown by Lord Kelvin[8] many years ago that the properties of small surface waves, called capillary waves or ripples, are mainly restored by the surface tension γ, in contrast to long waves where gravity g is the main force which tends to restore the position of the surface. In this context, it is well known that the presence of a monolayer of a surface active material at the surface affects the properties of surface waves. Indeed, a spread monolayer with viscoelastic behaviour produces a resistance against the periodic surface expansion and compression which accompany wave motion. As a result, the pattern of liquid flow underneath the surface is modified, giving rise to a higher rate of energy dissipation by viscous friction, and consequently of higher damping than would be expected for the surface of a pure liquid. It is important to mention that Levich was the first to highlight the indirect relationship between elastic surface properties and wave damping.[9]

In the present chapter, we will describe a device designed and developed for the study of the high frequency dynamical behaviour of several interfacial complex systems, like polymers, surfactants, etc., spread in the air–water interface. Concretely, we report the set up developed of a new technique able to excite surface capillary waves in the air-water interface in the frequency range from 10*Hz* to 2*kHz* by application of an electric field (~500*V*) trough a blade positioned close to the interface. The wave vector *q* and the corresponding spatial damping coefficient β of the electrocapillary waves formed are determined by optical reflectometry of a laser beam. These two parameters allow us to determine the dilational viscoelasticity using the dispersion curve of the surface modes take into account from the surface hydrodynamics theoretical approach.[5] Indeed, capillary waves come out from the linearized Navier–Stokes equation subject to boundary conditions at the fluid–fluid interface where a dispersion relation is defined in terms of the surface tension γ and dilational elasticity ε. Finally, when a monolayer is spread into a fluid surface, the propagation characteristics of this capillary waves on the surface of the fluid vary turning in complexity and thus provide us information about the dilational interfacial viscoelasticity.[10]

This chapter is organized as follows: Section 2 describes the theoretical background necessary to understand how to relate the transversal waves excited onto a fluid surface covered by a polymer or surfactant monolayer and its dilational viscoelasticity. The experimental set up developed is further described in Section 3. The methods of data analysis are presented in Section 4. The calibration of the technique is discussed in detail in Section 5. Finally, in Section 6, data on monolayers of a synthetic polymer such as poly (vinyl acetate) (PVAc) is reported as an example of the application of this method. This system is chosen because it has been previously studied.[11, 12]

2. Theoretical background

2.1 Monolayers viscoelasticity

Monolayers exert a resistance against various types of surface deformation. In the Krammers treatment[5, 13, 14], the monolayer is assumed to be isotropic in the surface plane. The elastic free-energy density is given by $f = (1/2)k_1(u_{xx}+u_{yy})^2 + (1/2)k_2 u_{zz}^2 + (1/2)k_3(u_{xx}+u_{yy}) u_{zz} + (1/2)k_4[(u_{xx}+u_{yy})^2 + 4u_{xy}^2] + 2k_5(u_{xz}^2+u_{yz}^2)$, where *z* is the direction of the surface normal, *u* is the surface displacement, and $u_{ij} = (1/2)(\partial u_i/\partial x_j + \partial u_j/\partial x_i)$. The K_i are elastic coefficients. For thin monolayers *u* is larger than the film thickness *h*, and consequently all the z derivatives vanish. By integration of *f* over *z* in the case where *u* is only function of *x*, one obtains the elastic free energy per unit area:

$$F = \frac{1}{2}\varepsilon\left(\frac{\partial u_x}{\partial x}\right)^2 + \frac{1}{2}G\left(\frac{\partial u_y}{\partial x}\right)^2 - \frac{1}{2}\gamma\left(\frac{\partial u_z}{\partial x}\right)^2 \qquad (3.1)$$

The stress tensor is $\sigma_{ij}=\partial F/\partial u_{ij}$, and the force per unit area is $F_i = \partial \sigma_{ij} / \partial x_j$. Its components are:

$$F_x = \varepsilon\frac{\partial^2 u_x}{\partial x^2}; \quad F_y = G\frac{\partial^2 u_y}{\partial x^2}; \quad F_z = -\Pi\frac{\partial^2 u_z}{\partial x^2} \qquad (3.2)$$

where ε, G and Π are positive coefficients as it will be explained latter. When there is no monolayer at the interface there is already a force per unit area exerted on the surface, $F_z = \gamma_0(\partial^2 u_z / \partial x^2)$, where γ_0 is the *bare* surface tension. As a result the total vertical force is

$$F_z = \left(\gamma_0 - \Pi\right)\frac{\partial^2 u_z}{\partial x^2} = \gamma\frac{\partial^2 u_z}{\partial x^2} \qquad (3.3)$$

The surface tension in the presence of the monolayer is decreased by the surface pressure, Π. Thus, the free energy variation when the surface area varies by δA is $\delta F= \gamma\, \delta A= (\gamma_0 - \Pi)\, \delta A$.

Pure shear deformations are represented by traceless u_{ij} tensor.[13] Any deformation can be written as the sum of pure shear and compression terms; for a motion in the surface plane ($u_z = 0$) $u_{ij}=(1/2)(u_{xx}+u_{yy})\delta_{ij} + (1/2)k_2\, u_{zz}^2 + [u_{ij} - (1/2)\,(u_{xx}+ u_{yy})\,\delta_{ij}]$. F can be rewritten as:

$$F = \frac{1}{2}\left(\varepsilon - G\right)\left(u_{xx} - u_{yy}\right)^2 + G_{ij}\left[u_{ij} - \frac{1}{2}\left(u_{xx} - u_{yy}\right)\delta_{ij}\right]^2 \qquad (3.4)$$

where it is seen that the compression modulus is $\varepsilon - G$, and the shear one is G. In the case of interfaces with an adsorbed film the modulus acting in the horizontal force parallel to Ox is then the sum of the pure compression ε and pure shear module G, $\varepsilon(t) = \varepsilon + G$. This fact is due to uniaxial compression always involves shear. Indeed, it is well known that shear modulus is nonzero only in solid or gel–like monolayers.[15, 16] This compression modulus is usually called as *dilational viscoelasticity:*

$$\varepsilon\left(t\right) = -A_0\,(\partial\Pi/\partial A) \qquad (3.5)$$

which this time-dependent modulus take account the elastic energy storage on dilating the monolayer, δA. However, the shear component can be independently measured with specific devices,[17, 18] but *usually* the whole dilational modulus is the dominant parameter in surface rheology. [15] The longitudinal restoring force is then proportional to the dilational modulus as shown the definition of F_x in Equation 3.2. In the case of the molecules cannot exchange between the

monolayer and the bulk liquid, both viscoelastic parameters govern, coupled together, the longitudinal interfacial motion, or Marangoni flow, which is driven by the surface tension gradient due to surface increase in the area A. Indeed, the horizontal force F_x is due to surface tension gradients (Marangoni force) $F_x = \partial\gamma/\partial x = (\partial\gamma/\partial\Gamma)(\partial\Gamma/\partial x)$, and the surface concentration Γ depends on x as all the other surface variables. Because the monolayer is insoluble, the conservation of matter in the surface gives the definition for the dilational modulus as:

$$\varepsilon = -\Gamma \frac{\partial \gamma}{\partial \Gamma} = \Gamma \frac{\partial \Pi}{\partial \Gamma} \qquad (3.6)$$

which is consistent with Equation 3.5. When the monolayer is soluble, i.e., when it can exchange matter between surface an bulk, Γ changes due to dissolution/re-adsorption process. Equation 3.6 can only be used when the rate of compression is faster than the rate of dissolution. When this is not the situation, models have been proposed to assume that desorption and adsorption proceed freely, without energy barriers.[19] More complex situations like the presence of adsorption/desorption barriers, exchange with micelles, etc., are explained in ref. [19]. These models are valid only for non-ionic amphiphilic molecules. For ionic ones, they can be refined to take into account the influence of surface potential in the diffusion process.[20]

In the context of the viscoelasticity theory, for a small amplitude oscillatory motion [$\delta A(t) \sim e^{i\omega t}$] of frequency ω, the linear response of the system can be described by a complex moduli:

$$\tilde{\varepsilon}(\omega) = \varepsilon(\omega) + i\omega\kappa \qquad (3.7)$$

Where ε is the elastic modulus and κ is the dilational viscosity.[10] This viscoelastic dilational modulus contains information about how the surface pressure changes on dilating the film, and thus, about the changes on the adsorption rate and the molecular conformation stressed by the external deformation. These changes are dependent of the time scale of the rheological experiment, in our case of the frequency of the applied deformation in surfaces waves experiment. In addition, the force per unit area is now the sum of elastic and viscous terms. For oscillatory deformations, the force components are still given by Eq. 3.3; however ε and *G* are replaced by the correspondent complex numbers: ε+iωκ and G+iωη. The surface tension, γ is an equilibrium property and cannot be treated as a response function.

2.2 Surfaces Modes and dispersion equation

Fluid surfaces are not perfectly flat, even under equilibrium conditions, they are in a state of continual fluctuation around the equilibrium position of the

interface due to stochastic thermal perturbations ~ k_BT (noise level depending on temperature).[5] They thus present some time-dependent roughness as shown the scheme of Figure 3.1. As a result, under thermal agitation or by mechanical stress, any displacement of the fluid interface with respect to the flat level shape could be conceived as a surface motion driven by an externally force (random or otherwise), and restored trough of the viscoelastic response of both the adjacent phases and eventually the interface itself.

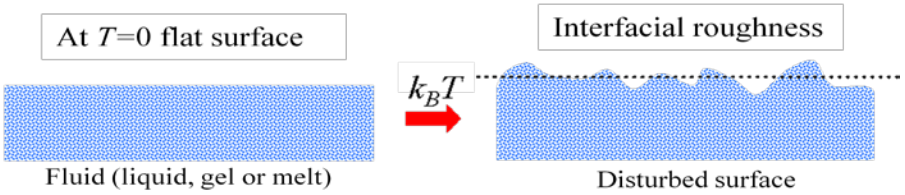

Figure 3.1. Scheme of the surface roughness explained by the fluctuations of the fluid interface about the equilibrium position due to stochastic thermal perturbations. The roughness generates extra area and indeed the so created excess of surface energy act as a restoring force of the flat shape. Any surface curvature induced by thermal roughness tends to be restored by the Laplace overpressure (see Eq. 3.3).

For thermal random motion, the interfacial shape can be described by a Fourier series of independent plane waves propagating within the $xy-$ plane and slightly penetrating the bulk phases adjacent to the interface. If the equilibrium level position of the interfacial plane is placed at z=0, displacements of the surface $u(r,t)$ can be written as follows:

$$u(r,t) = \sum_q u_q(q)\, e^{i(q\cdot r-\omega t)} \qquad (3.8)$$

where the sum extends over all wave vectors, q, the magnitude of which are defined by the wavelength of these surface capillary waves as $q=2\pi/\lambda+i\beta$; hence, the imaginary part is related to the damping coefficient β. This time and space evolution can be described by a dispersion equation, which relates q and the frequency, $\omega(q)$. The response is linear and single surface modes are excited. Therefore, u_x describes compression deformation modes, u_y shear modes and u_z transverse modes (see Figure 3.2). The total surface energy is described as:

$$F = \frac{1}{2}\varepsilon q^2 u_x^2 + \frac{1}{2}Gq^2 u_y^2 + \frac{1}{2}\left(\gamma q^2 + \Delta\rho g\right)u_z^2 \qquad (3.9)$$

In which several contributions have been added to Equation 3.2. i.e.: bare surface tension contribution, $\gamma_0 = \gamma - \Pi$ and gravity contribution, where$\Delta\ \rho=\rho_1-\rho_2$ is the density difference between lower and upper bulk phases. When q is smaller than $q_1 = \sqrt{\Delta\rho g}/\gamma$, u_z modes are gravity modes, however when q is larger than q_1, they are capillary modes. Very high q modes are not usually observed excepted in

synchrotron scattering experiments.[21] In thin monolayers, surface tension γ is considered as a main restoring force for *capillary waves* (out-of-plane deformations of the interface with respect to the flat equilibrium shape) (see Figure 3.3). Indeed, any local curvature causes a γ-governed *Laplace* stress which tends to restore the planar equilibrium shape of the interface. Gravity is also a relevant restoring force, however for much longer waves than ripples.[22]

The surface modes can be thermally excited and give rise to scattering of light. According to Eq. 3.9 the deformations u_x, u_y, u_z are statistically independent, and their mean square values are:

$$\left\langle u_x^2 \right\rangle = \frac{kT}{\varepsilon q^2};\ \left\langle u_y^2 \right\rangle = \frac{kT}{Gq^2}$$
$$\left\langle u_z^2 \right\rangle = \frac{kT}{\gamma q^2 + \Delta\rho g} \qquad (3.10)$$

Only u_x and u_z are associated to local density variations and scatter light due to the corresponding refractive index variations. It is noteworthy that only capillary waves (u_z) scatter an appreciable amount of light.[5]

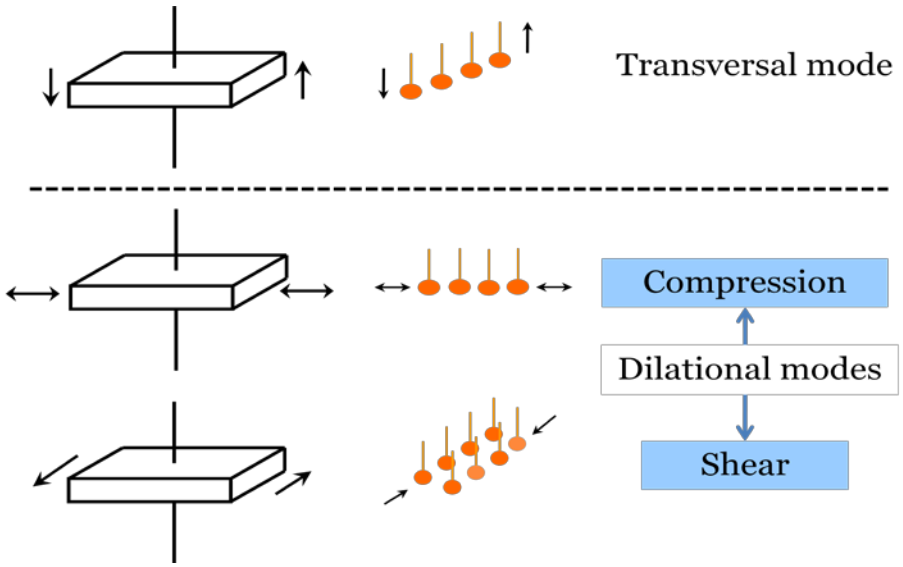

Figure 3.2. Different types of surface modes: Transversal (out of plane) and Dilational (in plane) composed by two different motions: Compression and Shear. Adapted from Ref.4.

The resolution of the hydrodynamic equations in terms of an oscillatory motion proposed by the Eq. 3.8 for a monolayer at a flat fluid–fluid interface lead us to a Dispersion equation where the motion along y evolves independently from the motion along *x* and *z*. Shear modes are then completely decoupled from capillary and compression modes: Both their amplitude and time evolution are independent. On the other hand the displacements associated with capillary and compression modes are statically independent, as shown Eq. 3.9 which does not

contain any cross term $u_x u_z$, so according to the equipartition theorem $< u_x u_z > = 0$.[5] However, their evolution is coupled, even if $u_x\,(t=0)=0$ when a capillary mode is excited, $u_z\ (t=0)\neq 0$, u_x becomes non zero at later times. This coupling also appears in the dispersion equation as seen before.

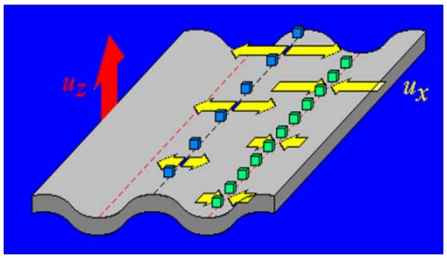

Figure 3.3. Transverse u_z and Longitudinal (dilational) u_x motions at a fluid interface. The cubes represent surface-active molecules (in short surfactants) responsible of a surface-tension decrease and the horizontal arrows represent the Marangoni stress due to surface tension gradients created by the surfactant concentration gradient.

Capillary waves are dispersive and thus a dispersion relation has been formulated for monolayers at an air–water interface taking in account the boundary conditions for the transverse and longitudinal motions of the interface explained before.

$$D(q,\omega) = T(q,\omega;\gamma)\cdot L(q,\omega;\tilde{\varepsilon}) + C(q,\omega) = 0 \qquad (3.11)$$

Where:

$$\begin{aligned} T(q,\omega;\gamma) &= \left[\gamma q^2 + i\eta_1\omega(q+m_1) + i\eta_2\omega(q+m_2) - \frac{(\rho_1+\rho_2)\omega^2}{q}\right] \\ L(q,\omega;\tilde{\varepsilon}) &= \left[\tilde{\varepsilon}(\omega)q^2 + i\eta_1\omega(q+m_1) + i\eta_2\omega(q+m_2)\right] \\ C(q,\omega) &= \left[\eta_1\omega(q-m_1) - \eta_2\omega(q-m_2)\right]^2 \ \text{(Coupling term)} \end{aligned} \qquad (3.12)$$

Here, η_i represent the bulk viscosity and ρ_i the bulk density with i=1,2 means the lower and upper phase respectively. The inverse of penetration depth of the surface velocity field, m_i is defines as $m_i = (q^2 - i\omega\rho_i/\eta_i)^{1/2}$, $Re(m) > 0$ showing a dependency on the density ρ_i and viscosity η_i of each phase.

It should be mention that the constant C controls the coupling between the Capillary term $T(\gamma)$ governed by surface tension and the Longitudinal one $L(\varepsilon)$ which only depends on the dilational viscoelasticity modulus. Furthermore, this coupling constant only depends on density ρ_i and shear or dynamic viscosity η_i of the adjacent bulk phases. From Equation 3.10 and 3.11 it is possible to conclude that the coupling between capillary and compression modes disappears when $\rho_1=\rho_2=\rho$ and $\eta_1=\eta_2=\eta$, i.e., when the monolayer is placed in the interface between identical fluids. This is never the case, however when the two fluids have

different properties, for instance, water and alkane, the decoupling is already significant.[7] The perfect decoupling is also found in bilayers immersed in water, where a theoretical description is also available. For a generic liquid-gas interface, $\eta_2 << \eta_1 = \eta$, $\rho_2 << \rho_1 = \rho$, and the coupling between capillary and compression modes is the largest.

In the framework of the Dispersion equation for a monolayer in the air-water interface, capillary and dilational modes are found coupled together. We thus obtain the dilational viscoelasticity modulus of a monolayer spread at the free surface of a liquid from the analysis of the propagation characteristics of capillary waves probed by transverse wave devices.[5] The dispersion relation obtained has two different solutions corresponding to two propagating modes: capillary and longitudinal or dilational waves.[22] The capillary mode is approximately given by:[8, 9]

$$\omega_c \approx \left(\frac{\gamma q^3}{\rho}\right)^{1/2} + \frac{2i\eta q^2}{\rho} \tag{3.13}$$

The dilational mode is approximately given by[9, 14]

$$\omega_d \approx \frac{\sqrt{3}}{2}\left(\frac{\varepsilon^2 q^4}{\eta\rho}\right)^{1/3} + \frac{i}{2}\left(\frac{\varepsilon^2 q^4}{\eta\rho}\right)^{1/3} \tag{3.14}$$

It should be noted that for wave motions on monolayers with non-zero viscosity will always be accompanied by dissipation of mechanical energy into heat. This fact means that wave motion is no longer pure sinusoidal, and the decay amplitude in distance should be accounted for by an imaginary part of q. Indeed, it is a complex number as: $q = 2\pi/\lambda + i\beta$, where the distance damping coefficient β is real and positive number. For bare interfaces a limiting solution can be obtained. One is the Kelvin's law for the frequency of capillary waves propagating on the free surface of a liquid:

$$\omega_q^2 = \frac{\gamma}{\rho} q^3 \tag{3.15}$$

and the other is Stoke's law accounting for the spatial damping due to the viscous friction with the bulk liquid:

$$\beta = 2\frac{\eta}{\rho} q^2 \tag{3.16}$$

If viscoelastic dilational effects exist, the capillary damping exceeds this minimum value expected for bare interfaces. Recently, Buzza et al. have shown that the surface tension γ is a real quantity and has to be equal to the equilibrium static surface tension.[6, 23] They have developed theoretical modifications

clarifying the previous models proposed by Goodrich and Krammer[14] which considered a complex surface tension. The important practical consequence of Buzza's analysis is the fact that if γ is measured independently and simultaneously of the propagation of capillary waves, it is then plausible to get the viscoelasticity modulus from the analysis of the spatial dependence of q and β in term of the dispersion relation proposed.

As a final remark, the coupling between capillary and compression points out that the use of capillary waves is worth to measure dilational viscoelasticity. As shown above, the accuracy will be better for monolayer at air-fluid interfaces. It is should be noted that the damping of waves is maximum at a surfactant concentration for which the frequency of the capillary and compression waves are about equal $\omega_c \approx \omega_d$. This is the resonance phenomenon where the propagative parameters of the capillary waves are sensible to ε, and as a consequence meaningful values of ε and κ can be obtained. Taking account the definitions of both frequencies from Equations 3.13 and 3.14 we thus define a resonance wavenumber q_R as follows:

$$q_R = \left(\frac{3}{4}\right)^3 \frac{\varepsilon^4 \rho}{\gamma^3 \eta^2} \tag{3.17}$$

As an experimental thumb rule, the resonance condition can be obtained from the definition of the coupling parameter β when $\omega_c \approx \omega_d$.[5]

$$\beta_R = \left(\frac{\varepsilon}{\gamma}\right)_R = \left(\frac{q\eta^2}{\gamma\rho}\right)^{1/4} \approx 0.1 - 0.5 \tag{3.18}$$

When the compression elasticity and viscosity are too large, the capillary waves are no longer affected by these parameters, and the surface behaves as a solid plate. Therefore the sensitivity of the damping coefficient of transverse capillary waves to the surface elasticity decreases strongly with the increase of the surface elasticity as pointed out the resonant condition showed by Eq. 3.18.

3. Experimental set up

This section describes the experimental set up of a method based on exciting capillary waves or ripples by the propagation of monochromatic transverse waves excited at a given frequency by electrical actuators. The technique designed and developed here is similar to the one previously describe by Ito et al.[24] and Jayalakshmi et al.[25] We thus have designed a new device which incorporates new improvements in relation to the previous. i.e., it makes possible to enlarge the frequency range accessible as well as to generate transversal waves with higher

amplitudes which able us to study the non-linear viscoelastic region. This technique leads us to generate capillary waves in the frequency range from 10*Hz* to 2 *kHz* at the air–water interface upon application of an *AC* electric field trough a blade positioned within 100μm to the interface. The spatial wave vector q ($=2\pi/\lambda$) and the corresponding wave damping coefficient β are determined by measuring the optical diffraction of a laser beam moving along the xy-plane parallel to the interface. At the same time, the device is able to measure the surface tension γ. All of these characteristic parameters of the ripples are then used to obtain the dilational viscoelasticity behaviour of the monolayer placed at the air–water interface by means of the Dispersion relation.[5] A schematic view of the set up of the device generator and detector of capillary waves *(ECW)* designed is shown in Figure 3.4. To get better insight in the design of the technique a set of pictures of this set up is also shown in Figure 3.5.

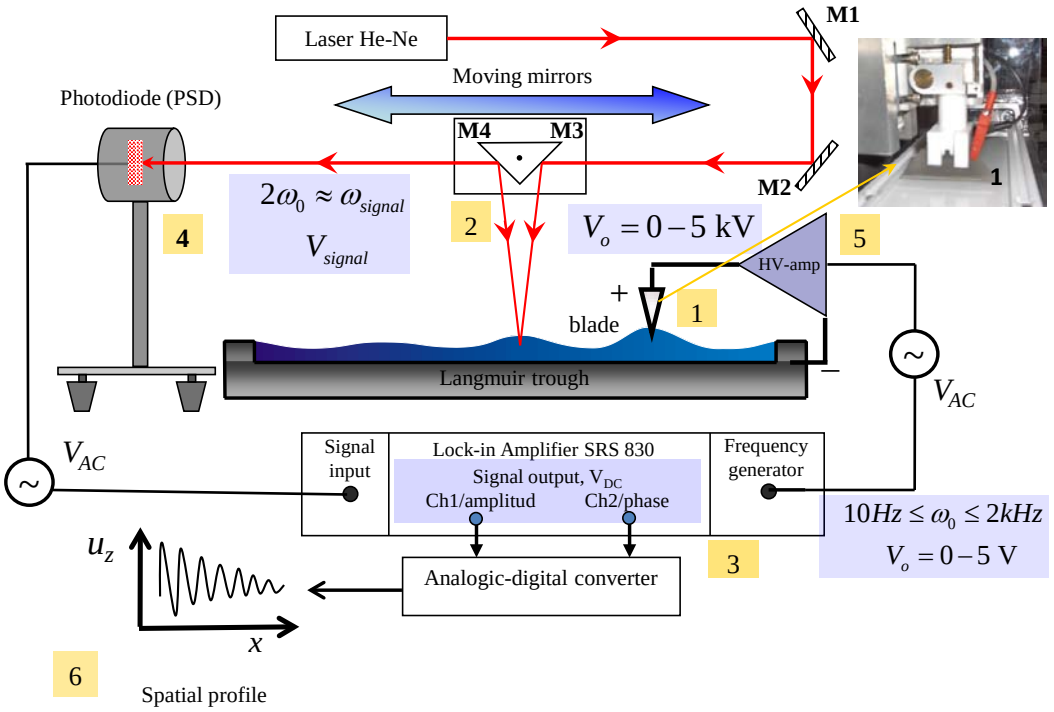

Figure 3.4. Scheme of the optical set up of the device generator and detector of capillary waves. Each part of the optical train noted by a number is described in the main text. This diagram shows the laser beam which scans the entire air–water interface (red solid line). All the main components of the device are also show in this scheme. (3) The Frequency generator applied a sinusoidal voltage in the range of 0–5V amplified thanks to the high voltage amplifier by a factor of 100 reaching up to 500V (5) between the blade (1) and the fluid surface located close to the blade. Generated capillary waves are detected by reflection of the laser beam with the fluid surface. This laser beam scanning the interface in the direction parallel to the propagation of waves by the moving mirrors component (2). The position sensitive photodiode (4) captures the laser beam on its surface and the resulting electrical signal is redirected to the Lock-in amplifier (3). Here, the resulting signal is multiplied with the reference signal and obtains a spatial profile containing information from the characteristic parameters of the capillary waves generated. All of these components are automatically controlled by the software programme implemented.

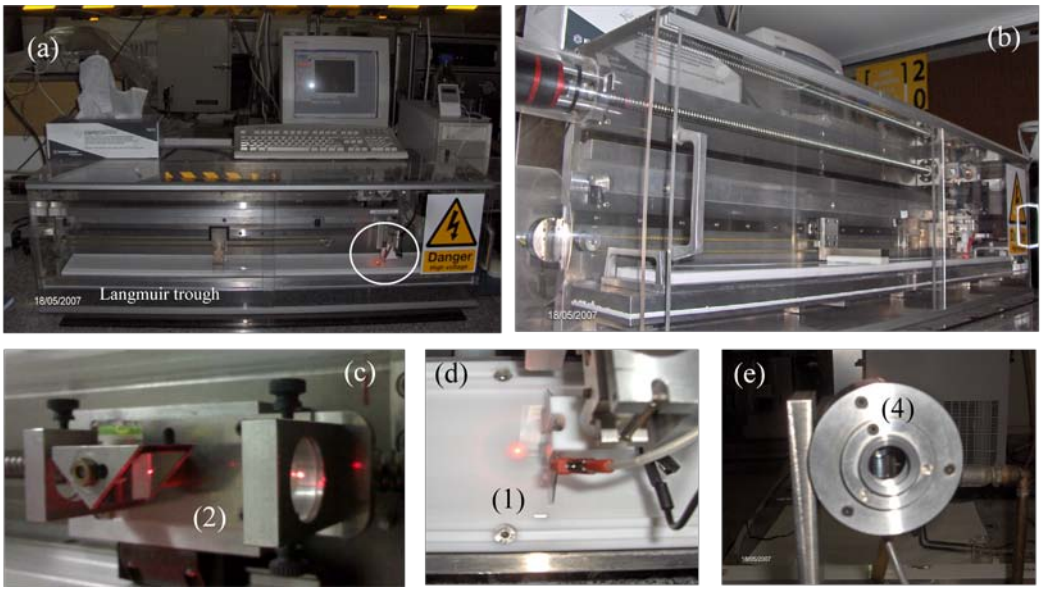

Figure 3.5. Set of pictures of the device generator and detector of capillary waves. (a) General view of the instrument set up placed in the laboratory. The circle shows the blade where the potential is applied onto the fluid interface. (b) Other perspective of the device where is possible note several parts of it. (c) Moving mirrors mechanism which focuses the laser beam onto the interface. It screens all the spatial profile of the capillary waves generated. (d) upper view of the blade above the Langmuir trough. (e) Detail of the Photodiode sensible to position (PSD) which detects the different positions of the laser beam.

The scheme in Figure 3.4 shows all the components of the device. The polymer or surfactant is spread on the water surface placed in the Langmuir trough. The transversal waves are generated by an sinusoidal electric field of frequency ω_0 from a function generator (3) amplified by a high voltage amplifier (5), and applied to the air–water interface by a steel blade located close to the fluid surface (1) (Fig. 3.5.d). Also, the reference electrode is placed inside the fluid. The generated field reaches high voltages (~100–500*Vac*). The spatial profile of the capillary waves generated is obtained by laser reflectometry, i.e., by means of the reflection of laser beam in a point on the fluid surface. Indeed, the laser beam reflected is *re*directed to a position sensitive photodiode (*PSD*) which detects the different directions of this laser beam. Because the mirrors responsible of the reflection of the beam on the surface are located on a mobile device (2), it is possible to measure the amplitude of the capillary waves in the direction of propagation (Fig. 3.5.c). In other words, it is possible to measure the whole wave profile from the point where it is generated to the point where amplitude becomes zero by the effect of damping. Lock-in amplifier is responsible for amplifying the electrical signal from the detector *PSD* (4) by a signal filtering to improve the signal-noise ratio, and it also convolutes the signal with a reference signal generated by the same lock-in (Fig. 3.5.e). As a result a *dc* electrical signal with information about the amplitude and phase of the capillary wave generated and detected is obtained. The software implemented allows us to get analog signals,

after conversion into digital lock-in amplifier for the amplitude and phase of the capillary wave generated in terms of the displacement of the positioning of mirrors on the blade, which is monitored through the spatial profile of the wave (6).

3.1 Wave generation

In our experimental set up, we used a high electric field for the generation of transversal waves along the monolayer placed in the air-water interface; this phenomenon called electrocapillarity as it was pointed out by Miyano et al.[26] Concretely, we apply a high sinusoidal voltage between a steel blade and a monolayer deposited onto an air-water interface in a Teflon trough (Fig. 3.5.a,b). The sinusoidal voltage generated ($V_0 \approx V_0^0\ sin\ (\omega_0 t) \sim 0–5V$) by a function generator (*Lock in amplifier 830 Stanford Research System*) works properly in the frequency range from about 10 *Hz* to approximately 2*kHz*. This reference signal is amplified by a factor of 10^2 using a high voltage amplifier (supplied by TREK, model 601C) and applied between the sharp edge of the blade and the trough where the monolayer is deposited on the air-water interface, as shown Figure 3.6. The blade, situated just above the trough in its right end, must be very close to the interface (≈100μm), and placed straight and parallel to the surface in order to generate a plane wave without any noise associated to the edge of the blade. Because of the dielectric constant of water ($\varepsilon_1 \sim 80$) is much greater than that of air ($\varepsilon_0 \sim 1$), the monolayer in the interface tend to rise up to the blade. In opposition to this motion, there are two restoring forces: surface tension γ and gravity *g*, the latter being unimportant at capillary wavelengths.

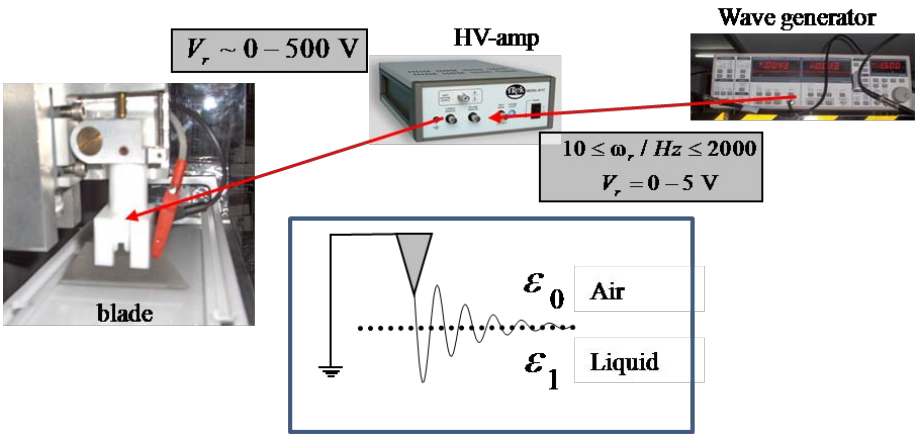

Figure 3.6 Scheme of the components in charge of the generation of capillary waves by application of a sinusoidal voltage between the blade and the air–liquid interface. These components are the wave generator which produces the oscillating electric field, the high-voltage amplifier which magnifies from 0 to 500*V* the electric signal and the steel blade; also the reference electrode would be located inside the fluid. As shown in the scheme the electrocapillary waves propagate along the air-liquid interface in the direction perpendicular to the blade.

It should be noted that the total electric energy change of the system, ΔE promoting the transversal displacement of the fluid (u_z) due to the fixed potential, Vr is given by[27, 28]

$$\Delta E = (1/8\pi)\int (D_1 \cdot E_0 - E_1 \cdot D_0)\,dx\,dz \qquad (3.19)$$

where E is the electric field, D is the electric displacement and the subscripts 0 and 1 refer to the situations before and after elevation of the ground surface with the application of the electric field. Due to the fact that $\varepsilon_1 > \varepsilon_0$, E is nearly perpendicular to the surface ($E_x \sim 0$). Assuming the boundary condition that D_z ($\approx u_z$) is continuous across the surface implies $D_0 \sim D_1$, and as a result Eq. 3.19 is reduced to

$$\Delta E = \left(\frac{1}{8\pi}\right)\frac{\varepsilon_0(\varepsilon_1 - \varepsilon_0)}{\varepsilon_1}\int_{A'} |E_0|^2\,dx\,dz \qquad (3.20)$$

Finally, the force acting on the surface given by $F = \partial E / \partial h$ taking into account the sinusoidal voltage applied, is given by[26, 27]

$$F = \left(\frac{1}{16\pi}\right)\frac{\varepsilon_0(\varepsilon_1 - \varepsilon_0)}{\varepsilon_1}\omega t)\,g(x,0)V dx(1+\cos 2 \quad \int_{\Delta x} | \quad |^2 \quad ^2 \qquad (3.21)$$

where g is a geometric factor related to the applied voltage.[28] It is well known that the electrical force is balanced by the surface tension due to the surface deformation u_z, thus the response of the surface is a stationary wave at twice of the applied frequency ($\omega = 2\omega_0$) with amplitude proportional to V_0^2. We thus confirm that the propagative characteristics of capillary waves come from the relation $u_z \Delta\varepsilon V \quad _r^2 \cos 2\omega\, t \quad _r$. It is also noteworthy that if the applied potential contains both an *dc* component an *ac* one at frequency ω_0, then the analysis of the electric force using $V_r = V_d + V_a \cos \omega_0 t$ it given by:

$$F \approx V_d^2 + V_a^2/2 + 2 \cdot V_d V_a \cos \omega_0 t + V_a^2/2 \cdot \cos 2\omega_0 t \qquad (3.22)$$

Figure 3.7 highlights that the capillary waves generated on the surface of a fluid have a characteristic frequency twice the excitation frequency. We thus represent the electrical signal gained by the position-sensitive detector (PSD) with a FFT-spectrum analyzer for an excitation frequency ω_r of 400*Hz* on the surface of pure water (*quality milliQ - RG*). It is noteworthy that the most important signal of the spectrum is predominantly at 800Hz, this frequency is twice that the excitation ($\omega = 2\omega_r$) as discussed above. This fact is due to the electrical effect which characterizes the formation of capillary waves. Also in the spectrum appear the 2nd harmonic order with respect to the fundamental frequency at 1600Hz as expected for a *dc* component; however it has a negligible amplitude (<1%). Finally, the excitation frequency appears at 400Hz and is a signal with very small amplitude

of the order of 2% respect to the capillary one. Thus, the fundamental signal of the spectrum of Figure 3.7 shows the formation of capillary wave on the surface of water and the other signals in the spectrum such as those existing at the excitation frequency and higher harmonic frequencies are not relevant because of its low intensity.

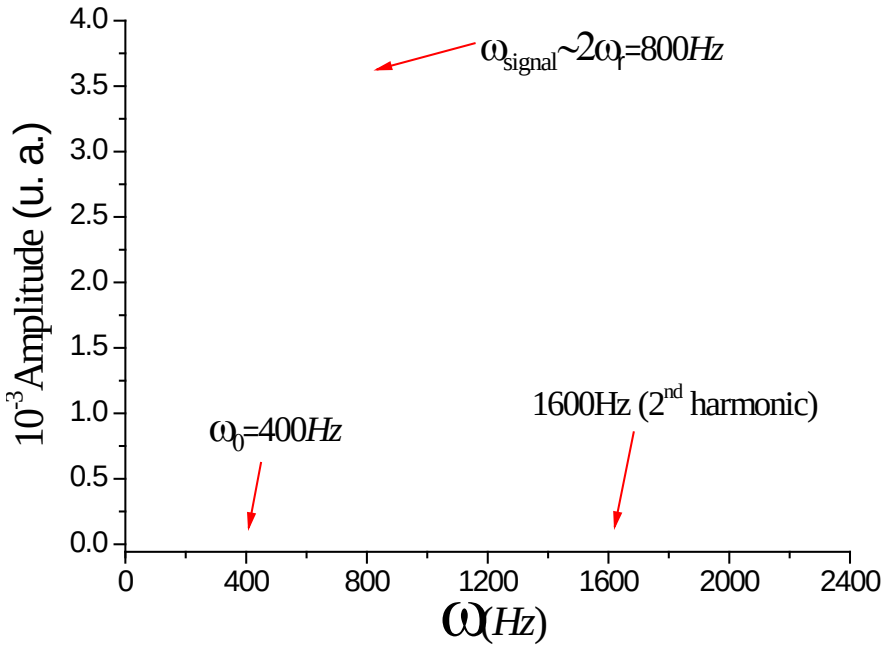

Figure 3.7 Fourier transform spectrum of amplitude of a capillary wave generated by the device as a function of the frequency ω. This spectrum which is obtained by an FFT-spectrum analyzer (*Stanford Research*, model *SR670-FFT)* corresponds to an experiment with ω_r = 400*Hz*. It is should be note that the frequency of the capillary wave is just the double of the reference $\omega = 2\omega_r$=800 *Hz*; this fact demonstrates the generation of a capillary wave according to the electrodynamics approach.[28] Also, a low intensity signal (~1%) appears in a frequency correspond to the second harmonic (1600 *Hz*).

3.2 Langmuir trough

The Langmuir trough used in this device is shown in Figure 3.5.a. It is made of *Teflon* with the following dimensions: length *L*=100 cm, width *B* =7 cm and total area A_0 = 700 cm^2; this large dimensions are useful for the damped capillary waves have sufficient space to move without being constrained by the size of the trough. A Pt Wilhelmy balance placed at the air-water interface was used as the surface force sensor. The instrument is placed inside a polyethylene box to control the atmosphere of the system. The temperature inside the box was controlled by passing thermostated water through the jacket of the trough. Near the interface, the temperature was measured with a precision of 0.01ºC, and the temperature control was better than ±0.05 ºC.

3.3 Optical train

Figure 3.8 illustrates schematically the optical set up of the instrument. The spatial profile of the excited electrocapillary wave is then scanned by laser reflectrometry. The laser beam comes from a 15*mW He-Ne* laser source with a wavelength of 633nm (*Coherent*). To be sensitive to a surface wave of wavelength λ the laser beam diameter is small compared to $\lambda/2$. Indeed, the shortest detectable wavelengths are limited by the size of the laser beam. Experimentally we have detected wavelengths less than 0.5*mm* on water corresponding to frequencies close to 1.5*kHz*. The optical set up leads the low intensity laser beam to be focused and then reflected by the interface. Indeed, the mirrors M1–M2 direct light from the laser to the mobile part where in it is located the mirrors responsible of the reflection M3–M4.[*] Indeed, Figure 3.8.b shows the configuration of the mirror M3 to direct the laser beam to the fluid surface and then when a fraction of the light is reflected redirect to the *PSD* detector by M4.

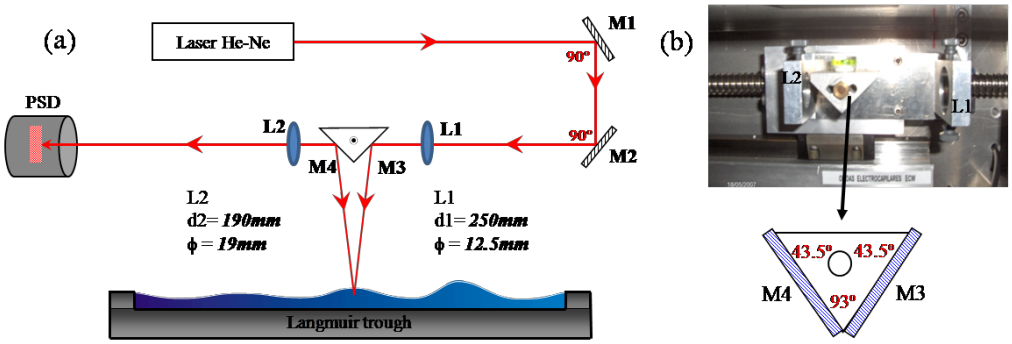

Figure 3.8 (a) Diagram of the optical set up. Each part of the optical train is described in the text. The diagram clearly shown the trajectory of the reference laser beam which focuses in the fluid surface (it acts as a mirror reflecting the beam) and then this spatial deflection is detected by a position sensitive photodiode (PSD). (b) A detail of the mechanism where the mirrors M3, M4 and the lenses L1, L2 are placed. This component is able to move in the xy-plane screening the entire whole fluid surface. It is fundamental in the design because with it is possible to get the spatial profile of the capillary waves generated.

More specifically, this component of the device consists of an aluminium prism with two mirrors inserted into its two sides. The prism has two angles of 43.5 º and one at 93 º, M3 mirror direct the beam to the surface of the fluid deposited in the trough. The reflected beam is directed to the position-sensitive photodiode (PSD) by the mirror M4 inserted into the other side of the prism. The circular achromatic lenses L1 (d=250*mm*) and L2 (d=190*mm*)[†] perform two tasks; L1 converges the reference beam to a single spot at the fluid interface and thus

[*] The lateral dimensions of the mirrors M1–M4 are 25.0 ± 0.25mm with a thickness of 1.0± 0.25mm. model 01 MFG 007/028 from *Melles Griot.*

[†] L1 correspond to the model 01 LAO 78 and L2 to the 01 LAO 588 from *Melles Griot.*

ensuring the beam diameter at the surface is not greater than 1mm. L2 converges the beam reflected onto the surface in the front plane of the photodiode, situated about 1*m* after the surface. Also L1 ensures that the diameter of the beam reaching the detector is not more than 1mm, one important factor in the sensitivity of the detection of the capillary waves. In order to get the spatial profile of the excited electrocapillary wave the mirrors M3–M4 mounted in the mentioned prism and the lenses L1–L2 move in the direction of propagation from the blade in a range from 1–750 mm (see Figure 3.8).

3.4 Detection system

The transversal waves are detected by the deflection of a laser beam reflected from the fluid surface. For this fact we used a position sensitive photodiode *PSD* (*Hamamatsu*) where the the absolute position of the laser beam determined by the center of mass of the light intensity distribution on the face of the photodiode is converted to an equivalent *ac* electrical signal. It makes possible to scan the fluid surface with an accuracy ±0.1*mm*. The *PSD* essentially consists in a photocurrent divider with two output leads (x_1, x_2). The difference between the two output currents (I_1, I_2) normalized by their sum lead us to known exactly the absolute position of the light beam $(I_1-I_2)/(I_1+I_2) \approx 2x$. Thus, a submicrometer detection is possible even thought the size of the laser beam may be larger than 1*mm*. The relation between the difference and sum of the currents is necessary to offset the light intensity variation of the laser beam itself o due to other factors.

It is noteworthy that the existence of experimental noise is mainly due to the oscillations of the fluid surface caused by vibrations of the device. To minimize it, the device is mounted onto an active damping anti-vibration platform and situated in a draft-proof enclosure. With this isolation unit active, the laser beam reflected from the liquid surface appears very stable. It is essential to minimize this noise because this amplitude is usually orders of magnitude larger than the signal one. The low s/n ratio inherent to this detection system is solved using a *lock-in* amplifier coupling between excitation and detection. Concretely we used a *lock-in* (830 *Stanford Research System*) to detect weak *ac* signals from the PSD detector at a frequency and a specific phase distinguishing over the noise components. The signal is amplified and combined with the first harmonic of the reference signal ($2\omega_0$) generated getting a product of two *ac* signals as follows

$$\begin{aligned} V &= V^0_{signal}\omega_{l}\cos\left(\ _{signal}\ -V\phi\cos\right) 2\omega^0_0\ t\ \ \left(\ \ _0\ +\phi_0\right) = \\ &= \frac{1}{2}V^0_{signal}\cdot V^0_0\omega\cos\left[\left(2\omega_{signal}-\ \ _0\right)+\phi_{signal}-\phi_0\right]- \\ &-\frac{1}{2}V^0_{signal}\cdot V^0_0\omega\cos\left[\left(2\omega_{signal}+\ \ _0\right)+\phi_{signal}+\phi_0\right] \end{aligned} \qquad (3.23)$$

where one of the two *ac*-resulting signals has the frequency difference ($\omega_{signal} - 2\omega_0$) for the multiplied signals, and other one the frequency sum ($\omega_{signal} + 2\omega_0$). This signal obtained is passed through a low-pass filter and then the *ac* components are removed. If both frequencies are identical ($\omega_{signal} \approx 2\omega_0$) the time average leads to a *dc* signal proportional to the signal amplitude, V_s.

$$\begin{aligned}\langle V(t)\rangle &= \langle V_{señal}^0 t \cos(\cdot V_{señal} \cos\phi_{señal}) t_0^0 \quad (\quad_0 + \phi_0)\rangle = \\ &= \lim_{T\to\infty}\frac{1}{T}\int_0^T V_{señal}^0 \cos(\quad_{señal} \cdot V + \phi_{señal}) 2\omega_0^0 t \quad (\quad_0 + \phi_0) = \\ &= \frac{1}{2} V_{señal} V_0 \cos(\phi_{señal} - \phi_0)\end{aligned} \tag{3.24}$$

It is interesting to note that the phase dependence of the *dc* signal should be directly eliminated by the lock in giving us two signals, one dependent on *cos* ϕ and the other on *sin* ϕ (where $\phi = \phi_s - \phi_0$) according to the following expressions:

$$\begin{aligned} V_1 &= V_{signal} \cos\phi \\ V_2 &= V_{signal} \sin\phi \end{aligned} \tag{3.25}$$

We thus acquire the amplified signal without any noise from the average of V_1 and V_2 obtained by the *lock–in*, both of them represent the signal as relative vector defined directly by $R = (V_1 + V_2)^{1/2}$ and $\phi\,(= tan^{-1}(V_2 / V_1))$. The configuration of the *lock–in* allows us to work in a range of voltages from -10 to 10V with the maximum intensity of 10 mA.

The *IU4* communication interface (*Nima technologies*, UK) provides us the analogical–digital conversion of the acquired electrical signals making possible to monitories the spatial profile of the electrocapillary wave in a real time. Indeed, the *IU4* unit allow us to control by a computer the different components of the device.

3.5 Global control of the device

To control not only the generation of the capillary waves but also their detection by laser reflectrometry we used a graphic interface (GUI) from a specific software package *701.OEC* (*Nima, UK*) implemented in *Labview (National instrument, USA)*. It thus monitorizes the averaged signal obtained from the *lock–in*, V_s as a function of the horizontal displacement of the capillary wave, i.e., getting the spatial profile of the capillary waves generated with an accuracy of ±0.1*mm*. At the same time, it is possible to measure the surface tension γ of the fluid surface as well as to change the effective area of the Langmuir trough part of the device. Figure 3.9 shows an example of the graphical interface used that controls the device and allows one to perform an standard experiment of detection

of previously excited capillary waves. In particular, the use of this graphical interface makes possible to scan the spatial evolution of the capillary wave generated, and to get the useful parameters, such as the spatial profile and the detector signals, from the *lock–in* in real-time. A reliable measure of the surface tension, it is also possible with the software control in a standard experiment.

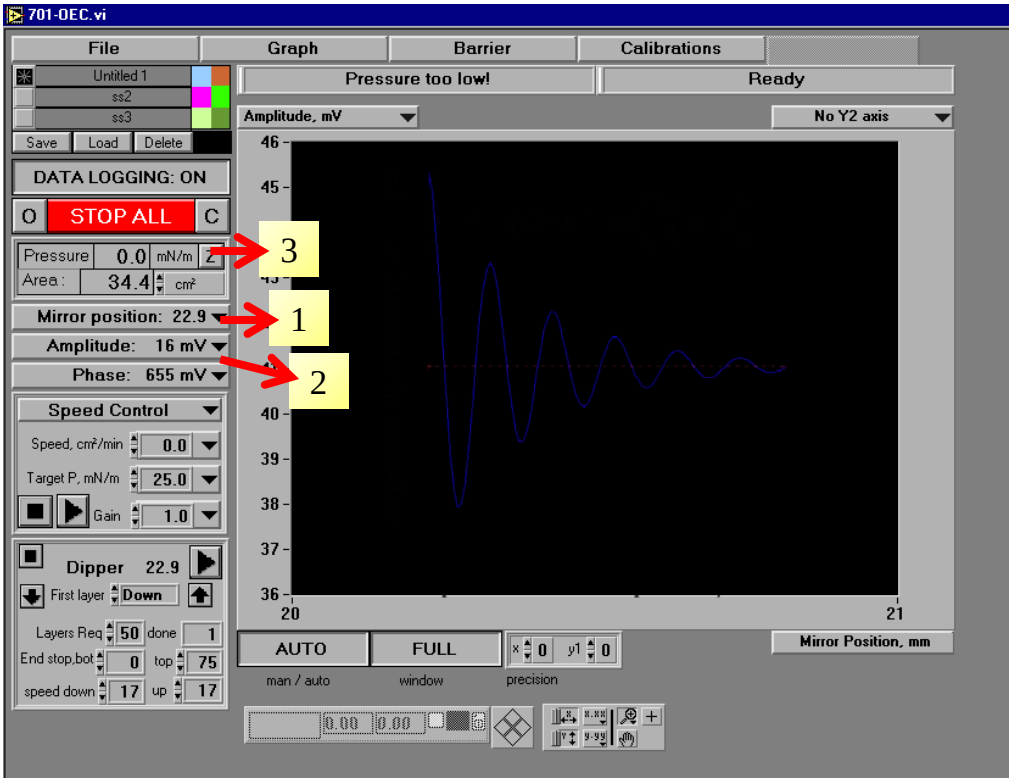

Figure 3.9. Display of the software implemented based on a graphic interface performed in *Labview* (National Instruments, USA) to control the generation and detection of the capillary waves on an arbitrary experiment. The picture shows the display corresponding to a generic experiment where an arbitrary capillary wave is generated and detected onto an arbitrary fluid surface; the software makes possible to evaluate the spatial evolution of the capillary wave in real-time. The program allow one to scan the whole surface by the mirror position control (1), and also to get the signals from the detection channels: amplitude and phase (2). In addition, the software provides an accurate measure of the surface pressure (Π) of the system perfectly coupled with the other parameters as a function of time (3).

3.6 Technical details

This instrument is very sensitive to surface vibrations. The *PSD* is able to detect very small displacements, and then it is very sensible to any experimental noise. It is necessary to reduce the mechanical noise by isolating the device to the surrounding media. However, the noise frequency is mostly below 10*Hz*, which is far away from the usual experimental frequencies, and can be easily filtered out by the *lock–in*. Under our experimental conditions, the amplitude of the noise oscillation on the liquid surface is several orders of magnitude larger than that of

the signal; however measurements with the device can be done perfectly with band-pass filtering and a dynamic reserve of more than 80*dB.* The fact that the detection is done at $2\omega_0$ instead of the excitation performed at ω_0 allows us to reduce the leakage noise coupled in the detection side from the generator.

The optical alignment of the set up is crucial. The laser beam must be accurately focused on the fluid surface to get the properly spatial profile of the capillary wave generated. Indeed, to make a perfect scan of the fluid surface, the translation stage where the prism is placed should be moved in the direction parallel to the fluid with a relative low speed (ca. $2 \cdot 10^{-2}$ *mm/s*) to avoid further random noise in the system, and thus making possible to carry out experiments in a continuous way. We thus perform measurements of the amplitude and the phase of the capillary wave as a function of the beam reflection point in the fluid surface in *continuous* without any inherent noise. Because of the generator has no mechanically moving parts, its noise is insignificant. However it is sensitive to changes in the fluid level, and then it is necessary to avoid any vibration during a common experiment. As commented in detail above, to minimize these vibrations the device is carefully isolated.

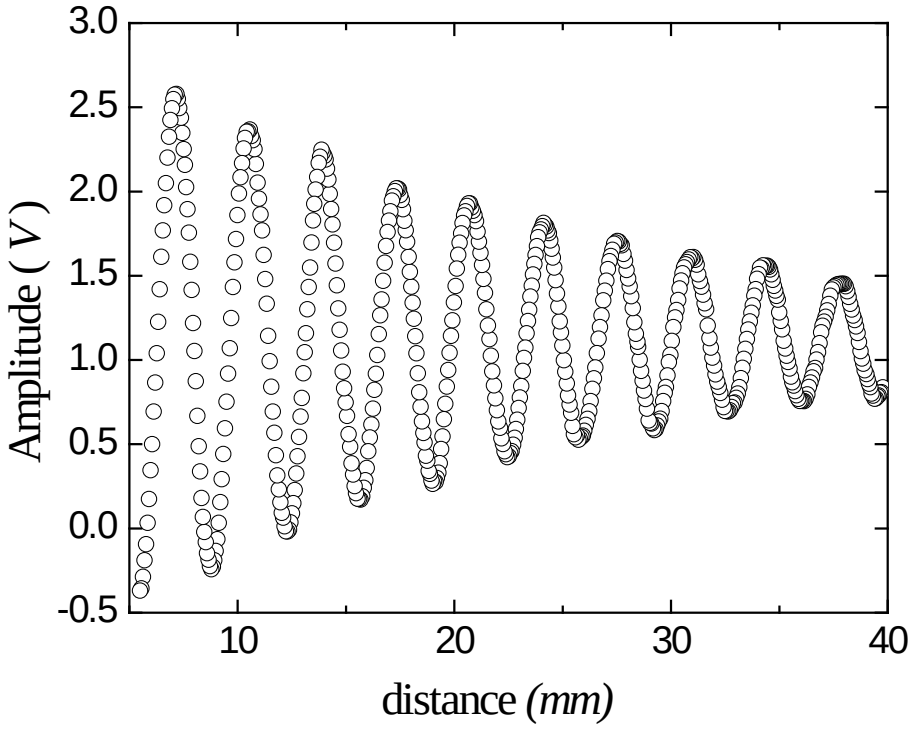

Figure 3.10. Spatial profile of a capillary wave generated and detected with our device. Concretely, it is showed the amplitude of the excited electrocapillary wave from the *lock in* as a function of the beam reflection point in an arbitrary air-water surface. It is important to note that the continuous scan over the whole surface begin close to the blade where the wave is excited and screening far away the damping of the wave is high. As commented in the text, the speed of the scan is very low ~ 2×10^{-2} *mm/s* and the accuracy in the determination of the distance ±0.1*mm.*

In a standard use of the instrument, the propagative parameters of the wave generated, scattering vector q(ω) and damping coefficient β(ω), as well the instrument configuration are calibrated at the beginning of each experimental session. This is done by studying the measured spatial profile of a pure liquid (typically water). Figure 3.10 illustrates a typical spatial profile of an arbitrary capillary wave generated and detected in the air-water interface covered by a monolayer of surfactant or polymer. The amplitude of the wave from the *lock–in* is measured as a function of the distance of the beam reflection point onto the surface studied to the generation of the wave by the blade. At the beginning of the scanning, close to the blade the amplitude of the wave is the highest. If we move far away from the origin of the wave the spatial damping increase until its amplitude is zero.

Our device, sketched in Figure 3.4, is based on the design of previous instruments following a pattern which has become fairly conventional.[5, 11, 26] However, we have performed new improvements not only in the set up, but also in the data analysis to get further insight in the dilational rheology of monolayers in a regime of moderate high frequencies. Indeed, the set up has been designed to generate and detect the transversal waves in a continuous experiment scanning the whole fluid surface. The configuration of the instrument is also designed to prevent all the mechanical noises. The dimensions of our trough are optimal for the propagation of the transversal waves generated. In addition, the control of the amplitude of the excited electrocapillary wave leads us to perform experiments even in non-linear regimes where new physical insights could be studied. Finally, the possibility to perform continuous experiments as well as the control of all the processes by a specific software implementation leads us to reduce the experimental time.

4. Data analysis

The suitable information about the propagative parameters of the excited electrocapillary waves in the air–water interface is obtained by fitting the experimental data previously commented directly by means of a damped sine function:

$$u_z(x) \approx V_s(x) \sim e^{-\beta x} \cos\left(\frac{2\pi}{\lambda} x + \phi\right) \qquad (3.26)$$

This expression related the amplitude of the capillary waves by means of this spatial profile obtained by reflectrometry. In Eq. 3.26, λ (= 2π/*q*), is the capillary wavelength, β is the spatial damping constant of the capillary wave oscillations, and ϕ is a phase term obtained as a function of the excitation frequency ω_0 of the

ECW. β can be related to the spectrum frequency width, $\Delta\omega$, using the capillary wave group velocity, $U = \partial\omega/\partial q$, through $\Delta\omega = U\beta$. No knowledge of the nature of the interface is required for this analysis, and this fitting procedure is very stable. In the literature, it is often found that experimental data is fitted to Eq. 3.26 obtaining the most reliable surface parameters.[5] One of the advantages of this phenomenological fitting approach is that the fit remains stable over the whole frequency range. However the fit becomes unstable and can yield un-physical values of the dilational parameters at the boundary of the region of strong coupling between transversal and longitudinal modes is approached, as discussed in detail in the previous section.

Data analysis to study the dilational behaviour of monolayers of surfactant or polymer at the air-water interface must be performed by means of the numerical solution of the dispersion relation (Eqs. 3.11–3.12) which must be resolved for given propagation parameters values, ω and $q = (2\pi/\lambda) - i\beta$. We follow Levich's approach for data analysis taking account that surface tension γ is a real quantity suggested by Buzza.[6] Our fitting and data analysis program is coded in *MATLAB* (it is shown in the appendix). In essence, the spatial profile of the electrocapillary waves obtained for a determined frequency (see figure 3.9) is fitted to the Eq. 3.26, and then, the propagative parameters q (λ, β) for a fixed ω and separately γ (measured simultaneously by a Wilhelmy plate method in the device) allow us by means of the dispersion relation to directly get the dilational properties of a monolayer (elasticity ε, and the viscosity κ).

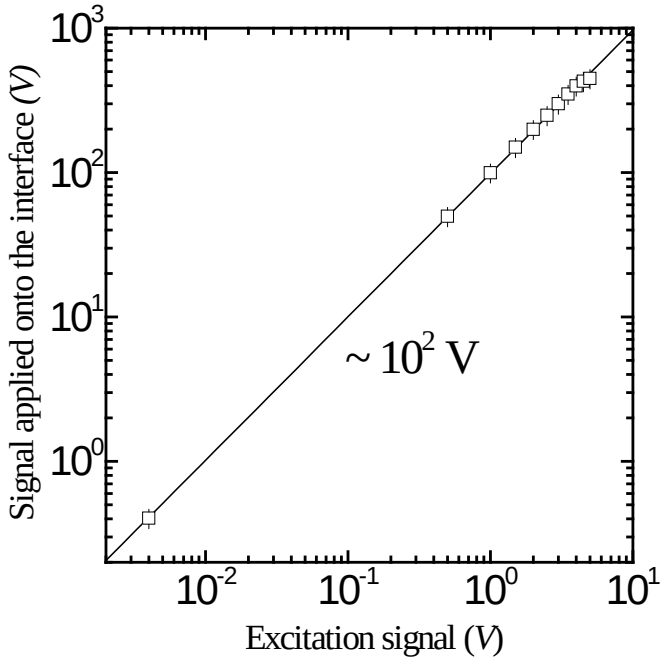

Figure 3.11. Amplified output voltage as a function of the amplitude of the excitation signal from the function generator. The experimental dates follow a linear fit which demonstrates that the factor of 10^2 is satisfied in the whole range of the excitation signal (0 – 5*V*).

5. Calibrations

This section illustrates the calibration of the instrument by the analysis performed for pure liquid, concretely ultrapure water. The instrumental parameters (V, ω, q, β) are calibrated by analysing the spatial profile from the capillary waves generated in a clean surface of water, for which both bulk and surface parameters are usually known precisely.

First of all, we have to test whether the sinusoidal voltage generated (≈ 0–5V) by a function generator is properly amplified by a factor of 10^2 using a high voltage amplifier (TREK, model 601C), when it is applied between the sharp edge of the blade and the trough where the monolayer is deposited on the air-water interface. We thus measured the output voltage from the frequency generator as a function of the amplitude of the amplitude of the capillary wave generated (see Figure 3.11), and confirmed that the actual voltage applied between the blade and the fluid surface is the amplitude of the excitation signal, multiplied by a factor of 100.

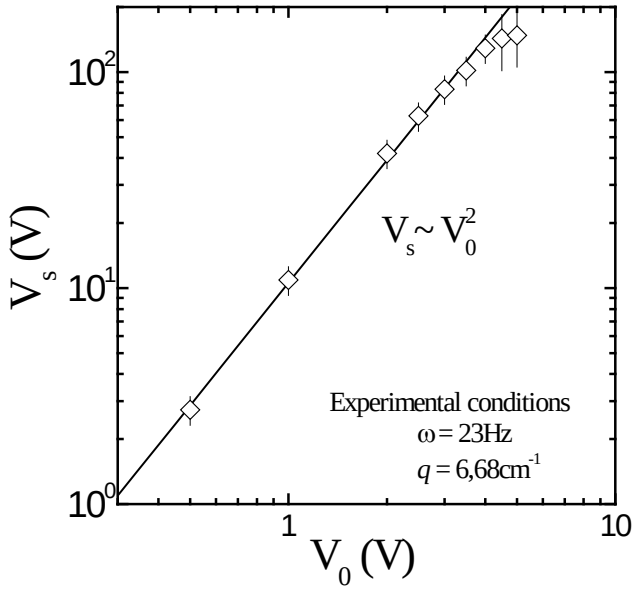

Figure 3.12. Amplitude of the excited signal as a function of the amplitude of the applied field. The experimental dates follow a power law behaviour showed by the straight line which demonstrates that $V_s \sim V_0^2$ is satisfied in the range from 0 – 4*V*.

It is well known that the dielectric ponderomotive deformation is proportional to the square of the applied field $u_z \sim E^2 \sim (\omega_0) \sim (cos\ \omega_0)^2 \sim cos(2\omega_0)$, where the response has a frequency twice of the applied field ($\omega = 2\omega_0$) typical of parametric excitation dynamics.[5] Therefore, we have checked that the propagative characteristics of capillary waves arise from the ponderomotive assumption. Figure 3.12 shows the amplitude of an arbitrary capillary wave generated in the

bare air-water interface as a function of the amplitude of the applied field over the accessible range of data. A quadratic relationship has been found pointing out the validity of the assumption $V_s \approx V_0^2$; however, above 4*V* the power law behaviour is not followed properly; this fact is not a problem because the standard range of work in our device is around 1– 4*V*.

We also have checked the frequency of the capillary waves generated in terms of the frequency and amplitude of the applied field. Figure 3.13 points out that the capillary waves generated on the surface of a fluid have a characteristic frequency twice that of the excitation frequency independently of the applied field. We also show the Fourier transform of the amplitude of the different excited electrocapillary waves using a *FFT*-spectrum analyzer for an excitation frequency ω_r =11.5*Hz* on the surface of pure water (*quality milliQ - RG*). It is noteworthy that the most important signal of the spectrum is predominantly at 23*Hz*, this frequency is twice that the excitation ($\omega = 2\omega_r$) as discussed in detail above. Also in the spectrum the 2nd harmonic order appears (fundamental frequency, ω_0 = 46Hz) but only at high excitation voltages (3.5–4V) as expected for the apparition of a *dc* component. However these signals are only ca. 10% of the fundamental.

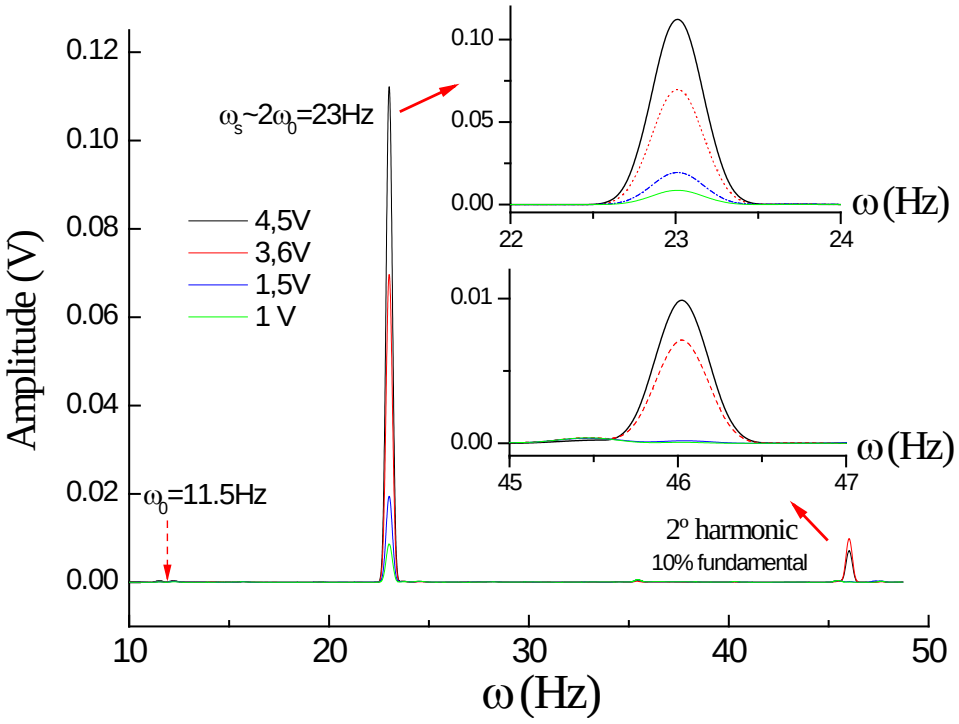

Figure 3.13. Fourier transform of the amplitude of different excited electrocapillary waves generated by the device as a function of the frequency ω. This spectrum correspond to an experiment with a excitation frequency ω_r = 11.5*Hz*. It is should be note that the frequency of the capillary wave is just the double of the reference $\omega = 2\omega_r$=23*Hz*; this fact demonstrates the generation of a capillary wave according to the electrodynamics approach. The apparition of a 2nd harmonic of the fundamental signal appears only when the applied field is high enough (3.5–4*V*).

To finish this section, we have carried out a systematic study of the ω–dependence of electrocapillary waves propagated along the surface of pure water (*quality milliQ - RG*) to check not only the instrumental calibration of our device but also the theoretical description used to get the dilational behaviour in the framework of the interfacial hydrodynamics. We thus plot in Figure 3.14 a typical spatial profile of excited capillary waves at a frequency $\omega = 400Hz$ onto the surface of pure water in the following experimental conditions: $T = 23ºC$ and $\gamma = 72mN/m$. It is should be mentioned that the experimental data have been fitted by means of Eq. 3.26 to get the ω–dependence of the propagative parameters λ and β.

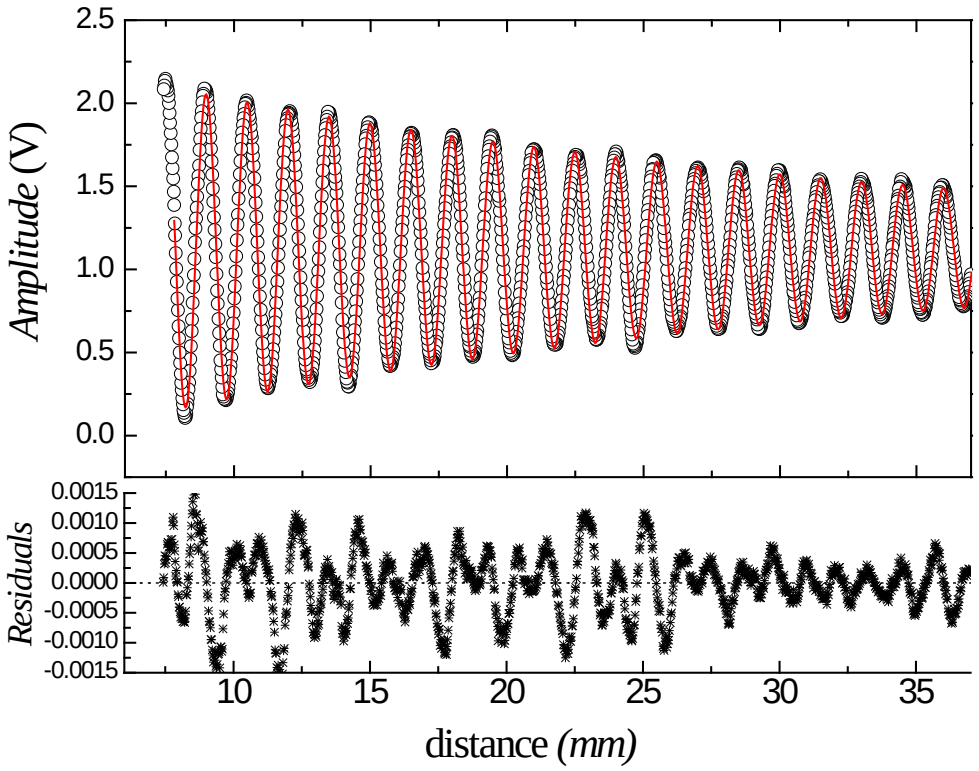

Figure 3.14. Spatial profile of a capillary wave generated at $\omega = 400Hz$ in the bare air-water interface (Experimental conditions: T=25ºC, γ =72*mN/m*). Experimental data (○) are fitted in terms of Eq. 3.26 (solid line). The residuals of the fit appear random pointing out the validity of the fitting equation used.

This representation points out the behaviour of capillary waves in the surface of a pure fluid like water. Here, we show that the phenomenological fitting equation proposed for the data analysis provides a good description of the propagative behaviour of the waves excited. The validity of this fitting equation is confirmed by the existence of a random distribution of residuals. The log-log plots in Figure 3.15 highlight the ω–dependence of the propagative parameters of the excited capillary waves onto the pure water surface (capillary wavelength λ and

spatial damping constant, β). The power-law behaviour observed for the propagation wavelength $\lambda \sim \omega^{(2.67\pm0.01)}$ follows rather well the potential law expected for an ideal interface; i.e., Kelvin's law for the frequency of capillary waves propagating on the free surface of a liquid (Eq. 3.15). Furthermore, we find a power-law behaviour of the damping coefficient $\beta \sim \omega^{(1.33\pm0.01)}$ following the Stokes' law for a bare surface of an ideal fluid ($\beta \approx (2/\eta)\, q^2 = (2/\eta)(\rho/\gamma)^{2/3}\, \omega^{3/4}$).

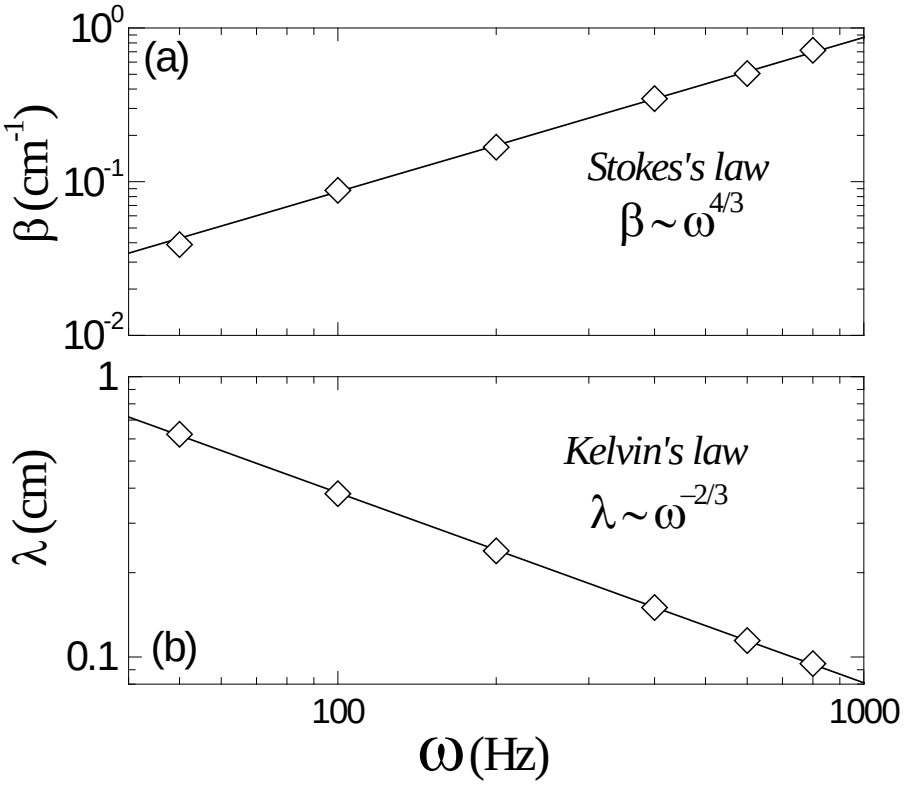

Figure 3.15. Frequency dependence of the propagative parameters of the excited electrocapillary waves onto the surface of pure water (Experimental conditions: *T*=25ºC, γ =72*mN/m*). (a) Spatial damping coefficient as a function of the frequency of capillary waves generated. Experimental data follow power law behaviour in terms of the Stokes' law, $\beta \sim \omega^{(1.33\pm0.01)}$. (b) Capillary wavelength as a function of the frequency. Experimental data follow power law behaviour in terms of the Kelvin's law, $\lambda \sim \omega^{(2.67\pm0.01)}$.

The results presented here confirm the validity of the determination of the propagation parameters by the fitting process in the whole frequency range covered by the study of propagation of capillary waves onto the surface of pure water by means of the Kelvin and Stokes laws for an ideal interface.

To summarize, all these experiments shown in this section allow us not only to calibrate all the technical details of the device but also to test the validity of the propagation parameters obtained by means of the theoretical approach of an ideal interface as the surface of the pure water.

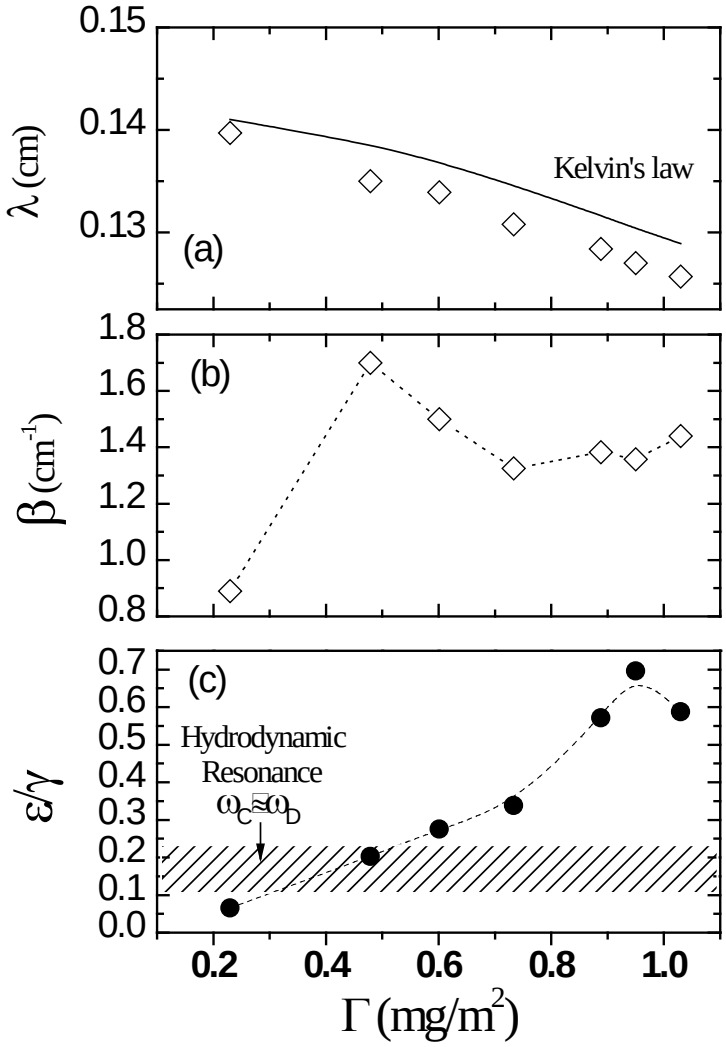

Figure 3.16. Γ-dependence of the propagation parameters of the excited electrocapillary waves onto the surface of water covered by a PVAc monolayer. Variation of (a) Capillary wavelength λ and (b) damping coefficient β of electrocapillary waves excited on the PVAc monolayer at a fixed frequency, ω = 400*Hz* generated, as a function of Γ. The solid line in (a) represent the behaviour of an ideal fluid interface pointed out by the Kelvin's law. (c) Probes of the dependence of the capillary damping on hydrodynamics trough the dimensional parameter ε/γ (≈ 0.15±0.05). It accounts for the resonance condition where the longitudinal and transversal waves are coupling.

6. Results: *ECW* in Langmuir monolayers

In this section we describe and analyze data on monolayers of a synthetic polymer Poly (vinyl acetate) (PVAc) as an example of the applicability of the ECW technique. This system was chosen because it was previously studied by similarly techniques,[11, 12, 29] and then allows us to get further insight into the role of the set up details and the right running of the technique developed. PVAc monolayer, for which the air-water interface can be considered a '*good–solvent*', within the two-dimensional semi-dilute statistical model for polymer. It can be considered a very appropriate system to study this moderate–high frequency range

rheology by our device and data analysis methods. We studied the effect of the surface concentration Γ on the dilational modulus and viscosity for a monolayer of PVAc (M_w = 90*kDa* and *Polydispersity index*, M_w/M_n=1.3) purchased from *Polysciences*, (Germany). The spreading solution was a mixture of benzene and tetrahydrofurane (5:1) and had a concentration ca. 0.1*mg/ml*. The monolayers were prepared directly in the trough of the device at *T*=23*ºC*.

Figure 3.16 shows the Γ-dependence of the propagation parameters (λ, β) characteristics of the capillary mode of the PVAc monolayer spread at the air-water interface obtained by the fitting (in terms of Eq. 3.26) of the spatial profile of the capillary waves generated onto that interface at a fixed frequency, ω = 400*Hz.* For the sake of comparison, the solid line in Fig. 3.16(a) represents the Kelvin's law for λ at the fixed frequency. It is should be mentioned that as Γ increases evident deviations for this borderline behaviour are found, thus pointing out the existence of dilational viscoelasticity. The highest value observed of β at Γ≈ 0.45mg/m^2 may be associated to the hydrodynamic coupling between the transversal and dilational modes. This fact implies energy transfer between them and strong dissipation in the capillary mode.[7] The resonance condition ($\omega_c \approx \omega_D$) takes place when $\varepsilon/\gamma \approx 0.15 \pm 0.05$ where ε is the dilational elasticity and γ is the surface tension measured. In effect, for the case of PVAc monolayer, we thus demonstrate that the calculated value of the ratio ε/γ showed in Fig. 3.16(c) perfectly agrees with the resonance condition determined in terms of Eq. 3.18 when the capillary damping reaches its upper limit according to the experimental results showed in the Fig. 3.16.(b)

As described in the previous sections, we obtain the dilational behaviour of the PVAc monolayers from the propagation experimental dates analyzed by means of the *Dispersion relation*[5] programmed in *MATLAB* code. Figure 3.17 shows the dependence of the dilational viscoelasticity parameters of PVAc monolayers on the surface concentration Γ at a fixed frequency of 400*Hz*. To test the validity of these parameters obtained, we include the hydrostatic equilibrium elasticity ε_0, calculated from the relative slope of the Π–Γ isotherm of PVAc. In the whole range of Γ studied, the viscoelastic response of the PVAc film obeys the *Krammers-Kronig* relationships, from which one can conclude that the elastic response increases monotonically with the frequency, $\varepsilon(\omega) \geq \varepsilon_0$.[30] Concretely, we thus found that $\varepsilon(400Hz) > \varepsilon_0$. An additional proof of the validity of these results is the fact that $\varepsilon(\omega) \geq \omega\kappa(\omega)$ according to the theoretical description for this kind of polymeric films previously explained.[30] Therefore, it seems reasonable to assume that the values obtained for the dilational parameters are in rather good agreement with others previously published for the PVAc monolayers spread at the air–water interface.[11, 12] Furthermore, these results allow us to get further

insight about the precision of the method, and to estimate the range of validity of the parameters obtained. In general, it is clear that the region of good coupling between the transverse and longitudinal modes is quite sharply delimited. Thus, the values of ε and ωκ which obey the resonance condition ($\varepsilon/\gamma \approx 0.15\pm0.05$) have been obtained with further precision; as a result, these are the most reliable surface parameters. However, outside the zone of perfect coupling of the modes the accuracy of the values are poorer, as shown the error bars for the parameters ε and ωκ in the Figure 3.17. It is should be mention that the measured error in the surface data depends not only on the experimental conditions of each test ($\gamma\pm\delta\gamma$, $\omega\pm\delta\omega$, $T\pm\delta T$), but also on the fitting parameters ($\lambda\pm\delta\lambda$, $\beta\pm\delta\beta$) which determine the *s/n* ratio of the technique. Therefore, the main difficulty to get perfectly reliable results arise from the sensitivity and accuracy of β and λ from the fitting process.

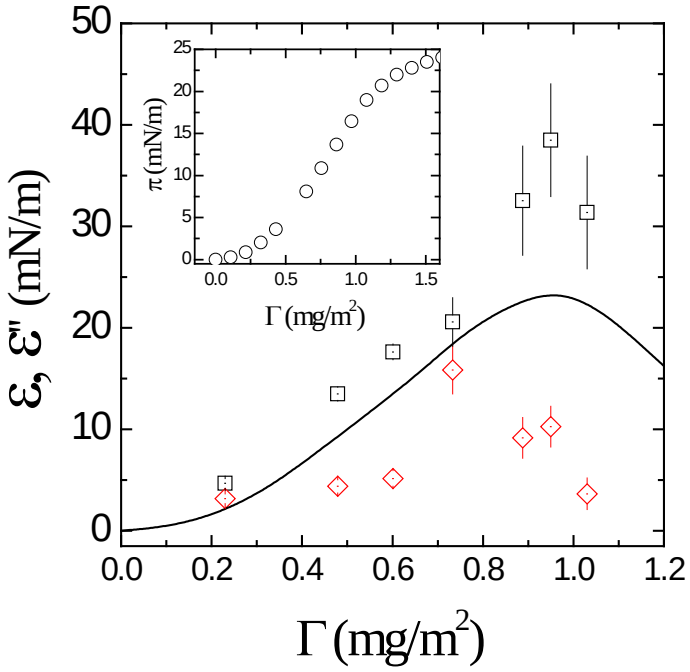

Figure 3.17. Γ–dependence of the dilational viscoelasticity parameters for PVAc monolayer at a fixed frequency, ω =400*Hz*.Symbols as follows: ε' (□), ε''= ωκ (◊). For the sake of comparison we include the hydrostatic equilibrium elasticity, ε_0 (solid line) calculated from the relative slope of the π–Γ isotherm of PVAc showed in the inset.

7. Conclusions

The method mainly based in the generation and detection of capillary waves onto the surface of a fluid is a non-invasive and sensitive technique that could be used to get further insight in the *moderate-high* frequency dependence of the dilational rheology of polymer and surfactants monolayers on a liquid subphase. The theoretical framework and the experimental set up designed and developed have been described in depth. Furthermore, the method of data analysis used has

been properly discussed and the experimental data on PVAc monolayers presented here give us an example of this method running. Thus, it has been shown that reliable fits can be obtained for a limited range of surface parameters by means of the resonance condition. However, it has been emphasized that for large values of the dilational modulus, such as will be related to polymer monolayers or fatty acid layers, both of them in a concentrated regime, the accuracy in the determination of the magnitude of dilational viscoelasticity modulus from capillary waves is not as reliable as expect.

From an experimental point of view, the technique presented here leads us several developments in relation to other related equipments. The frequency range used varies from $10Hz$ to $2kHz$; however, it depends on the system studied. In general, it provides us surface information for many interfacial systems in a broader spectral region. The generation and detection of *ECW* is considered as an absolute experimental technique that requires no preliminary calibration and therefore the results obtained do not have to compare with patterns or standards. Finally, it can be used to investigate the non-linear behaviour; i.e., the generation of capillary waves in a nonlinear viscoelastic region. In principle, this could be investigated by changing the amplitude of the deformation.

8. References

1. Holmberg, K.; Jönsson, B.; Kronberg, B.; Lindman, B., *Surfactants and Polymers in Aqueous Solution.* John Wiley & Sons: Chichester, 2002.
2. Hubbell, J. A., Bioactive biomaterials. *Current Opinion in Biotechnology* **1999,** 10, (2), 123-129.
3. Dickinson, E.; Walstra, P., *Food Colloids and Polymers: Stability and Mechanical Properties*. Royal Soc. Chem.: Cambridge, 1993.
4. Kawaguchi, M., Thermodynamic, structural and rheological properties of polymer films at the air-water interface. *Prog. Polym. Sci.* **1993,** 18, 341.
5. Langevin, D., *Light Scattering by Liquid Surfaces and Complementary Techniques*. Marcel Dekker: New York, 1992; Vol. 41.
6. Buzza, D. M. A.; Jones, J. L.; Mcleish, T. C. B.; Richards, R. W., Theory of surface light scattering from a fluid-fluid interface with adsorbed polymeric surfactants. *Journal of Chemical Physics* **1998,** 109, 5008-5024.
7. Lucassen, E. H.; Lucassen, J., Properties of Capillary waves. *Advances in Colloid and Interface Science* **1969,** 2, 347-395.
8. (Lord Kelvin) Thomson, W., *Philosophical Magazine* **1871,** 42.
9. Levich, V. G., *Physico-Chemical Hydrodynamics*. Prentice Hall: 1962.
10. Landau, L. D.; Lifshitz, E. M., *Theory of Elasticity*. Pergamon: Oxford, 1986.
11. Kawaguchi, M.; Sauer, B. B.; Yu, H., Polymeric monolayer dynamics at the air water interface by surface light-scattering. *Macromolecules* **1989,** 22, (4), 1735-1743.
12. Monroy, F.; Ortega, F.; Rubio, R. G., Dilatational rheology of insoluble polymer monolayers: Poly(vinylacetate). *Physical Review E* **1998,** 58, (6), 7629-7641.
13. Landau, L. D.; M, L. E., *Theory of Elasticity*. Pergamon: Oxford, 1986.
14. Krammer, L., Theory of light scattering from fluctuations of membranes and monolayers. *Journal of chemical physics* **1971,** 55, 2097.
15. Edwards, D. A.; Brenner, H.; Wasan, D. T., In *Interfacial Transport Processes and Rheology*, Butterworth-Heinemann: Boston, 1991.
16. Maestro, A.; Ortega, F.; Monroy, F.; Kragel, J.; Miller, R., Molecular Weight Dependence of the Shear Rheology of Poly (methyl methacrylate)

Langmuir Films: A Comparison between Two Different Rheometry Techniques. *Langmuir* **2009,** 25, (13), 7393-7400.

17. Sacchetti, M.; Yu, H.; Zografi, G., Inplane steady shear viscosity of monolayers at the air-water-interface and its dependence on free area. *Langmuir* **1993,** 9, (8), 2168-2171.
18. Kragel, J.; Siegel, S.; Miller, R.; Born, M.; Schano, K. H., Measurement of interfacial shear rheological properties - an automated apparatus. *Colloids and Surfaces a* **1994,** 91, 169-180.
19. Van den Tempel, M.; Lucassen-Reynders, E., Relaxation processes at fluid interfaces. *Adv Colloid Interface Sci* **1983,** 18, 281.
20. Bonfillon, A.; Langevin, D., Electrostatic model for the viscoelasticity of ionic surfactant monolayers. *Langmuir* **1994,** 10, (9), 2965-2971.
21. Gourier, C.; Daillant, J.; Braslau, A.; Alba, M.; Quinn, K.; Luzet, D.; Blot, C.; Chatenay, D.; Grubel, G.; Legrand, J. F.; Vignaud, G., Bending energy of amphiphilic films at the nanometer scale. *Physical Review Letters* **1997,** 78, (16), 3157-3160.
22. Birikh, R. V.; Briskman, V. A.; Velarde, M. G.; Legros, J. C., *Liquid Interfacial systems. Oscillations and inestability*. Marcel Dekker: New York, 2003.
23. Buzza, D. M. A., General theory for capillary waves and surface light scattering. *Langmuir* **2002,** 18, (22), 8418-8435.
24. Ito, K.; Sauer, B. B.; Skarlupka, R. J.; Sano, M.; Yu, H., Dynamic interfacial properties of poly(ethylene oxide) and polystyrene at toluene water interface. *Langmuir* **1990,** 6, (8), 1379-1388.
25. Jayalakshmi, Y.; Ozanne, L.; Langevin, D., Viscoelasticity of surfactant monolayers. *Journal of Colloid and Interface Science* **1995,** 170, (2), 358-366.
26. Sohl, C. H.; Miyano, K.; Ketterson, J. B., Novel technique for dynamic surface-tension and viscosity measurements at liquid-gas interfaces. *Review of Scientific Instruments* **1978,** 49, (10), 1464-1469.
27. Landau, L. D.; Pitaevskii, L. P.; Lifshitz, E. M., *Electrodynamics of Continuous Media*. 2 ed.; Butterworth-Heinemann: 1960; Vol. 8.
28. Jackson, J. D., *Classical Electrodynamics*. Wiley: New York, 1962.
29. Esker, A. R.; Zhang, L. H.; Sauer, B. B.; Lee, W.; Yu, H., Dilational viscoelastic behaviors of homopolymer monolayers: surface light scattering analysis. *Colloids and Surfaces A* **2000,** 171, 131-148.

30. Ferry, J. D., *Viscoelastic Properties of Polymers*. 3 ed.; Wiley: New york, 1980.

Chapter 4

Capillary waves to study the rheology of Langmuir polymer films: From '*poor*' to '*good*' solvent conditions

Abstract

We address an experimental study on the high frequency dynamical behaviour of Langmuir polymer films performed by the analysis of excited electrocapillary waves (*ECW*) onto the interface. For polymer monolayers, it is the quality of the air-water interface as a polymer solvent that defines the different conformational scenarios, from a near-collapsed chain at *poor*-solvent conditions to a swollen random-coil at *good*-solvent ones. Hence, we demonstrate the existence of a further correlation between the dilational viscoelastic parameters determined in a broad frequency range ($\omega \approx 10Hz - 1.2kHz$) and the conformation adopted by the polymer at the interface. In fact, we have studied two different polymer monolayers: a glass-forming polymer, poly (methyl methacrylate) (PMMA) for which the air-water interface is considered a *poor* solvent, and a flexible one poly(*tert*-butyl-acrylate) (PTBA) corresponding to *good* solvent conditions. The dilational high-frequency rheological behaviour obtained for both systems are in further agreement not only with the mechanical dilational rheology performed at low frequency range but also with the theoretical predictions corresponding to different conformations; i.e., the existence of a percolated gel in PMMA monolayers, and the reptation motion characteristic of an entangled gel in PTBA films.

1. Introduction

The dynamics of Polymers confined to two dimensions (*2D*) is rather unexplored and less well-understood than polymer dynamics in bulk solutions. This fact is due to the restricted dimensionality of the interface which strongly reduces the available configurations for these systems. This could be expected to dramatically affect the mechanical properties. For these reason, exploring the viscoelasticity of adsorbed polymer films allows one to obtain further insight into its physicochemical state as a function of surface concentration Γ, chain length *N* and temperature *T*. It is important due to its technological interest in many industrial processes and in understanding biological phenomenon.[1, 2]

Polymer films confined at interfaces as Langmuir monolayers represent a near flat two dimensional topology. Indeed, they can be considered as complex quasi-bidimensional systems, compatible with a flattened conformation thinner than the bulk coil. This scenario suggests that monolayers behave as very stiff systems characterized by a set of 2D viscoelastic parameters larger than the analogue ones for bulk systems.[1, 3] Within this perspective, we thus addressed in *part II* an experimental study of the rheological behaviour of polymers showing different conformational scenarios, from a near-collapsed chain at *poor*-solvent conditions to a swollen random-coil at *good*-solvent ones.

Here, we point out that poly(methyl methacrylate) (PMMA) Langmuir monolayer behaves as a system under *poor*–solvent conditions at the air-water interface; under this assumption, the polymer coils rearrange in collapsed pancakes at the interface. The dependence of the polymer chain length (*N*) and the surface polymer concentration (Γ) in the viscoelasticity parameters shows a strong power-law behaviour compatible with the existence of a quasi-2D gel-state based on the *percolation* of the PMMA pancakes. This percolated gel behaviour found has been explored seeking the existence of a 2D-glassy-state. On the other hand, we also have studied poly(*tert*-butyl-acrylate) (PTBA) monolayers for which the air-water interface is a good-solvent scenario, where the polymer chains present an extended configuration with most monomers adsorbed at the interface, thus leading to the existence of an entangled polymer chains. The dependencies of the mechanical rheological parameters at long-time lengths on chain concentration and polymer size are compatible with the existence of diffusional reptation motions controlling the molecular transport in the monolayer. In addition, the correlation found between the dynamical behaviour and the solvent quality of the interface, responsible of the conformational scenario proposed for each polymer monolayer, has been found to be in accordance with previous studies about the relation between equilibrium features and high-frequency dynamical behaviour performed by Esker et al.[4, 5]

The study of the propagation of electrically excited capillary waves on polymer monolayers at the air-water interface yield the dilational viscoelasticity of in the frequency range from 10*Hz* to 1*kHz*. Hence, we can extend the rheological study performed at low frequencies ($\omega < 1Hz$) to higher ones by means of the this technique. The rheology of both PMMA and PTBA monolayers at the air-water interface can be described in terms of the coupling between capillary (T) and dilational modes (L).[6] Indeed, surface hydrodynamics is relevant to the rheological behaviour of polymer monolayers; i.e., it leads to a dispersion equation which relates the propagation characteristics of the transversal waves (frequency ω, wavelength λ and damping β) to the constitutive parameters of the monolayer attached to the interface (surface tension γ, dilational elasticity ε and viscosity κ).[7, 8]

$$D(q,\omega) = T(q,\omega;\gamma)\cdot L(q,\omega;\tilde{\varepsilon}) + C(q,\omega) = 0 \qquad (4.1)$$

For a viscoelastic monolayer adsorbed at an air–water interface $L(\varepsilon, q, \omega)$ and $T(\gamma, q, \omega)$ functions of the Dispersion relation become:

$$\begin{aligned} L(\varepsilon,q,\omega) &= \varepsilon(\omega)q^2 + i\omega\eta_i(q+m_i) \\ T(\gamma,q,\omega) &= \gamma q^2 + i\omega\eta_i(q+m_i) - \omega^2\rho/q \end{aligned} \qquad (4.2)$$

Where $q=2\pi/\lambda - i\beta$ is a complex number representing the wave vector, γ is the surface tension and $\tilde{\varepsilon}$ is the dilational complex elasticity modulus. ρ_i and η_i are the density and viscosity of water (i=1) and air (i=2), respectively, and $m_i=(q^2 - i\omega\rho_i / \eta_i)^{1/2}$ is the inverse penetration depth.

It is well known that gel-like systems support shear elasticity[9]; however, only for dense polymer monolayers, shear effects could be comparable to compression ones. Similarly to bulk rheology, the dilational modulus is a complex quantity, $\varepsilon(\omega) = \varepsilon'(\omega) + i\varepsilon''(\omega)$; where $\varepsilon'(\omega)$ is the dilational storage component and the imaginary part $\varepsilon''(\omega)$ is the loss component. As expected for an oscillatory motion of frequency ω, the loss modulus is related to the viscous term, $\varepsilon''(\omega)=\omega\kappa$, where κ is the dilational viscosity.

The aim of this chapter is to extend our previous rheological studies performed at low frequencies to high frequencies by using ECW experiments leading to a high frequency range (from 10*Hz* to 1.2 *kHz*). Indeed, further investigation of the ω–dependence of the dilational viscoelasticity confirms the description of both PMMA and PTBA monolayers in concordance with their different quasi-2D conformational scenario previously demonstrated (see Part II).[10, 11] The next sections of the chapter will be organized as follows: Section 2 briefly summarizes the polymeric materials used and the experimental conditions of the performed ECW experiments. Section 3 contains the dilational rheological

studies of PMMA monolayers performed at high frequencies and the comparison with the mechanical rheology at low frequencies. The results can be explained by means of a percolation theory. Finally, section 4 points out the dependence on polymer concentration of the dilational dynamics of PTBA monolayers in a short time domain (≈ μs) getting further insight in the conformation as an entangled gel, which highlight the existence of a reptation motion.

2. Materials and Methods

2.1 Chemicals

We have used three different samples of *atactic* poly (methyl methacrylate) (PMMA) obtained from Polymer Source, Canada, with molecular weights and the respectively polydispersity index (M_w/M_N) between parenthesis : 14×10^3 (1.4), 80×10^3 (2.0) and 270.8×10^3 g·mol^{-1}(1.85). On the other hand, two different poly (*tert*-butyl-acrylate) (PTBA) samples, also purchased from Polymer Source, were chosen, with different molecular weights and low polydispersity index: 16.3×10^3 (1.13) and 1.56×10^3 g·mol^{-1} (1.07). These two samples correspond to polymer lengths *N's* above and below the critical size N_e (≈100 monomers) respectively.

Chloroform (Sigma Aldrich, 99% of purity) was used as spreading solvent. The concentration of the spreading solution was 0.01mg/ml. Double distilled and deionized water from a MilliQ-RG system was used to prepare the subphase, having a resistivity higher than 18mΩ·cm-1 and a surface tension of $\gamma = 72.6 mN\cdot m^{-1}$ at 20ºC. For the *ECW* measurements, the spreading solution was slowly applied by a micro syringe at different places onto the surface. The surface concentration Γ was changed by subsequent additions of the polymer solution waiting adequate time to reach the equilibration of surface pressure.

2.2 Method

The moderately high frequency dependence of the dilational viscoelasticity of PMMA monolayers were studied by the ECW technique (in the range from 10*Hz* to 1.2 *kHz*). The transversal waves are excited by application of an external *ac* electric field (~ $400V$) locally applied trough a blade electrode placed right above the interface (~100μm). Due to the existence of different dielectric constant between both sides of the interface, the deformation follows the direction of the applied electric field. The spatial profile (u_z) of the excited electrocapillary wave is then scanned by laser reflectometry. After the signal is processed the spatial profile of the ECW follow:

$$u_z(x) \approx e^{-\beta x} \cos\left(\frac{2\pi}{\lambda} x + \phi\right) \quad (4.3)$$

Data analysis must be performed trough the numerical solution of the dispersion equation (Eqs. 4.1 and 4.2) which may be solved for the propagation parameters ω and $q = (2\pi/\lambda) - i\beta$.

For the sake of comparison, together with experimental data of *ECW* we included measurements of the dilational rheology at low frequencies ($\omega < 1Hz$) performed by oscillatory and relaxation experiments (described in the methods summary, appendix 1).

3. Results and discussion

3.1 Poly(*methyl*-methacrylate) (PMMA) Langmuir monolayers

PMMA monolayers are considered as a glassy-former system. This conjecture is well supported by the knowledge that PMMA coils at poor solvent conditions have monomer–monomer interactions that largely exceeds the adsorption energy, thus promoting a conformation scenario based in soft disk-coils (pancakes) which reveal the plausible existence of a percolation-glass transition. This fact demonstrates that the existence of a glassy-state appears as a reliable scenario for an amorphous 2D solid.[10, 12]

Percolated PMMA networks are viscoelastic, as previously demonstrated in chapter II, thus surface wave experiments allow us to study the linear viscoelastic response of Langmuir PMMA films at high frequencies. The dilational parameters contain information about the changes in the adsorption state and the molecular conformation of the polymer film stressed by an external deformation. These characteristics depend on the time scale probed in a particular rheological experiment, i.e., on the frequency ω of the applied deformation in surface waves experiments. Furthermore, the constitutive viscoelastic parameters $\varepsilon(\omega)$ and $\kappa(\omega)$ measured as a function of ω contains the time-dependent response of the system subject to a small disturbance.

3.1.1 *Polymer concentration dependence: A percolation approach*

From the perspective above denoted about the viscoelasticity of percolated PMMA networks, we now discuss the dependence of the surface concentration Γ on the dilational modulus and viscosity for a monolayer of PMMA spread at the air-water interface (M_w = 270.8*kDa;* M_w/M_n=1.85). Figure 4.1 shows the Γ-dependence of the propagation parameters (λ, β) characteristics of the capillary

mode when a PMMA monolayer is attached at the air-water interface at a fixed frequency, $\omega = 400Hz$.

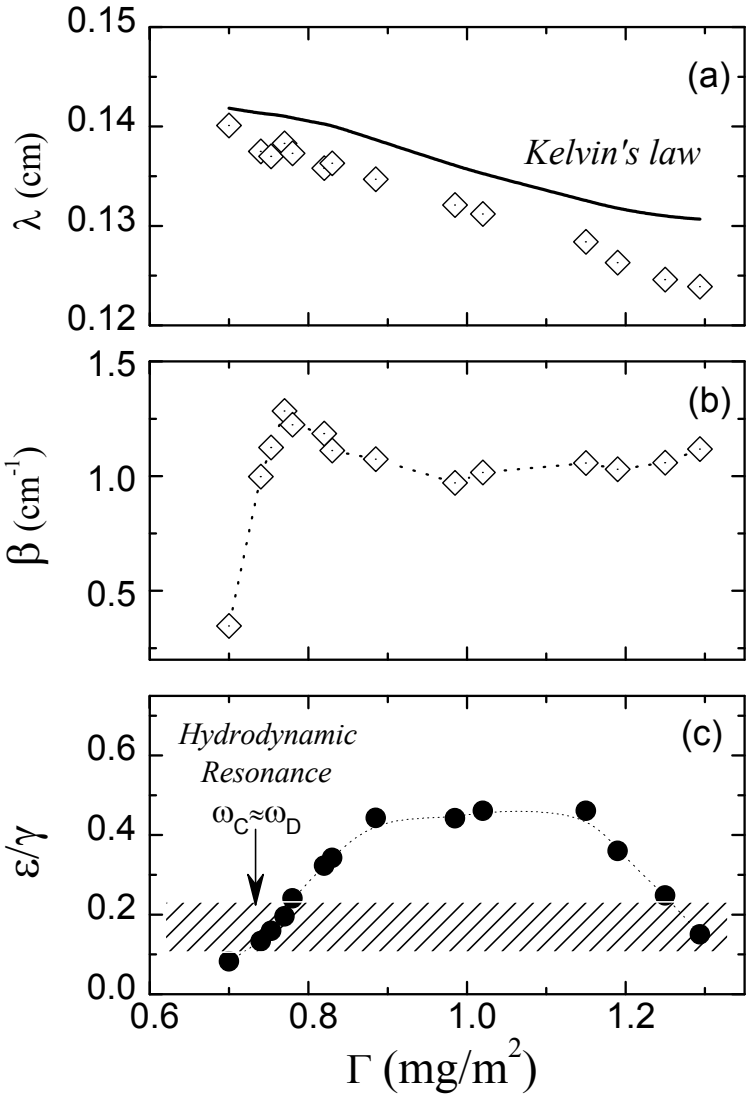

Figure 4.1. Γ-dependence of the propagation parameters of the excited electrocapillary waves onto the surface of water covered by a PMMA monolayer (M_w = 270.8*kDa;* M_w/M_n=1.85). Variation of (a) Capillary wavelength λ and (b) damping coefficient β of electrocapillary waves excited at a fixed frequency, ω = 400*Hz*, as a function of Γ. The solid line in (a) represent the behaviour of an ideal fluid interface (Kelvin's law). (c) Probes of the dependence of the capillary damping on hydrodynamics trough the dimensional parameter ε_0/γ (≈ 0.15±0.05). That accounts for the resonance condition where the longitudinal and transversal waves are highly coupled.

For the sake of comparison, the solid line in Fig. 4.1(a) represents the Kelvin's law ($\lambda^3 = \gamma 8\pi^3/\rho\omega^2$) at the experimental frequency. It should be mentioned that as Γ increases evident deviations for this ideal behaviour are found, thus pointing out the existence of a viscoelastic system. The highest value observed of β at $\Gamma \approx 0.6 - 0.8 mg/m^2$ may be associated to the hydrodynamic coupling between the transversal and dilational modes. This fact implies energy transfer between both modes and strong dissipation in the capillary one.[8] This

resonance phenomenon which takes place when $\omega_C \approx \omega_D$ promotes that the propagation parameters of the capillary waves are further sensible to the dilational viscoelasticity of the PMMA monolayer and then meaningful values of ε and κ can be obtained. At $\omega_C \approx \omega_D$ the resonance coupling parameter β can be approximated by:

$$\beta_R = \left(\frac{\varepsilon}{\gamma}\right)_R = \left(\frac{q\eta^2}{\gamma\rho}\right)^{1/4} \approx 0.15 \pm 0.5 \qquad (4.4)$$

Where ε is the dilational elasticity and γ is the surface tension, both observed at the resonance. Indeed, for PMMA monolayers, we found that the experimental values of the ratio ε/γ shown in Figure 4.1 (c) are in agreeement with the resonance condition determined by means of Eq. 4.4 correspond to the higher values of capillary damping pointed out by the experimental results shown in the Figure 4.1(b). We thus distinguish two regions of concentration where the resonance condition is obeyed, i.e., at $\Gamma \approx 0.7 \pm 0.1 mg/m^2$ and at $\Gamma \approx 1.30 \pm 0.05$ mg/m^2. Hence, more accurate dilational viscoelastic parameters should be expected at these Γ values. In the framework of the equilibrium properties of PMMA monolayers pointed out in the chapter 2, $\Gamma \approx 0.7 \pm 0.1 mg/m^2$ is enclosed in the semidilute regime where the polymer chains become into lateral contact, and then a flatten pancake conformation is expected.[14] On the other hand, $\Gamma \approx 1.30 \pm 0.05$ $mg/m^2 > \Gamma^{**}$ corresponds to the concentrated regime where the surface solvent is almost excluded, and the film becomes purely polymeric (see Figure 4.2).

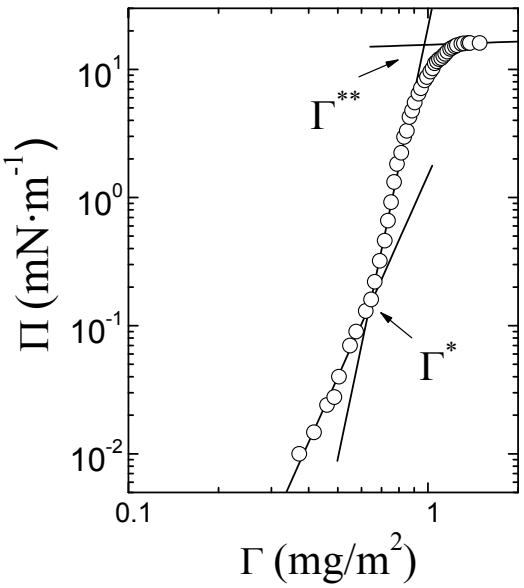

Figure 4.2. Logarithmic plot of the π-Γ isotherm of PMMA monolayer (M_w = 270.8*kDa*).[10] Γ^* marks the transition from the *dilute* to the *semidilute* regime and Γ^{**} the transition to the *concentrated* regime. Hence, in the semidilute regime is plausible the analysis by means of the *de Gennes* scaling laws.[15]

Figure 4.3 shows the dependence of the dilational viscoelasticity parameters (ε and ωκ) of PMMA monolayers (M_w = 270.8*kDa*) on the surface concentration Γ at a fixed frequency of 400*Hz*. For the sake of comparison, the values of hydrostatic equilibrium elasticity, ε_0 (calculated from the relative slope of the Π – Γ isotherm, see Fig. 4.2) are also plotted in Figure 4.3. It seems reasonable that the dilational response of the measured system should obey the *Krammers-Kronig* relationships, which established that the elastic response increases monotonically with the frequency: $\varepsilon(\omega) \geq \varepsilon_0$.[16] Indeed, we found that $\varepsilon(400Hz) > \varepsilon_0$ in the whole range of Γ studied. From this perspective we found also that $\varepsilon(\omega) \geq \omega\kappa(\omega)$ also in accordance with the *Krammers-Kronig* causality relation. Our experimental values of the dilational viscoelasticity for PMMA films in the high frequency regime are in quantitative and qualitative agreement with those reported in the literature for the same system using light scattering by thermal capillary waves.[3-5]

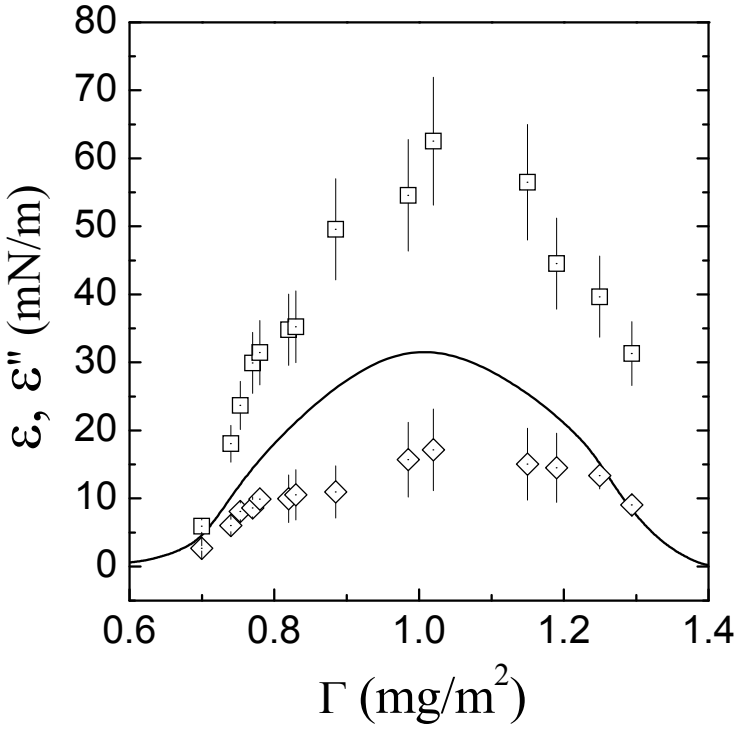

Figure 4.3. Γ–dependence of the dilational viscoelasticity parameters for PMMA monolayer at a fixed frequency, ω =400*Hz*.Symbols as follows: ε' (□), ε''= ωκ (◊). For the sake of comparison we have included the hydrostatic equilibrium elasticity, ε_0 (solid line) calculated from the relative slope of the π–Γ isotherm showed in Fig. 4.2.

As explained before, it is well known that the region of enhanced coupling between the transverse and longitudinal modes is quite sharply delimited. Hence, the values of ε and ωκ obtained close to the resonance condition ($\varepsilon / \gamma \approx 0.15 \pm 0.05$) have more precision as can be seen by the smaller error bars in Figure 4.3. However, outside the region of coupling the accuracy of the values are poorer, as shown by the larger error bars.

Our *ECW's* studies performed on PMMA monolayers have been restricted to $\Gamma > \Gamma^*$ (see Figs. 4.2 and 4.3). In this regime, we thus found, within the experimental error, the existence of a clearly Γ-dependence of the dilational parameters obtained in further agreement to the equilibrium elasticity dependence. An increasing tendency of the mechanical rigidity is shown in the semidilute regime ($\Gamma > \Gamma^*$), reaching a maximum value at Γ^{**} as expected for a percolated 2D network of semirigid solid disks at increasing compression. At higher densities, in the concentrated regime ($\Gamma > \Gamma^{**}$), as a consequence of the strong decrease of the available free area, and thus of the conformational degrees of freedom of the coils the system is less able to store energy and as a result the dilational parameters decrease.

To get further insight into the dependence of the dilational parameters of the PMMA monolayers, at a fixed high frequency with the plausible conformation adopted by the polymeric chains, it is interesting that these viscoelastic behaviour could be interpreted by means of the dynamic scaling laws predicted by de Gennes[15]. Therefore, dynamical experiments previously performed at low frequencies ($\omega < 1Hz$) point out the existence of a scaling-law behaviour in the semidilute regime; it should be remarked that we found interesting relations between the scaling properties of both equilibrium and dynamical parameters, and this was the subject of the chapter 2. To test the validity of the scaling hypothesis of the dynamical parameters at a high frequency Figure 4.4.a highlights that both real and imaginary part of the dilational viscoelastic modulus are strongly dependent on Γ, exhibiting a power-law behaviour as $\varepsilon \sim \omega\kappa \sim \Gamma^y$. The power-law exponent is found to be $y \approx 11 \pm 1$. This value suggests a strong correlation between the dilational parameters at high frequency and the molecular packing as shown by our previous studies. It should be mentioned that the scaling description of ε and ωκ is not suitable in the concentrated regime ($\Gamma > \Gamma^{**}$); in fact, it is restricted to the semidilute regime according to de Gennes theory.[15] We have found the same power-law behaviour not only with the dilational modulus and shear modulus measured at low frequencies (*G', G''*, ε and $\omega\kappa \sim \Gamma^y$), but also with the equilibrium surface pressure and compression elasticity ($\pi, \varepsilon_0 \sim \Gamma^y$).[3, 10, 17] Based on the scaling approach,[3] the scaling exponent $y = 2\nu/(2\nu-1)$, is related to the Flory exponent ν that for polymer chains at *poor*-solvent conditions adopt a value of 0.55.[10, 18]

In the present work, we show that a universal power-law is found for the Γ-dependence of the dilational parameters not only at low frequencies (mechanical experiments) but also at higher ones (ECW experiments). According to this universal behaviour, it can be hypothesized that both energy storage and dissipation follow the same mechanism trough the whole frequency range. From

a percolation perspective, the scaling behaviour found points out that the strong dependence of dilational viscoelasticity is based on a percolated scenario formed by polymer gels at poor-solvent conditions; where above the overlapping threshold defined by Γ^*, there is a high connectivity between the interacting pancakes given rise to the formation of a percolation network.[19]

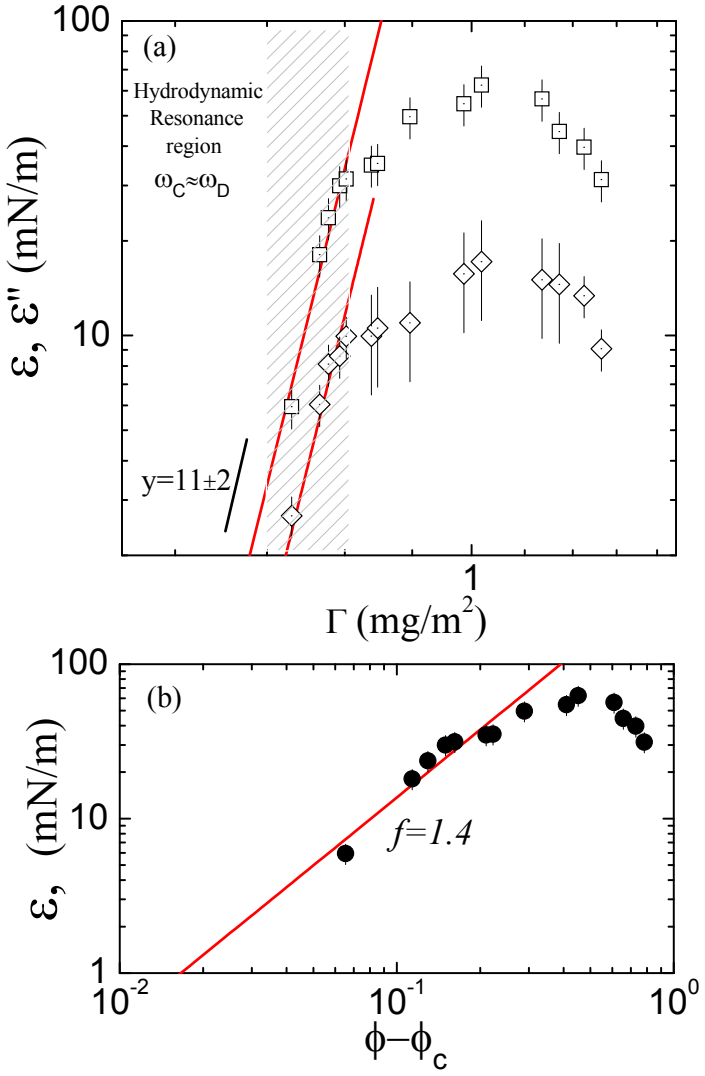

Figure 4.4. (a) Logarithmic plot of the dilational viscoelastic parameters, ε' (□) and , ε'' (◇) as a function of the polymer concentration Γ from the semidilute to concentrate regime for PMMA monolayer at a fixed frequency, $\omega = 400Hz$. Straight lines represent power-law fits, ε', $\varepsilon'' \sim \Gamma^{y}$, with exponent *ca.* 11±2 in all cases. (b) Dilational Elastic moduli, ε as a function of the difference between the packing fraction (ϕ) and the percolation threshold (ϕ_c). Straight line represent power-law fits in terms of a percolation behaviour: $\varepsilon \sim (\phi-\phi_c)^{f}$; where f=1.4 is in accordance with the *Central Force* (*CF*) model of the percolation theory.

Based on the percolation argument,[10, 20] It is expected that PMMA monolayer can be structurally conceived as a percolation network, which describes a disordered gel phase, in which the polymer coils come into random physical contact and form an interconnected 2D–network.[19] The sol-gel transition

takes place at a threshold in the polymer fractional area ϕ_c.[21] Therefore, if the fractional area ϕ is increased above ϕ_c the system freezes into a rigid gel state and dilational elasticity modulus follows a power law behaviour like:

$$\varepsilon(\phi) \approx \varepsilon_0 (\phi - \phi_C)^p \qquad (4.5)$$

Our previous mechanical results preformed at low frequencies point out the existence of a percolation network for the PMMA monolayers according to the power-law dependency obeyed by the dilational elasticity (Eq. 4.5). This dependency were explained in terms of a *Central Force* approach *(CF)*, where the structural rigidity of the system exclusively arises from the tensile stiffness of elemental clusters defining the network, consequently high rigidity requires not only stiff cross-links but also high connectivity, similarly to a pure entropic situation.[22] Within this approach, Figure 4.4(b) re-plots the experimental dilational, in reduced units, i.e., $\varepsilon/\varepsilon_0$ as a function of the fractional area of gel phase, $\phi - \phi_c$. This plot highlights the reasonable explanation of the high-frequency dynamics in terms of a *Central Force (CF)* approach. Hence, Dilational elasticity shows a power-law behaviour as $\varepsilon(\phi) \sim (\phi - \phi_c)^p$, with $p \approx 1.4$. This exponent is rather compatible with a *CF* model driven by rotationally-invariant osmotic forces.

The frequency dependence of the dilational viscoelastic parameters has been studied in the range 20*Hz*–1*kHz* by *ECW*. In accordance with the effect of surface concentration Γ in the dynamics of PMMA monolayers, our study has been restricted to the regions of Γ where the accuracy in the determination of the propagation characteristics of the excited capillary waves allows us to obtain reliable values of the dilational parameters. Thus, two different Γ's have been studied, corresponding respectively to regions obeying the hydrodynamic coupling of capillary and dilational modes; i.e., $\Gamma = 0.75 \pm 0.05 mg/m^2 \approx \Gamma^*$ just above the percolation threshold, in a disordered gel phase and $\Gamma = 1.30 \pm 0.05 mg/m^2 > \Gamma^{**}$ in the concentrated regime. The effect of the frequency in the dilational rheology of PMMA films at these two Γ values is shown in Figures 4.5 and 4.6, respectively. Concretely for each Γ, we have determined the frequency-dependent dilational storage moduli $\varepsilon'(\omega)$, and loss moduli $\varepsilon''(\omega) = \omega\kappa$ and the dilational viscosity $\kappa(\omega)$. In the whole frequency range studied the storage moduli is larger than the loss one ($\varepsilon > \omega\kappa$) pointing out the solid character of the PMMA film above the percolation threshold. The relaxation behaviour observed at $\Gamma = 0.75 mg/m^2$ (Fig. 4.5) might be explained by means of the rearrangement of the density distribution of a collection of individual coils on the surface. As a first approximation, it may be reasonable to fit the viscoelastic relaxation found to a

Maxwell-type dependency. Hence, the expected ω-functionality of the dilational viscoelasticity modulus is given by[13, 16]:

$$\tilde{\varepsilon}(\omega) = \varepsilon(\omega) + i\omega\kappa = \varepsilon_0 + \varepsilon_1 \frac{\omega^2\tau^2 + i\omega\tau}{1+\omega^2\tau^2} \qquad (4.6)$$

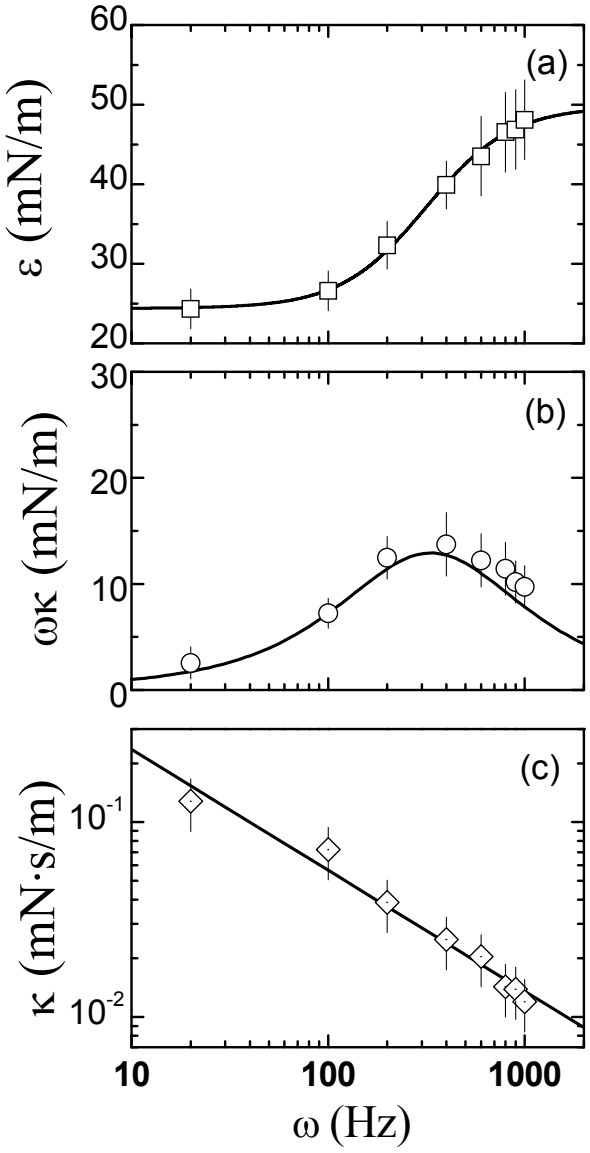

Figure 4.5. Frequency dependence of the dilational viscoelastic parameters for PMMA monolayer (270.8kDa) at $\Gamma = 0.75 \approx \Gamma^*$. (a) dilational elasticity ε (□); (b) loss modulus $\varepsilon'' = \omega\kappa$ (○) and (c) dilational viscosity k (◇). Solid lines correspond to the fit to a Maxwell-type dependency (see Eq. 4.6).

At $\Gamma \approx \Gamma^*$ the value of $\varepsilon_0 = 23.9 \pm 0.4$ *mN/m* is in further agreement with the dilational elasticity values obtained at low frequencies, it will be show below, and $\varepsilon_1 = 25.4 \pm 0.6$ mN/m, accounts for the amplitude of the relaxation process. At this surface concentration, the relaxation time is $\tau^* = 3.4 \pm 0.9$ *ms*. Taking into account that the diffusive relaxation of an isolated coil of radius $R_F \approx 14.9$nm is determined

by $\tau_0 = R_F^2/D \approx 0.01 ms^*$, the observed relaxation time ($\tau^* > \tau_0$) may be associated to the diffusion-driven density relaxation of a collection of polymer coils in a flatten pancake conformation when compressed by the surface waves.

Earlier experiments on the high-frequency viscoelastic relaxation of other polymer monolayer, in *poor* solvent conditions, points out a similar behaviour.[13]

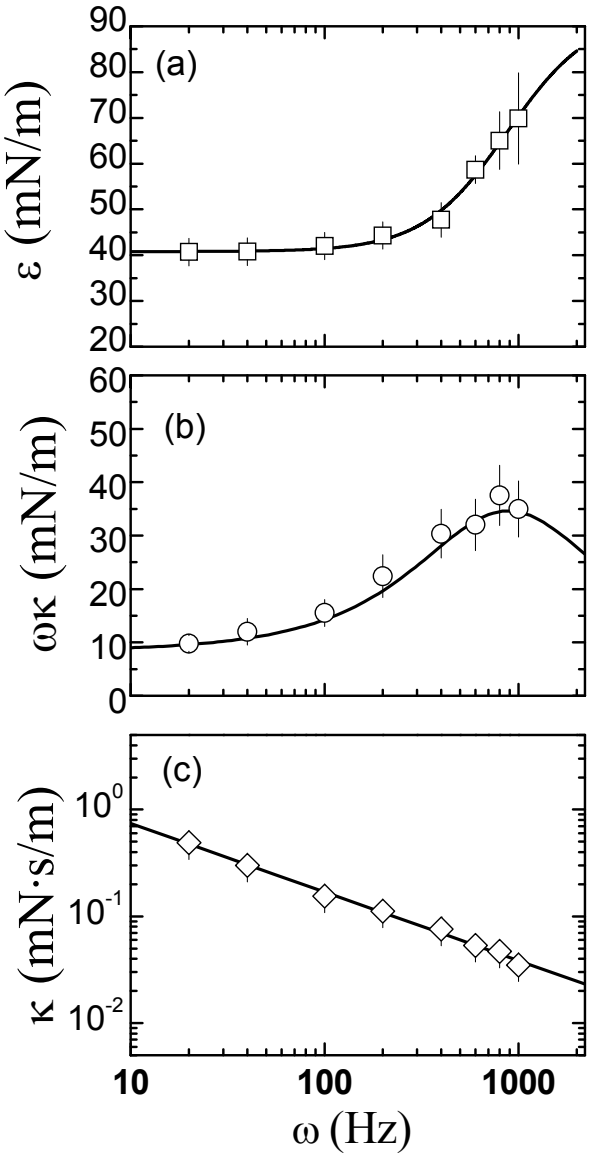

Figure 4.6. Frequency dependence of the dilational viscoelastic parameters for PMMA monolayer (270.8kDa) at $\Gamma = 1.3 > \Gamma^{**}$. (a) dilational elasticity ε (□); (b) loss modulus $\varepsilon'' = \omega\kappa$ (○) and (c) dilational viscosity k (◇). Solid lines correspond to the fit to a Maxwell-type dependency (see Eq. 4.6).

For the experimental data corresponding to $\Gamma > \Gamma^{**}$ (Figure 4.6), there is an apparent correlation with the behavior of the elastic properties at lower concentration. In this concentrated regime, the values of ε and ωκ are larger than

[*] The self–diffusion coefficient of a sphere of radius R_F, defined by the *Stokes-Einstein* relation is calculated as: $D = K_B T/6\pi\eta R_F \approx 1.5 \cdot 10^{-11}$ m^2/s.

at $\Gamma \approx \Gamma^*$ but also show a relaxation process. Thus, the data corresponding to both storage and loss moduli could be interpreted by a Maxwell-type relaxation (Eq. 4.6). At $\Gamma = 1.30 mg/m^2$, well above Γ^{**}, the relaxation time obtained is $\tau^{**} = 1.1 \pm 0.2$ *ms*. The relation between the relaxation times obtained at increasing Γ ($\tau^{**}/\tau^* \approx 0.3$) points out the existence of different relaxation mechanism because diffusion should be slowed down on increasing Γ. An explanation could arise by means of the coupling model drawn by Ngai which describes the behaviour of systems wherein the motion of the basic units is constrained by mutual interactions.[23] In this context, the observed relaxation times suggest some cooperativity that may correspond to collective motions of PMMA coils as pointed out $\tau > \tau_0$. As expected, above Γ^{**}, in the concentrated regime the polymer density is high enough, this fact leads to a further increase of the molecular connectivity and as a consequence $\tau^{**} < \tau^*$.

The dilational viscoelastic results presented here demonstrate the *non-Newtonian* behaviour of the PMMA monolayers (Figs. 4.5 and 4.6). It should be noted that the experimental values of the surface dilational viscosity κ decreases with increasing ω. This tendency, characteristic of a *non-Newtonian* response of the system, may be interpreted by a power law: $\kappa \sim \omega^{-f}$, where $f \approx 0.6 \pm 0.1$ suggests a solid-like description of the system. This exponent is consistent with a rheological model of a soft glass proposed for materials close to the glass transition.[24] The same power-like behaviour has been obtained for dilational experiments at low frequencies not only for the present system, but also for other polymer monolayers in similar conditions.[13] Also, it has been found from shear experiments in protein monolayers with a similar conformational picture.[25]

Within this perspective, Figure. 4.7 highlights the rheological parameters, over the whole frequency range accesible, at the regimes of Γ's previously studied. Here, we have included the results carried out by oscillatory experiments at low frequencies (0.002–0.2 *Hz*)[†] and the results at high-frequencies from *ECW* experiments above explained. As expected, the low frequency limit of the dilational elasticity extrapolates rather well at the value of equilibrium elasticity $\varepsilon'(\omega \to 0) \approx \varepsilon_0$, and the loss modulus extrapolates to a near-zero value indicating the absence of relaxation processes when the deformation if slow enough ($\omega < 0.001 Hz$). The relaxation spectra (Figure 4.7) show clearly the existence of two consecutive relaxation processes which may be described very accurately be the sum of two independent Maxwell relaxation modes[26]

[†] The dilational viscoelastic parameters corresponding to oscillatory barrier experiments that were presented in the chapter 2 (Figure 2.7), and have been included here for the sake of comparison with dynamical results obtained by ECW.

$$\tilde{\varepsilon}(\omega) = \varepsilon(\omega) + i\omega\kappa = \sum_{j=1,2} \frac{\varepsilon_{0,j}\omega\tau_j}{1+i\omega\tau_j} \qquad (4.7)$$

The values of τ_j obtained from the fit to ε and ωκ experimental results were coincident to the fit of the single Maxwell processes at high frequency. The existence of more than one Maxwell mode was already pointed out in polymer monolayers at *poor* solvent conditions.[13] From the experimental point of view, a good agreement between the *ECW* and the oscillatory rheology results was also found in PMMA monolayers. It thus supports the analysis by means of a bimodal relaxation process (Eq. 4.7).

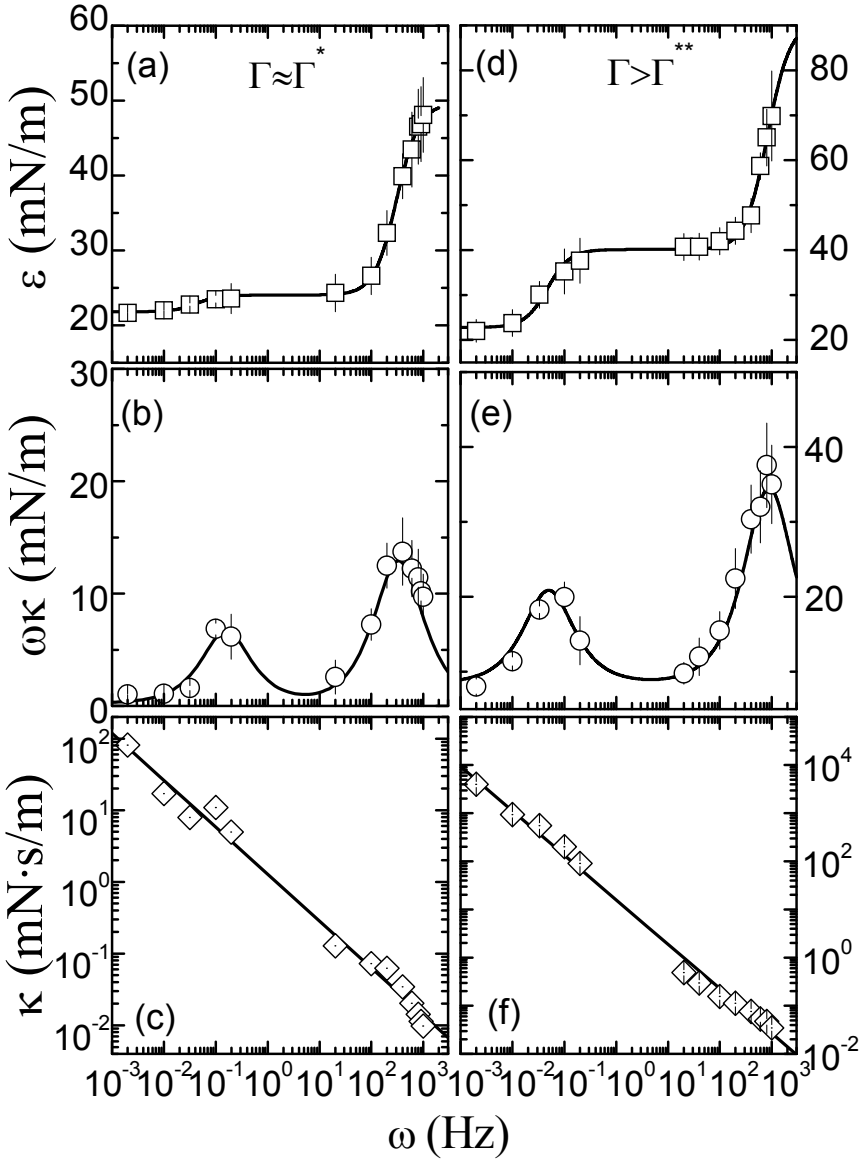

Figure 4.7. Frequency dependence of the dilational viscoelastic parameters for PMMA monolayer (270.8kDa) at two different surface concentrations: Γ= 0.75mg/m^2 ≈ Γ* and Γ= 1.3mg/m^2 < Γ**. (a), (d) dilational elasticity ε (□); (b), (e) loss modulus $\varepsilon'' = \omega\kappa$ (○) and (c), (f) dilational viscosity k (◊). Solid lines correspond to the fit to a bimodal Maxwell process.

As stated above, the characteristic time of a relaxation process depends on the diffusion coefficient and on the spatial scale a on which it operates, more precisely $\tau \sim a^2/D$.[13, 16] Assuming that the motion of the coils is diffusive, the spatial characteristic scale of the relaxation process pointed out by *ECW* would be $a^* \approx 0.2\mu m$ and $a^{**} \approx 0.1\mu m$ respectively for each regime studied. This values are quite less to the characteristic wavelength ($\lambda \approx 10^3 \mu m$) of the concentration longitudinal wave, or *Lucassen* wave, driven by surface tension gradients (*Marangoni* gradients) induced in the ECW experiments.[8] The propagation frequency of the so-created *Lucassen* wave disperses as $\omega = (\sqrt{3}/2)(\varepsilon^2 q^4/\eta\rho)^{1/3}$ (where q is the wavevector of the longitudinal wave, ρ is the density and η the viscosity of the subphase)[27] Thus, the longitudinal waves developed in the PMMA monolayer at the two regimes studied are characterized by a Lucassen wavelength $\lambda(=2\pi/q) \approx \varepsilon^{1/2}\omega^{3/4} \approx 0.8\text{–}1\times10^3\mu m$. This fact means that this relaxation process would be associated to the diffusion-driven density relaxation of a collection of polymer coils when compressed by a longitudinal wave. Furthermore, the relation $a^*/R_F \approx 10$ (R_F take in account the size of a polymer coil) leads to understand that the relaxation process showed at high frequencies correspond to a reduced collection of PMMA coils.

On the other hand, the spatial characteristic scale of the relaxation process pointed out by *oscillatory rheology* would be $a^* \approx 9\mu m$ and $a^{**} \approx 38\mu m$ respectively for each regime studied. In this case, the characteristic *Lucassen* wavelength associated takes a *macroscopic* dimension $\lambda \approx 10^4 mm$ quite larger than the spatial dimensions associate to the polymer coils. This fact means than the relaxation process found at long times would be related to the collective dynamics of polymeric domains. The concentration gradient created by the dilational wave by means of the oscillatory rheology has a macroscopic dimension. It leads to the polymer density profile along the surface is homogeneous; i.e., the strain function distributes homogeneously along the monolayer.

It is remarkable that in both Γ-regimes studied well above of the percolation threshold two Maxwell relaxation processes have been found: The primary *macroscopic* relaxation of the large-wavelength concentration waves. This process, which is located at low frequencies, corresponds to the large-spatial relaxation collective motions of polymeric domains. The second microscopic relaxation, which is located at high frequencies, is related to the short-spatial motion of a collection of polymer coils driven by diffusion. It is noteworthy that the increase of the mechanical rigidity above Γ^* is due to the polymer conformation adopted in a dense monolayer arrangement. Accordingly, the

relaxation processes are more intense at $\Gamma > \Gamma^{**}$ where exists high density of polymer. Therefore, at Γ^{**} is expected a stronger viscous dissipation.

To summarize, a bimodal structure is found for PMMA films; indeed, we suggest a model with two consecutive Maxwell relaxations to describe the frequency dependence of the viscoelastic parameters of PMMA monolayers. The dilational viscosity strongly decreases with increasing frequency, following a power law $\kappa \sim \omega^{-f}$, where $f \approx 0.6 \pm 0.1$. This *dynamical-thinning* effect is obeyed in the whole frequency range, and points out the *non-Newtonian* behaviour of the PMMA monolayers as explained above. The present results clearly show quite similar relaxation spectra for both Γ's pointing out a similar energetic mechanism above Γ^* (which marks the percolation transition).[19]

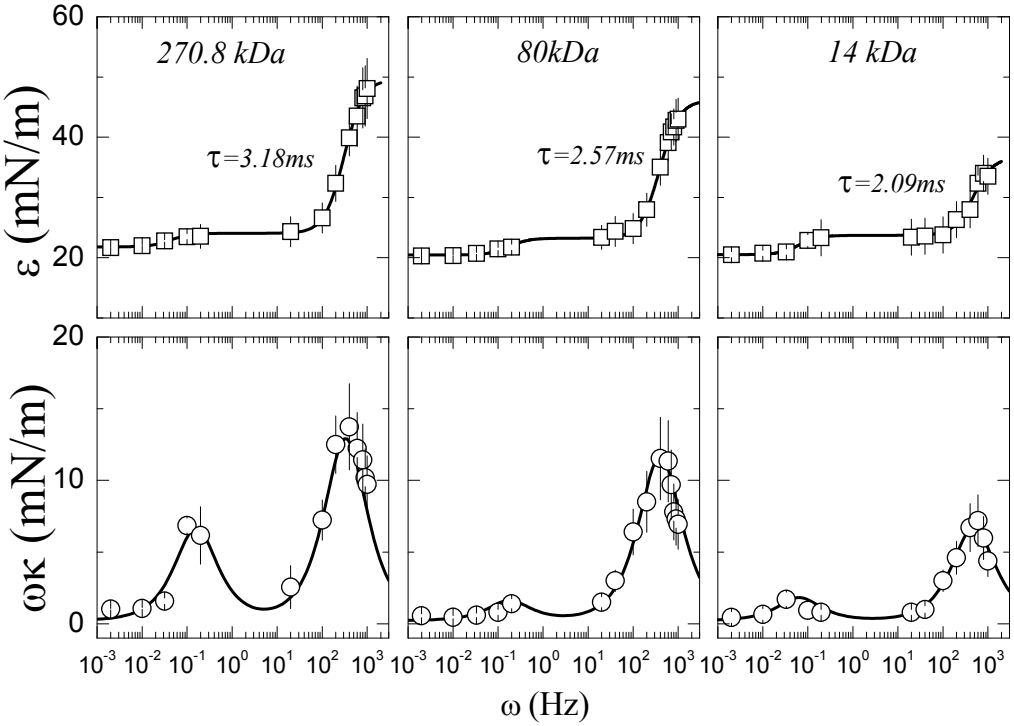

Figure 4.8. Frequency dependence of the dilational viscoelastic parameters for PMMA monolayer at $\Gamma = 0.75 mg/m^2 \approx \Gamma^*$ with different polymer weights. From left to right: $270.8 \cdot 10^3$; $80 \cdot 10^3$ and $14 \cdot 10^3$ *kDa*. Dilational elasticity ε (□); loss modulus $\varepsilon'' = \omega\kappa$ (○). Solid lines correspond to the fit to a model composed by two independent Maxwell processes.

3.1.2 Molecular Weight dependence

To get further insight into the dynamical behaviour of PMMA monolayers, we addressed the study of the effect of the polymer weight in the ω-dependence of the dilational viscoelastic parameters. For our purpose, we have studied three different M_w (270.8, 80 and 14 *kDa*) covering a broad range of polymer chain lengths N ($=M_w/M_0$) $\approx (1.4 - 27) \times 10^3$. Furthermore, we have considered two different Γ's regime as in previous results. Figure 4.8 shows the ω-dependence of

ε and ωκ for PMMA monolayers with different chain length at Γ= 0.75mg/m^2 ≈ Γ*. To study a broad frequency range, we included oscillatory experimental data performed at low frequencies and the *ECW* results at higher ones. Experimental values of ε corresponding to monolayers with different *N* are found between 20 and 50 mN/m. These data are in quantitative agreement and show identical trends. As expected, in all the cases the low frequency limit of ε extrapolates rather well at the equilibrium value ε'(ω→0) ≈ ε_0 and the loss modulus extrapolates to a near-zero value. A bimodal relaxation process corresponding to the sum of two Maxwell processes (Eq. 4.7) is followed for all the molecular weights. The parameters, which characterize the bimodal Maxwell relaxation, are shown in Table 4.1.

Table 4.1. Parameters of the model composed by two consecutives Maxwell-like processes for PMMA monolayers with different *N* at Γ ≈Γ*.

M_w *(kDa)*	$\varepsilon_0 \pm 0.5$ *(mN/m)*	$\varepsilon_1 \pm 0.75$ *(mN/m)*	$\tau_1 \pm 0.5$ *(s)*	$\varepsilon_2 \pm 0.75$ *(mN/m)*	$\tau_2 \pm 0.3$ *(ms)*
270.8	21.7	12.8	6.3	25.4	3.2
80	20.3	2.8	5.7	22.9	2.6
14	20.5	3.2	5.6	13.0	2.1

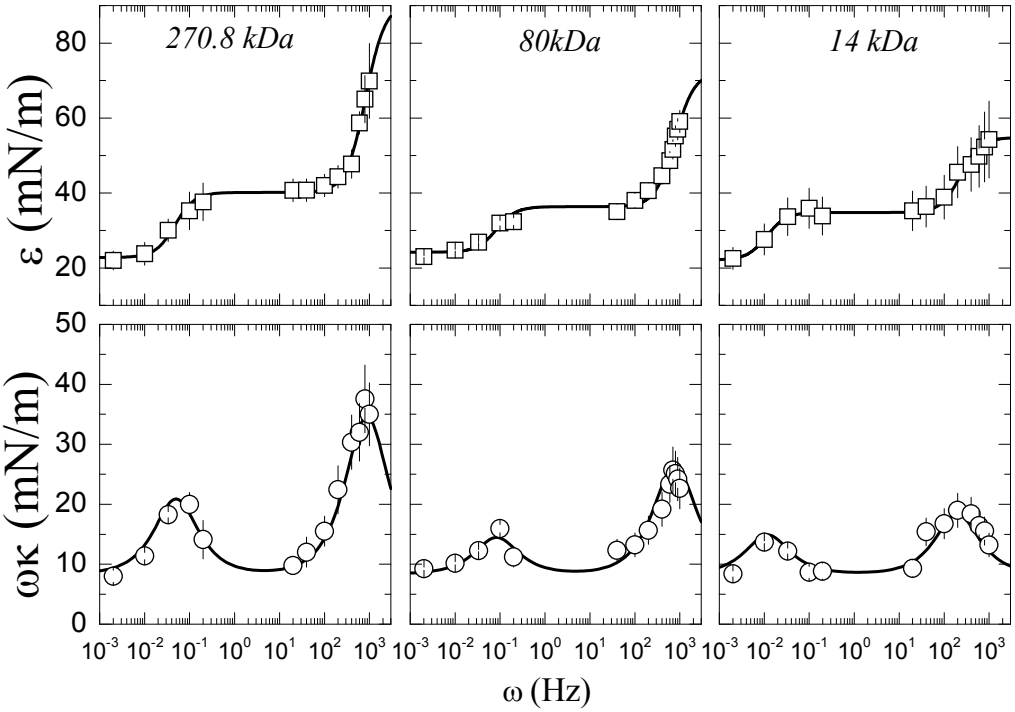

Figure 4.9. Frequency dependence of the dilational viscoelastic parameters for PMMA monolayer at Γ= 1.30mg/m^2 > Γ** with different polymer weights. From left to right: 270.8·10^3; 80·10^3 and 14·10^3 *kDa.* Dilational elasticity ε (□); loss modulus $\varepsilon'' = \omega\kappa$ (○). Solid lines correspond to the fit to a two Maxwell-like processes.

It is should be note that at decreasing *N* we found less intense relaxation peaks corresponding to weak viscous dissipation. This characteristic behaviour

suggests that dimensionality (viewed as chain length *N*) influences the network rigidity, as a reduction in the spatial dimension implies a loss of configurational entropy. On the other hand, the values of τ_i are found to be nearly chain-size independent ($\tau_i \sim N^0$) as expected for an interpretation of the PMMA monolayer above Γ^* in terms of a *central-for*ce (*CF*) percolation network.[28, 29] Within this framework, a further explanation arise from the fact that the relaxation times only depend on the high connectivity between the polymeric pancakes similarly to the pure entropic network as demonstrates the *CF* percolation model.[22]

In agreement with the results obtained just above Γ^*at different *N*'s Figure 4.9 highlights the ω-dependence of the parameters ε and ωκ for PMMA films with different *N* at $\Gamma = 1.30 mg/m^2 > \Gamma^{**}$. As explained above the broad frequency range shown corresponds to the mechanically oscillatory rheology and the ECW experiments performed. As expected, the experimental values of ε are found higher than those previously obtained at Γ^*. In fact, these data are in quantitative agreement and show identical trends. Furthermore, the low frequency limit of ε extrapolates rather well at the value of ε_0. Similarly, to the previous results, a bimodal relaxation process is described by means of a model constituted by two consecutive Maxwell-like processes (Eq. 4.7). The parameters corresponding to the model proposed, are shown in Table 4.2.

Table 4.2. Parameters of the model composed by two consecutives Maxwell-like processes for PMMA monolayers with different *N* at $\Gamma > \Gamma^{**}$.

M_w *(kDa)*	$\varepsilon_0 \pm 0.5$ *(mN/m)*	$\varepsilon_1 \pm 0.75$ *(mN/m)*	$\tau_1 \pm 1.0$ *(s)*	$\varepsilon_2 \pm 0.75$ *(mN/m)*	$\tau_2 \pm 0.3$ *(ms)*
270.8	22.8	25.0	20.2	52.4	1.1
80	24.2	12.1	12.0	35.9	1.3
14	22.5	13.2	70.1	21.7	1.5

Hence, the results at Γ^{**} are in further agreement with those obtained just above Γ^*. We thus find the same dependency of the intensity of the relaxation processes at decreasing *N* while the values of τ_i are found to be nearly chain-size independent ($\tau_i \sim N^0$) as expected well above Γ^* for a *central-for*ce (*CF*) percolation network.[29]

To summarize, we address an experimental study about the dilational viscoelasticity of PMMA monolayers covering a broad frequency range (0.002 *Hz* –1 *kHz*) by using mechanical oscillatory rheology and excited electrocapillary waves. Indeed, the Γ-dependence of the dilational elasticity modulus ε and dilational viscosity κ show a power law dependency like the equilibrium variables ($\Pi, \varepsilon_0 \sim \Gamma^{10}$; $\nu = 0.52$), and then compatible with the existence of a percolation network of PMMA soft-disk coils at 'poor' solvent conditions.[10, 18] From the ω-

dependence of the viscoelastic parameters at the two well defined regimes $\Gamma \approx \Gamma^{*}$ and $\Gamma > \Gamma^{**}$, we point out the existence of two relaxation modes conveniently modelled by two independent Maxwell-like processes. The first macroscopic relaxation corresponds to the large-wavelength concentration waves accounting for the large-spatial relaxation collective motions of polymeric domains. The second microscopic one corresponds to the short-spatial motion of a collection of polymer coils diffusing over a distance compatible with the domain size ($a \approx 0.1\mu m$). Finally, from the analysis of the effects produced by decreasing N in the dilational rheology we found that the rigidity of the system as well as the viscous dissipation decreases as expected for a percolation system dominated by entropy. In addition, within this perspective, the N-dependence of the relaxation times found $\tau \sim N^{0}$ could arise from the conjecture that the system is viewed as a *Central-force* percolation system in two dimensions.[28, 29]

3.2 Poly(*tert*-butyl-acrylate) (PTBA) Langmuir monolayers

In this section, we address an experimental study about the dilational rheology of PTBA monolayers adsorbed onto the air-water interface at frequencies in the range $10Hz–1kHz$ by using excited electrocapillary waves. In chapter 2, we have reported the existence of reptation motion in PTBA monolayers by means of equilibrium measurements as well as dynamical ones, in the low frequency range. The resulting dependencies on both chain concentration and size are compatible with the existence of diffusional reptation motions controlling molecular transport inside the monolayer. We found that monolayers of PTBA are adsorbed at the air-water interface in *good* solvent conditions explored by the scaling dependence of polymer concentration Γ and chain length N on the surface pressure Π, compatible with theoretical scaling laws.[15] In fact, these scaling dependences have been interpreted as a signature of the existence of a characteristic length ξ, which varies as $\xi \sim \Gamma^{-\nu/(2\nu-1)} N^0$, and defines the mean distance between entanglements points, i.e., the size of a blob in bulk, or the pancake segment conformation in quasi-2D. Hence, the value of the 2D-Flory exponent, $\nu = 0.78 \pm 0.03$ from $\pi \sim K_B T/\xi^2 \sim \Gamma^{2\nu/(2\nu-1)} N^0$ dependence for the PTBA monolayers above a critical size N_e ($\approx$100 monomers) corresponds with the behaviour expected for an entangled two-dimensional arrangements of flexible chains at *good*-solvent conditions.[11, 30]

Within the perspective of a *2D*-entangled network, polymer motion in the semidilute regime of a quasi-2D system, as Langmuir monolayer, is viewed as the surface diffusion of a chain (*reptation* motion). Thus, two time scales might be expected for this scenario: a short one over an unconstrained polymer flattened conformation of size ξ equilibrates on its own size, and a long time or reptation scale characterized by a characteristic time, τ_{rep}, over which the center of mass of the polymer chains diffuses through a tube defined by the topological constraints imposed by the surrounding chains. Accordingly, from the dynamical measurements performed on PTBA monolayers at low frequencies our results pointed out that long enough flexible chains can entangle in the monolayer evidencing reptation-like motion. Indeed, for polymers above N_e the terminal relaxation times, τ follow a scaling law $\tau \sim \Gamma^3 N^3$ suggesting that reptation is the dominant mechanism for molecular transport in the studied polymer layers.[15]

Under the reptation arguments proposed above, let us now extend the dynamical behaviour of PTBA monolayers to short time scale (higher frequency) by means of *ECW* experiments. Hence, we have studied the effect of the polymer concentration Γ on the dilational viscoelastic modulus for a PTBA film (M_w = $16.3kDa$; M_w/M_n=1.13) spread at the air-water interface at a fixed frequency, ω =

200*Hz*. The Γ-dependence of the propagation parameters (λ, β) characteristics of the spatial profile of the capillary waves generated onto that interface are shown by Figure 4.10.

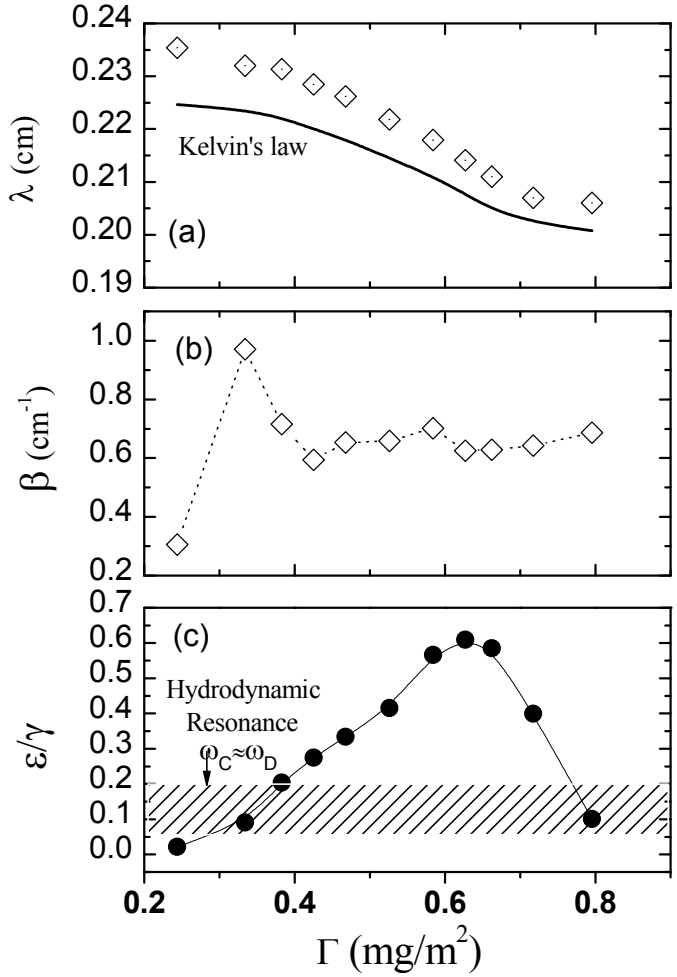

Figure 4.10. Γ-dependence of the propagation parameters of the excited electrocapillary waves onto the PTBA Langmuir monolayer (M_w = 16.3*kDa;* M_w/M_n=1.13). Variation of (a) Capillary wavelength λ and (b) damping coefficient β parameters at a fixed frequency, ω =200*Hz* generated, as a function of Γ. The solid line in (a) represent the behaviour of an ideal fluid interface pointed out by the Kelvin's law. (c) Probes of the dependence of the capillary damping on hydrodynamics trough the dimensional parameter ε_0/γ (≈ 0.15±0.05). It accounts for the resonance condition where the longitudinal and transversal waves are coupling.

The solid line in Fig. 4.10(a) represents the Kelvin's law ($\lambda^3 = \gamma 8\pi^3/\rho\omega^2$) at the fixed frequency. We found evident deviations for this limit behaviour, which points out the existence of a viscoelastic system. The highest value observed of β at $\Gamma \approx 0.3 - 0.4 mg/m^2$ may be associated to the hydrodynamic coupling between the transversal and dilational modes ($\omega_C \approx \omega_D$).[8] This resonance condition imply that the propagation parameters of the capillary waves are further sensible to the dilational viscoelasticity of the monolayer. Figure 4.1.c shows that the resonance condition determined by means of Eq. 4.4 correspond to the higher values of capillary damping β (Fig. 4.1.b). Hence, an enhanced accuracy of the ECW

method is expected at Γ's where the resonance condition is obeyed. Out of resonance, the dilational parameters could be affected by larger experimental errors due to the lack of coupling.

As commented above, there is a well-defined relation between the flatten pancake conformation with most monomers adsorbed at the interface adopted by the flexible chains of PTBA and their dynamical behaviour. We thus study the dilational viscoelastic modulus of the PTBA monolayer (M_w = 16.3*kDa, N*>N_e) at a short time scale, from the analysis of the propagation parameters characteristics of the excited electrocapillary waves at ω=200*Hz*.[6] The Γ–dependence of ε and ωκ for PTBA film is shown in Figure 4.11, above the overlapping concentration Γ^*=0.2 *mg/m*^{2}. The values of equilibrium elasticity ε_0 (calculated from the relative slope of the Π – Γ isotherm, see inset of Fig. 4.11) are also included in the Figure 4.11. As expected, we found that ε (400*Hz*) > ε_0 in the whole range of Γ studied, obeying the *Krammers-Kronig* relationship.[16]

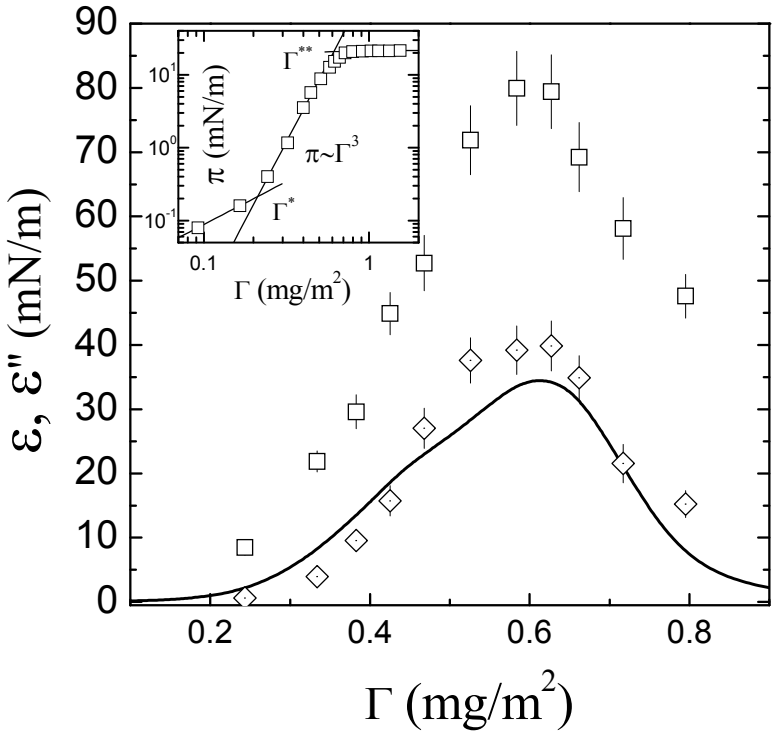

Figure 4.11. Γ–dependence of the dilational viscoelasticity parameters for PTBA monolayer at ω =200*Hz*.Symbols as follows: ε' (□), ε''= ωκ (◊). For the sake of comparison we have included the hydrostatic equilibrium elasticity, ε_0 (solid line) calculated from the relative slope of the π–Γ isotherm. Inset: Logarithmic plot of the π–Γ isotherm which points out three well defined concentration regimes. Γ^* separates the dilute from the semidilute and Γ^{**} defines the onset of the concentrated regime. The semidilute regime is described by the universal, *N*-independent, scaling law $\pi \sim \Gamma^3 N^0$ (*d* = 2, ν = ¾).

Looking at Figure 4.11 it seems reasonably to get further insight into the Γ-dependence of the dilational properties by analyzing the data in terms of the

dynamic scaling laws proposed by de Gennes[15]. We plot in Figure 4.12.a the dilational elasticity modulus ε as a function of Γ; as expected, ε scales as $K_BT/\xi^2 \sim \Gamma^{2\nu/(2\nu-1)} \sim \Gamma^3$ with $\nu = 0.78 \pm 0.03$. The value of this 2D-Flory exponent found for the Γ-dependence of ε suggests a strong correlation between the dilational viscoelasticity at a high frequency and the equilibrium properties pointed out in the chapter 1. Hence, as expected for cohesive adsorption forces between the polymer and the interface corresponding to 'good' conditions, the semidilute regime can be thought as a 2D gel made of entangled chains where the elasticity modulus scales with Γ. It should be mentioned that the scaling description shown is restricted to the semidilute regime according to the de Gennes theory.[15]

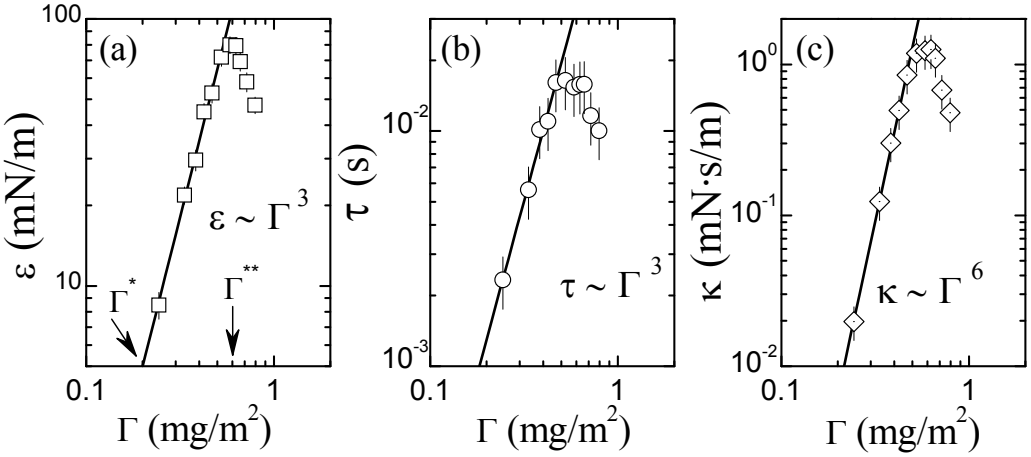

Figure 4.12. (a) Scaling behaviour of the dilational elasticity modulus ε as a function of Γ within the semidilute regime marked by Γ^* and Γ^{**} obtained from the ECW experiments of the PTBA monolayer at $\omega = 200Hz$. (b) Typical concentration dependence of the relaxation times ($\pi \sim \Gamma^3$) for flexible polymers with $N > N_e$. (c) Power-law dependency of the dilational viscosity $\kappa \sim \Gamma^6$ within the perspective for the predictions of 2D reptation of flexible polymers.

It is possible to define a relaxation times τ involved in the time scale defined by ECW experiment as the ratio between the dilational viscosity and the dilational elasticity at a fixed frequency ($\tau = \kappa / \varepsilon$). Figure 4.12.b shows the Γ-dependence of the relaxation times observed for a PTBA monolayer with $N > N_e$. These relaxation times follow a scaling law $\tau \sim \Gamma^3$, in rather agreement with the predictions for 2D reptation of flexible polymers. This dependence suggests that reptation is the dominant mechanism for molecular transport in this polymer film.[15] The mechanical relaxation results, reported in chapter 1, point out a power law dependence of the long time relaxation of PTBA films which is in agreement with the one shown here. Obviously, the temporal scale involved in each experiment is completely different. Thus, mechanical relaxation provides terminal relaxation times as correspond to long time scales ($\tau >> 1s$), while ECW experiments provide cooperative segmental relaxation in a short time scale ($\tau \approx 1ms$). Within this perspective, let us now evaluate the temporal scale in the

ECW experiments performed. At Γ=0.24mg/m^2 just above Γ^* the relaxation time, τ =2.33*ms*. Assuming that the motion of the polymer coils is diffusive, the molecular mobility is calculated as $D^*_0=K_BT/6\pi\eta R_F$ =1.42×10^{-11}*m*^{2}*/s* ($R_{F,PTBA}$ =15.4*nm; N=112*). The isolated chain Rouse-like self-diffusion $D^*_{Rouse}=D_0^*/N$ =1.265×10^{-13}*m*^{2}*/s*. Therefore, the polymer chains diffuses a distance of the order of its own size R_F during a characteristic time, called the Rouse time τ_R.[31] At $\Gamma\approx\Gamma^*$ $\tau_R^*\sim R_F^{\,2}/D^*_{Rouse}$ = 1.8*ms*, value significantly lower than the τ measured at the same polymer concentration by ECW (Figure 4.12.b).

To test our hypothesis about the existence of entanglements in PTBA monolayer making possible a reptation-like motion, we now discuss about the length scale involved in an ECW experiment. Thus, it is well known that topological constraints do not influence the polymer chains motion on length scales smaller than the size of an entanglement scenario. It is noteworthy that the power law found ($\tau\sim\Gamma^3$) can be interpreted as an indirect proof of the existence of a correlation length ξ related to the size of the polymer chains segments between entanglement points[1, 18]. Hence, we evaluate these characteristic times obtained by ECW which depend on the diffusion coefficient *D* and on the spatial scale *a* on which it operates, more precisely $\tau\sim a^2/D$.[13, 16] The spatial characteristic length scale of the relaxation process pointed out by *ECW* at $\Gamma\approx\Gamma^*$ would be $a^*\approx$73*nm*. At the overlapping concentration Γ^*, the characteristic length calculated as $\xi\approx R_F(\Gamma^*/\Gamma)^{3/2}$ leads to a value of $\xi^*\approx R_F\approx$15.4*nm*. As a conclusion, the fact that the spatial scale a^* are larger than ξ^* ($a^*>\xi^*\approx R_F$) means that the motion of flexible coils can be described by the reptation model.[31] It allows us to describe the relaxation times obtained by ECW by means of the reptation model due to $\tau>\tau^*$ which leads to larger *a*'s compared to the characteristic length ξ.

The dilational viscosity κ follows a strong dependence with Γ, above Γ^*, as $\kappa\sim\Gamma^6$ (Figure 4.11.c). This power-law behaviour is in further agreement with the scaling prediction of the reptation model for flexible polymers at good solvent conditions in 2D:[32, 33] $\kappa\sim\varepsilon\tau\sim(K_BT/\xi^2)\,\tau\sim N^3\Gamma^6$. The viscous dissipation of this system increases strongly with the chain size and polymer concentration as expected from a highly entangled system. We must remark that, above Γ^{**}, in the concentrated regime, not only the relaxation time but also the dilational elasticity and viscosity decrease strongly. This may be explained because ξ decreases at increasing Γ, leading to a blob size that probably falls below a critical value in which it does not support enough entropic elasticity. Therefore, the blob mobility increases, and then the dilational parameters ε, κ and τ decrease.

To summarize, this set of power-laws for the Γ-dependence of the dilational viscoelastic parameters can be explained by means of the reptation theory of

semidilute 2D-polymer solutions at good-solvent conditions. In addition, these results are in agreement with the long-time mechanical relaxation experiments performed in Langmuir films of a flexible polymer in good-solvent conditions, such as poly(vinyl acetate) (PVAC) by Monroy et al.[34] Furthermore, similar power-law dependencies of dilational rheological parameters for PVAC monolayers has been obtained from measurements of surface dynamic light scattering (SQELS) by Cicuta and Hopkinson.[35] It is well known that mechanical relaxation experiments point out the meso-macroscopic dynamics.[36] Indeed, this technique leads to probe large spatial scale collective motions, where it is plausible to identify the whole polymeric chain moving along the tube in terms of the reptation model. However, in time scales shorter than the longest relaxation time, which could arise from the ECW experiments, the reptation dynamics leads to correlated (coherent) motion of different portions (segments) in a given chain. Within this perspective, in accordance with our results in a high frequency domain performed by ECW, some experimental studies detect the motion of particular portions in the chain (collective segmental motion) by using different experimental techniques.[37] It should be noted that techniques working on a temporal scales ranged in the millisecond could revealed several characteristic featured of entangled chains as the faster relaxation of chain ends compared to the chain center. Further work may be necessary to clarify the possibility of evaluate the relaxation of polymer chain ends by ECW.

To get further insight in the dynamics of PTBA monolayer at short times, we have studied the frequency dependency in the range $10Hz-1kHz$ of the dilational viscoelastic modulus at two Γ*'s* well above Γ^*. Indeed, Figure 4.13 shows ε and $\omega\kappa$ as a function of the frequency at Γ=0.4 mg/m^2 >Γ^* and Γ= 0.6 $mg/m^2 \approx \Gamma^{**}$.

The relaxation spectra at both Γ's, can be described in terms of a Maxwell model (Eq. 4.6);[26] the characteristic parameters of this Maxwell-like viscoelastic relaxation are shown in Table 4.3. As expected, the low frequency limit of $\varepsilon(\omega\rightarrow 0)$ extrapolates to the value of equilibrium elasticity ε_0 (Figure 4.11), and $\omega\kappa$ extrapolates to a near-zero value at the two polymer concentrations studied. From this analysis in terms of a Maxwell dependence, the collective segmental polymer relaxation can be evaluated. Thus, the Maxwell relaxation times τ obtained here in the microsecond window are in agreement with the corresponding τ's shown in Figure 4.12. In fact, as the spatial scale involved are higher than the characteristic length, $a > \xi \approx R_F\,(\Gamma^*/\Gamma)^{3/2}$, the relaxation assumed here corresponds to highly correlated segmental motions along the confining tube. Furthermore, there is a delay in the relaxation between the experimental time found and the Rouse time, $\tau > \tau_{Rouse}$ due to constraining the chain's Rouse motion

to the tube. Assuming the Maxwell-type relaxation proposed, there is a shift on the dynamics towards longer times ($\tau \sim 1/\omega$) as Γ increases. Indeed, the characteristic relaxation time τ for the correlated segmental motion increases as increasing the polymer concentration. This fact can be explained molecularly by the existence of an increasing entangled network, which imposes serious constraints on the motion of the polymer chains, within the framework of the reptation approach.[32, 33]

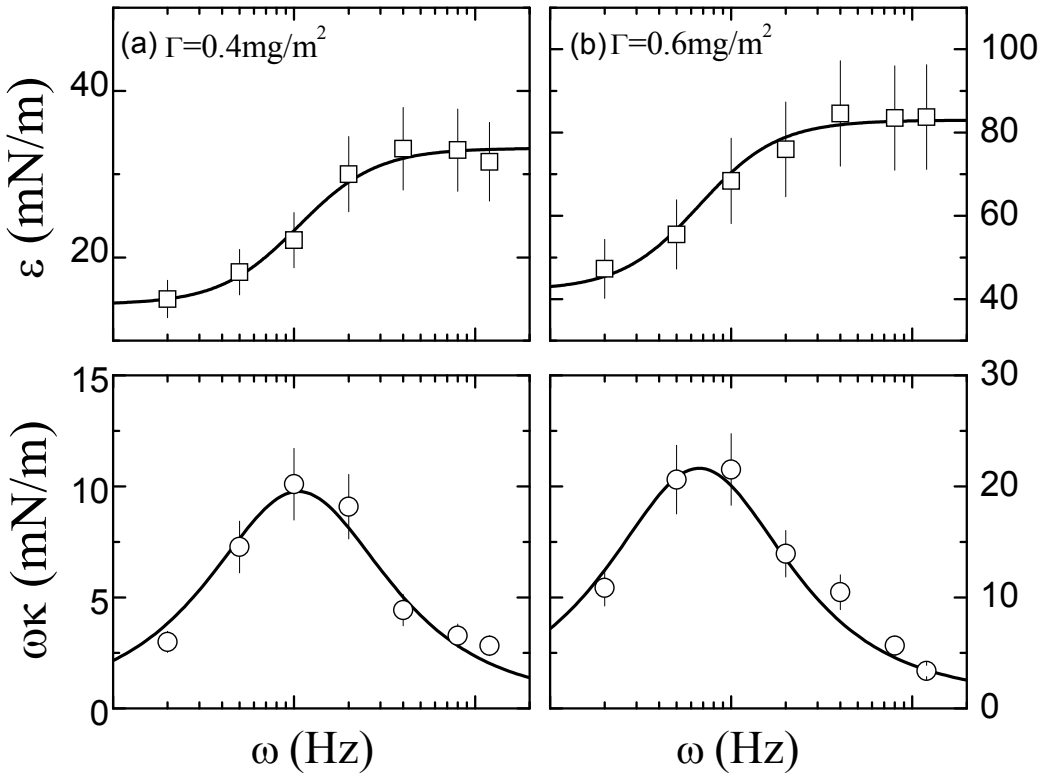

Figure 4.13. Frequency dependence of the dilational viscoelastic parameters for PTBA monolayer (16.3kDa, N=140 < N_e) at (a) $\Gamma = 0.4 mg/m^2 > \Gamma^*$ and (b) $\Gamma = 0.6\ mg/m^2 \approx \Gamma^{**}$. Symbols as follows: dilational elasticity ε (□) and loss modulus $\varepsilon'' = \omega\kappa$ (○). Solid lines reflects a Maxwell relaxation. (see Eq. 4.6).

Furthermore, both elastic modulus and viscosity values obtained suggest that relaxation of the molecular polymer conformation is strongly retarded by the entangled structure of the polymer chains. This description in terms of a Maxwell-type viscoelastic dependency leads to assume that the polymer monolayer behaves as an entangled gel, above Γ^*, in the semidilute and concentrated regime. The relaxation process, which belongs to a spatial scale larger than the characteristic length ξ as demonstrated above, describes the displacement of polymer chains in the direction parallel to the air-water interface restricted by a topological constraints imposed by the surrounding chains.

Table 4.3. Parameters of the Maxwell-like process for PTBA monolayer (16.4*kDa*).

Γ *(mg/m²)*	$\varepsilon_0 \pm 0.5$ *(mN/m)*	$\varepsilon_1 \pm 0.75$ *(mN/m)*	$\tau \pm 1.0$ *(ms)*
0.4	14.4	18.35	9.5
0.6	43.3	40.88	15.0

To test the validity of our hypothesis about the scaling-laws dependencies, we performed similar experiments, as the above described, in a PTBA monolayer (M_w = 1.45*kDa;* M_w/M_n=1.07) with N=10.9 <N_e ≈100 monomers. Figure 4.14 shows the Γ-dependencies found for the dilational viscoelastic parameters obtained by the analysis of the excited ECW on this PTBA film at the air-water interface. As expected, a much weaker dependence is experimentally observed for the relaxation time, below the critical entanglement size, pointing out a nearly linear dependence with the concentration, $\tau \sim \Gamma^{1.4}$ for $N<N_e$. This situation typical of non-entangled chains, demonstrates that amoeboid-like motion is also plausible in the crowded environment accessible to a given chain, highlighting a sub-diffusive transport mechanism characterized by weaker dependence than the expected from the Rouse model.[32] This experiment allow us to understand that only long enough flexible chains could entangle in a Langmuir monolayer giving rise to a reptation-like motion.

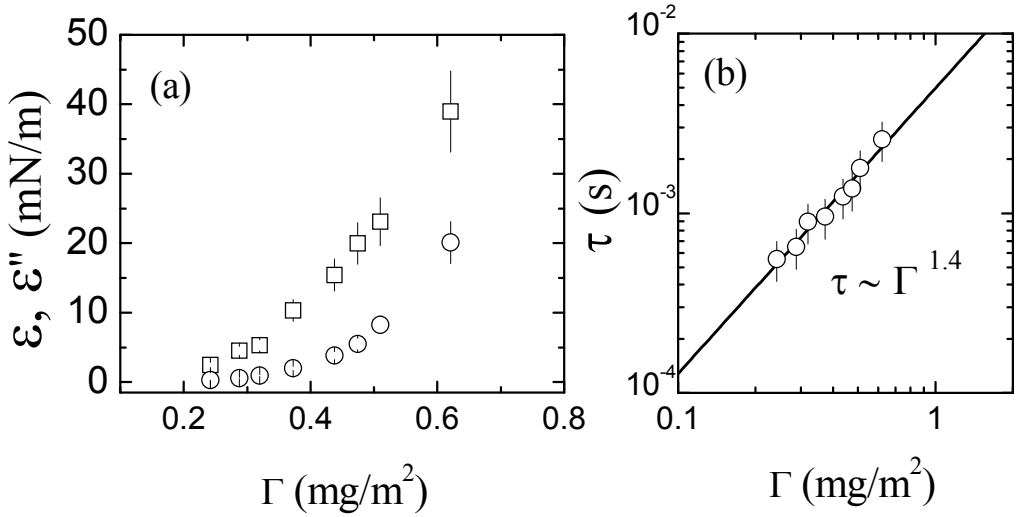

Figure 4.14. (a) dilational viscoelastic parameters ε and ωκ as a function of Γ obtained from the ECW experiments of the PTBA monolayer (M_w = 1.45*kDa*) at ω =200*Hz*. (b) Typical concentration dependence of the relaxation times ($\tau \sim \Gamma^1$) for flexible polymers with $N < N_e$, within the perspective for the predictions of 2D *amoeba*-like motion.

To summarize, in this section we stress that the concentration dependence of the dilational viscoelasticity of PTBA Langmuir monolayer studied by ECW are in agreement with the theoretical scaling laws proposed by de Gennes for an entangled 2D-system governed by reptation motion. Indeed, we have found that, as in bulk, above a N_e exists a crossover from a non-entangled to entangled

system. In addition, we address that from the analysis of the high-frequency rheological data obtained from capillary experiments, correlated segmental motions can be pointed out for the PTBA monolayer. The segmental relaxation times obtained in the millisecond window leads to understand better the collective segmental motions along the tube by means of the reptation model.

As a final remark, to explore the relation between the high-frequency dilational rheology and the interactions of the polymer with the air-water interface, we address the comparison between a PMMA monolayer ($M_w = 14kDa$) adsorbed at '*poor*' conditions at the A/W interface and PTBA one ($M_w = 16.3kDa$) considered adsorbed at '*good*' conditions. From the structural point of view, good-solvent conditions correspond to cohesive adsorption interaction between PTBA and the interface leading a flexible worm-like conformation and poor-solvent is related to a weak adsorption, as compared to the monomer-monomer interaction, and leads to a compressed coil conformation to minimize the contacts with the interface. Figure 4.15 highlights the relaxation spectra of both polymer monolayers in the concentrated regime, at $\Gamma \approx \Gamma^{**}$. These ω-dependencies have been interpreted by means of a Maxwell relaxation process (Equation 4.6). As expected, the existence of noticeable differences in the Maxwell relaxation used to fit the experimental data point out that the dilational response of a 2D polymer system depends on the conformation adopted at the interface. Concretely, PTBA monolayer leads to higher values of elasticity moduli; furthermore, the Maxwell-like relaxation observed for this flexible polymer is characterized by a rather large strength $\varepsilon_1/\varepsilon_0 \approx 1$. However, PMMA film, at the same polymer concentration, shows shorter strength of the relaxation mode $\varepsilon_1/\varepsilon_0 < 1$ leading to supports less dilational elasticity. These remarkably differences found suggest that expanded polymer monolayer at good solvent conditions are more elastic than condensed polymer ones at a poor solvent environment. On the other hand, for PMMA monolayer, the loss modulus $\omega\kappa$ which accounts the viscous friction between polymeric pancakes is not far from the elasticity values contrary to the further differences between $\omega\kappa$ and ε in PTBA. This difference behaviour, in terms of viscous dissipation, points out also the differences between the conformation adopted by the polymers. This results are in agreement with previous results of Yu et al. which denotes that the difference in the high-frequency dependence dilational rheology of polymer monolayers measured by SQELS is related to the solvent-quality of the A/W interface.[5, 38]

Within the perspective of the difference dilational rheology comes from the conformation adopted by the polymer at the interface, it is remarkably to analyze the different relaxation characteristic times τ obtained for the Maxwell viscoelastic process pointed out by both polymers films. We found that τ_{PTBA}

=15*ms* > τ_{PMMA}=1.5*ms*.Once again, it is plausible to explain this difference in terms of the conformation of the polymers. At Γ^{**}, a PMMA monolayer can be viewed as a percolated gel of soft disk-shaped coils (pancakes) under the *SAW (Self-avoiding walk)* conformation proposed by de Gennes[15] while PTBA monolayer can be described as an entangled gel constituted by flexible polymer chains which are able to entangle. The main difference between both scenarios proposed is that the existence of entanglements, well supported in 2D by previous studies[11]. This entangled scenario highlights a delay in the relaxation; In fact, this slowing arises because of the chain must move along the confining tube formed by the surrounding chains.

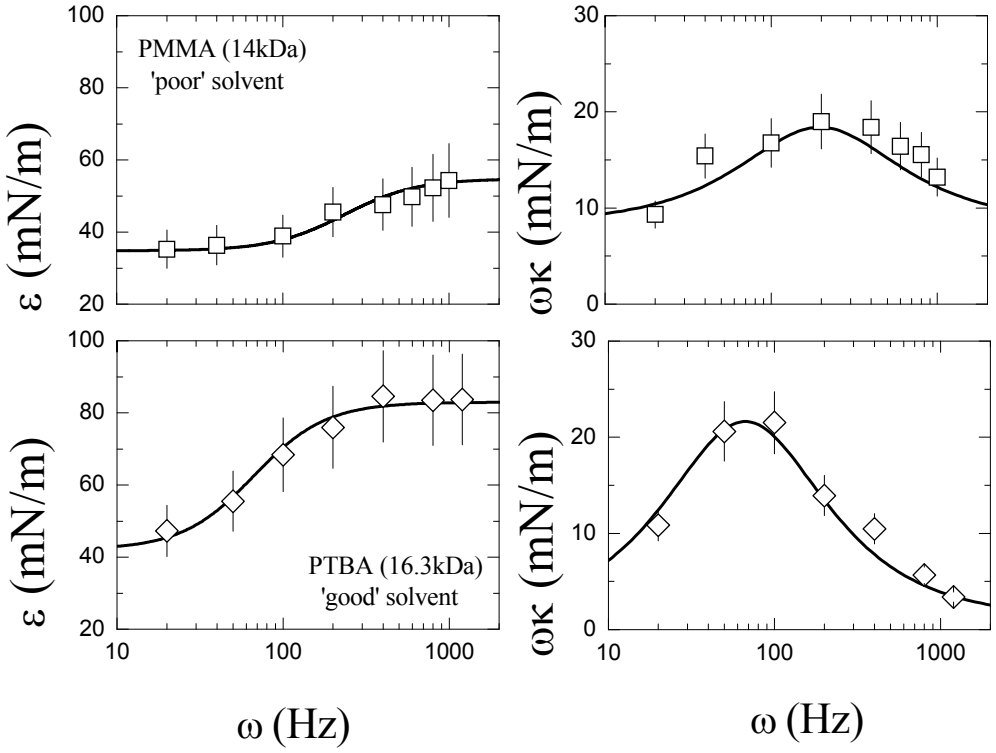

Figure 4.15. Relaxation spectra for both PMMA (14*kDa*) and PTBA (16.3*kDa*) monolayers at $\Gamma \approx \Gamma^{**}$. Symbols as follows: dilational elasticity ε (□) and loss modulus $\varepsilon'' = \omega\kappa$ (◊). Solid lines reflects the Maxwell-type dependency of the relaxation processes. (see Eq. 4.6).

4. Conclusions

In this chapter, we have addressed a direct proof of the correlation between the dynamical behaviour at short time domains, mainly at microsecond window, and the conformation of polymer monolayers adopt at the air-water interface. Indeed, we highlight that the solvent-character of the interfaces play a key role not only in the structure expected for the polymeric system but also in their dynamics. To test our hypothesis, we have studied two polymers at different adsorption

conditions demonstrating that the viscoelastic character of each one depends on the conformation adopted at the interface.

We have addressed the dilational viscoelastic behaviour of PMMA monolayers, which are described by means of a flattened pancake conformation, covering a broad frequency ($0.002Hz–1kHz$) range by means of mechanical oscillatory rheology and *ECW*. From the relaxation spectra we have found two viscoelastic Maxwell relaxation processes. One macroscopic mode placed at the long-time domain (low frequencies) which accounts the large-spatial relaxation collective motions of polymeric domains. At short time domain, we found a microscope relaxation mode accounting to the motion of a collection of polymer coils diffusing over a distance compatible with the domain size. From the Γ-dependence of the dilational viscoelasticity, we have found a power-law behaviour compatible with the existence of a percolation network of PMMA pancakes at *poor*-solvent conditions.

On the other hand, we have addressed the dynamics of PTBA monolayers in a short time domain ($\approx \mu s$) as expected for ω*'s* in the order of *Hz*'s. Within the perspective of A 2D-entangled network at *good*-solvent conditions which has been plausible hypothesized for PTBA monolayers, our results have pointed out the description of the viscoelastic parameters as well as the relaxation times in terms of the scaling-laws predicted by de Gennes for an entangled network highlighting the existence of a reptation-like motion. Despite of the amazing short times found is plausible correlate them to the diffusion of segments of chains constrained by the neighbouring chains according to the reptation mode, since $\tau > \tau_{Rouse}$.

5. References

1. Jones, R. A. L.; Richards, R. W., *Polymers at Surfaces and Interfaces*. Cambridge Univ. Press: Cambridge, 1999.
2. Bae, S. Y.; Granick, S., Molecular Motion at Soft and Hard Interfaces: From Phospolipid Bilayers to Polymers and Lubricants. *Annual Review of Physical Chemistry* **2007,** 58, 353-374.
3. Kawaguchi, M., Thermodynamic, structural and rheological properties of polymer films at the air-water interface. *Prog. Polym. Sci.* **1993,** 18, 341.
4. Esker, A. R.; Zhang, L. H.; Sauer, B. B.; Lee, W.; Yu, H., Dilational viscoelastic behaviors of homopolymer monolayers: surface light scattering analysis. *Colloids and Surfaces A* **2000,** 171, (1-3), 131-148.
5. Esker, A. R.; Kim, C.; Yu, H., Polymer monolayer dynamics. *Functional Materials and Biomaterials* **2007,** 209, 59-110.
6. Langevin, D., *Light Scattering by Liquid Surfaces and Complementary Techniques*. Marcel Dekker: New York, 1992; Vol. 41.
7. Levich, V. G., *Physico-Chemical Hydrodynamics*. Prentice Hall: 1962.
8. Lucassen, E. H.; Lucassen, J., Properties of Capillary waves. *Advances in Colloid and Interface Science* **1969,** 2, 347-395.
9. Edwards, D. A.; Brenner, H.; Wasan, D. T., In *Interfacial Transport Processes and Rheology*, Butterworth-Heinemann: Boston, 1991.
10. Maestro, A.; Ortega, F.; Monroy, F.; Kragel, J.; Miller, R., Molecular Weight Dependence of the Shear Rheology of Poly (methyl methacrylate) Langmuir Films: A Comparison between Two Different Rheometry Techniques. *Langmuir* **2009,** 25, (13), 7393-7400.
11. Maestro, A.; Hilles, H.; Ortega, F.; Rubio, R. G.; Langevin, D.; Monroy, F., Reptation in Langmuir polymer monolayers. *Soft Matter* **2010,** accepted 2010.
12. Maestro, A.; Langevin, D.; Monroy, F., Amorphous freezing in two dimensions: from soft coils to rigid particles. *Eur. Phys. J E* **2010,** 31, 89-94.
13. Monroy, F.; Rivillon, S.; Ortega, F.; Rubio, R. G., Dilational rheology of Langmuir polymer monolayers: Poor-solvent conditions. *Journal of Chemical Physics* **2001,** 115, (1), 530-539.
14. Kawaguchi, M.; Sauer, B. B.; Yu, H., *Macromolecules* **1989,** 22, 1735.

15. Gennes, P.-G. d., *Scaling Concepts in Polymer Physics*. Cornell University Press: Ithaca, 1979.

16. Ferry, J. D., *Viscoelastic Properties of Polymers*. 3 ed.; Wiley: New york, 1980.

17. Maestro, A.; Ortega, F.; Rubio, R. G., Surface Rheology of poly (methyl methacrylate) Langmuir monolayers: Evidences of a Glassy-like dynamic. *in preparation* **2010**.

18. Vilanove, R.; Rondelez, F., Scaling description of two-Dimensional Chain Conformations in Polymer monolayers. *Phys. Rev. Lett.* **1980,** 45, (18), 1502.

19. Monroy, F.; Ortega, F.; Rubio, R. G.; Ritacco, H.; Langevin, D., Surface rheology of two-dimensional percolating networks: Langmuir films of polymer pancakes. *Physical Review Letters* **2005,** 95, (5).

20. Stauffer, D.; Aharony, A., *Introduction to Percolation Theory*. London, 1992.

21. Adam, M.; Lairez, D., *Physical Properties of Polymeric Gels*. Willey: Chichester, UK, 1996.

22. Feng, S.; Sen, P. N., Percolation on elastic networks - new exponent and threshold. *Physical Review Letters* **1984,** 52, (3), 216-219.

23. Angell, C. A.; Ngai, K. L.; McKenna, G. B.; McMillan, P. F.; Martin, S. W., Relaxation in glassforming liquids and amorphous solids. *Journal of Applied Physics* **2000,** 88, (6), 3113-3157.

24. Sollich, P.; Lequeux, F.; Hebraud, P.; Cates, M. E., Rhelogy of Soft Glassy Materials. *physical Review Letters* **1997,** 78, (10), 2020-2023.

25. Cicuta, P.; Stancik, E. J.; Fuller, G. G., Shearing or compressing a soft glass in 2D: time-concentration superposition. *Physical Review Letters* **2003,** 90, (23), 236101/1-4.

26. Riande, E.; Diaz-Calleja, R.; Prolongo, M.; Masegosa, R.; Salom, C., *Polymer Viscoelasticity. Stress and Strain in practice*. Marcel Dekker: New York, 2000.

27. Lucassen, J.; Van der Tempel, M., Dynamic measurements of dilational properties of a liquid interface. *Chemical Engineering Science* **1972,** 27, (6), 1283.

28. Kantor, Y.; Webman, I., Elastic properties of random percolating systems. *Physical Review Letters* **1984,** 52, (21), 1891-1894.

29. Arbabi, S.; Sahimi, M., Mechanics of disordered solids .1. percolation on elastic networks with central forces. *Physical Review B* **1993,** 47, (2), 695-702.

30. Kawaguchi, M., Thermodynamic, structural and rheological properties of polymer films at the air-water interface. *Prog. Polym. Sci.* **2007,** 18.

31. Rubinstein, M.; Colby, R. H., *Polymer Physics*. Oxford Univ. Press: New York, 2003.

32. De Gennes, P. G., Dynamics of entangled polymer solutions. I. The Rouse model. *macromolecules* **1976,** 9.

33. De Gennes, P. G., Dynamics of Entangled Polymer Solutions. II. Inclusion of Hydrodynamic Interactions. *macromolecules* **1976,** 9, 594-598.

34. Monroy, F.; Hilles, H. M.; Ortega, F.; Rubio, R. G., Relaxation dynamics of Langmuir polymer films: A power-law analysis. *Physical Review Letters* **2003,** 91, (26).

35. Cicuta, P.; Hopkinson, I., Scaling of dynamics in 2d semi-dilute polymer solutions. *Europhysics Letters* **2004,** 68, (1), 65-71.

36. Monroy, F.; Ortega, F.; Rubio, R. G.; Velarde, M. G., Surface rheology, equilibrium and dynamic features at interfaces, with emphasis on efficient tools for probing polymer dynamics at interfaces. *Advances in Colloid and Interface Science* **2007,** 134-35, 175-189.

37. Russell, T. P.; V.R., D.; Dozier, W. D.; Felcher, G. P.; Agrawal, G.; Wool, R. P.; Mays, J. W., Direct observation of reptation at polymer interfaces. *Nature* **1993,** 365, 365-367.

38. Esker, A. R.; Zhang, L. H.; Sauer, B. B.; Lee, W.; Yu, H., Dilational viscoelastic behaviors of homopolymer monolayers: surface light scattering analysis. *Colloids and Surfaces A* **2000,** 171, 131-148.

Chapter 5

Dynamical behaviour of Nanoparticle – Surfactant interfacial mixed Layers

Abstract

The hydrophobicity of the particles' surface can be modified by adding surfactants, which would change the surface free energy of attachment to a liquid interface. The study of the dynamical and equilibrium behaviour of mixed particle – surfactant layer may provide insight in the strong influence of the hydrophobic – hydrophilic balance of the particle; i.e., in their affinity for the fluid interfacial environment. Here, we address an experimental study of the dilational viscoelasticity of the interfacial mixed layers formed by the mixture of colloidal silica nanoparticles and cationic surfactants. The results indicate that the interaction between silica nanoparticles and surfactant molecules at fluid interfaces affects the macroscopic interfacial dynamics, which is in agreement with results previously published for similar systems in the low frequency range. Thus, we found, by the viscoelastic behaviour over a broad frequency range that an important role in the mixed particle-surfactant layer is played, not only by the adsorption of particle-surfactant complexes from the bulk to the interface controlled by diffusion, but also by an other kinetic process at shorter characteristic time which is expected to be related to the surfactant redistribution between the particle surface and the fluid interface.

1. Introduction: Nanoparticles at Interfaces

The hydrophilic – hydrophobic character of colloidal nanoparticles plays a key role in their affinity for fluid interfaces. Hence, by the addition of surfactants, they turns less hydrophilic and as a consequence they can be adsorbed at a fluid interface creating an interfacial layer[1]. Systems formed by colloidal nanoparticles and surfactants adsorbed at fluid interfaces is currently a subject of increasing interest, mainly for their use in the formation and stabilization of foams and emulsions.[1-4] However, the mechanism of this stabilization is not completely understood yet. Actually, it is hypothesized that the efficiency of particles in the stabilization process is related to the particle attachment energy.[2] Solid particles generally adsorb irreversibly at the interface, with adsorption energies in the order of thousands of *kT*. This can be understood in terms of basic interface thermodynamics. In fact, the free energy, ΔE_p, associated with the transference of one spherical particle of radius *R* from the bulk phase to a planar fluid interface can be expressed in terms of the contact angle, θ of the particles with the interface as well as the air-water interfacial tension γ.[2]

$$\Delta E_p = -\pi R^2 \gamma \left(1 \pm \cos\theta\right)^2 \qquad (5.1)$$

The sign in the bracket corresponds to particles centers below (–) or above (+) the interface. As can be seen from Equation 5.1 indicates that micro- or nanoparticles non-completely wetted ($0 < \theta < 180º$) are strongly attached to fluid interfaces. Indeed, these interfacial energy, ΔE_p, exceeds usually the thermal energy (~*kT*) leading to an irreversible adsorption of the particles; i.e., at $\theta = 90º$, $\Delta E_p \approx \gamma R^2\ kT$, indicating that $\Delta E_p >> kT$.[5] This situation is schematically shown in Figure 5.1(a) where completely hydrophilic ($\theta = 0º$) or hydrophobic particles ($\theta = 180º$) reside in the respective bulk phase water or air/oil phase. Only if the particles are partly hydrophilic/hydrophobic ($0 < \theta < 180º$), they may attach irreversibly to interfaces. Increasing of the wetting angle θ (from left to right) results in changing the particle's position at the interface.This irreversibly adsorbed behaviour shown by particles partly hydrophobic is in contrast to surfactant molecules which adsorb and desorb on a relatively short timescale.[1] From Equation 5.1 one may expect a strong dependence of the interfacial energy ΔE_p on the wettability of the particles accounted by θ. In a surfactant-nanoparticle system, by the addition of surfactants molecules the wettability of these nanoparticles may be modified. Hence, their attachment to a fluid interface might be controlled as schematically shown Figure 5.1(b). Here, when cationic surfactants interact with a negatively charged colloidal particle surface, the composite system becomes more hydrophobic. Therefore,

particles first soluble in water, could move to the air/oil phase due to their hydrophobization by surfactants.[1, 3]

Nanoparticles attached at fluid interfaces adopt different structures according to the different interactions between particles adsorbed at fluid interfaces.[6] These interactions depend on the size and shape of the particles, as well as on the nature and composition of the bulk phases, e.g. on the presence of surfactants and/or polyelectrolytes. Attraction forces between the particles can result in their aggregation and formation of clusters of different shape at the interface,[7] whereas, repulsion forces lead to formation of ordered arrays of particles.[8] In summary, spherical charged colloidal nanoparticles are subject to attractive capillary interactions, to Columbic repulsion due to their vertically asymmetric charge distribution, and to long range attraction due to non-uniform horizontal charge distribution.[9]

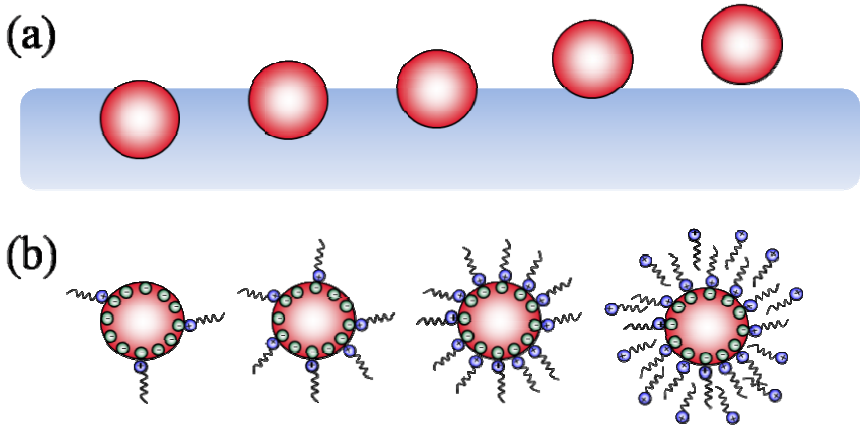

Figure 5.1. (a) Position of a particle in an arbitrary fluid-fluid interface depending of the free energy of their attachment ΔE_p accounting by the phase contact angle θ. From left to right correspond to an increase of the hydrophobicity of the particle; i.e., from θ =0º totally hydrophilic particle to θ=180º totally hydrophobic one. (b) Change of the hydrophobicity of an arbitrary colloidal particle negatively charged due to their interactions with cationic surfactants. At high enough surfactant concentration, hydrophobic interactions lead to the adsorption of additional surfactant molecules.

From a theoretical approach, composite systems formed by solid colloidal particles attached in a fluid biphasic environments has been further investigated, mainly the thermodynamic description of the partitioning of particles between aqueous bulk and fluid interfaces.[10, 11] Thus, the influence of the particle wetting on the thermodynamic properties of particles layers have been extensively studied.[1, 12] It is noteworthy that the interfacial layer formed by nanoparticles should be viewed as a multiphase nanometric region composed by three interfaces, one between two fluid interfaces, i.e., air/oil–water, and when the particles are partially wetted, two solid interfaces.[13]

The macroscopic mechanical properties of fluid interfaces are controlled by the interfacial tension, the dilational and shear surface complex elastic moduli. These variables can be strongly modified by the attachment of particles which contribute to the stabilization.[14] The interaction between ionic surfactants and charged nanoparticles may add significant complexity to the structure and dynamics of the laden interfaces, and in particular to the mechanical properties of the interface.[10]

The aim of this work is to get further insight into the interaction between nanoparticles and fluid interfaces, in relation to the surfactant adsorption on the particle surface, and to quantify its effect on the macroscopic interfacial dynamical behaviour. We thus highlight a study on the relation between the dilational viscoelastic behaviour of nanocomposite adsorbed layers formed by nanoparticles and surfactants and the interfacial structure adopted, which depends strongly on the surfactant concentration. We have carried out an experimental study of the dilational complex elasticity modulus of the interfacial layer formed by silica nanoparticles and two cationic surfactants (Alkyl trimethylammonium bromide, C_nTAB, with CTAB for n=16 and DTAB for n=12). The whole frequency range has been covered by combining three different methods: Drop profile analysis tensiometer (*PAT*)[15], from 0.01 to 0.2*Hz*, Capillary pressure tensiometer (*CPT*)[16] (0.5−100*Hz*), and Electrocapillary waves (*ECW*) (25*Hz*−1.5*kHz*). A theoretical model already presented in the literature has been used to analyze the dilational viscoelasticity behaviour of the colloidal nanoparticle-surfactant mixed layers. The analysis of the data points out the existence of two different relaxation processes associated to the adsorption dynamics and the effect of these kinetics on the viscoelastic behaviour of the adsorbed layers studied. Furthermore, we found a close link between the rheological response of the nanocomposite system and their adsorption mechanism, which highlights the molecular characteristics of surfactants as well as the transport and kinetic processes involving them. Indeed, the interpretation of dilational rheology by means of suitable models allows one to understand the physicochemical mechanisms related to the adsorption process. In fact, the change in the viscoelasticity behaviour of the composite interfacial layer can be attributed to the mass transfer and to the modification of the surface composition.

Ellipsometric measurements have been performed to clarify the nanocomposite layer structure generated. Hence, we have used a two-layer model recently described in the literature,[17, 18] which allows one to evaluate not only the thickness of the nanometric non-homogeneous interfacial layers, but also the wetting contact angle θ of the nanoparticles attached to the fluid interface. These results confirm the change in hydrophobicity of the nanoparticles due to the

interaction of these surfaces with the surfactants. As a final remark, our ellipsometric results show a strong influence of the particle hydrophobicity and surface composition on the structure of the layer pointing out a further agreement with the dilational macroscopic dynamics measured.

For the sake of clarity, the chapter is organized as follows: Section 2 describes briefly the model proposed by Ravera et al.[13, 19] for the description of the dilational dynamics of the interfacial system studied. The materials and methods used are described in section 3. Finally in section 4, we address the dynamical experiments performed in the broad frequency range studied pointing out the effect of the surfactant adsorption to the nanoparticles surface and the ellipsometric measurements which demonstrate the existence of a mixed nanocomposite layer in the air-water interface.

2. Theoretical background

It is well known that the frequency dependence of the dilational viscoelastic module ε is due to the existence of relaxation processes in the interfacial layer.[20] Hence, dilational rheology is used to study the dynamical behaviour of the surfactant adsorption and the process involved in it; i.e., molecular diffusion and secondary rearrangements in the adsorbed layer. To get further insight in the mechanism governing the adsorption and/or the re-organization of the interfacial layer and to quantitative evaluate the characteristic times of such processes, it is then important not only to measure the dilational viscoelasticity (or complex viscoelastic modulus) as a function of the frequency in a broad range, but also to analyze these data by a suitable model.

The classical Lucassen van der Tempel model[21] has been extensively employed to describe the diffusion controlled adsorption of soluble surfactant systems.[22, 23] Ravera et al. have proposed an extension of this classical approach taking into account other re-organization processes inside the adsorbed layer like molecular reorganization[24] or chemical reactions[19] leading to a general expression for the dilational viscoelasticity, ε (ω), where diffusion is considered together with other kinetic surface processes.[19] The key assumption adopted by this approach is to consider that, to describe the state of the interfacial system out of equilibrium, it is necessary an additional variable for each kinetic process involved respecting the equilibrium state. This fact means, that out of equilibrium, the surface tension (or surface pressure) is dependent not only on the total adsorption Γ, but also on other variables, such as the average surface area per molecule when re-orientable adsorbed molecules are considered in the interfacial layer.

Hence, taking in account a generic interfacial process described by a generic variable X, the dependence of the surface pressure on X has to be considered when calculating the total adsorption Γ, i.e., $\pi = \pi(\Gamma, X)$. In accordance to the definition of dilational viscoelasticity ε (= $d\gamma/dlnA$), it can be expressed as,

$$\varepsilon = -\varepsilon_{0\Gamma} \frac{d \ln \Gamma}{d \ln A} - \varepsilon_{0X} \frac{d \ln X}{d \ln A} \tag{5.2}$$

Where, $\varepsilon_{0\Gamma} = \partial\Pi / \partial ln\Gamma$ and $\varepsilon_{0X} = \partial\Pi / \partial ln\, X$, are thermodynamic quantities calculated from the surface equation of state. Within the framework of Lucassen van der Tempel approach, the high frequency limit elasticity, also known as Gibbs elasticity, is defined as $\varepsilon_{0G} = d\Pi / dln\Gamma$, and can be written as:

$$\varepsilon_{0G} = \varepsilon_{\Gamma} + \varepsilon_{0X} \frac{d \ln X_0}{d \ln \Gamma} \tag{5.3}$$

As explained in detail by Ravera et al.[19], solving the mass balance at the interface together with the kinetic equation for the relaxation process, in accordance to a harmonic perturbation scheme, leads to an expression of ε. In the situation of a single surface kinetic process, besides diffusion, described by a generic variable X, ε is given by:

$$\varepsilon = \frac{\varepsilon_{0\Gamma} - i\lambda\varepsilon_{0G}}{-(1+\xi-i\xi)i\lambda + 1 + G + \xi - i\xi/(1+G)} \tag{5.4}$$

Where $\xi = (\omega_D / 2\omega)^{1/2}$, being ω_D the characteristic frequency of the diffusion transfer and, $\lambda = \omega_k/\omega$, being ω_k the characteristic frequency of the surface kinetic process, while *G* is a thermodynamic quantity, $G = 1 - (dc_s/d\Gamma)/(\partial c_s/\partial\Gamma)$. Here, c_s is the sub-layer concentration.

The limit case of Eq. 5.4 for very fast equilibration of the relaxation process ($\omega_k >> \omega$) provides:

$$\varepsilon = \varepsilon_{0G} \frac{1 + \xi + i\xi}{1 + 2\xi + 2\xi^2} \tag{5.5}$$

which is the classical Lucassen-van den Tempel equation. It is noteworthy that, in the general case proposed, the high frequency limit of the elasticity given by Eq. 5.4 is $\varepsilon_{0\Gamma}$ which differs from the Gibbs elasticity.

Within the perspective of the model proposed by Ravera et al.[19] Figure 5.2 shows the dilational viscoelastic complex modulus ε(ω) calculated by means of Equation 5.4 for arbitrary values of the characteristic parameters. For the sake of comparison, we also have plotted the limit case expressed by the Lucassen van den Tempel model (Equation 5.5) as well as the other limit case obtained for

vanishing ξ, corresponding to the situation of an insoluble layer. In this case, Equation 5.4 becomes:

$$\varepsilon = \frac{\varepsilon_{0\Gamma} - \varepsilon_{0G}\lambda^2}{1+\lambda^2} + \left(\varepsilon_{0\Gamma} - \varepsilon_{0G}\right)\frac{i\lambda}{1+\lambda^2} \qquad (5.6)$$

It should be noted that the presence of a relaxation process confers to ε particular characteristics. In fact, at the corresponding characteristic frequency one can observe a maximum in the imaginary part, ωκ, and inflection points in the real part, ε.

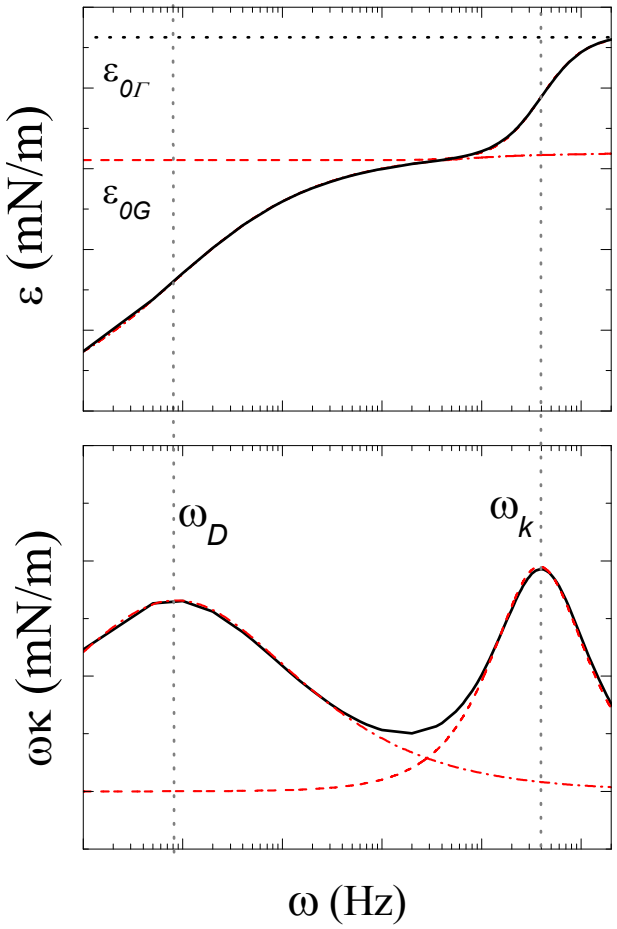

Figure 5.2. (Solid line) Theoretical curves of the real, ε, and imaginary, ωκ part of the dilational viscoelasticity as a function of the frequency ω obtained by means of the general mixed kinetic model proposed of Ravera et al. (Eq. 5.4). (Dashed-dot line) Theoretical curve corresponding to the diffusion-controlled model proposed by Lucassen van der Tempel (Eq. 5.5). (Dashed line) Theoretical curve corresponding to an insoluble monolayer with a kinetic process characterizes by Eq. 5.6. For the sake of comparison, in correspondence of the characteristic frequencies of the diffusion transfer, ω_D and of the surface kinetic process ω_k, ε has an inflection point and ωκ a maximum.

As a final remark, the present approach has been developed and applied so far to soluble and insoluble surfactant systems. One requirement for its application is that the system has linear behaviour. This fact is usually true for surfactant-

adsorbed layer and in general for interfacial layer not far from the equilibrium. We thus have used the model proposed by Ravera et al.[19] for modelling the rheological behaviour showed by the mixed surfactant-nanoparticle systems.

3. Materials and Methods

3.1 Chemicals

We used a commercial colloidal silica dispersion *Levasil 200/30* kindly supplied by (H. C. Stark-Bayern). *Levasil* is a colloidal dispersion at 30.38 wt. % of spherical silica nanoparticles, free from stabilizing additives and then more suitable as a model dispersion. In fact, the dispersion has pH 9.2 due to negatively charged nanoparticles. These are characterized by a specific *BET* area of 200 m^2/g.

Dynamic light scattering experiments were performed to characterize the size and polydispersity of the nanoparticles in water using an ALV (CGS-8) apparatus, working is pseudocross-correlation mode with an argon ion laser (λ=514.5*nm*). In dynamic light scattering, the temporal decay of the scattered intensity due to refractive index (n) fluctuation is measured as a function of the scattering angle θ between the incident and the scattered radiation. The scattering vector q is defined as $q = 4\pi n\lambda^{-1}\sin(\theta/2)$. From The normalized second-order correlation function were analyzed using inverse Laplace algorithms. From this analysis, we have calculated a hydrodynamic radius R_h, by means of the Stokes-Einstein relation, $R_h = kT/6\pi\eta D = 15\pm2nm$ (where kT is the thermal energy, η is the viscosity of the solvent, i.e., water and D is the diffusion coefficient).[25] We have measured the ζ-potential (Zeta Nanosizer, Malvern Instruments, USA) of our colloidal silica dispersion obtaining $\zeta = -42\pm1mV$, which corroborates that the particles are negatively charged.

Scheme 5.1. Chemical structure of the (a) hexadecyl trimethylammonium bromide CTAB and (b) dodecyl trimethylammonium bromide DTAB

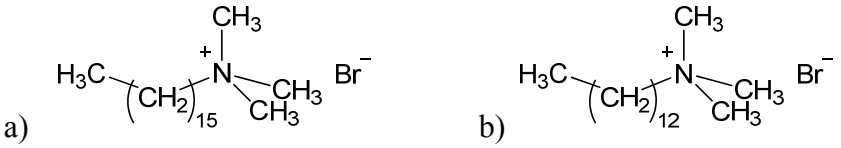

We have used two cationic surfactants, hexadecyl trimethylammonium bromide, CTAB (M_w = 346.46 g/mol) and dodecyl trimethylammonium bromide DTAB (M_w = 308.35 g/mol), both purchased from Sigma–Aldrich, with a purity ≥ 99%, and utilized without further purification. The double distilled and deionized water used in this work was produced by a MilliQ-RG system from Millipore,

having a resistivity higher than $18m\Omega \cdot cm^{-1}$ and a surface tension of $\gamma = 72.6 mN/m$ at 20ºC. As usual for studies involving ionic surfactants, salt was added to the surfactant solutions to promote its adsorption. Hence, for all the experiments addressed here, surfactant solutions always include $1mM$ of NaCl, purcharsed from Sigma-Aldrich, which has been roasted at 600ºC for 24 h before used in order to eliminate any surfactant impurity. The purity grade of the salt aqueous solution was checked by measuring the surface tension γ over a long time. A stable value of $\gamma = 72.5 \pm 0.2\ mN/m$ was found at 20ºC.

Furthermore, to avoid any particle aggregation during the dispersion preparation, the original Levasil dispersion was diluted to 1 wt. % by adding drop-by-drop the surfactant solution, while applying a continuous stirring, according to previous studies addressed by Ravera et al.[13]

3.2 Methods

We have carried out dynamic surface tension measurements of the nanocomposite complex studied using a drop shape tensiometer. This technique can be applied to study air-water interfaces. For our measurements, a pendant drop of the aqueous dispersion is formed at the tip of a Teflon capillary tube. Thus, the aging of the interface can be accurately characterized by measuring the dynamical interfacial tension of a drop with constant interfacial area.

To evaluate the dilational viscoelasticity behaviour of the nanocomposite interfacial layers, we used three different techniques covering a broad range of frequencies. The Drop profile analysis tensiometer (*PAT-1* from Sinterface, Germany) allows for the measurement of the dilational rheology by analyzing the interfacial tension response to controlled harmonic perturbations of the interfacial area in the range of frequencies from 0.01 to $0.2Hz$.[15] The Capillary pressure tensiometer (*CPT*) allows one to measure the dilational rheology by means of the fast oscillating drop-technique in the range from 0.5 to $100Hz$.[16] Finally, at high-frequencies can be explored by the excitation of electrocapillary waves (*ECW*) at the interfacial fluid layer covering the frequency range from $25Hz$ to $1.5kHz$. Finally, we have used an imaging ellipsometer (EP^3-Nanofilm, Germany) with a single wavelength of 532 nm to obtain information about the mixed nanocomposite system organization in the interfacial region. The aqueous dispersions were placed in a quartz dish (diameter: 10 *cm*, depth=5*cm*) and the laser beam was directed at the surface in the middle of the cell where the meniscus effect is negligible. We adopted a multiple angle of incidence and 4-zone averaging nulling scheme. Brewster angle microscopy was also performed in the same set up. By this method, one can obtain information about the organization of particles in the interface plane. Thus, we have demonstrated the non-existence of

nanoparticles aggregates on the air-water interface with dimensions bigger than 1μm. All the experiments performed in this chapter have been conducted at room temperature: 20±1 ºC. The details of each experimental method are given in the Appendix 1 (Methods summary).

4. Results and Discussion

In this section, we address a set of experimental results in an attempt to elucidate the relation between the interfacial structure of the nanocomposite mixed layers formed by silica particles and cationic surfactants (CTAB and DTAB) and their dilational rheology. It is well known that the macroscopic mechanical behaviour of these interfacial systems could be strongly affected by the organization and structure of the particles attached to the interface.[13]

4.1 Organization of particle–surfactant nanocomposites at the air-water interface: Effects of surfactant concentration

4.1.1 Interfacial tension measurements of adsorbed layers

The surface of the silica nanoparticles negatively charged can be modified by the adsorption of cationic surfactants, such as CTAB and DTAB. The main purpose of the Silica surface modification is to achieve an appropriate hydrophobicity to facilitate the attachment of the silica nanoparticles at the air-water interface. Non-chemically modified silica particles have a strong hydrophilic character. The surface tension of their dispersions is independent of the particle concentration, and no appreciable particle adsorption at the air-water interfaces take place.[13] On the other side, it is well known that CTAB and DTAB cationic surfactants adsorb at air-water interface very fast. The equilibrium surface tension γ as a function of the surfactant concentration is shown in Figure 5.3. Here, continuous lines represent the fits obtained with the Frumkin equation of state. [26] According to this model the relation between the surface tension γ, the bulk surfactant concentration *C* and the surface coverage θ (=Γ/Γ$_\infty$) is given by:

$$c = a\frac{\theta}{1-\theta}e^{2h\theta}$$
$$\gamma = \gamma_0 + RT\Gamma^{\infty}\left[\ln(1-\theta) - h\theta^2\right] \qquad (5.7)$$

Here, *h* is the Frumkin interaction parameter, Γ$_\infty$ is the saturation adsorption and *a* is the Langmuir-Szyszkowsky constant, which accounts the surface activity of the adsorbing species. These characteristic parameters from the fit of the measured surface tension of both surfactants in terms of Frumkin equation of state are addressed in Table 5.1. It is should be noted that the characteristic parameters

obtained are in further agreement with other previously appeared in the literature for similar systems.[27, 28]

Table 5.1. Parameters from the Frumkin equation of state corresponding of each surfactant

Surfactant	$1 / \Gamma_\infty$ (nm^2 / mol)	*a* (mM)	*h/RT*
CTAB	0.439	0.66	1.85
DTAB	0.468	8.35	*1.40*

The dilational viscoelastic parameters as well as the ellipsometric results have been obtained below the break point of the curves, which accounts the *cmc* of the surfactants. (CTAB $cmc=9.2\times10^{-4}M$ and DTAB $cmc=1.3\times10^{-2}M$). The values obtained of the *cmc* of both surfactant correlate well with values previously reported by other authors.[28]

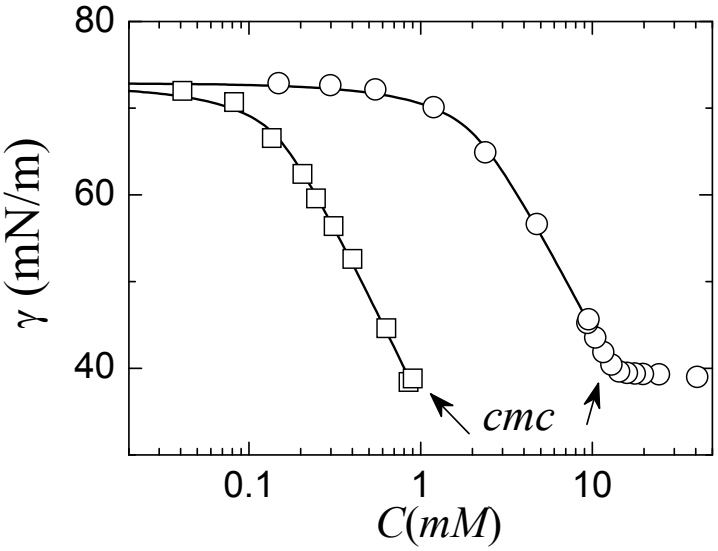

Figure 5.3. Equilibrium interfacial tension as a function of the surfactant concentration; symbols as follows: CTAB (□) and DTAB (○). Solid lines represent the fits with the Frumkin equation of state with the parameters addressed in Table 5.1. The break points of both curves indicate respectively the *cmc* of the surfactants.

To evaluate the effect of surfactant on the transfer of silica nanoparticles into the liquid-air interface, we have measured the dynamic surface tension during the aging of fresh 1 wt % dispersion-air interfaces for different surfactant concentrations. This allows for evaluating the existence of different states of the silica surface due to the different adsorption degrees. The dispersions here investigated were composed by 1 wt % of silica nanoparticles in surfactant solutions at concentrations below their respective *cmc*.

To evaluate the depletion of the surfactant solution due to surfactant adsorption into the nanoparticle surface, previous results obtained by Ravera et al.[13], based on the centrifugation of the dispersions, have been considered. From

these results it follows that, for the here considered surfactant concentrations and for nanoparticle concentration larger than 0.4 wt %, the surfactant is nearly completely removed form the bulk aqueous phase. Thus, for the here investigated compositions, there is no free surfactant available in the bulk, and the decrease of the interfacial tension can be completely attributed to the attachment of nanoparticles at the air-water interface.

Within this perspective, Figure 5.4 shows the time evolution of the dynamic surface tension γ of the composite nanoparticle-surfactant systems for a range of surfactant concentrations studied. The time behaviour of γ is similar for all the concentrations of surfactant. It could be considered as reproducible for all the samples in its main features. Thus, in general for both surfactants CTAB and DTAB the time evolution of γ can be related to the existence of a long-time relaxation process ($\geq 10^3$s).

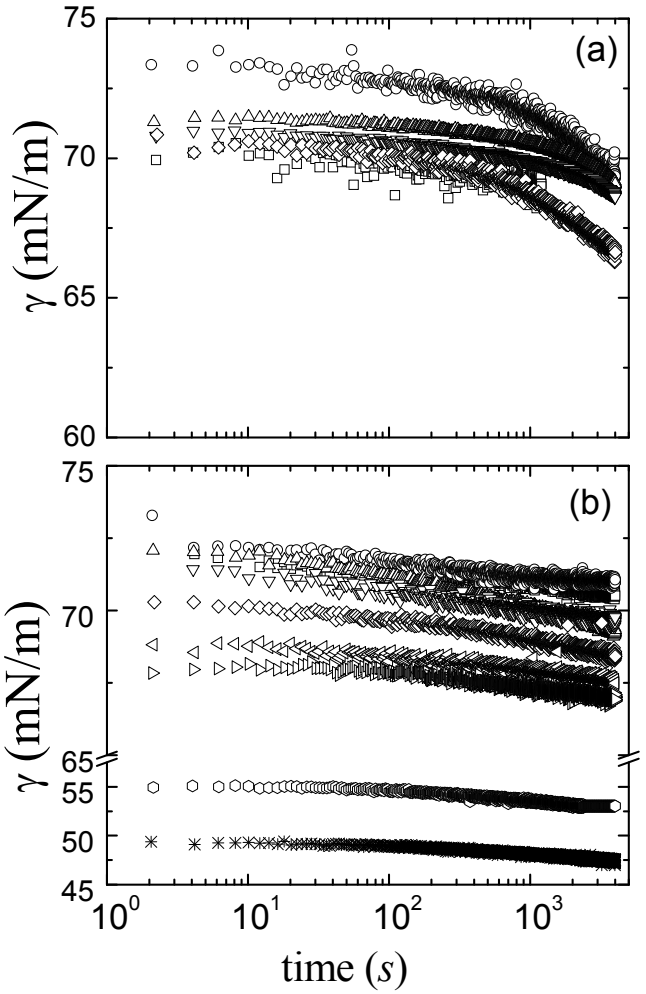

Figure 5.4. Dynamic surface tension as a function of time corresponding to the equilibration of freshly formed 1 wt % silica nanoparticles aqueous dispersion-air interface and using different surfactants concentrations. (a) CTAB: (□) $5\times10^{-5}M$; (○)$10^{-4}M$; (△) $2\times10^{-4}M$; (▽) $5\times10^{-4}M$ and (◇) $8\times10^{-4}M$. (b) DTAB: (□) $10^{-5}M$; (○) $5\times10^{-5}M$; (△)$10^{-4}M$; (▽) $2\times10^{-4}M$; (◇) $5\times10^{-4}M$; (◁) $8\times10^{-4}M$; (▷) $10^{-3}M$; (◇) $5\times10^{-3}M$ and (✳) $10^{-2}M$.

The simplest adsorption mechanism assumes that all the existing surfactant molecules are adsorbed at the SiO_2 surface. Indeed, the decrease of γ would be associated to the adsorption of the partly hydrophobized particles to the air-liquid interface. However, other related processes, such as the rearrangement of the adsorbed particles, and/or the reorganization of the surfactant adsorbed on the nanoparticles surface. A preliminary test of this assumption is to compare the characteristic diffusion coefficient of a nanoparticle in the bulk towards the surface over a characteristic length *d* larger than its size ($d >> R$ = 15nm). Within this perspective, the self-diffusion coefficient D_{SE} of a sphere of radius *R*, can be calculated by the Stokes-Einstein relationship obtaining $D_{SE} = kT/6\pi\eta R = 1.6\times10^{-11}$ m^2/s.

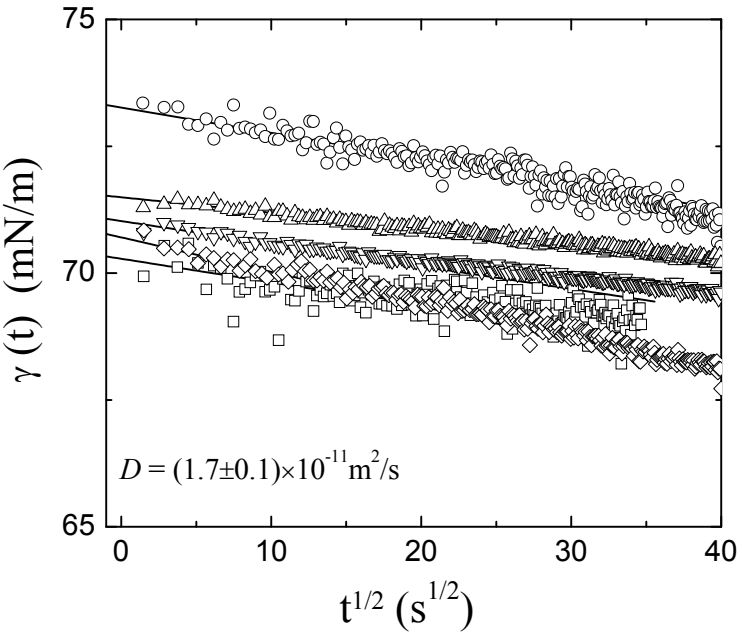

Figure 5.5. Analysis of the Dynamic surface tension at short times by Eq. 5.8 proposed by Word and Tordai for the experimental data corresponding to the equilibration of freshly formed 1 wt % silica nanoparticles aqueous dispersion-air interface and using different surfactant concentrations of CTAB: (□) $5\times10^{-5}M$; (○)$10^{-4}M$; (△) $2\times10^{-4}M$; (▽) $5\times10^{-4}M$ and (◇) $8\times10^{-4}M$.

We can obtain an experimental value of *D* evaluating the dynamical surface tension curves addressed in Figure 5.4 in terms of the *Ward* and *Tordai* equation at the short-time regime ($t \to 0$).[29, 30] This is based in the assumption that at short adsorption times, reorganization process of the molecules is not taken into account in the dynamic surface tension of complex systems adsorbed at the interface from the bulk. In this situation, *Word* and *Tordai* propose the following relationship for the dynamical surface tension γ:

$$\gamma(t) = \gamma_0 - 4RTc\left(\frac{Dt}{\pi}\right)^{1/2};\ t \to 0 \qquad (5.8)$$

where γ_0 is the solvent surface tension and D is the diffusion coefficient at short times. For instance, let us evaluate the dynamic surface tension of the SiO_2-CTAB complex in terms of the Equation 5.8 as it is shown in Figure 5.5. We have obtained a reproducible value of the diffusion coefficient $D = (1.7\pm0.1)\times10^{-11}$ m^2/s at different surfactant concentrations, which is in further agreement with the theoretical D_{SE} for the diffusion of a single nanoparticle. This fact means that the diffusion of nanoparticle-surfactant complex from the bulk to the interface does not depend on the surfactant concentration. Indeed, the equilibration process of the interfacial systems appears more complicated because depends not only on the diffusion of the nanocomposite complex to the interface but also, on the exchange of surfactant molecules attached to the particle surface and in the particle-particle interactions.[13]

As a remark, the diffusion of nanoparticles from the bulk to the fluid interface does not imply necessarily a further change in the interfacial tension and neither does the reorganization of surfactant molecules adsorbed on the silica surface. Within the hypothesis that the surfactant is initially totally adsorbed onto the silica surface, the mechanism responsible of the surface tension slight decrease at long time scales ($t > 10^3$s) could be the result of the rearrangement of the composite interfacial layer with a possible redistribution of the surfactant between the particle surface and the air-fluid interface. It is expected from the time dependence of the interfacial tension γ shown in Figure 5.4 that the higher the surfactant concentration, the faster is the surface tension decrease and the lower is the final surface tension value. For a fixed particle content, increasing the surfactant concentration leads to an increase of the surface coverage of silica particle, and as a consequence, not only exist the electrostatic attraction between the cationic surfactant and the SiO^- groups on the surface, but also, hydrophobic interactions between the nonpolar chains of the surfactants becomes more important. Hence, the weak decrease of the equilibrium interfacial tension can be due to the adsorption of additional surfactant molecules oriented preferentially with their head group away from the particle surface by hydrophobic interaction, making the complexes more hydrophilic and thus less surface active. To summarize, Particles could start to interact above a certain coverage degree of the interfacial layer. In this situation, the surface tension behaviour of the interfacial complex depends not only on the surfactant adsorption-desorption at the fluid interface, but also, on the particle-particle and particle-surfactant interactions.

To test the above assumptions, we define the surface status of the silica particles by means of the adsorption of surfactant on particle surface (Γ_s) estimated according to:[13]

$$\Gamma_s = \frac{C_{surf}}{a_s \chi_{pw} \rho} \tag{5.9}$$

where C_{surf} is the total surfactant concentration in the dispersion studied, χ_{pw} is the weight fraction particles (0.01 for the present work), ρ is the density of the dispersion and a_s is the specific silica surface area ($200 m^2/g$) given by the BET value provided by the producer for the *Levasil* 200/30. We plot in Figure 5.6 the values of the equilibrium interfacial tension as a function of the corresponding calculated values of Γ_s. For both surfactants, Γ_s has been found to be lower than the saturation values for the silica surface.[31, 32] This fact confirms that the particles are covered by unsaturated surfactant monolayers, with polar heads on the particle surface and hydrophobic tails toward the water phase. The decrease of γ at higher Γ_s's shown by the nanoparticle-DTAB mixed system can be due to a higher amount of surfactant adsorbed at the particle surface.

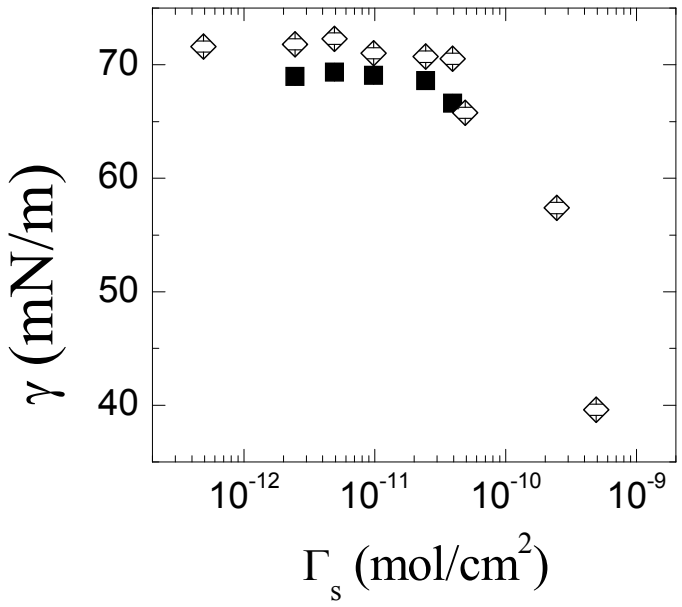

Figure 5.6. Interfacial tension for silica nanoparticle-surfactant mixed interfacial layer as a function of the adsorption of surfactant on the silica particle. Symbols as follows: CTAB: (■) and DTAB: (◇).

4.1.2 Ellipsometry of nanoparticle-surfactant networks at air-water interface

In this part, we provide experimental evidences of the adsorption and arrangement of the nanocomposite silica particle-surfactant at the air-water interface of particle dispersions. Thus, we have performed ellipsometric measurements to get information on the layer thickness and the three-phase contact angle of the silica nanoparticles as a function of the surfactant concentration by means of a two layer model proposed by Hunter *et al*.[18]

In ellipsometry, the well known equation $r_p/r_s = tan\ \Psi\ exp(i\Delta)$ relates the ratio of the Fresnel reflection coefficients polarization with the measured ellipsometric angles Ψ and Δ as a function of the incident angle φ. Thus, it is sensitive to the dielectric profile across the interface. At fluid interfaces, the ellipsometry signal depends on several contributions: surface roughness driven by thermal fluctuations (capillary waves), presence of adsorbed species at the interface an optical anisotropy of interfacial material. Here the nanoparticles are spherical-like, so no optical anisotropy contribution is expected. In addition, the particle-surfactant mixed layers have a thickness well above the amplitude of capillary waves (<1nm) and therefore the monolayer is expected to dominate the Ellipsometry signal.

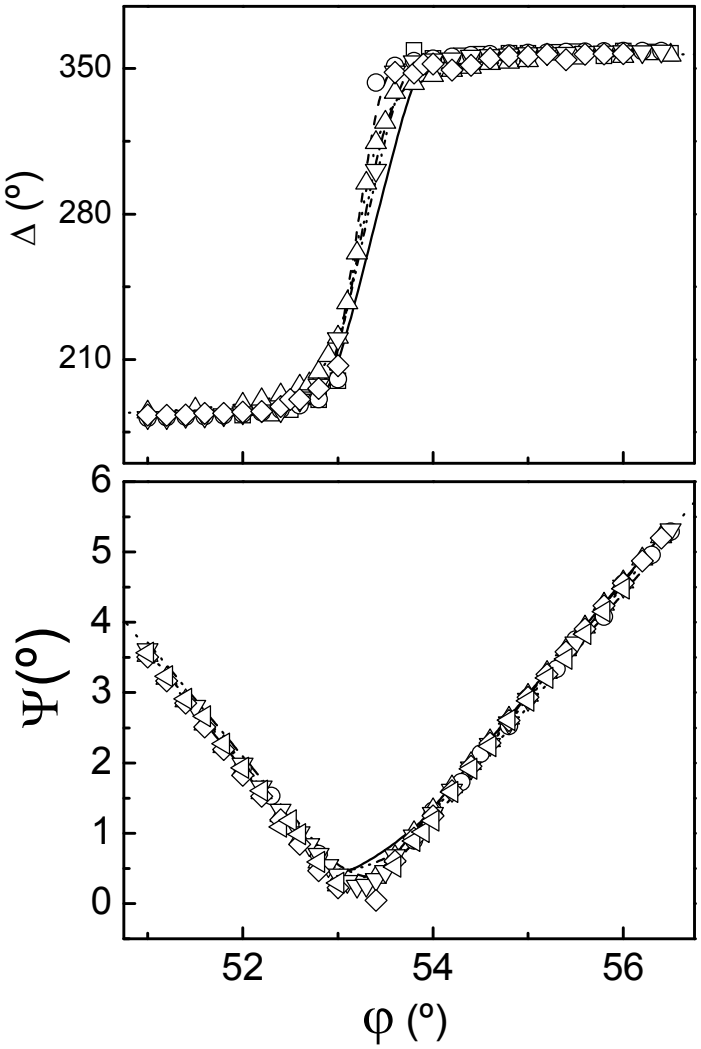

Figure 5.7. Results of ellipsometric scans performed around the Brewster angle of the nanocomposite interfacial layer formed by silica and CTAB as a function of the surfactant concentration. Symbols as follows: CTAB: (□) $5\times10^{-5}M$; (○)$10^{-4}M$; (△) $2\times10^{-4}M$; (▽) $5\times10^{-4}M$ and (◇) $8\times10^{-4}M$. Solid lines correspond to the fits to the experimental angles performed by Drude's equation.[33]

Let us first illustrate the ellipsometric scans performed to layers of the nanocomposite interfacial system as a function of the surfactant concentration around the Brewster angle [= $arctan(n_{water}/n_{air})$ = 53.12º] Concretely, Figure 5.7 shows the angular dependence of Δ and Ψ of a spread layer of silica nanoparticles (1 wt %) and different concentrations of CTAB. From these experimental values obtained, we can obtain structural information on the interfacial mixed layer.

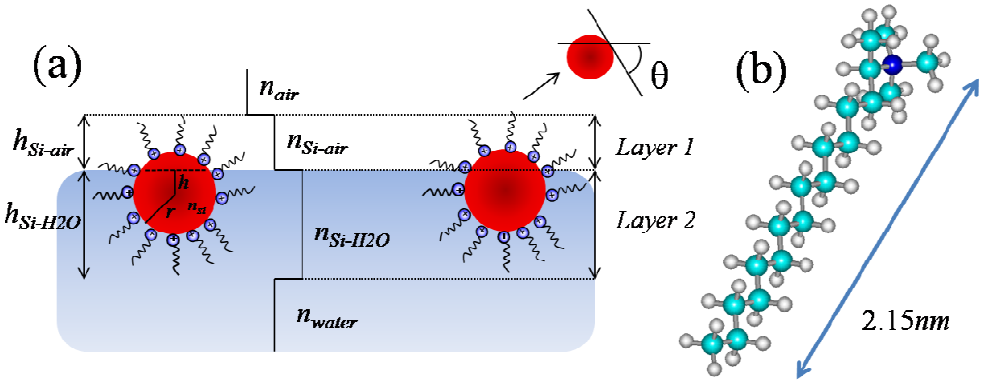

Figure 5.8. (a) Scheme of the two-layer ellipsometric model used to analyze the nanocomposite interfacial system formed by silica and CTAB. The silica spheres of radius *r* and refractive index n_{si} are attached at the air-water interface, note that surfactant molecules are adsorbed onto particles surface. *h* is the vertical distance between the centre of the sphere and the air-water interface. $h_{si\text{-}air}$ and $h_{si\text{-}H2O}$ represent the thickness of the two layers respectively; i.e., the part of the nanocomposite in air and water respectively. θ is the contact angle of the particle at the air-water interface measured into water. (b) Schematic representation of one molecule of CTAB, where it is possible to distinguish both hydrophobic chain and hydrophilic head. Its size (≈ 2.15nm) has been theoretically calculated by molecular modeling performed in *Hyperchem (Hypercube, Inc.)*.

The experimental ellipsometric data (Δ, Ψ) of the adsorbed silica-surfactant nanocomposite layer is then analyzed using a two-layer reflectance model[18, 34]. It is based on the existence of air/silica and silica/water layers, and takes into account the finite contact angle θ of the silica nanoparticles at the air-water interface as shown in Figure 5.7. Here, it is assumed that the upper layer (Layer 1) comprises a mixture of silica nanoparticles with surfactant molecules adsorbed onto their surface and air, while the lower layer (Layer 2) comprises a mixture of the nanocomposite silica-surfactant and water. It is also taken into account that Layers 1 and 2 behave as distinct homogeneous reflectance layers and then any influence of particle light scattering is ignored. This assumption has been previously found to be valid for nanoparticle layers.[35] Indeed, $h_{si\text{-}air}$ and $n_{si\text{-}air}$ are the thickness and the complex refractive index of the upper silica-air layer, and $h_{si\text{-}H2O}$ and $n_{si\text{-}H2O}$ are the thickness and the complex refractive index of the lower silica-water layer. The complex refractive index of each layer is composed by the real refractive index and the imaginary extinction coefficient ($n = n - ik$). The

sketch in Figure 5.8, shows a clear relation between the particle contact angle θ and the upper layer thickness ($h_{si\text{-}air}$) by means of the following equation[18]:

$$\cos\theta = 1 - \frac{2h_{Si-Air}}{d} \qquad (5.10)$$

where $d = h_{si\text{-}air} + h_{si\text{-}H2O}$, and therefore, it has been found that $h_{si\text{-}air}$ governs the wettability of the silica nanocomposite at the air-water interface. To get reliable values of the two layers thickness, as well as the phase contact angle, the ideal response is modelled by means of the effective medium approximation (EMA).[36] Here, the real refractive index of air (n_a=1.0) and water (n_w=1.337) are known,[37] while the refractive index of the silica nanoparticles was taken to be n_{si}=1.46.[18] This allows to calculate the effective real refractive index of each two mixed layer ($n_{si\text{-}air}$ and $n_{si\text{-}\ H2O}$) assuming that the extinction coefficient of each pure substance was assumed to be zero. Within this framework, silica particles are assumed to form a hexagonal close-packed layer at the interface characterized by the following parameters: r is the silica sphere radius (15nm), h accounts the distance from the centre of the particle to the air-water interface (we adopted the convention $h > 0$ for $\theta \leq 90^{\circ}$ and $h < 0$ for $\theta > 90^{\circ}$) and ϕ is the surface coverage of particles in the interfacial layer (= total particle cross-sectional area/ total area).[17] Therefore, Layer 1 is characterized by a thickness $r - h$ and the second one by a thickness $r + h$. Since the interfacial layers have spherical particles, it is useful to use the Maxwell-Garnett EMA[36], which consider that the nanocomposite system is a dispersed spherical component (B) completely surrounded by a host component (A). Here, the dielectric constant ε_1 of a heterogeneous layer can be obtained by the relation:

$$\varepsilon_1 = \varepsilon_A \frac{\varepsilon_B(1+2f_B) - \varepsilon_A(2f_B - 2)}{\varepsilon_A(2+2f_B) - \varepsilon_B(1+f_B)}, \qquad (5.11)$$

where f_A and f_B are the volume fractions ($f_A + f_B = 1$). The equation 5.10 is then applied for each of the two layers previously described. The mixture silica nanoparticle-surfactant is component B in all the cases while, for the first layer, component A is air and $f_B = \phi\ V_{sa}/V_{ca}$ and for the second one, A is water and $f_B = \phi\ V_{sw}/V_{cw}$. In this approach, V_{sa} ($=\pi[2/3r^3 - (r^2h - h^3/3)]$) and V_{sw} ($=\pi[2/3r^3 + (r^2h - h^3/3)]$) are the portions of volume occupied by a silica sphere in air and water respectively (see Figure 5.7) and V_{ca} ($=\pi r^2\,[r - h]$), V_{cw} ($=\pi r^2\,[r + h]$) accounting the volume of the corresponding cylinders of base πr^2 (= particle cross section).[17, 35] The refractive index n ($=\sqrt{\varepsilon}$) for the two layers proposed can be calculated from Eq. 5.11 and then, it is possible to obtain their thickness, and the phase contact angle of the silica nanoparticles θ. This two-layer model used to analyze the ellipsometric scans, has been implemented in a non-linear minimization method

(*Simplex*)[38, 39] that allows to fit the ellipticity parameter (r_p/r_s) obtained for each angle using the Drude's formalism.[33]

Figure 5.9 shows the ellipsometric thickness obtained by means of the two-layer model[17, 18] for the silica-surfactant nanocomposite layers at the air-water interface. The averaged values of the thickness for the layer 1 ($h_{si\text{-}air}$) and the layer 2 ($h_{si\text{-}H2O}$) have been plotted as a function of the surfactant concentration. The same quantity of nanoparticles have been used in all the experiments performed (1 wt%), which allows to understand the behaviour of the surfactant molecules in the interfacial layer. Thus, similar qualitative trends have been found for the two different surfactants studied (CTAB and DTAB) which only differ in the length of the hydrocarbon tail. For both systems, $h_{si\text{-}air}$ increase as the surfactant concentration increases, reaching the maximum value at $10^{-4}M$. Above this value, the thickness of the layer 1 decreases as the surface concentration increases, approaching to its *cmc*. However, as expected, the thickness of the second layer ($h_{si\text{-}H2O}$) has the opposite behaviour (see Figure 5.9). From a quantitative point of view, similar results have been found for these surfactants ruling out any effect of the chain length on the attachment and organization of nanoparticles at the air-water interface. Contrarily, we highlight that surfactant concentration plays a key role in the particle-network at the air-water interface as shown Figure 5.9.

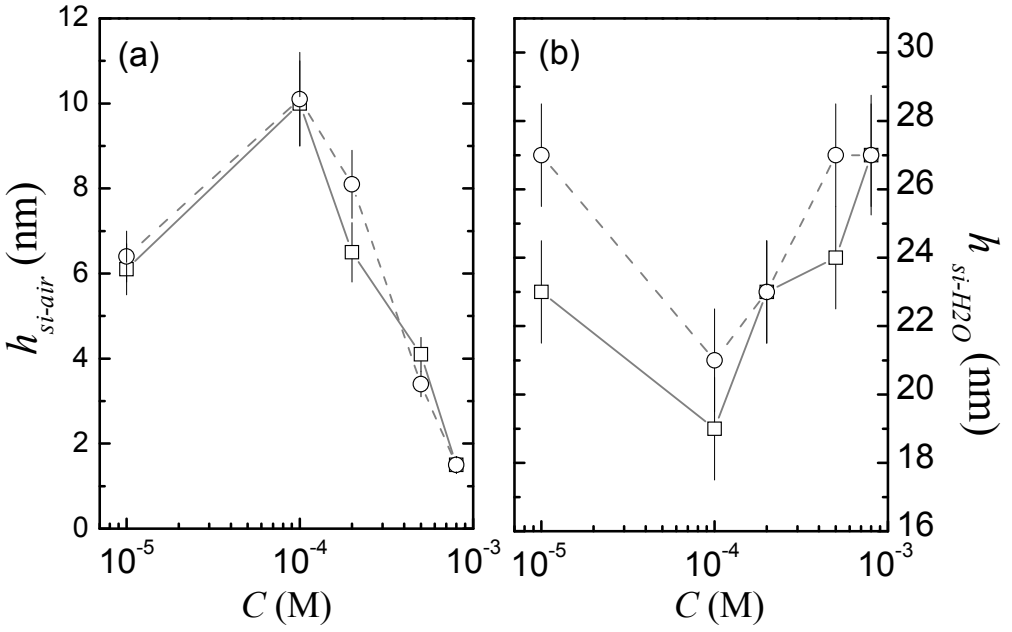

Figure 5.9. Averaged ellipsometric thickness obtained by means of the two layer model, for the silica-surfactant nanocomposite at the air-water interface as a function of the surfactant concentration, symbols as follows: CTAB (□) and DTAB (○). In (a), it is represented the thickness of the silica- air layer ($h_{si\text{-}air}$) while in (b), it is represented the thickness of the silica-water layer ($h_{si\text{-}H2O}$).

The existence of an increased amount of surfactant molecules adsorbed at the surface particle leads to a change in the wettability of the particle, turning them more hydrophobic. Then, an increase on the $h_{si\text{-}air}$ is expected at larger surfactant concentration. Despite of this fact, we have found lower $h_{si\text{-}air}$ at concentrations above 10^{-4}M. This fact can be explained by the existence of hydrophobic interactions between surfactants attached to the particle surface, which start to be important at higher surfactant concentrations. Then, this situation promotes the existence of a thinner thickness, or in other words, the change of the particle's position at the interface after becoming more hydrophilic.

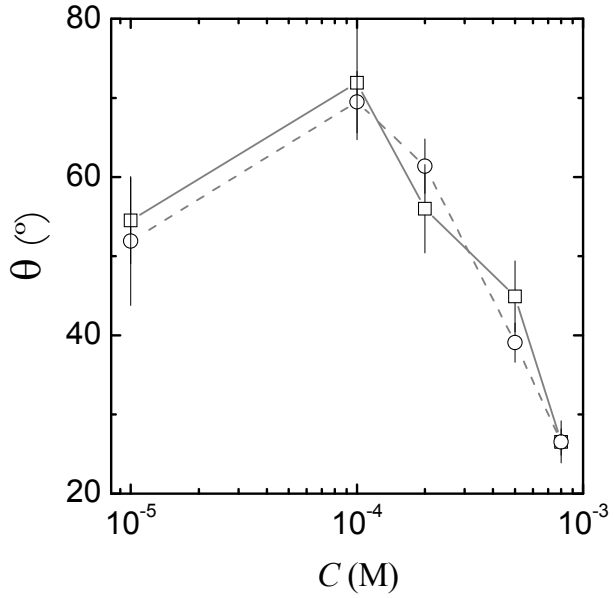

Figure 5.10. Contact angle, obtained from the analysis of the ellipsometric results by means of the two layer model proposed, for the silica-surfactant nanocomposite at the air-water interface as a function of the surfactant concentration, symbols as follows: CTAB (□) and DTAB (○).

As a conclusion of the ellipsometric thickness variation as a function of the surfactant concentration, two competition processes have been pointed out. The increase of the $h_{si\text{-}air}$ with the number of surfactant molecules interacting with the particle surface via electrostatic attraction, dominates at low concentrations. At higher C 's there is a global decrease of $h_{si\text{-}air}$ because of the competition of the previous process and the hydrophobic interaction between the non polar chains of the surfactants. Hence, Figure 5.10 shows the phase contact angle θ of the nanoparticles attached to the air-water interface as a function of the surface concentration from the analysis of the ellipsometric results in terms of the two layer model.[34] As expected from the results of figure 5.9 the values of θ for CTAB and DTAB are equal within the experimental error. This rules out the existence of chain length effect in the nanoparticle-surfactant interfacial layers.

In summary, the tendency of θ is in further agreement with the ellipsometric thickness previously showed. Thus, the nanoparticles become more

hydrophobic as the surface concentration increases until 10^{-4}M. Then, they become more hydrophilic as surface concentration approaches to the *cmc*. This complex behaviour has been found related to the existence of two kinetic processes previously commented, at low surfactant concentrations is more important the coating of the particle surface with surfactant molecules while at high concentrations, the hydrophobic interaction between surfactants attached to particle surface becomes more predominant leading to increase the hydrophilic behaviour of the nanoparticles.

As a final remark concerning to the nature of the surfactants, the ellipsometric measurements have shown that an increase of the surfactant hydrophobicity, by means of the large chain length exhibit of CTAB to DTAB, does not result in a stronger adsorption in the thick layer regions. This behaviour has been also observed by Monteux et al. for adsorbed layers of PSS with C_nTAB.[40, 41]

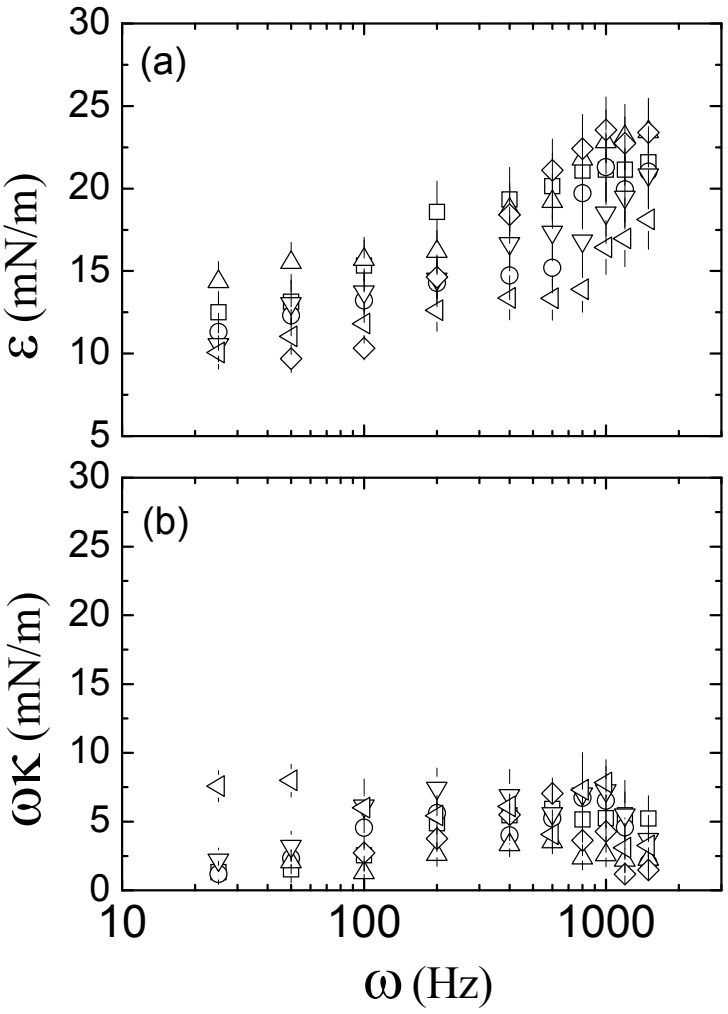

Figure 5.11. Frequency dependence of the dilational storage modulus ε (a) and loss modulus ωκ (b) of the 1 wt % silica nanoparticles aqueous dispersion-air interface using different CTAB concentrations performed by excited electrocapillary waves. Symbols as follows: (□) 10^{-5}*M;* (○) 5×10^{-5}*M;* (△) 1×10^{-4}*M;* (▽) 2×10^{-4}*M*; (◇) 5×10^{-4}*M* and (◁) 8×10^{-4}*M*.

4.2 Dilational rheology of silica-surfactant nanocomposites

In this part, we discuss the dilational rheological properties of the nanocomposite SiO_2–surfactant interfacial layer. The dilational storage modulus ε and loss one ωκ have been measured as a function of the frequency ω. These quantity are the real and the imaginary part, respectively, of the dilational viscoelasticity as defined in section 2. Different techniques have been combined to cover a broad frequency range (from 0.02Hz to 1.5kHz) to get further insight in the role of the surfactant in the organization of silica nanoparticles at the air-water interface. For our purpose, we have performed experiments at fixed 1 wt % silica dispersion varying the surfactant concentration. Preliminary experiments carried out on 1 wt % dispersions without surfactant, pointed out that null dilational viscoelastic complex module were found when the system contains the silica nanoparticles alone. This result, in accordance with the previous measurements of the interfacial tension, is a definitive proof that these nanoparticles are not adsorbed at the fluid interface unless they are modified by the presence of surfactant. In all the rheological experiments performed, we waited *ca.* 3600s in order to assure the formation of an equilibrium interfacial mixed layer according to the previous dynamical tension experiments (Figure 5.4).

4.2.1 *High-frequency dilational rheology: Excited capillary waves*

Let us first evaluate the dilational properties of the SiO_2-CTAB interfacial systems in the frequency range from 25Hz to 1.5kHz by means of the excitation of capillary waves onto the dispersion-air interface at 1wt % of silica particle concentration and different CTAB bulk concentrations. The frequency dependence of the experimental values of ε and ωκ obtained are shown in Figure 5.11. For this mixed interfacial system, it was not possible to work over 1.5kHz because of the strong decrease of the signal intensity leading to a very low sensitivity. This set of results at different CTAB concentrations shows a remarkably increases of ε with frequency, thus pointing out the existence of a dynamic relaxation process in this frequency regime. It should be noted that, under these conditions, the system uses some of the received energy for a re-organization process to return to the equilibrium state. As expected, at higher frequencies ($\omega \to \infty$) our interfacial system behaves as a pure-elastic body because the deformation is very fast and, the system does not have enough time to respond. Figure 5.11 shows that in this frequency regime the values of storage modulus are much larger than the loss ones ($\varepsilon >> \omega\kappa$), indicating that the system does not have time to dissipate energy by viscous friction. The general trend observed for ε as well as for ωκ points out the existence of a relaxation mode compatible with a re-organization and/or re-orientation process. This relaxation

process appears at times shorter than diffusion.[19, 42] Thus, it might be related to the existence of a re-organization process of the surfactants molecules at the particle's surface, which is governed by the re-distribution of the surfactant molecules between the particle's surface and the air-liquid surface.

In addition, the dynamical behaviour shown by all the SiO_2–CTAB systems are in qualitative agreement and show identical trends. From a quantitative point of view, we thus found remarkable correlation between the dilational viscoelastic parameters (ε, ωκ) and the CTAB concentration within the error limits as could be seen in Figure 5.11. It seems reasonably to attribute these noticeable differences in the dilational viscoelastic behaviour observed at this short-time domain (high frequencies) to the existence of an increased number of surfactant molecules, which leads to promote the existence of re-arrangement process in the interfacial layer. In fact, it is well known that the variation of the molecular structure of a mixed system adsorbed at the interface could influence the response to external forces of the interfacial layer.[19, 43]

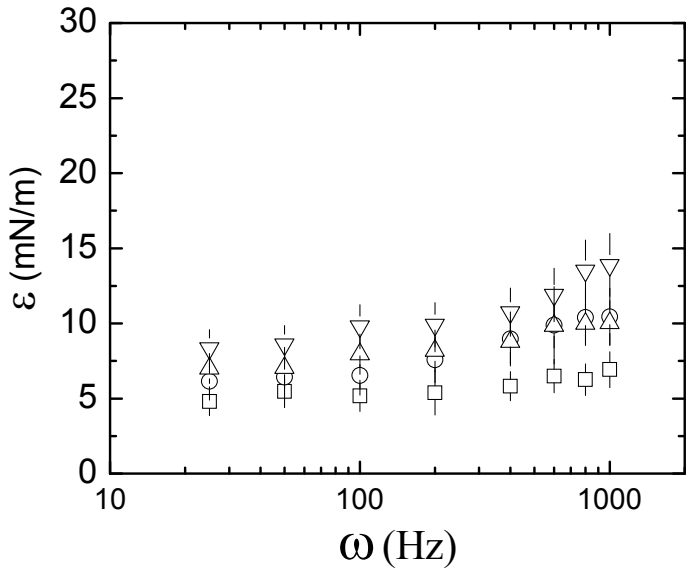

Figure 5.12. Frequency dependence of the dilational storage modulus (ε) of the CTAB aqueous solution – air interface performed by excited electrocapillary waves. Symbols as follows: (□) $10^{-5}M$; (○) $10^{-4}M$; (△) $2\times10^{-4}M$ and (▽) $8\times10^{-4}M$.

For the sake of comparison, we report in Figure 5.12 the frequency dependence of the dilational viscoelastic modulus of different CTAB solution-air interfaces. Without SiO_2 particles, the experimental values of ε of the CTAB solution-air interface are lower than those obtained for the mixed system for all the CTAB concentration. These results also point out the existence of a dynamic relaxation process in this frequency regime as in the previous nanocomposite system. Hence, one might try to describe it in terms of a kinetic process involving the surfactant molecules attached to the air-solution interface. As expected, the

noticeable differences in the values of ε can be explained by the nature of the interfacial layer in each situation.

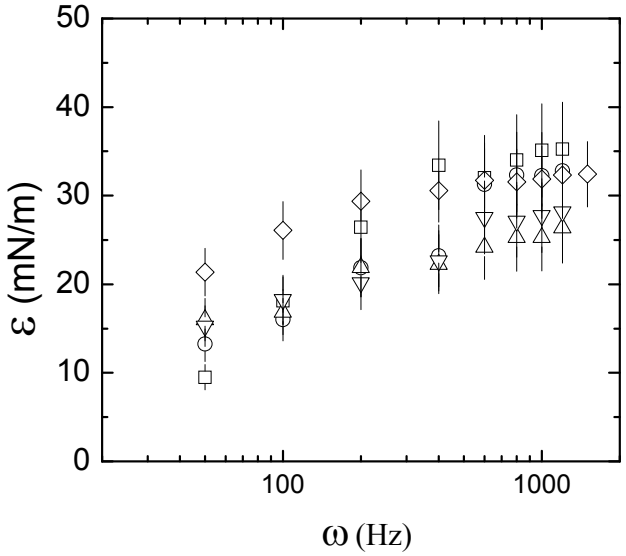

Figure 5.13. Frequency dependence of the dilational storage modulus ε (a) of the 1 wt % silica nanoparticles aqueous dispersion-air interface using different DTAB concentrations performed by excited electrocapillary waves. Symbols as follows: (□) $10^{-5}M$; (○)$1\times10^{-4}M$; (△) $5\times10^{-4}M$; (▽) $8\times10^{-4}M$ and (◇) $1\times10^{-3}M$.

To further explore the effect of the surfactant on the macroscopic rheology shown by nanocomposite interfacial systems, we have also studied the frequency dependence of the dilational elastic module ε of the SiO_2-DTAB interfacial systems at 1wt % of silica particle concentration and different DTAB bulk concentrations. The set of results obtained are plotted in Figure 5.13. Here, they are in qualitative agreement and show identical trends than the nanocomposite system formed by CTAB, highlighting the existence of a relaxation mode. From a quantitative point of view, the values of ε obtained for DTAB mixtures are appreciably larger in this frequency range than for the CTAB ones. This behaviour is surprising because it is expected that the elasticity increases with the chain length of surfactant interfacial layers. However, in our mixed systems formed by particles and surfactants molecules attached to their surface, this opposite behaviour can be attributed to the existence of a larger number of DTAB surfactants interacting with the particle surface in accordance with the previous ellipsometric results (see Figure 5.9). It can be assumed that this fact may be due to the apparition of steric impediments in the attachments of CTAB molecules with larger chain length, onto the particles surfaces. Furthermore, in SiO_2–DTAB interfacial layers, we found also a weak dependence of ε on DTAB bulk concentration, which suggest the existence of a relaxation mechanism in this short-time domain similar to the one discussed previously for CTAB nanocomposites. Therefore, it is necessary to evaluate quantitatively the dilational

viscoelasticity as a function of the frequency in a range as large as possible, and then interpreting these data by an appropriate theoretical model, which accounts the mechanism governing the interfacial layer.

4.2.2 Low – Moderate frequency regime: PAT + CPT methods

To explore further the role of the interaction between silica nanoparticles and surfactant at fluid interfaces on their macroscopic rheology, we extend our study to cover the frequency range from 5×10^{-3} to 100Hz by using two different techniques: Capillary pressure tensiometer (CPT) and drop profile analysis tensiometer (PAT). The complex dilational viscoelastic moduli of the SiO_2-CTAB interfacial system, for different surfactants concentrations are shown in Figures 5.14–5.15. The behaviour found in the range from 0.5 to 100Hz by CPT[16] indicates that there is no evidence of the existence of any relaxation process, contrary to what was found in the previous ECW experiments. Moreover, ε and ωκ show a weak dependence on the surfactant concentration except for a 10^{-4}M, where the values of elasticity are rather larger than for the other CTAB concentrations. This singular behaviour at C =10^{-4}M is related to the results previously found in the ellipsometric study (Figs. 5.9–5.10), which highlight an increase in the particle hydrophobicity and then a thicker particle interfacial network.

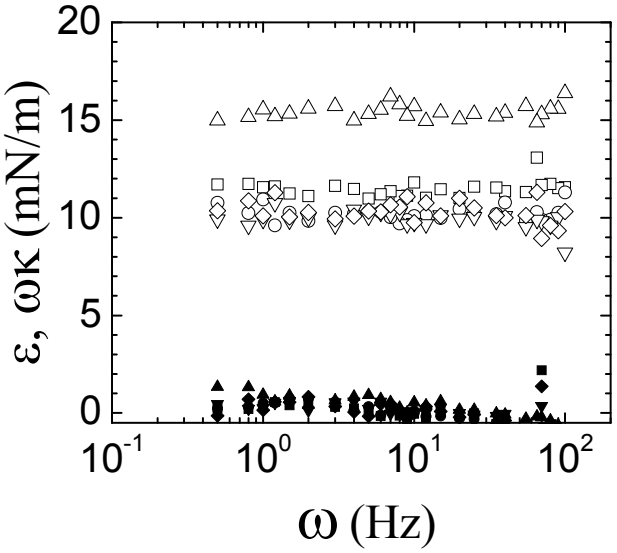

Figure 5.14. Frequency dependence of the dilational storage modulus ε and loss modulus ωκ of the 1 wt % silica nanoparticles aqueous dispersion-air interface using different CTAB concentrations measured in the capillary pressure tensiometer (CPT). Symbols as follows: (□,■) $10^{-5}M$; (○,●) $10^{-4}M$; (△,▲) $2\times10^{-4}M$ and (▽,▼) $5\times10^{-4}M$. Open symbols correspond to ε and filled ones to ωκ.

Within this frequency regime, we also found that the dilational loss modulus for each sample studied takes values close to zero (ωκ ≈ 0). This fact means that the system cannot dissipate energy by viscous friction in this frequency domain,

and the interfacial mixed layer behaves as a pure elastic body. This sets of data obtained show a good matching with the previous obtained by ECW in the overlapping frequency range. We studied the dilational parameters in the low frequency range accessible by means of the PAT technique[15]. Figure 5.15 shows the ω-dependence of ε and ωκ for each sample with different CTAB bulk concentration. In this low-frequency domain, we found remarkably similarities with the previous studies performed by both ECW and CPT at higher frequencies. Indeed, this set of results is in qualitative agreement and points out the existence of a relaxation process as the dilational elastic module, ε increase with ω. However, no strong differences have been found taking in account each CTAB concentration used. In addition, the loss modulus of each sample, which takes lower values than the storage one (ωκ << ε), shows a tendency according to the existence of a relaxation process. At this low-frequency domain ($t \rightarrow \infty$), this relaxation process can be interpreted as a diffusive process where the nanoparticle-surfactant system could be exchanged from the bulk to the air-solution interface.

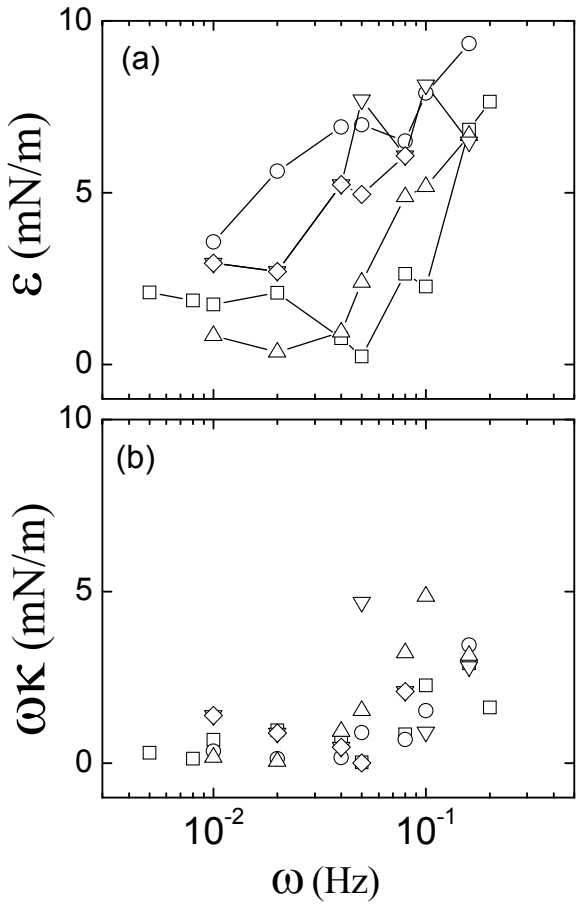

Figure 5.15. Frequency dependence of the dilational storage modulus ε (a) and loss modulus ωκ (b) of the 1 wt % silica nanoparticles aqueous dispersion-air interface using different CTAB concentrations performed by the drop profile analysis tensiometer (PAT). Symbols as follows: (□) $10^{-5}M$; (○) $5\times10^{-5}M$; (△) $1\times10^{-4}M$; (▽) $2\times10^{-4}M$; (◇) $5\times10^{-4}M$ and (◁) $8\times10^{-4}M$.

To summarize, we found different relaxation process in the broad frequency range accessible for the adsorbed interfacial mixed system studied. Indeed, it is necessary to understand this complex behaviour by means of a proper theoretical approach that will be discussed in the next section.

4.2.3 *Experimental viscoelasticity vs. frequency: extended mixed-kinetic theoretical approach*

Let us discuss now the validity of a theoretical approach to relate the dilational viscoelasticity as a function of the frequency of the SiO_2–surfactant adsorbed layer, leading to provide further insight on the dynamical behaviour of the interfacial layer. It is well known that the effect of a relaxation process on the interfacial dynamics is the appearance of a maximum in the loss modulus ωκ as a function of the frequency and an inflection point in the storage modulus ε, corresponding to the characteristic frequency of the considered relaxation process. This assumption has validity because come directly from the consideration of the relaxation phenomena as a linear kinetic process.

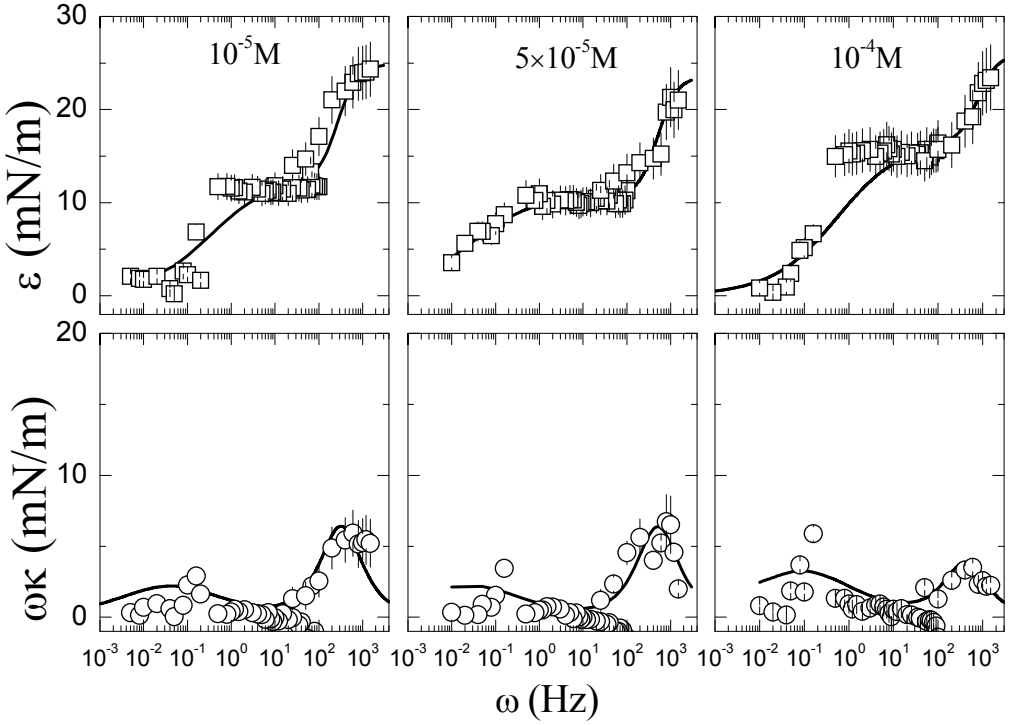

Figure 5.16. Frequency dependence of the dilational storage modulus ε (□) and loss modulus ωκ (○) of the 1 wt % silica nanoparticles aqueous dispersion-air interface using different CTAB concentrations (10^{-5}M, 5×10^{-5}M and 10^{-4}M) performed by combining techniques working in different frequency ranges: ECW, CPT and PAT. The straight lines correspond to the fit of the experimental data in terms of the model proposed by Ravera et al. (Eq. 5.4)

The results presented above can be explained by assuming the existence of two different relaxation modes in the frequency range studied as shown in Figures 5.13-5.15. To explain this behaviour, we address the frequency dependence of the

dilational viscoelastic parameters measured for the SiO_2-CTAB interfacial systems in Figures 5.16 and 5.17. For the sake of comparison, we have included different CTAB bulk concentrations (from 10^{-5} to 5×10^{-4}M), and the measurements were performed at the same experimental conditions. The set of data obtained by the three different methods used show a good matching in the overlapping frequency range for all the concentration studied, both for the real and the imaginary part.

The theoretical curves reported in Figures 5.15-16 correspond to the fit of the experimental data by means of the model proposed by Ravera et al. (Equation 5.4). As already stated, this model also predicts the time dependence of the surface tension, and allows one to obtain information about the kinetics of the relaxation process on the interfacial layer.[19] It is a diffusive control model assuming the existence of further relaxation process, like internal transformation or reorganization of the adsorbed layer, besides its diffusion. It is assumed as an extension of the Lucassen – van der Tempel approach[21], which considers the instantaneous coupling between the surface rheology and the adsorption kinetics. The presence of other relaxation process besides diffusion has the effect of changing the behaviour of ε and ωκ at the high-frequency domain as pointed out in Figures 5.16 and 5.17.

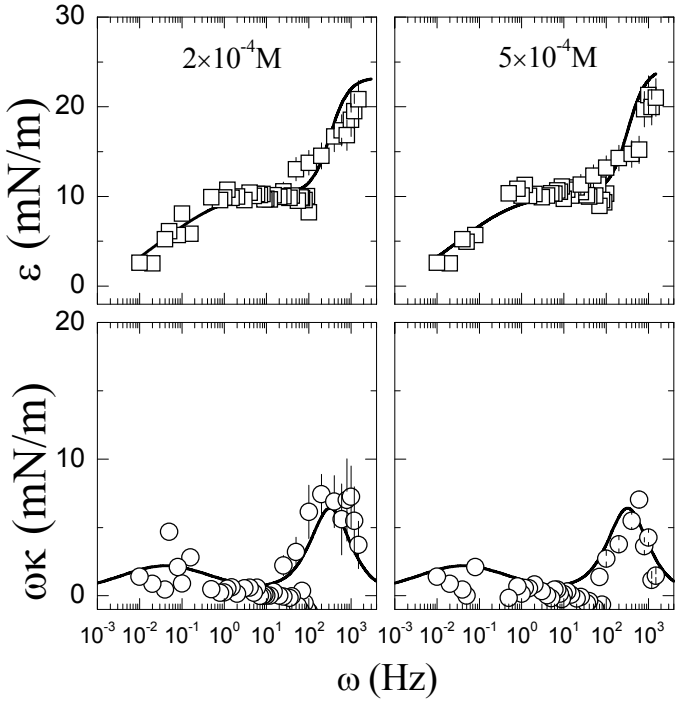

Figure 5.17. Frequency dependence of the dilational storage modulus ε (□) and loss modulus ωκ (○) of the 1 wt % silica nanoparticles aqueous dispersion-air interface using different CTAB concentrations (2×10^{-4}M and 5×10^{-4}M) performed by combining techniques working in different frequency ranges: ECW, CPT and PAT. The straight lines correspond to the fit of the experimental data in terms of the model proposed by Ravera et al. (Eq. 5.4)

Figure 5.16 and 5.17 shows that the model is able to describe quite accurately the experimental behaviour of ε and ωκ. According to this model, we found two characteristic frequencies, ω_D accounting for the diffusion transfer process and ω_k, which represents an arbitrary surface kinetic process. In the model proposed, ε_{0G} represents the frequency limit elasticity of the diffusion controlled mechanism, also known as Gibbs elasticity, while $\varepsilon_{0\Gamma}$ accounts for the high-frequency limit of the elasticity, which differs from the Gibbs elasticity. The values of these parameters for each sample studied are given in Table 5.2

Table 5.2. Parameters of the theoretical model proposed by fit the experimental rheology parameters of the interfacial nanocomposite systems formed by SiO_2 and CTAB

C (M)	*ε_{0G} ±0.5 (mN/m)*	*$\varepsilon_{0\Gamma}$ ±0.5 (mN/m)*	*ω_D ±0.025 (Hz)*	*ω_k ±0.25 (Hz)*
1×10^{5}	13.09	25.02	0.339	250.40
5×10^{5}	10.90	23.54	0.024	506.87
1×10^{4}	15.51	25.41	0.080	478.01
2×10^{4}	10.62	23.29	0.041	319.10
5×10^{4}	10.58	24.37	0.039	319.48

The characteristic times of the surface kinetic process are in the domain of the milliseconds (ms) further away of the characteristic time where the diffusion process takes place (about tens of seconds). In this time domain, the system behaves according to diffusion controlled mechanism where the characteristic times (τ_D) found are in agreement with the characteristic times of the relaxation process evidenced by the dynamic interfacial tension data shown in a previous section. These results strongly suggest that particle-surfactant diffusion is one of the processes governing the system equilibration. However, at concentrations high enough, also a surface re-organization process becomes important. The characteristic times for this process (τ_k) are in the domain of milliseconds, where the dynamic interfacial tension is difficult to be to be experimentally evaluated. From that, one might assume the existence of a kinetic process in the millisecond regime, which is in further agreement with the theoretical model previously proposed by Ravera et al. for a soluble monolayer.[19] A re-organization process in the range of ms could be due to the re-equilibration of the surfactant molecule distribution on the particle surface and the air-liquid interface. Thus, the amount of surfactant molecules plays an important role in the dynamical behaviour of the mixed interfacial system.

To explore the effect of the density of surfactant molecules in the coupling between the macroscopic surface rheology and the adsorption kinetics, we report in Figure 5.18.a the characteristic times (τ_D and τ_k) as a function of the CTAB concentration. The tendencies shown by the values of τ_D and τ_k are remarkably

different. τ_D slightly depends on the number of molecules of CTAB while τ_k does not show a strong dependence.

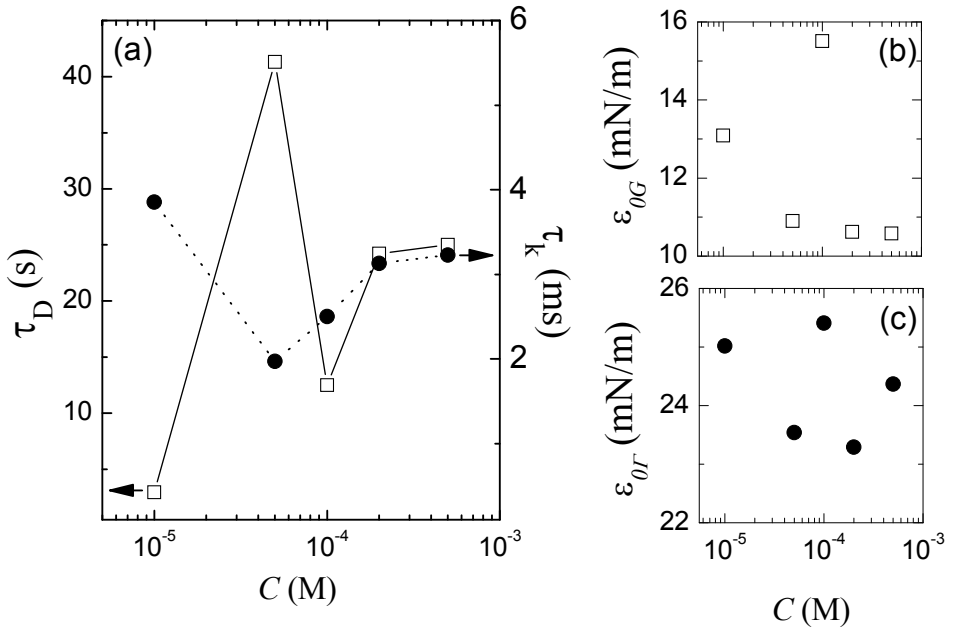

Figure 5.18. (a) Characteristic times of the diffusion process τ_D (□) and the kinetic process τ_k (●) obtained by means of the theoretical fit applied to the experimental data of the 1 wt % silica nanoparticles aqueous dispersion-air interface at different CTAB concentrations. (b) and (c) represent the respective parameters ε_{0G} ,which represent the frequency limit elasticity of the diffusion controlled mechanism and $\varepsilon_{0\Gamma}$, which accounts for the high-frequency limit of the elasticity, as a function of the CTAB concentrations.

As can be seen in Figure 5.18.a, we found that at 5×10^{-5}M, τ_D reaches its maximum value, and then decreases taking constant values at larger concentrations. A reasonable explanation is the formation in bulk of the nanocomposite mixed system driven by electrostatic interaction between the surfactant molecules and the nanoparticles. At increasing concentration, nanoparticle's hydrophobicity enhancement induced by the interaction with surfactants, promotes to their adsorption at the air-fluid interface in a flat-like configuration according to the ellipsometric thickness measured (Figure 5.9) and then the diffusion times (τ_D) increase with the surfactant concentration. However, at enough concentration, τ_D decreases because the hydrophobic interaction between surfactants, which leads to an immersion of the complex to the bulk solution. Then, the diffusion process turns faster.

The re-organization kinetic process does not show any strong dependence on the surfactant concentration as can be observed by the not stronger differences found in the values of τ_k for different concentrations. It should be noted that small differences in the values of τ_k are in accordance to the definition of a kinetic process based on the re-distribution of the surfactant molecules from the particle

surface to the interface, which only weakly depends on the surfactant concentration.

Figure 5.17.b-c shows the characteristic parameters ε_{0G} and $\varepsilon_{0\Gamma}$ as a function of the CTAB concentration. As it can be seen, both elastic moduli reach the highest values at the same surfactant concentration (10^{-4} M), thus highlighting that strongest interaction between the particles surface and the CTAB molecules occurs at this concentration. This interfacial viscoelastic behaviour is in agreement with the interfacial structure proposed by the ellipsometric thickness measured (Figure 5.9). These findings leads to connect the remarkably change in the interfacial dynamic elasticity with the structural changes in the layer associated to changes in the contact angle. The evolution of the ellipsometric signal and of the surface elasticity, is similar to that found for several interfacial mixed systems constituted by polyelectrolytes and surfactants, providing evidence of the surface microheterogeneity.[40]

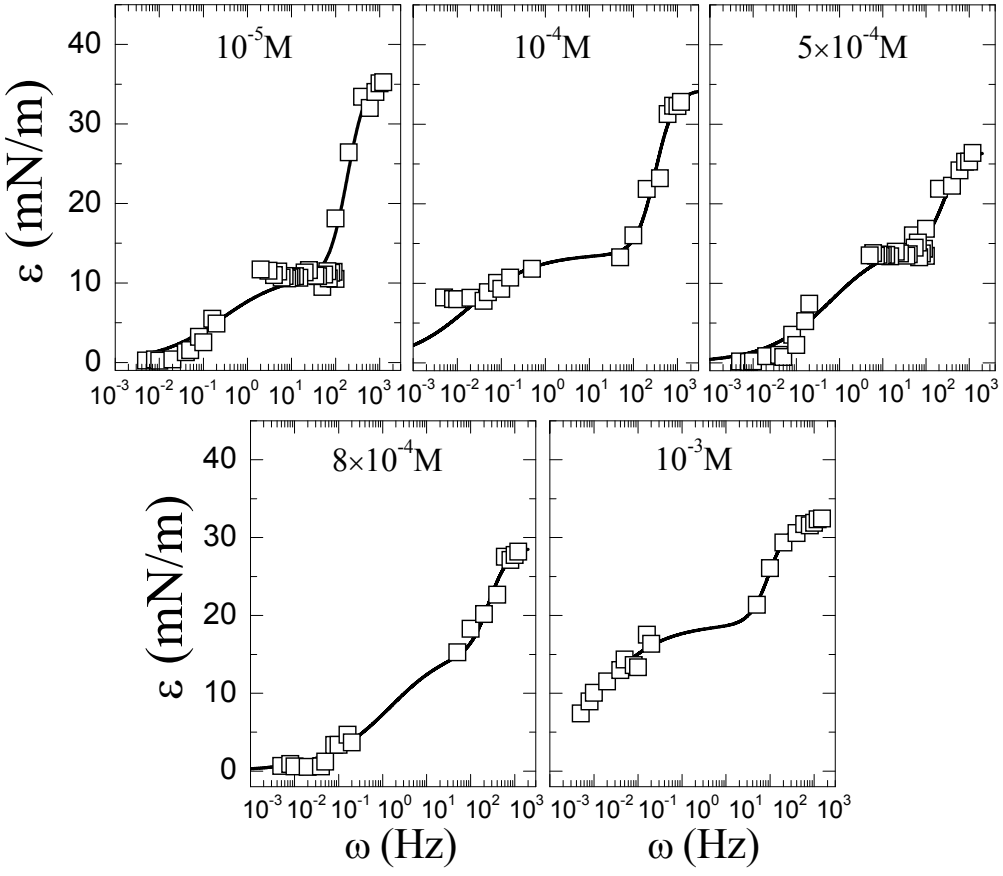

Figure 5.19. Frequency dependence of the dilational storage modulus ε (□) of the 1 wt % silica nanoparticles aqueous dispersion-air interface at different DTAB concentrations (10^{-5}M, 10^{-4}M, 5×10^{-4}M, 8×10^{-4}M and 10^{-3}M) performed by combining techniques working in different frequency ranges: ECW, CPT and PAT. The straight lines correspond to the fit of the experimental data in terms of the model proposed by Ravera et al. (Eq. 5.4)

Let us now evaluate the effect of the surfactant chain length in the theoretical description of our experimental data. We also have fitted by means of the theoretical approach proposed by Ravera et al.[19] the frequency dependence of the dilational elastic module of the SiO_2-DTAB nanocomposite systems. Again, the compatibility between the results obtained with the three different techniques is remarkable. Figure 5.19 shows that the overall quality of the fittings is similar to that found for the systems with CTAB. Here also exists a clear correlation between the experimental data and the theoretical fit.

Table 5.3. Parameters of the theoretical model proposed by fit the experimental rheology parameters of the interfacial nanocomposite systems formed by SiO_2 and DTAB

C (M)	ε_{0G} ±0.5 *(mN/m)*	$\varepsilon_{0\Gamma}$ ±0.5 *(mN/m)*	ω_D ±0.025 *(Hz)*	ω_k ±0.25 *(Hz)*
1×10^{5}	11.39	36.70	0.280	180.00
1×10^{4}	13.77	34.40	0.018	310.54
5×10^{4}	15.65	26.85	0.080	255.18
8×10^{4}	16.65	29.28	0.041	249.54
1×10^{3}	18.99	32.08	0.039	194.34

Within the perspective of the model proposed, the characteristic parameters for each sample studied are summarized in Table 5.3. The analysis leads to similar conclusions that previously discussed for CTAB.

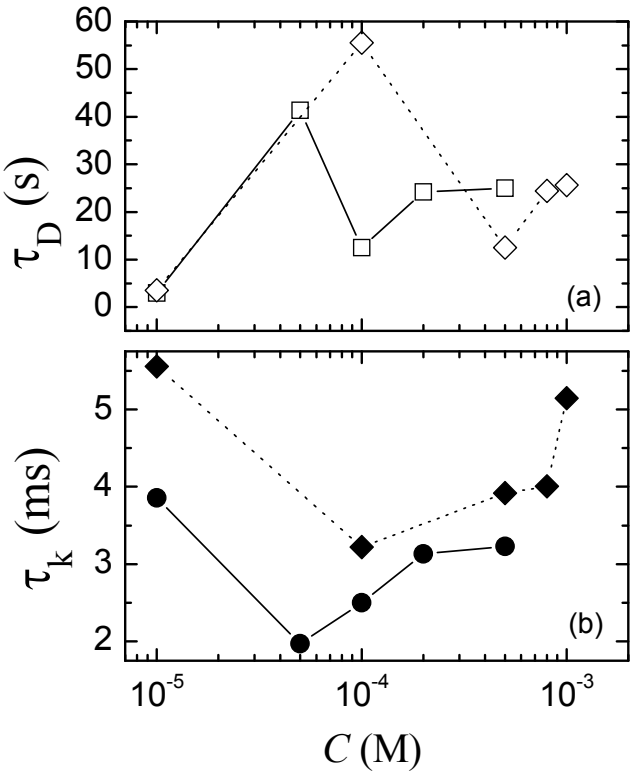

Figure 5.20. (a) Characteristic times of the diffusion process τ_D (□:CTAB; ◇:DTAB) and (b) the kinetic process τ_k (●: CTAB; ◆:DTAB) obtained by means of the theoretical fit applied to the experimental data of the 1 wt % silica nanoparticles aqueous dispersion-air interface at different surfactant concentrations.

To explore the effect of surfactant chain length in the relation between the macroscopic surface rheology and the adsorption kinetics, Figure 5.20.*a-b* shows the characteristic times (τ_D and τ_k) as a function of the surfactant concentration. From a qualitative point of view, the respective tendencies showed by the values of τ_D and τ_k are remarkably similar independently of the chain length of the surfactant within the experimental errors. However, we found that over the whole concentration range, the characteristic times for DTAB samples are slightly larger than those of CTAB. This general trend observed for the two kinetic processes can be explained taking in account that the size of the hydrophobic tails plays a key role not only in the formation of bulk complexes via hydrophobic interactions and latter adsorption to the interface but also, in the re-organization process that occurs at the interface. Hence, the larger characteristic times for DTAB could be related with lower hydrophobic interactions between nonpolar surfactant chains. Several authors have showed the effect of the surfactant chain length in the formation of interfacial systems such like polyelectrolyte-surfactant.[41, 44]

5. Conclusions

We have addressed an experimental study of the dilational rheology of the interfacial nanocomposite system constituted by silica nanoparticles interacting with cationic surfactants such as C_nTAB, with CTAB for n=16 and DTAB for n=12. It is well known that the addition of surfactants modified the intrinsic hydrophobicity of the particles and then their affinity for the fluid interfacial environment. We thus pointed out that the interaction between the particles negatively charged and the cationic surfactant molecules plays a key role in the macroscopic interfacial dynamics, which has been found in further agreement with the conformational scenario pointed out by ellipsometry measurements. Hence, we have interpreted the ellipsometric results in terms of a two layers model in order to get further insight in the plausible structure adopted by the mixed layers at the air-water interface. This model allows us to know the particle's hydrophobicity and determinate the grade of affinity for the fluid interfacial environment. To get a better understanding of the interaction of nanoparticles and the role showed by the surfactant, we have performed a study about the dilational viscoelastic behaviour of our complexes covering a broad range of frequencies by means of the combination of different experimental techniques. To this aim, we also correlate the experimental data with a theoretical approach involving various kinetic processes in the instantaneous coupling between the surface rheology and the adsorption kinetics. Indeed, besides the Brownian motion of particles in the bulk, an important role is also played by the internal reorganization of the mixed particle-surfactant system at the interface.

6. References

1. Binks, B. P.; Horozov, T. S., *Colloidal Particles at Liquid Interfaces*. Cambridge University Press: Cambridge, U.K., 2006.
2. Binks, B. P., Particles as surfactants - similarities and differences. *Current Opinion in Colloid & Interface Science* **2002,** 7, (1-2), 21-41.
3. Miller, R.; Fainerman, V. B.; Kovalchuk, V. I.; Grigoriev, D. O.; Leser, M. E.; Michel, M., Composite interfacial layers containing micro-size and nano-size particles. *Advances in Colloid and Interface Science* **2006,** 128, 17-26.
4. Aveyard, R.; Binks, B. P.; Clint, J. H., Emulsions stabilised solely by colloidal particles. *Advances in Colloid and Interface Science* **2003,** 100, 503-546.
5. Pieranski, P., Two-Dimensional Interfacial Colloidal Crystals. *physical Review Letters* **1980,** 45, 569-572.
6. Frydel, D.; Dietrich, S.; Oettel, M., Charge renormalization for effective interactions of colloids at water interfaces. *physical Review Letters* **2007,** 99, 118302
7. Tarimala, S.; Ranabothu, S.; Vernetti, J.; Dai, L., Mobility and In Situ Aggregation of Charged Microparticles at Oil−Water Interfaces. *Langmuir* **2004,** 20, 5171-5173.
8. Aveyard, R.; Clint, J. H.; Nees, D.; Paunov, V. N., Compression and structure of monolayers of charged latex particles at air/water and octane/water interfaces. *Langmuir* **2000,** 16, (4), 1969-1979.
9. Chen, W.; Tan, S.; Ng, T.-K.; Ford, W. T.; Tong, P., Long-Ranged Attraction between Charged Polystyrene Spheres at Aqueous Interfaces. *physical Review Letters* **2005,** 95, (21).
10. Paunov, V. N.; Binks, B. P.; Ashby, N. P., Adsorption of charged colloid particles to charged liquid surfaces. *Langmuir* **2002,** 18, (18), 6946-6955.
11. Fainerman, V. B.; Kovalchuk, V. I.; Lucassen-Reynders, E. H.; Grigoriev, D. O.; Ferri, J. K.; Leser, M. E.; Michel, M.; Miller, R.; Mohwald, H., Surface-pressure isotherms of monolayers formed by microsize and nanosize particles. *Langmuir* **2006,** 22, (4), 1701-1705.
12. Aveyard, R.; Binks, B. P.; Fletcher, P. D. I.; Rutherford, C. E., Measurement of contact angles of spherical monodisperse particles with surfactant solutions. *Colloids and Surfaces A* **1994,** 83, (1), 89-98.

13. Ravera, F.; Santini, E.; Loglio, G.; Ferrari, M.; Liggieri, L., Effect of nanoparticles on the interfacial properties of liquid/liquid and liquid/air surface layers. *Journal of Physical Chemistry B* **2006,** 110, (39), 19543-19551.

14. Lucassen, J., Capillary forces between solid particles in fluid interfaces. *Colloids and Surfaces.* **1992,** 65, (2-3), 131-137.

15. Loglio, G.; Pandolfini, P.; Miller, R.; Makievski, A.; Ravera, F.; Ferrari, M.; Liggieri, L., In *Studies in Interface Science Series*, Mobius, D.; Miller, R., Eds. Elsevier: 2002; Vol. 11.

16. Liggieri, L.; Attolini, V.; Ferrari, M.; Ravera, F., Measurement of the surface dilational viscoelasticity of adsorbed layers with a capillary pressure tensiometer. *Journal of Colloid and Interface Science* **2002,** 255, (2), 225-235.

17. Zang, D. Y.; Stocco, A.; Langevin, D.; Wei, B. B.; Binks, B. P., An ellipsometry study of silica nanoparticle layers at the water surface. *Physical Chemistry Chemical Physics* **2009,** 11, (41), 9522-9529.

18. Hunter, N. T.; Jameson, J. G., Adsorption of Submicrometer-Sized Cationic Sterically Stabilized Polystyrene Latex at the Air-Water Interface: Contact Angle determination by Ellipsometry. *Langmuir* **2009,** 25, 3440-3449.

19. Ravera, F.; Ferrari, M.; Liggieri, L., Modelling of dilational visco-elasticity of adsorbed layers with multiple kinetic processes. *Colloids and Surfaces a-Physicochemical and Engineering Aspects* **2006,** 282, 210-216.

20. Miller, R.; Liggieri, L. Eds., *Interfacial Rheology*. VSP: UK, 2009.

21. Lucassen, J.; Van der Tempel, M., Dynamic measurements of dilational properties of a liquid interface. *Chemical Engineering Science* **1972,** 27, (6), 1283.

22. Miller, R.; Loglio, G.; Tesei, U., Exchange of matter at the interface between 2 liquid-phases. *Colloid and Polymer Science* **1992,** 270, (6), 598-601.

23. Fainerman, V. B.; Kovalchuk, V. I.; Aksenenko, E. V.; Michel, M.; Leser, M. E.; Miller, R., Models of two-dimensional solution assuming the internal compressibility of adsorbed molecules: A comparative analysis. *Journal of Physical Chemistry B* **2004,** 108, (36), 13700-13705.

24. Ravera, F.; Ferrari, M.; Miller, R.; Liggieri, L., Dynamic elasticity of adsorption layers in the presence of internal reorientation processes. *Journal of Physical Chemistry B* **2001,** 105, (1), 195-203.

25. Berne, B.; Pecora, R., *Dynamic light Scattering*. John Wiley: New York, 1975.

26. Prosser, A.; Franses, E., Adsorption and surface tension of ionic surfactants at the air–water interface: review and evaluation of equilibrium models. *Colloids and Surfaces A* **2001,** 178, 1.

27. Szymzyk, K.; Janezuk, B., The adsorption at solution-air interface and volumetric properties of mixtures of cationic and non-ionic surfactants. *Colloids and Surfaces A: Physicochemical and Enginnering aspects* **2007,** 293, 39-50.

28. Szymzyk, K.; Janezuk, B., A Study of the Interactions of Ternary Surfactan Systems at the Water-Air Interface. *Langmuir* **2010,** 26, 2491-2496.

29. Ward, A. F.; Tordai, L., Time-Dependence of Boundary Tensions of Solutions I. The Role of Diffusion in Time-Effects. *J Chem Phys* **1946,** 14, 453.

30. Fainerman, V. B.; Makievski, A. V.; Miller, R., The analysis of dynamic surface-tension of sodium alkyl sulfate-solutions, based on asymptotic equations of adsorption kinetic-theory. *Colloids and Surfaces A* **1994,** 87, (1), 61-75.

31. Atkin, R.; Craig, V. S. J.; Wanless, E.; Biggs, S., The influence of chain length and electrolyte on the adsorption kinetics of cationic surfactants at the silica-aqueous solution interface. *Journal of Colloid and Interface Science* **2003,** 266, 236-244

32. Wang, W.; Gu, B.; Liang, L.; Hamilton, W., Synthesis of rutile (alpha-TiO2) nanocrystals with controlled size and shape by low-temperature hydrolysis: Effects of solvent composition *Journal of physical Chemistry B* **2004,** 108, 17477.

33. Drude, P., Ueber die reflexion und brechung ebener fichtwellen beim durchgang durch eine mit oberflächenschichten behaftete planparallele Platte. *Annalen fur Physik (Wiedemann Annalen)* **1891,** 279, 126-157.

34. Hunter, N. T.; Jameson, J. G.; Wanless, E., Determination of Contact angle of Nanosized Silica Particles by Multi-Angle Single-Wavelength Ellipsometry. *Aust. J. Chem* **2007,** 60, 651-655.

35. Nagy, N.; Deak, A.; Horvolgyi, Z.; Fried, M.; Agod, A.; Barsony, I., Ellipsometry of Silica Nanoparticulate Langmuir−Blodgett Films for the Verification of the Validity of Effective Medium Approximations. *Langmuir* **2006,** 22, 8416-8423.

36. Aspnes, D. E., Optical properties of thin films. *Thin Solid Films* **1982,** 89, 249.

37. *CRC Handbook of Chemistry and Physics*. 85 ed.; CRC Press: Boca Raton, Florida, 2004.

38. Fakhraai, Z.; Valadkhan, S.; Forrest, J. A., Qualitative discrepancy between different measures of dynamics in thin polymer films. *European Physical Journal E* **2005,** 18, (2), 143-148.

39. Bertsekas, D. P., *Non Linear Programming*. Scientific Belmont: Athens, 1999.

40. Noskov, B. A.; Loglio, G.; Miller, R., Dilational viscoelasticity of polyelectolyte/surfactant adsorption films at the air/water interface: Dodecyltrimethylammonium bromide and sodium poly(styrenesulfonate). *Journal of Physical Chemistry B* **2004,** 108, (48), 18615-18622.

41. Monteux, C.; Fuller, G. G.; Bergeron, V., Shear and dilational surface rheology of oppositely charged polyelectrolyte/surfactant microgels adsorbed at the air-water interface. Influence on foam stability. *Journal of Physical Chemistry B* **2004,** 108, (42), 16473-16482.

42. Ivanov, I. B.; Danov, K. D.; Ananthapadmanabhan, K. P.; Lips, A., Interfacial rheology of adsorbed layers with surface reaction: On the origin of the dilatational surface viscosity *Advances in Colloid and Interface Science* **2005,** 114.

43. Liggieri, L.; Ferrari, M.; Mondelli, D.; Ravera, F., Surface rheology as a tool for the investigation of processes internal to surfactant adsorption layers. *Faraday Discussions* **2005,** 129, 125-140.

44. Noskov, B. A.; Grigoriev, D. O.; Lin, S. Y.; Loglio, G.; Miller, R., Dynamic surface properties of polyelectrolyte/surfactant adsorption films at the Air/Water interface: Poly(dially1dimethylammonium chloride) and sodium dodecylsulfate. *Langmuir* **2007,** 23, (19), 9641-9651.

Chapter 6

Capillary waves study of adsorbed β–Casein / Surfactant mixed layers

Abstract

We address the study of the dilational rheological behaviour of adsorption layers of the milk protein β–casein (BCS) mixed with the non-ionic dodecyl dimethyl phosphine oxide (C_{12}DMPO), and with the cationic dodecyl trimethyl ammonium bromide (DTAB). Combining the drop profile tensiometry (PAT-1) and the excited capillary waves method (ECW) it is possible to get the dilational parameters over a broad frequency range. The adsorption mechanism can be discussed from dilational rheology experiments. Indeed, the formation of the mixed adsorption layer is based on a modification of the protein molecules via electrostatic and/or hydrophobic interactions with the surfactant molecules, and a competitive adsorption of the resulting complexes with the free surfactant. Depending on the surfactant concentration, these adsorption mixed layers contain different amounts of protein. One may expect that increasing the surfactant concentration should decrease the amount of adsorbed proteins. However, due to the much larger adsorption energy, proteins are rather strongly bound to the interface and via competitive adsorption surfactants cannot easily displace them.

1. Introduction: Mixed protein-surfactant interfacial layers

It is well known that surfactants added to a protein solution modify the adsorption layer properties at liquid-fluid interfaces.[1-3] Mixed systems containing proteins and low molecular weight surfactants are commonly used for the stabilization of foams and emulsions in many technological process, like food processing and pharmaceutical industry.[2] Specifically, the interfacial properties of such mixed layers play a key role in the formation and stabilization of foams and emulsions.[4] In the adsorbed state, the interaction between proteins and surfactant differs from that in the bulk, and hence, the interfacial complexes are different and, leads to different surface tension values, and surface rheological behaviour.[5] The interactions stabilizing these complexes can be of hydrophobic and/or electrostatic nature.[6-9] Thus, the conformation of the protein molecules in the bulk or at the interface change depending on the nature of their interaction with the surfactant molecules.[10] The surfactant concentration strongly affects the complexation process and the adsorption layer composition of the protein-surfactant mixtures. By increasing the amount of surfactant, the free surfactant molecules can gradually displace the protein molecules from the surface layer due to a competitive adsorption mechanism. At surfactant concentrations high enough, depending on the nature of the protein and the surfactant as well as the ionic strength of the solvent, protein molecules can be completely displaced by surfactants, thus leading to a significant change of the interfacial layer composition.[5] In short, the understanding of the interaction between proteins and surfactants allows one to describe the complex formation and the protein displacement from the interface to the bulk at high surfactant concentrations. The adsorption dynamics of protein-surfactant complex has been quantitatively described,[11] while the exact mechanism for protein displacement is not yet completely understood. Hence, different mechanisms have been suggested based on the competitive adsorption combined with protein modification via complexation.[5] A scheme of the competitive adsorption mechanism between a *β–casein* molecule and surfactant ones at increasing their concentration is shown in Figure 6.1.

Recently, the theoretical basis for the adsorption kinetics, the equilibrium state of adsorption, and the corresponding models for the dilational rheology as well as the experimental data have been presented for mixtures adsorbed at the air/oil-water interface, containing β–lactoglobulin (BLG) and β–casein (BCS) mixed with various surfactants, such as alkyl dimethil phospine oxides (C_nDMPO), sodium dodecyl sulphate (SDS), and dodecyl trimethil ammonium bromide (DTAB).[5, 11-13]

For food proteins that form a highly close-packed network at the interface, such as the globular proteins (BLG, ovoalbumin, etc.), a dilational deformation of the interface might not be expected to result in a uniform change in the surface coverage of molecules. Instead, a much more patchy, localised depletion of adsorbed protein molecules might be expected for a random-coil protein such as BCS. It is well known that for an individual protein molecule to become adsorbed a certain, minimum length of the polypeptide chain must become associated with the surface. When the protein must change its conformation for this to occur, e.g., with a globular protein such as BLG, the one might expect an energy barrier to adsorption.[14-21]

The random coil structured $\beta - casein$ (BCS), a bovine milk protein, is used in this work. BCS has been studied for many years, and thus its adsorption dynamics, thermodynamics and rheological behaviour are well-know.[22, 23] The BCS structure differs from those other proteins. Despite the common ordered three-dimensional structures typical for proteins, BCS is disordered and flexible. This molecule behaves like a block-copolymer, and has a strong tendency for self-assembling.[24]

The surfactants used in this study are the non-ionic dodecyl dimethil phospine oxide (C_{12}DMPO) and the cationic dodecyl trimethyl ammonium bromide (DTAB). The surface properties of both surfactants at the air-water interface have been extensively studied by different methods such as tensiometry,[25, 26] neutron reflectivity[27] and excited capillary waves.[28] Protein-surfactant mixed layers at the air-water interface can be built using two different methodologies: simultaneous and sequential adsorption of the respective components. Both strategies lead to compatible results of the thermodynamic and rheological behaviour of BCS-surfactant complex as previously was demonstrated by Kotsmar et al.[12]

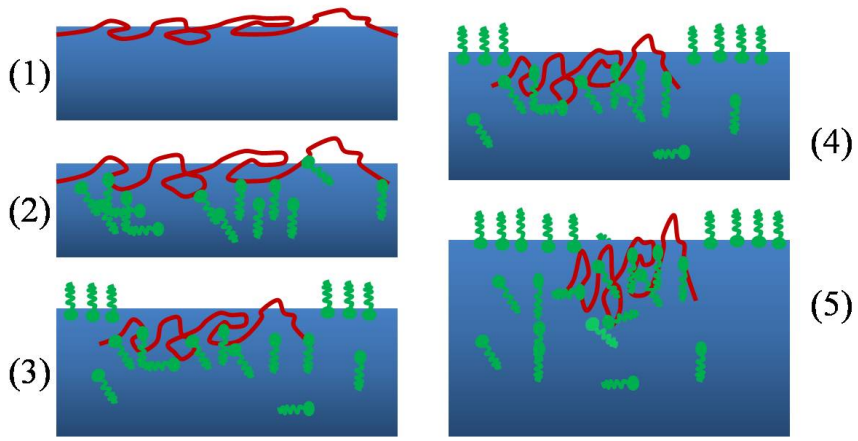

Figure 6.1. Possible conformational changes of the β-casein (BCS) molecule at the air-water interface at increasing surfactant concentration.

Lately, theoretical models that describe the thermodynamic and the adsorption kinetics of proteins and protein surfactant mixtures at the air/liquid interfaces have already been published.[5, 21, 29] It is necessary to assume multiple adsorption states of protein molecules at the surface, and an intrinsic compressibility of the surface layer formed.[30] Theoretical models to describe the dilational rheological behaviour of protein-surfactant and surfactant-surfactant mixtures have been developed recently.[5, 31] Indeed, the theory of Lucassen-van den Tempel[32] for interfacial layers of single surfactants has been generalized for the mixed adsorption kinetic of an arbitrary number of surface active species.[31]

The aim of this work is to get further insight on the interaction between mixed protein and surfactants at fluid interfaces. The adsorption dynamics formed from mixed solutions, and their dilational rheological behaviour will be studied. The interfacial layers are formed by simultaneous adsorption of the two components, which interact already in bulk. Non-ionic (C_{12}DMPO) and cationic (DTAB) surfactants are combined with the BCS. Their dilational viscoelastic behaviour has been measured by oscillating drop profile tensiometry and excited capillary waves covering a broad frequency range, from 0.005Hz to 1.2kHz. The understanding of the dynamics of adsorption of BCS-surfactant complex to the air-water interface allows one to describe the competition between proteins and surfactant on their adsorption at the interface, although they have different adsorption energies, certainly lower for surfactants. Thus, we analyze the displacement of the random-coil structured BCS from the air-water interface upon their interaction with the non-ionic and ionic surfactants. The structural changes and displacement of the protein are compared and discussed from the point of view of the dilational viscoelastic behaviour of the different species involved, such as BCS and the surfactants.

For the sake of clarity, the chapter is organized as follows: Section 2 describes briefly a theoretical background about the thermodynamic and rheological description of the formation of protein-surfactant complex and its dynamics of adsorption layers. The materials and methods used are described in section 3. Finally in section 4, we address the dynamical experiments performed in the broad frequency range studied pointing out the effect of the surfactant addition to the β-casein layer at the air-water interface.

2. Theoretical background

The surface dilational viscoelastic modulus ε is defined as the increase in surface tension γ for a small increase of surface area A by the expression originally proposed by Gibbs:

$$\varepsilon = \frac{d\gamma}{d\ln A} \tag{6.1}$$

The viscoelastic module ε is a frequency dependent complex quantity.[32-34] This is characterized by a storage term, which considers the elastic energy, and an imaginary loss term, which considers the energy dissipated. The common notation to define the complex dilational modulus ε reads:

$$\varepsilon = \varepsilon' + i\varepsilon'' = \varepsilon' + i\omega\kappa \tag{6.2}$$

where the real element ε' is the dilational storage component and the imaginary part ε'' is the loss component. For a small amplitude oscillatory motion of frequency ω, the loss modulus is related to the viscous friction $\varepsilon'' = \omega\kappa$, where κ is the dilational viscosity.

The dilational viscoelastic module of the surface layer containing single surfactants were derived by Lucassen and van den Tempel assuming that the mechanism of matter exchange between the bulk and the interface is diffusion controlled:[32, 34]

$$\varepsilon = \varepsilon_0 \left(\frac{d\Gamma}{dC}\sqrt{\frac{i\omega}{D}} \right) \Big/ \left(1 + \frac{d\Gamma}{dc}\sqrt{\frac{i\omega}{D}} \right) = \frac{1 + \zeta + i\zeta}{1 + 2\zeta + 2\zeta^2} \tag{6.3}$$

where the surface dilational elasticity ε_0 is the high frequency limit, and the characteristic parameters of the diffusional exchange of matter between bulk and surface ζ and ω are given by $\varepsilon_0 = d\Pi/d\ln\Gamma$; $\zeta = (\omega_D / \omega)^{1/2}$ and $\omega_D = D/2\,(dc/d\Gamma)^2$. Γ accounts for the surfactant adsorption at the interface and C is the bulk concentration.

For mixed protein-surfactant adsorption layers, the relations are similar in structure but more complex. The theory available takes into account the diffusion coefficients and relevant thermodynamic parameters related to all the components.[31] The general expressions were adapted to mixtures of two surfactants with the surface tension $\gamma = \gamma(\Gamma_1, \Gamma_2, T)$ and with the adsorption of each component $\Gamma_j = \Gamma_j(Cs_1, Cs_2)$, where Γ_j is the adsorption, and Cs_j is the corresponding sub-surface concentration of component j in the mixture. Assuming diffusion controlled mechanism for the adsorption layer relaxation and harmonic oscillations at a frequency ω and a small area amplitude ΔA the following mass balance equation results:

$$i\omega\Delta\Gamma_j + i\omega\Delta\Gamma_j \frac{\Delta A}{A} + \left(i\omega D_j\right)^{1/2} \Delta C_{sj} = 0 \tag{6.4}$$

where D_j is the diffusion coefficient of component j. Equation 6.4 leads to the complex viscoelasticity of a mixed layer:[31]

$$\varepsilon = \frac{1}{B}\left(\frac{\partial \Pi}{\partial \ln \Gamma_1}\right)_{\Gamma_2}\left[\sqrt{\frac{i\omega}{D_1}}a_{11} + \sqrt{\frac{i\omega}{D_2}}a_{12}\frac{\Gamma_2}{\Gamma_1} + \frac{i\omega}{\sqrt{D_1 D_2}}\left(a_{11}a_{22} - a_{12}a_{21}\right)\right] + \\ + \frac{1}{B}\left(\frac{\partial \Pi}{\partial \ln \Gamma_2}\right)_{\Gamma_1}\left[\sqrt{\frac{i\omega}{D_1}}a_{21}\frac{\Gamma_1}{\Gamma_2} + \sqrt{\frac{i\omega}{D_2}}a_{22} + \frac{i\omega}{\sqrt{D_1 D_2}}\left(a_{11}a_{22} - a_{12}a_{21}\right)\right], \quad (6.5)$$

where C_1 and C_2 are the bulk concentrations of the components and, a_{ij}= $(\partial\Gamma_i / \partial Cj)|\, c_{k\neq j}$ are the partial derivatives to be determined from the adsorption isotherm. The coefficient B represents the mechanism of the dynamics of the interfacial layer, here assumed as diffusion controlled:

$$B = 1 + \sqrt{\frac{i\omega}{D_1}}a_{11} + \sqrt{\frac{i\omega}{D_2}}a_{22} + \frac{i\omega}{\sqrt{D_1 D_2}}\left(a_{11}a_{22} - a_{12}a_{21}\right) \quad (6.6)$$

For two components, only adsorption and desorption process can be possible in these systems and both of them are controlled by diffusion. To determine the dilational parameters it is necessary to assume a model of the equilibrium surface adsorption layer obeying the correspondent equations of state and adsorption isotherms.

For mixtures of a protein with a non-ionic surfactant governed by different adsorption models, it would be necessary to derive the following equation of state of the surface layer:[5, 12]

$$\frac{-\Pi\Omega_0^*}{RT} = \ln\left(1-\theta_P-\theta_S\right) + \theta_P\left(1-\Omega_0/\Omega_P\right) + a_P\theta_P^2 + a_S\theta_S^2 + 2a_{PS}\theta_P\theta_S \quad (6.7)$$

where the subscripts P and S refer to the protein and surfactant molecules, respectively. Π is the surface pressure, R is the gas constant and T is the absolute temperature, Γ_i, Ω_i and a_i are the adsorption, average molar area and interaction constant for the component i. $\theta_i = \Omega_i\Gamma_i$ is the surface coverage by surfactant molecules of component i, and Ω_0 is the molar area at zero surface pressure. The parameter a_{PS} accounts for the interaction between the protein and surfactant molecules.

The adsorption behaviour of a protein mixed with an ionic surfactant is somewhat different. For a protein molecules with m-ionize groups, the Coulomb interaction with ionic surfactants causes the formation of complexes, which are determined by the average activity of ions $(c_p^{\,m}c_s)^{1/(1+m)}$. The resulting equation of state of the surface layer is similar to Equation 6.7:

$$\frac{-\Pi\Omega_0^*}{RT} = \ln\left(1-\theta_{PS}-\theta_S\right) + \theta_{PS}\left(1-\Omega_0/\Omega_P\right) + a_{PS}\theta_{PS}^2 + a_S\theta_S^2 + 2a_{SPS}\theta_{PS}\theta_S \quad (6.8)$$

Here $\theta_{PS} = \Omega\,\Gamma$ is the coverage of the interface by adsorbed protein-surfactant complexes and a_{SPS} is the parameter which describes the interaction of the no associated surfactant with the protein-surfactant complexes. It was shown that the assumption of an intrinsic compressibility of surfactant of the form: $\Omega_s=\Omega_{s0}\ (1-\varepsilon_s\Pi\theta_s)$ improves the quality of the data description. Here, Ω_{s0} ($\Omega_0 \approx \Omega_{s0}$) is the molar area of surfactant at zero surface pressure and ε_s is the two-dimensional relative surface layer compressibility of the surfactant molecules in the surface layer. The influence of aggregation was approximately taken into account by introducing a difference of the average molar area of adsorbed molecules. It is clear at this point that other complex phenomena related to protein surface layers remains far from the possibilities of quantitative description by this thermodynamic description. This general picture of the equilibrium adsorption of mixed adsorption layers have been described in detail in ref. 5.

3. Materials and Methods

3.1 Chemicals

The double distilled and deionized water used for the preparation of all solutions in this work was produced by a MilliQ-RG system from Millipore, having a resistivity higher than $18 m\Omega\cdot cm^{-1}$ and a surface tension of $\gamma = 72.6 mN/m$ at 20ºC. Na_2HPO_4–NaH_2PO_4 buffer solution (Flukka, assay > 99%) with pH=7 and surface tension $\gamma = 72.2 mN/m$ at 22ºC was used to prepare the solutions of β–Casein studied (3×10^{-7} and 10^{-6} M) as well as the surfactant solutions. BCS from bovine milk (purity > 90%) with a molecular weight of 24kDa and an isoelectric point ca. pH=5.2 was purchased from Sigma-Aldrich Chemical co. (Germany) and used without further purification. The nonionic surfactant Dodecyl dimethyl phospine oxide, C_{12}DMPO (M_w = 246.4g/mol), synthesized at the MPI by Haage,[35] was added to the BCS bulk solution at concentrations ranging between 10-6M and the critical micelle concentration (cmc) at 5×10^{-4}M. The anionic surfactant Dodecyl trimethyl ammonium bromide, DTAB (M_w = 308.35g/mol), purchased from Fluka (Switzerland), was used at concentrations ranging between 10-6M and the critical micelle concentration (cmc) at 1.3×10^{-2}M. Scheme 6.1 shows the molecular structure of both C_{12}DMPO and DTAB.

All experiments were performed at a constant temperature of 22ºC. The mixed protein-surfactant solution were prepared mixing the respective protein and surfactant solution during 30min before starting the measurements to ensure that the protein-surfactant complexes are perfectly formed.

Scheme 6.1. Chemical structure of the (a) dodecyl dimethyl phospine oxide C_{12}DMPO and (b) dodecyl trimethylammonium bromide DTAB

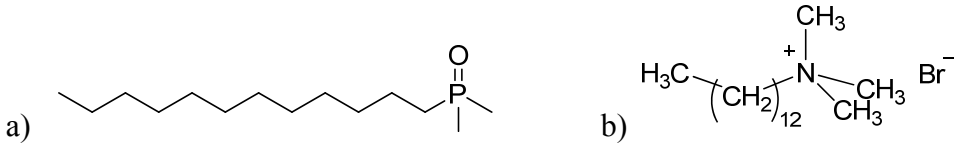

3.2 Methods

The dilational viscoelastic behaviour of BCS-surfactant mixed system adsorbed at the air-water interface were studied by the detection of electrocapillary waves (ECW) onto the interfacial fluid layer formed covering the frequency range from 25 *Hz* to 1 *kHz*.

For the sake of comparison with the experimental data at high frequencies performed by *ECW*, we included in this study measurements of the dilational rheology at low frequencies ($\omega < 1Hz$) performed by drop profile analysis tensiometer[5, 36] (PAT, Sinterface Technologies, Germany). It is based on harmonic area oscillations of the drop surface at low frequencies, and is further described in the methods summary, appendix 1.

4. Results and Discussion

In this section, we address the macroscopic dynamical properties of mixed β-casein / surfactant interfacial layers at higher frequencies by means of the detection of excited electrically capillary waves (ECW) onto the air-mixed protein–surfactant solution interface. We thus report the dilational viscoelasticity of the mixed BCS-surfactant adsorption layers to get further insight into their mechanism of adsorption to the interface. The layers are formed by simultaneous adsorption of the two components because they have already been in contact with each other in the solution bulk. We performed the rheology measurements by ECW and PAT-1 covering a broad frequency range from 5×10^{-3}Hz to 1kHz, after the adsorption kinetics reached the equilibrium state ($\approx 2\times10^{3}$s) according to the adsorption isotherms previously measured by Kotsmar et al.[11] It was not possible to work beyond this region due to the strong decrease of the signal intensity leading to very low measurement sensibility in the ECW method.

4.1 Adsorption isotherms: a brief summary of the equilibrium features of the mixtures BCS/surfactant

To summarize the equilibrium experiments previously performed by Kotsmar et al.[11, 12], Figure 6.2 shows the adsorption isotherms of the surfactants C_{12}DMPO and DTAB and their mixtures with BCS measured by profile analysis

tensiometry. [11, 12] The mixed adsorption layers were built up in two different ways, with sequential and with simultaneous adsorption of the different components. The isotherms of the respective mixtures built up in the two different ways do not differ significantly, indicating, that the composition of the mixed layers is very similar. Despite these tensiometric data the surface dilational investigations showed that the compositions of the layers differ.

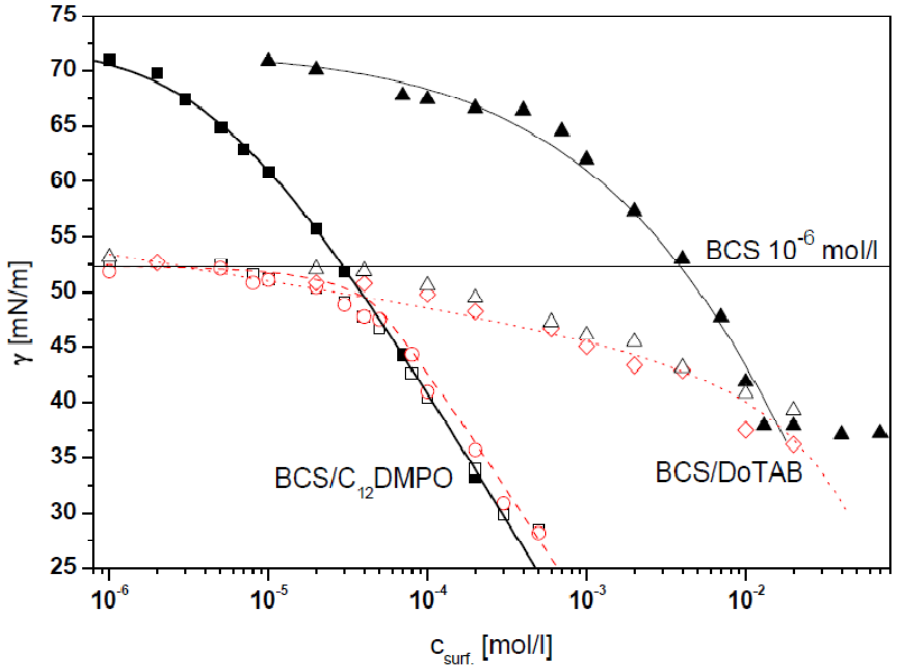

Figure 6.2. Adsorption isotherms of the surfactants C12DMPO (■) and DTAB (▲) and their mixtures with BCS built up in two different ways; BCS/C12DMPO via sequential (□) and simultaneous adsorption (○) BCS/DTAB via sequential (△) and simultaneous adsorption (◇);horizontal line indicates the equilibrium surface tension value of 10^{-6} mol/l BCS solution; solid curves correspond to the theoretical fitting for C12DMPO and DTAB, dashed line and dotted line are the fittings for the BCS/C12DMPO and BLG/DTAB mixtures, respectively, formed via simultaneous adsorption. Adapted from ref. 12.

By the comparison of the isotherms of the mixtures containing the nonionic C_{12}DMPO and the cationic DTAB, one can see, that the isotherms of BCS–C_{12}DMPO mixtures merge with the isotherm of the pure surfactant already before reaching its CMC. It suggests that BCS is displaced from the surface layer by the C_{12}DMPO already before reaching this concentration value. The surface rheological data also support these findings for both ways of mixed layer formation (we will show below). Ellipsometric and foam film measurements using the simultaneous adsorption route showed the same results.[37] For the BCS–DTAB mixtures the curves meet the pure DTAB isotherm only around its CMC (**Fig. 1)**, showing that the ionic surfactant with the same hydrocarbon chain length cannot displace the BCS as effective as the non-ionic C_{12}DMPO. The surface activity of DTAB molecules is also much smaller, as compared to that of

C_{12}DMPO, due to the charged head group. The curves on the figure represent the theoretical fitting for the surfactants and for the mixtures formed via simultaneous adsorption (see ref. 12 for details).

4.2 Dilational Rheology of single component solutions

Let us first evaluate the dilational viscoelastic behaviour of the single components adsorbed onto the air-water interface; i.e., the random coil structured β-casein (BCS) and the two different surfactants used, such as the non-ionic C_{12}DMPO and the cationic DTAB.

4.2.1 β-casein (BCS)

We report in Figure 6.2 the frequency dependence of the dilational storage module ε and the loss module ωκ, components of the complex viscoelastic module ε (ω) for two different bulk concentrations of BCS solution. The reason for using $3\times10^{-7}$and 10^{-6}M is to evaluate the region of concentration ($c^*=4\times10^{-7}$M), where the adsorption layer is saturated with the protein molecules and where the formation of a second layer or surface aggregation starts.[12]

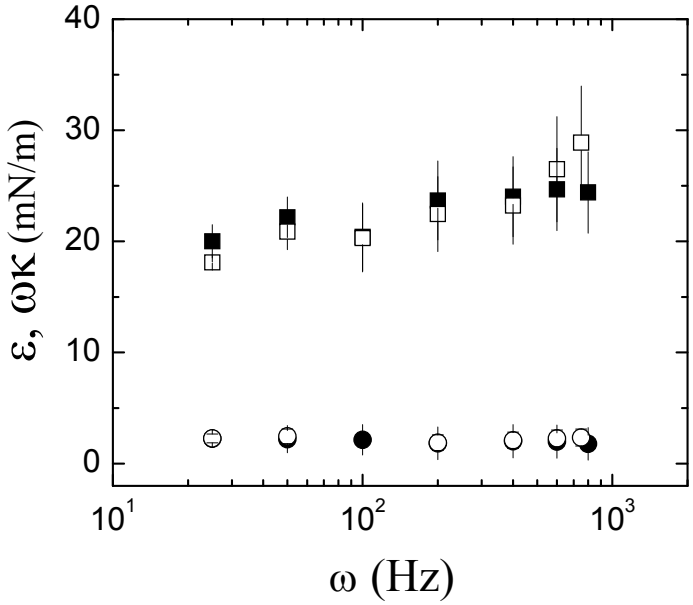

Figure 6.3. Frequency dependence of the dilational elastic module ε (□, ■) and the loss module ωκ (○, ●) measured by means of the ECW method, taking in account different BCS bulk concentrations (open symbols: 3×10^{-7}M and filled symbols: 10^{-6}M).

As it can be seen in Figure 6.3, the set of results at different BCS bulk concentration shows a slight increase of ε with frequency, which levels off at higher frequencies pointing out the existence of a dynamic relaxation process in this frequency range. However, the dilational loss modulus ωκ at different BCS concentrations remains constant at increasing frequency and both reaches values

close to zero as it is expected beyond a sufficiently high frequency.[32] It is noteworthy that, at higher frequencies ($\omega \rightarrow \infty$), the BCS interfacial layer behaves as a pure-elastic body because the deformation is very fast and do not have enough time to respond, and therefore to dissipate energy. As aconsequence, in this frequency regime the values of storage modulus are much larger than the loss ones ($\varepsilon >> \omega\kappa$).

These results point out that, within the experimental uncertainty, thre is no concentration dependence of ε and $\omega\kappa$ in this frequency range. This can be understood considering that the BCS concentrations studied are in the precritical region where the adsorption layer is saturated with protein molecules. Hereinafter, to describe properly the dilational rheological features of the BCS–surfactant solution we will assume that the concentrations of the protein used in this study are located close to the precritical region, which will allow us describing the interface as initially saturated by BCS and/or BCS-surfactant complex.

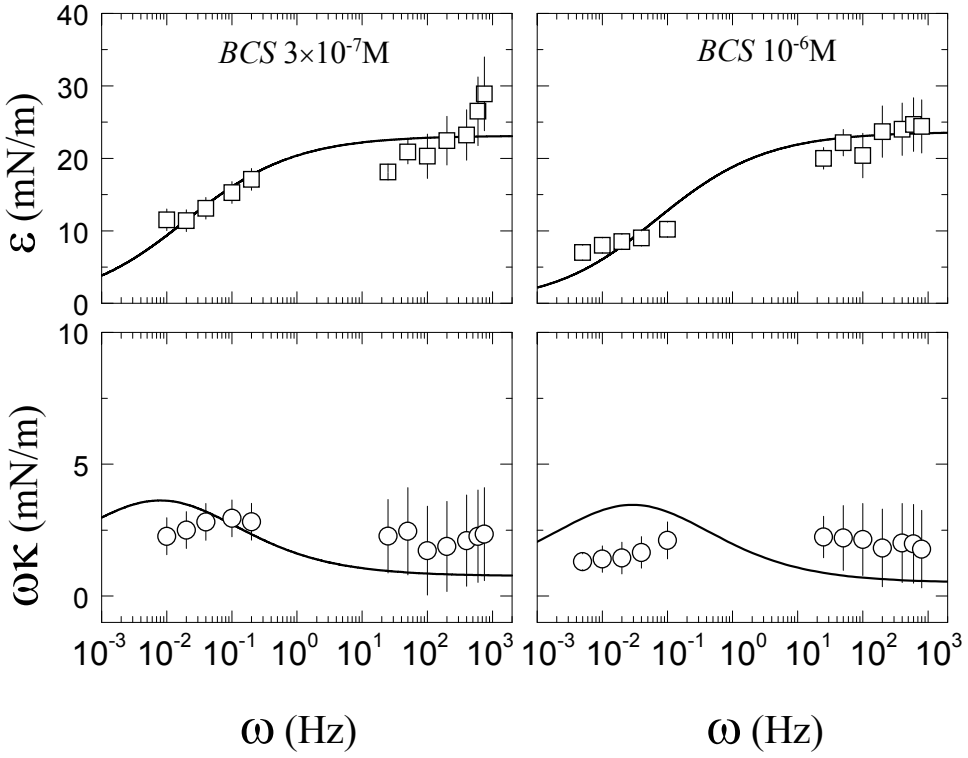

Figure 6.4. Frequency dependence of the dilational elastic module ε (□) and the loss module $\omega\kappa$ (○) for BCS interfacial layer at different concentrations (3×10^{-7} and 10^{-6}M) measured by combining ECW and PAT methods. The lines represent the theoretical fitting of the experimental data by the Lucassen-van den Tempel (LVT) model (Eq. 6.3)

These experimental results can be compared with those obtained for the same system at lower frequencies performed by PAT tensiometer. Figure 6.4 shows the dilational viscoelastic parameters covering a broad frequency range, from 10^{-2}Hz to 1.2kHz. The experimental values obtained from both

methodologies are in reasonable agreement pointing out a similar trend in accordance to a single relaxation process. In the whole frequency range, ε increases with frequency and levels off at higher frequencies. However, the values of ωκ do not show any clear feature. It has been possible to describe semi-quantitatively the viscoelastic behaviour in terms of a Lucassen-van den Tempel (LVT) diffusion controlled mechanism (Eqs. 6.1–6.3).[32] Figure 6.4 shows the fits obtained. The dilational elastic modulus is found in rather good agreement with the theoretical fit within the experimental errors, while the predictions of the loss modulus are less satisfactory over the whole frequency range. An explanation may be that proteins do not relax according to a diffusional exchange mechanism.[12, 21] To clarify this point, the value of diffusion coefficient obtained for the BCS by the LVT theoretical approach, $D_{BCS} = 3\times10^{-11}$m^2/s has been found in agreement with previous values of D obtained from fitting the adsorption isotherm of BCS by the theoretical models appeared in the literature.[11, 12]

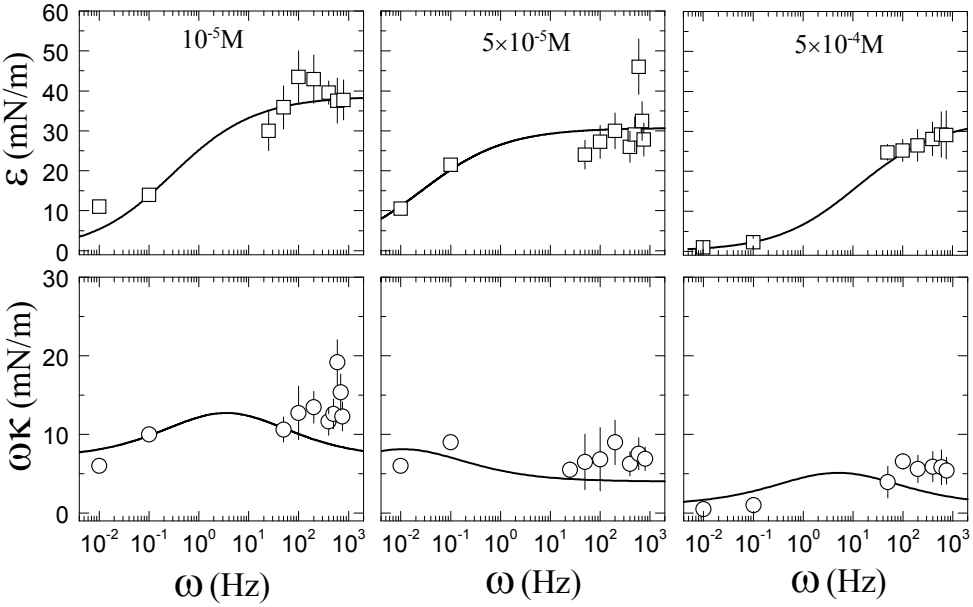

Figure 6.5. Frequency dependence of the dilational elastic module ε (□) and the loss module ωκ (○) for C_{12}DMPO adsorbed monolayers at the air-water interface, taking in account different C_{12}DMPO bulk concentrations. The broad frequency range has been covered by combining ECW and PAT methods. The lines represent the theoretical fitting of the experimental data by the Lucassen-van der Tempel (LVT) model (Eq. 6.3)

4.1.2 C_{12}DMPO

The frequency dependence of the dilational viscoelastic parameters ε and ωκ of C_{12}DMPO interfacial layers has been systematically studied as a function of the surfactant concentration as shown in Figure 6.4. We have combined the ECW measurements and the those performed with the PAT method.[12] The data presented in Figure 6.5 show the remarkably accordance between the results

obtained in the low frequency range (0.01–0.1 Hz) with the ones at higher frequencies (25Hz–1kHz).

The qualitatively frequency dependence of ε and ωκ is the same already observed in Figure 6.4 for BCS layers. Similar results have been found at all concentrations studied (from 10^{-5} to 5×10^{-4} M) highlighting the existence of a single relaxation process over the frequency range studied. In fact, we have fitted the experimental results addressed in Figure 6.5 with the LVT model[32] assuming a diffusion-controlled exchanged matter mechanism as expected for a surfactant system. The theoretical fit proposed is in remarkable agreement not only with the experimental dilational elastic module ε, but also, with the storage modulus ωκ. The mean value of diffusion coefficient, $D_{CDMPO} = 3\times10^{-10}$m^2/s has been found in concordance with previous values of *D* appeared in the literature for the same surfactant.[11, 12] Moreover, previously studied performed by Wantke et al.[38] and Kovalchuk at al.[25] covering a broad frequency range are in rather good accordance with the dilational rheological behaviour of C_{12}DMPO adsorbed layers shown in this work.

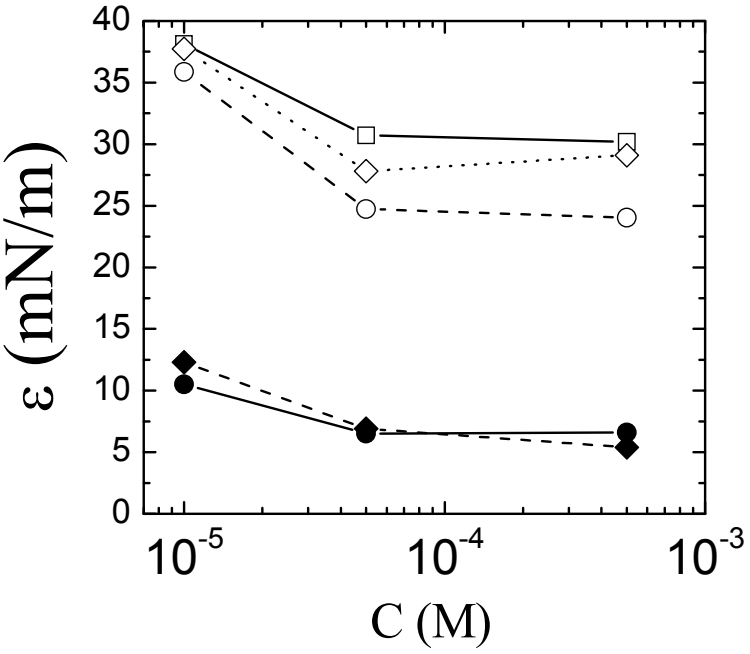

Figure 6.6. Dilational elastic module ε and loss module ωκ part of the complex viscoelasticity as a function of C_{12}DMPO concentrations at two frequencies 50Hz (○,●) and 750Hz (◇,◆): filled symbols correspond to ε and open symbols to ωκ. It is also included the high frequency limit of the dilational elastic module ε_0 (□) from the correspondent analysis of the experimental data by LVT model.

To evaluate the role of the surfactant concentration, Figure 6.5 plots the experimental viscoelastic parameters ε and ωκ at two different frequencies (50 and 750 Hz) as a function of the C_{12}DMPO concentration. For the sake of

comparison, we also include in Figure 6.5 the high frequency limit of the dilational elasticity module ε_0 obtained from the analysis of the experimental data by means of the LVT model. As it can be observed, all the data addressed point out qualitative trends compatible with the existence of a higher value of ε and ωκ at 10^{-5}M. The values of these dilational moduli decrease as the surfactant concentration increases, as it usually happens for surfactant adsorption layers.[32, 39]

4.1.3 DTAB

The frequency dependence of the dilational viscoelastic parameters ε and ωκ of DTAB interfacial layers is also systematically studied as a function of the surfactant concentration as shown Figure 6.7. Again there is a good accordance between the experiments performed in the low frequency range (0.01–0.1 Hz) by the PAT[12] and the ones at higher frequencies (25Hz–1kHz) obtained by ECW.

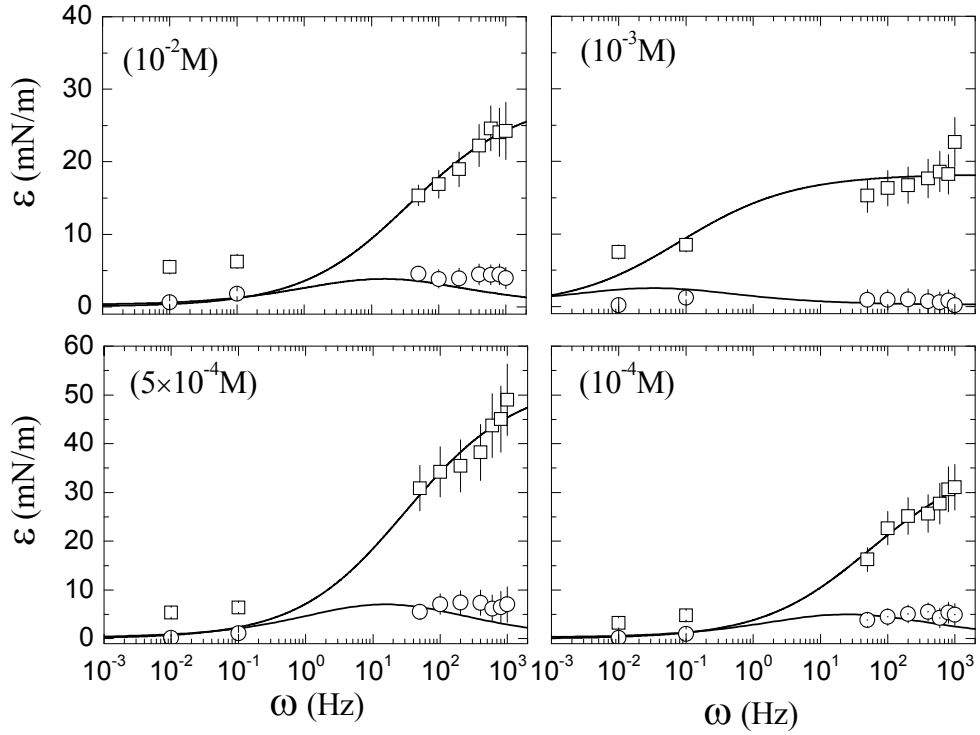

Figure 6.7. Frequency dependence of the dilational elastic module ε (□) and the loss module ωκ (○) for DTAB adsorbed monolayers at the air-water interface, taking in account different DTAB bulk concentrations. The broad frequency range has been covered by combining ECW and PAT methods. The lines represent the theoretical fitting of the experimental data by the Lucassen-van den Tempel (LVT) model (Eq. 6.3)

Similarly to the viscoelastic behaviour of C_{12}DMPO, here, ε increases with frequency levelling off at higher frequencies while the values of ωκ show little variation. The results point out the existence of a relaxation process in the experimental frequency window. Similar qualitative results were found for different DTAB concentration.

Again, we have analyzed the experimental results with the LVT theoretical model.[32] In the high frequency domain the model describes ε within the experimental uncertainty, and gives a reasonable prediction of ωκ, although it slightly underestimates the experimental results. However, the theoretical model slightly falls to describe the low frequency dilational behaviour, clearly underestimating the elastic modulus. The mean value of diffusion coefficient, $D_{DTAB} = 3\times10^{-10}m^2/s$, obtained for the fit of the dilational parameters by LVT model have been found in good agreement with the values appeared in the literature for the same surfactant.[12]

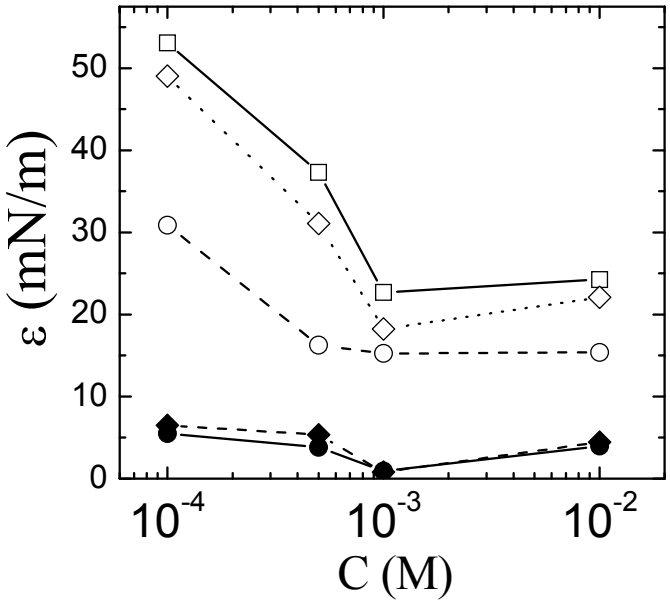

Figure 6.8. Dilational elastic module ε and loss module ωκ part of the complex viscoelasticity as a function of DTAB concentrations at two frequencies 50Hz (○,●) and 800Hz (◇,◆): filled symbols correspond to ε and open symbols to ωκ. It is also included the high frequency limit of the dilational elastic module ε_0 (□) from the correspondent analysis of the experimental data by LVT model.

Figure 6.8 shows the experimental viscoelastic parameters ε and ωκ at two different frequencies (50 and 800 Hz) as a function of the DTAB concentration. For the sake of comparison, we also include in Figure 6.7 the high frequency limit of the dilational elasticity module ε_0 obtained from the analysis of the experimental data by means of the LVT model. As it can be observed, all the data point out qualitative trends compatible with the existence of a higher value of ε and ωκ at 10^{-4}M.

In addition, we found that he experimental viscoelastic parameters shown by the DTAB samples are quantitatively similar to the dilational parameters obtained for the C_{12}DMPO interfacial layers. However, the location of the highest viscoelastic module is shifted to larger concentrations in the case of DTAB. As it

will be discussed below, the location of the maximum in ε and ωκ plays a key role in the explanation of the viscoelastic behaviour of the mixed interfacial layers.

4.3 Dynamical behaviour of BCS/surfactant interfacial systems

The role of the surfactant addition on the dynamical behaviour of BCS adsorption layers at air-water interface has been studied by the ECW and PAT techniques. The protein-surfactant complexes have been previously formed in bulk and latter adsorbed at the air-water interface. We have used surfactants of different chemical nature (C_{12}DMPO and DTAB) in a well-defined concentration regime. It is well known that the surfactant nature and its bulk concentration play a key role in the existence of diverse interactions between proteins, and surfactants leading to protein-surfactant complexes with different structure.[29]

4.3.1 BCS – C_{12}DMPO adsorption layers

Figure 6.9 shows the frequency dependence of dilational viscoelastic parameters ε and ωκ of BCS–C_{12}DMPO interfacial layers for different surfactant concentrations (from 10^{-6} to 10^{-4} M), and for fixed protein concentration (10^{-6}M).

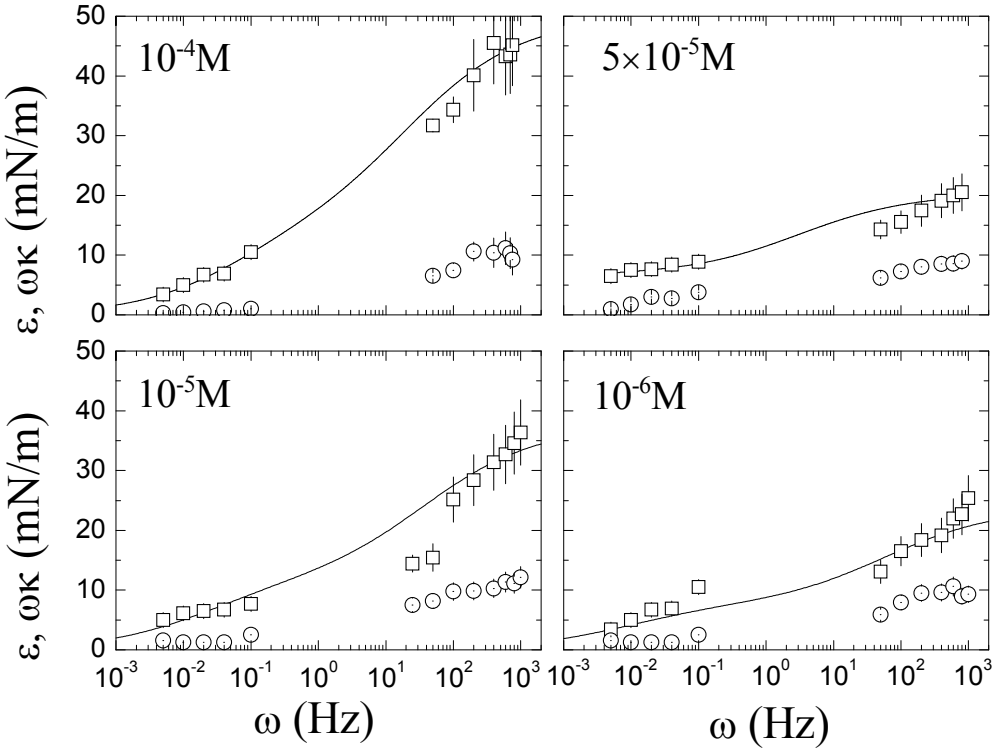

Figure 6.9. Frequency dependence of the dilational elastic module ε (□) and the loss module ωκ (○) for *BCS-C_{12}DMPO* adsorbed layers at the air-water interface, taking in account different C_{12}DMPO bulk concentrations at fixed protein concentration (10^{-6}M). The broad frequency range has been studied by combining ECW and PAT methods. Continuous lines correspond to the fit of the experimental data by Eqs. 6.6-6.7.

It can be observed that the values of ε increase with frequency and then level off at a high frequency limiting value, usually at frequencies ω ≈ 0.8 –1kHz, which is quite similar to the behaviour of the non-ionic C_{12}DMPO pure layers at different concentrations (Figure 6.5). Again the results suggest the existence of well-defined relaxation process. As for the pure components, the frequency dependence of the dilational loss modulus (ωκ) at different C_{12}DMPO concentrations is smaller than that of the elasticity modulus.[32] As discussed above, it is reasonable that in the high frequency limit (ω→∞), ε >> ωκ, because the interfacial layer is essentially rigid. Figure 6.9 also contains the theoretical curves corresponding to the fit of the experimental elastic module by means of the theoretical model proposed in section 2. [31] These fits have been calculated by the analytic expressions for the complex elasticity modulus of mixed protein+surfactant samples (Eqs. 6.5–6.7) taking into account the necessary thermodynamic parameters given in table 6.1, obtained in a previous thermodynamic description of the system.[11, 12]

Table 6.1. Fit Parameters from the Adsorption isotherm of BCS-C_{12}DMPO mixture obtained from ref. 11. These parameters are also necessary to fit the dilational rheology of these mixtures.

	Ω_0 $(10^5 m^2/mol)$	Ω_1 $(10^6 m^2/mol)$	Ω_{max} $(10^7 m^2/mol)$	a_{ps}
BCS	2.2	3.0	2.7	1.1
	Ω_{S0} $(10^5 m^2/mol)$	a_s	as_{ps}	ε_s $(10^{-3} m/mN)$
DTAB	2.5	0.0	0.0	9.0

The theoretical model already proposed in the literature[31] describes rather well the dilational viscoelastic behaviour of the BCS–C_{12}DMPO interfacial layers in the entire surfactant concentration regime. However, this model based in the diffusion relaxation is not sufficient for understanding the complex behaviour of mixed adsorption layers. It is necessary to take into account additional effects accounting for other processes, such as molecular re-conformation, aggregation, etc. This direct fitting of the data by this diffusion relaxation model, leads to effective diffusion coefficients for both C_{12}DMPO and BCS–C_{12}DMPO complex. Indeed, the effective diffusion coefficient obtained, correspond to a composition of the diffusivities of the involved species, i.e., the complex and the free surfactant. Hence, we have found that the *effective* diffusion coefficient slightly vary with surfactant concentration. Hence, we have calculated a mean value of $D_{complex}$ = 2.9±0.4×$10^{-11}$$m^2$/s and D_{CDMPO} = 3.1±0.4×$10^{-10}$$m^2$/s which have been found in concordance with the respective diffusion coefficients for the pure BCS and DTAB previously studied.

We have studied the effect of decreasing the protein concentration on the dilational behaviour of BCS – C_{12}DMPO adsorbed layers from 10^{-6}M (just above

to the critical region of concentration, c^*) to 3×10^{-7}M (close to $c^*=4\times10^{-7}$M). The results shown in Figure 6.10 have been obtained at different surfactant concentration by the excited capillary waves method (ECW).

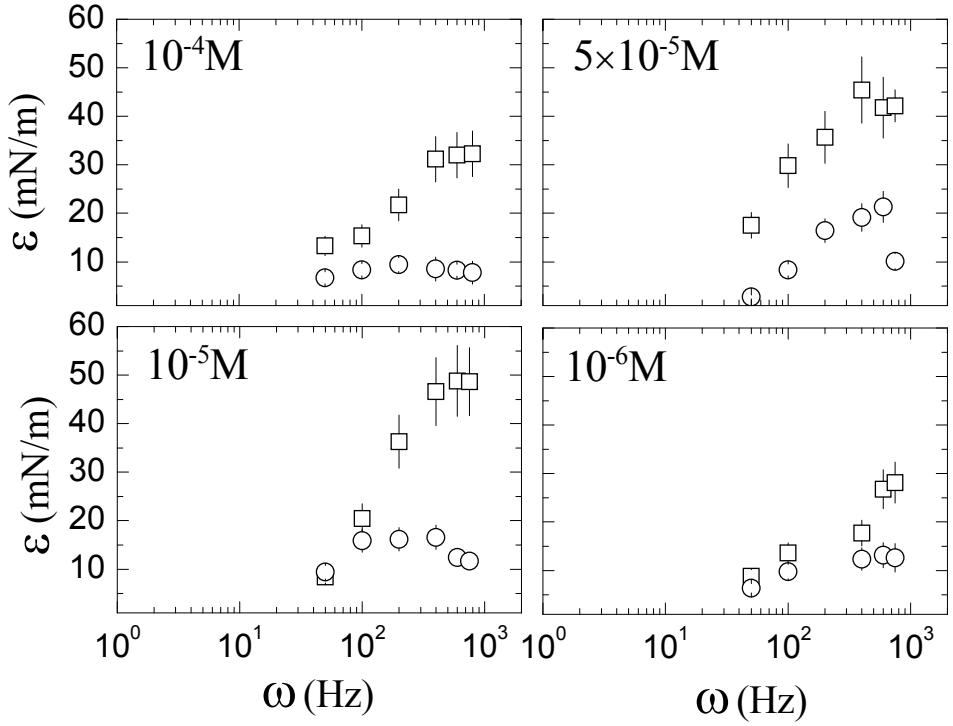

Figure 6.10. Frequency dependence of the dilational elastic module ε (□) and the loss module ωκ (○) for *BCS-C_{12}DMPO* adsorbed layers at the air-water interface, taking in account different C_{12}DMPO bulk concentrations at fixed protein concentration (3×10^{-7}M). This set of results has been obtained by ECW method.

Here, the general trend shown by the values of ε and ωκ are similar to that of the results shown in Figure 6.9 for $c=10^{-6}$M. A comparison of the viscoelastic moduli is shown in Figures 6.5, 6.9 and 6.10 indicates that they depend strongly not only on the surfactant concentration, but also on the protein concentration. For instance, Figure 6.11 shows the dilational viscoelastic parameters ε and ωκ as a function of C_{12}DMPO concentration for the BCS–C_{12}DMPO adsorbed layers at two different BCS concentrations (10^{-6} y 3×10^{-7}M) at the same frequency (800Hz). For the sake of comparison, we have included the viscoelastic moduli of the pure C_{12}DMPO adsorbed layer.

For both complexes, which only differ in the BCS concentration, the general trend of ε as a function of the C_{12}DMPO concentration is similar; i.e., ε increases, pass through a maximum, and finally decreases. The general behaviour of the viscoelastic moduli with respect to the surfactant concentration is related to the assumption of a successive replacement of BCS by surfactant at the interfacial layer as shown schematically in Figure 6.1.

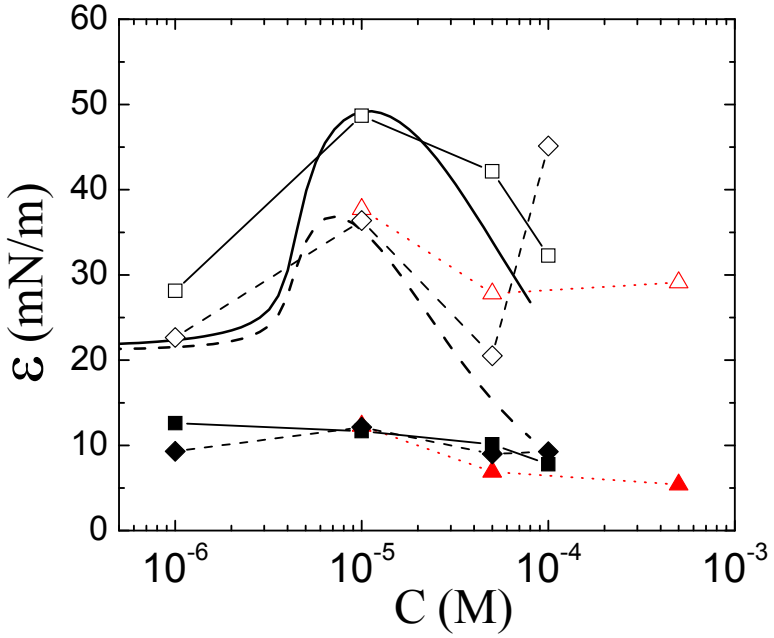

Figure 6.11. Dilational elastic modulus ε and loss modulus ωκ for *BCS-C_{12}DMPO* adsorbed layers at 800Hz as a function of *C_{12}DMPO* concentration comparing different *BCS* concentrations: 3×10^{-7}M (□,■) and 10^{-6}M (◇,◆); filled symbols correspond to ε and open ones to ωκ. It is also included the parameters ε (△) and ωκ (▲) of pure *C_{12}DMPO* adsorbed layers from Fig 6.4. Curves are theoretical fittings using Eqs. 6.6–6.7.

It should be noted that at $c > 10^{-6}$M, simultaneous adsorption of BCS – C_{12}DMPO complex and free surfactant molecules coexist as previously pointed out by dynamical tension experiments performed by Kotsmar et al.[10, 11] It has been reported that during the initial steps of adsorption, mainly surfactant molecules go to the surface due to their higher diffusion coefficient. After that, the surface concentration of the complex increases gradually, and hence the surface elasticity increases.[5] At relatively high surfactant concentrations it is expected that the structure of the protein-surfactant complex changes; i.e., the complexes are formed due to hydrophobic interactions between the non-ionic C_{12}DMPO and the BCS (see Figure 6.12), and increasing the surfactant molecules leads to changes of the adsorption layer structure, and as a consequence change of the surface elasticity.[5] As it can be seen in Figure 6.11, in the low concentration range the slight decrease in the dilational module ε is caused by the increasing amount of surfactant, which according to Figure 6.4, have small contribution to ε. Thus, in this concentration regime the surfactant dominates the interfacial layer, in further agreement with previously results using different methodologies.[10, 37] From the assumption that further increasing of non-ionic surfactant concentration, simultaneously to the hydrophobic interaction with protein segments, the number of free surfactants increases, leading to a stronger competition at the interface. Both effects lead finally to a progressive depletion of the protein form the interface. The curves in Figure 6.11 represent the theoretical fittings that describe

both complexes with different BCS concentration (Eqs. 6.5–6.7).[31, 40] The theoretical approach is in agreement with the experimental data and describes rather well the maximum in the dilational elastic modules. The BCS–C_{12}DMPO adsorbed layer with BCS at 3×10^{-7}M is in agreement with the above picture, while for the one with BCS (10^{-6} M) this behaviour is valid in the entire concentration regime studied except for 10^{-4} M. Here, the amazing increasing of ε can be explained by the relaxation of bound surfactants, which can be released upon expansion and rebound upon compression during the propagation a longitudinal wave onto the interface. This fact has been suggested by Kotsmar et al.[12] but further work is necessary to clarify this point. Moreover, we found that the values of ε corresponding to the complex with BCS (3×10^{-7}M) are larger than the ones with BCS (10^{-6}M), this fact can be explained by the molar ratio of the free surfactant molecules to the protein-surfactant complex. Thus, higher concentrations of BCS leads to an increase of this ratio and then smaller values of ε closed to the pure surfactant, as shown the values at 10^{-6}M in Figure 6.10.

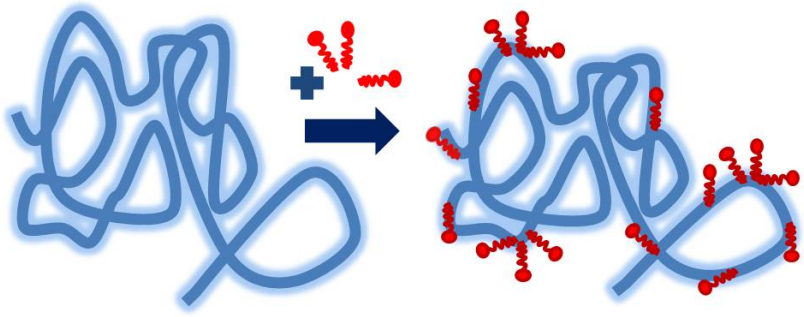

Figure 6.12. The addition of a non-ionic surfactant, such as C_{12}DMPO, to a BCS solution leads to a complex formation which is more hydrophilic and thus less surface active than the original protein.

4.3.2 BCS – DTAB adsorption layers

We have measured the dilational viscoelastic moduli of BCS–DTAB interfacial layers at different surfactant concentrations (from 10^{-4} to 10^{-2}M) and fixed protein concentration, just above the critical concentration (10^{-6}M > c^*). The dilational viscoelastic parameters ε and ωκ of the BCS–DTAB complex as a function of the frequency are shown in Figure 6.13. For mixed adsorption layers containing different amounts of cationic surfactant the absolute values of ε increase with frequency levelling off at a high frequency limiting value, as occurs for non-ionic surfactants. The dilational loss modulus ωκ at different DTAB concentrations remains relatively constant at increasing frequency with values smaller than the correspondent storage modules (ε >> ωκ). In general terms, the

shape of the experimental data shown in Figure 6.13 is qualitatively similar from those of the pure DTAB measured (Figure 6.7).

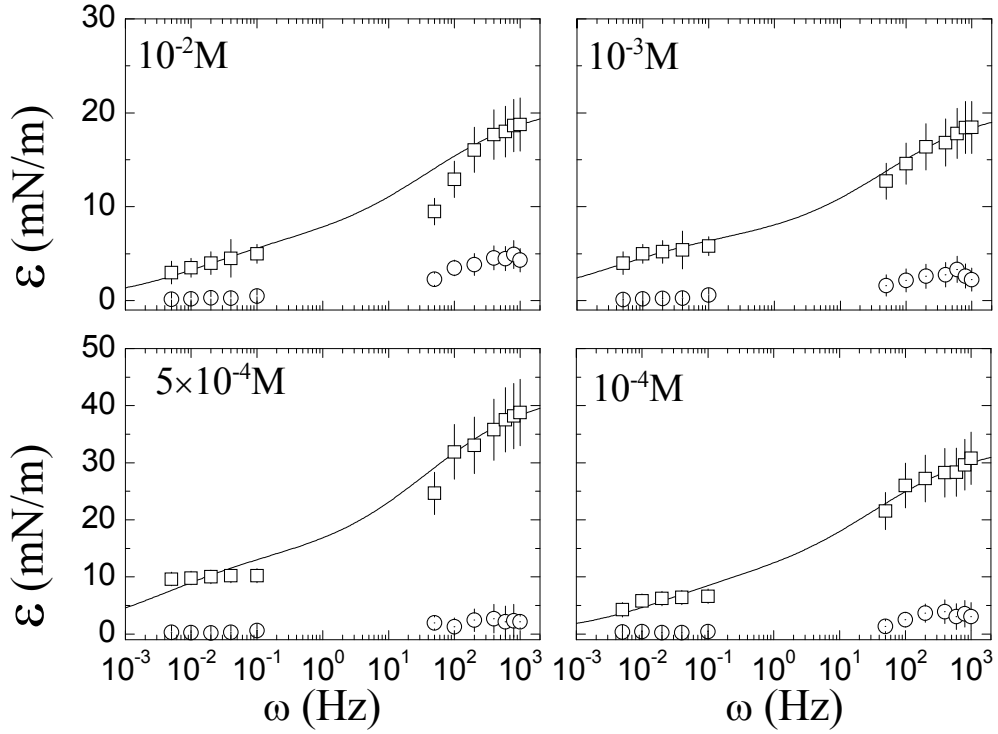

Figure 6.13. Frequency dependence of the dilational elastic modulus ε (□) and the loss modulus ωκ (○) for *BCS-DTAB* adsorbed layers at the air-water interface, taking in account different DTAB bulk concentrations at fixed protein concentration (10^{-6}M). The broad frequency range has been studied by combining ECW and PAT methods. Continuous lines correspond to the fit of the experimental data by Eqs. 6.6-6.7.

In addition, Figure 6.13 also shows the theoretical curves predicted by the theoretical model proposed in section 2 (Equations 6.5–6.7).[31, 40] with the thermodynamic parameters given in Table 6.2 obtained in a previous thermodynamic description of the BCS–DTAB adsorption layers.[11, 12] The predictions are reasonable over the whole surfactant concentration range. However, as explained above this model,[31] is not enough for understanding the complex behaviour of mixed adsorption layers. This direct fitting of the data leads to effective diffusion coefficients; we have found that the *effective* diffusion coefficient slightly vary with surfactant concentration. The mean value of $D_{complex}$ = 2.9±0.4×$10^{-11}$$m^2$/s and D_{DTAB} = 3.1±0.4×$10^{-10}$$m^2$/s which have been found are in concordance with the respective diffusion coefficients for the pure BCS and DTAB.

The different values found between the complex and the pure DTAB layers are related to the structure adopted by the BCS–DTAB layer, which depends strongly on the surfactant concentration, as expected from previous studies about the adsorption thermodynamic of these systems.[11, 31] The dilational viscoelastic

behaviour of the BCS–DTAB interfacial layers as a function of surfactant concentration is shown in Figure 6.14. We have evaluated two values of frequency measured by ECW (50 and 800Hz), and the viscoelastic behaviour of the pure DTAB adsorbed layer at the same frequencies.

Table 6.2 Fit Parameters from the Adsorption isotherm of BCS-DTAB mixture obtained from ref. 11. These parameters are also necessary to fit the dilational rheology of these mixtures.

	Ω_0 $(10^5 m^2/mol)$	Ω_1 $(10^6 m^2/mol)$	Ω_{max} $(10^7 m^2/mol)$	a_{ps}	
BCS	2.2	3.0	4.0	1.1	
	Ω_{S0} $(10^5 m^2/mol)$	a_s $(10^6 m^2/mol)$	as_{ps} $(10^7 m^2/mol)$	ε_s $(10^{-3} m/mN)$	m
DTAB	2.1	0.0	0.0	8.0	8.0

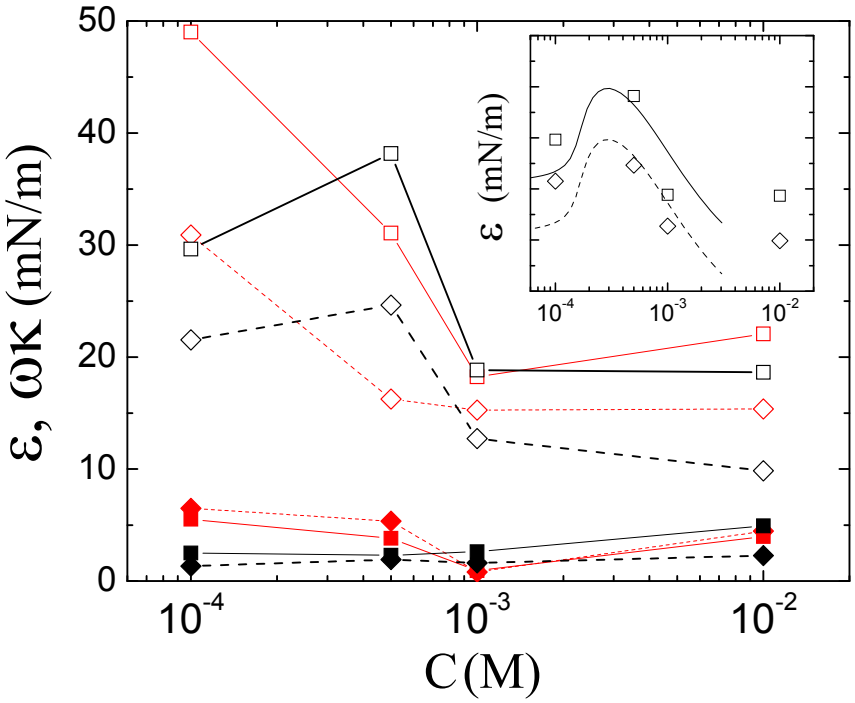

Figure 6.14. Dilational elastic module ε and loss module ωκ for *BCS-DTAB* adsorbed layers as a function of *DTAB* concentration. Two frequencies were evaluated: 800Hz (□,■) and 50Hz (◇,◆); filled symbols correspond to ε and open ones to ωκ. It is also included the parameters ε (△) and ωκ (▲) of pure *DTAB* adsorbed layers at the same frequencies: 800Hz (□,■) and 50Hz (◇,◆) from Figure 6.6. Curves are theoretical fittings using Eqs. 6.5–6.7. Inset: Experimental points as in the main figure and curves correspond to the theoretical fittings using Eqs. 6.5–6.7.

It is well known that ionic surfactants, such as DTAB, fix more strongly the proteins to the interface that the non-ionic ones. The formation of the complex is based on ionic and hydrophobic interactions, and depends strongly on the surfactant concentration (see Figure 6.15). Indeed, the observed viscoelastic behaviour is due to the superposition of the contributions of the protein-surfactant complex and the free surfactant molecules. As expected, with increasing total concentration of surfactant the elasticity pass trough a minimum due to the protein

hydrophilization, and then increases due to the increasing amount of adsorbed surfactant. The subsequent decrease is caused by the increasing exchange of surfactant molecules. The curves in the inset of Figure 6.14 represent the theoretical fitting as explained above. There is a good agreement between the theory and the experimental data in the description of the maximum in the dilational elastic module. However, at high DTAB concentration the theory fails; the deviation between the theory and the experiments at high surfactant concentrations can be explained by the fact that, the theory does not properly take into account the depletion of the protein by surfactants interaction.

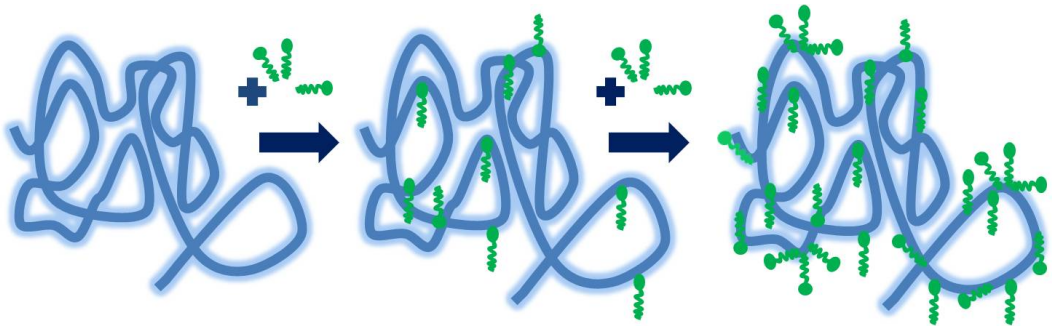

Figure 6.15. The addition of a cationic surfactant, such as DTAB, to a BCS solution leads to a complex formation, first via stronger ionic interaction resulting in an increased hydrophobicity and hence higher surface active complexes, and then by additional hydrophobic interactions leading again to a more hydrophilic and therefore less surface active complex as compared with the original protein.

This general picture is in agreement with previously studies of Mackie et al., which assumed the existence of a competitive adsorption of both surfactant and complex at lower surfactant concentrations followed by a displacement of the protein by the surfactant at higher concentrations.[41-43] Besides this assumption, it is also convenient to indicate that the displacement of protein-surfactant complex via the displacement of the protein must be due to its molecular hydrophilization via hydrophobic interaction with surfactant molecules as suggested Kotsmar et al. in a previous work.[5]

As a final remark, we have found larger values of dilational elastic module for mixtures with C_{12}DMPO compared with DTAB in the whole surfactant concentration regime shown by Figures 6.11 and 6.14. This fact can be explained by small changes in the structure of the BCS due to the interaction with the surfactants, which in turn allows a more effective interaction between the protein molecules. The results suggest, that these changes are more pronounced for C_{12}DMPO than for DTAB. The reason can probably be found in the different types of interaction between the different species, i.e. hydrophobic and electrostatic.

5. Conclusions

The dilational viscoelastic behaviour of BCS–C_{12}DMPO and BCS–DTAB adsorption layers at the air-water interface have been investigated by the combination of the drop profile analysis tensiometry in the low frequency range and excited capillary waves in the high-frequency domain. Previously experiments performed by other authors[11, 12], which study the adsorption isotherms of the single components and the mixtures suggest, that the BCS molecules can be displaced from the surface by the surfactant molecules. The dilational rheology studied in this work confirms these findings. The interfacial dynamical experiments show that the composition of the layers can differ depending on the surfactant concentration and nature. Our results suggest that for both complex BCS–surfactant the characteristics of the mixed layers are essentially corresponding to a competitive adsorption mechanism. Hence, we have demonstrated that further increase of the surfactant concentration results in a decrease of the viscoelastic module values indicating the protein displacement. It is remarkable that the different values found for both surfactants, in the whole surfactant concentration, mainly higher in mixtures with C_{12}DMPO as compared to those with DTAB. Indeed, probably C_{12}DMPO displaces the protein molecules more efficiently from the surface, which correlates to its higher surface activity as compared to DTAB. This fact could be due by small changes in the structure of the BCS due to interaction with the surfactants because C_{12}DMPO interacts more efficiently with BCS than DTAB.

We have used a theoretical model previously published by other authors[5, 31] for a quantitative description of the dilational rheology of the surface layers of single components and their mixtures. There is some mismatch between the experimental results and the theoretical curves for the dilational rheology in the region of interfacial competition. This can be explained by the fact, that the theory requires refinement in order to better account for the particular interfacial properties of the protein-surfactant complexes in this concentration range.

6. References

1. Dickinson, E.; Walstra, P., *Food Colloids and Polymers: Stability and Mechanical Properties*. Royal Soc. Chem.: Cambridge, 1993.
2. Dickinson, E.; Miller, R., *Food Colloids - Fundamentals of Formulation; Special Publication n°258*. Royal Society of Chemistry: London, 2001.
3. Miller, R.; Fainerman, V. B.; Makievski, A. V.; Kragel, J.; Grigoriev, D. O.; Kazakov, V. N.; Sinyachenko, O. V., Dynamics of protein and mixed protein/surfactant adsorption layers at the water/fluid interface. *Advances in Colloid and Interface Science* **2000,** 86, (1-2), 39-82.
4. Kragel, J.; Grigoriev, D. O.; Makievski, A. V.; Miller, R.; Fainerman, V. B.; Wilde, P. J.; Wustneck, R., Consistency of surface mechanical properties of spread protein layers at the liquid-air interface at different spreading conditions. *Colloids and Surfaces B-Biointerfaces* **1999,** 12, (3-6), 391-397.
5. Kotsmar, C.; Pradines, V.; Alahverdjieva, V. S.; Aksenenko, E. V.; Fainerman, V. B.; Kovalchuk, V. I.; Kragel, J.; Leser, M. E.; Noskov, B. A.; Miller, R., Thermodynamics, adsorption kinetics and rheology of mixed protein-surfactant interfacial layers. *Advances in Colloid and Interface Science* **2009,** 150, (1), 41-54.
6. Green, R. J.; Su, T. J.; Joy, H.; Lu, J. R., Interaction of Lysozyme and Sodium Dodecyl Sulfate at the Air−Liquid Interface. *Langmuir* **2000,** 16, 5797-5805.
7. Green, R. J.; Su, T. J.; Lu, J. R.; Pendfold, J. J., The Interaction between SDS and Lysozyme at the Hydrophilic Solid−Water Interface. *J Phys Chem B* **2001,** 105, 9331-9338.
8. Kragel, J.; O'Neill, M.; Makievski, A. V.; Michel, M.; Leser, M. E.; Miller, R., Dynamics of mixed protein-surfactant layers adsorbed at the water/air and water/oil interface. *Colloids and Surfaces B-Biointerfaces* **2003,** 31, (1-4), 107-114.
9. Vysotsky, Y. B.; Bryantsev, V. S.; Fainerman, V. B.; Vollhardt, D.; Miller, R.; Aksenenko, E. V., Transition state for aggregation and reorganization of normal fatty alcohols at the air/water interface. *Journal of Physical Chemistry B* **2004,** 108, (24), 8330-8337.
10. Kotsmar, C.; Grigoriev, D. O.; Makievski, A. V.; Ferri, J. K.; Kragel, J.; Miller, R.; Mohwald, H., Drop profile analysis tensiometry with drop bulk exchange to study the sequential and simultaneous adsorption of a mixed

beta-casein/C12DMPO system. *Colloid and Polymer Science* **2008,** 286, (8-9), 1071-1077.

11. Kotsmar, C.; Grigoriev, D. O.; Xu, F.; Aksenenko, E. V.; Fainerman, V. B.; Leser, M. E.; Millert, R., Equilibrium of Adsorption of Mixed Milk Protein/Surfactant Solutions at the Water/Air Interface. *Langmuir* **2008,** 24, (24), 13977-13984.
12. Kotsmar, C.; Kragel, J.; Kovalchuk, V. I.; Aksenenko, E. V.; Fainerman, V. B.; Miller, R., Dilation and Shear Rheology of Mixed beta-Casein/Surfactant Adsorption Layers. *Journal of Physical Chemistry B* **2009,** 113, (1), 103-113.
13. Pradines, V.; Kragel, J.; Fainerman, V. B.; Miller, R., Interfacial Properties of Mixed beta-Lactoglobulin-SDS Layers at the Water/Air and Water/Oil Interface. *Journal of Physical Chemistry B* **2009,** 113, (3), 745-751.
14. Makievski, A. V.; Fainerman, V. B.; Bree, M.; Wustneck, R.; Kragel, J.; Miller, R., Adsorption of proteins at the liquid/air interface. *Journal of Physical Chemistry B* **1998,** 102, (2), 417-425.
15. Mellema, M.; Clark, D. C.; Husband, F. A.; Mackie, A. R., Properties of beta-casein at the air/water interface as supported by surface rheological measurements. *Langmuir* **1998,** 14, (7), 1753-1758.
16. Fainerman, V. B.; Miller, R., Equation of state for concentrated protein surface layers at the water/air interface. *Langmuir* **1999,** 15, (5), 1812-1816.
17. Makievski, A. V.; Loglio, G.; Kragel, J.; Miller, R.; Fainerman, V. B.; Neumann, A. W., Adsorption of protein layers at the water/air interface as studied by axisymmetric drop and bubble shape analysis. *Journal of Physical Chemistry B* **1999,** 103, (44), 9557-9561.
18. Miller, R.; Fainerman, V. B.; Makievski, A. V.; Grigoriev, D. O.; Kragel, J., Dynamic properties of proteins at liquid interfaces. *Abstracts of Papers of the American Chemical Society* **1999,** 217, 016-PMSE.
19. Mackie, A. R.; Husband, F. A.; Holt, C.; Wilde, P. J., Adsorption of beta-Lactoglobulin variants A and B to the air-water interface. *International Journal of Food Science and Technology* **1999,** 34, (5-6), 509-516.
20. Sukhishvili, S. A.; Granick, S., Adsorption of human serum albumin: Dependence on molecular architecture of the oppositely charged surface. *Journal of Chemical Physics* **1999,** 110, (20), 10153-10161.
21. Mobius, D.; Miller, R., *Proteins at Liquid Interfaces. Studies in Interface Science*. Elsevier: Amsterdam, 1998.

22. Maldonado-Valderrama, J.; Martin-Molina, A.; Martin-Rodriguez, A.; Cabrerizo-Vilchez, M. A.; Galvez-Ruiz, M. J.; Langevin, D., Surface properties and foam stability of protein/surfactant mixtures: Theory and experiment. *Journal of Physical Chemistry C* **2007,** 111, (6), 2715-2723.

23. Noskov, B. A.; Latnikova, A. V.; Lin, S. Y.; Loglio, G.; Miller, R., Dynamic surface elasticity of beta-casein solutions during adsorption. *Journal of Physical Chemistry C* **2007,** 111, 16895-16901.

24. Horne, D. S.; Leaver, J., Milk proteins on surfaces. *Food Hydrocolloids* **1995,** 9, 91-95.

25. Kovalchuk, V. I.; Kragel, J.; Makievski, A. V.; Ravera, E.; Liggieri, L.; Loglio, G.; Fainerman, V. B.; Miller, R., Rheological surface properties of C12DMPO solution as obtained from amplitude- and phase-frequency characteristics of an oscillating bubble system. *Journal of Colloid and Interface Science* **2004,** 280, (2), 498-505.

26. Fainerman, V. B.; Leser, M. E.; Michel, M.; Lucassen-Reynders, E. H.; Miller, R., Kinetics of the desorption of surfactants and proteins from adsorption layers at the solution/air interface. *Journal of Physical Chemistry B* **2005,** 109, (19), 9672-9677.

27. Lee, L. T.; Mann, E. K.; Guiselin, O.; Langevin, D.; Farnoux, B.; Penfold, J., Polymer surfactant films at the air-water-interface .2. a neutron reflectivity study. *Macromolecules* **1993,** 26, (25), 7046-7052.

28. Stenvot, C.; Langevin, D., Study of viscoelasticity of soluble monolayers using analysis of propagation of excited capillary waves. *Langmuir* **1988,** 4, (5), 1179-1183.

29. Miller, R.; Alahverdjieva, V. S.; Fainerman, V. B., Thermodynamics and rheology of mixed protein-surfactant adsorption layers. *Soft Matter* **2008,** 4, (6), 1141-1146.

30. Miller, R.; Fainerman, V. B.; Leser, M. E.; Michel, M., Kinetics of adsorption of proteins and surfactants. *Current Opinion in Colloid & Interface Science* **2004,** 9, (5), 350-356.

31. Aksenenko, E. V.; Kovalchuk, V. I.; Fainerman, V. B.; Miller, R., Surface dilational rheology of mixed Surfactants layers at liquid interfaces. *Journal of Physical Chemistry C* **2007,** 111, 14713-14719.

32. Lucassen, J.; Van der Tempel, M., Dynamic measurements of dilational properties of a liquid interface. *Chemical Engineering Science* **1972,** 27, (6), 1283.

33. Liggieri, L.; Ferrari, M.; Mondelli, D.; Ravera, F., Surface rheology as a tool for the investigation of processes internal to surfactant adsorption layers. *Faraday Discussions* **2005**, (129), 125-40.

34. Lucassen, J.; Vandente.M, Longitudinal waves on viscoelastic surfaces. *Journal of Colloid and Interface Science* **1972,** 41, (3), 491-498.

35. Lunkenheimer, K.; Haage, K.; Miller, R., On the adsorption properties of surface-chemically pure aqueous solutions of n-alkyl-dimethyl and n-alkyl-diethyl phosphine oxides. *Colloids and Surfaces* **1987,** 22, (2), 207-214.

36. Loglio, G.; Pandolfini, P.; Miller, R.; Makievski, A. V.; Ravera, F.; Ferrari, M.; Liggieri, L., Drop and bubble shape analysis as a tool for dilational rheological studies of interfacial layers. *Novel Methods to Study Interfacial Layers* **2001,** 11, 439-483.

37. Kotsmar, C.; Arabadzhieva, D.; Khristov, K.; Mileva, E.; Grigoriev, D. O.; Miller, R.; Exerowa, D., Adsorption layer and foam film properties of mixed solutions containing beta-casein and C12DMPO. *Food Hydrocolloids* **2009,** 23, (4), 1169-1176.

38. Wantke, K. D.; Fruhner, H., Determination of Surface Dilational Viscosity Using the Oscillating Bubble Method. *Journal of Colloid and Interface Science* **2001,** 237, 185-199.

39. Miller, R.; Liggieri, L. Eds., *Interfacial Rheology*. VSP: UK, 2009.

40. Kotsmar, C.; Pradines, V.; Alahverdjieva, V. S.; Aksenenko, E. V.; Fainerman, V. B.; Kovalchuk, V. I.; Kragel, J.; Leser, M. E.; Noskov, B. A.; Miller, R., Thermodynamics, adsorption kinetics and rheology of mixed protein-surfactant interfacial layers. *Adv Colloid Interface Sci* **2009,** 150, (1), 41-54.

41. Mackie, A. R.; Gunning, A. P.; Wilde, P. J.; Morris, V. J., Orogenic displacement of protein from the air/water interface by competitive adsorption. *Journal of Colloid and Interface Science* **1999,** 210, (1), 157-166.

42. Mackie, A. R.; Gunning, A. P.; Ridout, M. J.; Wilde, P. J.; Patino, J. R., In situ measurement of the displacement of protein films from the air/water interface by surfactant. *Biomacromolecules* **2001,** 2, (3), 1001-1006.

43. Gunning, P. A.; Mackie, A. R.; Gunning, A. P.; Woodward, N. C.; Wilde, P. J.; Morris, V. J., Effect of surfactant type on surfactant-protein interactions at the air-water interface. *Biomacromolecules* **2004,** 5, (3), 984-991.

Part IV

Particle monolayers:
Two dimensional microrheology

Aim

Recently, a new emergent rheological tool denominated *microrheology* has appeared. It makes possible to study the rheology of bidimensional systems such as surfactant or polymer monolayers at fluid interfaces by measuring the Brownian trajectories of microparticles also attached at the interfaces. Within this perspective, the part is organized as follows:

In **chapter 7,** we address a systematic study of several factors that affects to the particles attached at fluid-liquid interfaces to understand well the attachment process. We have demonstrated that the contact angle of the particles adsorbed at interfaces, which marks their hydrophobicity, could be affected by the spreading solvent used, as well as their chemical nature and size. To obtain reliable values of the contact angle we have used different techniques. In **chapter 8,** we address the study of the shear viscoelasticity of PTBA monolayers spread at the air-water interface by following the passive motion of beads also spread at the interface. We have used different theoretical approaches for describing the hydrodynamic of a particle trapped at a polymer monolayer, in order to compare the results obtained.

Chapter 7

Contact angle of microparticles at fluid interfaces: Spreading solvent effect and comparison of measuring methods

Abstract

We address a systematic study of the three-phase contact angle, θ of microparticles at flat fluid–liquid interfaces by using different experimental methods. We measured the dependence of θ not only on the particle chemical composition and size, but also on the solvent used to spread the microparticles onto the fluid interface. We found a non-expected and non-regular dependence of θ with size, chemical nature and spreading solvent used for the different particles studied. We propose that these dependences are due to porosity/roughness of the particles that allows the adsorption of the spreading solvent onto the solid particle surface. This conclusion is supported by the values of the line tensions estimated for the different systems.

1. Introduction

Colloidal particles can accumulate onto the interface dividing two immiscible fluid phases and stabilize foams and emulsions by slowing down the three processes that lead to the phase separation: drainage, coarsening and coalescence[1]. This fact was discovered at the beginning of the last century by Ramsden[2] and rediscovered by Pickering[3, 4] some years later but then forgotten until the appearance of the work of Menon and coworkers on water-oil emulsions in 1987.[5] Since those early works the interest on dispersed systems stabilized by particles has increased much due to the new way for producing nano or micro structured materials, and the range of applications of such particles. For instance, Dinsmore et al.[6] reported a novel method to fabricate permeable solid capsules by assembling particles at the surface of an aqueous drop in a continuous oil phase. These capsules called *Colloidosomes*, allow one to encapsulate a wide range of active molecules, which may be delivered in a controlled way. Particles at fluid interfaces are also important from the environment point of view (e.g. by reducing the use of standard surfactants) in water treatment and recycling flotation process.[7] Recently, particles attached to fluid interfaces or in confined environments (membranes, cells) have been used as probes to measure the surface shear viscoelasticity of those systems by following their Brownian motion. This methodology leads to a new rheological technique called micro- or nano-rheology, depending of the size of the particles, with several advantages over traditional methods.[8]

The behaviour of particles at interfaces (structure, interaction forces and dynamics) is also important because they can be used as a model system to study 2D or quasi-2D colloidal organization. The structure and dynamics of these systems has been studied mainly at flat fluid-fluid interfaces (air/oil-water) such as Langmuir films[9-11]. To prepare Langmuir monolayers of particles, they are deposited onto an interface using a spreading solvent, usually an alcohol. The basic knowledge on particles at flat liquid interfaces was reviewed by Aveyard et al. and Binks et al. [12, 13]. The traditional method to characterize these particle monolayers are based in the study of the surface pressure–area (Π–A),[14-17] isotherms. For microparticles, these monolayers can be also characterized by video-microscopy obtaining information about their structure and dynamical behaviour.[18] The forces between particles at the monolayer have been studied by using laser tweezers, and also different theoretical models of the pair interaction potential have been propoused.[12, 19-21].

The wettability of the particles has been found to be a key factor in controlling the static and dynamic behavior of particle at the fluid interfaces. This wettability is characterized by the three-phase contact angle θ which is defined as

the angle between the tangents to the solid surface and the interface measured through one of the phases. When the lower subphase is water, particles with angles between $0º < \theta < 90º$ are called hydrophilic, because the particle area immersed into the water phase is larger than the area in contact with the upper phase. On the contrary, particles are called hydrophobic when $90º < \theta < 180º$. Nowadays, it is well known that the contact angle θ determines the type of foam or emulsion formed; for instance, *foams* or *water-in-oil emulsions* are formed if $\theta < 90º$ while *aerosols* or *oil-in-water emulsions* are formed when $\theta > 90º$. The wettability of the particles remarkable affects the free energy of particle detachment, ΔG_d, and thus the particle capability to stabilize foams and emulsions. Pieranski[19] has calculated the detachment free energy for the case of a planar fluid interface as a function of the three phase contact angle:

$$\Delta G_d = \pi a^2 \gamma_0 \left(1 - \left|\cos\theta\right|\right)^2 \qquad (7.1)$$

where a is the particle radius and γ_0 the surface tension. This equation yields a maximum in the free energy of particle detachment at $\theta = 90º$, where ΔG_d is several orders of magnitude greater than the thermal energy $k_B T$, (k_B being the Boltzmann constant), and sufficient to make the particle attachment almost irreversible. On the other hand, ΔG_d decreases to zero at $\theta = 0º$ and $\theta = 180º$ and particles can exhibit a reversible attachment-detachment behaviour.

Different authors have demonstrated that the particle wettability has a dramatic effect on the particle interactions resulting in ordered or disordered structures or aggregation depending on the θ.[12] For instance, Kralchevsky et al.[22] have shown that very hydrophobic silica particles adsorbed at the octane-water interface, with $\theta \approx 130º$, lead to well-ordered monolayers over large distances, while less hydrophobic particles ($\theta \approx 118º$) form large aggregates. Lin and Chen found a 2D solid-like phase, which melts through a hexatic phase for charged polystyrene particles adsorbed at decane-water interface with $\theta \approx 70$.[23, 24] Fernandez-Toledano et al. have proposed a theoretical model of interactions between particles in monolayers, and they have calculated the total pair potential by computing the different interaction terms.[25] The computation of their potential has been done using the Derjaguin approximation over the emergent and immersed parts of the particles which depends on the three phase contact angle. These authors obtained a dependence of the repulsive dipolar interaction potential on θ for different inter-particle distances with a maximum near to 90º in all cases. However above the dipolar interaction decreases several orders of magnitude for θ below 20º and above 120º.[25]

Particles can be used as probes to measure the surface shear viscosity of Langmuir monolayers made of different materials in micro- and nano-rheology experiments. To extract useful information from these experiments one needs to understand the Physics underlying the motion of the particles in a 2D or quasi-2D environment. Here, the contact angle plays a key role in calculating the interfacial shear viscosity from the Brownian trajectories of the particles, as described by Danov et al. and Fischer et al.[18, 26, 27] These authors have calculated the drag force on a small spherical particle attached to interfaces with different viscosities as a function of the contact angle.

The contact angle, measured trough the lower subphase, is given in its simplest way by the Young´s equation, and depends only on the interfacial tensions between the upper (air or oil) and lower (water) phases (γ_0) and the ones between the solid particle and both upper (γ_{po}) and lower phases (γ_{pw}),

$$\cos\theta = \frac{\gamma_{po} - \gamma_{pw}}{\gamma_{wo}} \qquad (7.2)$$

In the last decades increasing number of publications have appeared describing different methods to measure the contact angle θ for microparticles at interfaces.[28] They can be classified in two families: "in situ" methods, based in the direct observation of the particle at the interface; [14] and those in which the forces involved in the adsorption are measured.[28, 29] In contrast to other particle properties, like charge or size, this parameter is hardly accessible experimentally. The direct determination of θ is restricted to particles of sufficiently large size because of the magnification limits. Thus, direct optical microscopy methods are suitable for particle diameters of several tens of micrometers. The determination of θ from a force-distance dependence measured by AFM is also limited by the size of a particle glued to the tip of the cantilever. For further discussion about the direct and indirect methods see ref. [28].

Here we present a systematic study of the contact angle of microparticles adsorbed onto flat liquid-liquid and liquid-gas interfaces as a function of the particle chemical nature and size. We explore for the first time, the influence of the spreading solvent on the measured contact angle and found that the chemical nature of the solvent used strongly modify the measured angles. We have used three different methodologies to measure θ. Concretely, we have used the gel-trapping technique developed by Paunov[30, 31], the method based on the measurement of collapse pressure in a particulate monolayer upon compression in the Langmuir trough[32] and the method based on the excluded-area formalism. [30] It will be shown that the three methods lead to comparable values of θ.

2. Materials and Methods

2.1 Chemicals

Microparticles of different chemical nature and sizes were used in the experiments. (a) Negatively charged surfactant-free polystyrene (PS) microparticles with sulphate functional groups on the surface (Interfacial Dynamics Corporation, USA), with diameters ranging from 0.5 to 5.7 μm. All of them have similar surface charge density (≈ −6 μC / cm^2). (b) Poly(methyl methacrylate) (PMMA) microparticles (Microparticles GmbH, Germany) with two diameters, 1.0 and 2.0 μm. The first ones are electrostatically stabilized by sulphate groups on their surface and the second ones are sterically stabilized by PVAc adsorbed on the surface. (c) Silica-sphere particles (SiO_2) with OH groups at their surface and 1.0 μm in diameter (Sigma-Aldrich, Germany). Water with a resistivity higher than 14 MΩ obtained from a *milli*-Q (Millipore) was used and n-octane (Sigma-Aldrich) filtrated trough an alumina (Al_2O_3) column was used as the oil-subphase. The spreading solvents used were: 2-propanol (*IPA*) (99%) and methanol (MetOH) (99%), used as received from Sigma-Aldrich (Germany).

2.2 Methods

We have used the gel trapping technique (*GTT*) to measure the three-phase contact angle of different sets of PS, silica and PMMA particles spread onto air-water and octane/water interfaces by using MetOH and IPA as spreading solvents. [33] In this technique a non surface active gelling agent (Gellan) is added to the water, the particles are spread onto the interface at about 50 ºC, and after gelling the water phase by cooling the system at room temperature (25ºC), the particle monolayer is detached by using polydimethylsiloxane (PDMS), which is first poured on top of the water and then cured. The surface of PDMS with the particles trapped is imaged with a Scanning Electron Microscope (SEM). The position of the particles with respect to the PDMS surface can then be determined from the SEM images, which provides the necessary information for the determination of the particle contact angle at the initial air-water or oil-water interface. Figure 7.1 shows a typical SEM image. We have chosen this technique because it can also be used to observe the behaviour of all different types of solid particles (nature and size) and at both liquid interfaces[33]. We have also used the method described by Clint and Taylor [32] in which θ is obtained from the Π-A isotherms of the particle monolayers. The surface pressure is defined as usual, $\Pi=\gamma_0-\gamma$, being γ_0 and γ the surface tension of a bare interface and with the monolayer, respectively, and A is the interfacial area. The contact angle is related to the collapse pressure, $\Pi_{collapse}$ (see Figure 7.2) through:

$$\cos\theta = \pm\sqrt{\frac{\Pi_{collapse}\,2\sqrt{3}}{\pi\gamma}} - 1 \qquad (7.3)$$

where $2\sqrt{3}$ is a geometry constant that comes from the hexagonal packing of the particles at the collapse. Hence, by measuring the interfacial tension and collapse pressure we obtain the contact angle.

The third method makes use of the excluded-area formalism[17]. Monolayers composed of a mixture of an insoluble polymer and the microparticles are considered as a binary surfactant monolayer with complete immiscibility of its components. The area occupied by the particles at the interface is then inaccessible for the polymer chains, and therefore, the Π–A isotherms for the mixed monolayer should show a shift towards higher molecular areas, A, when increasing the number of particles, N_p. From the slope of the excluded area as a function of surface pressure, ΔA/Π, the averaged interfacial area occupied by the particles and θ can be calculated as:

$$\frac{d\Delta A}{d\Pi} = -\frac{2N_p\pi a^2{\gamma_0}^2\cos^2\theta_p^0}{\gamma^3} \qquad (7.4)$$

being θ_p^0 the contact angle measured against the liquid phase in the initial uncovered state.

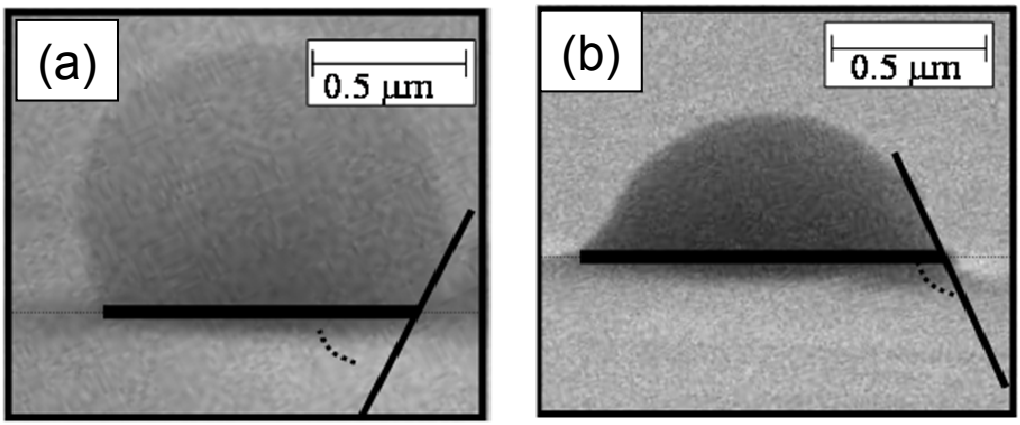

Figure 7.1. Set of SEM images of SiO_2 particles with 1.0 μm in diameter spread onto the octane-water interface with (a) isopropanol and (b) methanol obtained for the GTT methodology. Straight lines show the contact line of the particle at the PDMS surface which allows one to calculate θ.

3. Results and Discussion

Let us first report the different methodologies to determinate θ used in this work. Figure 7.1 shows a set of images obtained by SEM of SiO_2 particles trapped in PDMS using the GTT technique corresponding to identical particles spread

with methanol (Fig. 7.1a) and with isopropanol (Fig 7.1.b) onto the octane-water interface.

One can clearly observe that the contact angles depend on the spreading solvent. This change in the contact angle θ could be due to the different surface activity of the alcohols that will change γ_0 and according to Young's equation. To test this possibility, we have performed control experiments by spreading the same amounts of methanol and isopropanol that are added when spreading the particles. The surface tension measured at both interfaces (air/octane-water) did not change with the added amount of alcohols, (volume spread is less than 0.1%) which means that the change in the contact angle cannot be attributed to the adsorption of the alcohols onto the interface. Table 7.1 summarizes all the contact angle measured by the GTT technique of particles with different chemical nature (PS, PMMA, and SiO_2) attached to the air-water and oil-water interface as a function of their diameter σ, and for two different spreading solvents (methanol and isopropanol).

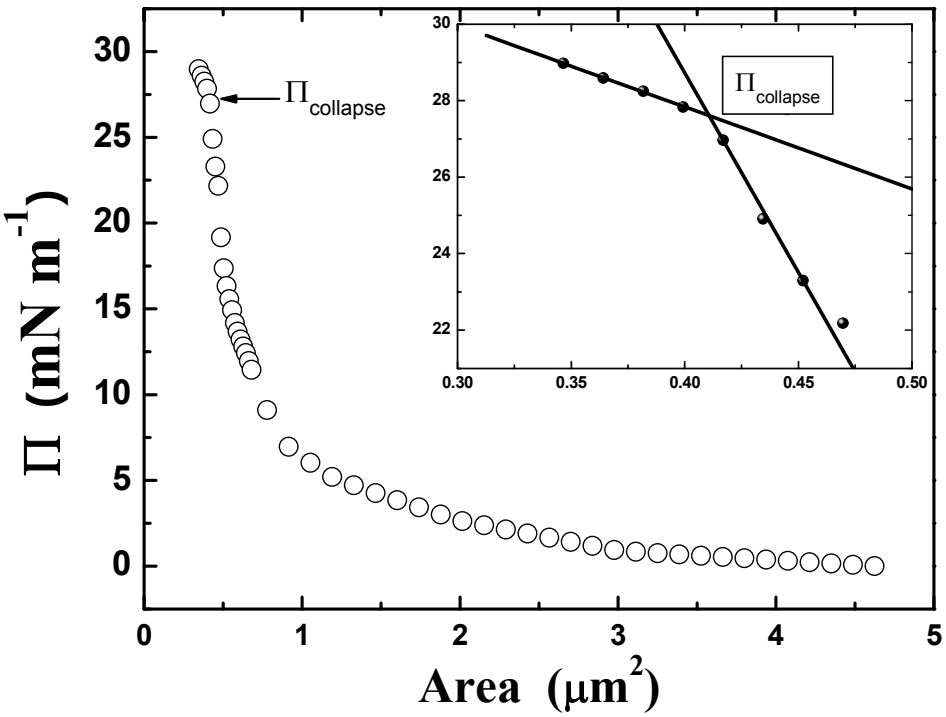

Figure 7.2. Surface preasure-area isotherm for 0.5 μm PS particles at octane-water interface. The inset shows the collapse presure, $\Pi_{collapse}$, obtained by the locus of the change slope. The surface presure due to the spreading solvent is neglectid because the small amount inyected vs. the total water volume.

Figure 7.2 shows as example a surface pressure-area (Π–A) isotherm of a monolayer of PS particles (σ = 0.548 mm) at the octane-water interface. At high areas the surface pressure is very low, when the area is reduced particles begin to

interact and the surface pressure increases until a kink which corresponds with the collapse pressure ($\Pi_{collapse}$) of the monolayer. We have calculated the $\Pi_{collapse}$ as the locus of the slope change (inset in Figure 7.2). From $\Pi_{collapse}$ and using Equation 7.3 we obtained two solutions $\theta = 77.6º$ and 102.4º. As can be seen in the Table 7.1 the first value is in accordance with the contact angle obtained by the GTT technique.

Table 7.1. Three-phase contact angle of microparticles with different nature attached to air/oil-water interfaces and different spreading solvent, i.e., methanol and *iso*propanol.

	Diameter (μm)	*Water / Air*		*Octane / Water*	
		MetOH	*IPA*	*MetOH*	*IPA*
PS	**0.5**	---	---	---	74±5
	1.0	63±7	120±20	0	140±10
	1.6	89±8	88±22	56±6	120±12
	2.9	76±6	59±2	120±18	135±10
	5.7	37±2	0	120±22	120±9
PMMA	**1.0**	18±6	36±6	---	---
	2.0	29±4	56±2	---	---
SiO_2	**1.0**	41±10	70±10	68±6	148±5

Figure 7.3 is an example of the third methodology used to obtain the contact angle based in the excluded-area formalism. It shows the surface pressure-area isotherms Π–A of a monolayer formed by a mixture of a polymer, poly(methyl methacrylate) (PMMA, Molecular weight *Mw* = 270.8 *kDa*) and ca. 12×10^6 and 20×10^6 particles of PMMA (diameter $\sigma = 2\mu m$), respectively. Similar shifts were obtained for other particle concentrations and for the rest of PMMA particles. The inset in Figure 7.3 shows the excluded area by the PMMA particles; i.e., the difference between the area of the monolayer with PMMA particles attached and the area of the monolayer only formed by the polymer. From the slope of the excluded area versus surface pressure $\Delta A/\Pi$ the averaged interfacial area occupied by the particles can be calculated, and from it the contact angle θ of the particles at the interface (Eq. 7.4). For instance, for the PMMA particles (σ = 2μm) both slopes in Figure 7.3, $\Delta A/\Pi$ corresponding to $N=12\times10^6$ and 20×10^6 particles, lead to a mean value of $\theta = 56\pm1º$, which is in excellent agreement with the value obtained by the GTT technique, $\theta_{GTT} = 56\pm2º$. All values obtained with this method agree within 5-10% with the results from the GTT technique.

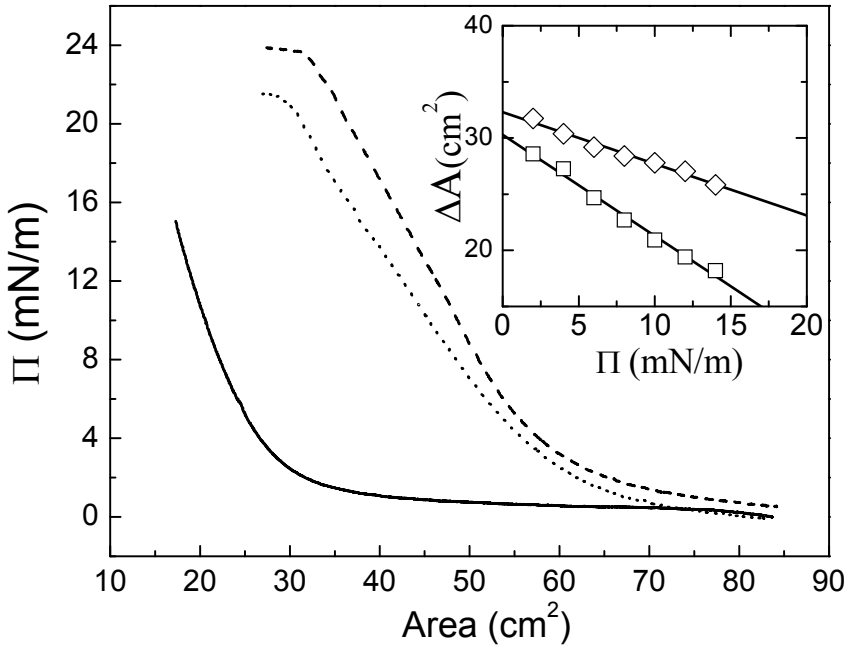

Figure 7.3. Surface pressure-area isotherms Π–A measured for monolayers of poly(methyl methacrylate) (PMMA) Langmuir films. Solid line represent the bare PMMA monolayer, dot line and dashed line represent the PMMA monolayer with 12×10^6 and 20×10^6 particles of PMMA with a diameter $\sigma = 2$ μm respectively. The inset shows the excluded area, i.e., the difference between the area of the monolayer with PMMA particles attached and the area of the monolayer only formed by the polymer as a function of the surface pressure Π. Solid line represent the linear fit of the experimental data. The slope of the fit ΔA/Π is related to the contact angle of the PMMA particles.

The values of θ shown in Figure 7.4 denote the existence of a non-general behavior in the relation of θ with the spreading solvent, hereinafter '*solvent effect'*. The behavior of the contact angle as particle size and spreading solvent change cannot be explained by the Young relation (Eq. 7.1), because it does not take into account the particle size, and it is only valid when particles are completely smooth and adsorbed at the interface without spreading solvent (Gibbs monolayers) as will be demonstrated in the next paragraph. It is well known that real solid surfaces are usually rough and chemically heterogeneous, especially for polymeric/gel particles, which show porosity and high surface roughness.[23, 34] It should be emphasized that the roughness and/or the existence of a heterogeneous surface lead to two important effects. The first one is that roughness magnifies the line tension effect. Three phases in contact meet at a line and then there exist a *line tension* which is expressed as a force or energy per unit length. Line tension can be viewed as the equivalent to the surface tension (energy per unit area for a 2D interface dividing two phases), and it should be considered that for spherical microparticles the effect of τ becomes more important as the radius decreases. In the limit of ideal flat surface $\tau\rightarrow0$ and the original Young equation is recovered. The relevant modification of the Young equation reads:[35]

$$\cos\theta = \cos\theta_{young} - \frac{\tau}{a_c \gamma_{wo}}, \qquad (7.5)$$

where θ_{Young} is the three-phase contact angle from the Young relation, a_c is the radius of the contact line between the three phases and τ is the line tension[36, 37]. Taking into account the roughness of the particles, the second effect mentioned above is related to traces of solvent that could be trapped at the particle surface in the spreading process. Therefore, the surface tensions related by the Young equation (Eq. 2) and then the three-phase contact angle, are affected by the trapped solvent as sketched in Scheme 7.1. In addition, this adsorption will also change the length of the contact line.

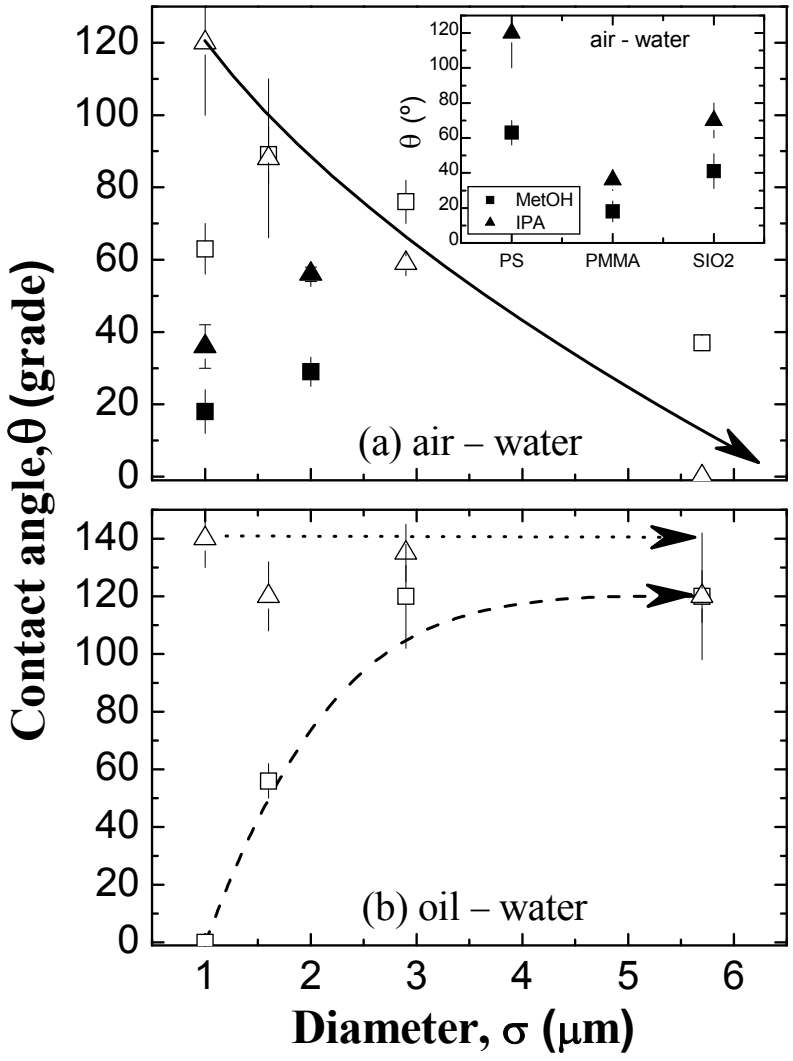

Figure 7.4. Three-phase contact angle θ as a function of the diameter ϕ of the particles attached to the interface (a) air-water and (b) oil-water. The nature of the particles and the spreading solvent as follows: Polystyrene (PS) particles solved in methanol (□), in isopropanol (Δ). Poly(methyl methacrylate) (PMMA) particles in methanol (■) and isopropanol (▲). In (a) the general θ–σ dependency is denoted by a solid line and in (b) the θ–σ behaviour for MetOH and IPA is denoted by a dashed and dot line respectively. Upper inset: Contact angle as a function of the nature of the particles attached at the air-water interface.

Figure 7.4 shows the experimental contact angle θ of particles whose surfaces have different chemical nature (PS, PMMA and SiO_2) attached to the air-water interface (Figure 7.4.a) and octane-water interface (Figure 7.4.b) as a function of their diameter σ, taking into account the different spreading solvent used. We found a general tendency for the values of θ corresponding to PS particles at the air-water interface (spread with both IPA and MetOH); i.e., θ decreases as the diameter of the particle increases which is pointed out by the solid line (Figure 7.4.a.). Particles with different nature (PS, PMMA and SiO_2) spread with IPA leads to higher contact angles than using MetOH, (see inset in Figure 7.4). Figure 7.4.b shows the experimental θ*′s* obtained for PS particles at the oil-water interface. Here, two different behaviors were found: the contact angle θ increases (PS spread from MetOH) or remain constant (from IPA) as the diameter increases. This behaviour is contrary to that described previously for the A/W interface. Thus, we propose that particles spread with IPA are at this interface completely covered with the alcohol molecules leading to a constant contact angle as a function of the particle diameter. To test our hypothesis we have measured the contact angle of PS particles with equal size (2.9 μm), and different charge surface density, (-5.7 and -9.7 μC / cm^2), similar contact angle values were obtained. A possible explanation of this behaviour is that particles are completely covered by a layer of the spreading solvent and as a consequence the nature of the surface does not affect the contact angle.

Scheme 7.1. Detail of the spreading solvent trapped on the roughness of the particle's surface for an arbitrary oil-water interface.

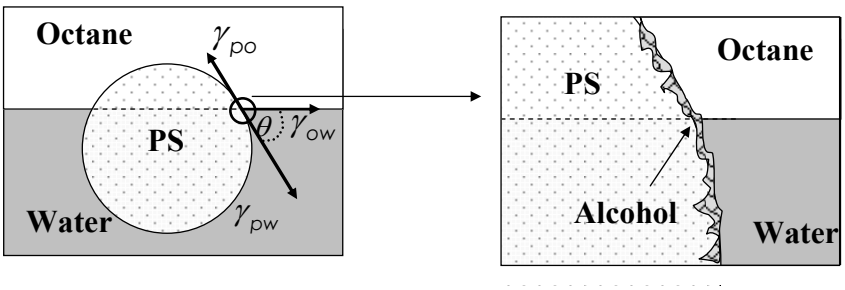

In particular, PS particles with size ranging from 1.0 to 1.6 μm behaves as a completely hydrophilic (θ < 90º) when are spread from MetOH, and are hydrophobic (θ > 90º) when IPA is used as the spreading solvent. IPA is less hydrophilic than MetOH, thus, the contact angle of particles spread with IPA lead to higher contact angles than the same particles spread with MetOH.

In general, the *solvent effect* seems to be more important for small particles. This fact could be due to an increase of roughness and porosity as diameter particles decreases. However, when the particle size increase we suppose that the solvent does not cover completely the surface, thus leading to similar contact

angle for particles spread from different solvents. Unfortunately there are no available experimental data showing the dependence of roughness/porosity on the particle size.

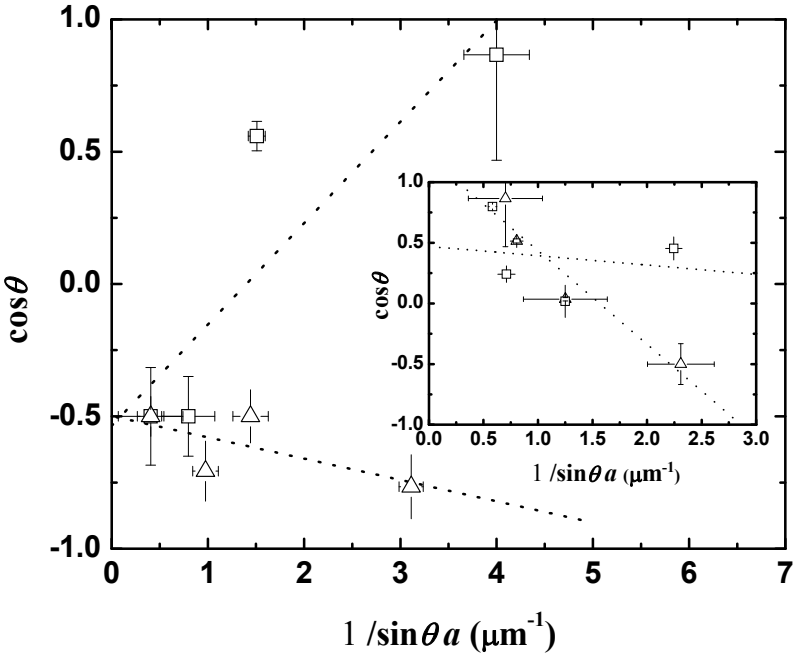

Figure 7.5. *Cos* θ as a function of 1/*a*c (where *ac* = sinθ *σ/2*) PS particles with different diameter (σ) at the oil-water interface. Symbols as follows: Particles spread with methanol (□) and isopropanol (Δ). Dot line represents the best fit of the experimental data by Equation 5. The slope of the fit is related to the line tension τ. Inset: Similar results at the air-water interface.

In addition, we estimate the value of the line tension for our systems using Eq. 7.4. In Figure 7.5, we have plotted *cos* θ as a function of (*a sin* (θ))$^{-1}$ for PS particles spread with both solvents at the octane-water interface and also at the air-water interface as shown the inset in Figure 5. We have consider smooth particles where $a_c = a \sin \theta$. Considering $\gamma_0 = 72$ mN/m for the air-water interface we found $\tau \approx 0.5$ nN and $\tau \approx 5$ nN from the slope for respectively Methanol and IPA. The line tension is much higher for IPA than for Methanol which is a further indication of an interaction between the spreading solvent and the solid particles. For the octane-water interface ($\gamma_0 = 51$ mN/m) and PS particles, we found a negative line tension, $\tau \approx -0.20$ nN for methanol and a positive one with IPA, ($\tau \approx 0.20$ nN), being again a clear indication of a preferential adsorption of the spreading solvent onto the surface of the particles. This is also supported by the values of the ordinate y-intercept of the fitting lines in Figure 7.5, which gives us an estimation of the $\cos(\theta_{Young})$. For the water-octane interfaces these values are negative indicating that the difference between the particle-octane interfacial tension (γ_{po}) minus the particle-water one (γ_{pw}) is negative, i.e $\gamma_{po} < \gamma_{pw}$ which is consistent with the presence of methanol or isopropanol adsorbed onto the solid

surface (the surface tension between methanol or isopropanol and octane is lower than between them and water).

4. Conclusions

This study reveals the non-regular behaviour of the contact angle of particles adsorbed at fluid interfaces with the chemical nature and size of the particles and with the spreading solvent. We have used three different methods to measure the contact angle (explained in the main text) which leads to similar results. We demonstrate how the contact angle θ depends strongly on many commented factors not taken into consideration previously. Our results point out that the roughness and/or porosity of particles plays a key role in the hydrophobicity/hydrophylicity balance of the particles accounting by θ. We highlight the existence of a solvent effect: molecules of solvent can be trapped at the particle surface in the spreading process changing quantitatively the contact angle. This conclusion is supported by the values of the line tensions estimated for the different systems

5. References

1. Stocco, A.; Drenckhan, W.; Rio, E.; Langevin, D.; Binks, B. P., Particle-stabilised foams: an interfacial study. *Soft Matter* **2009,** 5, (11), 2215-2222.
2. Ramsden, W., "Separation of solids in the surface-layers of solutions and 'Suspensions' (Observations on surface-membranes, bubbles, emulsions, and mechanical coagulation). Preliminary Account." *Proceedings of the Royal Society of London* **1903,** 72, (479), 156-164.
3. Pickering, S. U., Emulsions. *J Chem Soc* **1907,** 97.
4. Lucassen-Reynders, E.; van den Tempel, M., Wave damping and Gibbs elasticity for nonideal surface behavior. *J Phys Chem.* **1963,** 67.
5. Menon, V. B.; Nagarajan, R.; Wasan, D. T., Separation of fine particles from nonaqueous media - free-energy analysis and oil loss estimation. *Separation Science and Technology* **1987,** 22, (12), 2295-2322.
6. Dinsmore, A. D.; Hsu, M. F.; Nikolaides, M. G.; Marquez, M.; Bausch, A. R.; Weitz, D. A., Colloidosomes: Selectively permeable capsules composed of colloidal particles. *Science* **2002,** 298, (5595), 1006-1009.
7. Nguyen, A. V.; Schulze, H. J., *Colloidal Science of Flotation*. Marcel Dekker: New York, 2003; Vol. 1.
8. Ortega, F.; Ritacco, H.; Rubio, R., Interfacial microrheology: Particle tracking and related techniques *Current Opinion in Colloid and Interface Science* accepted 2010.
9. Schuker, H., *Kolloid-Z* **1967,** 380, 216.
10. Sheppard, E.; Tcheurekdjian, N., Multiparticle Effects on the Interactions of Complex Colloidal Dispersions. *Journal Colloid Interface Science* **1971,** 28, 481.
11. Doroszkowski, A., *J. Poymer Sci.* **1971,** 34, 253.
12. Binks, B. P., *Colloidal Particles at Liquid interfaces*. UK, 2006.
13. Binks, B. P., Particles as surfactants-similarities and differences. *Current Opinion in Colloids & Interface Science* **2002,** 7, 21.
14. Averyard, R.; Clint, J.-H.; Paunov, V. N., Compresion and structure of monolayers of charged latex particles at air/water and octane interfaces. *Langmuir* **2000,** 16, 1996.
15. Averyard, R.; Clint, J.-H.; Nees, D.; Quirke, N., Structure and Collapse of Particle Monolayers under Lateral Pressure at the Octane/ aqueus Surfactant Solution Interface. *Langmuir* **2000,** 16, 8820.

16. Horozov, T. S.; Averyard, R.; Binks, B. P.; Clint, J. H., Structure and Stability of Silica particles Monolayers at Horizontal and Vertical Octane-Water interfaces. *Langmuir* **2005,** 21, 7405-7412.

17. Hórvölgyi, Z.; Nëmath, S.; Fendle, J. H., Monoparticulate layers of silanizad glass spheres at the water/air interface: particle-particle and particle-subfase interactions. *Langmuir* **1996,** 12, 997-1004.

18. Fischer, T. M.; Dhar, P.; Heinig, P., The viscous drag of spheres and filaments moving in membranes or monolayers. *Journal of Fluid Mechanics* **2006,** 558, 451-475.

19. Pieranski, P., Two-Dimensional Interfacial Colloidal Crystals. *Phys. Rev. Lett.* **1980,** 45, (7), 569.

20. Aveyard, R.; Binks, B. P.; Clint, J. H.; Fletcher, P. D. I.; Horozov, T. S.; Neumann, B.; Paunov, V. N., Measurement of Long-Range Repulsive Forces between Charged Particles at an Oil-Water interface. *Physical Review Letters* **2002,** 88, (24).

21. Martínez-López, F.; Cabrerizo-Vílchez, M. A.; Hidalgo-Alvarez, R., Colloidal Interaction at the Air Liquid Interface. *Journal Of Colloid and Interface Science* **2000,** 232, 303.

22. Kralchevsky, P. A.; Paunov, V. N.; Ivanov, I. B.; Nagayama, K., Capillary meniscus interaction between colloidal particles attached to a liquid-fluid interface. *Journal of Colloid and Interface Science* **1992,** 151, (1), 79-94.

23. Chen, W.; Tan, S. S.; Ng, T. K.; Ford, W. T.; Tong, P., Long-ranged attraction between charged polystyrene spheres at aqueous interfaces. *Physical Review Letters* **2005,** 95.

24. Lin, B. J.; Chen, L. J., Phase transitions in two-dimensional colloidal particle system

observed in Langmuir trough. *Colloids and Surfaces A: Physicochem. Eng. Aspects* **2006,** 284-285, 239-245.

25. Fernandez-Toledano, J. C.; Moncho-Jorda, A.; Martinez-Lopez, F.; Hidalgo-Alvarez, R., Self-assembly in two-dimensions of colloidal particles at liquid mixtures. *Langmuir* **2006,** 22, (16), 6746-6749.

26. Petkov, J. T.; Denkov, N. D.; Danov, K. D.; Velev, O. D.; Aust, R.; Durst, F., Measurement of the drag coefficient of spherical-particles attached to fluid interfaces. *Journal of Colloid and Interface Science* **1995,** 172, (1), 147-154.

27. Danov, K. D.; Dimova, R.; Pouligny, B., Viscous drag of a solid sphere straddling a spherical or flat surface. *Physics of Fluids* **2000,** 12, (11), 2711-2722.

28. Grigoriev, D. O.; Kragel, J.; Dutschk, V.; Miller, R.; Mohwald, H., Contact angle determination of micro- and nanoparticles at fluid/fluid interfaces: the excluded area concept. *Physical Chemistry Chemical Physics* **2007,** 9, (48), 6447-6454.

29. Clint, J. H.; Taylor, S. E., *Colloids Surf* **1992,** 65, 61.

30. Aveyard, R.; Clint, J. H.; Nees, D.; Paunov, V. N., Compression and structure of monolayers of charged latex particles at air/water and octane/water interfaces. *Langmuir* **2000,** 16, (4), 1969-1979.

31. Paunov, V. N., Novel method for determining the three-phase contact angle of colloid particles adsorbed at air-water and oil-water interfaces. *Langmuir* **2003,** 19, (19), 7970-7976.

32. Clint, J. H.; Taylor, S. E., Particle-size and interparticle forces of overbased detergents - a langmuir trough study. *Colloids and Surfaces* **1992,** 65, (1), 61-67.

33. Paunov, V. N., Novel Method for Determininig the three-Phase Contact Angle of Colloid Particles Adserbed At Air-Water and Oil-Water Interfaces. *Langmuir* **2003,** 19, 7970-7976.

34. Tan, S. S.; Sherman, R. L.; Qin, D. Q.; Ford, W. T., Surface heterogeneity of polystyrene latex particles determined by dynamic force microscopy. *Langmuir* **2005,** 21, (1), 43-49.

35. Good, R. J.; Koo, M. N., Effect of drop size on contact-angle. *Journal of Colloid and Interface Science* **1979,** 71, (2), 283-292.

36. Wolansky, G.; Marmur, A., The Actual Contact Angle on a Heterogeneus Rough Surface in Three Dimensions. *Langmuir* **1998,** 14, 5292-5297.

37. Marmur, A.; Krasovitski, B., Line Tension on Curved Surfaces: Liquid Drops on Solid Micro- and Nanospheres. *Langmuir* **2002,** 18, 8919-8923.

Chapter 8

Particle tracking to characterize the rheology of insoluble Langmuir polymer monolayers

Abstract

We have studied the surface shear viscoelasticity of poly (*tert*-butyl-acrylate) (PTBA) Langmuir monolayers spread at the air–water interface by tracking the Brownian diffusion of tracer particles with different chemical nature and size also spread at the interface. We also report the surface shear moduli calculated from the diffusion coefficients (*D*) of the particles, combined with different theoretical approaches for describing the hydrodynamics of a particle trapped at a polymer monolayer matrix. It has been found that these different theoretical approaches lead to comparable values of the shear interfacial viscosity at different polymer concentrations (Γ) and chain lengths (*N)*. The results demonstrate the consistency of the microrheology techniques used, and also that the existence of entanglements in PTBA monolayers is a reasonable hypothesis, as previously discussed in Chapter 2. However, the values obtained for the interfacial viscosity have been found to be up to 3 orders of magnitude lower than the previous data obtained with macroscopic interfacial shear rheometers.

1. Introduction

Many of the diverse properties of soft materials (polymer solutions, gels, filamentous proteins in cells, etc.) derive from their complex structures and dynamics with multiple characteristic length and time scales. A wide variety of technologies, from paints to foods, from oil recovery to processing of plastics, all rely heavily on understanding the flow of complex fluids.[1, 2]

Rheological measurements on complex materials reveal viscoelastic responses, which depend on the time scale at which the sample is probed. To characterize the rheological response one usually measures the shear or the Young modulus as a function of frequency by applying a small oscillatory strain; typically, commercial rheometers probe frequencies from mHz up to tens of Hz.

Despite standard rheological measurements have been very useful in characterizing soft materials and complex fluids, they are not always well suited for all systems. They need sample volumes larger than a milliliter, thus precluding the study of rare or precious materials, including many biological samples that are difficult to obtain in large quantities. Moreover, conventional rheometers provide an average measurement of the bulk response, and do not allow for local measurements in inhomogeneous systems. To address these issues, a new rheological methodology has emerged that probes the material response on micrometer length scales. *Microrheology* is a term that does not describe one particular technique, but rather a number of approaches that attempt to overcome some limitations of traditional bulk rheology. Advantages over macrorheology include a significantly higher range of frequencies available without time-temperature superposition,[2] the capability of measuring material inhomogeneities that are inaccessible to macrorheological methods, and rapid thermal and chemical homogeneization that allow the transient rheology of evolving systems to be studied.[3] Microrheology methods typically use embedded micron-sized probes to locally deform the sample, permitting the use of very small volumes (~ μl). Macro- and microrheology probe different aspects of the material: the former makes measurements over extremely long (macroscopic) length scales using a viscometric flow field, whereas the latter effectively measures material properties on the scale of the probe itself (since flow and deformation fields decay on this length scale). Detailed descriptions of the methods and applications of microrheology to the study of bulk systems have been given in review articles published in recent years.[4-6]

Interfaces play a dominant role in the behaviour of many complex fluids. Interfacial rheology has been found to be a key factor in the stability of foams and emulsions, compatibilization of polymer blends, flotation technology, fusion of

vesicles, etc.[7] Particle-laden interfaces have attracted much attention in recent years. The tendency of colloidal microparticles to become (almost irreversibly) trapped at interfaces and their behaviour once there, has lead to their use in a wide variety of systems including drug delivery, stabilization of foams and emulsions, froth, flotation, or ice cream production. The high trapping energy of particles at interfaces provides a route to use fluid interfaces as a substrate for the self-assembly of particles into materials of specific mechanical, optical or magnetic properties.[8]

The interactions of the particles at interfaces are expected to be more complex than in the bulk,[9] indeed, the dynamic properties of particle-laden interfaces are strongly influenced by direct interparticle forces (capillary, steric, electrostatic, van der Waals, etc.) and complicated hydrodynamic interactions mediated by the surrounding fluids.[9, 10] At macroscopic scales, the rheological properties of particle-laden fluid interfaces can be viewed as those of a liquid-liquid interface with some effective surface viscoelastic properties described by effective shear and compressional viscoelastic moduli. A significant fact is that for the simplest fluid-fluid interface, different dynamic modes have to be taken into account: the capillary (out of plane) mode, and the in-plane mode, which contains dilational (or extensional) and shear contributions. For more complex interfaces, such as thicker ones, other dynamic modes (bending, splaying) have to be considered.[10] Moreover, the coupling of the abovementioned modes with adsorption/desorption kinetics may be very relevant for interfaces that contain soluble or partially soluble surfactants, polymers or proteins.[11, 12]

In recent years a number of experimental techniques have been developed for studying the dilational rheology in a broad range of frequencies (1mHz – 100 kHz), both in the linear an non-linear regimes.[13, 14] The extended frequency range is a key advantage of the microrheology. Traditional measurements using a macroscopic rheometers can be extended over a limited range, determined primarily by the inertia of the measuring tool. Thus, extending the frequency range is only possible in a limited number of cases trough the use of time-temperature supersposition.[15] In the case of surface shear rheology, most of the information available has been obtained using macroscopic interfacial rheometers which have a sensibility limit of about 10^{-6} $N \cdot s \cdot m^{-1}$,[10, 16, 17] but many important systems have surface shear viscosities below this limit. Particle tracking techniques have been emerged as a powerful method to study the dynamics of interfaces with shear viscosities as low as 10^{-10} $N \cdot s \cdot m^{-1}$. In spite that the measurement of diffusion coefficients of microparticles attached to interfaces is relatively straightforward with modern microrheological techniques, one has to rely on hydrodynamic models of the viscoelastic surroundings traced by the particles in order to obtain variables such as monolayer elasticity or shear

viscosity. The more complex the structure of the interface the stronger are the assumptions of the model, thus resulting in more difficulties in checking their validity.

In general, interface microrheology techniques are adaptations of bulk microrheology techniques. For studying the interfacial viscoelasticity of the probe environment there are two broad types of experimental methods: active methods, which involve probe manipulation, and passive methods, that relay on thermal fluctuations (Brownian motion). Passive techniques are typically more useful for measuring low values of predominantly viscous moduli, whereas active techniques can extend the measurable range to samples with significant elasticity modulus. Concretely, here we use the particle tracking by videomicroscopy, which is a passive bulk microrheology technique adapted to interfaces. From a experimentally point of view, we have chosen it among others because it is the most suitable and simple technique for studying interface microrheology.

The aim of the present work is to briefly demonstrate the validity of the experimental techniques applied to interface dynamics based on the video-analysis the Brownian motion of particles tracers attached at the fluid interface. We will summarize the available theoretical models for calculating the shear viscoelastic complex moduli of polymer Langmuir monolayers from particle tracking experiments. We also discuss the validity of the experimental results of particle tracking performed on poly (*tert*-butyl-acrylate) monolayers at air-water interface using beads with different chemical nature and size as tracers. Finally, we conclude that different microrheological methodologies lead to comparable results, which nevertheless are orders of magnitude far from previously macroscopic ones. The chapter has been organized as follows: Section 2 addresses a theoretical description of the theoretical models suitable for the analysis of the particle trajectories providing the values of the shear complex moduli. Section 3 describes the experimental set-up used and the materials necessary to perform these experiments. Finally, section 4 summarizes the experimental results obtained, and includes a discussion on the validity of the methods in relation to the study of the interfacial shear rheology of polymer monolayers.

2. Theoretical background

2.1 Fundamentals of videomicroscopy particle tracking

The main idea in particle tracking is to follow the trajectories (Brownian motion) of probes introduced into (onto) the system by videomicroscopy. The time evolution of the mean square displacement $< \Delta r^2(\tau) >$ of the particles, either in bulk or on surfaces, can be measured by videomicroscopy. The mean square

displacement (MSD) of the beads reflects the response of the material to the stress applied to it by the thermal motion of the beads and is related to the diffusion coefficient, *D* by the dimensions in which the translational motion takes place, *d* trough the following expression:

$$\left\langle \Delta r^2(\tau) \right\rangle = 2dD\tau^{\alpha} \tag{8.1}$$

where the brackets indicate the average over all the particles.

In case of diffusion in a purely viscous material (or interface), α is equal to 1, and the usual linear relation is obtained between the MSD and the lag time τ. For highly viscous materials or interfaces (like condensed surfactant, lipid monolayers and dense polymer monolayers), or when the system is dominated by the probe particles interactions (being this particularly important at high particle surface coverage) Equation 8.1 does not fully apply. The movement of nano- and micro-particles in these solid-like interfaces cannot simply be interpreted assuming sub-diffusivity $\alpha<1$. In fact, if we consider a Maxwell viscoelasticity model the mean square displacement adopts the form of

$$\left\langle \Delta r^2(\tau) \right\rangle = \frac{\sigma}{G} + \frac{\sigma\tau}{\eta} \tag{8.2}$$

where σ is the stress, *G* is the elasticity modulus and η the viscosity coefficient and all of them refer to pure shear deformations. The characteristic Maxwell time is given by τ_c (= η/G). Anomalous diffusion $\alpha<1$ has been invoked in many systems of biological interest where the Brownian motion of the particles is hindered by obstacles, or even constrained to defined regions (corralled motion).[18]

The diffusion coefficient *D* is related to the friction coefficient, *f*, by the Einstein relation:

$$D = \frac{k_B T}{f} \tag{8.3}$$

In 3D, *f* is given by Stokes law, $f = 6\pi\eta\, a$, where *a* accounts the radius of the spherical beads. For pure viscous fluids the shear viscosity can be directly obtained from the diffusion coefficient $\eta = k_B T/(6\pi\, Da)$. By contrast, the motion of the probe particles in an elastic medium will be constrained and the MSD will reach an average plateau value $< \Delta r^2_p >$ that is set by the elastic modulus of the material.

In general, for the case in which the particles are embedded in a viscoelastic fluid, particle tracking experiments allow one to obtain the viscoelastic moduli of the fluids. Manson and Weitz first in an ad-hoc way, and later Levine and Lubensky in a more rigorous way, proposed a generalization of the Stokes-

Einstein equation (GSE), which accounts the full frequency dependence of the viscoelastic moduli obtained from the MSD:[19, 20]

$$\left\langle \Delta\tilde{r}^2(s) \right\rangle = \frac{2k_BT}{3\pi as\tilde{G}(s)} \tag{8.4}$$

Where $\left\langle \Delta\tilde{r}^2(s) \right\rangle$ is the Laplace transform of the MSD and $\tilde{G}(s)$ is the Laplace transform of the stress relaxation modulus. *s* and *a* account the Laplace frequency, and the radius of the particles respectively. This expression allows one to determinate the macroscopic viscoelasticity of the system from the local response assuming that the bulk stress relaxation has the same behaviour as the local relaxations that affect the bead dynamics. An alternative expression for the GSE equation can be written in the Fourier domain to allow comparison with mechanical measurements where the elastic and viscous moduli are expressed in the Fourier frequency domain.[21] Concretely, The complex shear modulus has been estimated algebraically from the dynamics of the probe particles by using a local power law to describe the MSD of the beads in the complex fluid. The power law behaviour is obtained from the logarithmic time derivate of the MSD. For a particle in a purely viscous medium undergoing diffusive motion, the slope of the logarithmic time derivative of MSD will be one, while for a probe in an elastic environment, where its motion is completely arrester, the slope of the MSD will be zero. Thus, for a complex viscoelastic fluid, the logarithmic time derivative of the MSD will lie between zero and one. In this method the GSE is expressed in the Fourier space domain as follows:[21]

$$\tilde{G}(\omega) = \frac{k_BT}{\pi ai\omega\Im\left\{\left\langle \Delta r^2(\tau) \right\rangle\right\}}, \tag{8.5}$$

where $\Im\left\{\left\langle \Delta r^2(\tau) \right\rangle\right\}$ is the Fourier transform of the MSD. Taking into account a local power law form for $<\Delta r^2(\tau)>$ leads to the following expression for the elastic $G'(\omega)$ and the loss $G''(\omega)$ moduli:

$$\begin{aligned} G'(\omega) &= G(\omega)\cos\left[\pi\alpha(\omega)/2\right] \\ G''(\omega) &= G(\omega)\sin\left[\pi\alpha(\omega)/2\right] \end{aligned} \tag{8.6}$$

Where:

$$G(\omega) = \frac{k_BT}{\pi a\left\langle \Delta r^2(1/\omega) \right\rangle\Gamma\left[1+\alpha(\omega)\right]} \tag{8.7}$$

In Equation 8.7 $<\Delta r^2(1/\omega)>$ is the magnitude of $<\Delta r^2(\tau)>$ evaluated at $\tau = 1/\omega$. The local power law $\alpha(\omega)$ is given by $\left[\partial \ln\left\langle \Delta r^2(\tau) \right\rangle / \partial \ln\tau\right]_{\tau=1/\omega}$ and Γ denotes the

gamma function, which is a result of the Fourier transform of the MSD. Equations 8.5-8.7 satisfy the Kramers-Kronig relations.[15] The GSE equation is valid under the following approximations: (a) The medium around the sphere may be treated as a continuum material, which requires that the size of the particle be larger than any structural length scale of the material. (b) No slip boundary conditions. (c) The fluid surrounding the sphere is incompressible; and (d) there are no inertial effects.

Recently, other different methods have been devised to obtain $\tilde{G}(s)$ from the experimental MSD.[22-24] For instance, Felderhof has presented an alternative method for calculating the shear complex modulus from the velocity autocorrelation function, that can be calculated from the particle trajectories.[24]

When the samples are heterogeneous at the scale of particle size (a situation rather frequent specially in biological systems[18, 25, 26]), single particle tracking gives erroneous results and the so-called "two-point" correlation method is recommended.[27] Two-point microrheology is based on cross correlating the motion of pairs of embedded tracers motion using video particle tracking. Hence, the fluctuations of pairs of particles at a distance R_{ij} are measured for all the possible values of R_{ij} within the system. Vector displacements of individual particles are calculated as a function of lag time, τ, and initial absolute time, t: Then the ensemble averaged tensor product of the vector displacements is calculated: [5, 27, 28]

$$D_{\alpha\beta}(r,\tau) = \left\langle \Delta r_{\alpha}^{i}(r,\tau)\Delta r_{\beta}^{j}(r,\tau)\delta\left[r - R_{ij}(t)\right]\right\rangle_{i\neq j,t}$$
$$\Delta r_{\alpha,\beta}^{i,j}(r,\tau) = r_{\alpha,\beta}^{i,j}(t+\tau) - r_{\alpha,\beta}^{i,j}(t) \qquad (8.8)$$

where i and j label two particles, α and β are coordinate axes and R_{ij} is the distance between particles i and j. The average corresponding to i = j represents the one-particle mean-squared displacement. Two-point microrheology probes dynamics at different lengths from distances much larger than the particle radius down to the particle size, which reflects extrapolation of long-wavelength thermal fluctuations of the medium to the particle size.[29]

2.2 Dynamics of particles at fluid interfaces: Models

For interfaces the situation is more complex than for bulk, and the calculation of the surface shear viscosity has relied on the use of hydrodynamic models of the interface. Only very recently Song et al.[30] have performed computer simulations that indicate that the GSE can be applied to fluid interfaces and has applied the GSE to the study of interfaces in oil-water emulsions.[31] More recently, Kandar et al. have also applied the GSE to particles embedded in Langmuir

monolayers.[32] So far, no comparison has been made between the surface shear viscosity calculated by hydrodynamic models and the GSE.

For particles trapped at interfaces Einstein's equation, Eq.(8.3), is still valid. However, one cannot calculate the friction coefficient using Stokes equation and directly substituting the interfacial shear viscosity. Instead, *f* is a function of the viscosities of the adjacent phases (η's), the geometry of the particle (e.g., the radius "*a*" for spheres), the contact angle between the probe particle and the interface (θ), etc. There is no solution for the slow viscous flow equations for steady translational motion of a sphere in an ideal 2D fluid (Stokes paradox). This problem was first solved by Saffman and Delbrück.[33]

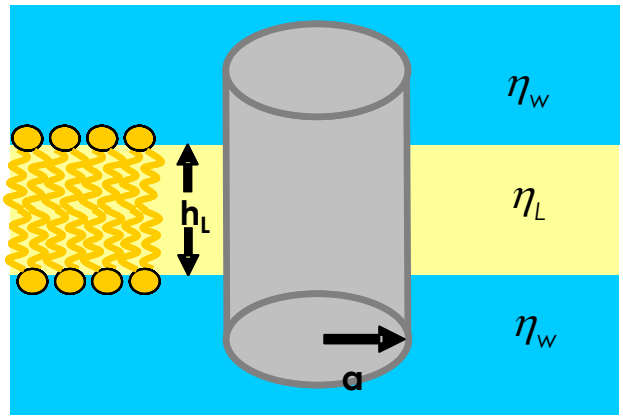

Figure 8.1. Scheme of the *Saffman-Delbrük* model for the diffusion of a cylinder with radius *a* in a fluid membrane of thickness *h*. η_L and η_w represent the viscosities of membrane and liquids respectively.

2.2.1 The Saffman-Delbrük equation

Saffman and Delbrück solved the hydrodynamic problem of a cylinder of radius *a* moving in a highly viscous membrane of thickness *h*.[33] The membrane is considered of infinite size and both phases, above and below the membrane, to be infinite aqueous phases. The cylinder is allowed to move in the plane of the membrane and to rotate around the z-axis. A non-slip boundary condition is assumed at the surface of the cylinder and membrane. The motion of the cylinder produces flow fields in both up and down phases in two ways: directly by the particle surface in contact with the fluid phases and by coupling to the 2D membrane flow fields (note that now the system is 3D avoiding the Stokes' paradox). They obtained the following expression for the translational mobility,

$$b_T = \frac{1}{f} = \frac{1}{4\pi\eta_L h}\left(\ln\left(\frac{\eta_L h}{\eta_w R} - \gamma\right)\right) \qquad (8.9)$$

where η_L and η_w accounts the viscosities of membrane and liquids respectively, and γ the Euler constant. Note that there is no dependence on the cylinder height, because in the derivation it was assumed that $\eta_w <<< \eta_L$.

The Saffman and Delbrück model has been extended for a motion of a thin disk immersed in a membrane of arbitrary viscosity, η_L separating two phases of viscosities η_1 and η_2.[34] The model assumes infinite phases surrounding the membrane. The case of a disk moving in an incompressible surfactant layer overlaying a sub phase of finite depths has been solved by Barentin et al.[35] On the basis of the assumption that the depth of the sublayer is small compared to the radius of the moving disk (lubrication approximation). Stone and Ajdari[36] have solved the problem for sublayers of an arbitrary depth. The solution is given in the form of a system of integral equations that must be solved numerically.

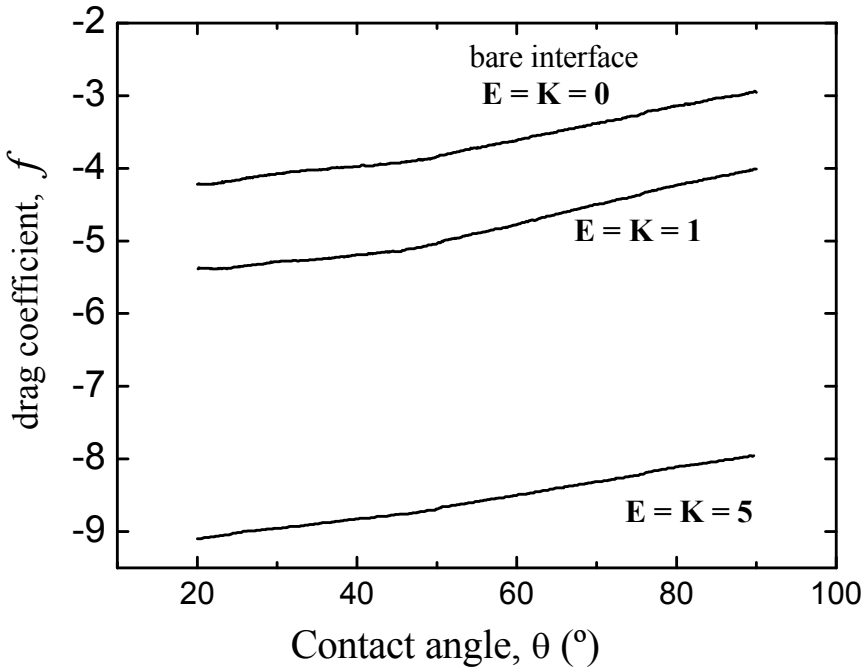

Figure 8.2. Effect of contact angle (θ) on the drag coefficient of a particle trapped at a fluid interface according to Danov's theory.[37, 38] The different lines correspond to the following values of E (=K): 0; 1 and 5.

2.2.2 *Danov's model for a sphere in a compressible surfactant layer*

The above theories are limited to non protruding particles (or high membrane viscosities) however, in particle tracking experiments the spherical particles used as probes are partially immersed in both fluid phases separating the interface. Danov et al. have calculated the hydrodynamic drag force and the torque acting on a micro spherical particle trapped at different interfaces.[37, 38] The interfaces were modeled as a *compressible* 2D-fluid characterized by two

dimensionless parameters K and E defined as $E = \eta_{sh}/(\eta a)$ and $K = \eta_d/(\eta a)$, being η_{sh} and η_d the surface shear and dilational viscosity respectively. Danov et al. assumed that: (1) the movement implies low Reynolds number, thus they ignore any inertial term; (2) the moving particle is not affected by capillarity or electro-dipping; (3) the contact line does not move with respect to the particle surface, and (4) they considered E=K, i.e. the interface is compressible. Taking into account these assumptions, they solved numerically the Navier-Stokes equation to obtain the values of the drag coefficient *f* as a function the contact angle and of E (or K). They addressed their results in graphical form, which are reproduced in Figure 8.2. These curves can be used to obtain the shear viscosity of compressible surfactant layer once one has obtained the diffusion coefficient of the particles by particle tracking experiments, at a surfactant free interface, and in the presence of the surfactant layer.

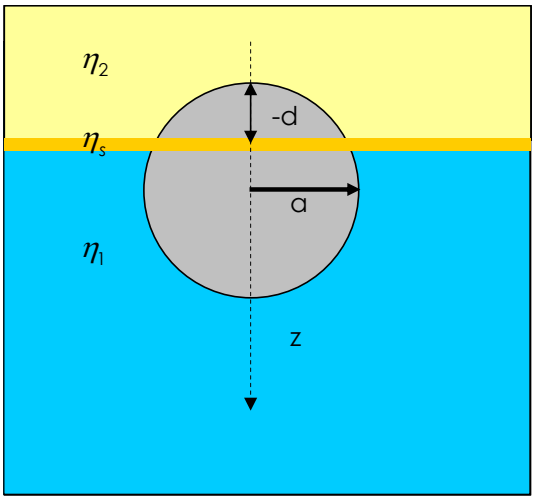

Figure 8.3. Sketch of a sphere immersed in a surface of viscosity η_s between two liquids of infinite depth and viscosity η_1 and η_2.

2.2.3 Fischer's theory for a sphere in a compressible surfactant layer

Fischer, on the basis of that a Langmuir film cannot be considered as a compressible monolayer, has criticized Danov's theory.[39, 40] In the presence of a surfactant, Marangoni forces (forces due to surface tension gradients) strongly suppress the motion of particles that compress or expand the interface due to the corresponding gradient in the surface pressure. Such gradients are instantly compensated by the fast motion of the surfactant at the interface, thus leading to a constant surface pressure, and then behaving as an incompressible monolayer (Fischer assumes that the velocity of the 2D surfactant diffusion is faster than the motion of the beads). The fact that the drag on a disk in a monolayer is that of an incompressible surface has been verified experimentally.[41]

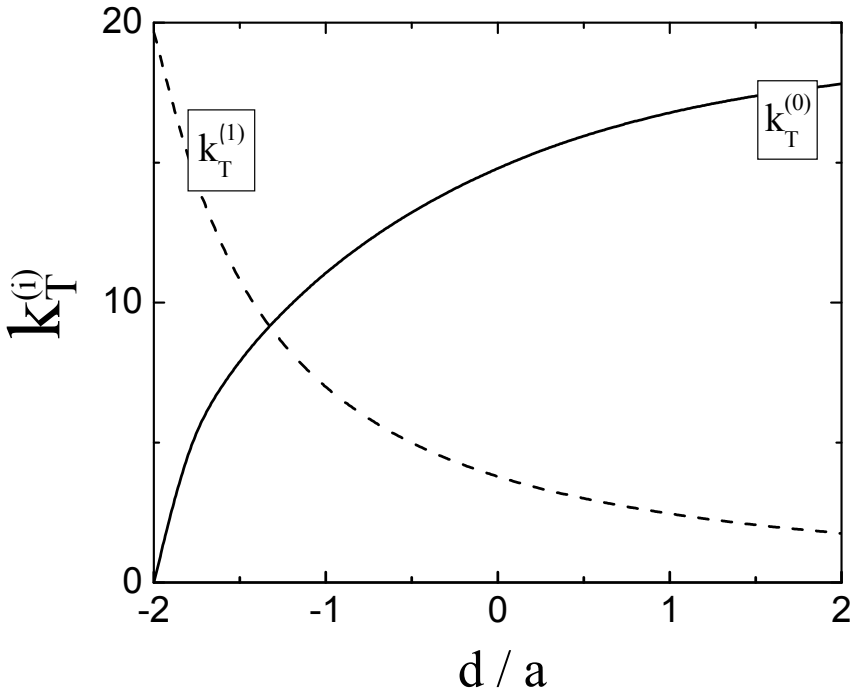

Figure 8.4. Numerical solution for the drag coefficients as a function of the distance of the north pole from the monolayer surface for zero Boussinesq number (*B*=0).

Fischer et al. have numerically solved the problem of a sphere trapped at an interface with a contact angle θ moving in an *incompressible* surface[39] (see Figure 8.3). They showed that contributions due to Marangoni forces account for a significant part of the total drag. This effect becomes most pronounced in the limit of vanishing surface compressibility. In this limit the Marangoni effects are simply incorporated to the model by approximating the surface as incompressible. They resolve the fluid dynamics equations for a 3D object moving in a monolayer of surface shear viscosity, η_s between two infinite viscous phases. The monolayer surface is assumed to be flat (no electrocapillary effects). Then the translational drag coefficient, $k_{T,}$, was expressed as a series expansion of the Boussinesq number, $B = \eta_s / \left((\eta_1 + \eta_2) \times a \right)$, *a* being the radius of spherical particle:

$$k_T = k_T^0 + B k_T^1 + O(B^2) \tag{8.10}$$

For B=0, and for an air-water interface (η_1, η_2=0), the numerical results for $k_T^{(0)}$ and $k_T^{(1)}$ are fitted with an accuracy of 3% by the following expressions:

$$k_T^0 \approx 6\pi \sqrt{\tanh\left(32\left(\frac{d}{R} + 2 \right) \Big/ \left(9\pi^2 \right) \right)} \tag{8.11}$$

$$k_T^{(1)} \approx \begin{cases} -4\ln\left(\frac{2}{\pi}\arctan\left(\frac{2}{3}\right)\right)\left(\frac{a^{3/2}}{(d+3a)^{3/2}}\right) & (d/a>0) \\ -4\ln\left(\frac{2}{\pi}\arctan\left(\frac{d+2a}{3a}\right)\right) & (d/a<0) \end{cases} \quad (8.12)$$

Where d is the distance from the apex of the bead to the plane of the interface (which defines the contact angle). Figure 8.4 plots $k_T{}^{(0)}$ and $k_T{}^{(1)}$ as a function of d/a calculated by Eqs. 8.12–8.13. It is noteworthy that if d goes to infinity, $k_T^0 = 6\pi$, which is the correct theoretical value for a sphere in bulk (Stokes law). They found that, even in the absence of any appreciable surface viscosity, the drag coefficient of an incompressible monolayer is higher than that of a free interface, and the MSD data cannot be used to extract the surface shear viscosity using Danov's theory especially in the limit of low surface viscosities.

3. Materials and Methodology

3.1 Chemicals

To study the shear rheology of poly(*tert*-butyl-acrylate) (PTBA) Langmuir monolayers by particle tracking, we have used several different highly monodisperse samples of PTBA obtained from Polymer Source, Canada, with molecular weights ranging from 1.44×10^3 to 1.095×10^6 g·mol^{-1}. The properties of the samples used have been previously summarized in the Table 2.1 (see Chapter 2). Chloroform (Sigma Aldrich, 99% of purity) was used as spreading solvent. The concentration of the spreading solution was 0.1mg/ml for all the samples. Double distilled and deionized water from a MilliQ-RG system was used to prepare the subphase, having a resistivity higher than 18mΩ·cm^{-1} and a surface tension of γ =72.6mN/m at 20ºC.

Small aliquots of the spreading solution (10-20 μl) were slowly dispensed at different places onto the A/W interface with a Hamilton microsyringe. The polymer concentration was changed by subsequent additions of the spreading solution. Times ranging 15 to 50 min were allowed for solvent evaporation and equilibration. The temperature of the monolayers was controlled by a thermostat and a water jacket of the trough. Near the interface, the temperature was measured with a precision of 0.1ºC, and the temperature control was better than ±0.05 ºC. Care was taken to avoid any changes on the height of the monolayer during the experiments due to evaporation.

Micron-sized spherical particles of different chemical nature and size were used as interfacial probes in the particle tracking methodology performed in this work. (a) negatively charged surfactant-free polystyrene (PS) microparticles with sulphate functional groups on the surface (Interfacial Dynamics Corporation, USA), with diameters 1.6 and 5.7 μm. They have a surface charge density of about - 6 μC / cm^2. (b) Poly(methyl methacrylate) (PMMA) microparticles (Microparticles GmbH, Germany) with two diameters, 1.0 and 2.0 μm. The first ones are electrostatically stabilized by sulphate groups on their surface and the second ones are sterically stabilized by grafted chains of poly (vinyl-acetate) (PVAc) adsorbed on their surface. (c) Silica-sphere particles (SiO_2) with OH groups at their surface and 1.0 μm in diameter (Sigma-Aldrich, Germany). All of them have been spread at the air–water interface using methanol (MetOH) with a purity of 99%, as received from Sigma-Aldrich (Germany). The spreading solution was slowly applied by a micro syringe at different places onto the surface. We have used the gel trapping technique (*GTT*) [42] to measure the three-phase contact angle θ of different sets of PS, silica and PMMA particles spread

onto the air-water interface by using MetOH as spreading solvent (Further information about the determination of θ in chapter 7). Table 8.1 summarizes the properties of the microparticles used in this study.

Table 8.1. Properties such as diameter (σ) and Three-phase contact angle (θ) of microparticles with different nature attached to air -water interfaces by using methanol as spreading solvent.

Chemical nature	*Diameter σ (μm)*	*Contact angle* θ (°)*
PS	**1.6**	**89±8**
	5.7	**37±2**
PMMA	**1.0**	**18±6**
	2.0	**29±4**
SiO_2	**1.0**	**41±10**

*Measured by different experimental techniques (see Chapter 7)

3.2 Particle tracking by videomicroscopy: Methodology

3.2.1 Experimental Set-up

Figure 8.5 shows a sketch of a typical set-up for interface particle tracking experiments. A CCD camera (Hamamatsu photonics UK, about 60-100 fps) is connected to a microscope (Nikon Elipse 80i) that permits to image the interface prepared onto a Langmuir Through (Nima technologies, U.K.). The series of images are transferred to a computer to be analyzed and to extract the trajectories of a set of particles. The experimental set-up has already been described elsewhere.[43] All the experiments performed in this chapter have been conducted at controlled temperature, being 23±1 *ºC*.

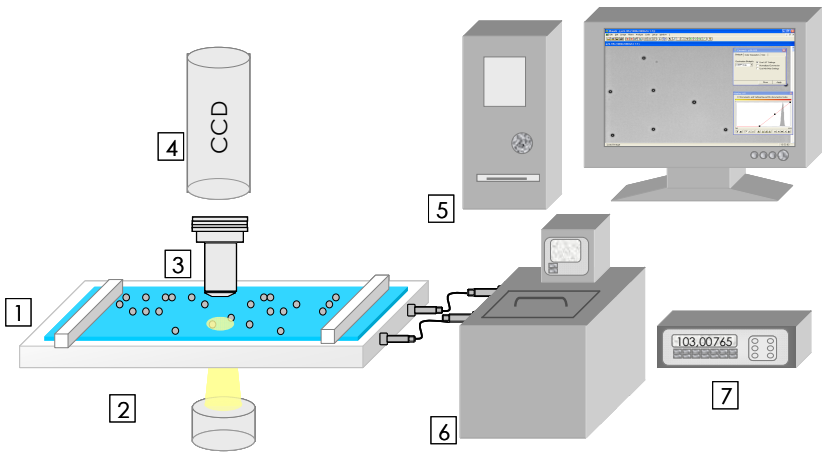

Figure 8.5. Typical particle tracking set-up for 2D microrheology experiments. Components as follows: (1) Langmuir trough; (2) illumination; (3) microscope objective; (4) CCD camera; (5) computer; (6) thermostat and (7) electronics for measuring the surface pressure.

Different strategies of experimental realization have been done in order to test if not only the polymers, but also the microparticles used as probes are adsorbed together at the air-water interface. The mixed Langmuir monolayer formed by polymers and particles were built in two different ways, with sequential spreading, and simultaneous coupling of both components on the air-water (A/W) interface. In brief, the sequential methodology consists in spreading the particles onto the A/W interface when the polymer monolayer has already been formed and stabilized. When the spreading solvent of the particles is evaporated a mixed layer is created on the A/W interface. On the other hand, in the case of simultaneous coupling, the Langmuir trough is separated in two well defined sections, one for the polymer monolayer and the other one for the particles monolayer by a moving barrier. When the spreading solvents have been evaporated and the respectively monolayers have been formed, the two separated regions are put in contact by the mobile barrier, and by diffusion a mixed Langmuir monolayer is created. It is noteworthy that we have demonstrated by a systematically set of experiments that both methods lead to comparable results.

In addition, to minimize the macroscopic drift currents of the particles at the air-water interface due to thermal convection promoted by temperature gradients along the monolayer, a set of homemade stainless steel rings has been used in accordance to the previous works of Klinger and McConell.[44, 45] Once the mixed monolayer of particles and polymer is deposited on the air-water interface and the respectively solvents are evaporated, the height of the interface is adjusted by removing volume of the aqueous phase until the monolayer becomes "trapped" in the upper edge of the ring, as schematically shown Figure 8.6.

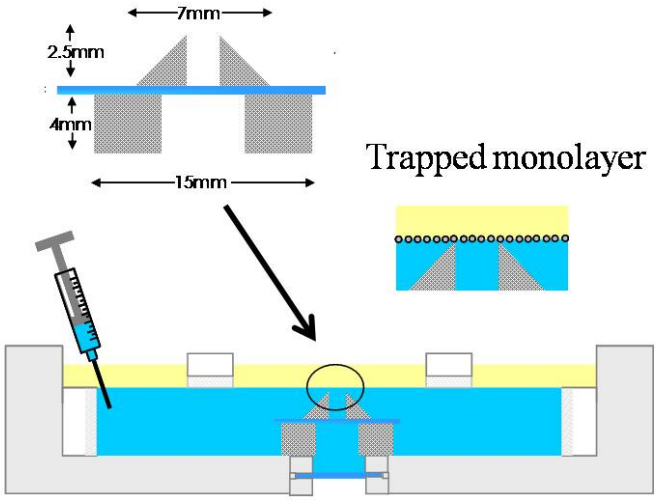

Figure 8.6. Sketch of the Set of rings to eliminate the drift movements that affect the monolayer. Firstly, the dispersion of particles is spread onto the interface, and then the level of the interface is adjusted to the height of the ring by removing volume of the aqueous phase with a precision microsyringe.

The microparticles are imaged by bright-field microscopy with a 50× objective (working distance 10.1 mm), numerical aperture n =0.55, at a spatial resolution of 233nm/pixel and a frame rate of 102fps. For each sample, movies of 3×10^3 frames (≈ 600 s) are recorded with a CCD camera (Hamamatsu photonics) that has $10^3\times10^3$ pixel resolution, with a few number of particles lying within the field of view. The images were digitalized and analyzed off-line, using methods described elsewhere[43] in order to determine the position of the particle tracers for every frame by particle tracking.[46] (i.e., Particle tracking methodology consists in first locating all particles in each image and then identifying each particle in subsequent images based on the proximity to its position in previous images.) It is noteworthy that the motion of the particles consists of random diffusive motion and collective drift induced by the both phases in contact to the mixed monolayer. Thus, any global motion is subtracted from the particles' displacements.

It is well known that at higher density of particles there are interactions between them, mainly due to electrostatic and capillary forces.[47] In order to study such interactions, we have measured the pair correlation function $g(r)$. Control experiments were performed at lower particle density (less than 15 particles for each frame), where it is expected that $g(r)$ has no structure when plotted as a function of r.

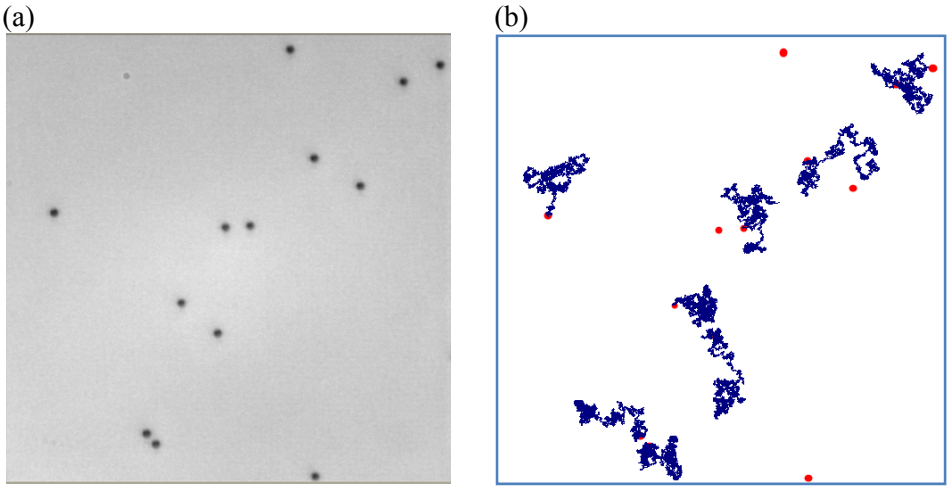

Figure 8.7. Set of images of the particle tracking analysis. (a) Mixed monolayer of PTBA and PMMA particles (σ = 2μm) imaged by the CCD camera. This picture corresponds to the initial state of the particles onto the interface at the beginning of the film. (b) Picture of the trajectories of the particles shown in (a) obtained from the analysis of their Brownian motion due to thermal energy (*kT*).

3.2.2 *Image Analysis: Evaluation of MSD and Diffusion Coefficient*

The series of images obtained allow us to get the trajectories of a set of particles by analyzing their MSD. For instance, Figure 8.7 shows a typical image analysis performed on a mixed monolayer of PTBA (Π = 3.6 mN/m; Γ= 0.4

mg/m^2) and PMMA particles (σ =2μm) at the air-water interface. Figure 8.7.a shows a picture of a patch of the mixed monolayer, with only 12 PMMA particles adsorbed at the air-water interface. In (b) the trajectories of the particles calculate by the Particle tracking methodology are shown. The relative mean square displacement of pairs of particles is calculated as:

$$MSD_{rel} \equiv \left\langle \Delta r_{rel}^2(\tau) \right\rangle = \left\langle \left(\Delta \vec{r}_{ij}(t+\tau) - \Delta \vec{r}_{ij}(t) \right)^2 \right\rangle = 8Dt \qquad (8.13)$$

where $\vec{r}_i$ and $\vec{r}_j$ accounts the position of the particles over a time τ. These averages are taken over all the pairs of particles and initial times, t, of the system.

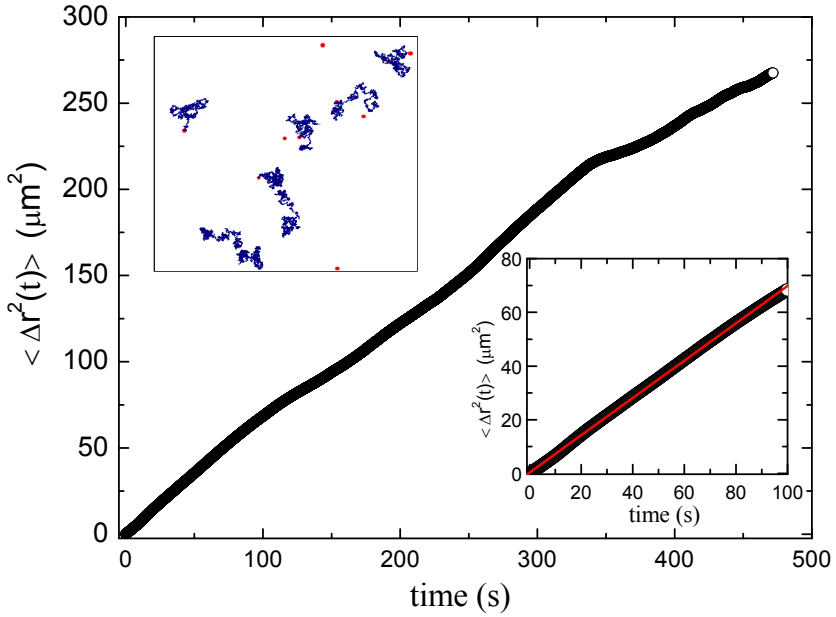

Figure 8.8. Relative mean square displacements as a function of time obtained from the trajectories of several PMMA particles (σ =2 μm) adsorbed at the air–water interface where previously a PTBA monolayer is spread. The MSD shows a sub-diffusive behavior (α<1 according to Eq. 8.1). Upper inset: Particle's trajectories over 600s. Lower inset: Detail of the first 100s where $<\Delta r^2>$ has a linear behaviour (α =1). Straight line shows the fit of the experimental data.

Figure 8.8 shows a typical result for the MSD of the system of PMMA particles (σ =2μm) spread at the air-water interface where previously a PTBA monolayer (Π = 3.6 mN/m; Γ= 0.4 mg/m^2) is spread. The analysis of MSD_{rel} in terms of Equation 8.7 in the linear range (lower inset of Figure 8.8) allows one to obtain D. However, it must be taken into account that for laden interfaces, even below the threshold of aggregation or fluid-solid phase transitions, the MSD shows a sub-diffusive behavior (α < 1 in Equation 8.1). Therefore, only physically meaningful values of D can be obtained in the limit of short times, and this should be taken into account when extracting the surface microrheology parameters from D. Here, since the density of particles is low, the behaviour found is the one

expected for particles following a Brownian motion in two dimensions, and considering that both thermodynamic and hydrodynamic interaction are negligible.

4. Results and Discussion

As stated above, we have performed 'particle tracking' experiments on PTBA monolayer using particles with different chemical nature and size. Our aim is to get further insight, not only on the validity of the different theories used to calculate the interfacial viscosity, but also to compare the results obtained with those obtained using conventional macroscopic interfacial rheometers.

4.1 Diffusion of microparticles at the bare water surface

Let us first describe the measurements of the diffusion coefficient D_0 of the particles used in this study on clean water surfaces at 22ºC. From a hydrodynamic point of view, a free water surface is to be considered as compressible, in the sense that a moving object creates a compressible flow.[39] The particles' diffusion was obtained by the MSD analysis of their individual trajectories over 10 sequences on 5 different samples. In these experiments, the inter-particle distance (r) is about 60 times the particle diameter (σ) ensuring the lineal behaviour of the MSD, and avoiding the possibility of hydrodynamic coupling between particles. Table 8.2 summarizes the resulting D_0 obtained.

Table 8.2. Diffusion coefficient D_0 of the microparticles used in this study attached to the bare air/water interface by using methanol as spreading solvent.

Chemical nature	*Diameter σ (μm)*	*Contact angle θ (°)**	*Diffusion Coefficient D_0 (μm2/s)*
PS	**1.6**	**89±8**	**0.216±0.004**
	5.7	**37±2**	**0.070±0.020**
PMMA	**1.0**	**18±6**	**0.278±0.002**
	2.0	**29±4**	**0.493±0.009**
SiO_2	**1.0**	**41±10**	**0.41±0.05**

*Measured by different experimental techniques (see Chapter 7)

It is important to note that the motion of particles trapped at a fluid interface is strongly influenced by the presence of the other particles. Figure 8.9 shows the behavior of D on the bare air–water interface as a function of particle surface coverage fraction, $\phi = \rho \pi a^2$, (ρ is surface concentration of particles and a the particle radius). Results for different particle radius are shown. The diffusion coefficient follows $D(\phi) = D_0 - k\phi$, where D_0 is the diffusion coefficient at infinite

dilution, and k is a parameter that depends on both thermodynamic and hydrodynamic interaction. For particles trapped at fluid interfaces, hydrodynamic theories usually describe D_0 as the value of diffusion coefficient in the low density particle regime. Such a regime will be characterized by an inter-particle separation distance of about thirty times its diameter, that cannot always be obtained because in many systems of biological or technological interest there is no way to modify ϕ in a controlled way.

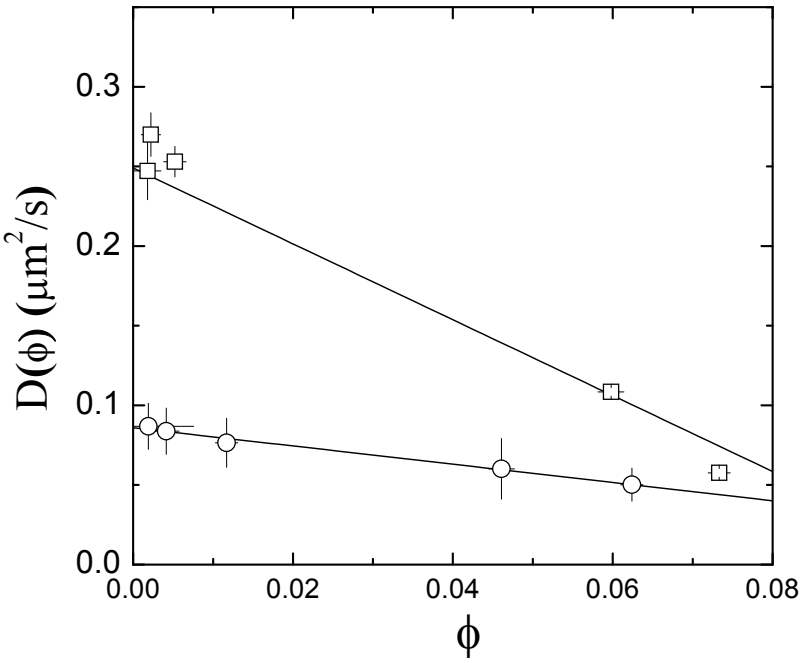

Figure 8.9. Diffusion coefficient (D) of PS particles at the air-water interface as a function of the particle packing density (ϕ). Symbols represent to the experimental results for particles of different sizes: (□) 1.6μm and (○) 5.7μm.

It is well known that the Stokes-Einstein relation can be generalized to two-dimensional scenario; hence, it may allow obtaining the drag coefficient f from D_0 measurements ($f = kT / D_0$). As explained in the theoretical section, there are different theories that relate f with the contact angle θ and the size of spheres moving in an arbitrary interface. Danov et al.[38] have demonstrated the dependence of f as a complex function of θ and a (=σ/2) as: $f = \pi\eta_1 f_{Danov}(\theta,\eta_1,\eta_2)\, a$. On the other hand, accordingly to the model proposed by Fischer et al.[39] $f = \eta_1 f_{Fischer}(d / a, B)\, a$; where, B is the Boussinesq number.

Figure 8.10 shows the friction coefficient for PS particles at the air–water interface obtained from single particle tracking experiments. For the sake of comparison, it also shows the values calculated from Danov's and from Fischer's theories (notice that for the bare interface E = B =0) and an experimental datum obtained from a similar experiment performed by Sickert and Rondelez,[48] which is in further agreement with our experimental result at the same θ. Figure 8.10

clearly shows that both theories underestimate the experimental values over the whole θ range. Moreover, they lead to values of f lower than the limiting value corresponding to the 3D-Stokes equation at 0º (6π), which would represent a spherical particle in the water subphase. We have tested that the increased drag is not due to contamination of the interface by other species. We have also eliminated the possibility of hydrodynamic coupling between the PS beads by ensuring a large separation between them. The discrepancies between our measurements and the theoretically expectations may be due for the following factors: (1) The effect of the air viscosity ($\eta_{air} = 18.6\times10^{-6}$N·s/m^2) has not been taken into account. (2) Slight hydrodynamic effects at the bead surface (slip, no-slip conditions) may lead to an extra dissipation. (3) If the water-bead-air contact line is not perfectly planar, a displacement of the sphere is accompanied by a vertical displacement of the adjacent water sheet, an effect that would significantly increase the energy dissipation. (4) Rotational-translational coupling mode effect could induce an extra dissipation. Thus, we have performed an 'ad-hoc' correction based on an empirical factor of $f'(\theta) = f(\theta)_{exp} / f(\theta)_{Fisher} = 1.8\pm0.2$ that brings the values calculated with Fischer's theory in good agreement with the experiments at all the contact angle values (see continuous line in Figure 8.10). This empirical factor is valid for the air–water interface, while a value of 1.2 was found for the air–octane interface.[43]

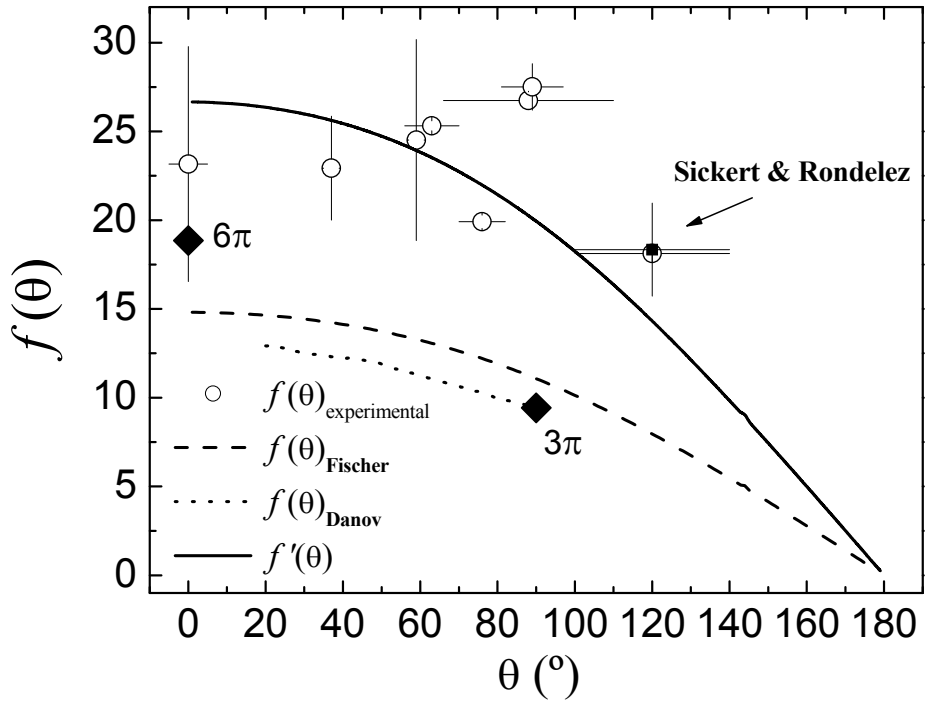

Figure 8.10. Friction coefficient f calculated from the experimental diffusion coefficients D_0 of PS particles at the air/water interface measured by particle tracking experiments (symbols), by Danov's theory (dotted line), by Fischer's theory (dashed line), and by the corrected Fischer's theory (continuous line).

In the following, we have analyzed our experimental results in terms of the Fischer's model[39] because it allows one to determinate the shear viscosity over the whole range of superficial concentration Γ of the monolayer studied. The model proposed by Danov is limited to the range $D/D_0 < 0.23$.[38] Furthermore, Fischer model can be applied for the wide θ-range (0 –180º), while in the case of Danov's theory, results have been presented graphically for particular values of the contact angle (30º, 50º, 70º, etc.). Figure 8.11 shows the parameters $k_T^{(i)}$ for i=0,1 from the Fischer's model, and from the model corrected by the 'ad-hoc' parameter above mentioned.

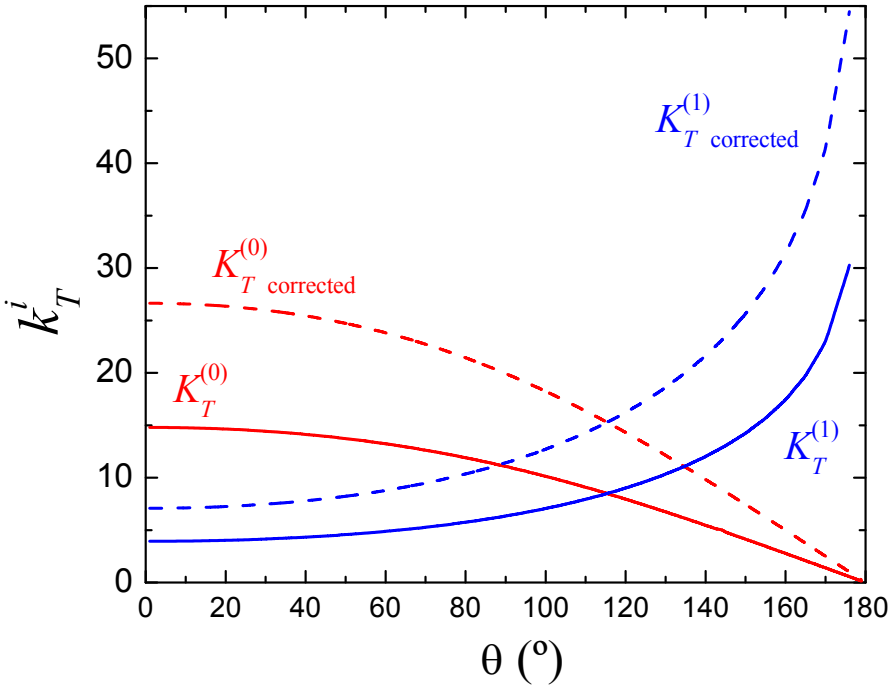

Figure 8.11. $k_T^{(0)}$ and $k_T^{(1)}$ parameters obtained from the Fischer's theory (straight lines) and from the corrected Fischer's theory by the 'ad-hoc' proceeding (continuous line) as a function of the contact angle θ at the air/water interface.

4.2 Surface shear viscosity of PTBA monolayers by Fischer theoretical approach

Let us first discuss the surface shear viscosity of a PTBA monolayer with M_w=4.6 kDa by using particles with different chemical nature and size as tracers (see Table 8.1). The modified Fischer theoretical model will be used to calculate the interfacial shear viscosity (η). This monolayer has a chain size below a critical number of monomers $N < N_e$ (≈100 monomers) above which chain entanglements are suggested to exist.[49, 50] Thus, segregated quasi-2D coils structure has been suggested for this Langmuir PTBA film assuming good solvent conditions. This implies that the polymer chains are adsorbed at the air-water interface in a flat pancake conformation with most monomers adsorbed at the interface.[51] A

network of entangled chains is characterized by a mesh length scale ξ which represent the mean distance between entanglements, i.e., the size of a pancake segment in 2D.

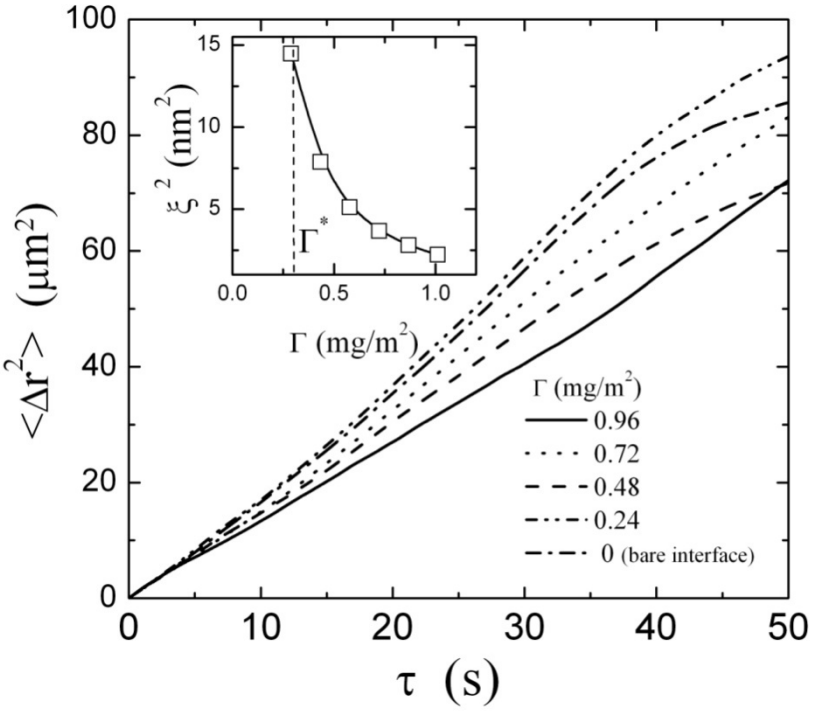

Figure 8.12. Time evolution of the mean square displacement of PMMA particles (σ = 2μm) for different surface concentration Γ of a PTBA monolayer (4.6kDa) attached at the air/water interface. The Inset depicts the square of the mesh size ξ as a function of Γ for the PTBA monolayer calculated using Eq. 8.14. Note that the MSD of the particles are greater than ξ^2 in the whole range of Γ studied. Vertical straight line marks the overlapping concentration Γ*.

All the beads used in this work are significantly larger than the mesh size ξ, ensuring a continuum response of the polymer monolayer to the thermal strains imposed by the beads. The mesh size for the polymer monolayer has been calculated through the following relation:

$$\xi = R_F \left(\Gamma^*/\Gamma\right)^{\nu} \qquad (8.14)$$

where R_F is the Flory radius of the PTBA. Γ^* and Γ denote the overlapping concentration and the surface concentration for the polymer monolayer, respectively. It is well known that Γ^* marks the onset of the semidilute regime of a polymer monolayer and it is defined as the concentration at which the neighbouring polymer coils start to overlap with each other. Concretely, the PTBA monolayer (4.6 kDa) adsorbed at the air-water interface is characterized by the overlapping concentration Γ^*=0.31mg/m^2 and R_F=3.7nm as pointed out equilibrium experiments performed in Chapter 2.

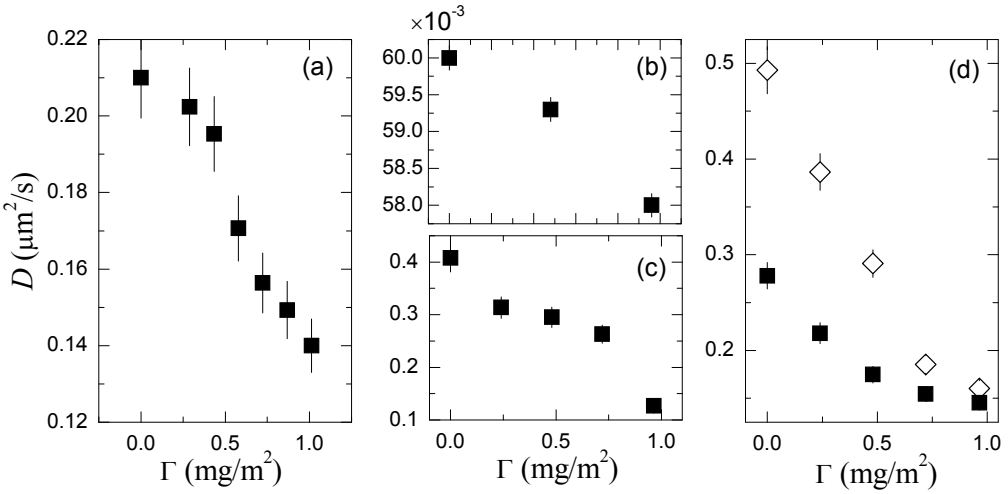

Figure 8.13. Diffusion coefficient *D* of different microparticles as a function of the surface concentration Γ of a PTBA monolayer (4.6kDa) at the air/water interface: (a) PS particles (σ = 1.6μm). (b) PS particles (σ = 5.7μm). (c) SiO_2 (σ = 1μm). (d) PMMA particles with σ = 2μm (◇) and 1μm (■).

As an example of the relative mean square displacement obtained for the PTBA monolayer, Figure 8.12 shows the time evolution of the MSD of PMMA particles with 2μm of diameter at different surface concentration of PTBA. The MSD for the different Γ's show the same trend: at short times MSD rises diffusively, and becomes sub-diffusive at larger times. The main difference between the samples is due to the fact that higher polymer concentrations constrain the motion of the particles to for the same value of time. At each concentration studied, the particles diffuse according to Equation 8.1. The monotonic decrease of the MSD with increasing Γ reflects an increase of the shear viscoelastic moduli of the samples as expected. As expected, the MSDs are greater by several orders of magnitude than the square of the mesh size, which together with the fact that, $\xi < \sigma$ ensures that the Brownian motion of the particles should not be affected by inhomogeneity effects.

The experimental data obtained from diffusion experiments are presented in Figure 8.13, which shows the diffusion coefficient *D* corresponding to the different beads used as a function of the polymer concentration. As it can be seen, each different type of bead used as tracer (chemical nature and size) leads to different values of *D*, whereas the regular trend shown reveals a strong decrease of the diffusion coefficient as Γ increases. As expected, greater values of *D* are shown by the smaller size particles independently of its chemical nature. In addition, we have observed for all the samples studied that *D* is smaller than the diffusion coefficient of the beads at a bare compressible surface D_0 (see Table 8.2) due to the incompressibility effect of the polymer monolayer adsorbed at the air-water interface. This fact is due the monolayer was in a semidilute regime (Γ >

Γ^*) where the polymer chains are close to each other, and inter-chain frictions are probable. Moreover, the highest diffusion coefficient, that was measured at very low surface concentrations is always lower than the reference value (D_0) for bead diffusing on a bare water interface. This fact points out the existence of a contribution of the polymer monolayer on the diffusive motion of the beads attached at the interface.

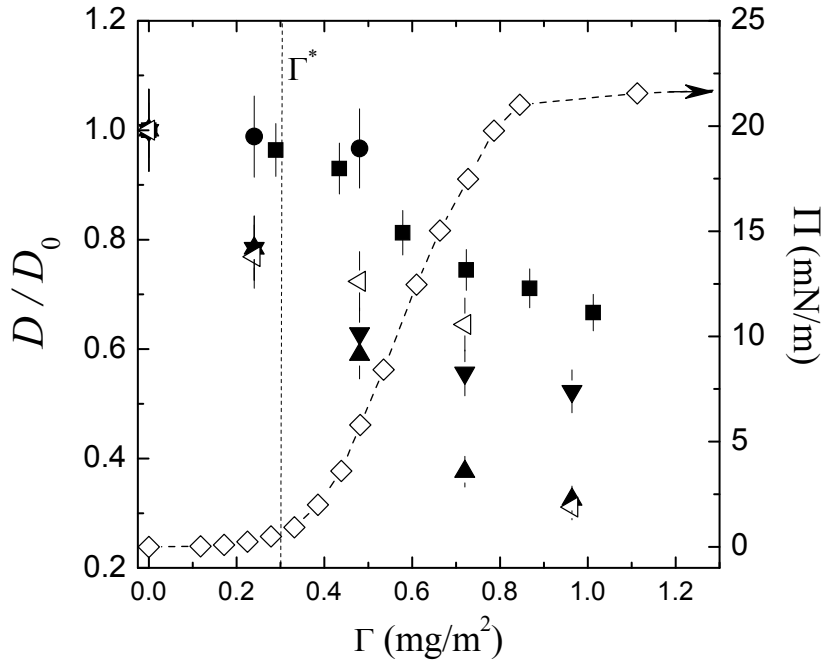

Figure 8.14. Diffusion coefficient D relative to the diffusion coefficient for a clean water interface D_0 of microparticles as a function of the surface concentration Γ of a PTBA monolayer (4.6kDa). Symbols as follows: (■) PS (σ = 1.6μm); (●) PS (σ = 5.7μm); (▼) PMMA (σ = 2μm); (▲) PMMA (σ =1μm); (◁) SiO_2 (σ = 1μm). It is also included the surface pressure vs. surface concentration isotherm (Π–Γ) of the PTBA monolayer (4.6kDa) (◇).

The diffusion coefficient D for the different particles expressed relative to the diffusion coefficient D_0 at a bare air–water interface are shown in Figure 8.14 as a function of Γ. It should be noted that this procedure is useful to minimize the influence of systematic effects such as long-range hydrodynamic interactions between the probe particles.[52] As stated above the diffusive motion of the particles attached at the air-water interface with the PTBA monolayer depends strongly on their size. Figure 8.14 also shows the surface pressure isotherm (Π–Γ) of the PTBA monolayer and the values of Γ^* from where the relation D/D_0 is expected to decrease as Γ increases. As it can be observed in Figure 8.14, the particles with smaller diameters (1μm) show a stronger reduction of the relation D/D_0 as Γ increases (e.g. $D/D_0 \approx 1.0$ to 0.3 in the case of PMMA with 1μm of diameter). We also have found that the relation $D_0/ D_{\to 0}$ ($D_{\to 0}$ accounts for the value of an incompressible monolayer for which the surface concentration is tending to zero) is not equal 1 ($D_0/ D_{\to 0} \approx 0.9$-0.8). This behavior at low surface coverage is an

example of the apparent paradox that a small amount of surface active substance (i.e., $\Pi \approx 0$) such as a polymer can affect the hydrodynamics of the diffusing bead. This situation was also observed by Barentin et al.[35] and by Lee. et al.[3] for different systems.

In order to calculate the surface shear viscosity η of the PTBA monolayer at increasing surface concentration Γ, we have used the numerical method proposed by Fischer et al.[39] In their notation, the drag coefficient f ($=kT / D$) has been expressed as: $f(\theta) \approx K_T^{(0)}(\theta)+B\ K_T^{(1)}(\theta)$; where the coefficients $K_T^{(i)}$ are functions of the contact angle θ. Thus, we have taken into account the 'ad-hoc' correction performed on the drag coefficient (f) mentioned above (see Figure 8.10). The values of θ have been corrected by using the Young's equation that accounts for its dependence on the interfacial tension (γ) at increasing polymer concentration. The Young´s relation ($cos\ \theta = \gamma_{pa}+ \gamma_{pw} / \gamma$) shows that θ depends only on the interfacial tensions between the upper (air) and lower (water) phases ($\gamma_{aw} \approx \gamma$) and the ones between the solid particle and both upper(γ_{pa}) and lower phases(γ_{pw}).

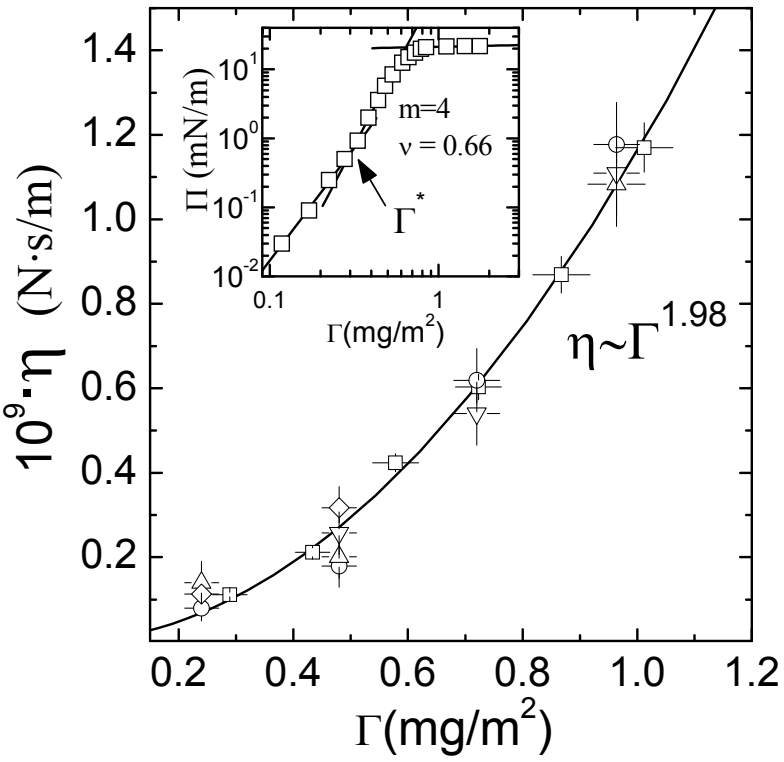

Figure 8.15. Surface shear viscosity η as a function of the surface concentration Γ of a PTBA monolayer (4.6kDa). Symbols correspond to different particles used as tracers: (□) PS (σ = 1.6μm); (◇) PS (σ = 5.7μm); (○) PMMA (σ = 2μm); (△) PMMA (σ =1μm); (▽) SiO_2 (σ = 1μm). The straight line shows the power law dependency $\eta \sim \Gamma^2$ followed by the experimental data. Inset: log-log plot of the Π–Γ isotherm of the PTBA monolayer. Γ^* marks the start of the semidilute regime where the power law description is plausible obtaining a Flory exponent ν = 0.67±0.02.

The dependence of η on the surface concentration of PTBA monolayer with M_w = 4.6kDa has been plotted in Figure 8.15. We have included all the experimental shear viscosities obtained from the measurements of *D* using different particles as tracers. The observed surface shear viscosity values range from 1×10^{-10} to 1.25×10^{-9} N·s/m. As it can be seen in Figure 8.15 particles with different chemical nature and size lead to the same shear viscosity values in the whole range of Γs studied. Indeed, we address for the first time a systematic study of how different microparticles to be followed by particle tracking lead to the same values of the surface shear viscosity. This universal-behaviour suggests that the surface adsorption of the probe particles does not affect the measurement of the viscoelasticity, and that the shear viscosity is not affected by an adsorbed layer of polymer on the surface of the beads. It is noteworthy that the uncertainties in the diffusion coefficient introduces significant uncertainty in the determination of *B,* and consequently on the surface shear viscosity as evidenced in Figure 8.15. We have fitted the experimental data to the following power-law dependency $\eta\sim\Gamma^{\beta}$ where β accounts for the scaling exponent of the concentration dependency. The power-law behaviour of our experimental data is shown by the continuous line in Figure 8.15. The scaling exponent obeyed for the experimental shear viscosities correspond to β =1.98±0.06.

Taking into account the theoretical argument proposed by de Gennes [51, 53] and that the PTBA monolayer considered (4.6kDa) has a chain size N = 46, smaller than the critical one (N_e ≈100), allow us to describe the surface shear viscosity by the Rouse model in the following terms:

$$\eta_{Rouse} \sim Na\left(a^2\Gamma\right)^{\frac{\nu-1}{1-2\nu}} \qquad (8.15)$$

where a is the monomer length and ν is the Flory exponent for the Radius of gyration ($R_F \sim N^{\nu}$). This model assumes that the force exerted on a polymeric coil is the hydrodynamic drag force exerted by the subphase. When the polymer chain is displaced, each coil drags the water volume under it and generates a subphase flow. These flow fields decay over a distance comparable to the mesh size ξ. Hence, the surface shear viscosity has its origin in the hydrodynamic coupling of the coils to the subphase. If we relate the experimental scaling exponent β with the scaling description of η provided by the Rouse model, one can write the relation ν = (β+1)/(1+2β), which leads to a value that corresponds to ν = 0.60±0.05. This demonstrates that the PTBA (at $N<N_e$) in a *quasi*-two dimensional scenario is a strongly segregated and entanglements may appear in the soft periphery of a chain playing only a minor role. To test our hypothesis about the power-law behaviour shown by η, a log-log representation of the Π–Γ isotherm (see inset of Figure 8.15) allows one to point out that the surface pressure obeys a power law as a

function of Γ above Γ^* characterized by an exponent *m* that is directly related to the Flory exponent ν by the relation m=2ν/(2ν−1). We have obtained a Flory exponent of ν=0.67±0.02 which is compatible with the one obtained from the shear viscosity measurements by means of the Rouse model proposed for these experimental conditions. To summarize, the Rouse model provides a theoretical framework to understand the power law dependence on the polymer concentration of the surface pressure and of, the surface shear viscosity. Concretely, the power law behaviour found $\eta \sim \Gamma^{\beta}$ may be due to the absence of entanglement and a decoupling of the behaviour of the chains as expected for polymer monolayers below N_e as pointed out the Rouse theory.

Let us now study a PTBA monolayer with higher molecular weight in order to get further insight about the dependence of η on Γ at chain sizes above a critical number of monomers ($N_e \approx 100$ monomers) for which chain entanglements become possible. We have used PS particles (1.6μm) as tracers, and a monolayer of PTBA with molecular weight M_w=103kDa. The Γ-dependence of η taking into this chain length (N=1030 monomers) is shown in a log-log representation, in Figure 8.16. The surface viscosities measured for PTBA monolayers range between 1×10^{-10} and 5×10^{-8} N·s/m. As it can be observed, the values of η depend on the polymer weight; i.e., in the whole regime of polymer concentrations, the values of η increase as M_w increases.

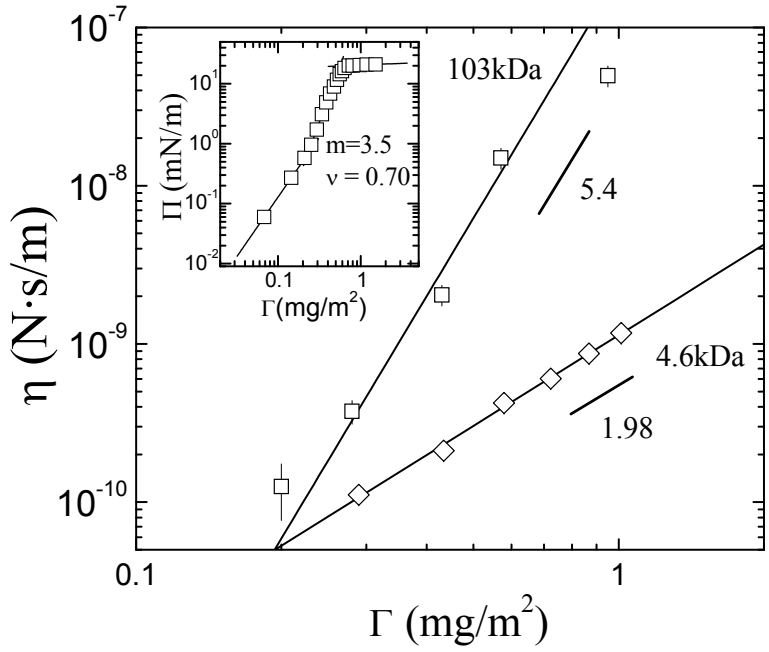

Figure 8.16. Surface shear viscosity η as a function of the surface concentration Γ of PTBA monolayers with different molecular weight (M_w) using PS particles (σ =1.6μm) as tracers. Symbols as follows: (□) 103kDa, and (◇) 4.6kDa. Straight lines shows the power law dependency $\eta \sim \Gamma^{\beta}$ followed by the experimental data. Inset: log-log plot of the Π–Γ isotherm of PTBA monolayer with polymer weight 103 kDa.

Concretely, for a PTBA monolayer with $N < N_e$ we have demonstrated the existence of a power-law dependence of the form: $\eta \sim \Gamma^{\beta}$ with $\beta = 1.90 \pm 0.06$. This is in agreement with a Rouse theoretical description of the system. On the other hand, deviations from this scaling-behaviour have been found at increasing N above N_e which is reflected by the β parameter: 5.4±0.2 for PTBA with 103kDa. These different values of β (from 1.98 to 5.4) could be due not only to the existence of inter-chain frictions at the periphery of the polymer coils, but also to internal frictions as expected for flexible PTBA chains long enough to entangle in the monolayer. Thus, additional dissipations could arise from the entangled two-dimensional arrangement of flexible chains. This behaviour found for PTBA with 103kDa is close to the expected for an entangled system where the viscous friction scales with an exponent β close to 6.[49, 50] Accordingly, the Flory exponent obtained from the scaling analysis of the Π–Γ isotherm of the monolayer studied, $\nu_{103kDa} = 0.70 \pm 0.03$ (see Inset in Figure 8.16) is compatible with the description of a system in terms of a *good-solvent* scenario where the entanglements may exist (see Chapter 2).

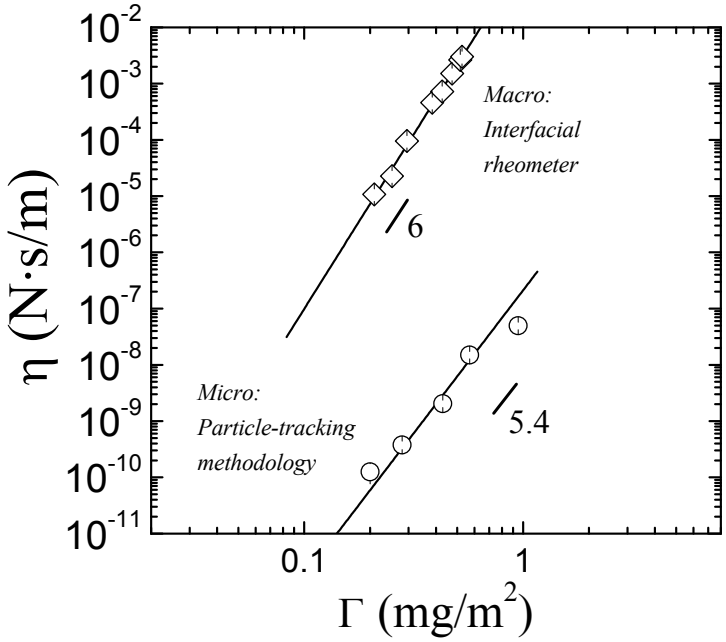

Figure 8.17. Surface shear viscosity for a PTBA monolayer with M_w =103 KDa as a function of the surface concentration Γ. (○) correspond to data obtained from particle-tracking whereas (◇) correspond to data obtained from conventional interfacial shear rheometry. The scaling- behaviour of both set of ηs are in further agreement with an entangled scenario.

In general, the values of η obtained from this methodology are more than three orders of magnitude lower than the values measured by conventional macroscopic rheometers as can be seen in Figure 8.17.[50] However, the power-law found for the shear viscosities ($\eta \sim \Gamma^{5.4\pm0.2}$) is in reasonable agreement with the oscillatory shear experiments previously performed on PTBA monolayers, which

have pointed out by that the viscous friction scale as $\eta \sim \Gamma^6$ as expected from a highly entangled system following a reptation-like motion.[51, 53, 54] In addition, strong evidences for reptation-like shear viscoelasticity have been also reported in the literature.[55] The discrepancy between the values of η obtained well above N_e from micro- and macro-rheology measurements has not a clear answer so far. In spite of the fact that $\xi << \sigma$, this discrepancy between micro and macro interfacial shear viscosity values might arise from the existence of a non-homogeneous polymer monolayer, mainly due to the adsorption of microparticles at the interface after the polymer monolayer was formed. This situation can affect strongly the polymer monolayer. Hence, further work is necessary to clarify this point.

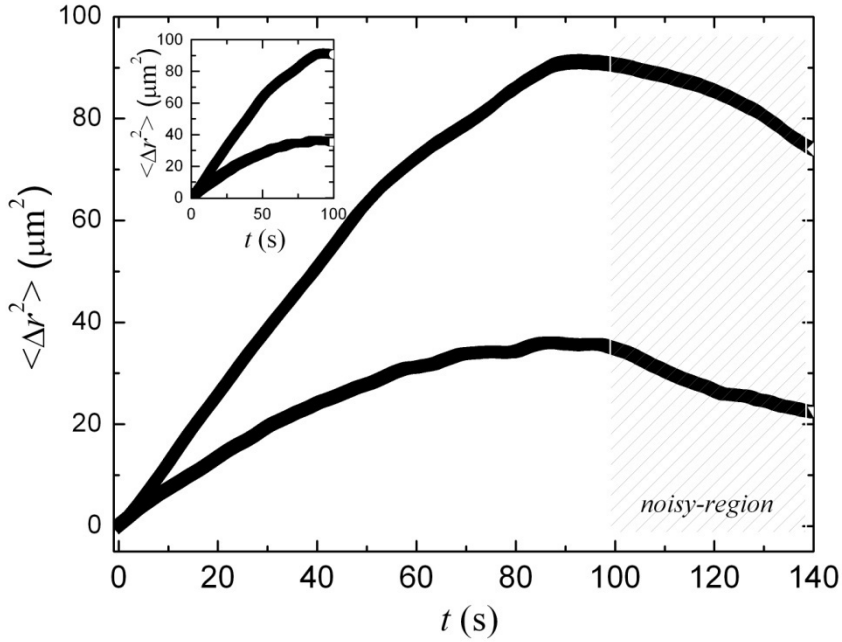

Figure 8.18. Example of the existence of noisy regions (narrow zone) in the time evolution of the mean square displacement of PMMA particles (σ = 2μm) for two arbitrary surface concentration Γ of a PTBA monolayer (103kDa) attached at the air/water interface. The Inset depicts the zones valid to obtain the shear viscoelastic moduli by the GSE equation (Eqs. 8.4–8.7).

4.3 Shear Viscoelasticity moduli of PTBA monolayers by using the generalized Stokes-Einstein equation (GSE)

The modified algebraic form of the generalized Stokes-Einstein equation (GSE) given in Eqs. 8.4–8.7 is used to calculate the storage (*G'*) and loss modulus (*G''*) from the MSD data. The noisy regions of the MSD data are not included in the calculation of the shear complex moduli $G(\omega)$. An example of the existence of noisy regions in the time evolution of the MSD data is shown in Figure 8.18. As expected, when the sphere moves diffusively, the slope of the MSD is close to unity, and according the GSE equation (Eqs. 8.4–8.7) *G''* dominates, whereas when the sphere is confined by the elastic structure of the polymer monolayer, the

slope approaches to zero, and *G'* dominates. At higher times the slope decrease below zero showing an inconsistency in the motion of the particles. This fact could be due to poor-statistics of the MSD data at higher acquisition times.

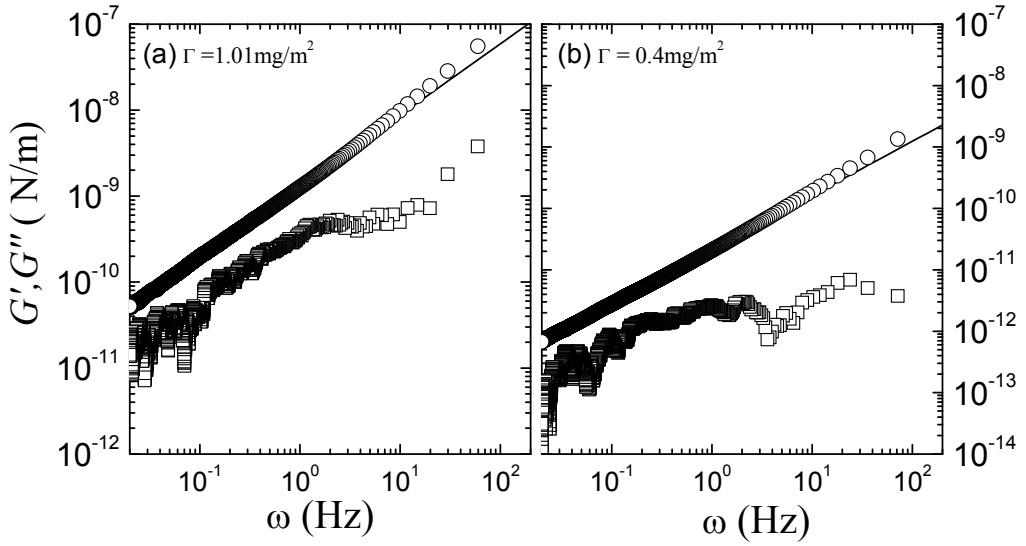

Figure 8.19. Frequency dependence of the storage (*G'*) and loss (*G''*) moduli of PTBA monolayers (M_w=4.6kDa) with different surface concentration Γ: (a) 1.01mg/m^2 and (b) 0.43mg/m^2 using PS particles (σ =1.6μm) as tracers and the Generalized Stokes-Einstein equation (Eqs. 8.4–8.7). Symbols as follows: *G'* (□) and *G''* (○); straight lines shows the power law behaviour of the experimental loss module: $G'' \sim \omega^{0.8\pm0.1}$.

The temporal limits for the data depend on the bead size used as probes. Moreover, as stated above, an important requirement obeyed is that the size of our beads (≈ μms) are significantly larger than the characteristic mesh size ξ of our PTBA monolayers (in the range of nms; for instance, see inset in Fig. 8.12). The way to estimate the frequency range accessible by this methodology has been described by Levine and Lubensky. [20] The lower limit (ω_B), is the time scale at which longitudinal modes become significant compared to the shear modes that are excited in the system. For $\omega > \omega_B$, the elastic network is coupled to the incompressible fluid, and longitudinal modes of the network are suppressed. In this regime, the probe motion is entirely due to excited shear modes of the material. An estimation of the ω_B can be obtained by balancing local viscous and elastic forces leading to the expression:

$$\omega_B \geq \frac{G'\xi^2}{\eta_w \sigma^2} \tag{8.16}$$

For instance, in a PTBA monolayer (4.6kDa), the storage modulus at low frequencies is independently of the frequency and could be approximated by $G' \approx G_0 \approx k_BT/A_f \approx 0.1$ μN/m. It depends on the free-area available of the polymer monolayer $A_f = \pi R_F (1-\xi) / \xi \approx 31\text{nm}^2$, with a mesh size ($\xi = R_F = 3.7$nm). As a

result, the lower limit of the frequency accessible, $\omega_B = 2.56\times10^{-2}$ Hz. The upper frequency limit exists due to the onset of the inertial effects of the polymer monolayer at the length scale of the bead. Typically these inertial effects can be expected to be significant only for frequencies larger than 1MHz.[5]

Figure 8.19 shows the frequency dependence of the surface shear storage (*G'*) and loss module (*G''*) of the PTBA monolayer (4.6kDa) from the microrheology experiments using PS particles (σ =1.6μm), and calculated by the GSE relation (Eqs. 8.4–8.7). To take into account the effect of increasing the polymer concentration in the rheological behaviour of our polymer monolayer, two surface concentrations have been studied: 0.4 and 1.01 mg/m^2; both above the overlapping concentration ($\Gamma^* \approx 0.3$ mg/m^2). The values of *G'* and *G''* are ranging from 5×10^{-14} to near 10^{-7} N/m over the accessible frequency regime. A predominantly viscous response $G''(\omega) > G'(\omega)$ is observed over the whole surface concentration range. Moreover, the loss modulus follows a power law with ω: $G'' \sim \omega^{0.8\pm0.1}$. This predominantly viscous behaviour over the entire frequency range studied at both concentrations points out the non existence of a crossover frequency, at least at the frequencies probed by our measurements. The behaviour shown might be qualitatively anticipated from the monotonic decrease of the MSD with increasing Γ shown in Figure 8.12. This situation is in qualitative agreement with the macroscopic shear rheology measurements performed in a PTBA monolayer at $N < N_e$.[50] From a quantitative point of view, the results obtained are at least three orders of magnitude lower than those measured by macroscopic interfacial rheometers.

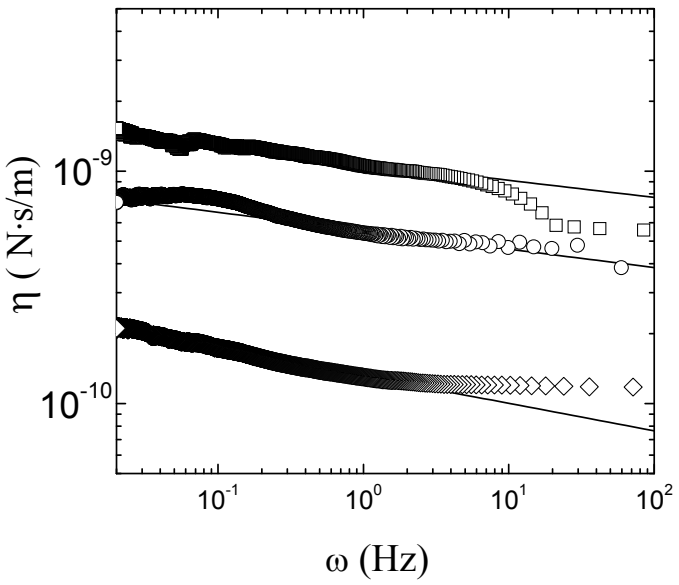

Figure 8.20. Frequency dependence of the surface shear viscosity η of a PTBA monolayer (4.6kDa) at different surface concentrations Γ: (□) 1.01mg/m^2 ; (○) 0.72 mg/m^2 and (◇) 0.43mg/m^2 measured by using PS particles (σ =1.6μm) as tracers. Straight lines show a power-law behaviour of the experimental data: $\eta \sim \omega^{-0.10\pm0.02}$.

To compare the results obtained from the analysis of the experimental MSDs corresponding to PS particles by the GSE equation with those previously obtained by the Fischer theoretical model, we have obtained the shear viscosities η attributed to the PTBA monolayer through the frequency dependence of the loss module *G''* shown in Figure 8.19. The surface shear viscosity calculated as $\eta = G''/\omega$ is shown in Figure 8.20. Here, η is plotted as a function of the frequency for the PTBA monolayer at different polymer concentration Γ (1.01 mg/m^2; 0.72 mg/m^2 and 0.43 mg/m^2). In general, the shear viscosity decreases with increasing frequency, as expected for a non-Newtonian fluid, and in accordance with the ω-dependence of *G''* shown previously. The straight lines in Figure 8.20 show also the power-law behaviour followed by the correspondent values of viscosity obtained ($\eta \sim \omega^{-0.10\pm0.02}$). As it can be observed, η increases with Γ in the whole frequency regime studied. This situation is clearly observed in the previous results obtained by means of the Fischer methodology (Section 4.2) at fixed value of frequency. The agreement between the shear viscosity values obtained by the GSE equation (Figure 8.19) and the previously obtained by the modified-Fischer methodology (Figure 8.15-8.16) will be discussed later.

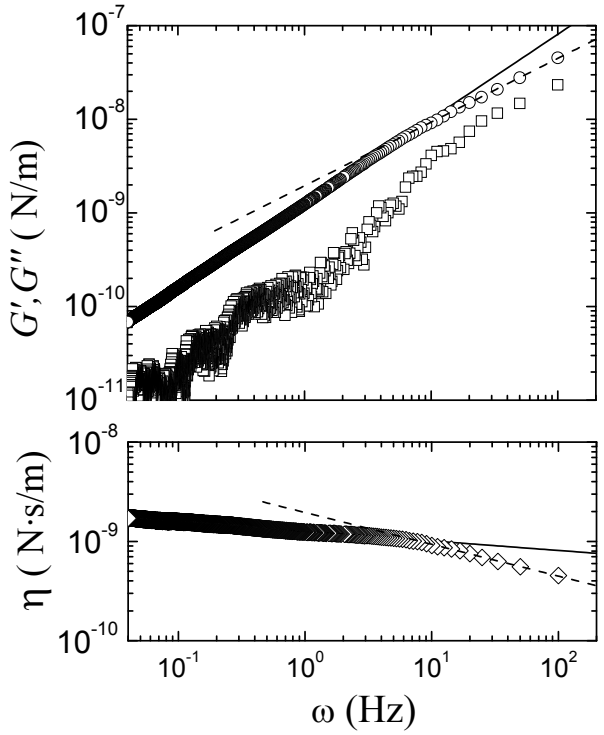

Figure 8.21. (a) Frequency dependence of the storage (*G'*) and loss (*G''*) moduli of PTBA monolayers (M_w=103kDa) at the surface concentration of Γ= 0.41mg/m^2 using PMMA particles (σ =2μm) as tracers and determined by the GSE equation (Eqs. 8.4–8.7). Symbols as follows: *G'* (□) and *G''* (○). Straight and dashed lines show the different power laws behaviour of the experimental loss module as $G'' \sim \omega^{0.9\pm0.1}$ and $G'' \sim \omega^{0.7\pm0.1}$ respectively (b) Surface shear viscosity η as a function of the frequency for a PTBA monolayer at the same conditions that in (a). Straight and dashed lines show the different power laws behaviour of the shear viscosity as $\eta'' \sim \omega^{-0.10\pm0.05}$ and $\eta'' \sim \omega^{-0.3\pm0.1}$ respectively.

Let us now to discuss about the shear viscoelasticity behaviour of PTBA monolayer for a chain size above a critical value ($N > N_e$) for which entanglements become possible. Concretely, we have measured the frequency dependence of *G'* and *G''* obtained by the GSE equation for a PTBA monolayer (103kDa) at Γ=0.41mg/m^2 (above Γ^*), and using PMMA particles as tracers (σ =2μm), the results are shown in Figure 8.21.a. At increasing chain length we also observe a predominantly viscous response $G''(\omega) > G'(\omega)$ over the whole Γ range, as in the case of the lower polymer weight. However, the ratio G''/G' decreases as M_w increases, tending to one ($G''/G' \rightarrow 1$) at the highest frequencies studied; hence, the results suggest the existence of a crossover at higher frequencies not probed by our measurements. This crossover frequency is shifted to lower frequencies for this higher molecular weight in relation to the lower previously studied. Owing to its larger chain length, the longer polymer chain the larger the time for reptating trough the network, and this will result in a crossover at a lower frequency when compared to a polymer with a shorter chain length. Moreover, the loss modulus rises quasi-linearly with ω ($G'' \sim \omega^{0.9\pm0.1}$) at low frequencies while at increasing frequency ($\omega \geq 10$Hz) the slope changes: $G'' \sim \omega^{0.7\pm0.1}$, as expected for a shear-thinning material.[15]

It is unfortunate that we cannot measure directly the crossover point $G'=G''$ for the monolayers with $N < N_e$. For a polymer for which reptation is the correct dynamic mechanism, it is possible to write the relaxation times for the different reptation modes as τ_p (reptation) = τ_d / p^2, with p being an odd natural number. The terminal relaxation time (p =1), can be written as $\tau_d \approx 1/\omega_x$, where $G'(\omega_x) = G''(\omega_x)$.[56] It had been worth to compare these values of τ_d with those obtained from relaxation experiments even though they correspond to different viscosities.

We also have calculated the frequency dependence of the shear viscosity η (= G''/ω) as shown Figure 8.21.b. Here, the trend followed by η also points out the shear-thinning behaviour. From a quantitative point of view, the values of η obtained are in concordance with those previously obtained for the same monolayer using the modified-Fischer theory.

A test of the reliability of the surface shear viscosity values obtained using the GSE equation is to compare them with the values obtained using the modified Fischer's theory. Figure 8.22 shows the values of $\eta(\omega \rightarrow 0)$, as a function of the polymer concentration. It is clear that both calculation methods lead to almost indistinguishable surface shear viscosities of PTBA monolayers with N smaller and larger than N_e. Furthermore, this is true for probe particles of rather different chemical nature and size. The use of particles of different chemical composition allows us to discard any effect of polymer adsorption on the beads concerning to the results obtained. Thus, we have demonstrated the non-dependence of the shear

viscosity values on the particles used as tracers as remarks the non-existence of adsorbed polymer layer on the bead surface.

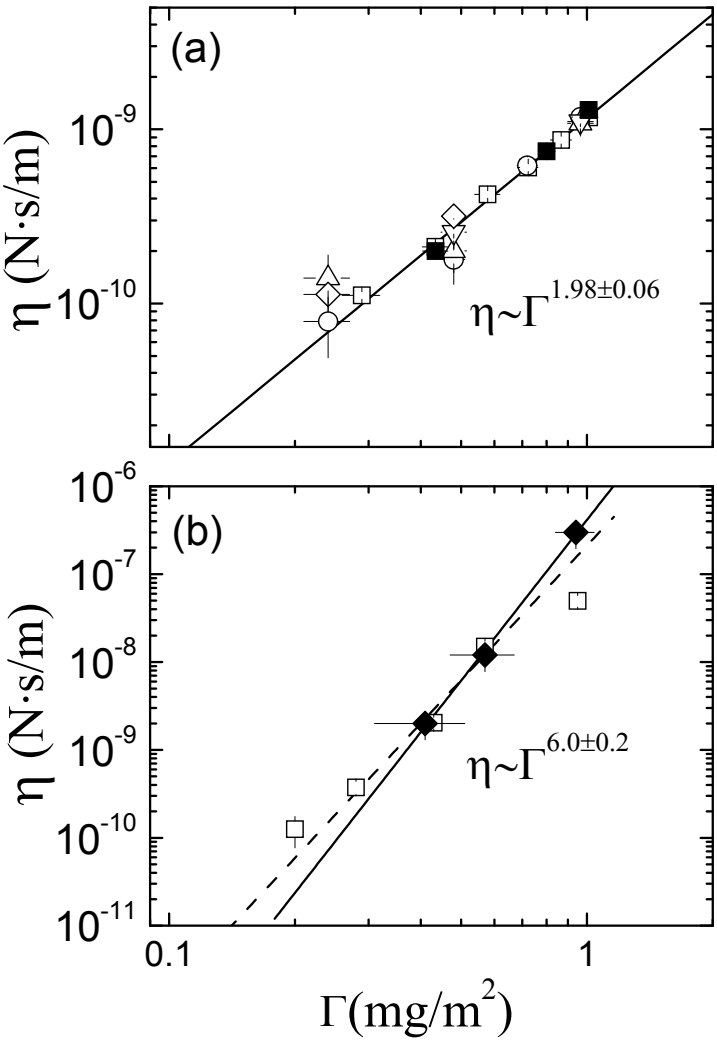

Figure 8.22. (a) Surface shear viscosity η as a function of the surface concentration Γ of a PTBA monolayer (4.6kDa) calculated from the GSE equation in the limit of lower frequencies (■: PS particles with 1.6μm of diameter). We also include the η values obtained from the Fischer methodology (open symbols). Symbols correspond to different particles used as tracers: (□) PS (σ = 1.6μm); (◇) PS (σ = 5.7μm); (○) PMMA (σ = 2μm); (△) PMMA (σ =1μm); (▽) SiO_2 (σ = 1μm). The straight line shows the power law dependency $\eta \sim \Gamma^{1.98}$ followed by the experimental data. (b) Γ-dependence of η for a PTBA monolayer with higher molecular weight (103kDa). Close symbols correspond to the calculus by the GSE equation and using PMMA particles (2μm) and open ones correspond for the Fischer methodology using PS particles (1.6μm). The straight line shows the power law dependency $\eta \sim \Gamma^{6}$ shown by the values of η from the GSE calculation. Dashed line shows the power law $\eta \sim \Gamma^{5.4}$ followed by the values corresponding to the Fischer methodology.

In Figure 8.22.b, we also have compared both methodologies for a PTBA monolayer at larger polymer weight (103kDa). Again, similar results were obtained using the two theoretical analysis and for all the probe particles. However, the two shear viscosity values at higher surface concentration (Γ ≈

1mg/m^2) are different. Hence, the method based in the GSE equation provides a more reasonable higher viscosity and leads to a power-law dependence of η with Γ close to the reptation predictions ($\eta \sim \Gamma^6$) for flexible polymer monolayer above N_e than the previous shown by the results from Fischer's method ($\eta \sim \Gamma^{5.4}$). In spite of this fact, both methodologies leads to a power-law behaviour in agreement with the previously shown by macroscopic measurements and based on the stated theories proposed for polymer monolayers depending on its polymer weight.[50]

4.4 Two-particle microrheology of PTBA monolayers

As stated above, this methodology is based on the cross-correlated thermal motions of pairs of particles. It has been demonstrated by Prasad and Weeks that the correlated motion of two beads is driven by long-wavelength modes in the system and is thus independent of the local environment of the tracers.[28] The comparison of this method with the previous ones can point out the existence of heterogeneities of the order of the bead size and above.[57, 58]

Concretely, we look at the correlated motions of particles adsorbed at the air-water interface in the presence of a PTBA monolayer taken from particle tracking measurements. This is performed as a function of particle separation r and lag times t, for correlated motion along the line joining the centers of particles, $D_{rr}(r,t)$, and in the perpendicular direction, $D_{\theta\theta}(r,t)$. In particular, we focus on the diagonal elements of the tensor products of the averaged cross-correlated particles motions (Equation 8.8): $D_{rr}(r,t)$ and $D_{\theta\theta}(r,t)$ which are calculated according to the vector displacements of the tracers. The Brownian motion of a single bead is the superposition of such modes with wavelengths greater than the particle radius, a. The correlated motion of two beads is driven by those modes with wavelengths greater than their separation r, since shorter wavelengths modes do not move the tracers in phase. In this way, Prasad and Weaks have defined a mean square displacement, $\langle \Delta r^2(t) \rangle_D$; which depends on the correlation motion of two particles $D_{rr}(r,\tau)$ according to:

$$\left\langle \Delta r^2(t) \right\rangle_D = \frac{2r}{a} D_{rr}(r,t) \qquad (8.17)$$

This expression accounts for the thermal motion obtained by the extrapolation of the long-wavelength thermal fluctuations of the medium down to the bead size. In practice, we have obtained the respective D_{rr} over the length scale from 3.2 to 80μm, and then we use the average value obtained from *Drr* over that range to calculate $\langle \Delta r^2(t) \rangle_D$ from Equation 8.17. Finally, to obtain the complex shear viscoelastic moduli $G^*(\omega)$, we substitute the defined $\langle \Delta r^2(t) \rangle_D$ instead of the

$<\Delta r^2(t)>$ in the GSE equation previously defined (Equations 8.4–8.7). The use of these local algebraic expressions allows one to calculate the shear storage (G') and loss module (G'').[21]

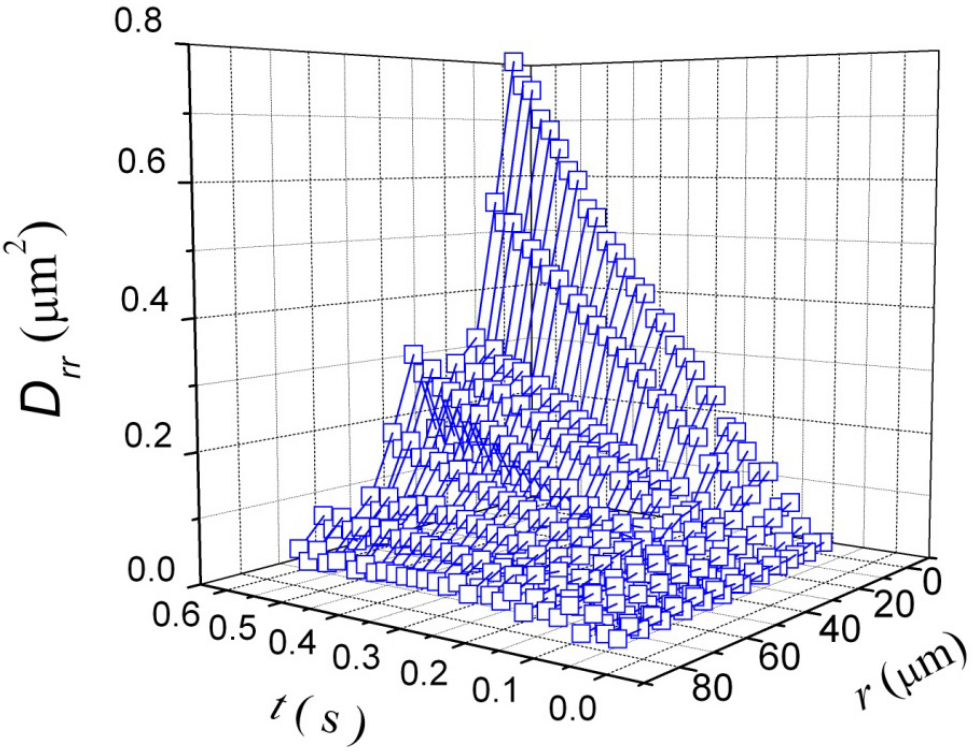

Figure 8.23. Two-point correlation function D_{rr} (r,t) as a function of r and t, for PS beads with diameter 1.6μm adsorbed at a air-water interface where a PTBA monolayer (4.6kDa, Γ=1.01mg/m^2) has been previously attached. In This triple-log plot, the spaced correlation functions imply that $D_{rr} \sim t/r$.

Figure 8.23 shows D_{rr} as a function of r for different lag times t, for a PTBA monolayer (4.6kDa) with Γ=1.01mg/m^2. These measurements correspond to the particle-tracking experiments performed with PS particles with 1.6μm of diameter. It is important to note that $D_{rr} \sim t/r$ within the statistical error. As expected, the motion of a tracer particle creates a flow field that affects the motion of other particles. This flow field decays as we move further out from the particle. Hence, the correlated motions (D_{rr}) decay as a function of particle separation (r) for all lag times considered as it can be observed in Figure 8.22. For the sake of clarity we do not plot $D_{\theta\theta}$, which obeys similar a tendency ($D_{\theta\theta} \sim t/r$). The linear scaling of the correlation functions enable the estimation of r-independent quantities (rD_{rr}), which depend only on t and allows one to calculate $< \Delta r^2(t) >_D$.

Figure 8.24.a shows the time dependence of $< \Delta r^2(t) >$ and $< \Delta r^2(t) >_D$ for the same PTBA monolayer considered in Figure 8.23. We found that both parameters are coincident and linearly depend on time within statistical errors.

This points out the non-existence of local heterogeneities that might affect the measurements of the MSD's. $G'(\omega)$ and $G''(\omega)$ have been calculated respectively from $< \Delta r^2(t) >$ and $< \Delta r^2(t) >_D$ using the GSE equation. Figure 8.24.b shows that the shear parameters calculated from the two-particle correlation function are in reasonable agreement with the results obtained from the one-particle microrheology (previously shown in Figure 8.19). In particular, the values of *G''* from both methodologies are close to each other within the estimated combined errors. However, the values of *G'* from the two-particle microrheology are only close to the ones obtained from the one-particle methodology until high frequencies where increase the discrepancy between both. Thus, two particle-correlation leads to larger values of *G'*, which are close to the values of *G''* in the upper frequency limit suggesting the existence of a crossover frequency. On the other hand, one-particle microrheology provides lower values of the storage module which completely fails to detect any crossover.

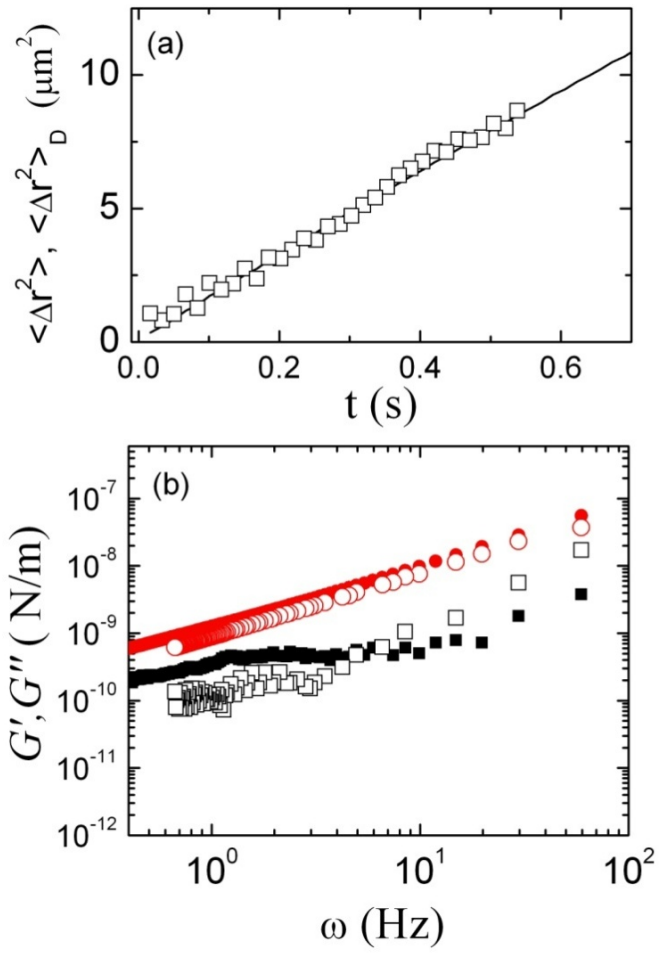

Figure 8.24. (a) Time dependence of $< \Delta r^2(t) >_D$ calculated from the average value of rD_{rr} (○) overlaid on $< \Delta r^2(t) >$ (straight line) for PS beads with diameter 1.6μm adsorbed at a air-water interface where a PTBA monolayer (4.6kDa, Γ=1.01mg/m^2) has been previously attached. (b) Frequency dependence of the storage, *G'* (■,□) and loss module, *G''* (●,○) of the monolayer considered in (a) calculated from one-particle (closed symbols) and two-particle microrheology (open symbols).

Let us now discuss the shear viscoelastic behaviour of a PTBA monolayer with larger molecular weight (103kDa), with N well above N_e. In this situation, the existence of 2D-entanglements, could affect the local motion of the tracers leading to a different viscoelastic scenario which has been previously demonstrated.[50] Figure 8.25.a shows the time evolution of $< \Delta r^2(t) >$ and $<\Delta r^2(t)>_D$ for the PTBA monolayer (103kDa) at $\Gamma = 0.4 mg/m^2$ using the same beads as tracers (PMMA, $\sigma = 2\mu m$). Significantly, $<\Delta r^2(t)>$ is larger than $<\Delta r^2(t)>_D$, suggesting that most of the motion of the beads occurs in a non-homogeneous environment formed by the PTBA monolayer. Any differences between both MSDs highlight the presence of heterogeneities, and this will be reflected in the calculated shear moduli; Figure 8.24.b shows the results obtained. Contrary to the behaviour shown in Figure 8.23 for a PTBA with lower molecular weight, the agreement between the values of *G'* of both methods is reasonable. However, two-particle correlation leads to lower values of *G''* than one-particle microrheology over the whole frequency range studied. As a consequence, now the values of the storage and loss moduli are close to each other over the frequency range, contrary to the behaviour pointed out by one-particle microrheology. Again, for this polymer it is possible to obtain the crossover of *G'* and *G''*. We found a crossover point at $\omega = 16Hz$; and thus the respective relaxation time takes the value: $\tau_d \approx 2/\omega_x = 0.06s$. It should be noted that macrorheology shear viscosity experiments performed in this system, at the same Γ, lead to a relaxation time of $\tau_d = 42s$ which is several orders of magnitude higher than the one obtained for two-particle correlation. These differences in the relaxation times between macro and micro-experiments lead to the same conclusions previously mentioned.

Finally, the different behaviours obtained for $M_w = 4.6kDa$ and $M_w = 103kDa$ must arise from the existence of entanglements in the high molecular weight sample, which is the main difference between both samples. In particular, for the PTBA monolayer with $M_w = 103kDa$, the probe particles size ($\sigma = 2\mu m$) is also much larger than the characteristic correlation length for this high molecular weight ($\xi^* \approx R_F = 53.02nm$) so that the probes are considered to be dynamically coupled to a viscoelastic continuum not being affected by the existence of heterogeneity of the medium at length scales comparable with particle length. However, the existence of an entangled scenario could promote that polymer chains are depleted by entropic effects in the vicinity of a surface particle to distances of order of the coil radius.[6, 59] Schnurr et al. has suggested that in an entangled 3D system formed by flexible Actin filaments, the coil depletion would have implications for the dynamics of dispersed colloidal probes.[60] Accordingly, a

similar explanation in terms of the depletion of the quasi-2d polymer coils nearest to the beads could arise.

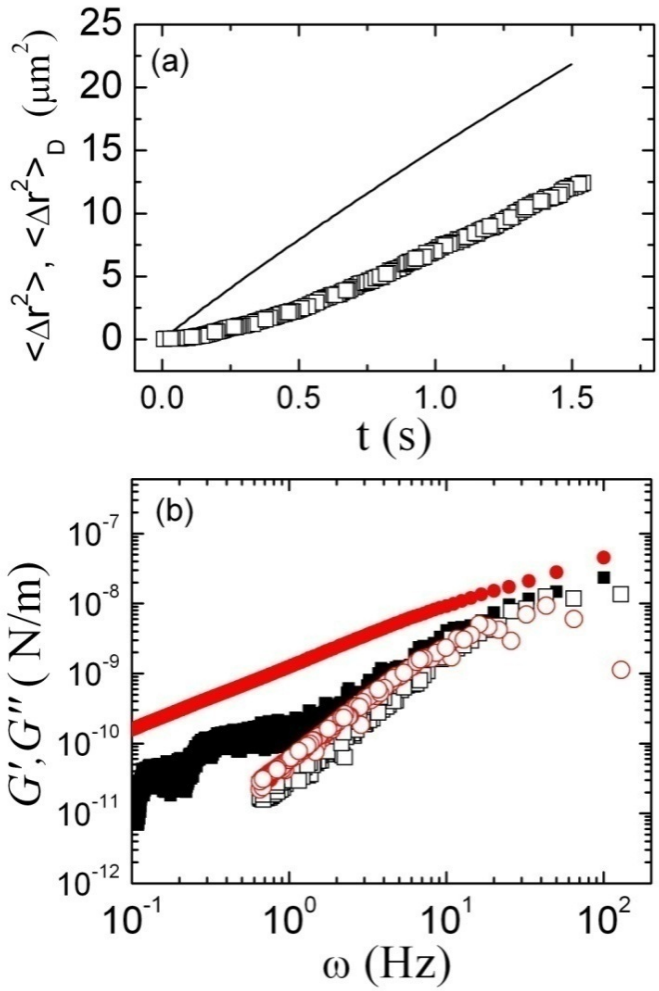

Figure 8.25. (a) Time dependence of $< \Delta r^2(t) >_D$ calculated from the average value of rD_{rr} (○) and $< \Delta r^2(t) >$ (straight line), for PMMA beads with diameter 2μm adsorbed at a air-water interface where a PTBA monolayer (103kDa, Γ=0.40mg/m^2) has been previously attached. (b) Frequency dependence of the storage, *G'* (■,□) and loss module, *G''* (●,○) of the monolayer considered in (a) calculated from one-particle (closed symbols) and two-particle microrheology (open symbols).

To test the hypothesis stated above, Figure 8.26 shows an example of a heterogeneous 3D system, such as polymerized F-actin with 0.47μm of average filament length and using PS beads as tracers (σ =0.20μm) obtained from ref. 57. It can be observed that $< \Delta r^2(t) >$ is up to 5 times larger than $< \Delta r^2(t) >_D$, suggesting that most of the motion of the beads is inside a "cage" formed by actin filaments. The linear viscoelasticity calculated from the one-particle methodology largely underestimates the bulk value by a factor of 5, which are in agreement with the two-particle correlation results. This experiment highlights the differences between one-particle and two-correlation particle microrheology for a heterogeneous system. In our experiments with polymer monolayers, the

differences between both MSDs found are always smaller than the difference found for a well known heterogeneous medium, such as F-actin.

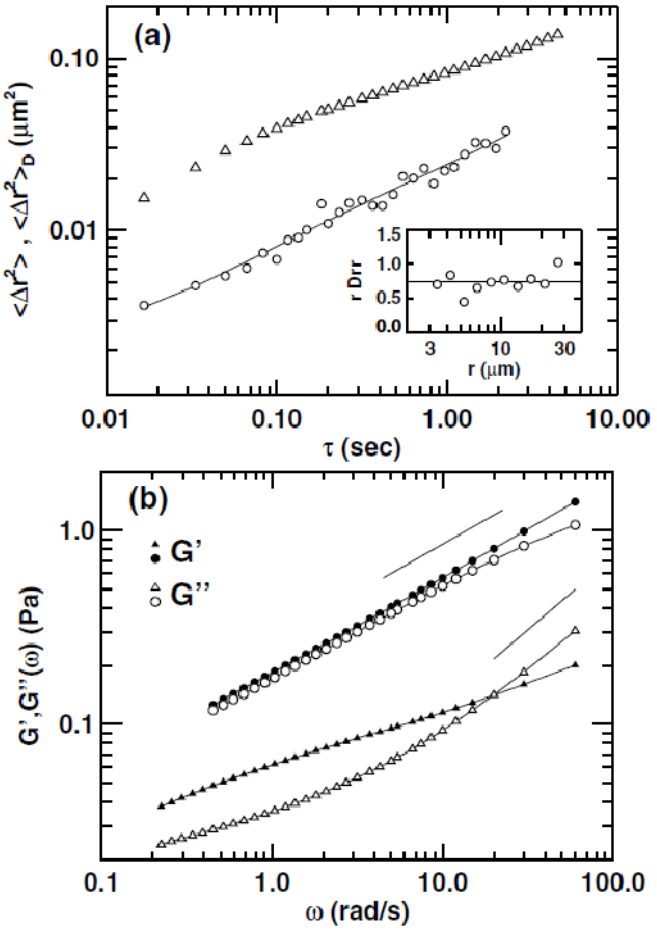

Figure 8.26. Comparison of the data from single-particle and two-particle correlation tracking experiments with F-Actin, an example of a 3D heterogeneous system. (a) Mean square particle fluctuations, triangles correspond to single particle ($< \Delta r^2(t) >$) and circles to two-particles correlation ($< \Delta r^2(t) >_D$). Inset shows the behaviour of two-point correlation function versus particle separation where the $1/r$ *behaviour* is emphasized. (b) The linear viscoelastic shear moduli calculated from the MSDs, circles correspond to the two particles and triangles one-particle technique. Continuous lines refer to bulk measurements of the shear moduli in fair agreement with data from cross-correlated particle motions. Adapted from Ref. 57.

4.5 Molecular weight effect on the shear viscoelasticity of PTBA monolayer: Comparison between Micro and Macro methodologies

As pointed out above there is a quantitative inconsistency between macro and micro-rheology results. To summarize, Figure 8.27 shows clearly the great difference found between micro- and macrorheology for monolayers of PTBA at the same experimental conditions. We have measured the shear viscosity (η) at the so-called Γ^{**} surface concentration (Π^{**}=16mN/m) for different polymer

weights (see Chapter 2 for details). η (Γ^{**}) has been measured using two different oscillatory macroscopic rheometers[17, 50] as be pointed out in Chapter 2. It has also been calculated for all the samples by the modified-Fischer theory previously shown, using PS particles with 1.6μm of diameter as tracers. It is noteworthy that similar results were found for other particles and for the calculation using the GSE equation from single particle tracking.

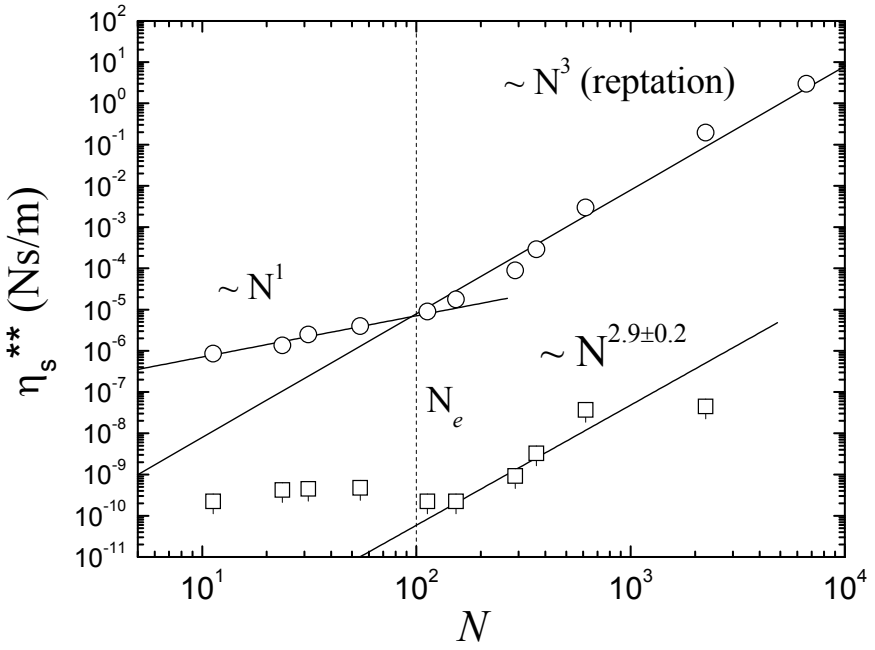

Figure 8.27. Surface shear viscosity for monolayers of PTBA as a function of the chain length at a dense state (Π**=16mN/m). The lower curve corresponds to data obtained from particle tracking while the upper curve was obtained from conventional oscillatory rheometers. Both plots represent the scaling behaviour of the shear viscosity at increasing molecular weight. N_e marks the critical chain size for which entanglements become possible.

From the macroscopic measurements of η (Γ^{**}) performed at the same state, we have already demonstrated that above the critical entanglement size ($N_e \approx$ 100), we found a reptation-like dependence of the shear viscosity on the molecular weight ($\eta \sim N^{3.0\pm0.3}$). A weaker linear dependence ($\sim N^1$) was expected below N_e. These values of η** obtained are in the range from 8×10^{-7} to 3 N·s/m. However, from microrheology measurements, in general, we have obtained much lower values of η (Γ^{**}) for all the samples studied, in the range from 2×10^{-10} to 4×10^{-8} N·s/m. The huge difference (about three orders of magnitude) cannot be attributed to specific interactions between the particles and the monolayer as it was demonstrated above. The values calculated by the GSE equation, allows us to conclude that these differences cannot be due to the accessible experimental frequency. On the other hand, it is important to note that the values of η (Γ^{**}) follow a similar trend at $N>N_e$ suggesting the existence of a *reptation* motion of the polymer chains attached to a 2D-enviroment. The agreement of the values of

η calculated by GSE equation and by Fischer's (or Danov's) theory, allows us to discard that the differences found are due to the different assumptions made by the distinct theories about the hydrodynamics considerations of a particle trapped at an interface. This discrepancy between micro- and macrorheology in the study of polymer monolayers has not a clear theoretical answer and further work is necessary to clarify this point.

5. Conclusions

In this chapter we have carefully demonstrated the validity of the microrheological measurements of polymer Langmuir monolayers attached at the air-water interface, where a low concentration of probe particles are added to the polymer film and the thermal motion of these particles is used to determine the viscoelastic response of the matrix polymer monolayer. We have focused here in the viscoelastic response of the poly (*terc*-butyl-acrylate) (PTBA) monolayers in different experimental conditions. We have evaluated different molecular weights in order to get further insight into the existence of entanglements in the bidimensional scenario proposed for this kind of flexible polymeric chains. We have found that microrheological experiments lead to values of the shear viscoelasticity complex up to three orders of magnitude lower than the ones measured by conventional macroscopic rheometers. However, from a qualitative point of view, the trend followed by both macro and micro experimental data are in agreement. Indeed, our results show that long enough flexible PTBA chains can entangle in the monolayer evidencing reptation-like motion.

Taking into account the different methodologies used to analysis the particle-tracking experiments, we have demonstrated that the modified Fischer approach leads to values of the experimental shear viscosity compatible with the ones obtained from the one-particle microrheology based on the GSE equation. This method also provides the complex shear viscoelasticity moduli over a broad frequency range (from 0.025 to hundreds of Hzs). From the comparison between the one-particle technique and the two-particle correlation one, we have obtained compatible results studying the PTBA with lower polymer weight while further discrepancies between *G'* and *G''* with PTBA at higher molecular weight. These differences could arise from the plausible existence of entanglements in the polymer matrix at increasing polymeric chain length. This situation based on an entangled scenario may provide heterogeneities on the polymer monolayer which lead to different viscoelastic response.

Finally, taking into account that the microrheology results of a polymer monolayer are in further agreement while exists great discrepancies with the macroscopic ones, further work is necessary to clarify this situation. One

explanation may arise from the local character of the microrheological results, mainly due to the motion of the particles are not conditioned to the whole polymer monolayer.

6. References

1. Larson, R. G., *The structure and rheology of complex fluids*. Oxford University Press: New York, 1999.
2. Riande, E.; Diaz-Calleja, R.; Prolongo, M.; Masegosa, R.; Salom, C., *Polymer Viscoelasticity. Stress and Strain in practice*. Marcel Dekker: New York, 2000.
3. Lee, M. H.; Reich, D. H.; K.J., S.; R.L., L., Combined passive and active microrheology study of protein-layer formation at an air-water interface. *Langmuir* **2009,** 25, 7976-7982.
4. Cicuta, P.; Donald, A. M., Microrheology: a review of the method and applications. *Soft Matter* **2007,** 3, (12), 1449-1455.
5. Gardel, M.; Valentine, M.; Weitz, D. A., Microrheology. In *Microscale diagnostic techniques*, Brauer, K., Ed. Springer: Berlin, 2005.
6. Waigh, T. A., Microrheology of complex fluids. *Rep. Prog. Phys.* **2005,** 68, 685-742.
7. Langevin, D., Influence of interfacial rheology on foam and emulsion properties. *Advances in Colloid and Interface Science* **2000,** 88, (1-2), 209-222.
8. Smith, R. K.; Lewis, P. A.; Weiss, P. S., Patterning self-assembled monolayers. *Prog. Surface Sci.* **2004,** 75, 1-68.
9. Binks, B. P., *Colloidal Particles at Liquid Interfaces*. Cambridge University press: UK, 2006.
10. Miller, R.; Liggieri, L., *Interfacial Rheology*. VSP: UK, 2009.
11. Langevin, D., *Light Scattering by Liquid Surfaces and Complementary Techniques*. Marcel Dekker: New York, 1992; Vol. 41.
12. Diez-Pascual, A. M.; Monroy, F.; Ortega, F.; Rubio, R. G.; Miller, R.; Noskov, B. A., Adsorption of water-soluble polymers with surfactant character. Dilational viscoelasticity. *Langmuir* **2007,** 23, (7), 3802-3808.
13. Monroy, F.; Ortega, F.; Rubio, R. G.; Velarde, M. G., Surface rheology, equilibrium and dynamic features at interfaces, with emphasis on efficient tools for probing polymer dynamics at interfaces. *Advances in Colloid and Interface Science* **2007,** 134-35, 175-189.
14. Liggieri, L.; Ferrari, M.; Mondelli, D.; Ravera, F., Surface rheology as a tool for the investigation of processes internal to surfactant adsorption layers. *Faraday Discussions* **2005,** 129, 125-140.

15. Ferry, J. D., *Viscoelastic Properties of Polymers*. 3 ed.; Wiley: New york, 1980.

16. Gavranovic, G. T.; Deutsch, J. M.; Fuller, G. G., Two-dimensional melts: Polymer chains at the air-water interface. *Macromolecules* **2005,** 38, 6672-6679.

17. Maestro, A.; Ortega, F.; Monroy, F.; Kragel, J.; Miller, R., Molecular Weight Dependence of the Shear Rheology of Poly (methyl methacrylate) Langmuir Films: A Comparison between Two Different Rheometry Techniques. *Langmuir* **2009,** 25, (13), 7393-7400.

18. Saxton, M. J.; Jacobson, K., Single-particle tracking: Applications to membrane dynamics. *Annu. Rev. Biophys. Biomol Struct* **1997,** 26, 373-399.

19. Mason, T. G.; Weitz, D. A., Optical measurements of frequency-dependent linear viscoelastic moduli of complex fluids. *Physical Review Letters* **1995,** 74, (7), 1250-1253.

20. Levine, A. J.; Lubensky, T. C., One- and two-particle microrheology. *Physical Review Letters* **2000,** 85, 1774-1777.

21. Mason, T. G., Estimating the viscoelastic moduli of complex fluids using tue generalized Stokes-Einstein equation. *Rheol. acta* **2000,** 39, 371-378.

22. Dasgupta, B. R.; Shang-You, T.; Crocker, J. C.; Frisken, B. J.; Weitz, D. A., Microrheology of polyethylene oxide using diffusing wave spectroscopy and single scattering. *Physical Review E (Statistical, Nonlinear, and Soft Matter Physics)* **2002,** 65, (5), 051505/1-10.

23. Wu, J.; Dai, L., One-particle microrheology at liquid-liquid interfaces. *Appl. Phys. Lett.* **2006,** 89, 094107.

24. Felderhof, B. U., Estimating the viscoelastic moduli of a complex fluid from observation of Brownian motion *J. Chem. Phys.* **2009,** 131.

25. Alexander, M.; Dalgleish, D. G., Diffusing wave spectroscopy of aggregating and gelling systems. *Current Opinion in Colloid & Interface Science* **2007,** 12, 179-186.

26. Hasnain, I.; Donald, A. M., Microrheology characterization of anisotropic materials. *Phys Rev E* **2006,** 73, 031901.

27. Chen, D. T.; Weeks, E. R.; Crocker, J. C.; Islam, M. F.; Verma, R.; Gruber, J.; Levine, A. J.; Lubensky, T. C.; Yodh, A. G., Rheological microscopy: Local mechanical properties from microrheology. *Physical Review Letters* **2003,** 90, (10).

28. Prasad, V.; Koehler, S. A.; Weeks, E. R., Two-particle microrheology of quasi-2D viscous systems. *Physical Review Letters* **2006,** 97, (17).

29. Liu, J.; Gardel, M. L.; Kroy, K.; Frey, E.; Hoffman, B. D.; Crocker, J. C.; Bausch, A. R.; Weitz, D. A., Microrheology probes length scale dependent rheology. *Physical Review Letters* **2006,** 96, (11), 118104/1-4.

30. Song, Y.; Luo, M.; Dai, L. L., Understanding nanoparticles diffusion and exploring interfacial nanorheology using molecular dynamics simulations. *Langmuir* **2009,** 26, 5-9.

31. Wu, C. Y.; Tarimala, S.; L.L., D., Dynamics of charged microparticles at oil-water interfaces. *Langmuir* **2006,** 22, 2112-2116.

32. kandar, A. K.; Bhattacharya, R.; Basu, J. K., Interfacial microrheology as a tool to study viscoelastic transtitions in nanoconfined soft matter. *Physical Review E* **2010,** 81, 041504.

33. Saffman, P.-G.; Delbrück, M., *Proc. Natl. Acad. Sci. USA* **1975,** 72, 3111-3113.

34. Hughes, B. D.; Pailthorpe, P. A.; White, L. P., The translational and rotational drag of a cylinder moving in a membrane. *J. Fluid Mechanics* **1981,** 110, 349-372.

35. Barentin, C.; Muller, P.; Ybert, C.; Joanny, J.-F.; di Meglio, J.-M., Shear viscosity of polymer and surfactant monolayers. *Eur. Phys. J E* **2000,** 2, 153-159.

36. Stone, H.; Ajdari, A., Hydrodynamics of particles embedded in a flat surfactant layer overlying a subphase of finite depth. *J. Fluid Mechanics* **1998,** 369, 151-173.

37. Danov, K. D.; Aust, R.; Durst, F.; Lange, U., Influence of the surface viscosity on the drag and torque coefficients of a solid particle in a thin liquid layer. *Chemical Engineering Science* **1995,** 50, (2), 263-277.

38. Danov, K. D.; Dimova, R.; Pouligny, B., Viscous drag of a solid sphere straddling a spherical or flat surface. *Physics of Fluids* **2000,** 12, (11), 2711-2722.

39. Fischer, T. M.; Dhar, P.; Heinig, P., The viscous drag of spheres and filaments moving in membranes or monolayers. *Journal of Fluid Mechanics* **2006,** 558, 451-475.

40. Fischer, T. M., Comment on "Shear viscosity of Langmuir monolayers in the low-density limit". *Physical Review Letters* **2004,** 92, (13), 139603/1.

41. Wurlitzer, S.; Schmiedel, H.; Fischer, T. H., Electrophoretic relaxation dynamics of domains in Langmuir-monolayer. *Langmuir* **2002,** 18, 4394.

42. Paunov, V. N., Novel method for determining the three-phase contact angle of colloid particles adsorbed at air-water and oil-water interfaces. *Langmuir* **2003,** 19, (19), 7970-7976.

43. Bonales, L. J. Microparticles at Fluid Interfaces. Ph.D. Thesis, Universidad Complutense de Madrid, 2009.

44. Klingler, J. F.; McConnell, H. M., Field-gradient electrophoresis of lipid domains. *J Phys Chem* **1992,** 97, 2962.

45. Klingler, J. F.; McConnell, H. M., Brownian motion and fluid mechanics of lipid monolayer domains. *J Phys Chem* **1993,** 96, 6096.

46. Crocker, J. C.; Grier, D. G., Methods of digital video microscopy for colloidal studies. *J Colloid Interface Sci* **1996,** 179, 298-310.

47. Aveyard, R.; Binks, B. P.; Clint, J. H.; Fletcher, P. D. I.; Horozov, T. S.; Neumann, B.; Paunov, V. N.; Annesley, J.; Botchway, S. W.; Nees, D.; Parker, A. W.; Ward, A. D.; Burgess, A. N., Measurement of long-range repulsive forces between charged particles at an oil-water interface. *Physical Review Letters* **2002,** 88, (24).

48. Sickert, M.; Rondelez, F., Shear viscosity of Langmuir monolayers in the low-density limit. *Physical Review Letters* **2003,** 90, (12), 126104/1-4.

49. Monroy, F.; Hilles, H. M.; Ortega, F.; Rubio, R. G., Relaxation dynamics of Langmuir polymer films: A power-law analysis. *Physical Review Letters* **2003,** 91, (26).

50. Maestro, A.; Hilles, H.; Ortega, F.; Rubio, R. G.; Langevin, D.; Monroy, F., Reptation in Langmuir polymer monolayers. *Soft Matter* **2010,** accepted 2010.

51. Gennes, P.-G. d., *Scaling Concepts in Polymer Physics*. Cornell University Press: Ithaca, 1979.

52. Sickert, M.; Rondelez, F.; Stone, H. A., Single-particle Brownian dynamics for characterizing the rheology of fluid Langmuir monolayers. *Europhysics Letters* **2007**, 66005 (6 pp.).

53. De Gennes, P. G., Dynamics of entangled polymer solutions. I. The Rouse model. *macromolecules* **1976,** 9.

54. De Gennes, P. G., Dynamics of Entangled Polymer Solutions. II. Inclusion of Hydrodynamic Interactions. *macromolecules* **1976,** 9, 594-598.

55. Ding, A. L.; Binks, B. P.; Goedel, W. A., Influence of particle hydrophobicity on particle-assisted wetting. *Langmuir* **2005,** 21, (4), 1371-1376.

56. Arendt, B. H.; Krishnamoorti, R.; Kannan, R. M.; Seitz, K.; Kornfield, J. A.; Roovers, J., Dynamics of Disordered Diblocks of Polyisoprene and Polyvinylethylene. *Macromolecules* **1997,** 30, 1138-1145.

57. Crocker, J. C.; Valentine, M. T.; Weeks, E. R.; Gisler, T.; Kaplan, P. D.; Yodh, A. G.; Weitz, D. A., Two-point microrheology of inhomogeneous soft materials. *Physical Review Letters* **2000,** 85, (4), 888-891.

58. Corrigan, A. M.; Donald, A. M., Passive Microrheology of Solvent-Induced Fibrillar Protein Networks. *Langmuir* **2009,** 25, 8599–8605.

59. Israelachvili, J. N., *Intermolecular and Surface Forces*. 2nd ed.; Academic Press: San Diego, 1991.

60. Schnurr, B.; Gittes, F.; MacKintosh, F. C.; Schmidt, C. F., Determining Microscopic Viscoelasticity in Flexible and Semifllexible Polymer Networks from Thermal Fluctuations. *macromolecules* **1997,** 30, 7781-7792.

Conclusions

The present Ph. D. Thesis contains an experimental study of the dynamic properties of interfacial systems and their relation with their corresponding equilibrium features. Both insoluble neutral polymer spread monolayers (Langmuir films), and soluble systems (proteins, nanoparticles and their mixtures with surfactants) forming Gibbs layers, have been studied.

In particular, a technique for measuring electrically excited capillary waves (ECW) has been built. The equipment is suitable for measurements of the dilational viscoelastic moduli in the 10Hz–2kHz frequency range, and can be used to study both Langmuir and Gibbs monolayers. It has been found to be an excellent complement to other low-frequency techniques, such as the based in mobile barriers (oscillation and compression) and the oscillating drop ones. The design details of the technique and its calibration are given in **Chapter 3**.

The main conclusions of this thesis are summarized below:

In **Part II** we have pointed out that, in the low frequency range, the physical mechanism for the dynamics of neutral polymer Langmuir monolayers at the air–water interface is reptation when the surface is a good solvent for the monolayer. On the other hand, for poor solvent conditions, the dynamics can be described as a percolation process leading to the existence of a *quasi*-bidimensional soft–glass.

Part III of the thesis was dedicated to high frequency studies of both Langmuir and Gibbs monolayers. In the case of the Langmuir monolayers of neutral polymers, the spatial scale involved in ECW experiments lies within the micrometers scale making possible the study of the relaxation of collective segmental motions. We have demonstrated from the Γ–dependence of the dilational features a power-law description compatible with the existence of a percolated PMMA network. For PTBA monolayers, the results have pointed out the description of the dilational viscoelastic parameters at high frequencies in terms of the scaling-laws predicted by de Gennes for the reptation motion characteristic of an entangled network. Thus the characteristic times found correlate relatively well with the collective diffusion of segments of chains.

In the case of mixtures of silica nanoparticles and a surfactant, the combination of high and low frequency results has pointed out that the interaction

between the particles negatively charged and the cationic surfactants molecules plays a key role in the interfacial dynamics. The correlation between the experimental data with a theoretical approach previously developed lead to demonstrate the instantaneous coupling between the surface rheology and the adsorption kinetics. Thus, besides the adsorption of the complex from the bulk, it is important the internal reorganization process of the mixed particle–surfactant at the interface.

In addition, for mixtures of the protein β–casein (BCS) and surfactants with different chemical nature and charge, again the combination of low and high-frequency data allowed us to conclude that the surface dilational behaviour of the mixtures has a strong dependence on the nature of the surfactant used. The results has been tested by the theoretical model previously suggested for Fainerman et al., based on the depletion of the proteins at the interfacial layers as the surfactant concentration increases. The results have been demonstrated that for both complex BCS–surfactant the behaviour of the mixed layers corresponds to a competitive adsorption mechanism.

Finally, **Part IV** was dedicated to the use of particle tracking as a microrheological technique. The study of insoluble neutral polymer monolayer lead to similar conclusions about the physical mechanism for the chain motion in both good and poor solvent conditions than the macrorheological techniques based in conventional interfacial rheometers. However, there is a big difference (2-3 orders of magnitude) between the values obtained by macro- and microrheology. So far no explanation has been found for this discrepancy.

To test the validity of the particle tracking technique, we have used particles with different chemical composition and size, as well as different theoretical approaches, such as Fischer's theory, and theories based on the *GSE* equation as one-particle treatment and two-point correlation, to obtain values in reasonable agreement of the shear viscosity, (or the complex shear modulus) for a Langmuir monolayer of poly (*tert*-butyl acrylate).

Moreover, we have revealed the non-regular behaviour of the contact angle of particles adsorbed at fluid interfaces. Our results have pointed out that roughness and/or porosity of particles play a key role in their hydrophobicity. Thus, we have highlighted the existence of a solvent effect supported by the values of the line tension estimated for the different systems studied.

To conclude, we can assert that the present thesis has studied some of the interesting problems deal with the relationship between equilibrium and dynamical behaviour of interfacial systems. This thesis thus contributes with

pieces of knowledge, getting further insight into the systems attached to fluid interfaces, which have been partially published and submitted for publication.

Appendix section

Appendix 1

Methods Summary

In this section, we will make a short description of the different experimental techniques that have been used in the experiments performed in this thesis. A classification is made as a function of the properties obtained from each one: (1) Equilibrium properties, and (2) both dilational and shear rheological features.

1. Langmuir Monolayers: Equilibrium properties

1.1 Preparation and Surface pressure-concentration isotherms

Langmuir monolayers are prepared by spreading a small amount of the surfactant, polymer and/or particle solution onto a bare air-water or oil-water interface, being chloroform or aliphatic alcohols used as preferred solvent. The spreading procedure consists on adding small aliquots of the stock solution (10µl, typically), with a Hamilton syringe at different places on the surface till reaching the desired surface concentration. Once the solvent evaporates, the surfactant surface concentration, Γ, which depend on the spread volume, on the concentration of the solution, and on the accessible surface area A_0, can be varied by moving the barriers that confine the surface, as shown in Figure A.1.

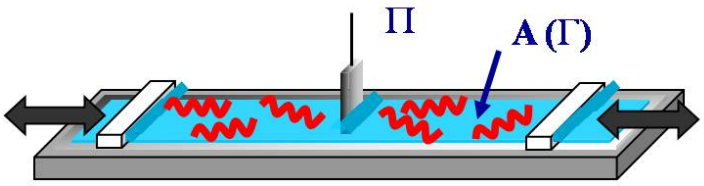

Figure A.1. Scheme of a Langmuir Balance: the trough and the barriers are usually made of *Teflon*, although *Delrin* can also be used as the material for the barriers, and the Wilhelmy plate is normally made of paper or of roughed Pt. The Teflon trough is glued to a thermostated metallic piece for temperature control. For very high surface pressures a continuous ribbon instead of barriers is preferred.

Usually the monolayers are formed on commercially available Teflon Langmuir trough. Hence, Figure A.2 shows the Langmuir troughs devices used in this work (KSV Instruments Minitrough, Finland, or Nima, Coventry, UK) both with computerized control.

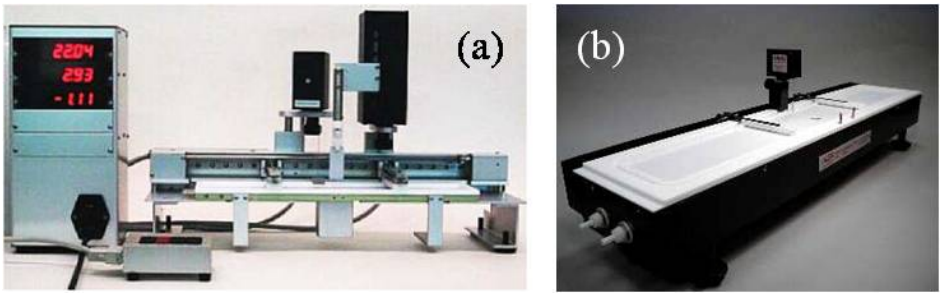

Figure A.2. Set of pictures of the Langmuir troughs commercially available used in this study. (a) KSV Instruments Minitrough from Finland and (b) Nima 701model, Coventry, UK.

A Platinum-Wilhelmy plate (or a rectangular piece of pure cellulose paper, chromatography quality) is used as a surface pressure sensor. The trough is made of Teflon while polyoxymethylene (Delrin) hydrophilic barriers are usually used to prevent the film leakage under the barriers at higher surface pressures. The

whole set-up is enclosed in a box to keep isolated the experimental realization. The temperature control of water in the trough is carried out by passing water through the jacket at the bottom of the trough from a thermostatic bath. The temperature close to the surface is measured with a calibrated Pt-100 sensor. The temperature of the box is kept constant within ±0.1ºC.

Surface tensions are measured from the maximum force needed to detach the plate from the liquid surface. If a Langmuir trough is used the Wilhelmy plate is the most valuable method because: (a) the relative force (monolayer/water), instead of the maximum detachment force, can be measured, and (b) this method does not need further corrections. The plate (made of rough platinum or chromatography paper) hanged from the hook of a microbalance is moved until it gets in contact with the air-water interface (see scheme on Figure A.3).

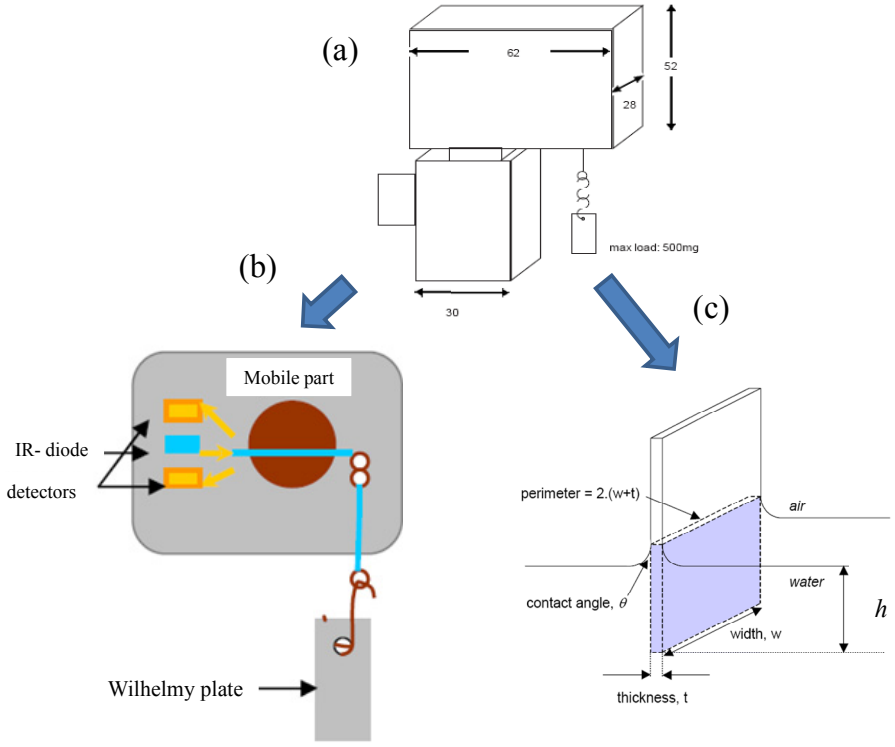

Figure A.3. Scheme of the microbalance and the plate which measure the surface tension (γ). (a) General aspect of the Wilhelmy plate hanged from the hook of the microbalance (dimensions in cm). (b) Internal scheme of the microbalance. (c) Detail of the Wilhelmy plate attached to an arbitrary interface.

When the plate is placed at an arbitrary interface, the weight (W) of the plate increase by the force (F) exerted by the interface, consequently, this increment of weight (ΔW) is related to the surface tension (γ) by the following expression:

$$\gamma = \frac{\Delta W}{L \cos\theta} \qquad \text{(A.1)}$$

Where L is the plate contour (see Figure A.3.c), and θ accounts for the contact angle between the liquid and the plate given by:

$$\left(\frac{h}{a}\right)^2 = 1 - \sin\theta \qquad \text{(A.2)}$$

a being the capillary length and h accounts for the height of the plate as shown in Figure A.3.b. The use of both plates (platinum and cellulose paper) assures that the contact angle $\theta \approx 0^{o}$ pointing out the existence of complete wetting conditions. Experimentally, in the microbalance device the detection of the surface tension γ is based on the deflection of a mechanical mobile part produced by the increment of weight (ΔW) of the plate fixed by a hook when it is placed at the interface (see Figure A.3.b). Each reading of the surface tension made by the microbalance is determined within ±10 μN/m. Control experiments performed assuming bare air-water interfaces and taking into account small changes of the position of the barriers the variation in the surface tension is around ±30 μN/m.

The force exerted on a Wilhelmy plate immersed in the water, measured with a microbalance, gives the surface pressure, Π, defined as the difference between, γ_0, the surface tension of pure water, and γ the surface tension in presence of the monolayer ($\Pi = \gamma_0 - \gamma$). The surface pressure is related to the surface concentration by the equation of state $\Pi = \Pi(\Gamma, T)$, where T is the temperature. It is noteworthy that if we measure the dependence of Π as a function of only Γ and T, it must be considered that other factors like pH, ionic strength and the composition of the subphase are held constant.

Equilibrium studies of monolayers consist in the determination of the Π–Γ isotherms, which are the usual route to study the phase behaviour of a given monolayer.

1.2 Ellipsometry and Brewster Angle Microscopy

Ellipsometry is a technique most frequently used for solid supported mono and multilayers, but with the use of lasers as the light source, and antivibrating devices to avoid mechanically induced oscillations on the liquid surface, it became a useful technique for liquid supported monolayers.

When a beam of light impinges on a surface part of beam is reflected and the rest is transmitted (in absence of other effects like scattering, etc.). Ellipsometry is based on the analysis of the state of polarization of the reflected light.[1, 2] A plane polarizing incident beam contains both p (polarized in the plane of incidence, PI) and s (polarized perpendicular to the plane of incidence) polarizations (see Figure A.4). Using Fresnel equations p and s reflectances (R^p,

R^s) – defined as the ratio of the reflected to the incident intensity or the square of the reflectance coefficients, R^p and R^s- can be calculated as a function of the angle of incidence (θ_1). R^s is always higher that R^p, and there is a particular angle called the Brewster angle (θ_B), at which there is a minimum in R^p ($R^p = 0$ in the case of non-absorbing materials), this is the reason for the high contrast obtained in Brewster angle microscopy. For the case of a bare water-air interface using the following equation

$$\theta_B = \tan^{-1}\left(\frac{n_2(\lambda)}{n_1(\lambda)}\right) \qquad \text{(A.4)}$$

We obtain: $\theta_B = 53.14^o$ for $\lambda = 532nm$.

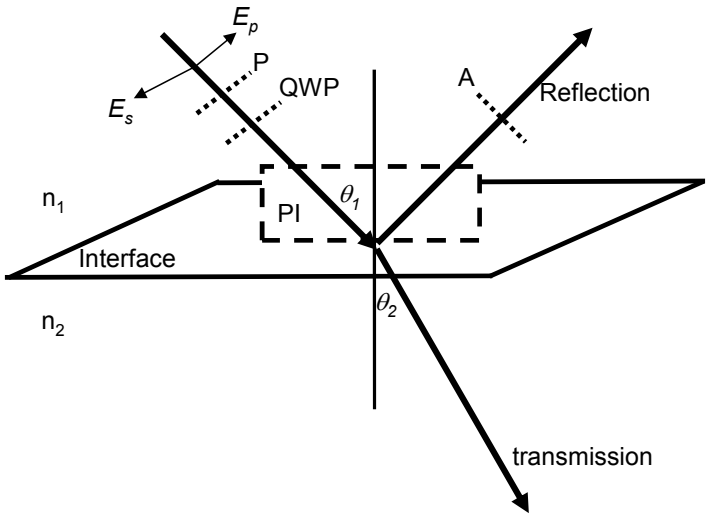

Figure A.4. Geometry of the incident, reflected and transmitted beams at a surface in a typical ellipsometer configuration.

In general for one or multiple piled interfaces the complex ratio of the total reflection coefficients, ρ, is related with the ellipsometric angles Δ and Ψ through:

$$\rho = \frac{R^p}{R^s} = \tan\Psi e^{i\Delta} \qquad \text{(A.5)}$$

where Δ and Ψ are the quantities measured by an ellipsometer. Δ is related to the phase differences between the parallel and perpendicular components of the incident δ_i and reflected δ_r beams, and its value can vary from zero to 360º:

$$\Delta = \delta_i - \delta_r \qquad \text{(A.6)}$$

and the tangent of Ψ is the ratio of the magnitudes of the *p* and *s* total reflection coefficients:

$$\tan \Psi = \frac{\left|R^{p}\right|}{\left|R^{s}\right|} \qquad (A.7)$$

There are several commercial apparatus which use slightly different setups, but the most versatile ones consist in a very stable laser (typ. power 50mW), which passes though a polarizer (P) and a quarter wave plate (QWP), and is reflected at a given angle of incidence by the interface. The reflected light is going through a analyzer (A) and finally detected with a PMT or a CCD camera (imaging ellipsometry). An scheme of these main parts is shown in Figure A.5. The angle of incidence can be varied (typ. 30-80º) and the optical components are motorized with rotatory stages. At a given angle of incidence, both P and A are rotated to null the detected intensity, there are 4 null point, two for the QWP fixed in 45º and two for -45º, and the more accurate measurements are obtained by averaging of the ellipsometric angles with the four sectors, although for faster measurements it is possible to use only one. For the sector corresponding to QWP 45º and 0º<A<90º and -45º<P<135º, avoiding redundancies for angles separated by 180º, the ellipsometric angles can be calculated by $\Delta=270º - 2P$ and $\Psi=A$.

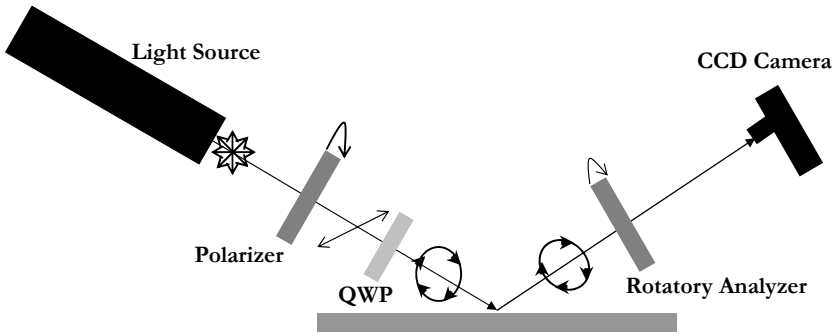

Figure A.5. Scheme of the main parts of the Ellipsometry technique.

Ellipsometry experiments were performed in a Nanofilm (Germany) EP^3 with a single wavelength of 532 nm, and all the experiments were carried out on a Langmuir through at a fixed angle of 56º. The ellipsometric angles △ and Ψ describe the changes in the state of polarization when the light is reflected at a surface. The accuracy of △ and Ψ were ±0.1 and ±0.05 degrees, respectively. To obtain the ellipsometric thickness (*h*) the system was modelled as three layers: the first layer was the aqueous subphase where the refractive index was taken as n = 1.34. The external layer (third layer) was the air with a refractive index equal to 1polymer solution. Finally the polymer layer (second layer of the model) thickness and refractive index has to be obtained from the fitting, using a Simplex minimization algorithm[3, 4] of △ and Ψ to the Fresnel equation[1] for the method of Drude.[5]

Brewster angle microscopy is a technique that allows one to make a direct observation of the meso-scale textures or domains formed in a monolayer under phase separation due to a 2D phase transition or to a 3D segregation of the monolayer material due to aggregation or collapse. In BAM *p*- polarized light from a laser is directed to the air-water interface at the Brewster angle (53.1º). Under these conditions no light is reflected from the interface, and we get a dark image. In these conditions the presence of a monolayer that modifies the Brewster angle give rise to reflected light which is detected with a CCD camera, the presence of domains with different surfactant concentration or different thickness can be easily imaged using a microscope objective before the camera. As it will be evident below BAM is no more than a low level ellipsometry.

2. Rheology of Langmuir monolayers

The viscoelastic behaviour of interfacial layers actually contains compression and shear components. Hence, the following techniques, that will be discussed in detail below, give information about both shear and compression rheology of monolayers adsorbed at fluid interfaces.

2.1. Oscillatory strain experiments

In this rheological technique the barriers of the Langmuir through are driven to a sinusoidal motion of constant frequency, ω, that imposes a oscillatory strain perturbation on the film. Fourier transform analysis of the strain must show the true sinusoidal character of the movement and the monochromaticity, i.e. absence of frequency components others than the fundamental one, ω.

The film is strained in the Langmuir trough by an uniaxial in-plane compression of amplitude u, ranging 0–100% of the initial surface area A_0. Since the Langmuir trough has a fixed width (B) the strain ratio is actually an elongation/compression ratio performed between the trough barriers placed at a distance L; since the available area is $A = B \times L$, one has:

$$u = \frac{A_0 - A}{A_0} = \frac{L_0 - L}{L_0} = 1 - \frac{L}{L_0} = 1 - \lambda \qquad \text{(A.8)}$$

λ ($= L/L_0$) being the compression ratio defined with respect to the initial position of the barriers (L_0). This ratio is lower than unity for the compression-like experiments considered in this work.

The barrier speed v must be conveniently changed in order to perform experiments at constant frequency but variable strain amplitudes ($v \approx \omega \times u$). As a consequence of the surface compression a negative surface pressure gradient

$\Delta\Pi$ appears, the so-named dilational stress σ_D. it acts as restoring force for recovering the initial state of the film when strain ceases:

$$\sigma_D = \Pi_0 - \Pi < 0 \tag{A.9}$$

It must be noticed that because of the uniaxial character of the compressive deformation, as the applied strain u as the response stress σ, contain both, hydrostatic compression (*xx*) and in-plane shear (*xy*) components. In terms of a generalized stress function $\sigma = -\sigma_D$, the dilational response function can be then written as follows:[6]

$$-\sigma_D = \sigma = \varepsilon(u)\cdot u \tag{A.10}$$

where $\varepsilon(u)$ is in general a strain-dependent dilational modulus, containing two components coupled together, the hydrostatic component (ε_0) and the shear one (G):

$$\varepsilon(u) = \varepsilon_0(u) + G(u) \tag{A.11}$$

At very small strains ($u \to 0$) the elastic response becomes linear, *i.e.* the dilational modulus is a strain-independent constant, which takes values close to the equilibrium compression modulus ε_0, which can be obtained from the equilibrium isotherms:

$$\varepsilon(u \to 0) \geq \varepsilon_0 \tag{A.12}$$

Since the applied strain of amplitude u_0 is sinusoidal in shape, its time dependence has the form:

$$u(t) = \frac{u_0}{2}\left[1 + \sin(\omega t + \phi_u)\right] \tag{A.13}$$

where ω is the strain frequency and ϕ_u is a phase factor which depends of the arbitrary choice of the initial time of the experiment.

Only in the linear regime (if $u \to 0$ then $\sigma = cte \times u$) the elastic response closely follows the sinusoidal shape of frequency ω imposed by the strain:

$$\begin{aligned} \Pi(t) &= \Pi_0 + \sigma(t) \\ \sigma(t) &= \frac{\sigma_0}{2}\left[1 + \sin(\omega t + \phi_\sigma)\right] \end{aligned} \tag{A.14}$$

here, σ_0 is the amplitude of the response, measured with respect to the pressure background Π_0, and ϕ_σ a phase factor accounting for the viscous delay in the response ($\phi_\sigma \geq \phi_u$). In fact, a pure elastic response leads to a zero phase difference, $\phi = \phi_\sigma - \phi_u = 0$, which reaches a maximum value of $\pi/2$ for a non-elastic viscous fluid. In the linear regime, the elasticity modulus ε and the dilational viscosity κ can be strictly obtained as follows:

$$\varepsilon = |\varepsilon| \cos\phi \quad \omega\kappa = |\varepsilon| \sin\phi$$
$$\textit{where} \qquad (A.15)$$
$$|\varepsilon| = \frac{\sigma_0}{u_0} \quad \textit{and} \quad \phi = \phi_\sigma - \phi_u$$

Figure A.6 shows a typically oscillatory experiment performed on an arbitrary monolayer trough the sinusoidal strain imposed by the barriers of a Langmuir trough. In addition, at higher strains, the viscoelastic response becomes non-linear, and obviously the sinusoidal model proposed cannot be a good description of the stress response. A Fourier analysis is necessary for a rigorous analysis of strongly non-linear responses.[7] However, an accurate description of the stress σ is given by the following expression:

$$\sigma = \sigma_0 \exp(i\omega t) + \sigma_1 \exp(i2\omega t) + \sigma_2 \exp(i3\omega t) + \ldots \quad (A.16)$$

where σ_1, σ_2,.. are the amplitudes of the harmonics.

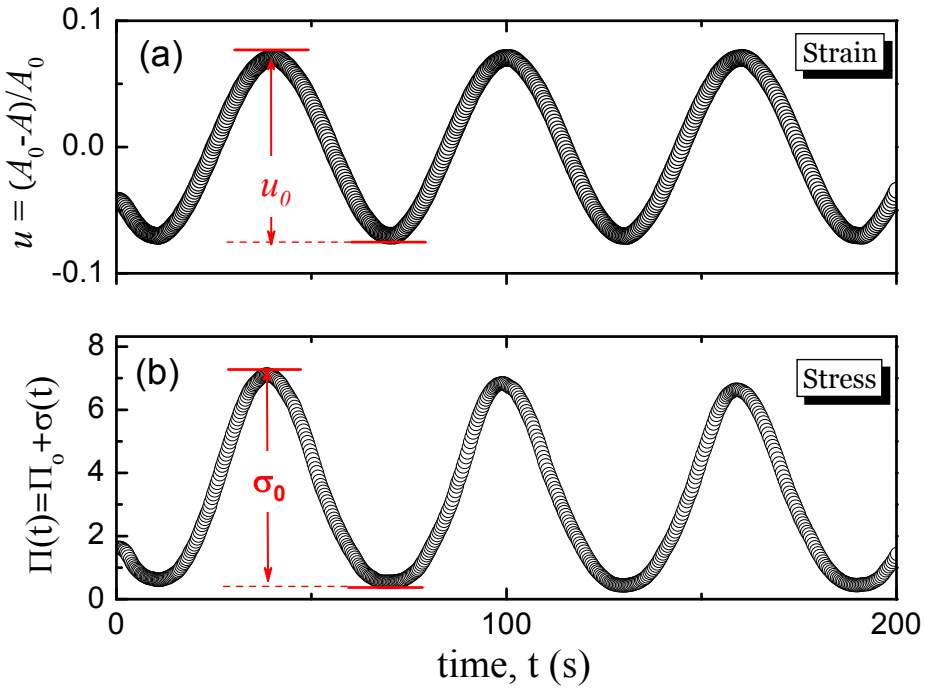

Figure A.6. Typically experiment of oscillatory strain performed on an arbitrary fluid monolayer at an air-water interface deposited on a Langmuir trough. (a) Sinusoidal strain (*u*) imposed by the barriers of the trough as a function of time. (b) Stress curve from the sinusoidal shape imposed by the strain.

2.2. Relaxation by step-compression experiments

The step-compression experiments are carried out in the Langmuir trough. The spread monolayer is suddenly strained upon a mechanical uniaxial compression imposed by the barriers of the Langmuir trough. The compression

ratio is adjusted to a few percent of the initial area depending of the system. It must be ensured that the viscoelastic response is linear, and the signal-to-noise ratio of the recorded signal is high enough. The relaxation of the surface pressure is then monitored as a function of time $\Pi(\Gamma,t)$ until the final equilibrium is reached $\pi(\Gamma,t\to\infty)$, thus the relaxation function can be easily determined from the compression stress $\sigma(t) = \pi(\Gamma,t) - \pi(\Gamma,t\to\infty)$. For instance, Figure A.7 shows a typical relaxation experiment by step-compression performed to a typical insoluble polymer monolayer in a Langmuir trough. Controls are regularly made by monitoring the surface tension of a bare water subphase, remaining constant within ±0.1mN/m for about one day. Additionally, relaxation curves not recovering a final steady-state compatible with the equilibrium isotherm are not considered.

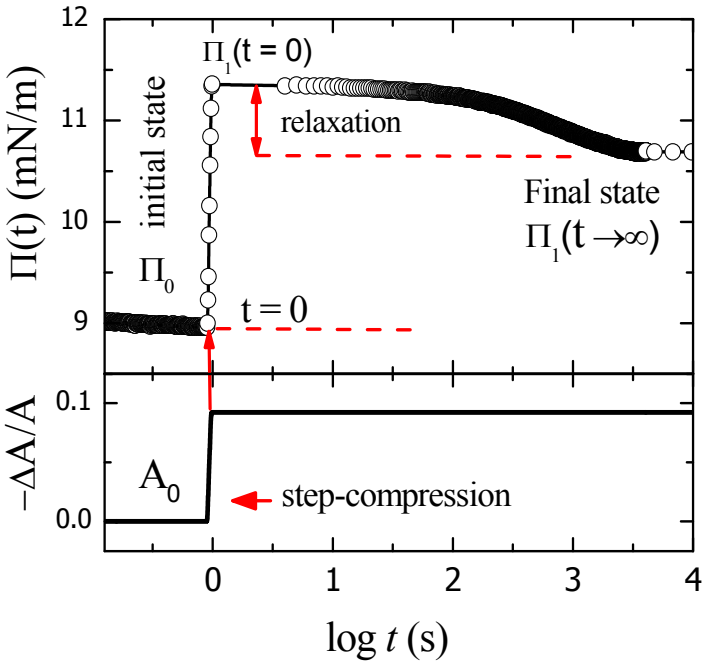

Figure A.7. Typically experiment of relaxation by step-compression performed on an arbitrary fluid monolayer at an air-water interface.

2.3 Capillary Pressure Tensiometer

The Capillary Pressure Tensiometer (CPT) is based on the measurement of the capillary pressure, ΔP_{cap}, across a spherical interface. In fact, under suitable mechanical quasi-equilibrium conditions, the Young Laplace equation holds,

$$\Delta P_{cap}(t) = \frac{2\gamma(t)}{R(t)} \qquad \text{(A.17)}$$

From this equation, $\gamma(t)$ can be derived by measuring simultaneously the capillary pressure and the interface curvature radius.[8] In a typical tensiometer a droplet is

formed inside a liquid, at the tip of a capillary. The pressure difference across the interface is monitored by a pressure transducer while the drop radius is measured by direct imaging, or it is calculated from the injected liquid volume; then, the dynamic interfacial tension is derived according to the Young-Laplace equation.

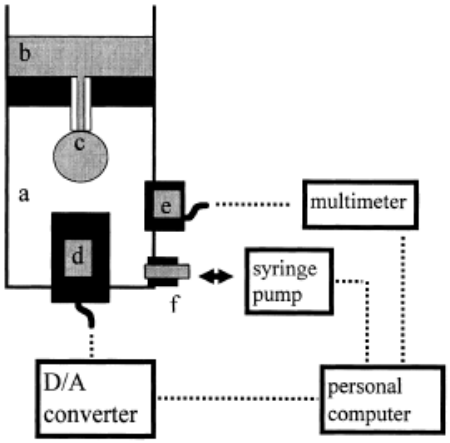

Figure A.9. Sketch of the capillary pressure tensiometer: a) liquid 1; b) liquid 2; c) capillary nd droplet; d) piezoelectric rod; e) strain gauge pressure transducer; and f) valve.

Since the technique relies on the sphericity of the interface, it requires negligible interface deformation, which can be obtained either by using very small drops or small difference of densities between the two fluids. This latter condition makes the method particularly suitable for investigating liquid/liquid systems. A sketch of a CPT utilised is shown in Figure A.9. The tensiometer is composed by two stacked chambers containing the two liquids and connected through a glass capillary. The upper part is open to the atmospheric pressure, while the other one is closed. The droplet is formed at the internal edge of the tip of a glass capillary, which protrudes in the closed chamber. The drop volume is accurately controlled by varying the length of a piezoelectric rod immersed in the closed room, a coarser positioning is provided by a syringe pump. The pressure transducer is connected to the closed chamber, thus, the measured pressure is the capillary pressure plus a nearly constant hydrostatic head, which is also evaluated. The internal diameter of the capillary is of approximately 0.5mm, while the typical drop diameters are of 1mm.

The CPT is a powerful tool for the study of the adsorption dynamics both of liquid/vapour and liquid/liquid interface. Basically, this technique may be used to investigate the interfacial tension response to different variations of the interfacial area getting further insight into different physicochemical aspects characterising the interface of a single sample.[8, 9] Since the volume change rates used are smaller than 10^{-1}mm^3/s, the dynamic contributions to the measured pressure P are

negligible. Thus P can be expressed by the sum of the capillary pressure and a constant term, P*, due to the hydrostatic contribution:

$$P = -\frac{2\gamma^{P}}{R} + P^{*} \qquad \text{(A.18)}$$

Accordingly the interfacial tension is calculated as half the slope of the straight line best fit to the pressure, P, and the curvature data, 1/R. P is measured during the formation of the droplet while the corresponding droplet radii are calculated from the droplet volume, V^{0}_{d}, according to the relationship

$$V_d^0 - wt - V_g^0\left(\frac{P^0}{P} - 1\right) = \frac{2}{3}\pi\left(R^3 - r^3\right) + \frac{\pi}{3}\sqrt{R^2 - r^2}\left(2R^2 + r^2\right) \qquad \text{(A.19)}$$

which also takes into account the presence of a gas volume V^{0}_{g} inside the closed phase of the cell which is either a real entrapped gas volume, or it simulates the compressibility of this phase. Usually, t =0 is assumed as the time corresponding to the hemispherical drop with radius *r*. This time reference is easily determined because it corresponds to a minimum in the pressure signal. Finally, V^{0}_{g} is estimated as the value that provides a linear relationship between the measured P and the calculated 1/R as expected by Equation A.18. Thus, it is possible to estimate V^{0}_{g} with an accuracy on the order of a few mm^3.

The CPT is also an effective technique to investigate the dilational rheology of the interfacial layer. In fact using the CPT according to the Oscillating Drop/Bubble method, which allows the measurement of the dilational visco-elasticity as a function of the frequency. In the oscillating drop experiment, after the adsorption equilibrium of a droplet/bubble slightly larger than the hemisphere is reached, a harmonic perturbation of the droplet volume is applied by means of the piezo rod immersed in the closed cell. During this oscillation of the drop volume also the area, A(t), oscillates with the same frequency ν, as well as the pressure, P(t), in the close part of the cell which is measured by the pressure sensor.[8] Thus, the volume of the piezoelectric rod, V_{pz}, is oscillated around its initial value V^{0}_{pz},

$$V_{pz} = V^{0}_{pz} + \widetilde{V}_{pz}\ \sin(\omega t) \qquad \text{(A.20)}$$

The amplitude $\widetilde{V}_{pz}$ is suitably set up to produce a relative oscillation of the interfacial area of a few percent. Under these conditions the system behaves as a linear system achieving, after a few oscillations, a stationary state characterised by nearly harmonic responses of all the physical and geometrical quantities: pressure, adsorption, surface tension, droplet volume, etc. Because of the viscoelastic

interface and of the cell/liquid ensemble response, the stationary oscillations of these quantities may present different phase shifts with respect to V_{pz}.

Thus, a sinusoidal pressure signal that is characterised by a given amplitude $\widetilde{P}$ and phase shift ϕ,

$$P = P^0 + \widetilde{P}\ \sin(\omega t + \phi) \tag{A.21}$$

where the superscript "0" will identify, from now on, the reference state, is expected. At given frequency, a couple $(\tilde{P},\phi)$ can be obtained, thus, ε is calculated, by using an appropriate experiment theory.

In fact, due to the highly dynamic aspect of the present method, besides the capillary contribution, the measured pressure also sums up the various contributions arising from different effects: the viscoelastic response of the interface, the intrinsic viscoelastic response of the cell and liquid bulks, the viscous flow through the capillary, the inertia of the moving liquid, and the weight of the liquid column. Thus, to get the dilational viscoelasticity data from the acquired pressure oscillating signal measured, a theoretical method is used in this work which models the closed part of the measurement cell as equivalent to an incompressible liquid containing gas volume V_g related to the pressure P by the perfect gas law.[10] This model is justified by the small pressure variations involved, and allows a simplified analysis of the cell/bubble system, valid for frequency not too large (≤ 100 Hz). Here, we recall that the capillary contribution, ΔP_{cap}, to the measured pressure is

$$\Delta P_{cap} = -\frac{2\gamma\Delta R}{R^{0^2}} + \frac{2}{R^0}\varepsilon\frac{\Delta A}{A^0} \tag{A.22}$$

according to the definition of dilational viscoelasticity which provides $\Delta\gamma = \varepsilon\,\Delta A/A^0$. This approach leads to the following expression of the visco-elasticity in terms of measured quantities:

$$\varepsilon = -\frac{\pi h^0 R^{03}}{2}\frac{\tilde{P}}{\tilde{V}_d}e^{i(\phi-\theta)} + \frac{\left(h^0 - R^0\right)R^0}{2h^0}\left[\frac{2\gamma^0}{R^0} - 4i\omega\left(\eta_1 - \eta_2\right) + \rho_1\omega^2 R^{02}\right] + \\ + \frac{\pi h^0 R^{03}}{2}\left(\omega^2 K_2 - i\omega K_1\right) \tag{A.23}$$

where:

$$K_1 = \frac{8\eta_2 L}{\pi a^4} \tag{A.24}$$

$$K_2 = \frac{4\rho_2 L}{3\pi a^2} \tag{A.25}$$

$\widetilde{V}_d$ and θ, are respectively the amplitude and the phase shift of the oscillating drop volume that can be found considering that, under the hypothesis of the present model;

$$\frac{dV_d}{dt} = -\frac{dV_{pz}}{dt} - \frac{dV_g}{dt} = -\frac{dV_{pz}}{dt} + \frac{V_g^0}{P^0}\frac{dP}{dt} \qquad \text{(A.26)}$$

Introducing the oscillating quantities, after some re-arrangements this condition provides the required expressions for $\widetilde{V}_d$ and θ, i.e.

$$\widetilde{V}_d = \widetilde{V}_{pz}\sqrt{1 + \frac{V_g^{0\,2}}{P^{0\,2}}\frac{\widetilde{P}^2}{\widetilde{V}_{pz}^{\;2}} - 2\frac{V_g^{0\,2}}{P^{0\,2}}\frac{\widetilde{P}}{\widetilde{V}_{pz}}cos\,\varphi} \qquad \text{(A.27)}$$

$$\theta = a\,cos\left(\frac{\frac{V_g^{0\,2}}{P^{0\,2}}\widetilde{P}\,cos\,\varphi - \widetilde{V}_{pz}}{\widetilde{V}_d}\right) \qquad \text{(A.28)}$$

The utilisation of Eq. A.23 requires the knowledge of the physical characteristics of the involved fluids like the density ρ and the viscosity η, and the geometrical characteristics of the capillary, radius a and length L. Moreover also the interfacial tension and the volume of the effective gas bubble as well as the geometrical characteristics of the drop at the reference state are required. These quantities can be evaluated by ancillary experiments. In fact the reference equilibrium surface/interfacial tension, γ^0, is measured, according to the Radius-Pressure Steps method described above. The reference drop radius and height are measured, just before the oscillation, by using a drop profile acquisition technique. $V_g^{\,0}$ is estimated using a growing drop experiment. In addition, Equation A.23 has been derived on the assumptions of incompressible and quasi stationary conditions of the fluid inside the capillary. This sets a frequency limitation in the applicability of this approach, depending on the value of the internal radius. For a typical value of a=0.3 mm, this limit frequency is of the order of 100 Hz, for liquid-gas (gas inside the capillary), and of 10Hz for liquid-liquid.[9]

2.4 Drop Shape Tensiometer (DST)

The Drop Shape Tensiometer (DST), which is commonly used for dynamic and equilibrium interfacial tension measurements on a static drop/bubble surface, can also be used to measure dilational viscoelasticity for frequencies below 1 Hz.[9, 10] A bubble or a drop of one liquid inside another fluid, under the gravity effect, assumes a shape which depends on the surface tension and on the density difference between the two fluids. This profile is provided by the Bashforth–

Adams equation for axis-symmetric drops which is an integration of the Laplace equation, expressing the mechanical equilibrium at each point of the surface.

$$2+\frac{\beta z}{b}=\left[\frac{1}{R^{*}/b}+\frac{\sin\phi}{x/b}\right] \qquad \text{(A.29)}$$

Where R^{*} is the curvature radius of the meridian section (see Figure A.10) at the point $P \equiv (x,z)$ and ϕ the angle between the normal to the surface at the same point and the vertical axes and b the curvature radius at the drop apex.

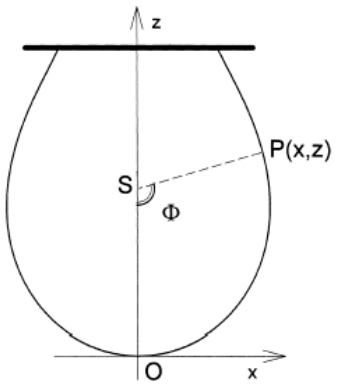

Figure A.10. Sketch of the meridian section of a pendant drop.

The surface tension can then be obtained by fitting such theoretical drop profile to the acquired one. In fact, changing γ a family of theoretical curves results, and the one that best fits to the experimental points (red points) then corresponds to the optimum value of the surface tension (See Figure A.11).

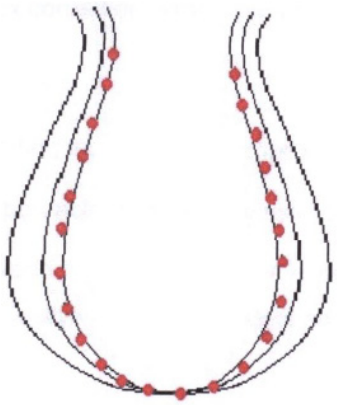

Figure A.11. Image of a pendant drop and the principle of fitting the Laplace equation to the drop profile.

This technique is applicable to liquids with appreciable density difference, otherwise the drop is spherical and the surface tension results undetermined. The dimensionless shape factor:

$$\beta = \frac{\Delta\rho g b^2}{\gamma} \tag{A.30}$$

where Δρ is the density difference between the internal and the external phases, g is the gravity acceleration taken with positive sign if directed accordingly to the z-axis. This factor gives an estimation of the level of drop deformation due to gravity effect. In many practical cases, with the most common acquisition systems, accurate data are obtained for $|\beta|>0.1$. Moreover, such technique is valid if the surface state is not far from the mechanical equilibrium. For this reason it is commonly used for measuring the dynamic interfacial tension during the ageing of a fresh surface at constant area (adsorption dynamics), or during slow variations of the surface area. Specific investigations have shown that for area oscillations with amplitude below 10%, the drop can be considered at mechanical equilibrium for frequencies below 1 Hz, when water–air systems are considered. For more viscous liquids or liquid–liquid the limit frequency reduces to about 0.1 Hz.

A typical DST is composed by a cell where a drop or a bubble is formed inside the other fluid, continuously monitored by a camera, which allows drop profile acquisition in an automatic way to control the drop volume and the area and to calculate the surface tension with a numerical fitting procedure. When the tensiometer is used for adsorption kinetics experiment the surface area is usually kept constant and the drop profile is acquired during the variation of the surface tension. For dilational visco-elasticity measurements, γ^0 is acquired while applying an harmonic small amplitude perturbation of the surface area, usually few percents. In practice the area of a drop, in an equilibrium state with surface tension, is forced to oscillate with frequency ν, around its reference value A^0, i.e.,

$$A = A^0 + \tilde{A}\sin(2\pi\nu t) \tag{A.31}$$

Where the symbol ~ indicates the amplitude of the oscillating area. For small amplitude perturbations the response is linear, thus surface tension is an oscillating quantity which, due to the visco-elastic character, is phase (Φ) shifted with respect to the area perturbation, i.e.,

$$\gamma(t) = \gamma^0 + \tilde{\gamma}\sin(2\pi\nu t + \Phi) \tag{A.32}$$

By a fitting procedure or by a numerical extraction of the harmonic with frequency ν, $\tilde{\gamma}$ and Φ are obtained from the γ measurements. Then, the real and imaginary part of the visco-elasticity can be calculated as:

$$\varepsilon = A^0 \frac{\tilde{\gamma}}{\tilde{A}}\cos(\Phi) + iA^0 \frac{\tilde{\gamma}}{\tilde{A}}\sin(\Phi) \tag{A.33}$$

2.5 Shear Rheology

It is very useful to use a oscillatory test to determine the interfacial shear properties of the polymer monolayers,[11] and to present the experimental results in terms of the components of the complex modulus: the interfacial shear storage modulus *G'* and the interfacial shear loss modulus *G''*. According to the oscillatory methodology used the dynamic surface modulus is defined as the proportionality factor related to the stress and the strain:[12]

$$\sigma = S^{*}u \tag{A.34}$$

where $u = u_0 e^{i\omega t}$ is the applied sinusoidal strain of frequency, ω, and amplitude, u_0. $\sigma = \sigma_0 e^{i(\omega t+\delta)}$ is the resultant stress at the same frequency with the amplitude, σ_0 and δ, the phase shift relative to the strain. Rearranging expression (A.34) and using the assumptions of the oscillatory test we can obtain $S^{*} = \sigma_0 u_0^{-1} e^{i\delta(\omega)} = G'(\omega) + iG''(\omega)$. Finally, each dynamic measurement at a given frequency provides simultaneously two independent parameters *G'* and *G''* related by $tan\delta = G''/G'$.

$$G' = \left(\frac{\sigma_0}{u_0}\right)\cos(\delta) \tag{A.35}$$

$$G'' = \left(\frac{\sigma_0}{u_0}\right)\sin(\delta) \tag{A.36}$$

We use two different oscillatory rheometers working in the plate (ISR-1, Sinterface) and bi-cone (MCR301-IRS, Anton Paar) geometries to measure the interfacial shear storage modulus, *G'*, and loss modulus, *G''*, of polymer monolayers at the air-water interface. In both cases, the rheometer tool is carefully placed at the interface and the linear mechanical response measured at a constant shear rate (0.1Hz). The oscillatory mode assigns the observed rheology to a plateau regime (almost independent on the deformation frequency).

One of the shear rheometers used in this thesis was the Interfacial Shear Rheometer ISR-1, from Sinterface (Germany); it consists of a ring with a sharp edge hanging on a tungsten torsion wire. After applying an impulsive torque by an instantaneous movement of the torsion head then the pendulum generates damped oscillations characterized by a damping factor, α and a radian frequency ω[13]. The angular position of the measuring body is registered by means of a mini laser and a position-sensitive photodiode with an accuracy of ± 0.01°. The mathematical relationships for an oscillating torsion pendulum in surface films was derived by Tschoegl[14]. The measuring cell consists of a circular trough. The geometric

dimensions of the device are: trough inner radius, R_1=*35mm*, measuring body radius, R_2=*25mm*. The measuring cell is surrounded by a temperature controlled water jacket. The accessible range of data for the interfacial shear viscosity is from 10^{-4} mN·s·m^{-1} to 1 mN·s·m^{-1} and for the interfacial shear elasticity from 10^{-3} mN·m^{-1} to 1 mN·m^{1}. The registered oscillation curve is fitted with a parameter model that allow one to determine α and ω.[13] From the difference in the values of the two variables in relation to those for the oscillation in a pure air-water interface the rheological parameters are calculated via the following expressions:

$$\eta = 2H_S I_r \left(\alpha - \alpha_0\right) \tag{A.37}$$

$$G' = H_S I_r \left(\alpha - \alpha_0^2 + \omega^2 - \omega_0^2\right) \tag{A.38}$$

where η is the shear viscosity modulus, *G'* is the shear storage modulus; H_S is a device constant, which depends on the shear field geometry; I_r is the moment of inertia of the measurement system; α_0 and ω_0 are determined from calibration measurements at the air-water interface.

The second rheometer used was the Interfacial Shear Rheometer (model MCR301-IRS) from Anton Paar. The set up consists of a biconical disk rigidly coupled to a driven motor and also a torque and normal force transducer unit. The edge of the disk is placed in the interface between the two different fluids, air/liquid or liquid/liquid. Both rotational and oscillatory mode can be performed using this instrument. For the best sensitivity in the measurements the direct strain oscillation mode (DSO) was selected. The device is able to measure in stress- and strain-controlled oscillation experiments, and we have used the strain-controlled option. In order to perform reproducible measurements the biconical disk must be placed correctly in the interface. In the positioning procedure the biconical disk is lowered slowly to the interface while the normal force is measured. When the edge of the biconical disk touches the surface a jump in normal force is observed. The positioning height can be calculated from the point of contact and the geometry of the disk[15]. The measuring cell consists of a circular trough made from glass. The geometric dimensions of the device are: trough inner radius, R_1=*40mm*, whole trough height, h=45mm, disk radius, R_2 =*34.14mm,* and cone angle, α =5º. For measurements at the air/liquid interface the cell is filled to a height of about 25mm. Also, a Peltier element is used to control the temperature of each experiment. The direct strain oscillation mode (DSO) allows us to work with a low angular resolution (0.1μrad) and low torques (0.01μN·m with DSO),[15,16] and to perform measurements of the rheological parameters with the lowest detection limits for the interfacial shear viscosity are about 10^{-2} mN·s·m^{-1} and interfacial shear elasticity modulus of about 10^{-2} mN·m$^{-1.}$ The maximum measurable values for both parameters are higher than for the ISR-1.

We have verified that the influence of the bulk motion on the dissipation of the interfacial stress can be neglected for the two techniques.[17] The degree of hydrodynamic interaction between the monolayer and the subphase is conveniently characterized by the Boussinesq number B_o[17, 18].

$$B_o = \frac{\text{interfacial viscosity}}{\text{bulk viscosity} \times \text{ length scale}} = \frac{\eta}{(\eta_1 + \eta_2) R} \qquad \text{(A.39)}$$

where η_1, η_2 are the lower and upper fluid viscosities respectively, η is the interfacial shear viscosity and R is the characteristic distance of the flow geometry. In our devices R is the radius of the probe located at the interface. For small Boussinesq numbers *(B_0<<1)* the interfacial flow is controlled by the bulk phase stresses. For intermediate values of B_0, subphase contributions to the interfacial viscosity are significant. Finally, for high values of Boussinesq number *(B_0>>1)* the bulk viscous effects are negligible and, as a result, the interfacial flow dominates over the flow in the subphase. For the two techniques used here we have confirmed that B_0>>1. This fact means that the interfacial flow is predominant to the flow of the adjacent phases and it is possible to measure the viscoelastic properties of the interface, considered as an isolated two dimensional fluid.

3. References

1. Azzam, R. M. A.; Bashara, N. M., *Ellipsometry and Polarized Light*. Elsevier: North-Holland, 1987.
2. Thompkins, H. G., *A user's guide to Ellipsometry*. Academic Press: Amsterdam, 1993.
3. Fakhraai, Z.; Valadkhan, S.; Forrest, J. A., Qualitative discrepancy between different measures of dynamic in thin polymer films. *Eur. Phys. J E* **2005,** 18, 143-148.
4. Bertsekas, D. P., *Non Linear Programming*. Scientific Belmont: Athens, 1999.
5. Drude, P., Ueber die reflexion und brechung ebener fichtwellen beim durchgang durch eine mit oberflächenschichten behaftete planparallele Platte. *Annalen fur Physik (Wiedemann Annalen)* **1891,** 279, 126-157.
6. Landau, L. D.; Lifshitz, E. M., *Theory of Elasticity*. Pergamon: Oxford, 1986.
7. Hilles, H.; Monroy, F.; Bonales, L. J.; Ortega, F.; Rubio, R. G., Fourier-transform rheology of polymer Langmuir monolayers: Analysis of the non-linear and plastic behaviors. *Advances in Colloid and Interface Science* **2006,** 122, (1-3), 67-77.
8. Liggieri, L.; Attolini, V.; Ferrari, M.; Ravera, F., Measurement of the surface dilational viscoelasticity of adsorbed layers with a capillary pressure tensiometer. *Journal of Colloid and Interface Science* **2002,** 255, (2), 225-235.
9. Liggieri, L.; Ferrari, M.; Mondelli, D.; Ravera, F., Surface rheology as a tool for the investigation of processes internal to surfactant adsorption layers. *Faraday Discussions* **2005,** 129, 125-140.
10. Ravera, F.; Ferrari, M.; Santini, E.; Liggieri, L., Influence of surface processes on the dilational visco-elasticity of surfactant solutions. *Advances in Colloid and Interface Science* **2005,** 117, (1-3), 75-100.
11. Brooks, C. F.; Fuller, G. G.; Frank, C. W.; Robertson, C. R., *Langmuir* **1999,** 15, 2450.
12. Ferry, J. D., *Viscoelastic Properties of Polymers*. 3 ed.; Wiley: New york, 1980.
13. Kragel, J.; Siegel, S.; Miller, R.; Born, M.; Schano, K. H., Measurement of interfacial shear rheological properties - an automated apparatus. *Colloids*

and Surfaces a-Physicochemical and Engineering Aspects **1994,** 91, 169-180.

14. Tschoegl, N. W., *Kolloid-Z* **1961,** 19, 181.
15. Erni, P.; Fisher, P.; Windhab, E. J.; Kusneszov, V.; Stettin, H.; Läuger, J., Stress- and strain-controlled measurements of interfacial shear viscosity and viscoelasticity at liquid/liquid and gas/liquid interfaces. *Review of Scientific Instruments* **2003,** 74, (11), 4916-4924.
16. Läuger, J.; Wollny, K.; Huck, S., *Rheol. acta* **2002,** 41, 356.
17. Edwards, D. A.; Brenner, H.; Wasan, D. T., In *Interfacial Transport Processes and Rheology*, Butterworth-Heinemann: Boston, 1991.
18. Boussinesq, M. J., *Ann. Chim. Phys.* **1913,** 29, 349.